Carbon-Nitrogen Bond-Forming Reactions in Supercritical and Expanded-Liquid Carbon Dioxide Media:

Green Synthetic Chemistry with Multiscale Reaction and Phase Behavior Modeling

by

Rocco P. Ciccolini

M.S. Chemical Engineering Practice
Massachusetts Institute of Technology, 2004

B.S. Chemical Engineering
New Jersey Institute of Technology, 2003

Submitted to the Department of Chemical Engineering in Partial Fulfillment of the Requirements for the Degree of

DOCTOR OF PHILOSOPHY IN CHEMICAL ENGINEERING

at the

MASSACHUSETTS INSTITUTE OF TECHNOLOGY
[June 2008]
May, 2008

© 2008 Massachusetts Institute of Technology
All Rights Reserved

ARCHIVE

MASSACHUSETTS INSTITUTE OF TECHNOLOGY
JUN 06 2008
LIBRARIES

Signature of Author: _____
Department of Chemical Engineering
May 19, 2008

Certified by: _____
Professor Jefferson W. Tester
Thesis Supervisor

Accepted by: _____
Professor William M. Deen
Chairman, Committee for Graduate Studies

CARBON-NITROGEN BOND-FORMING REACTIONS IN SUPERCRITICAL AND EXPANDED-LIQUID CARBON DIOXIDE MEDIA:

GREEN SYNTHETIC CHEMISTRY WITH MULTI-SCALE REACTION AND PHASE BEHAVIOR MODELING

by

Rocco P. Ciccolini

Submitted to the Chemical Engineering Department on May 19, 2008
in partial fulfillment of the requirements for the degree of
Doctor of Philosophy in Chemical Engineering

ABSTRACT

The goal of this work was to develop a detailed understanding of carbon-nitrogen (C-*N*) bond-forming reactions of amines carried out in supercritical and expanded-liquid carbon dioxide (CO_2) media. Key motivations behind this study were the importance of nitrogen-containing compounds in the pharmaceutical and fine chemical industries and a growing commercial interest in utilizing environmentally-friendly syntheses and processing with cost-efficient, green solvents. The thermodynamics and reaction engineering characteristics associated with the synthesis of several model C-*N* bond-forming reactions were examined both experimentally and theoretically. Operating conditions and engineering correlations were identified that will facilitate process scale-up and potential commercialization of these and other fundamentally-important CO_2-based processes.

Amine chemistry in CO_2-based media was complicated by the facility of nucleophilic amines to react with carbon dioxide to form carbamic acids, which sometimes interfered with desired reaction pathways. Experimental observations and a complimentary *ab initio* quantum chemical calculation study revealed that carbamic acid formation was suppressed when adding bulky *N*-substituents to primary amines and when operating at low pressures and/or high temperatures.

With a firm understanding of amine-CO_2 chemistry, we developed a synthetic protocol that produced classes of pharmacologically-significant nitrogen heterocycles known as tetrahydroisoquinolines and tetrahyrdo-β-carbolines. Our method involved (1) the *in situ* carbamation of amines from their reaction with carbon dioxide and a dialkyl carbonate and (2) the Pictet-Spengler cyclization of these carbamates by their reaction with an aldehyde in the presence of acid. The conversion of amines to their carbamate derivatives offered suitable *N*-protection against carbamic acid formation. For nearly all reactions studied, the Pictet-Spengler step proceeded nearly quantitatively.

The efficiency of amine carbamation via the CO_2/dimethyl carbonate (DMC) reaction system was highly sensitive to process operating conditions. Phase behavior, amine conversion, and carbamate yield and selectivity all varied appreciably with temperature, pressure, and amine feed concentration. For example at 130 °C, carbamate selectivity increased from 50 to 75% with increasing pressure up to the mixture critical pressure of the CO_2/DMC binary system ($P_{c,mix\ CO_2/DMC}$). Selectivity decreased to 55% for $P_{c,mix\ CO_2/DMC} < P <$ the $P_{c,mix}$ of the entire reaction system ($P_{c,mix\ system}$). Above $P_{c,mix\ system}$, selectivity increased to 80%. At 105 bar, decreasing temperature from 150 to 100 °C led to an increase in carbamate selectivity by 25%. Finally, decreasing the amine feed concentration from 4 to 1 M resulted in an increase in carbamate selectivity by 30%.

Mixture critical pressures ($P_{c,mix}$) and liquid-phase densities, species concentrations, and volume expansion were measured for the CO_2/DMC system over a wide range of operating conditions. Importantly, we developed an equation-of-state (EOS) model and several empirical engineering correlations that were used to predict vapor-liquid equilibrium properties in P-T-x_i regimes for which data were not available. Deviations from experimental data and empirical correlations were typically less than 9%. $P_{c,mix\ CO_2/DMC}$ data were measured for $37 < T < 150$ °C and were correlated well by a third-order polynomial. Liquid-phase carbon dioxide concentration ($[CO_2]_l$) varied linearly with pressure for 37 to 100 °C. Liquid-phase volume expansion (ΔV_l) measured for the same temperature range increased exponentially with increasing pressure. Maximum-possible values of $[CO_2]_l$ and ΔV_l decreased with increasing temperature. $[CO_2]_l$ was 2 to 4 times larger than that of pure CO_2 when compared at the same T and P.

We also developed and optimized a practical and high atom-economy CO_2-based synthetic protocol that afforded amides via the amination of ketenes generated *in situ* from the thermolysis of 1-alkynyl ethers. A variety of amines, 1-alkynyl ethers, and ketenes participated efficiently in the reaction and produced amides in yields comparable to those of conventional solvents. Experimental phase partitioning observations agreed well with EOS-based predictions and aided in the determination of process operating conditions. Amide yield varied in the order secondary > branched-primary > primary amines, which suggested that carbamic acid formation may have diminished reaction efficiency. *t*-butoxy-substituted 1-alkynyl ethers produced ketenes at rates faster than ethoxy-substituted ethers and allowed for a considerable reduction in operating temperature. Extension of the amide synthesis protocol to an intramolecular variant that afforded lactams resulted in a significant decrease in selectivity when compared to conventional solvents. We suspected that multi-phasic behavior led to this discrepancy and were able to increase selectivity by 25% using CO_2/co-solvent mixtures. Finally, an *ab initio* quantum chemical kinetic model was developed and was capable of qualitatively predicting observed amide formation dynamics. Product selectivity and amine consumption rate predictions, for example, agreed well with experimental data.

Thesis Supervisor: Jefferson W. Tester
Title: H. P. Meissner Professor of Chemical Engineering

ACKNOWLEDGEMENTS

338 pages, 100+ figures and tables, and dozens of reactions… yet somehow *this* section is the most difficult. I'm excited to finish! I'm sad to leave. Bitter-sweet, I guess.

I never would have made it this far had it not been for the love and encouragement from my family. Mom, Dad, and Anthony, everything that I have or will accomplish in life is for you.

Thank you for everything, Jeff. You were a great mentor and your ability to steer me in the right direction was matched only by your concern for my personal wellbeing. Gwen, my MIT mom, I will forever be thankful for your caring and thoughtful support. You're awesome.

Rick, Bill, and K.C., thank you for guiding the project and providing excellent feedback, even when chapters were in rough shape.

Josh, Xiao Yin, and Julia, thanks for teaching an engineer tons of synthetic organic chemistry.

Chad, Scott, Andy H., Hidda, Andy P., Kurt, Russell, Karl, Mike T., A. J., Russ, Jason, Morgan, Joany, Heather, Sean, Adam, Yi, and Mike M., thanks for all of the help in the lab and for making the place feel like it had windows.

My Massachusetts family — Dan, Sandeep, Curt, Ryan, Greg, Melissa, Justin, Brian H., Rob, Brian M., Adam, Biju, Andy M., Michelle, Kristen, Eliza, Earl, Ingrid, Rebecca, Mark, and

My New Jersey Family — Willie, Luis, Juan, Manny, Fabian, Otto, Steve, Sammy, Eddie, Adolfo, Bernard, Sandro, Ronald, Ronnie, Joey, Lou, Lisa, Aly, Ana, and Mercy — thanks so much for all that you've done to get me here, for keeping me sane, and for being there when I needed you most. I promise to return the favor.

Lastly, what's an acknowledgement page without sappy advice?...

I spent most of my early years as a graduate student worrying… what will the committee think of my proposal? Will I ever get data? Will the reactor hold pressure overnight? I've come to appreciate advice from Baz Luhrmann:

> *"Don't worry about the future… worrying is as effective as trying to solve an algebra equation by chewing bubblegum. The real troubles in your life are apt to be things that never crossed your worried mind; the kind that blindside you at 4pm on some idle Tuesday."*

Stay the course — grad school has a funny way of working itself out.

For my late father, Rocco E., and brother, Anthony.

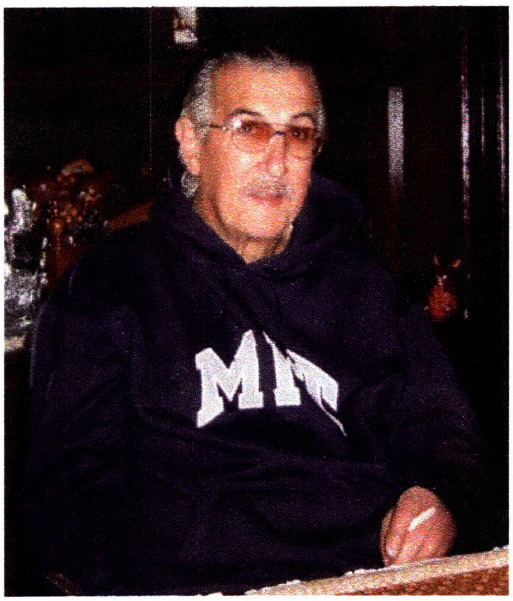

TABLE OF CONTENTS

Chapter 1: Introduction and Background..... 15
1.1. Motivation..... 15
1.2. Carbon Dioxide: An Alternative Reaction Media..... 18
1.2.1. Environmental and Economic Considerations..... 18
1.2.2. Physicochemical Properties and Considerations..... 20
1.3. Properties of CO_2/co-solvent Mixtures and CO_2-Expanded Liquids..... 26
1.4. CO_2-Based Media as a Solvent for Synthetic Chemistry..... 32
1.4.1. Solvation and Phase Behavior Effects..... 32
1.4.2. Representative Transformations..... 35
1.5. CO_2-Based Industrial Processing..... 40
1.6. Earlier Work on CO_2-Based Syntheses in the Tester-Danheiser Groups..... 41
1.7. The Cambridge-MIT Institute Partnership Program..... 45
1.8. References..... 48

Chapter 2: Objectives and Approach..... 53
2.1. Literature Assessment and Selection of Model Transformations..... 53
2.2. Expansion of Experimental and Analytical Capabilities..... 54
2.3. Experimental Reaction Screening and Process Engineering..... 55
2.4. Thermodynamic and Quantum Chemical Kinetic Modeling..... 55

Chapter 3: Experimental Equipment and Procedures..... 59
3.1. Motivation..... 59
3.2. The $scCO_2$ Delivery, Reaction, and Phase Behavior System..... 61
3.2.1. Data Acquisition System..... 64
3.2.2. High-Pressure Manifold..... 64
3.2.3. View Cells..... 68
3.2.4. Reactor..... 77
3.2.5. Sight Gauge..... 84
3.2.6. Cloud-Point Apparatus..... 90
3.2.7. Ultrasonic View Cell..... 92
3.3. Analytical/Sampling Equipment and Procedures..... 102
3.3.1. At-condition Sampling/Injection Units..... 102
3.3.2. Inverted-Buret Apparatus..... 105

TABLE OF CONTENTS

3.3.3. Volume Determination Unit 107
3.3.4. Off-gas Detection Unit 109
3.3.5. High-Pressure Liquid Chromatography System 110
3.4. Safety Considerations 113
3.5. Recommendations 114
3.6. Equipment and Instrumentation Symbol Key 115

Chapter 4: A Review of Carbon-Nitrogen Bond Formation in Carbon Dioxide-Based Media 119
4.1. Motivation 119
4.2. The Reaction of Carbon Dioxide with Amines 120
4.3. Review of Synthetic Transformations 125
4.3.1. Carbon Dioxide as both a Raw Material and Solvent 125
4.3.2. Carbon Dioxide as a Solvent 130
4.4. Conclusions and a Path Forward 133
4.5. References 134

Chapter 5: Amine Carbamation and Pictet-Spengler Reactions in Carbon Dioxide-Expanded Liquid Media 139
5.1. Motivation 139
5.2. Synthetic Methodology 141
5.2.1. Nitrogen Protection via Amine Carbamation 141
5.2.2. Synthetic Protocol and Variables Explored 146
5.3. Experimental Approach 147
5.4. Screening of the Amine Carbamation Reaction 148
5.4.1. Carbamation of β-arylethylamines 148
5.4.2. Carbamation of β-indolylethylamines 152
5.5. Screening of the Pictet-Spengler Reaction 155
5.5.1. Cyclization of Carbamates Derived from β-arylethylamines 155
5.5.2. Cyclization of Carbamates Derived from β-indolylethylamines 158
5.6. Conclusions and Recommendations 159
5.7. References 162

TABLE OF CONTENTS

Chapter 6: Phase Equilibria Data and Engineering Correlations for the Carbon Dioxide/Dimethyl Carbonate System 165

6.1. Motivation 165

6.2. Equation-of-State-Based Modeling Approach 166

6.3. Vapor-Liquid Equilibria Data and Modeling 170

6.3.1. Data Regression 170

6.3.2. Results and Discussion 171

6.4. Mixture Critical Points and Modeling of the *P-T* Envelope 176

6.4.1. Experimental Approach and Equipment Validation 176

6.4.2. Results and Discussion 177

6.5. Liquid-Phase Densities and Species Concentration Correlations 180

6.5.1. Experimental Approach and Equipment Validation 180

6.5.2. Results and Discussion 186

6.6. Liquid-Phase Volume Expansion Correlations 192

6.6.1. Experimental Approach and Equipment Validation 192

6.6.2. Results and Discussion 194

6.7. Investigation of Additional Carbon Dioxide/Dialkyl Carbonate Systems 197

6.8. Effects of Additives on Binary Carbon Dioxide/Dimethyl Carbonate Phase Equilibria 202

6.8.1. Methanol Composition Effects 202

6.8.2. Amine Composition Effects 208

6.9. Conclusions and Recommendations 211

6.10. References 213

6.11. Experimental Data, Correlation Parameters, and Supplementary Figures 215

6.11.1. Mixture Critical Pressure Data and Correlation Parameters 215

6.11.2. Liquid-Phase Densities and Species Concentration Data and Correlation Parameters 216

6.11.3. Liquid-Phase Volume Expansion Data and Correlation Parameters 222

6.11.4. Phase Equilibria Data and Correlation Parameters for other CO_2-based Mixtures 226

TABLE OF CONTENTS

Chapter 7: Revisiting Amine Carbamation in Carbon Dioxide-Expanded Liquid Media..... 231
7.1. Model Reaction and Variables Explored..... 231
7.2. Experimental Approach and Analytical Methods..... 232
7.3. Phase Behavior Considerations..... 235
7.3.1. The Amine/Dimethyl Carbonate System..... 235
7.3.2. The Carbon Dioxide/Dimethyl Carbonate System..... 235
7.3.3. The Carbon Dioxide/Amine System..... 237
7.3.4. The Carbon Dioxide/Carbamate System..... 238
7.3.5. The Dimethyl Carbonate/Carbamate System..... 238
7.3.6. The Reaction System..... 238
7.4. Kinetic Model Formulation..... 241
7.4.1. Reaction Networks..... 241
7.4.2. Carbamate Selectivity and Mechanism Validation..... 245
7.5. Coupling Reaction Kinetics and Phase Behavior..... 246
7.6. Reaction Performance..... 249
7.6.1. Pressure Effects..... 249
7.6.2. Temperature Effects..... 253
7.6.3. Composition Effects..... 255
7.7. Conclusions and Recommendations..... 258
7.8. References..... 262

Chapter 8: The Larock Indole Synthesis in Supercritical Carbon Dioxide..... 263
8.1. Motivation and Synthetic Methodology..... 263
8.2. Experimental Approach..... 264
8.3. Results and Discussion..... 264
8.4. Conclusions and Recommendations..... 270
8.5. References..... 271

TABLE OF CONTENTS

Chapter 9: Amide and Lactam Synthesis in Supercritical Carbon Dioxide..... 273
9.1. Motivation, Synthetic Methodology, and Variables Explored..... 273
9.2. Experimental Approach and Analytical Methods..... 274
9.3. Amide Synthesis..... 277
9.3.1. Model Reaction..... 277
9.3.2. Process Optimization and Phase Behavior Considerations..... 278
9.3.3. Scope of the Synthesis Protocol..... 284
9.4. Lactam Synthesis..... 291
9.4.1. Motivation and Model Reaction..... 291
9.4.2. Results and Discussion..... 294
9.5. Conclusions and Recommendations..... 298
9.6. References..... 300

Chapter 10: *Ab Initio* Insights towards Carbamic Acid and Amide Formation in Supercritical Carbon Dioxide..... 301
10.1. Motivation and Variables Explored..... 301
10.2. Methodology..... 301
10.2.1. Transition State Theory..... 301
10.2.2. Computational Approach..... 304
10.3. Model Reaction..... 306
10.4. Results and Discussion..... 308
10.4.1. Carbamic Acid Formation..... 308
10.4.2. Ketene Formation..... 319
10.4.3. Ketene Cycloaddition Product Formation..... 322
10.4.4. Amide Formation..... 326
10.5. Conclusions and Recommendations..... 332
10.6. References..... 335
10.7. Model Formulation and Kinetic Parameters..... 336

1. INTRODUCTION AND BACKGROUND

1.1. Motivation

Economies of industrialized nations rely heavily on their ability to manufacture and distribute chemical products. These products range widely in origin and application — be they refined hydrocarbons for transportation, commodity petrochemicals for plastic containers, consumer products for general hygiene, or pharmaceuticals for the treatment of ailments. Although their use generally provides great improvements to the quality of human life, their production processes have paradoxically resulted in the substantial release of toxic and hazardous waste to the environment. It is estimated that the United States Chemical Industry alone releases more than 3 billion tons of chemical waste each year to the environment, and spends approximately $150 billion per year in waste treatment, control, and disposal costs (Anastas et al., 1996). These environmental wastes and treatment costs are frequently a result of toxic and hazardous materials (including many organic solvents) that are used as reaction media or for phase separation purposes (Buncel et al., 2003; Marcus, 2002; Marcus, 1998; Murrell, 1994; Reichardt, 2003; Steinfeld, 1999; Tapia et al., 1996).

Toluene, for example, is an organic solvent commonly used for synthetic transformations in the pharmaceutical and fine chemical industries, and was listed as the 7th most frequently used by GlaxoSmithKline (GSK) in 2005 (Constable et al. 2007). Like many organic solvents, toluene poses significant health and safety threats to humans and the environment, as it is toxic, highly flammable, and a dermal and inhalation irritant. In addition to operator exposure risks, the use of solvents almost always results in their permitted and fugitive emission to the environment. According to the United States Environmental Protection Agency (US EPA), the US Chemical Industry in 2004 released approximately 54, 2, and 0.3 million pounds of toluene to the air, land, and water, respectively (US EPA, 2004). Environmental emissions for other commonly-employed organic solvents are given in **Table 1-1**.

The solvent emission figures listed in **Table 1-1** are not the complete story; additional environmental impacts are revealed when the specific details of the processes which involve these solvents are considered. In order to synthesize an active pharmaceutical ingredient (API), for example, several batch reaction steps in organic solvent media are typically performed.

Table 1-1. Estimated release (in pounds) of selected organic solvents to the United States environment in 2004 (US EPA, 2004).

	Solvent Emissions to the		
Solvent	**Land**	**Air**	**Water**
Methanol	21,644,000	166,814,000	10,966,000
Acetonitrile	11,987,000	700,000	11,000
Toluene	2,485,000	53,979,000	266,000
Dichloromethane	346,000	7,317,000	7,000
n-Hexane	376,000	39,402,000	14,000

Each reaction entails the risk of operator exposure and release to the environment. Following each reaction step, solvent- and energy-intensive operations (e.g., crystallization and distillation, respectively) are often necessary to isolate intermediates that ultimately form the API. These additional processing steps carry their own environmental burden, as waste and emissions are not only generated in the separation processes themselves, but also during auxiliary steps that provide their required material and energy inputs.

Researchers at the Sustainable Development in the Environmental Product Stewardship Team, Corporate Environment, Health and Safety Group at GSK conducted a study of several of their API production processes and revealed that organic solvent use accounted for 80 – 90% of mass utilization (Constable et al., 2007), 14 – 45% of total drug production costs (Constable et al., 2002), 60% of overall process energy consumption, and 50% of the total post-treatment greenhouse gas emissions (Jimenez-Gonzalez et al., 2005). In separate and earlier study, Sheldon (1994) estimated that although pharmaceutical and fine chemical process tonnages are less than that of other chemical industry sectors (e.g., $10^1 - 10^3$ and $10^2 - 10^4$, respectively vs. $10^6 - 10^8$ tonnes/yr for petrochemicals), they tend to generate larger amounts of chemical waste on a per capita basis (e.g., 25 – 100 and 1 – 50, respectively vs. ca. 0.1 kg byproducts/kg product for petrochemicals).

The following example illustrates the amount of solvent used in a typical API production process. Assume that a pharmaceutical company produces a drug that will be used by 20% of the US population (ca. 60 million people). With 20 mg of API per pill, one dose per day, and 85% of the mass associated with making that API being organic solvent, roughly 5.5 million pounds of solvent will be required per year. A 5% release to the environment during processing corresponds to 275,000 pounds per year. If we optimistically assume that 50% of the solvent

employed in the process is recovered, then 2.25 million pounds of waste per year is generated and will mostly likely undergo expensive treatment methods (chemical neutralization and combustion) and subsequently result in greenhouse gas emissions.

In order to address the rising trend of solvent emissions by the US Chemical Industry, the US EPA developed the Green Chemistry and Engineering Program under the Pollution Prevention Act of 1990 (which aims to prevent and reduce pollution at its source). The Green Chemistry and Engineering Program suggests the "design of chemical products and processes that reduce or eliminate the use and generation of hazardous substances (US EPA, 2008)." The program goes beyond the regulations in the Act by establishing environmentally-sustainable process design guidelines and resources for the scientific community. Major aspects of the Green Chemistry framework — the "12 Principles of Green Chemistry" — are delineated below (Anastas et al., 1998):

- design chemical products to be less hazardous to human health and the environment;
- use feedstocks and reagents that are less hazardous to human health and the environment;
- design syntheses and other processes to be less energy- and materials-intensive;
- use feedstocks derived from annually-renewable resources or from abundant waste, and
- design chemical products for increased, more facile reuse or recycling.

While it is difficult to accurately quantify the damaging effects of organic solvent exposure on human health (e.g., increase in cancer occurrences) and on environmental degradation (e.g., pollution and wildlife population decline), minimizing their use certainly is a step in the right direction to lower these impacts. An attractive action in line with the principles of green chemistry is to replace toxic and hazardous organic solvents with environmentally-benign materials. For over 15 years, Professor Jeff Tester's Sustainable Energy and Clean Chemical Processing group at the MIT Chemical Engineering Department has focused on the use of carbon dioxide and carbon dioxide-based media as a 'green' replacement of organic solvents and reagents for a variety of chemical transformations. The work discussed in this dissertation will therefore revolve around this theme.

1.2. Carbon Dioxide: an Alternative Reaction Media

1.2.1. Environmental and Economic Considerations

For the past 20 years, liquid and supercritical carbon dioxide ($scCO_2$) has attracted considerable attention as an alternative reaction and processing medium to organic solvents. Much of this attention stems from the environmentally-benign attributes of pure carbon dioxide, as it is non-toxic, non-flammable, odorless, non-explosive, and not corrosive. The threshold limit value (TLV) — "the airborne concentration at 298 K [25 °C] to which it is believed that nearly all workers may be repeatedly exposed day after day without adverse effects" — for carbon dioxide is 5000 ppm (Beckman, 2004), which is significantly higher than the TLV's for organic solvents such as ethanol (1800 ppm), acetone (750 ppm), pentane (600 ppm), dichloromethane (170 ppm), and chloroform (10 ppm) (Beckman, 2004; Clark et al., 2007). From an economic perspective, CO_2 is relatively inexpensive because it is a widely-available product of fermentation and combustion processes. As shown by **Figure 1-1**, liquid carbon dioxide costs approximately \$0.44/kg for industrial-grade and \$0.97/kg for high purity-grade, and is significantly less expensive (2 – 100x) than many commonly-used organic solvents.

There are, however, environmental and health concerns associated with carbon dioxide use. Like all gases other than oxygen, CO_2 in high airborne concentrations can act as an asphyxiant. Carbon dioxide is also a greenhouse gas that is believed to be the chief contributor to global warming. Although carbon dioxide emissions may have less of an observable environmental and human-exposure impact than those of organic solvents, care must still be taken to minimize CO_2 release. The addition of solvent recovery steps within CO_2-based processes would reduce these concerns.

Discussed in more detail below in the following section, the most attractive physicochemical properties of CO_2 are attained when it is used in a dense, pressurized state. Because of this, there are large capital investments (e.g., high-pressure reactors, pumps, and piping systems) and energy requirements (e.g., during compression) associated with CO_2-based processing. Contrary to conventional organic solvent-based processes, though, many of these costs are offset because: (1) CO_2 is an inexpensive raw material, (2) removal of CO_2 from a reaction or separation step often requires significantly less energy and processing steps (e.g., depressurization instead of distillation, extraction, or membrane separation), (3) CO_2 can be easily recovered and recycled, and (4) portions of the initial energy input associated with

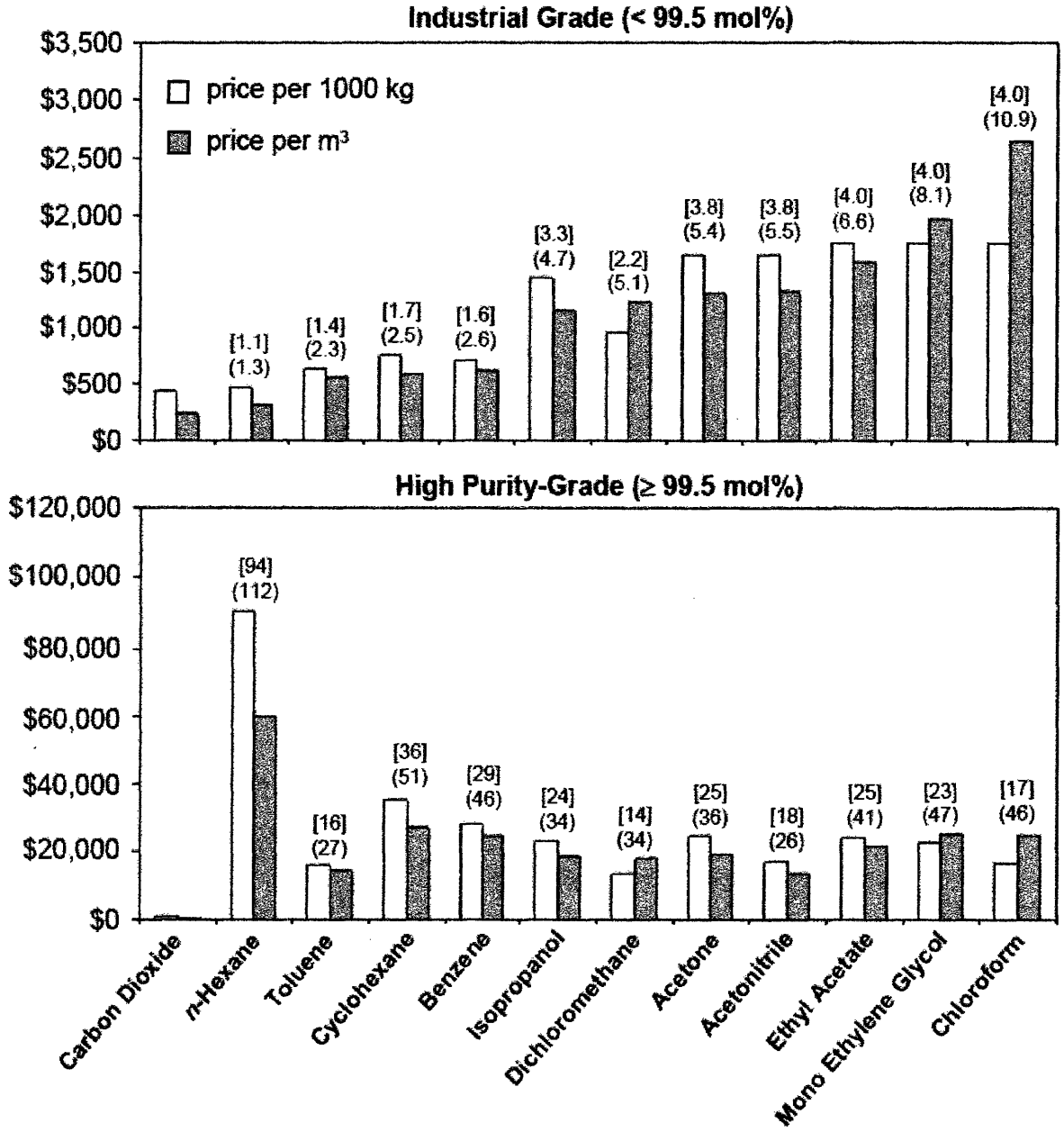

Figure 1-1. Price comparison for carbon dioxide and selected organic solvents (2006 values). Numbers listed in brackets indicate a per-mass multiple of CO_2 price; those listed in parentheses indicate a per-volume multiple. *Example: industrial-grade acetone is approximately 3.8 times more expensive than CO_2 on a per-mass basis and 5.4 times more expensive on a per-volume basis.* Data for industrial- and high purity-grade CO_2 (in liquid form at its vapor pressure) obtained from Airgas, industrial-grade solvents from ICIS, and high purity-grade solvents from Sigma-Aldrich. Density data for solvents obtained from (Poling et al., 2001) and correspond to conditions of 298 K (25 °C) and 1.01 bar. A CO_2 density of 550 kg/m^3 was used, which corresponds to an average of practically-attainable operating densities.

pressurization can be recovered during downstream depressurization steps (e.g., via electricity generation from turbine expansion).

1.2.2. Physicochemical Properties and Considerations

Carbon dioxide at ambient conditions (298 K [25 °C], 1.01 bar) is a gas, and like nearly all gases, is a poor solvent for reactions and separations because of its inability to solubilize liquid and solid materials in amounts feasible for practical application. To overcome this limitation, CO_2 is often employed in its supercritical fluid (SCF) state. A SCF is defined as a pure component or mixture in a fluid state above its critical pressure (P_c) and critical temperature (T_c), but below the pressure required for condensation to a solid state (Jessop et al., 1999). The supercritical fluid region of pure CO_2, with corresponding critical conditions of P_c = 73.8 bar and T_c = 304.1 K (31 °C) (Poling et al., 2001), is shown in **Figure 1-2**.

In practice, the supercritical state for CO_2 is achieved by isochoricly heating an equilibrium liquid-vapor mixture from ambient temperature along the co-existence curve. Along curve **a**, liquid and vapor CO_2 co-exist in equilibrium (with a system P corresponding to the vapor pressure; ca. 65 bar at ambient T) and the phase boundary is clearly visible (see **Figure 1-2**, "**a**"). As the two-phase mixture is heated, the densities of each phase approach one another and the boundary between them becomes less distinguishable (see **Figure 1-2**, "**b**"). Upon heating beyond T_c, the phase boundary disappears and a single supercritical phase forms (see **Figure 1-2**, "**c**"). Alternative approaches to reaching the supercritical state include isothermal compression at $T > T_c$ to arrive at $P > P_c$, or isobaric heating at $P > P_c$ to arrive at $T > T_c$.

Probably the most attractive aspect of a SCF in general is that its physicochemical properties (e.g., density, dynamic viscosity, self-diffusivity, solvent 'power,' etc.) are intermediate of gases and liquids, and can be varied appreciably with relatively minor changes in temperature or pressure (Beckman, 2004, Jessop, 1999, Rayner, 2007, Sun et al., 2002, and Subramaniam et. al., 1986). Shown in **Table 1-2** are typical order-of-magnitude values of some physicochemical properties of gases, SCFs, and liquids (Sun et al., 2002).

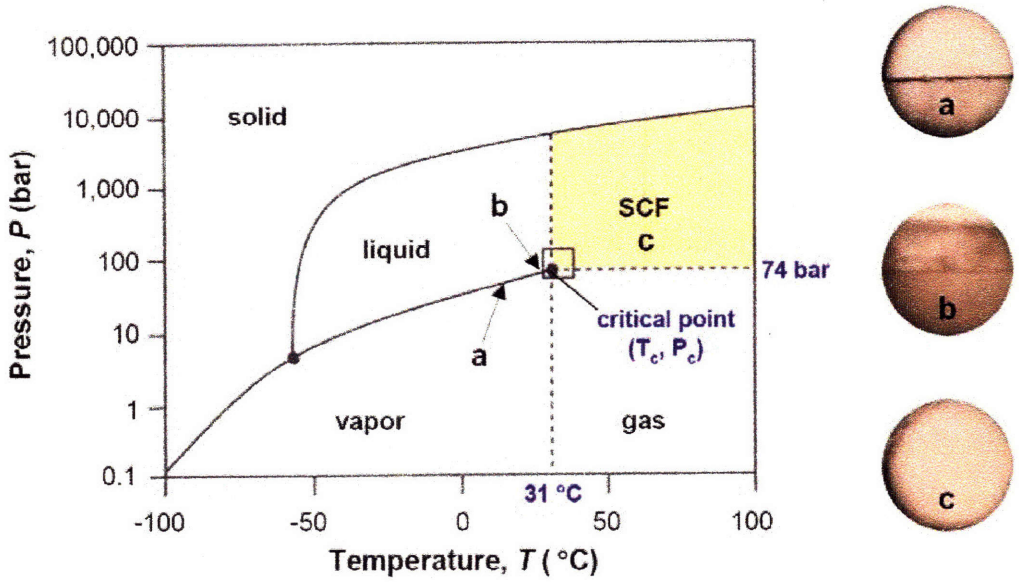

Figure 1-2. Pressure-temperature phase diagram for pure CO_2 (adapted from Jessop et al., 1999; original references cited therein). Phase behavior photographs courtesy of Professor Chris M. Rayner's Cleaner Synthesis Group at the University of Leeds.

Table 1-2. Order-of-magnitude comparison of the physicochemical properties of gases, SCFs, and liquids (adapted from Sun et al., 2002).

Physicochemical Property	Gases	SCFs	Liquids
Density, ρ ($g \cdot cm^{-3}$)	0.001	**0.2 – 1.0**	0.6 – 1.6
Dynamic viscosity, η ($g \cdot cm^{-1} \cdot s^{-1}$)	10^{-4}	$\mathbf{10^{-3}}$	10^{-2}
Self-diffusivity, D_{11} ($cm^2 \cdot s^{-1}$)	10^{-3}	$\mathbf{10^{-4}}$	10^{-5}

Selected physicochemical properties of CO_2 plotted as a function of P at 313.2 K (40 °C) in **Figure 1-3** show that $scCO_2$ has a liquid-like density, and a gas-like self-diffusivity and dynamic viscosity. Also noteworthy is that more than a three-fold increase in density and viscosity and a two-fold decrease in the self-diffusivity-density product can be realized when transitioning to pressures only slightly above P_c. These 'hybrid' and 'tunable' properties give $scCO_2$ unique solvation abilities (Sun et. al., 2002 and Rayner, 2007), as well as mass-transfer characteristics that may benefit multiphasic reaction and separation processes (Beckman, 2004; Subramanium, 1986). For example, $scCO_2$'s liquid-like density enables it to dissolve materials and also influence chemical reaction rates (unlike gaseous CO_2), while its gas-like self-diffusivity and dynamic viscosity facilitates mixing and interfacial mass-transport in the presence of liquid phases (unlike liquid CO_2).

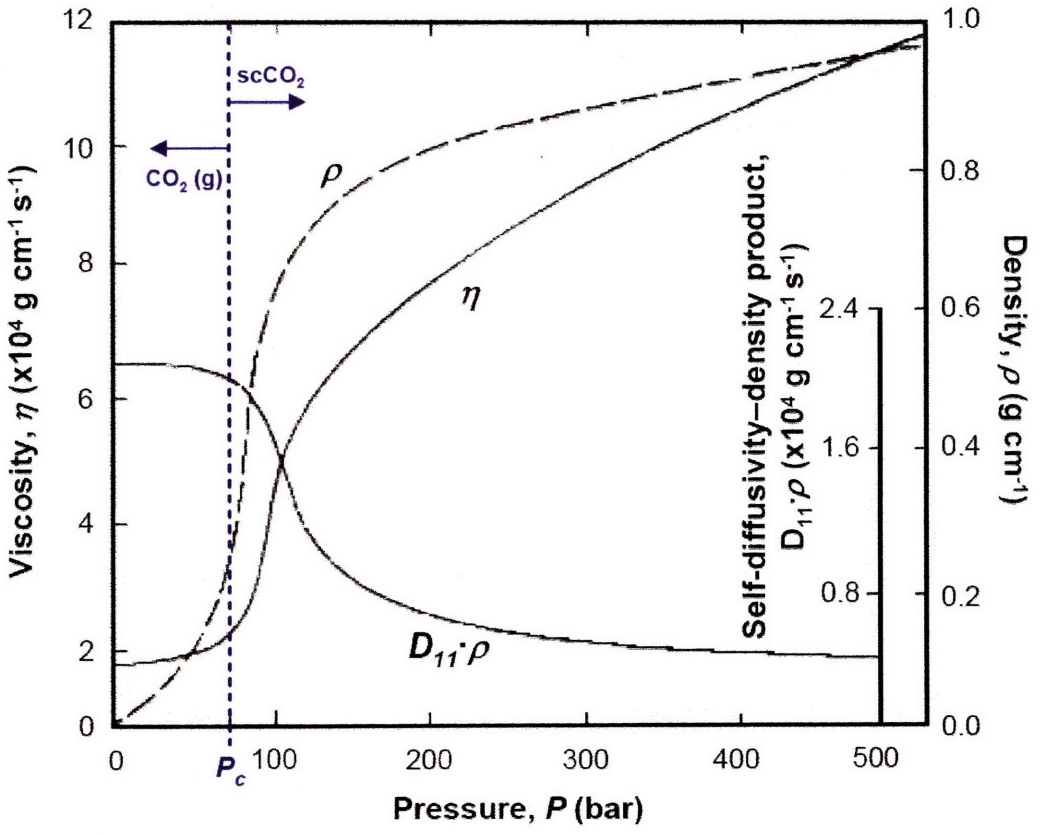

Figure 1-3. Selected physicochemical properties of pure carbon dioxide plotted as a function of pressure at 313.2 K (40 °C) (adapted from Subramaniam et al., 1986).

The ability of $scCO_2$ to solubilize materials or influence the course of a chemical reaction (e.g., phase behavior, rate, selectivity, etc.) typically correlates with fluid density. In practice, a particular operating density is attained via isothermal compression. The correlation of CO_2 density with pressure the Hildebrand solubility parameter (δ), a common — albeit simplistic — scale used for quantifying the solvent 'power' of liquid solvents (Jessop et al., 1999) is shown over a range of T and P in **Figure 1-4**.

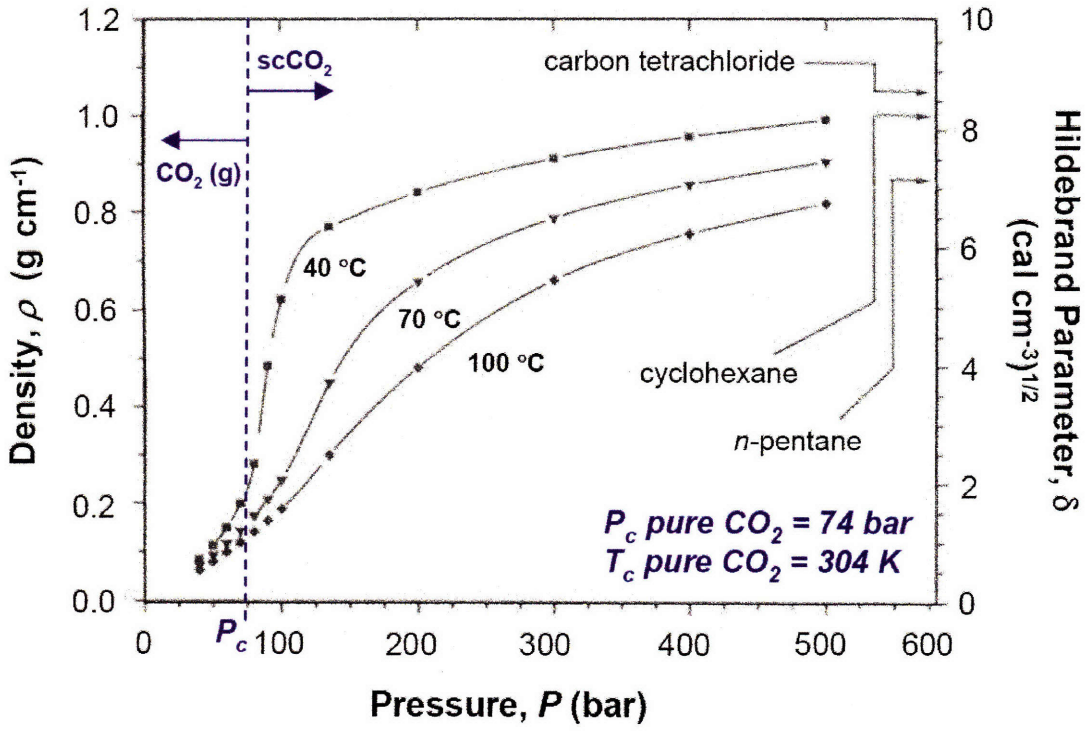

Figure 1-4. Density and Hildebrand parameter of carbon dioxide plotted as a function of temperature and pressure (adapted from Jessop et al., 1999; original references cited therein).

To further illustrate the relationship between fluid density and solubility in $scCO_2$, the solubility of solid caffeine in CO_2 is plotted as a function of T and P in **Figure 1-5**. For a given isotherm, the solubility of caffeine increases when the transitioning from gaseous to $scCO_2$, and continues to increase with increasing density (via an increase in P along an isotherm or a decrease in T along an isobar). Noteworthy is the dramatic increase in solubility in the vicinity of the critical point.

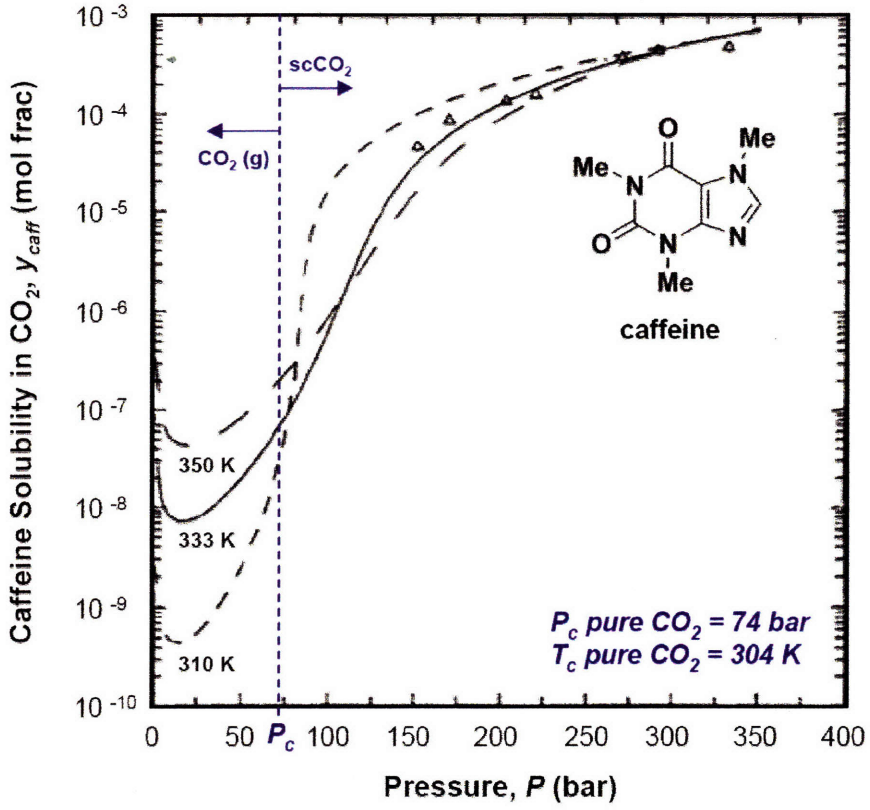

Figure 1-5. Solubility of caffeine in carbon dioxide plotted as a function of temperature and pressure (adapted from McHugh et al., 1994). Solid and dashed lines are predictions by the Peng-Robinson Equation-of-State with a single binary interaction parameter (k_{ij} = 0.059) fit from experimental data (Δ) at 333 K (60°C).

In addition to hybrid and tunable physicochemical properties of $scCO_2$, it possesses several other desirable solvent characteristics (Beckman, 2004):

- **The supercritical state of CO_2 is relatively mild.** Compared to other supercritical fluids, the critical point of CO_2 is readily accessible and is amenable to the synthesis of thermally-sensitive organic compounds (e.g., APIs and fine chemicals). Water, another potential 'green' supercritical solvent, for example, has a T_c = 647 K (374.2 °C) and P_c = 220.5 bar (Poling et al., 2001), making it less attractive from a synthetic chemistry standpoint. Some other pure materials besides water have 'mild' critical points — ethane, propane, and ammonia, for example — but are not considered 'green.'

- **CO_2 is a non-contaminating solvent.** Due to its high vapor pressure and minimal solubility of CO_2 in compounds at ambient or near-ambient conditions, depressurization typically results in its complete removal from final products that are in solid or liquid form (e.g., APIs, reagents, polymers, etc.). Similarly, depressurization to ambient conditions also results in the removal of solid and liquid contaminants from CO_2, hence affording facile recycle.
- **CO_2 in its vapor, gas, or supercritical state is completely miscible with all other pure components or mixtures that are also in their vapor, gas, or supercritical state.** Unlike conventional liquid organic solvents, CO_2 can be employed as a medium for gas-phase reactions without adding additional phase and mass-transfer limitations.
- **CO_2 can not be oxidized and is generally inert to free-radical attack.** As such, CO_2 is often employed in a variety of oxidation and free-radical small- and large-molecule (e.g., polymer) chemistries.

Several limitations exist, however, and detract from the widespread use of CO_2 as an alternative to organic solvents (Beckman, 2004):

- **CO_2 is non-polar and has a low dielectric constant** (ca. 1.5 for liquid CO_2 and 1.1 – 1.5 for $scCO_2$, compared to ca. 2 for toluene, 20 for acetone, and 80 for water at 298 K [25 °C] and 1 bar). As such, it is not particularly effective at dissolving very polar or high-molecular weight compounds (e.g., polymers, proteins, cellulose, etc.). Caffeine, for example, is a polar compound and only modest solubility in CO_2 is obtained in the practical operating pressure region (1 – 500 bar, see **Figure 1-5**). While operating at elevated pressures generally increases solute solubility, extremely polar compounds either remain essentially insoluble or impractical pressures would be required to achieve desired solubility levels. Adding relatively small amounts of a miscible co-solvents (e.g., 1 – 15 wt.% isopropanol, ethyl acetate, etc.) to CO_2 can dramatically effect solubility, as they increase the dielectric constant and polarity of the medium, hence giving the CO_2-rich mixture a greater ability to dissolve solutes in the practical operating pressure region. This phenomenon is discussed in greater detail in **Section 1.3**.

Because of its low dielectric constant, CO_2 is not particularly effective at stabilizing transition state complexes that involve charge separation, and for these types of reactions, generally offers slower reaction rates when compared to conventional organic solvents. In fact, there are only a limited number of cases in the literature which report on reactions that have significantly faster reaction rates or dramatic selectivity changes in pure CO_2.

- **CO_2 is an electrophile**. Carbon dioxide can therefore react with a variety of nucleophilic materials, namely those that contain amine, phosphine, alkyl anion, metal alkoxide, metal alkyl, and/or metal hydride functionality. For example, CO_2 reacts with some primary and secondary amines to form carbamic salts that are insoluble in $scCO_2$ and can also interfere with desired reaction pathways. To overcome this limitation, electron-withdrawing and/or bulky protecting groups are added in the vicinity of CO_2-reactive substrate sites. These groups serve to hinder the reaction with CO_2 via a decrease in substrate nucleophilicity and steric interference, respectively. An alternative to chemical modification is to operate in a *P-T* regime where the undesired reaction is unfavorable.
- **CO_2 lowers the pH of water.** CO_2, and to a greater extent $scCO_2$, dissolves in water, reacts to form carbonic acid, and a subsequently reduces its pH (as low as 2.9 at elevated pressures). This effect can be both advantageous (e.g., rate acceleration for acid-catalyzed aqueous reactions) and disadvantageous (e.g., reagent degradation and undesired pathways that favor lower-pH environments), and may require the use of corrosion-resistant materials and equipment.

1.3. Properties of CO_2/co-solvent Mixtures and CO_2-Expanded Liquids

In order to overcome many of the solubility and reaction rate limitations associated with a pure CO_2 medium, conventional organic solvents are often added as 'medium enhancers.' Depending on the operating conditions and amount of co-solvent employed, two distinct mediums can be achieved: (1) a single-phase CO_2/solvent mixture (CSM), or (2) a multi-phasic system consisting of a CO_2-rich phase and one or more CO_2-expanded liquid (CXL) phases. To fully understand the distinction between the two, consider the schematic representation of a

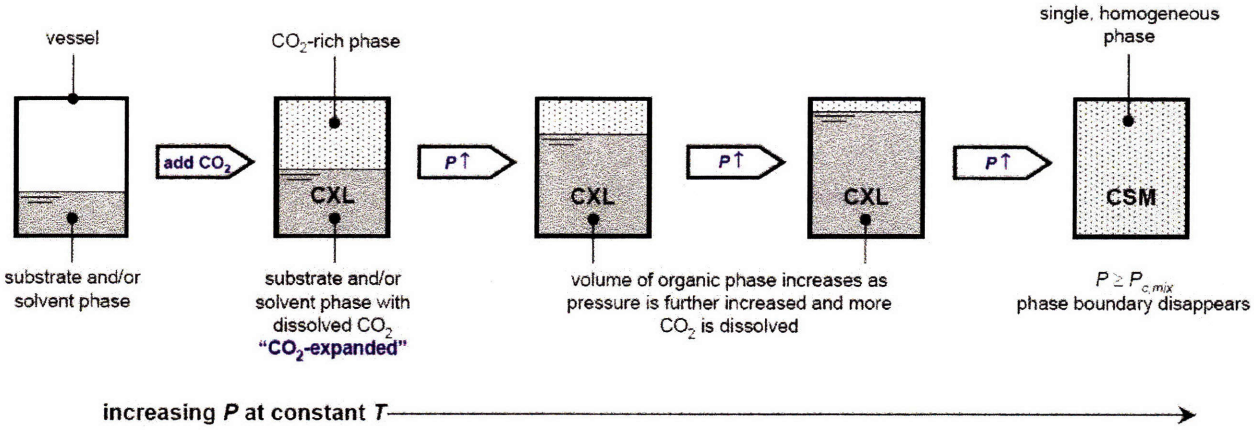

Figure 1-6. Schematic representation of isothermal solvent expansion in the presence of carbon dioxide.

typical CO_2/solvent mixing process and its associated thermodynamics shown in **Figure 1-6** and **Figure 1-7**, respectively.

Several liquid substrates, conventional organic solvents, and mixtures of the two readily dissolve carbon dioxide. Upon addition of CO_2 to a vessel containing a pure liquid (e.g., ethanol), a biphasic system is formed and consists of an upper, lower-density CO_2-rich phase and a lower, higher-density liquid phase. The system equilibrates to yield phase-specific compositions according to the principles of thermodynamics that govern vapor-liquid equilibrium (VLE). For a two-component system, this equilibrium is established when temperature and pressure are fixed. As shown by the equilibrium data for the CO_2/ethanol system presented in **Figure 1-7**, if T and P are fixed at 313.2 K (40 °C) and 30 bar, the corresponding liquid- and vapor-phase compositions (mole fractions x_i and y_i, respectively, where the subscript "i" is the component index) would be: $x_{CO_2} \approx 0.16$, $x_{ethanol} \approx 0.84$, $y_{CO_2} \approx 0.99$, and $y_{ethanol} \approx 0.01$. As the system pressure is increased isothermally (in practice, usually via the isochoric addition of compressed CO_2), a greater amount of CO_2 dissolves into the ethanol-rich liquid phase ($x_{CO_2} \uparrow$) and simultaneously results in an increase in its volume (see **Figure 1-6**).

CO_2 absorption into and volume expansion of the liquid phase both terminate when the mixture critical pressure ($P_{c,mix}$) is reached. As system P approaches $P_{c,mix}$ (ca. 82 bar for the CO_2/ethanol system at 313.2 K [40 °C]), the liquid phase expands to fill the entire vessel volume and the phase boundary begins to vanish. At $P > P_{c,mix}$ (but less than the P required to condense the mixture to a solid), the mixture is in its supercritical state, and only a single phase

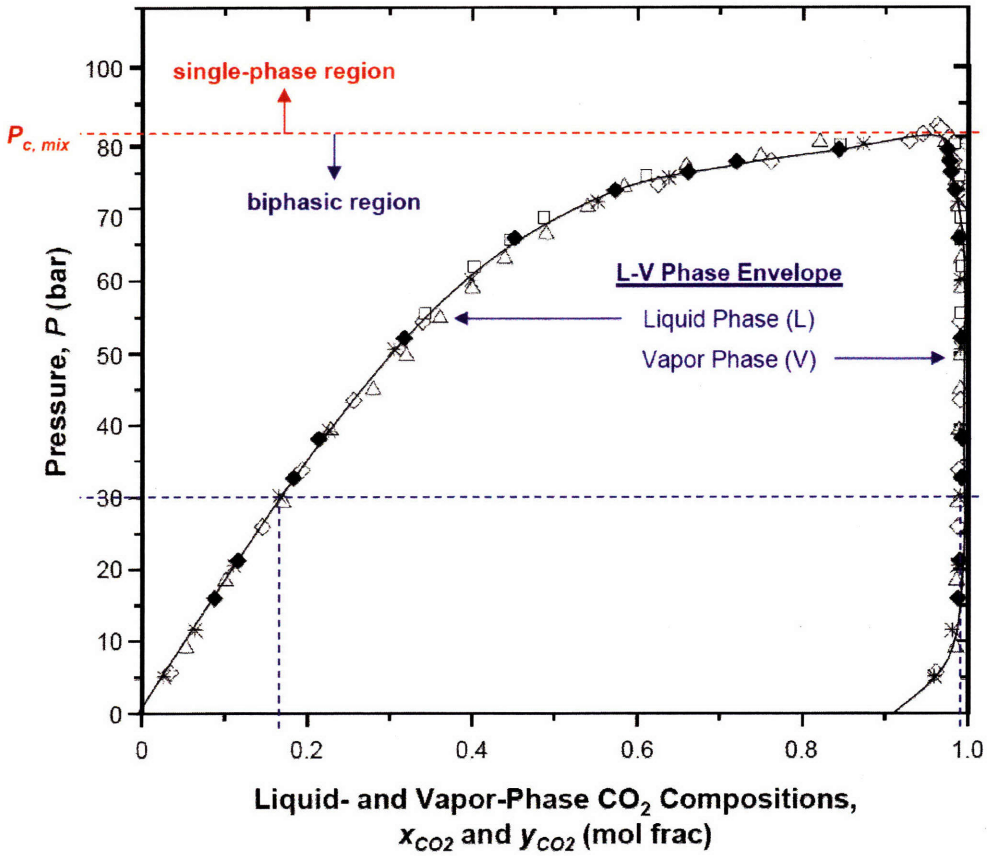

Figure 1-7. Vapor-liquid equilibrium data for the carbon dioxide/ethanol system at 313.2 K (40 °C) (♦) (adapted from Knez et al., 2008). All other data are comparisons from references cited within Knez, et al., 2008. The solid line is drawn to serve as a guide and no physical basis is intended.

exists with a composition corresponding to that of the initial solvent and total CO_2 charge. Each mixture has a unique $P_{c,mix}$ that varies with T and substrate composition. For $T \approx T_c$ of pure CO_2 and for $P \approx P_{c,mix}$, a liquid phase can contain as much as 99 mol% CO_2 (see **Figure 1-7**).

In the context of this work, a CXL will therefore refer to a liquid-phase mixture that contains appreciable amounts of dissolved CO_2 and is at $P < P_{c,mix}$ at a given T and substrate composition. A CSM will be defined as a CO_2-rich (e.g., ≥ 50 wt.% CO_2) binary mixture (that may also contain dissolved substrate) in a single, supercritical phase. Although it is also possible to obtain a single-phase CO_2/solvent mixture for $P < P_{c,mix}$ by adding the solvent in an amount less than the solubility limit at the given T and P, these amounts are often too small to significantly affect the bulk properties of the medium and will therefore be excluded from this discussion.

CSMs and CXLs offer several advantages, one of which is their ability to dissolve substrates that are not soluble in pure CO_2 in the practical operating pressure region (1 – 500 bar). Kopcak and coworkers (2005), for example, have demonstrated that the addition of alcohol co-solvents to CO_2 in relatively small amounts (5 and 10 wt.%) can lead to an almost order-of-magnitude increase in caffeine solubility, as shown in **Figure 1-8**. Their work also reveals that the level of solubility enhancement is dependent on co-solvent choice. Compared to isopropanol CSMs, ethanol mixtures at identical masses and operating conditions were shown to greater enhance caffeine solubility.

An increase in polar substrate solubility in CSMs is typical and believed to occur as a result of increased medium polarity (i.e., increases the dielectric strength) and electrostatic stabilization effects that result in a free energy reduction (see **Section 1.4.1**). For the previous example, it is hypothesized that caffeine is stabilized in CO_2/alcohol mixtures via hydrogen bond interactions. This hypothesis is also thought to explain the greater solubility of caffeine in CO_2/ethanol mixtures when compared to CO_2/isopropanol mixtures, as ethanol is a better H-bond donor and a larger H-bond density is achieved for CO_2/ethanol mixtures when adding equal masses of the alcohols. Much like $scCO_2$, CSMs have tunable physicochemical properties that are accessible by the manipulation of solvent choice and concentration, *T*, and *P*.

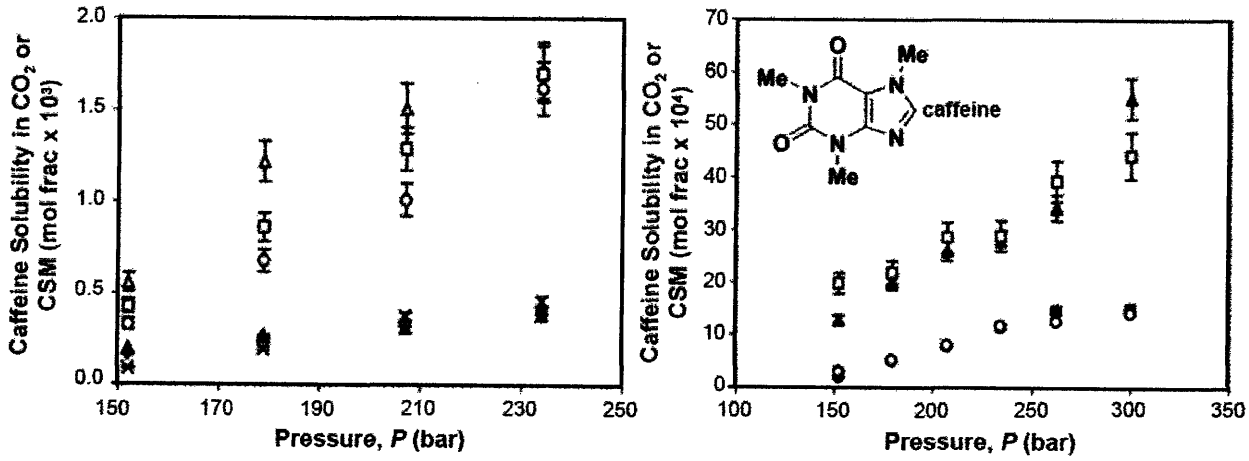

Figure 1-8. Solubility of caffeine in pure carbon dioxide and carbon dioxide/co-solvent mixtures plotted as a function of temperature and pressure (adapted from Kopcak et al., 2005). *Left:* experimental data for pure CO_2 at 313.2 K (40 °C), (▲), 323.2 K (50 °C) (◊), and 343.2 K (60 °C) (×) and CO_2/5 wt.% ethanol at 313.2 K (40 °C) (Δ), 323.2 K (50 °C) (□), and 343.2 K (60 °C) (○). *Right:* experimental data for CO_2/5 wt.% isopropanol 323.2 K (50 °C) (○), 343.2 K (60 °C) (•) and CO_2/10 wt.% ethanol at 323.2 K (50 °C) (□) and 343.2 K (60 °C) (▲). All conditions correspond to a CSM state (i.e., each $P \geq P_{c,mix}$).

CXLs are similarly tunable via solvent type and operating conditions. Jessop and Subramaniam (2007) provide a detailed review of the properties of CXLs, of which the most relevant to this work include:

- **Liquid-phase CO_2 solubility.** The ability of liquids to dissolve carbon dioxide — or their liquid 'CO_2-philicity' — depends on a variety of factors, some of which include molecular size and functionality, polarity, hydrogen bonding ability, viscosity, and the T and P at which they are employed. The variation of liquid-phase CO_2 composition ($[CO_2]_l$) of several solvents as a function of T and P is shown in **Figure 1-9**. Substantial differences in the CO_2-philicity exist for the liquids presented; larger pressures, for example, are required to obtain an identical $[CO_2]_l$ for water than for acetonitrile. In general, the largest $[CO_2]_l$ concentration is obtained when $T \approx T_{c,CO_2}$ and $P \approx P_{c,mix}$. Increasing T usually requires an increase in the P required to achieve a similar $[CO_2]_l$. Most noteworthy is how a continuum of liquid-phase CO_2 concentrations is achieved by the manipulation of system pressure. Operating at the lower-P end of this continuum results in physicochemical and solvation properties similar to the original solvent, while the higher-P end exhibits those of $scCO_2$. The medium can therefore be tuned to an intermediate pressure regime to arrive at conditions suitable for a variety of synthetic and processing applications.
- **Liquid-phase volume expansion.** The variation of liquid-phase volume expansion is directly proportional to its $[CO_2]_l$. As shown by **Figure 1-9**, large increases in liquid-phase volume can be achieved in the presence of CO_2; under certain operating conditions, solvents can experience expansion up to 1000%. A potential application of this CXL property is for unimolecular ring-closing chemistries that suffer from undesired competitive polymerization pathways. By expanding the solvent with CO_2, substrate concentration is reduced, hence inhibiting polymerization without the need for large dilutions with liquid solvents.

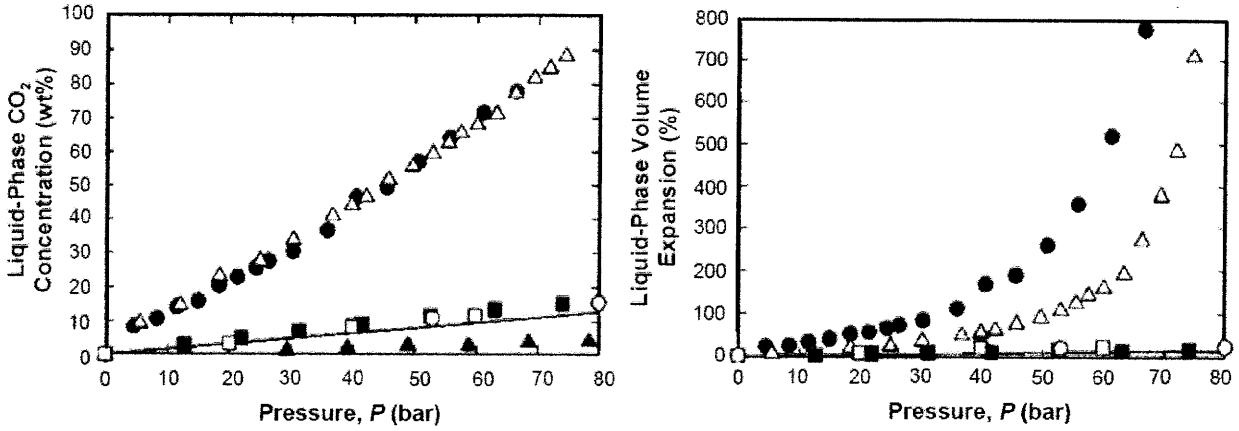

Figure 1-9. Liquid-phase solubility of carbon dioxide in (*left*) and volume expansion of (*right*) selected organic solvents plotted as a function of pressure (adapted from Jessop et al., 2007; original references cited therein). Experimental data for water (▲), ethyl acetate (•), acetonitrile (Δ), [bmim]BF_4 (■), crude oil (–), PEG (○), and PPG (□). All data at 313.2 K (40 °C) except for water and PPG (308.2 K [35 °C]) and crude oil (316.2 K [43 °C]). [bmim]BF_4 is an ionic liquid and "bmim" is the abbreviation for 1-*n*-butyl-3-methylimidazolium.

- **Enhanced gas solubility.** Compared to other gases (e.g., O_2, H_2, N_2, CO) at the same *T* and *P*, CO_2 tends to have a larger solubility in liquid solvents. Since CXLs are less polar than their neat liquid components, non- and slightly-polar gases often have higher solubilities in these mediums. As shown by **Figure 1-10**, the addition of CO_2 to an H_2/octene system increases the liquid-phase composition of H_2 by a factor of 4.

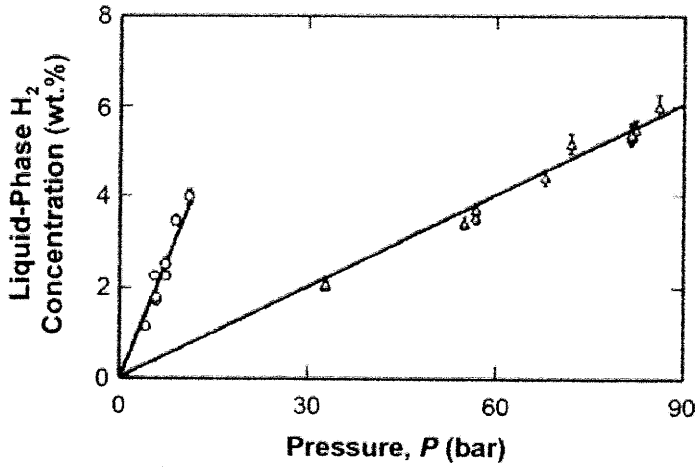

Figure 1-10. Liquid-phase solubility of hydrogen in pure octene (Δ) and carbon dioxide-expanded octene (○) plotted as a function of pressure at 333.2 K (60 °C) (adapted from Jessop et al., 2007; original references cited therein).

- **Enhanced mass transport.** CXLs also have tunable mass transport properties that are intermediate to that of their neat liquid components and pure $scCO_2$. With surface tensions and viscosities lower than conventional solvents, CXLs often have faster transport across the CO_2-solvent phase boundary and larger solute bimolecular diffusion rates.

It is worth nothing that the addition of substrates to CO_2-expanded solvent systems can have a significant impact on phase behavior. Depending on the type of substrate and its liquid-phase composition, volume expansion and CO_2-philicity can be diminished, for example. Substrate precipitation from the bulk liquid phase and the formation of additional liquid phases may occur under certain operating conditions. As P is increased isothermally for substrate/CXL systems, selective partitioning of either the substrate or solvent to the CO_2-rich phase can also occur.

In addition, some solvents and solvent/substrate mixtures in the presence of CO_2 may experience volume contraction as the $P_{c,mix}$ is approached and a single phase is formed. Multiple phases beyond the binary phase mixture illustrated in **Figure 1-6** may also appear due to further solubility limitations and extreme system non-idealities.

1.4. CO_2-Based Media Applied to Synthetic Chemistry

1.4.1. Solvation and Phase Behavior Effects

The density at which CO_2 is employed in both neat and CO_2-based solvent systems can often affect the course of the chemical reaction. Reaction rates and product selectivites, for example, can vary appreciably depending on system P, and may be significantly different when compared to conventional solvents at similar operating conditions (*vide infra*). A qualitative analysis of reaction transition state theory (TST) offers an explanation of this phenomenon.

Figure 1-11a schematically illustrates how the Gibbs free energy (G) varies along a 1-dimensional reaction coordinate for a generic chemical reaction, where reactants proceed to products via a transition state (TS) complex. The rate constant (k) associated with this transformation is exponentially proportional to the free energy barrier between the TS complex and the reactants (ΔG^{TS}) (Steinfeld et. al., 1999). A given reaction will have a ΔG^{TS} (and hence k) that is dependent on T and the solvent in which the reaction proceeds. At a fixed T,

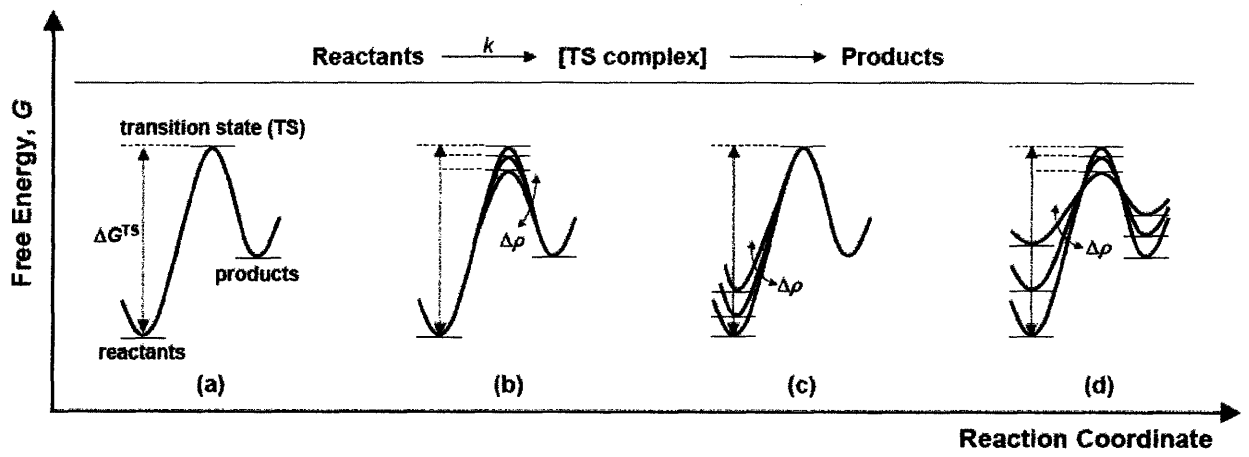

Figure 1-11. Generic reaction coordinate profile **(a)** and the illustration of solvation effects on only the TS complex **(b)**, only the reactants **(c)**, and the reactants, TS complex, and products **(d)**.

changing the reaction solvent can lead to the selective solvation of the TS complex and/or reactants, hence altering the free energy required for the transformation. Rate accelerations occur when there is a decrease in $G_{TS\ complex}$ relative to an unchanged $G_{reactants}$ (see **Figure 1-11b**), increase in $G_{reactants}$ relative to an unchanged $G_{TS\ complex}$ (see **Figure 1-11c**), or any combination of these (see **Figure 1-11d**) that results in a net decrease in ΔG^{TS}. Consider, for example, uncharged reactants that undergo a transition state with charge separation. Performing this reaction in a polar solvent with a high dielectric constant would preferentially solvate the TS complex relative to the reactant molecules, decrease ΔG^{TS}, and lead to an increase in reaction rate.

Unlike conventional incompressible, liquid solvents, the intensity of solvation effects in $scCO_2$ is a function of density. For example, altering the density of CO_2 (via isothermal compression) can simultaneously alter ΔG^{TS} and afford density-dependent reaction rate constants. This is also applicable to CSMs and CXLs, both of which have additional solvation effects due to the increased dielectric of the medium or electrostatic interactions of the added solvents with reactants and TS complexes.

Electrostatic interactions of CO_2 with nucleophilic sites of reactants and TS complexes may also alter the ΔG^{TS} and vary with fluid density. Stronger interactions with CO_2 (e.g., the reaction of CO_2 with these sites to form covalent bonds) may similarly affect the free energy of reactive species and could enhance or inhibit reactions as a result of interactions at these sites.

A three-density-region solvation model for supercritical fluid mixtures has been proposed to account for density-dependent spectroscopic and solvation responses (Sun et al., 2002). The model, shown schematically in **Figure 1-12**, provides a qualitative explanation of observed solvation behavior at various density regimes. Solute responses found in the low-density region ($0.1 < \rho_r < 0.5$, where ρ_r is reduced density, see **Figure 1-12a**) are strong functions of density, which is thought be attributed to the saturation of the solute's inner solvation shell. In the near critical-density region ($0.5 < \rho_r < 1.5$, see **Figure 1-12b,**), the fluid is considered microscopically-inhomogeneous and viewed as consisting of solvent-solvent and solute-solvent clusters and free volumes. Solvation properties do not change much in this region, and compression is thought to simply fill free volumes instead of disturbing the cluster structures. Increasing the density further results in the complete filling of free volumes to form a liquid-like state ($\rho_r > 1.5$, see **Figure 1-12c,**) and solvation properties once again begin to vary with density in a manner predicted by the dielectric continuum theory.

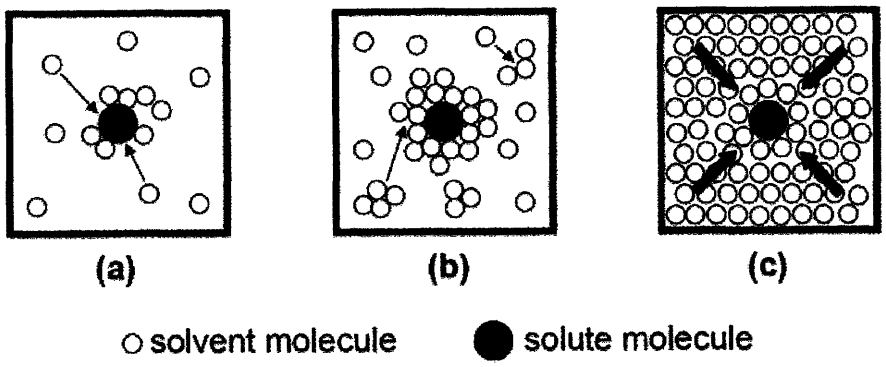

Figure 1-12. Schematic representation of the qualitative three-density-region solvation model (adapted from Sun et al., 2002; original references cited therein), depicting the molecular-level interactions for the low- or gas like-density region **(a)**, near critical-density region **(b)**, and the far above P_c in a more liquid like-density region **(c)**.

Although solvation properties are reported to not vary much in the supercritical region, solvent clustering is still thought to affect reaction pathways when compared to microscopically-homogeneous solvent mediums. The small molecular size of CO_2 relative to other solvents and solutes of interest facilitates its ability to form self- and CO_2-solute clusters. Consider, for example, the unimolecular ring-closing reaction discussed briefly in **Section 1.3**. In cases where a reactant can undergo unimolecular ring closure as well as undesired bimolecular

polymerization, the minimization of solute-solute interaction is key. While dilution is usually the common fix, it is also possible that solvent clusters (see **Figure 1-12b**) formed around individual solute molecules will help shield the molecule such that it preferentially undergoes ring-closure.

The quadrupole moment — a measure of the departure from spherical symmetry of a charge distribution — of CO_2 when compared to other non-polar (i.e., zero dipole moment) molecules is large (Bundgen et al., 1995) and is thought to contribute to its greater ability to solubilize non-polar materials and also affect the reactivity of dissolved solutes (Kauffman et al., 2001 and Jaeger et al., 2006).

In addition to solvation effects, phase behavior can also affect reaction rates and product selectivities. In CXLs, reactants may distribute to both the CO_2-rich supercritical-like phase and organic-rich liquid phases, where differences in the dielectric and physicochemical properties of the medium may play a role. For example, a reaction may proceed slower in the CO_2-rich phase and may also experience selectivities that are significantly different than those in the organic-rich phase.

The phase behavior during a single-phase reaction in CO_2 may also change as the reaction proceeds and the reactants and/or products may precipitate to form separate phases as solubility limits are exceeded. In the case of reactions limited by thermodynamic equilibrium, product precipitation can facilitate reaction completion in accordance to Le Chatlier's principle. Reactants may also partition to these newly-formed phases, where they could experience rate and selectivity changes or undergo alternate reaction pathways not occurring in the bulk CO_2-rich phase. Because much of this work is concerned with phase behavior effects, a more detailed discussion is presented in later chapters.

1.4.2. Representative Transformations

Several reviews for the application of CO_2 as a reactant and/or solvent are available and present a wide range of synthetic transformations (Abraham et al., 2002; Adams et al., 2004; Ahluwalia et al., 2004; Anastas et al., 1996; Anastas et al., 1998, Anastas and Williamson, 1998; Arai et al., 2002; Baiker, 1999; Beckman, 2004; Brunner, 2004; Clark et al., 2002; Clifford, 1999; DeSimone et al., 2003; Eckert et al., 2004; Hobbs, et al., 2007; Jessop, 2006; Jessop et al., 1999; Jessop et al., 2007; Kemmere et al., 2005; Leitner, 1999 and 2002; Liu et al., 2003; Matsuda et al., 2004; Mesiano et al., 1999; Mikami et al., 2005; Nelson et al., 2004; Oakes et al., 2001; Rayner, 2007; Sakakura et al., 2007; Subramaniam et al., 1986; Subramaniam et al.,

2002; Sun et al., 2002; Tundo et al., 2000). Although it is beyond the scope of this work to comprehensively review all of research focused on chemical transformations performed in CO_2 and CO_2-based media, a discussion of key examples that demonstrate novel behavior is presented here and is relevant to the model synthetic reactions selected for study in this thesis.

A striking example of novel reaction behavior in CO_2 was reported by Rayner and coworkers in their organosulfur oxidation study (Rayner, 2007), where *tert*-butyl hydroperoxide (TBHP) in the presence of Amberlyst sulfonic acid ion-exchange resin (IER) was used to oxidize *S*-methyl cysteine to its corresponding sulfoxide (see **Figure 1-13**).

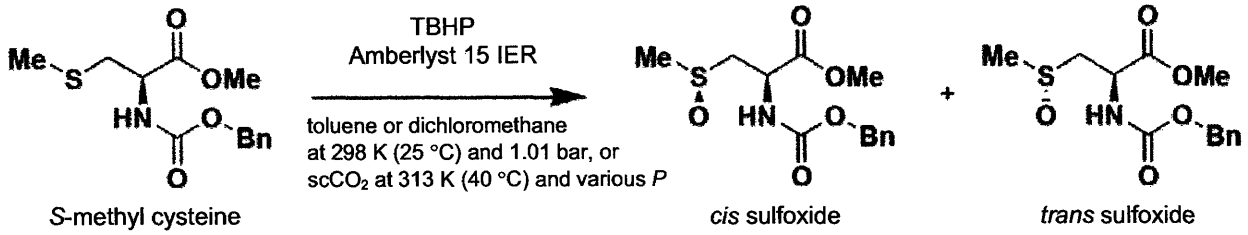

Figure 1-13. Diastereoselective oxidation of *S*-methyl cysteine with *tert*-butyl hydroperoxide in carbon dioxide.

In conventional organic solvents such as toluene and dichloromethane at ambient reaction conditions, no appreciable selectivity to either diastereomer was observed (i.e., ca. 50:50 *cis*:*trans* molar ratio, diastereomeric excess = 0). In fact, the only examples of diastereocontrolled sulfur oxidation in conventional solvents prior to this work were attained at very low temperatures (195 K [-78 °C]). However, when the reaction was performed in $scCO_2$ at 313.2 K (40 °C), selectivity towards the *trans* isomer observed, and was astonishingly found to vary as a function of density (via isothermal compression, see **Figure 1-14**). Nearly complete stereoselectivity for the *trans* sulfide was realized when tuning the reaction medium to $P \approx 110$ bar ($\rho \approx 0.7$ g/mL).

Rayner proposed that phase behavior and CO_2/substrate interactions were responsible for the observed trend. VLE calculations revealed a $P_{c,mix} \approx 110$ bar for the CO_2/*S*-methyl cysteine system, which coincided with the P at which optimal selectivity was observed. Rayner also indicated that the sulfoxide products precipitated from the CO_2 phase as they were formed.

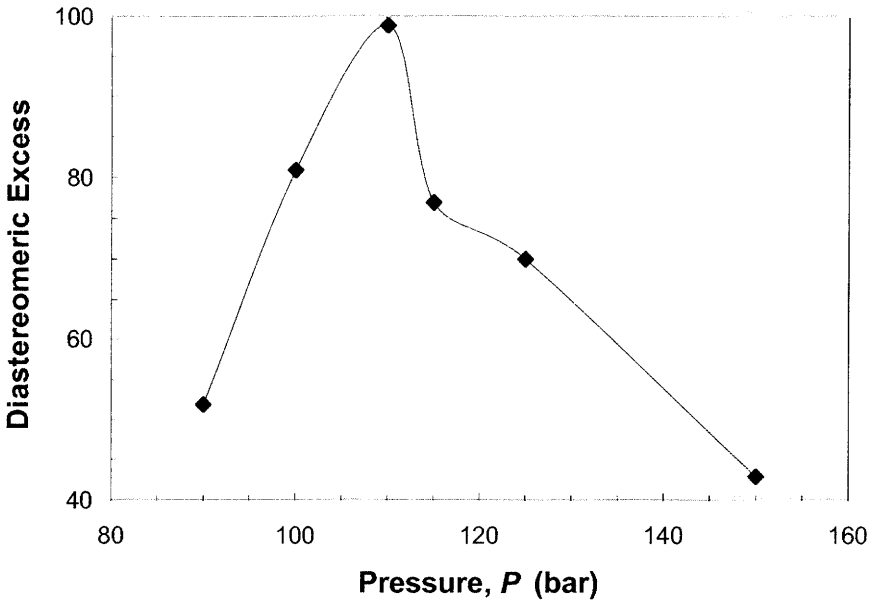

Figure 1-14. *S*-oxidation diastereoselectivity in carbon dioxide plotted as a function of pressure at 313.2 K (40 °C) (adapted from Rayner, 2007).

For $P < 110$ bar, the phase behavior of the system was biphasic and consisted of a substrate/sulfoxide/catalyst/TBHP-rich phase and a CO_2-rich phase. A biphasic system containing a sulfoxide-rich phase and CO_2/substrate/catalyst/TBHP-rich phase was observed for $P \geq 110$ bar. The reaction therefore took place in drastically different mediums; for the $P < 110$ bar regime, the reaction proceeded in the polar liquid phase, whereas for the $P \geq 110$ bar regime, the reaction proceeded in a non-polar, CO_2-rich supercritical-like phase. Differences in medium dielectric strength and phase-specific reactant partitioning could account for the observed changes in selectivity. In addition, the carbonyl carbon of CO_2 can interact with the double-bound oxygen sites in the substrate, quite possibly leading steric interference for the *cis* sulfide transition state coordination complex and/or the selective solvation of the *trans* sulfide complex.

In their homogeneous study of the Diels-Alder cycloaddition of 9-hydroxymethyl anthracene and *N*-ethylmaleimide (see **Figure 1-15**), Qian and fellow coworkers in the Tester research group (Qian et al., 2004) found that the reaction rate varied considerably with solvent choice and the density at which CO_2 was employed. An isothermal increase in CO_2 (via an

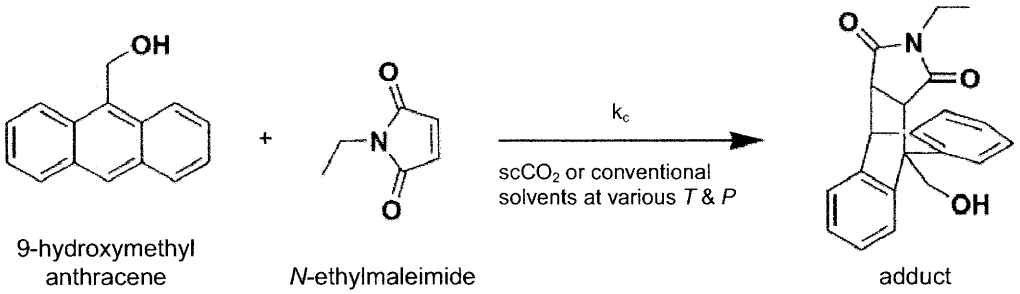

Figure 1-15. Diels-Alder cycloaddition of 9-hydroxymethyl anthracene and *N*-ethylmaleimide in carbon dioxide.

increase of system *P*) density was shown to decelerate the rate of reaction. As shown by **Figure 1-16**, at a given *T*, as much as a four-fold increase in reaction rate constant was realized when operating at pressures in the vicinity of $P_{c,mix}$. Comparing the reaction rate values in $scCO_2$ with those for selected organic solvents (see **Figure 1-16**), they found that the reaction proceeded faster in CO_2 (except when compared to water), and that rates similar to those observed in these solvents could be obtained by manipulating the density of the $scCO_2$ medium. The authors attribute the observed rate enhancements in CO_2 to preferential solvation of the

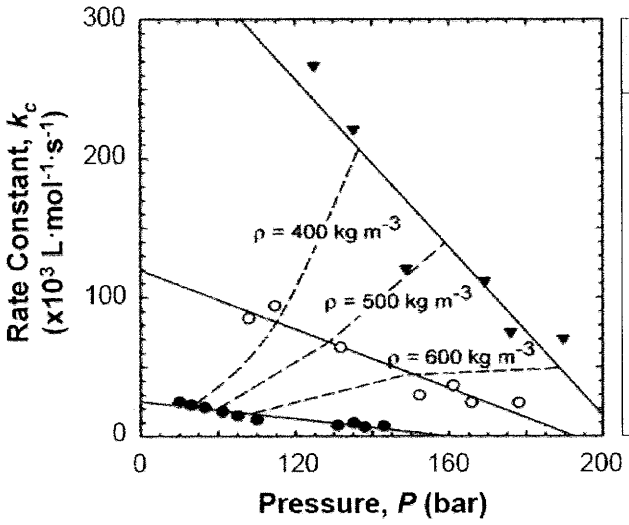

Solvent	Rate Constant, k_c ($x10^5$ L mol^{-1} s^{-1})
$scCO_2$ (ρ = 340 g·L^{-1})	2480 ± 250
$scCO_2$ (ρ = 560 g·L^{-1})	1490 ± 150
$scCO_2$ (ρ = 730 g·L^{-1})	740 ± 250
n-hexane*	776 ± 250
acetonitrile	100 ± 6
methanol*	337 ± 60
water	18400 ± 300

Figure 1-16. *Left:* Bimolecular reaction rate constants for the Diels-Alder cycloaddition of 9-hydroxymethyl anthracene and *N*-ethylmaleimide in carbon dioxide plotted as a function of temperature and pressure (adapted from Qian et al., 2004). Experimental data at 318.2 K (45 °C) (•), 333.2 K (60 °C) (○), and 348.2 K (75 °C) (▼). *Right*: Tabulated rate constant values for the reaction in $scCO_2$ and selected conventional organic solvents at 318.2 K (45 °C) (Qian et al., 2004). Values designated with a "*" were obtained from references cited within Qian et al, 2004.

reactants and/or transition state complex (i.e., lower reaction ΔG^{TS} in CO_2 compared to other solvents and in CO_2, ΔG^{TS} decreased with decreasing fluid density).

Song and coworkers (2007) found that the acid-catalyzed transesterification of glycol monostearate with methanol (see **Figure 1-17**) was accelerated with the addition of CO_2 to the reaction mixture. As seen by **Figure 1-18**, complete conversion of reactants in the absence of

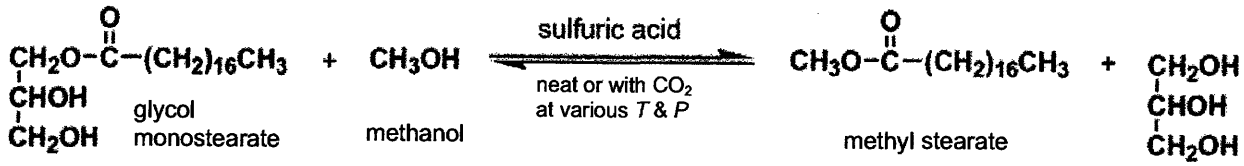

Figure 1-17. Transesterification of glycol monostearate with methanol in carbon dioxide.

CO_2 required greater than 36 hours and the phase behavior was biphasic and consisted of a lower-density methanol rich phase (top) and a higher-density glycerol monostearate-rich phase (bottom). The sulfuric acid catalyst partitioned to the methanol-rich phase to a larger extent, and hence the reaction was believed to proceed in this phase. Upon the addition of CO_2 to the reaction mixture, the phase behavior became triphasic and consisted of a lower-density CO_2-

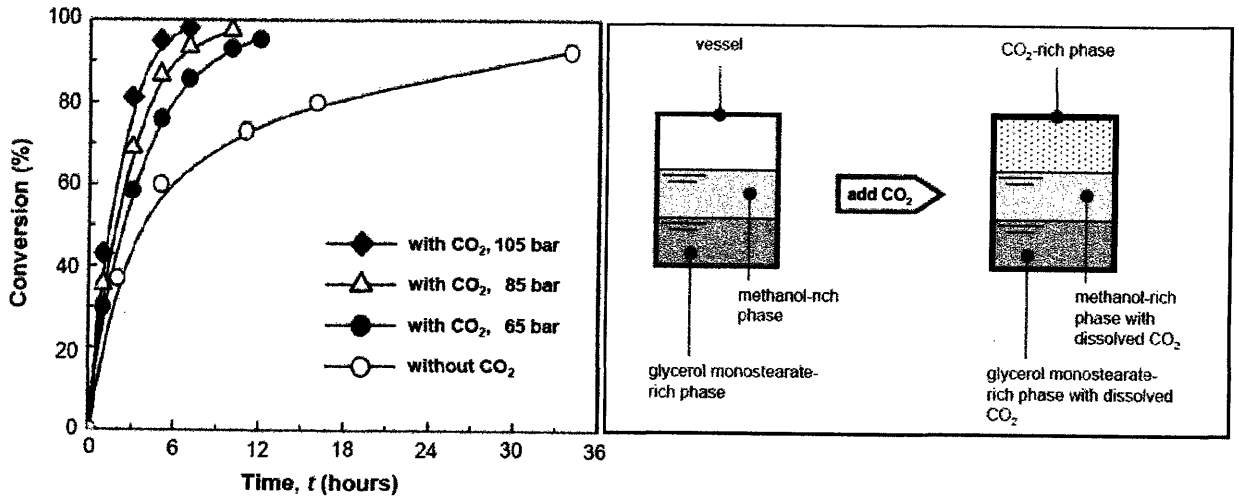

Figure 1-18. *Left:* Conversion of glycol monostearate in carbon dioxide plotted as a function of time and pressure at 333.2 K (60 °C) (adapted from Song et al., 2007). *Right*: Schematic representation of the reaction phase behavior.

rich phase (top), an intermediate-density methanol-rich CXL phase (middle), and a glycol monostearate-rich CXL phase (bottom).

Significant rate enhancements were achieved in the presence of CO_2; pressures as low as 65 bar were shown to decrease the *t* required for complete conversion by a factor of four. Song and coworkers believe that the observed rate enhancements were attributed to the physicochemical properties of CXLs. More specifically, the addition of CO_2 increased phase-specific reactant concentrations and diffusivities, lowered liquid-phase viscosity, and increased the interfacial mass-transport rate of glycol mono-stearate to the methanol-rich reaction phase — all of which accelerated the rate of reaction.

The reaction phenomena cited in these examples illustrate a means for achieving changes in both reaction rate and selectivity in CO_2-based media without having to use a different solvent, but rather by the simple change of system *P* and density.

1.5. CO_2-Based Industrial Processing

Coupled with environmental and economic advantages, the tunable physicochemical properties of CO_2 have led to its incorporation into a variety of commercial processes. The most popular example of a large-scale CO_2-based industrial process is the Maxwell House coffee decaffeination process implemented by Kraft General Foods (McHugh et al., 1994); CO_2 at 318 K (45 °C) and 300 bar is used to selectively extract caffeine from coffee beans. The extraction vessel used in this process is estimated to contain 100,000 lbs of coffee beans per batch and realizes a throughput of 60 million lbs/yr. Other non-synthetic commercial applications that use CO_2 and CSMs as extraction solvents include clothing dry-cleaning (Adam, 2000), the degreasing of metal surfaces (McHardy, 1998), and supercritical fluid chromatography applications. CO_2, CSMs, and CXLs are also commonly employed as anti-solvents in particle precipitation processes (Jessop et al., 2007).

From the commercial synthesis standpoint, DuPont uses CO_2 as a reaction medium for the production of fluoropolymers, including their blockbuster Teflon® product line (Beckman, 2004). Thomas Swan & Co. Ltd. uses a CXL medium for a pilot-scale hydrogenation process that yields the fine chemical trimethylcyclohexanone (Licence et al., 2003). These examples demonstrate how CO_2 and CO_2/solvent mixtures can be successfully employed on a large scale despite the need to operate with specialty equipment and at elevated pressures.

1.6. Earlier Work on CO_2-Based Syntheses in the Tester–Danheiser Groups

The work presented in this thesis builds on the results and ideas of former group colleagues and is the culmination of 15 years of research experience with $scCO_2$ and CO_2/H_2O mixtures as media for synthetic transformations. The involvement of the Tester group in this research area began with the doctoral work of Randy D. Weinstein (1993 – 1998) (Weinstein, 1998). Weinstein began his work with the design and construction of our first $scCO_2$ delivery system and several high-*P* reaction vessels. At the time, the use of CO_2 as an alternative solvent for chemical synthesis was relatively new, and as such, the goal of Weinstein's work was to gain a better understanding of its solvation effects on the rates and selectivities of several model organic synthesis reactions. Much of Weinstein's work was done in collaboration with fellow doctoral candidate Adam R. Renslo (1993 – 1998) of Professor Rick L. Danheiser's synthetic organic chemistry at the MIT Chemistry Department.

Specifically, Weinstein and coworkers probed the *P-T* and density space and found that the bimolecular rate constants of the single-phase Diels-Alder cycloaddition of ethyl acrylate and cyclopentadiene in $scCO_2$ were comparable to that of typical liquid media, and for fixed *T*, found to increase with increasing density by as much as 1.5 times (see **Figure 1-19**). A rigorous theoretical TST reaction rate constant model was derived and used to explain the observed rate enhancements (Weinstein et al., 1996).

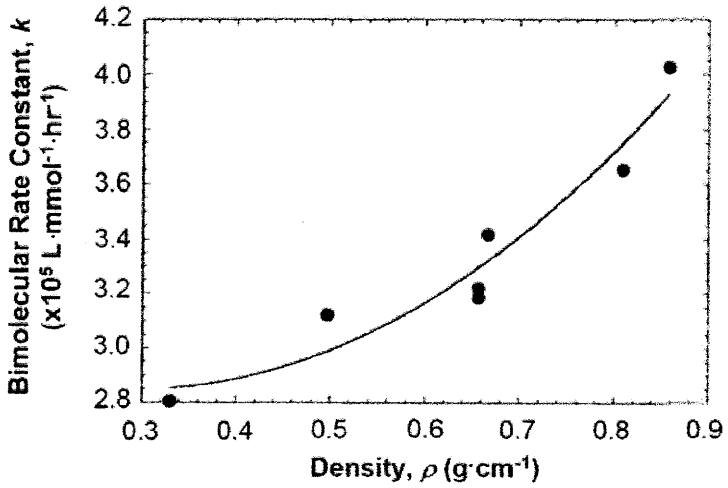

Figure 1-19. Bimolecular reaction rate constants for the Diels-Alder cycloaddition of ethyl acrylate and cyclopentadiene in carbon dioxide plotted as a function of density at 311.2 K (38 °C) (adapted from Weinstein, 1996).

In addition to rate constant measurements, Weinstein and coworkers investigated the effect of density on the stereo- (i.e., *endo* vs. *exo* adducts) and regioselectivity (i.e., *para* vs. *meta* adducts) of several additional Diels-Alder reactions in $scCO_2$. Increasing density isothermally during the Diels-Alder cycloaddition of ethyl acrylate and cyclopentadiene slightly increased stereoselectivity towards the *endo* adduct by 5%.

An earlier study of the Diels-Alder reaction of methyl acrylate and isoprene in CO_2 by Ikushima and coworkers reported a dramatic reversal in regioselectivity — from ca. 70:30 mol% *para*:*meta* for $P < P_c$ and $P > P_c$, to ca. 40:60 mol% at $P \approx P_c$) (Ikushima et al., 1990 and Ikushima et al., 1992). Intrigued by this observation, Weinstein and coworkers repeated Ikushima's reaction conditions but did not observe this shift in regioselectivity. They instead found that the selectivity remained essentially constant at a value of ca. 70:30 mol% *para*:*meta*. It was discovered that the reaction exhibited phase splitting which was not possible to observe in Ikushima's apparatus. Weinstein and coworkers believed that the reported reversal in regioselectivity was attributed to the improper sampling of a biphasic reaction mixture. In addition, no significant density-dependent changes in regioselectivity were observed for several other selected Diels-Alder reactions in CO_2 and the selectivities were similar to values obtained when performing the reactions in toluene at the same T (Renslo et al., 1997).

Weinstein and coworkers went on to study several carboxylation reactions, of which the only one found to proceed to appreciable yields in CO_2 was the Kolbe-Schmitt reaction. Lastly, they experimented with environmentally-benign heterogeneous catalysis in $scCO_2$ and found that silica slightly increased the reaction rate and selectivities of several Diels-Alder reactions (Weinstein, 1999). By way of adsorption isotherm studies, it was found that increased pressure inhibited the reaction rate, as reactants were partitioned from the catalyst surface to the CO_2-rich phase.

In a subsequent doctoral study in our group, Michael T. Timko (1998 –2004) (Timko, 2004) employed biphasic CO_2/H_2O mixtures as media for several model reactions. Timko, working with Professors Jefferson W. Tester and Kenneth A. Smith, routinely collaborated with Professors Rick L. Danheiser and Jeffrey I. Steinfeld of the MIT Chemistry Department.

Timko and coworkers used water to overcome solubility and reaction rate limitations associated with pure $scCO_2$ and to combine the unique solvation properties of each — all while maintaining an environmentally-benign reaction medium. Ultrasonic emulsification was used as an additive-free mechanical method of bringing CO_2- and H_2O-rich phases into intimate contact,

hence facilitating interfacial transport of reactants that partitioned between both phases. Given the importance of partitioning behavior in biphasic systems (e.g., for accurate reactor design and reaction rate analysis), they first measured the partition coefficients of several organic solutes and developed a linear solvation energy relationship capable of accurate predictions over a wide range of operating conditions (Timko, 2004).

Timko then developed an ultrasonic high-*P* reactor system capable of generating water-in-carbon dioxide and carbon dioxide-in-water microemulsions. The application of ultrasound to the reactor system was achieved by interrogation on of a titanium horn interfaced with a piezoelectric crystal and an electrical power supply. A schematic representation of emulsion formation in a CO_2/H_2O biphasic system is shown in **Figure 1-20**. Visual observation and turbidity measurements indicated that the emulsions were formed with a single ultrasonic pulse (of small minimal threshold power input, ca. 0.1 W cm^{-3}) and were stable up to 30 minutes, whereby they spontaneously phase split. Pulsing the medium regularly (e.g., every second) sustained the emulsion for up to several hours and was limited only by equipment failure (e.g., horn tip corrosion, piezoelectric crystal overheating, etc.). *In situ* video-enhanced microscopy was used to measure phase-specific droplet size distributions. The volume-surface area average diameter of H_2O droplets dispersed in the CO_2-rich phase (see **Figure 1-20a**) was 10 μm and 15 μm for CO_2 droplets dispersed in the H_2O-rich phase (see **Figure 1-20b**). Further characterization of the microemulsion size distributions revealed that sonication resulted in more than a 1000-fold increase in interfacial surface area.

Timko and coworkers went on to use ultrasonically-induced biphasic CO_2/H_2O microemulsions for several model benzoyl halide hydrolysis reactions in order to quantify reaction kinetics and transport effects (Timko et al., 2003; Timko, Diffendal et al., 2006). Benzoyl halides were essential water-insoluble, making the reactions impractical for large-scale production. Since many of the benzoyl halides were CO_2-soluble, and since water plays a chief role in hydrolysis reactions, these reactions were excellent candidates for study in CO_2/H_2O mixtures. Sonication accelerated the reaction rate for all systems studied, some up to 200 times faster when compared to reactions performed under silent conditions (i.e., without sonication). Rate enhancements were attributed to the increase in interfacial surface area achieved by the microemulsions. Physical models for both silent and sonicated conditions were also developed, which predicted the mass transport and reaction phenomenon taking place in these systems.

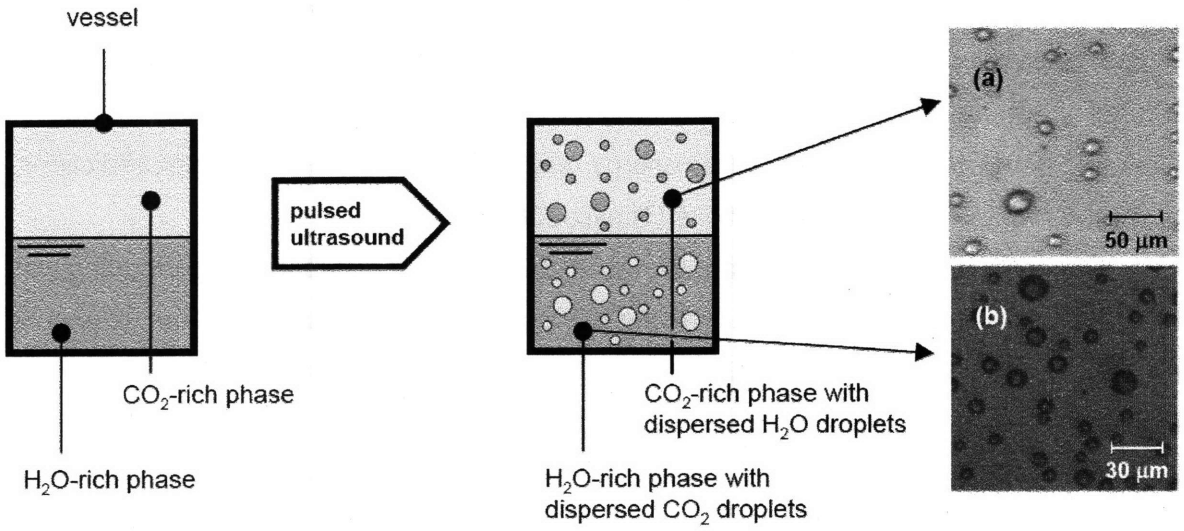

Figure 1-20. Schematic representation of a biphasic microemulsions formed by power ultrasound and representative micrographs of water-in-carbon dioxide **(a)** and carbon dioxide-in-water **(b)** microemulsions (micrographs adapted from Timko, 2004).

Timko and coworkers also studied the Diels-Alder cycloaddition of cyclopentadiene and methyl vinyl ketone (Timko, Allen, et al. 2006) and found that both sonication and the amount of water employed increased the reaction rate and selectivity between *endo* and *exo* adducts (see **Figure 1-21**). Similar to the benzoyl halide hydrolysis study, CO_2 served as a carrier of water-insoluble reactants to the water-rich phase where the reaction proceeded to a larger extent (the reaction rate constant in pure H_2O was found to be ca. 1000 times faster than in CO_2 under the same operating conditions). *Endo*:*Exo* selectivity ratios of 6 – 16 were obtained, which were intermediate to those of pure H_2O (ca. 20) and pure CO_2 (ca. 4). Given these results and considering the relatively slow reaction rate constant in pure CO_2 and reactant solubility limitations in pure H_2O, CO_2/H_2O microemulsions offered an attractive means for performing this and similar reactions.

Andrew J. Allen's master's thesis (2002 – 2004) (Allen, 2005) overlapped with the final stages of Timko's doctoral work. Allen focused initially on the previously-discussed sonically-enhanced Diels-Alder reaction in CO_2/H_2O mixtures. Allen and Timko at this time also worked with postdoctoral research assistant (2002 – 2003) Jin Qian on the pure CO_2 Diels-Alder study presented earlier in **Section 1.4.2.**

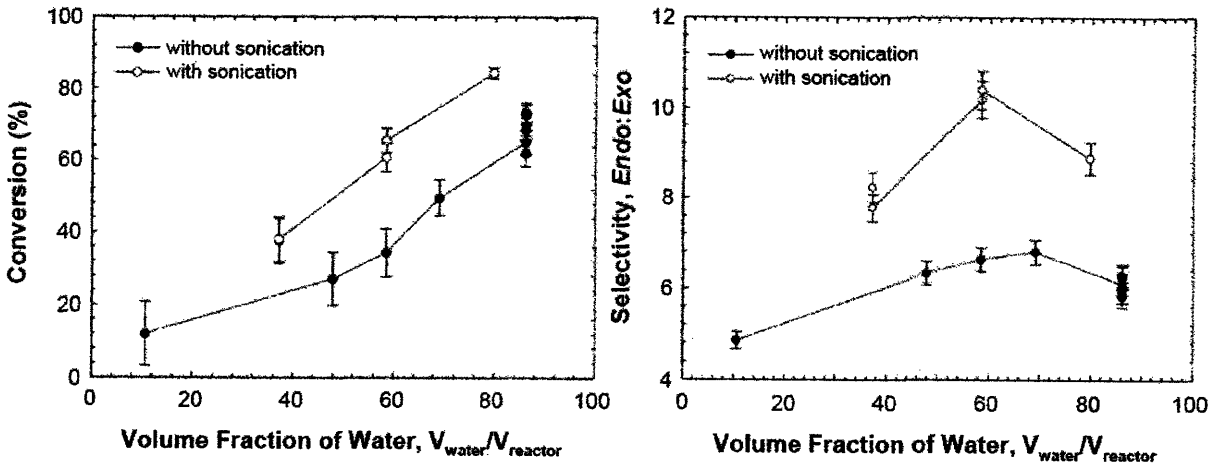

Figure 1-21. Experimental conversion *(left)* and selectivity data (*right*) for the Diels-Alder cycloaddition of cyclopentadiene and methyl vinyl ketone in a carbon dioxide/water mixture plotted as a function of water volume fraction with and without sonication (adapted from Timko, 2004). Reaction conditions: 303 K (30 °C), 80 bar, 20 kHz ultrasound frequency, 25 % duty (on a 1 s cycle), 0.55 W cm^{-3}.

1.7. The Cambridge-MIT Institute Partnership Program

Beginning in the Fall of 2003, the Tester and Danheiser groups engaged in a 3-year collaboration with Chemistry Professor Andrew B. Holmes of the University of Cambridge, UK under direct funding of the Cambridge-MIT Institute (CMI) Partnership Program. Formed in 2002 and ending in 2007, the CMI initiative supported multidisciplinary research efforts between MIT and the University of Cambridge, UK. In addition to providing financial support, the program focused on forming industrial partnerships for future funding purposes and also the potential commercialization of intellectual property.

Titled "Sustainable Chemical Processes in Environmentally-Friendly Media," our overall project objective was to develop a variety of synthetic reactions of importance to pharmaceutical and fine chemical industries in environmentally-benign reaction media and to develop new technologies that would provide a competitive edge to companies engaged these industry sectors. Specifically, our combined objectives were to:

1. develop methods and techniques for achieving important synthetic transformations in environmentally-friendly media;
2. establish the "added value" of the use of CO_2 and/or CO_2/H_2O microemulsions using physical methods of activation such as power ultrasound;

3. develop a thorough understanding of the phase behavior in CO_2 of the reactants and products employed in this study;
4. study the quantitative aspects of reaction kinetics and develop multi-scale models for predicting reaction rates and selectivity;
5. investigate the potential for rapid parallel synthesis in CO_2, and
6. identify ways in which this technology can be adopted by pharmaceutical and other industrial manufacturing processes.

Given the multidisciplinary aspects of the proposed work, Andrew J. Allen and I routinely collaborated with doctoral candidates Joshua R. Dunetz (2000 – 2005) and Xiao Yin Mak (2003 – present) of Professor Danheiser's synthetic organic chemistry group at MIT and Melanie W. S. Tsang (2003 – 2006) of Professor Holmes' chemistry group at the Universtiy of Cambridge.

CMI collaboration ended in the Spring of 2006 and resulted in several jointly-prepared peer-reviewed journal articles, patents, disclosure at scientific conferences, and specific engagement with industrial partners. Major technical achievements included:

1. the design and construction of several new high-*P* reactor, phase behavior, and sampling systems for carrying out exploratory and preparative reactions in CO_2 and CO_2-based media (MIT);
2. the "added value" of using CO_2 as a solvent was observed in the change in the regioselectivity in dipolar cycloadditions of nitrile oxides to alkenes and alkynes when compared with conventional solvents and for the control of diastereoselectivity in Lewis acid-mediated additions to allylic alcohols (Lee et al., 2005) (Cambridge, UK);
3. a preliminary study of batch and continuous flow coupling reactions in the presence of a solid-phase supported Pd catalyst demonstrated the potential for rapid parallel synthesis (Lee et al., 2004) (Cambridge, UK);
4. palladium-mediated C-C and C-X (X = heteroatom) coupling reactions were successfully performed in CO_2 (Smith et al., 2004) (Cambridge, UK);
5. a procedure for the preparation of substituted aromatic amines was developed using *N*-silyl aryl amines as precursors (Smith et al., 2005) (Cambridge, UK);

6. a general strategy was developed for achieving reactions of nucleophilic amines in supercritical carbon dioxide through "*in situ* protection" of the amines as carbamate derivatives (MIT);
7. demonstrated the utility of the in situ protection strategy by applying it in Pictet-Spengler synthesis of several classes of nitrogen heterocycles in CO_2-based media (Dunetz et al., 2005) (MIT);
8. identified and quantified phase behavior of reactions taking place in multiphasic CO_2-based media over a wide range of operating conditions (MIT), and
9. developed equation-of-state-based models to predict the dynamic partitioning of reactants in multiphasic CO_2-based media (MIT).

1.8. References

Abraham, M. A. and Moens, L., Eds. *Clean Solvents: Alternative Media for Chemical Reactions and Processing (ACS Symposium Series 819).* American Chemical Society: Washington, D.C., **2002**.

Adam, D. *Clean and green... but are they mean?* Nature, **2000**, *407*, 938-940.

Adams, D. J., Dyson, P. J., and Tavener, S. J. *Chemistry in Alternative Reaction Media.* Wiley: Chichester, **2004**.

Ahluwalia, V. K. *New Trends in Green Chemistry.* Kluwer Academic: Boston, **2004**.

Allen, A. J. *Green Chemistry: Dense Carbon Dioxide and Water as Environmentally Benign Reaction Media.* S. M. Thesis, Chemical Engineering Department, Massachusetts Institute of Technology, Cambridge, MA, **2004**.

Anastas, P. T. and Williamson, T. C., eds. *Green Chemistry: Designing Chemistry for the Environment* (ACS Symposium Series 626). American Chemical Society: Washington, D.C., **1996**.

Anastas, P. T. and Warner, J. C. *Green Chemistry: Theory and Practice.* Oxford University Press: New York, **1998**.

Anastas, P. T., and Williamson, T. C., Eds. *Green Chemistry: Frontiers in Benign Chemical Syntheses and Processes.* Oxford University Press: Oxford, **1998**.

Arai, Y., Sako, T., and Takebayashi, Y., Eds. *Supercritical Fluids: Molecular Interactions, Physical Properties, and New Applications.* Springer: Berlin, **2002**.

Baiker, A. *Supercritical Fluids in Heterogeneous Catalysis.* Chem. Rev. **1999**, *99*, 453-473.

Beckman, E. *Supercritical and Near-Critical CO_2 in Green Chemical Synthesis and Processing.* J. Supercrit. Fluids, **2004**, *28*, 121-191.

Brunner, G., Ed. *Supercritical Fluids as Solvents and Reaction Media.* Elsevier: Boston, **2004**.

Buncel, E., Stairs, R. A., and Wilson, H. *The Role of the Solvent in Chemical Reactions.* Oxford University Press: Oxford, **2003**.

Bundgen, P., Grein, F., and Thakkar, A. J. *Dipole and Quadrupole Moments of Small Molecules. An ab initio Study Using Perturbatively Corrected, Multi-Reference, Configuration Interaction Wave Functions.* J. Molec. Struc. (Theochem), **1995,** *334*, 7-13.

Clark, J. H. and Macquarrie, D., Eds. *Handbook of Green Chemistry and Technology.* Blackwell Science: Oxford, **2002**.

Clark, J. H. and Tavener, S. J. *Alternative Solvents: Shades of Green.* Org. Proc. Res. & Dev., **2007**, *11*, 149-155.

Clifford, T. *Fundamentals of Supercritical Fluids.* Oxford University Press: New York, **1999**.
Constable, D. J. C., Curzons, A. D., and Cunningham, V. L. *Metrics to 'Green' Chemistry — Which are the Best?* Green Chem., **2002**, *4*, 521-527.

Constable, D. J. C., Jimenez-Gonzalez, C., and Henderson, R. K. *Perspective on Solvent Use in the Pharmaceutical Industry.* Org. Proc. Res. & Dev., **2007**, *11*, 133-137.

DeSimone, J. M. and Tumas, W., Eds. *Green Chemistry using Liquid and Supercritical Carbon Dioxide.* Oxford University Press: New York, **2003**.

Dunetz, J. R., Ciccolini, R. P., Fröling, M., Papp, S. M., Allen, A. J., Holmes, A. B., Tester, J. W., and Danheiser, R. L. *Pictet-Spengler Reactions in Multiphasic Supercritical Carbon Dioxide/CO_2-Expanded Liquid Media. In Situ Generation of Carbamates as a Strategy for Reactions of Amines in Supercritical Carbon Dioxide.* Chem. Commun., **2005**, *35*, 4465-4467.

Eckert, C. A., Liotta, C. L., Bush, D., Brown, J. S., and Hallett, J. P. *Sustainable Reactions in Tunable Solvents.* J. Phys. Chem. B **2004**, *108*, 18108-18118.

Hobbs, H. R. and Thomas, N. R. *Biocatalysis in Supercritical Fluids, in Fluorous Solvents, and under Solvent-Free Conditions.* Chem. Rev. **2007**, *107*, 2786-2820.

Ikushima, Y., Ito, S., Asano, T., Yokoyama, T., Saito, N., Hatakeda, K., and Goto, T. *A Diels-Alder Reaction in Supercritical Carbon Dioxide Medium.* J. Chem. Eng. Jpn., **1990**, *23*, 96-98.

Ikushima, Y., Saito, N., and Arai, M. *Supercritical Carbon Dioxide as Reaction Medium — Examination of Its Solvent Effects in the Near-Critical Region.* J. Phys. Chem., **1992**, *96*, 2293-2297.

Jaeger, H. M., Swenson, D. W. H., and Dykstra, C. E. *Remarkable Features in the Interactions of Quadrupolar Molecules.* J. Phys. Chem. A., **2006,** *110*, 6399-6407.

Jessop, P. G., Ikariya, T., and Noyori, R. *Homogeneous Catalysis in Supercritical Fluids.* Chem. Rev. **1999**, *99*, 475-494.

Jessop, P. G. and Leitner, W., Eds. *Chemical Synthesis Using Supercritical Fluids.* Wiley-VCH: New York, **1999**.

Jessop, P. G., *Homogeneous Catalysis Using Supercritical Fluids: Recent Trends and Systems Studied.* J. Supercrit. Fluids **2006**, *38*, 211-231.

Jessop, P. G. and Subramaniam, B. *Gas-Expanded Liquids.* Chem. Rev., **2007,** *107*, 2666-2694.

Jimenez-Gonzalez, C., Curzons, A. D., Constable, D. J. C., and Cunningham, V. L. *Expanding GSK's Solvent Selection Guide — Application of Life Cycle Assessment to Enhance Solvent Selections.* Clean Techn. Environ. Policy, **2005**, *7*, 42-50.

Kauffman, J. F. *Quadrupolar Solvent Effects on Solvation and Reactivity of Solutes Dissolved in Supercritical CO_2.* J. Phys. Chem. A., **2001,** *105*, 3433-3442.

Kemmere, M. F. and Meyer, T., Eds. *Supercritical Carbon Dioxide in Polymer Reaction Engineering.* Wiley-VCH: Weinheim, **2005**.

Knez, Z., Skerget, M., Ilic, L., Lutge, C. *Vapor-Liquid Equilibrium of Binary CO_2-Organic Solvent Systems* J. Supercrit. Fluids, **2008**, *43*, 383-389.

Kopcak, U. and Mohamed, R. S. *Caffeine Solubility in Supercritical Carbon Dioxide/Co-Solvent Mixtures* J. Supercrit. Fluids, **2005**, *34*, 209-214.

Lee, C. K. Y., Holmes, A. B., Ley, S. V., McConvey, I. F., Al-Duri, B., Leeke, G. A., Santos, R. C. D., and Seville, J. P. K. *Efficient Batch and Continuous Flow Suzuki Cross-coupling Reactions under Mild Conditions Catalyzed by Polyurea-encapsulated Palladium(II) Acetate and Tetra-n-butylammonium Salts.* Chem. Commun., **2004**, *16*, 2175-2177.

Lee, C. K. Y., Holmes, A. B., Al-Duri, B., Leeke, G. A., Santos, R. C. D., and Seville, J. P. K. *Nitrile Oxide Cycloadditions in Supercritical Carbon Dioxide.* Chem. Commun., **2005**, *22*, 2622-2623.

Leitner, W. *Reactions in Supercritical Carbon Dioxide.* Topics in Current Chemistry (Vol. 206). Springer-Verlag: Berlin, **1999**.

Leitner, W. *Supercritical Carbon Dioxide as a Green Reaction Medium for Catalysis.* Acc. Chem. Res. **2002**, *35*, 746-756.

Licence, P. K., J., Sokolova, M., Ross, S. K., Poliakoff, M. *Chemical Reactions in Supercritical Carbon Dioxide: From Laboratory to Commercial Plant.* Green Chem., **2003**, *5*, 99-104.

Liu, C.-J., Mallinson, R. G., and Aresta, M., Eds. *Utilization of Greenhouse Gases (ACS Symposium Series 852).* American Chemical Society: Washington, D.C., **2003**.

Marcus, Y. *The Properties of Solvents.* Wiley: Chichester, **1998**.

Marcus, Y. *Solvent Mixtures: Properties and Selective Solvation.* Marcel Dekker: New York, **2002**.

Matsuda, T., Harada, T., and Nakamura, K. *Organic Synthesis using Enzymes in Supercritical Carbon Dioxide.* Green Chem., **2004**, *6*, 440–444.

McHardy, J. and Sawan, S. P., Eds. *Supercritical Fluid Cleaning: Fundamentals, Technology, and Applications.* Noyes: Westwood, **1998**.

McHugh, M. and Krukonis, V. *Supercritical Fluid Extraction, Second Edition.* Butterworth-Heinemann: Boston, **1994**.

Mesiano, A. J., Beckman, E. J., and Russell, A. J. *Supercritical Biocatalysis.* Chem. Rev. **1999**, *99*, 623-633.

Mikami, K., Ed. *Green Reaction Media in Organic Synthesis.* Blackwell: Oxford, **2005**.

Murrell, J. N. and Jenkins, A. D. *Properties of Liquids and Solutions.* Wiley & Sons: Chichester, **1994**.

Nelson, W. M., Ed. *Agricultural Applications in Green Chemistry (ACS Symposium Series 887).* American Chemical Society: Washington, D.C., **2004**.

Oakes, R. S., Clifford, A. A., and Rayner, C. M. *The Use of Supercritical Fluids in Synthetic Organic Chemistry.* J. Chem. Soc., Perkin Trans. **2001**, *1*, 917-941.

Poling, B. E., Prausnitz, J. M., and O'Connell, J. P. *The Properties of Gases and Liquids, Fifth Edition* McGraw-Hill: New York, **2001**.

Qian, J., Timko, M. T., Allen, A. J., Russell, C. J., Winnik, B., Buckley, B., Steinfeld, J. I., and Tester, J. W. *Solvophobic Acceleration of Diels-Alder Reactions in Supercritical Carbon Dioxide.* J. Am. Chem. Soc. **2004**, *126*, 5465-5474.

Rayner, C. M. *The Potential of Carbon Dioxide in Synthetic Organic Chemistry.* Org. Proc. Res. & Dev., **2007**, *11*, 121-132.

Reichardt, C. *Solvents and Solvent Effects in Organic Chemistry.* Wiley-VCH: Weinheim, **2003**.

Renslo, A. R., Weinstein, R. D., Tester, J. W., and Danheiser, R. L. *Concerning the Regiochemical Course of the Diels-Alder Reaction in Supercritical Carbon Dioxide.* J. Org. Chem., **1997**, *62*, 4530-4533.

Sakakura, T., Choi, J.-C., and Yasuda, H. *Transformation of Carbon Dioxide.* Chem. Rev., **2007**, *107*, 2365-2387.

Sheldon, R. A. *Consider the Environmental Quotient.* CHEMTECH, **1994**, *24*, 38-46.

Smith, C. J., Early, T. R., Tsang, M. W. S., Holmes, A. B., and Shute, R. E. *Palladium Catalyzed Cross-Coupling Reactions of Silylamines.* Chem. Commun., **2004**, *17*, 1976-1977.

Smith, C. J., Tsang, M. W. S., Holmes, A. B., Danheiser, R. L., and Tester, J. W. *Palladium Catalyzed Aryl Amination Reactions in Supercritical Carbon Dioxide. Org. Biomol. Chem.*, **2005**, *3*, 3767-3781.

Song, J., Hou, M., Jiang, T., Han, B, Li, X., Liu, Gang, and Yang, G. *Enhanceing Reaction Rate of Transesterification of Glycerol Monostearate and Methanol by CO_2.* J. Phys. Chem. A., **2007**, *111*, 12007-12010.

Steinfeld, J. I., Francisco, J. S., and Hase, W. L. Chemical Kinetics and Dynamics. Prentice Hall: Upper Saddle River, **1999**.

Subramaniam, B. and McHugh, M. A. *Reactions in Supercritical Fluids-A Review.* Ind. Eng. Chem. Process Des. Dev., **1986**, *25*, 1-12.

Subramaniam, B., Lyon, C. J., and Arunjatesan, V. *Environmentally Benign Multiphase Catalysis with Dense Phase Carbon Dioxide.* App. Cat. B: Environ. **2002**, *37*, 279–292.

Sun, Y.-P., Ed. *Supercritical Fluid Technology in Materials Science and Engineering: Syntheses, Properties, and Applications.* Marcel Dekker: New York, **2002**.

Tapia, O. and Bertran, J., Eds. *Solvent Effects and Chemical Reactivity.* Kluwer Academic: Dordrecht, **1996**.

Timko, M. T., Diffendal, J. M., Peters, W. A., Danheiser, R. L., Steinfeld, J. I., Smith, K. A., and Tester, J. W. *Ultrasonic Emulsification of Liquid, Near-Critical Carbon Dioxide-Water Biphasic Mixtures for Acceleration of a Hydrolysis Reaction.* J. Phys. Chem. A, **2003**, *107*, 5503-5507.

Timko, M. T. *Acoustic Emulsions of Liquid, Near-Critical Carbon Dioxide and Water: Application to Synthetic Chemistry through Reaction Engineering.* Ph.D. Thesis, Chemical Engineering Department, Massachusetts Institute of Technology, Cambridge, MA, **2004**.

Timko, M. T., Nicholson, B. F., Steinfeld, J. I., Smith, K. A., and Tester, J. W. *Partition Coefficients of Organic Solutes between Supercritical Carbon Dioxide and Water: Experimental Measurements and Empirical Correlations.* J. Chem. Eng. Data, **2004**, *49*, 768-778.

Timko, M. T., Allen, A. J., Danheiser, R. L., Steinfeld, J. I., Smith, K. A., and Tester, J. W. *Improved Conversion and Selectivity of a Diels-Alder Cycloaddition by Use of Emulsions of Carbon Dioxide and Water.* Ind. & Eng. Chem. Res., **2006**, *45*, 1594-1603.

Timko, M. T., Danheiser, R. L., Steinfeld, J. I., Smith, K. A., and Tester, J. W. *Reaction Rates in Ultrasonic Emulsions of Dense Carbon Dioxide and Water.* AIChE J., **2006**, *52*, 1127-1141.

Tundo, P. and Anastas, P., Eds. *Green Chemistry: Challenging Perspectives.* Oxford University Press: Oxford, **2000**.

United States Environmental Protection Agency (US EPA), *Toxic Release Inventory*, EPA Offices of Environmental Information, **2004**. Data accessed November **2006** via http://www.epa.gov/tri/.

United States Environmental Protection Agency (US EPA) Green Chemistry Program. Data accessed January **2008** via http://www.epa.gov/greenchemistry/pubs/whats_gc.html.

Weinstein, R. D., Renslo, A. R., Danheiser, R. L., Harris, J. G., and Tester, J. W. *Kinetic Correlation of Diels-Alder Reactions in Supercritical Carbon Dioxide.* J. Phys. Chem., **1996**, *100*, 12337-12341.

Weinstein, R. D. *Organic Synthesis in Supercritical Carbon Dioxide.* Ph.D. Thesis, Chemical Engineering Department, Massachusetts Institute of Technology, Cambridge, MA, **1998**.

Weinstein, R. D., Renslo, A. R., Danheiser, R. L., and Tester, J. W. *Silica-Promoted Diels-Alder Reactions in Carbon Dioxide from Gaseous to Supercritical Conditions.* J. Phys. Chem. B, **1999**, *103*, 2878-2887.

2. OBJECTIVES AND APPROACH

The goal of this work was to develop a detailed understanding of carbon-nitrogen (C-*N*) bond-forming reactions of amines carried out in supercritical and expanded-liquid carbon dioxide (CO_2) media. Key motivations behind this study were the importance of nitrogen-containing compounds in the pharmaceutical and fine chemical industries and a growing commercial interest in utilizing environmentally-friendly syntheses and processing with cost-efficient, green solvents. The thermodynamics and reaction engineering characteristics associated with the synthesis of several model C-*N* bond-forming reactions were examined both experimentally and theoretically. Operating conditions and engineering correlations were identified that will facilitate process scale-up and potential commercialization of these and other fundamentally-important CO_2-based processes. The end result of this research was the development of reaction processes that were not only attractive in terms of their synthetic chemistry and environmental attributes, but also from the standpoint of their practicality as feasible chemical processes. Specifically, the following research objectives were established:

2.1. Literature Assessment and Selection of Model Transformations

Objective 1: After reviewing the literature for reports of C-N bond-forming reactions in CO_2-based media, identify synthetic transformations of interest to the pharmaceutical and fine chemical industries that have not been previously studied in this media.

Given our lab's limited research experience with C-*N* bond-formation in CO_2-based media prior to this work, we began by performing a thorough review of the existing literature. Careful consideration of both the literature and needs of the pharmaceutical and fine chemical industries revealed several opportunities for exploration. One opportunity was the development of CO_2-based processes for the syntheses of a class of pharmaceutically-significant molecules known as nitrogen heterocycles (see **Chapter 4**). The identification of and decision to study these transformations was driven largely by suggestions from Professor Danheiser and Josh Dunetz, with selected input from others on the CMI team. Specifically, we selected three effective and conventional reaction methods that afforded this important class of molecules:

1. **The Pictet-Spengler Reaction:** the synthesis of tetrahydroisoquinolines via the condensation of β-arylethylamines with aldehydes in the presence of acid. We also extended the reaction to the synthesis of tetrahydro-β-carbolines via the condensation of β-indolylethylamines (see **Chapter 5**);
2. **The Larock Indole Synthesis:** the synthesis of indoles via the reaction of ortho-iodoanilines and disubstituted alkynes in the presence of a palladium catalyst and base (see **Chapter 8**), and
3. **Lactam Synthesis:** the synthesis of lactams via the cyclization of aminoketenes (see **Chapter 9**).

We also decided to study two other C-*N* bond-forming reactions that were relevant to the pharmaceutical and fine chemical industries:

4. **Carbamate Synthesis:** the synthesis of carbamates via the reaction of amines with carbon dioxide and dialkyl carbonates (see **Chapter 7**), and
5. **Amide Synthesis:** the synthesis of amides via the reaction of amines with ketenes (see **Chapter 9**).

A summary of the model transformations investigated in this work is provided in **Table 2-1**.

2.2. Expansion of Experimental and Analytical Capabilities

Objective 2: To design and construct the necessary reactor systems and sampling methods capable of performing desired synthetic reactions and phase-behavior studies over a wide range of operating conditions in supercritical and expanded-liquid CO_2 media.

Prior group research experience underscored the importance of characterizing phase behavior and mixing for reactions taking place in CO_2-based media. This need, coupled with the state of our experimental capabilities at the onset of this work, made it necessary to update much of Weinstein's original CO_2 delivery and reaction system. A newly-designed CO_2 delivery, reaction, and phase-behavior system was therefore developed (see **Chapter 3**). All reactors and phase-behavior units were equipped with co-axial visual access, mechanical, magnetic, ultrasonic, and/or recirculatory mixing, *T* control, *T* and *P* data acquisition, and capable of operating up to ca. 400 bar (6015 psia) at 150 °C. At-condition sampling methods were used in

conjunction with a newly-assembled High-Pressure Liquid Chromatography (HPLC) system to quantify species distributions during reaction and phase-behavior studies.

2.3. Experimental Reaction Screening and Process Engineering

Objective 3: To extensively characterize and optimize selected transformations by applying fundamental chemical engineering principles at the reaction screening and process engineering levels.

Several screening experiments were performed to assess the feasibility of using CO_2 as a medium for the proposed model C-*N* bond-forming reactions. The focus of this step was to quantify product distributions under conditions of complete reactant conversion. Importantly, screening studies revealed process engineering issues that warranted further study (e.g., system phase-behavior, solubility limitations, competitive byproduct formation reaction pathways, etc.). Provided reasonable reaction performance (e.g., $\geq$ 50% molar yield at complete conversion), reactions were selected for further investigation and subjected to rigorous studies pertaining to reaction engineering and thermodynamics. That is, reaction rates, conversion, selectivity, dynamic phase equilibrium and phase-specific species partitioning were examined all as a function of process operating conditions. In most cases, reactions were successfully optimized for application in CO_2-based media.

2.4. Thermodynamic and Quantum Chemical Kinetic Modeling

Objective 4: To develop a theoretical equation-of-state-based vapor-liquid equilibrium model and an ab initio quantum chemical kinetic model to facilitate experimental design and results interpretation.

Equation-of-state-based VLE models were constructed and used in combination with phase equilibrium data to predict the experimentally-observed phase-partitioning phenomena observed during carbamate (see **Chapter 6**) and amide synthesis (see **Chapter 9**). *Ab initio* quantum chemical kinetic models based on transition state theory were developed and qualitatively justified experimental global reaction rates and product selectivity data (see **Chapter 10**). Combined, these models were successful at predicting the effect of process

operating conditions on the phase-behavior and relative reaction rates of selected transformations in CO_2-based media.

Table 2-1. Model transformations selected for study in carbon dioxide-based media.

The Pictet-Spengler Reaction

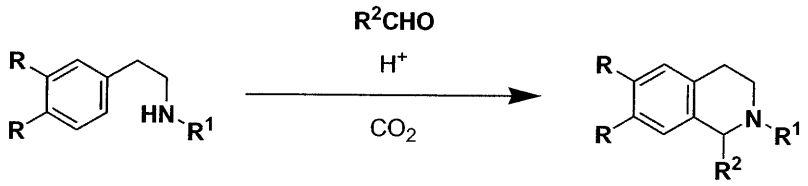

The Larock Indole Synthesis

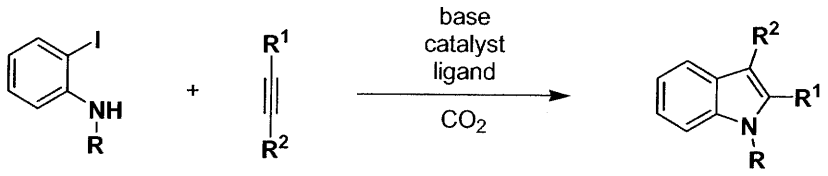

Lactam Synthesis

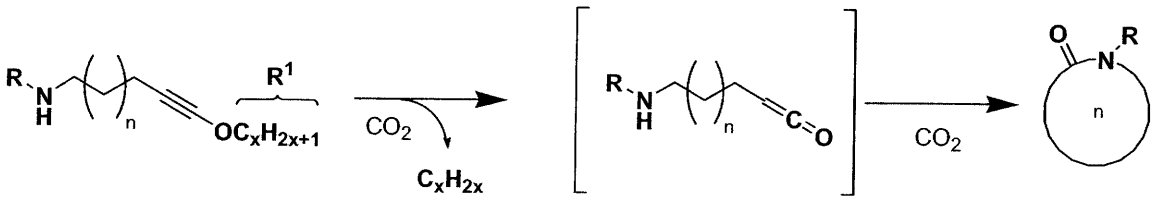

Carbamate Synthesis

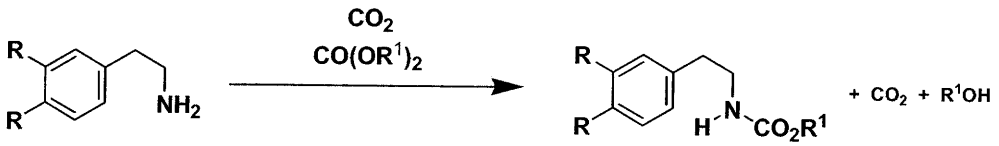

Amide Synthesis

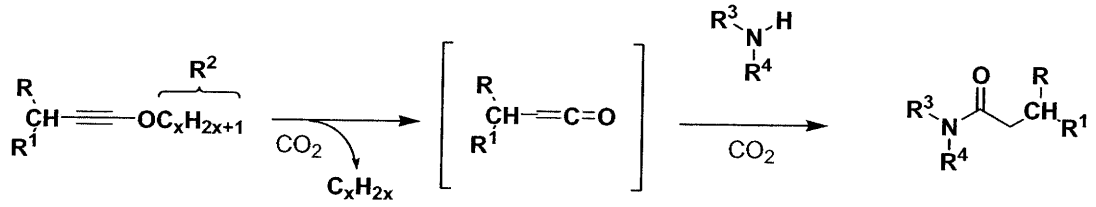

3. EXPERIMENTAL EQUIPMENT AND PROCEDURES

3.1. Motivation

Weinstein (1998) was the first member of our research group to explore the use of $scCO_2$ for organic syntheses and was responsible for the design and construction of our 'first generation' $scCO_2$ Delivery and Reaction System (G1 System). The chief components of Weinstein's apparatus included several custom-designed, MIT- fabricated view cells (ca. 25-mL volume) and a 1-L off-the-shelf stirred-tank reactor. Weinstein's system was slightly modified by Timko (2004) to include an ultrasonic reactor and an apparatus that measured solute partition coefficients in biphasic media. Details of the G1 System including all reaction vessels are well-documented in the doctoral theses of Weinstein and Timko.

At the start of this doctoral work, the G1 System — an excellent design at the time of its original construction and capable of producing accurate kinetic and thermodynamic data — was over 15 years old and in need of redesign and upgrading (see **Figure 3-1**). Specifically, a large portion of the piping infrastructure was inaccessible, with many lines either damaged or completely out of service. The G1 System also lacked a data acquisition (DAQ) system that would enable the user to continuously log *T*-*P*-time data for extended experiments.

Given the physical space constraints of the G1 System, it was difficult to add new pieces of equipment to the existing infrastructure. In addition, the G1 System's safety enclosure had been removed to accommodate additional equipment. A satellite enclosure was constructed as a quick fix to some of these problems and was used to house Weinstein-type view cells (see **Figure 3-2**) in the early phase of this research. Experimentation with these cells revealed several areas for improvement, as the vessels were (1) heavy and bulky due to their thick-walled stainless steel (SS) design, (2) damaged and had stripped ports and fittings that required refashioning, (3) tedious to heat isothermally given their irregular geometry, (4) difficult to agitate due to their narrow internal diameters, and (5) not easily visually-accessible because of their single (rather than coaxial) window design. In addition, it was difficult to seal the cells, as they often required rigorous polishing of their sealing surfaces, the delicate positioning of a custom-

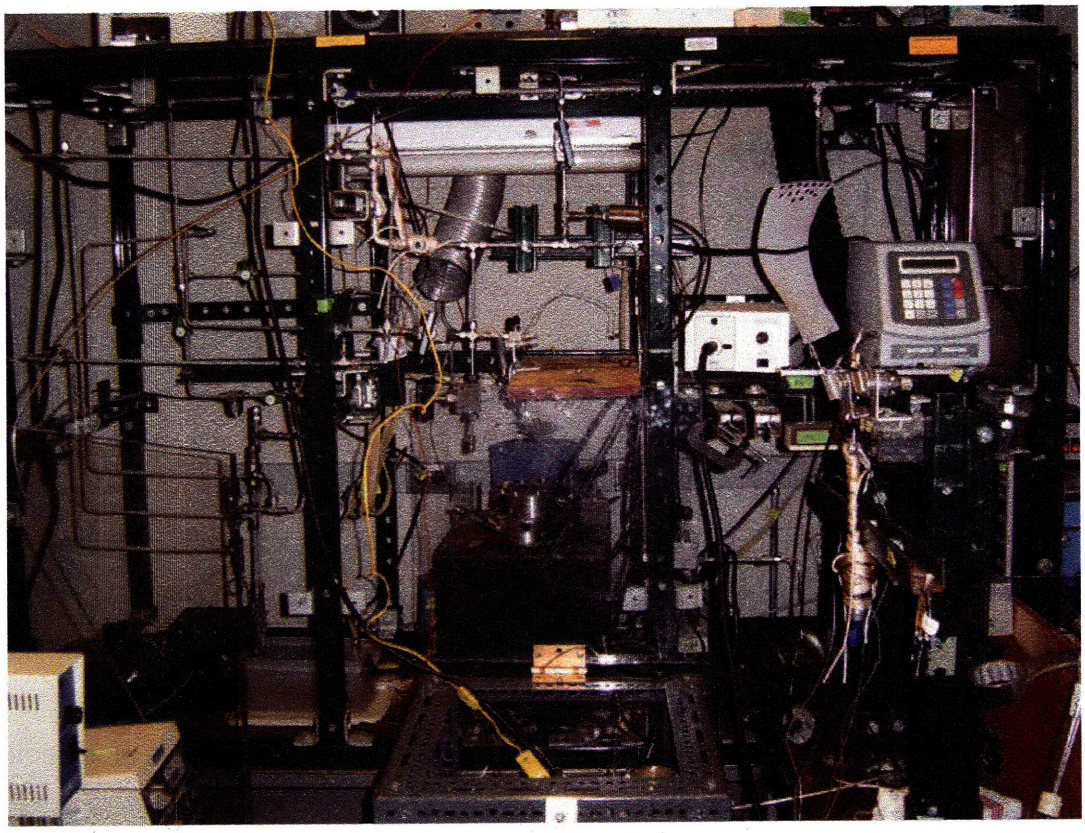

Figure 3-1. Photograph of the Tester Group's 'first generation' CO_2 Delivery and Reaction System at the start of this work, ca. May 2004 (photo/ Ciccolini).

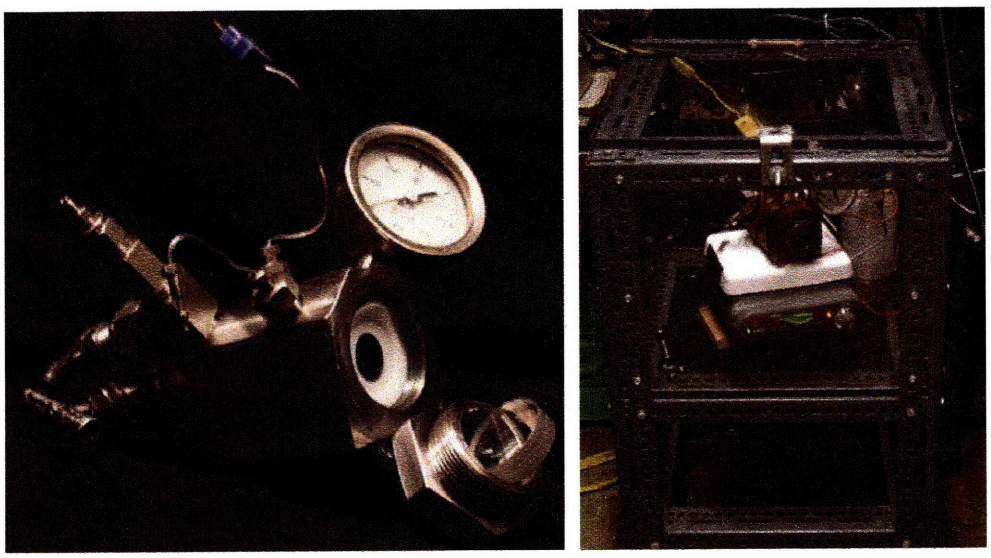

Figure 3-2. *Left:* Photograph of a typical view cell used in the theses of Weinstein (1998) and Timko (2004); view cell designed by Weinstein (1998) (photo/ Timko [2004]). *Right:* satellite enclosure designed and constructed in this work to utilize this and similar vessels (photo/ Ciccolini).

made Teflon® gasket (which frequently deformed and leaked at elevated *T*), and a large torque requirement on the cap to make the window/gasket seal.

In addition to replacing the G1 view cells, we also decided to forgo the use of other previously-designed vessels. For instance, it was not feasible to conduct reactions at a scale suitable for Weinstein's 1-L reactor since many of the compounds we selected for study were not commercially-available and required labor-intensive syntheses with only small amounts of reactants for study. The 1-L vessel was also less desirable due to its lack of visual access. Timko's ultrasonic reactor was redesigned for three main reasons: (1) due to its mass and difficulties in loading, (2) its rectangular geometry made it difficult to heat via an external source, and (3) it was unable to operate in the *P-T* regime of interest to this research.

3.2. The $scCO_2$ Delivery, Reaction, and Phase Behavior System

Motivated by limitations of the G1 System and using valuable knowledge documented by Weinstein and Timko, we decided to redesign and rebuild the experimental equipment to improve our ability to perform, observe, monitor, and analyze reaction and phase-behavior phenomena proceeding in CO_2 and CO_2-based media. The components and applications of the Tester Group's 'second generation' $scCO_2$ Delivery, Reaction, and Phase Behavior System (G2 System) are summarized below:

- **A high-pressure manifold** (see **Section 3.2.2**), used to deliver CO_2 and Argon (Ar) to reaction and phase behavior systems;
- **Three view cells** (see **Section 3.2.3**), (two 25-mL and one 50-mL) and their associated piping systems, used for reaction screening and for all syntheses. The cells and their piping configurations were often modified to accommodate phase-behavior studies (e.g., mixture critical point determination via cloud-point measurements). Due to their relatively small size, view cells were used for reaction and phase-behavior studies that did not involve at-condition aliquot sampling. Instead, these systems were monitored by *in situ* (e.g., UV/Vis spectroscopy and visual inspection) or post-reaction (e.g., HPLC) methods;
- **One reactor** (see **Section 3.2.4**), (100-mL) — equipped with additional ports and a more vigorous mechanical mixing system than the view cells — used for reaction

or phase-behavior experiments that required at-condition, phase-specific sampling;

- **A sight gauge** (see **Section 3.2.5**), used to quantify the volume expansion of CXLs, and
- **An ultrasonic view cell** (see **Section 3.2.7**), (a view cell equipped with an ultrasonic horn) used to generate emulsions, thereby facilitating mixing in multiphasic CXL systems. In order to insert the horn into the vessel, a custom high-*P* adapter was designed and constructed.

All of the reactor and phase-behavior vessels were capable of operating up to ca. 400 bar (6000 pisa) and 150 °C and were equipped with co-axial sapphire windows, the appropriate instrumentation to allow continuous *T* and *P* data acquisition (DAQ), and were enclosed by thick-walled plastic (Lexan®) safety shielding. In addition, all vessels, fittings, and piping sections of the G2 System were of 316 SS construction.

Several sampling and analytical methods and their associated equipment were also developed and included:

- **Two at-condition sampling/injection units** (see **Section 3.3.1**), used to procure phase-specific aliquots for further analysis or to inject liquids into vessels that were at elevated *T* and *P*;
- **An inverted-buret apparatus** (see **Section 3.3.2**), used to identify liquid-phase concentrations of CO_2 in CXLs;
- **A volume determination apparatus** (see **Section 3.3.3**), used to determine vessel and piping system volumes;
- **An off-gas detection unit** (see **Section 3.3.4**), used to measure the evolution of CO_2 from reaction mixtures, and
- **One High-Pressure Liquid Chromatography system (HPLC)** (see **Section 3.3.5**), consisting of hydrocarbon (C-18) and silica (Si) chromatography columns, column heater, dual-pump mobile phase delivery system, UV/Vis absorbance detector, and autosampler. Methods were developed that allowed for the quantification of product distributions for several model syntheses.

The G2 System, shown in **Figure 3-3**, was divided into three bays that each interfaced with the high-*P* manifold and DAQ system:

1. **A view cell bay**, which contained all of the view cell systems. This bay was used for all synthetic work and also for phase-behavior studies that involved view cells;
2. **A reactor bay**, which contained the reactor system and mainly used for phase-behavior studies, and
3. **An ultrasound bay**, which contained the ultrasound view cell. This bay was used proof-of-concept studies that involved emulsion formation in CXLs.

Not shown in **Figure 3-3** are the sight gauge, volume determination, and off-gas apparatuses that were connected to the G2 System manifold and located in an adjacent fume hood. Also not shown are the sampling/injection units and inverted-buret gas measurement apparatus, which were connected to the G2 System when needed.

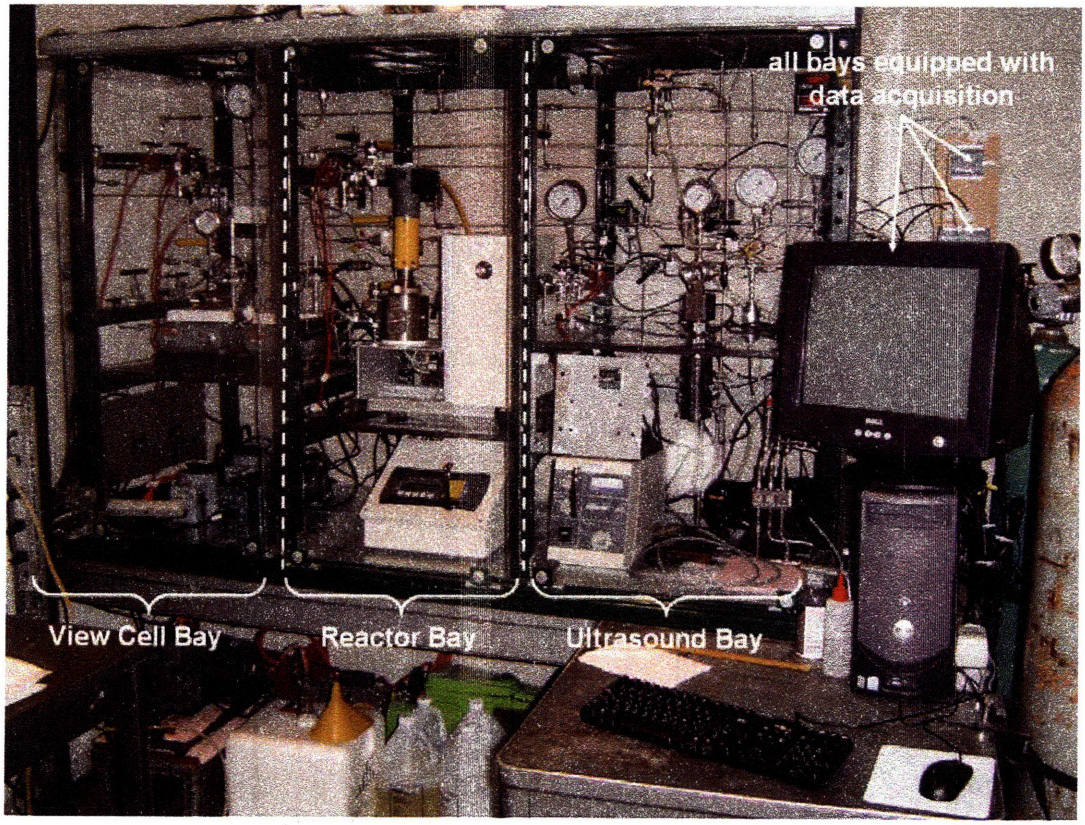

Figure 3-3. Photograph of the Tester Group's 'second generation' CO_2 Delivery, Reaction, and Phase Behavior System designed and constructed for this work (photo/ Ciccolini).

3.2.1. Data Acquisition System

We chose to integrate data acquisition into the G2 System because in addition to adding completeness to the design, it was especially important for troubleshooting equipment failure (e.g., overnight leaks) and for comparing operating conditions for multiple runs (e.g., *P-T*-time profiles). In general, DAQ for the G2 System was achieved by wiring pressure transducers and thermocouples to respective acquisition modules and interfacing these modules with a desktop computer via the universal serial bus (USB).

Temperature data were acquired by connecting one of the two output terminals of a J-type dual-element thermocouple (Omega, *SIC316SS-062U-6-DUAL*) to a temperature-specific acquisition module (Measurement Computing, *USB-TC*) via J-type thermocouple wire (Omega, *EXPP-J-20-TWSH-50*). Dual-element thermocouples were in order, as *T* readings were sent to multiple devices (e.g., one signal sent to the DAQ system, and the other to a control system). Splicing the output line of a single-element thermocouple was a crude substitute for the dual-output approach that often led to erroneous or fluctuating *T* readings. Pressure data was acquired by connecting the output terminal of a pressure transducer (Newark, *MSP-300 series*) to an acquisition module that accepted a direct current voltage (VDC) signal (Measurement Computing, *USB-1208FS*) via 18-gauge electrical wire. *P* transducers were powered with a 5 VDC (@ 500 mA) barrier strip-style power supply (Omega, *PSS-5A*).

Both DAQ modules were separately connected to a computer (Dell, *Dimension 1100n*) via the USB and interfaced with *TracerDAQ* acquisition software (Measurement Computing). *TracerDAQ* provided a user-friendly graphical user interface (GUI) and real-time and continuous logging of *P-T* data for the entire G2 system.

Nearly all DAQ connections to the G2 System were fully detachable (via quick-connects) so that vessels could be relocated. Detailed wiring diagrams for the *P* transducers, thermocouples, and DAQ modules are provided in their respective owner's manuals.

3.2.2. High-Pressure Manifold

A detailed piping and instrumentation diagram (PID) for the high-pressure manifold is shown in **Figure 3-4**. A legend for the symbols used in this all PIDs presented in this chapter can be found in **Table 3-2** of **Section 3.6**. The basic framework of the manifold closely resembled Weinstein's original G1 System design.

'Supercritical fluid extraction (SFE)/chromatography (SFC)-grade' (99.9999% purity) liquid carbon dioxide (Airgas, *CD SFC15AS*) was supplied from a cylinder at a pressure corresponding to its vapor pressure at ambient *T* (ca. 940 psia [65 bar] at 298 K [25 °C]) and entered the manifold via a dip tube and SFE/SFC transfer kit (**RG-1**; Airgas, *Y99TP14C320K*). The pressure of the cylinder remained essentially constant (at the vapor pressure corresponding to ambient *T*) and decreased only when nearly all of the liquid contents were removed. Consumption was monitored by a household-type balance and the cylinder was replaced when approximately 5% of the liquid remained (the tare mass of CO_2 within a new cylinder was ca. 39 lbs.). Cylinder *P* was monitored by a pressure gauge (**PI-1**; Swagelok, *PGI-100B-PG3000-LAOX*, ca. 0–200 bar [0–3000 pisa] span, accuracy ± 1% of span [2 bar or 30 pisa]) and a DAQ-interfaced transducer (**PT-1**; Newark, *MSP-300-2K5-P-4-N-1*, accuracy ± 1% of span [1.7 bar or 25 pisa]). Cylinder *T* was measured by a J-type dual-element thermocouple (**TI-1**; Omega, *SIC316SS-062U-6-DUAL*, accuracy ± 0.1 °C) interfaced with both a local digital display (Omega, *DP460*) and the DAQ system.

Prior to compression, it was necessary to subcool the CO_2, as potential vaporization would lead to cavitation within the pump (*vide infra*). CO_2 was therefore cooled in a custom-built counter-current shell-and-tube heat exchanger (**HX**) consisting of a process-side 1/4-in. pipe placed concentrically within a 1/2-in. pipe. The total length of the exchanger (ca. 6 ft.) was insulated with flexible polyethylene foam rubber insulation (McMaster-Carr, *4530K122*). Off-the-shelf antifreeze coolant at 273 K (0 °C) was supplied to the annulus of the exchanger via a refrigerated circulating bath at a rate of 15 $L \cdot min^{-1}$ (**CH**; Cole-Parmer, *01268-14*). The *T* of the cooling bath was monitored with a mineral spirit-filled general-purpose thermometer (**TI-4**; VWR, *61066-126*, accuracy ± 1 °C). The *P* and *T* at the exchanger outlet were measured by a pressure gauge (**PI-2**; [identical to **PI-1**]) and thermocouple (**TI-2**; [identical to **TI-1**]) interfaced with a local digital display (Omega, *CN9121A*). Exit temperatures of 283 K (10 °C) were typically observed.

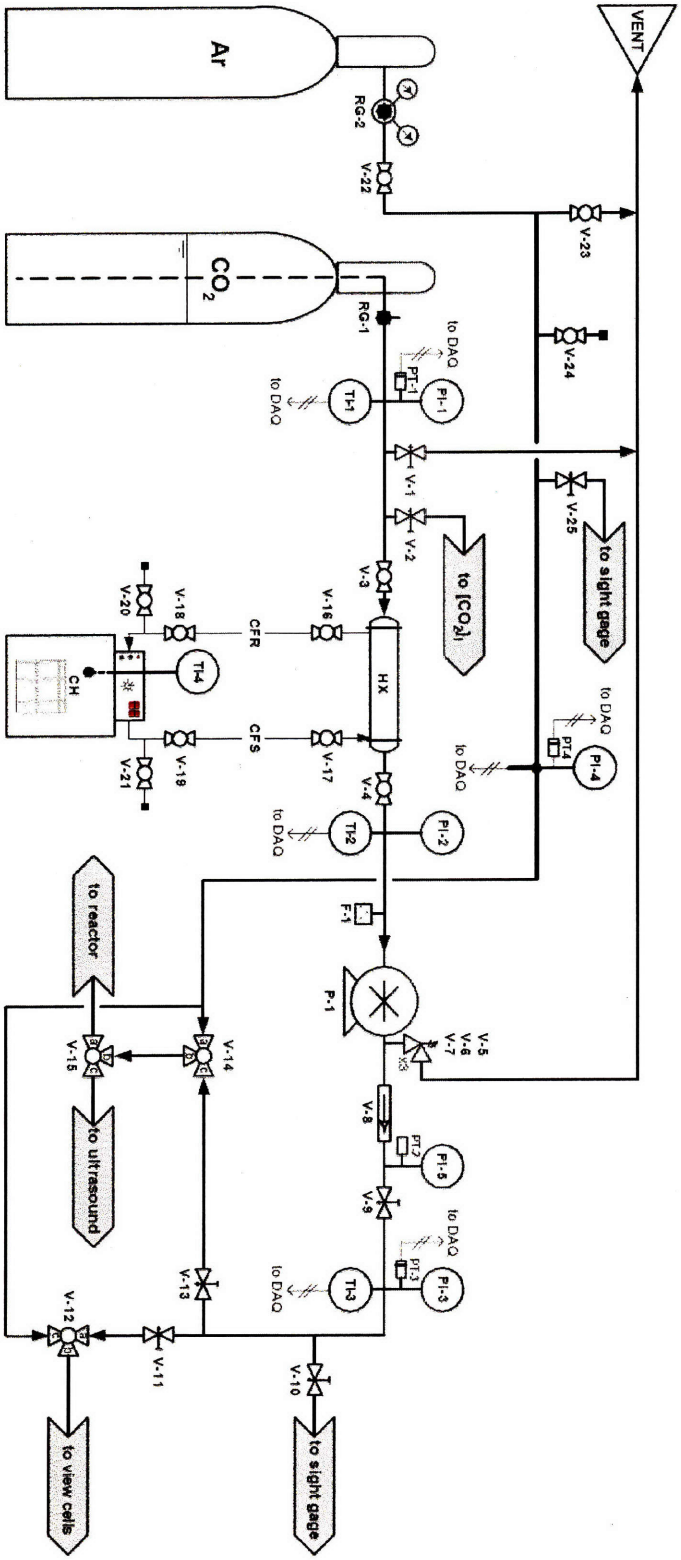

Figure 3-4. Piping and instrumentation diagram for the high-pressure manifold. A list of all piping and instrumentation symbols for this and all other diagrams of this type can be found in **Section 3.6**.

Chilled CO_2 was directed to a filter (**F-1**; Swagelok, *SS-4TF-7*) equipped with a 7-μm filter element (Swagelok, *SS-4F-K4-7*) before entering a positive-displacement reciprocating triple-piston metering pump (**P-1**; Eldex, *BBB-4*) that was capable of compression to ca. 414 bar (6000 pisa) at 100 mL·min^{-1}. The filter prevented particulates from clogging the pump inlet and potentially damaging the delicate sapphire pistons. Spring-loaded pressure relief valves (Swagelok, *SS-4R3A*) were set to 414 bar (via calibration by a pressure gauge and a manual pressure generator) and placed on each of the three pump heads. In the case of overpressurization, the valves opened and released the line contents to a dedicated vent line that was connected to the building's ventilation system. The pump heads typically heated during operation due to mechanical friction associated with gear and piston movement, leading to a 10 °C increase in *T*. Had the CO_2 not been chilled before entering the pump, vaporization would have likely to occurred, hence making it more difficult for a pump of this design to attain a desired *P*. Crushed ice (obtained from an ice machine located basement of Building 18) was often compacted around the pump head casing to further suppress frictional heating. A check valve (Swagelok, *SS-CHS4-1*) was placed at the exit of the pump to prevent contamination of the CO_2 cylinder by downstream chemical processing. The *P* at the pump outlet was measured by a pressure gauge (**PI-3**; Swagelok, *PGI-100B-PG6000-LAOX*, ca. 0–414 bar [0–6000 pisa] span, accuracy ± 1% of span [4 bar or 60 pisa]) and a DAQ-interfaced transducer (**PT-3**; Newark, *MSP-300-05K-P-4-N-1*, accuracy ± 1% of span [3.5 bar or 50 pisa]). The *P* was also displayed digitally (**PI-5**; Dynisco, *uPR 690*) via transducer (**PT-2**; Dynisco, G*832-000-3.5M*, ca. 0–240 bar [0–3500] span, accuracy ± 0.15% of span [0.4 bar or 5 pisa]). The *T* was measured by a thermocouple (**TI-3**; [identical to **TI-1**]) interfaced with a local digital display (identical to **TI-1**).

The G1 System manifold system was expanded to also deliver Argon, which was used to create inert environments prior to reaction and phase behavior studies, and for vessel volume determinations. 'Research Plus-grade' (99.9999% purity) gaseous Argon (Airgas, *AR RP300*) was supplied from a cylinder at ca. 175 bar (2640 pisa) at ambient *T* and entered the manifold via a pressure regulator (**RG-2**; Matheson Tri-Gas, *3040-CGA*). Cylinder *P* was monitored by a pressure gauge (**PI-4**; [identical to **PI-1**]) and a DAQ-interfaced transducer (**PT-4**; [identical to **PT-1**]). Temperature was measured by a J-type single-element thermocouple (Omega, *GJMQSS-062G-6*, accuracy ± 0.1 °C) interfaced with the DAQ system only. When needed, the G2 System was vented by opening **V-1** (CO_2 lines) and **V-23** (Ar lines).

General Operating Procedures

Compressed carbon dioxide was supplied to the manifold by performing the following steps:

1. opening the CO_2 cylinder **RG-1** valves;
2. powering the chiller and allowing the bath to reach a desired set-point temperature of 0 °C;
3. adding and compacting crushed ice around the heads of **P-1**, and
4. turning **P-1** on until a desired pressure was reached.

Argon was supplied to the manifold by opening the Ar cylinder valve and adjusting **RG-2** to the desired pressure. The Ar line *P* was usually maintained at ca. 35 bar (500 psia).

3.2.3. View Cells

View cells were used for reaction screening and for all synthetic work and were often reconfigured to accommodate phase-behavior studies (**Section 3.2.6**). A detailed PID for the view cells system is shown **Figure 3-5**. The system was divided into two identical sub-systems, with each capable of servicing one cell. The system's symmetric design afforded easy access, parallel processing, and the seamless interchanging of vessels and auxiliary equipment.

Two 25-mL (nominal) (**VC-1** and **VC-2**; Thar Technologies, *05422-2*) and one 50-mL (nominal) (**VC-3**; Thar, *05422-3*) off-the-shelf view cells were used in this study. The vessels were of cylindrical 316 SS construction, with the 25 mL-cells measuring 3.8 in. x 1.2 in. ID x 2.0 in. OD and the 50 mL-cell measuring slightly longer in length at 5.2 in. The vessels came standard with three 1/8-in. female national pipe thread (FNPT) ports and allowed visual access via two 1.25-in. coaxial window assemblies (1-in. viewable diameter). The assemblies were fully-removable and were the primary means of loading and unloading materials to and from the vessel. Each window assembly was comprised of a sapphire window (Thar, *03192*), fluoropolymer-encapsulated viton o-ring (McMaster-Carr, *93445K218*), and cap (Thar, *03218*). The seal was made by compressing the o-ring to the vessel's internal sealing surface with the cap and window via a 1.5-in. spanner wrench (Thar, *03224*). A variety of seal materials were investigated and it was found that the fluoropolymer encapsulated-type offered the best corrosion and deformation resistance.

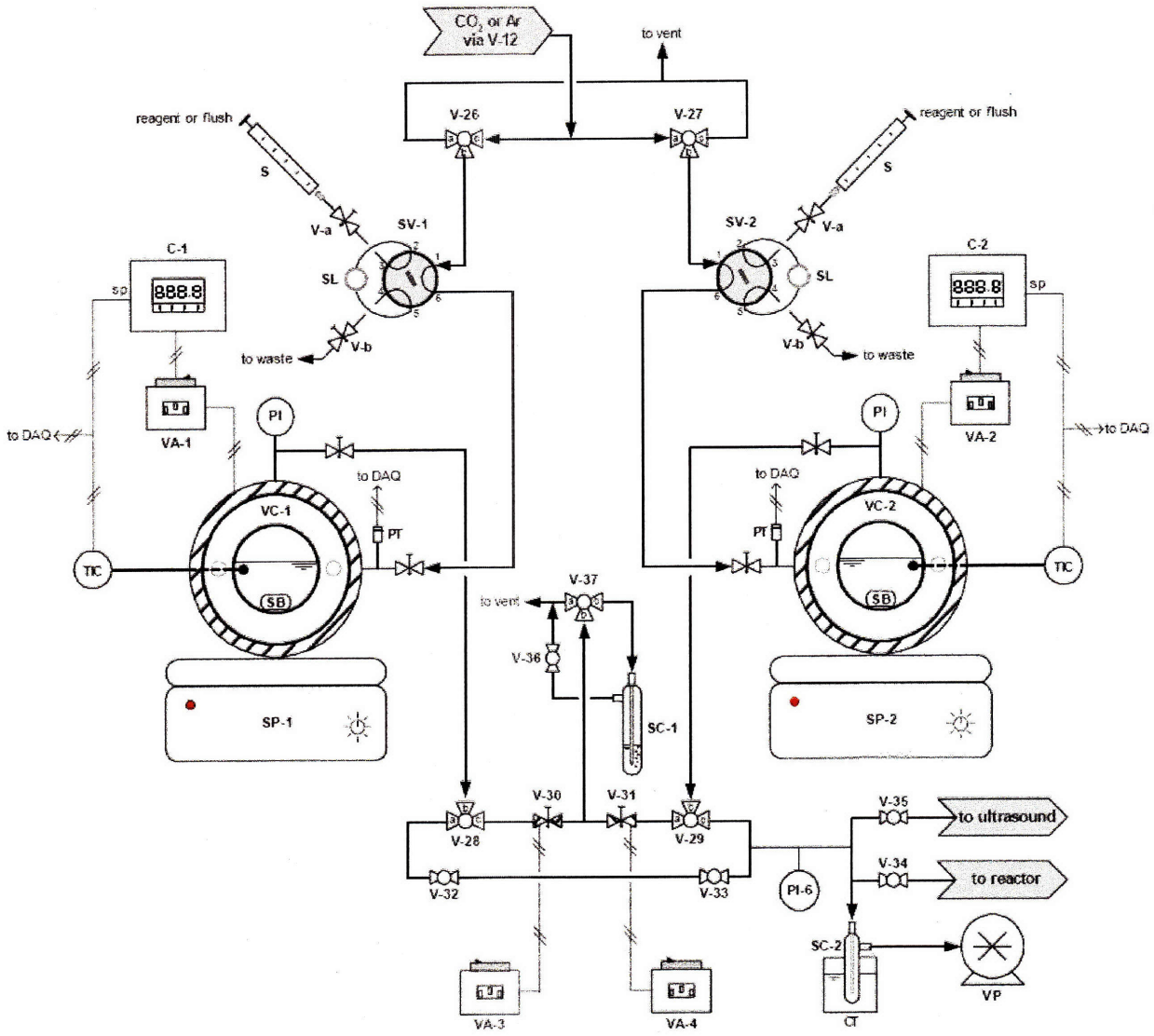

Figure 3-5. Piping and instrumentation diagram for the view cell systems.

A manufacturer (Thar Technologies) cut sheet that provides additional dimensions, port orientations, and the sealing configuration for the cells is provided in **Figure 3-6**.

The manufacturer-specified maximum allowable working pressure (MAWP) of the cells was 414 bar (6000 pisa) at 423 K (150 °C). The maximum allowable working conditions for the SS vessel were determined from wall thickness, sealing surface area, and deformation of o-rings at elevated *T*. Higher-*P* cells (MAWP of 689 bar [10,000 pisa]) were available, but required the use of smaller windows (5/8-in. viewable diameter) that would have restricted visual access, making phase behavior characterization more difficult.

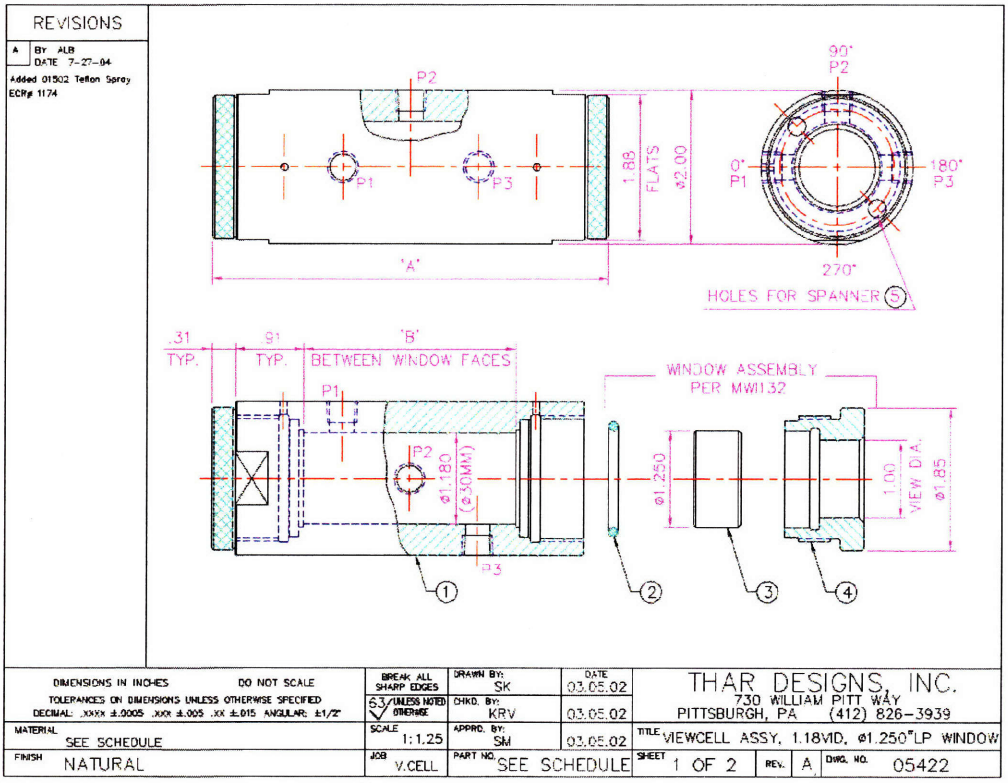

BILL OF MATERIALS / VIEWCELL ASSEMBLY AND QTY. SCHEDULE

ITEM	DESCRIPTION	DWG#	PART#	05422-1	05422-2	05422-3	05422-4	05422-5
1	VIEWCELL BODY, 10ML, 1.18VID, ø1.250" LP WINDOW	05421	05421-1	1	--	--	--	--
	VIEWCELL BODY, 25ML, 1.18VID, ø1.250" LP WINDOW	05421	05421-2	--	1	--	--	--
	VIEWCELL BODY, 50ML, 1.18VID, ø1.250" LP WINDOW	05421	05421-3	--	--	1	--	--
	VIEWCELL BODY, 100ML, 1.18VID, ø1.250" LP WINDOW	05421	05421-4	--	--	--	1	--
	VIEWCELL BODY, 250ML, 1.18VID, ø1.250" LP WINDOW	05421	05421-5	--	--	--	--	1
2	ORING, #218 TEFLON ENCAPSULATED SILICONE	--	04316	2	2	2	2	2
3	WINDOW, 1.250" DIA. LP SAPPHIRE	03192	03192	2	2	2	2	2
4	WINDOW NUT, 1.250" DIA. LP	03218	03218	2	2	2	2	2
5	WRENCH, SPANNER, 1.50" PIN CENTERS	--	03224	1	1	1	1	1
6	SPRAY, TFE DRY LUBRICANT, 10 OZ (Not Shown)	--	01502	1	1	1	1	1

VIEWCELL SPECIFICATIONS

ASSEMBLY			DIMENSIONS		PORTS			MATERIALS		PRESSURE RATING
PART#	VOLUME	WEIGHT LBS	'A'	'B'	P1	P2	P3	VIEWCELL BODY	WINDOW NUT	MAWP
05422-1	10ML	1.73	3.00	.56	1/8" NPT			316 STAINLESS STEEL	304 STAINLESS STEEL	6000 PSI @ 302°F (414BAR @ 150°C)
05422-2	25ML	2.21	3.84	1.39	1/8" NPT					
05422-3	50ML	3.00	5.23	2.79	1/8" NPT					
05422-4	100ML	4.61	8.02	5.58	1/8" NPT					
05422-5	250ML	9.42	16.39	13.95	1/8" NPT					

Figure 3-6. View cell dimensions and specifications (courtesy of Thar Technologies, Inc.).

Each view cell was custom-configured to meet the needs of the reaction and phase behavior studies described in latter chapters. The instrumentation components and fittings configuration for a 25-mL view cell (**VC-1**; [identical configuration for **VC-2** and **VC-3**]) is shown in **Figure 3-7**. Cell *P* was monitored by a pressure gauge (**PI**; Swagelok, *PGI-63C-PG6000-LAQX*, ca. 0–414 bar [0–6000 pisa] span, accuracy ± 1.5% of span [6 bar or 90 pisa]) and a DAQ-interfaced transducer (identical to **PT-3**). Cell *T* was measured by a J-type dual-element thermocouple (**TI**; Omega, *SIC316SS-125U-6-DUAL*, accuracy ± 0.1 °C) connected to both a local controller (**C-1**; Omega, *CN9121A*) and the DAQ system. Temperature set-points were attained (within ± 0.5 °C) by interfacing the controller with a variable autotransformer (**VA-1**; Powerstat, *3PN116B*) and insulated heating tape (Omega, *STH051-080*) wrapped tightly around the exterior cell wall. Inlet and outlet valves were needle-type (High Pressure Equipment [HiP], *15-21AM1NMA*) in order to adjust material flow to and from the vessel. The inlet valve was placed near the vessel's bottom surface in efforts to promote mixing between incoming

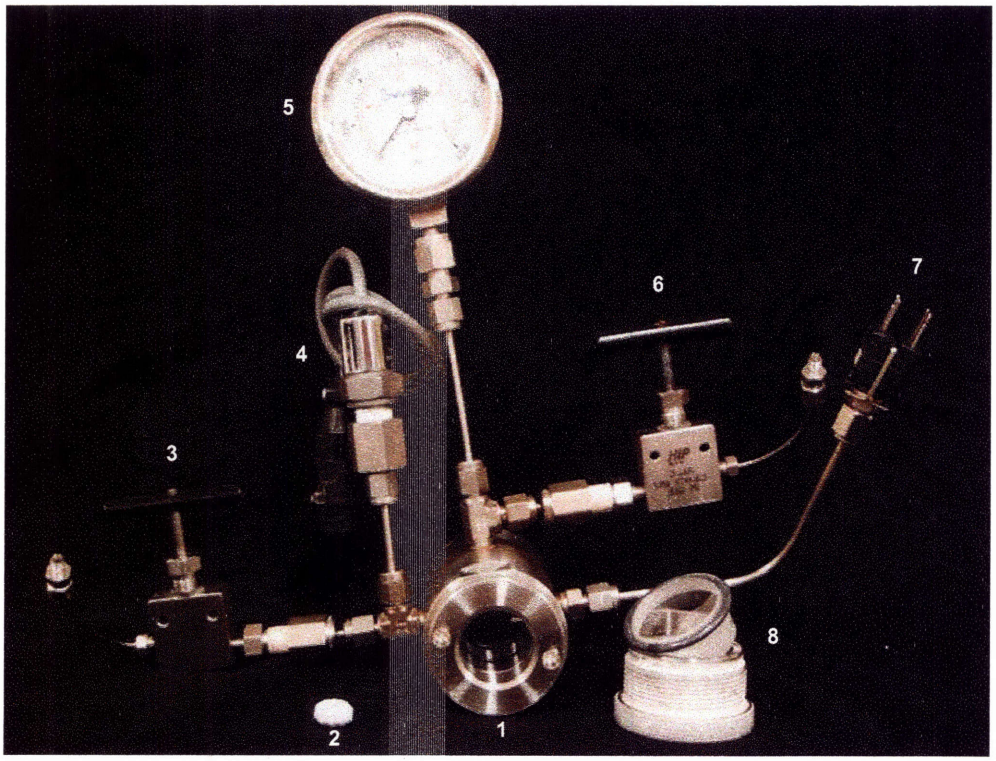

Figure 3-7. Photograph of a 25-mL view cell (**VC-1**) (photo/ Ciccolini): **(1)** 25-mL view cell with the front window assembly installed; **(2)** stir bar; **(3)** inlet valve; **(4)** pressure transducer; **(5)** pressure gauge; **(6)** outlet valve; **(7)** thermocouple; **(8)** back window assembly (from top to bottom: o-ring, window, cap). The configurations for **VC-2** and **VC-3** (not shown) were identical to that of **VC-1**.

materials with liquid-phase reagents already contained within the vessel. The outlet valve was placed near the vessel's top surface to prevent the loss of liquid-phase reagents during CO_2 or Ar venting. Agitation was provided by means of a Teflon®-coated octagon-shaped magnetic stir bar (**SB**; VWR, *58948-116*) driven externally by a stir plate (**SP-1**; Corning, *PC-410*). To prevent galling and seizing, all male NPT (MNPT) portions of vessel (and manifold) fittings were dressed with Teflon® thread sealant (McMaster-Carr, *45855K27*) prior to connection with their FNPT mates.

General Operating Procedures

General operating protocols for the view cells system are provided below. Given the symmetry of the system and identical cell design, procedures are only given for **VC-1** and its auxiliary components. In some cases, general procedures were modified to accommodate the needs of certain reactions and phase behavior experiments.

1. **Vessel preparation and loading.** To prevent galling and stripping of threads, the caps were sprayed with a Teflon®-based dry lubricant aerosol (Miller-Stephenson, *MS-122AD*). The windows were then inserted into their caps and o-rings were placed around the portion of the windows that protruded from the cap (per **Figure 3-6** and **Figure 3-7**). The vessel's internal sealing surfaces were cleaned with a cotton swap. A window assembly was inserted into the back end of the vessel and tightened securely by hand. Inlet and outlet valves were closed to prevent loss of material when handling the vessel.

   When charging liquid or solid materials to the vessel at ambient conditions, it was oriented in a vertical position with the pressure gauge face upwards and parallel to the floor (i.e., through the front end of the vessel). The stir bar was added before the charge to prevent splashing and subsequent material loss. Liquids were added either by a graduated polypropylene Luer-Lok® syringe (**S**; VWR, *309585 and other sizes*) equipped with a 16-gauge x 1.5-in. needle (VWR, *305198*) or a ca. 1-mL disposable glass pipet (VWR, *14672-380*) equipped with a latex bulb (VWR, *82024-554*). Solids were added directly by a SS spatula or from wax weighing paper (VWR, *12578-121*) shaped into a cone.

After all charges, the remaining window assembly was inserted into the front end of the vessel and tightened securely by hand. The vessel was then inserted into a vice with the pressure gauge facing downwards and parallel to the floor. The back cap was tightened by hand using the spanner wrench. When operating the vessel at $T > 100$ °C, a ca. 1-ft. pole was placed around the spanner wrench to create a longer lever-arm. The cap was then tightened one quarter-turn past the hand-tight position. The procedure was repeated for the front cap. Care was taken when transporting the vessel and orienting it within the vice so that materials within it would remain in the vessel's primary volume and not become entrained in dead-volume (e.g., the tube connecting the gauge to the vessel or the fittings leading to the outlet valve). Heating tape was wrapped tightly around the cylindrical portion of the vessel, starting from the front cap, weaving around the ports that connected to the thermocouple, transducer/inlet valve, and pressure gauge/outlet valve, and ending at the back cap. The remaining length of tape was wrapped around the fittings leading to the inlet and outlet valves. Nearly all metal surfaces were covered by the tape.

The vessel — sealed and insulated with heating tape — was inserted into the view cells system, centered on the stir plate, and the connections to the inlet and outlet valves were fastened. The vessel was secured to a ring stand (located under the stir plate) by a three-finger clamp placed around fittings in the pressure gauge line. The transducer was connected to the DAQ system. One of the thermocouple leads was connected to the DAQ system and the other to the controller. Finally, the heating tape was plugged into the variable autotransformer.

2. **Heating.** The desired temperature set-point (T_{sp}) was dialed into the controller and the variable autotransformer was turned on. Heating rate was controlled by the autotransformer setting; larger settings resulted in faster heating rates, but also larger overshoots. For experiments performed at $100 < T < 150$ °C, a transformer setting of 90% provided relatively fast heating ($T \rightarrow T_{sp}$ in < 5 minutes) and a modest overshoot (ca. 5 °C). For temperature-sensitive experiments (e.g., reactions), overshoot was avoided by setting the transformer initially to 90%, then reducing it to 60% when the temperature reached within 15 °C of the desired T_{sp}. For experiments

requiring 40 < *T* < 100 °C and T < 40 °C, 60% and 30% settings were used, respectively.

3. **Pressurization.** CO_2 from the high-*P* manifold entered the view cells system by placing **V-12** in the *a-b* position and was directed to either of the two identical cell sub-systems. Ar was added by placing **V-12** in the *b-c* position. With **V-26** in the *b-c* position, CO_2 (or Ar) passed through a six-way valve (**SV-1**; Valco, *C6UW*) where — depending on the valve position — it entered either the view cell directly or through a sample loop (**SL**; Valco, *SL100CUW* series) in order to pressure-inject liquid reagents into the cell. A detailed discussion of this injection method is presented in **Section 3.3.1**.

   The pressure of the cell was adjusted by controlling the amount of CO_2 (or Ar) added to the vessel via the inlet valve. Following pressurization, residual pressure that accumulated between the vessel inlet valve and manifold was vented by switching **V-26** to the *a-b* position while keeping **V-27** closed.

4. **Cooling.** Heating was terminated by turning off the autotransformer, unplugging the heating tape, and detaching the thermocouple leads connected to the controller. The heating tape was removed and the vessel was allowed to cool to ambient *T* via natural convection. For time-sensitive experiments or rapid quenching, the vessel was placed on a mound of crushed ice in polypropylene tub (VWR, *62662-026*) and ice was compacted around the walls and fittings. Care was taken so that ice was not in direct contact with window surfaces, as rapid cooling caused some windows to crack. For a vessel *T* = 130 °C, cooling to ambient *T* via natural convection required ca. 2 hours and ca. 5 minutes when cooling via ice.

5. **Venting.** CO_2 (or Ar) within the reactor was released only at ambient *T* and was sent either directly to the vent or to the sparge chamber (**SC-1**; Chemglass, *1821-01*). In order to release CO_2 directly to the vent, **V-28** was set to the *b-c* position and **V-37** to the *a-b* position. With **V-30**, **V-31**, and **V-36** closed, the vessel's outlet valve was opened. Finally, CO_2 was released by slowly opening **V-30**. **V-30** was insulated with heating tape and interfaced with a variable autotransformer (**VA-3**) set to 30% to prevent valve damage due to CO_2 expansion during the venting process. If expanded rapidly, CO_2 cooled to low temperatures and damaged the valve's sealing

components. It was especially important to vent the cell slowly as pressure was reduced to ambient *P* for experiments that involved liquids, as rapid evolution of CO_2 from the liquid-phase led to violent frothing and material loss to the outlet line.

When sent to sparge chamber **SC-1**, CO_2 slowly bubbled through ca. 20 mL of solvent (usually acetonitrile or dichloromethane) in order to extract any organic materials from the effluent stream prior to its release to the environment. A procedure similar to that of the preceding paragraph was used to direct the effluents to the sparge chamber, but by switching **V-37** to the *b-c* position and opening **V-36**.

6. **Vacuum.** The view cells system was connected to a vacuum system that was used in cases that required non-volatile liquid reagent charges of specific mass to **VC-1**. Reagent samples in sample vials (VWR, *66030-720*) were dissolved in dichloromethane and charged to the vessel via a disposable glass pipet equipped with a latex bulb. Vacuum was applied to the solution to selectively remove the volatile solvent, leaving behind the intended reagent charge. Graduated syringes were not used to charge neat reagents in these cases, as the density of the reagent was unknown (and in a quantity too small to calculate accurately). Pipets were not used because portions of the neat charge would be lost to the walls of the pipet.

   The vacuum system was driven by a duo-seal vacuum pump (**VP**; Welch, 1400), with pressure monitored by a vacuum gauge (**PI-6**; Varian, *801*). A cold trap — consisting of a bubbler (**SC-2**; [similar to **SC-1**]) housed in a Styrofoam® container and cooled by dry ice (Dry Ice Co.) — was used to condense solvent vapors before reaching the pump, as they would damage o-rings and reduce suction head. The vacuum system connected to the vessel's outlet valve and vacuum was achieved by powering the pump, switching **V-28** to the *a-b* position, closing **V-29**, **V-34**, and **V-35**, and opening **V-32** and **V-33**.

7. **Unloading and cleaning.** Following the vent step, the vessel was disconnected from the system and the heating tape was removed. The vessel was taken to the vice and the front cap was loosened with the spanner wrench. The vessel was taken to a fume hood, oriented with the pressure gauge facing upwards and parallel to the hood surface, and placed on a glass tray (similar to VWR, *46600-542*) that provided secondary containment in the event of a spill.

The front cap was removed and the threads were rinsed with HPLC-grade acetonitrile (VWR, *0043-08*) or dichloromethane (VWR, *4879-10*) via a solvent wash bottle (VWR, *16649 series*). All washes were collected in a 200-mL beaker. The front window was set on its side within the reactor and washed so that the solvent rinse entered the vessel. On rare occasions, the window was difficult to remove from the sealing surface and was gently pried off by leveraging the tip of a screw driver between the sides of the window and vessel. After visually-clean, the window was removed and placed aside in the cap. The vessel threads and internal components (i.e., ports and thermocouple) were rinsed thoroughly. A spatula was used to gently scrape the sides of the vessel to remove residual solids or films. A disposable glass pipet equipped with a latex bulb was used to transfer the rinses from the vessel to the rinse collection beaker.

After visually-clean, ca. 15 mL of solvent was added to the vessel and the front window assembly was refastened by hand. The contents were shaken vigorously to clean the ports and fitting dead-volumes not accessible by wash bottle rinses. The back cap was removed in the vice, the vessel was placed in the hood with the pressure gauge facing downwards and parallel to the hood surface, and the rinse procedure described in the preceding paragraph was repeated.

The inlet and outlet valves (and their associated fittings and tubing) were flushed with ca. 20-mL aliquots of solvent from a 50-mL beaker via a Luer-Lok® syringe (VWR, *309661*). The syringe was equipped with a SS Luer-Lok® needle (McMaster-Carr, *6710A65*) and compression fitting that enabled a leak-free connection to the valve lines. Because of its position on the cell, the inlet valve was in contact with reagents more frequently than the outlet valve and often required additional rinsing.

The front cap and window were removed and the stir bar and o-rings were placed in the rinse collection beaker. The windows were rinsed again to ensure that the surface covered by the o-rings were free of material.

All rinses were transferred to 100-mL collection bottles (VWR, *149-0125*) by way of a polypropylene funnel (VWR, *30252-907*), wrapped with Parafilm® (VWR, *52858-000)*, and stored for further analysis in a refrigerator at 4 °C. The required total rinse

volume varied for all experiments (i.e., some were easier to clean than others) and typically ranged from 100 – 300 mL.

For experiments in which CO_2 was vented through the sparge chamber, ca. 40-mL of solvent was flushed through the piping section of the view cells system that connected the outlet valve to the chamber. An identical syringe/needle combination used for flushing the vessel inlet and outlet valves was used for this step. The initial sparge chamber solvent charge and all piping rinses were added to the rinse collection beaker prior to its transfer to the sample bottles.

Finally, the vessel was cleaned thoroughly with deionized (DI) water (18.2 MΩ) supplied from our laboratory unit, soap (VWR, *56700-144*), and a flask-and-bottle brush (VWR, *17145-063*). Following several DI water rinses, the vessel and valves were flushed with acetonitrile and dried with high-velocity air (from a nozzle located in the fume hood) before its next use.

3.2.4. Reactor

The reactor was primarily used for phase behavior studies that required at-condition aliquot sampling. A PID for the reactor system is given in **Figure 3-8**. The reactor system expanded beyond the view cells system design to include continuous fluid recirculation among phases and phase-specific agitation and sampling. The vessel was an off-the-shelf model (Thar, *R-100-W-PCP-ST*) modified slightly by the manufacturer per our instructions to include additional ports. The body of the vessel (104 mL nominal volume) was cylindrical (4.2 in. length x 4.5 in. diameter external; 1.8 in. x 2.1 in. diameter internal), constructed of SS, and mounted on a portable stand assembly. Two 7/8-in. coaxial sapphire window assemblies (5/8-in. viewable diameter) afforded visual access into the vessel. The window assemblies and their sealing mechanisms were identical to those of the view cells, with the exception being their smaller size (window [Thar, 01269]; fluoropolymer-encapsulated viton o-ring [McMaster-Carr, *93445K212*]; window cap [Thar, *01568*]). The reactor contained one 1/8-in. FNPT and four 1/4-in. FNPT ports located on the side walls, two custom-added 1/8-in. FNPT ports located on the bottom wall, and two 1/4-in. FNPT ports on the primary seal cap. The manufacturer-specified MAWP of the reactor was 414 bar (6000 pisa) at 423 K (150 °C).

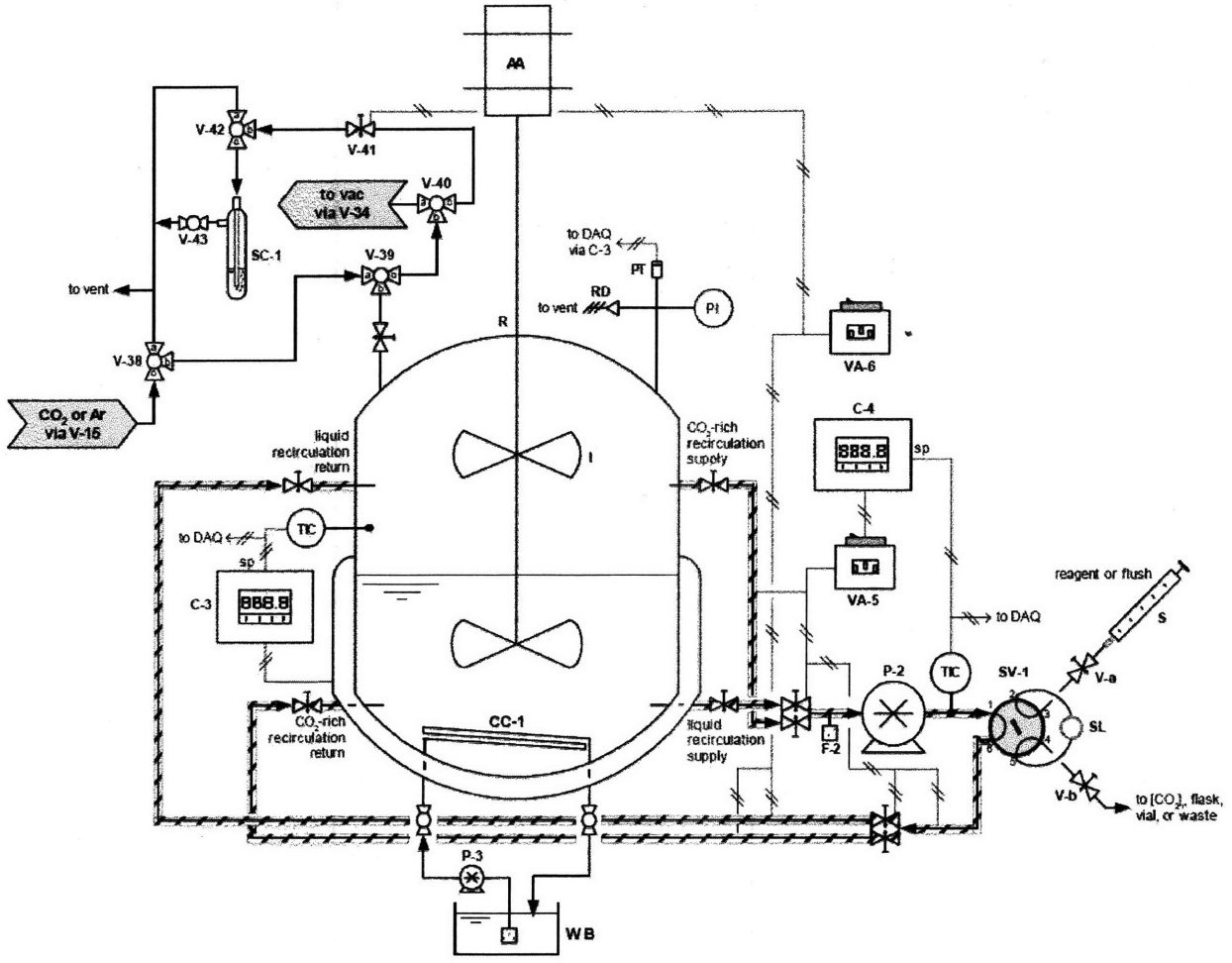

Figure 3-8. Piping and instrumentation diagram for the reactor system.

Agitation was provided by a variable-speed magnetically-coupled stirrer equipped with two turbine-type impellers (**I**; Thar, *05277-2*). Each impeller was fixed to the agitator shaft with a set screw and placed in a position that enabled phase-specific mixing. Agitation rates were adjusted by a knob located on the reactor's electrical enclosure. The agitator assembly connected to the vessel via the primary seal cap and was fully removable from both the vessel and cap.

The primary vessel seal was made by made placing a spring-loaded polyimide o-ring (Thar, *01076*) around the cap and by hand-tightening the cap/agitator assembly to the vessel. Unlike the view cells, the reactor seal was made by compressing of the o-ring against the top-portion of the vessel wall. Diagrams illustrating the vessel's port orientations, sealing mechanisms, and internal components are shown in **Figure 3-9**.

Reactor *P* was monitored by a pressure gauge (**PI**; Swagelok, *PGI-63B-PG6000-CAOX*, ca. 0–414 bar [0–6000 pisa] span, accuracy ± 1.5% of span [6 bar or 90 pisa]) and a transducer (identical to **PT-3**) interfaced with the reactor process control unit (**C-3**; Thar, *06137*). A rupture disc rated to 414 bar (6000 pisa) directed the vessel contents to the event of pressures exceeding the MAWP. Cell *T* was measured by a J-type dual-element thermocouple (**TI**; Omega, *SIC316SS-125U-6-DUAL*, accuracy ± 0.1 °C) interfaced with the controller. The controller achieved desired set-point temperatures (within ± 0.2 °C) by manipulating the electrical power fed to four heating cartridges located within the vessel walls. The controller unit displayed reactor *P* and *T* locally and sounded an alarm if these values exceeded user-input maximums. Real-time process data was collected in ASCII format by interfacing the controller with the DAQ computer's HyperTerminal applet via the serial (9-in) port.

The vessel was equipped with a custom-made cooling coil (**CC-1**) fabricated from 1/16-in. SS tubing and placed near the bottom vessel wall with adequate clearance between the lowest impeller. Chilled water from an ice/water bath (**WB**; VWR, *62662-026*) was recirculated through the coil via dual-piston metering pump (**P-3**; Laboratory Data Control, *92014903*) at 8 $mL \cdot min^{-1}$.

A single-piston metering pump (**P-2**; Eldex, *B-100-S*) equipped with a 7-μm inlet filter (**F-2**; Swagelok, *SS-2TF-7*) was used to recirculate fluids between phases at a rate of 8 $mL \cdot min^{-1}$ and also provide well-mixed phase-specific samples. Depending on the positions of the three-way two-stem valves (HiP, *15-15AF2*) mounted at the pump inlet and outlet, it was possible to recirculate and sample (see **Section 3.3.1**) a CO_2-rich phase into a liquid phase and *vice versa*. To ensure that sampling was representative of the vessel contents, all tubing and fittings placed between the vessel and inlet side of the sampling/injection unit were wrapped tightly with insulated heating tape and maintained at the vessel *T* (within ± 0.5 °C) via a thermocouple/controller (**C-4**)/variable autotransformer (**VA-5**) combination identical to the view cells *T*-control system (see **Section 3.2.2**). Tubing and fittings on the outlet side of the sampling/injection unit were also wrapped in heating tape and heating was provided by a transformer (**VA-6**) set at 50%.

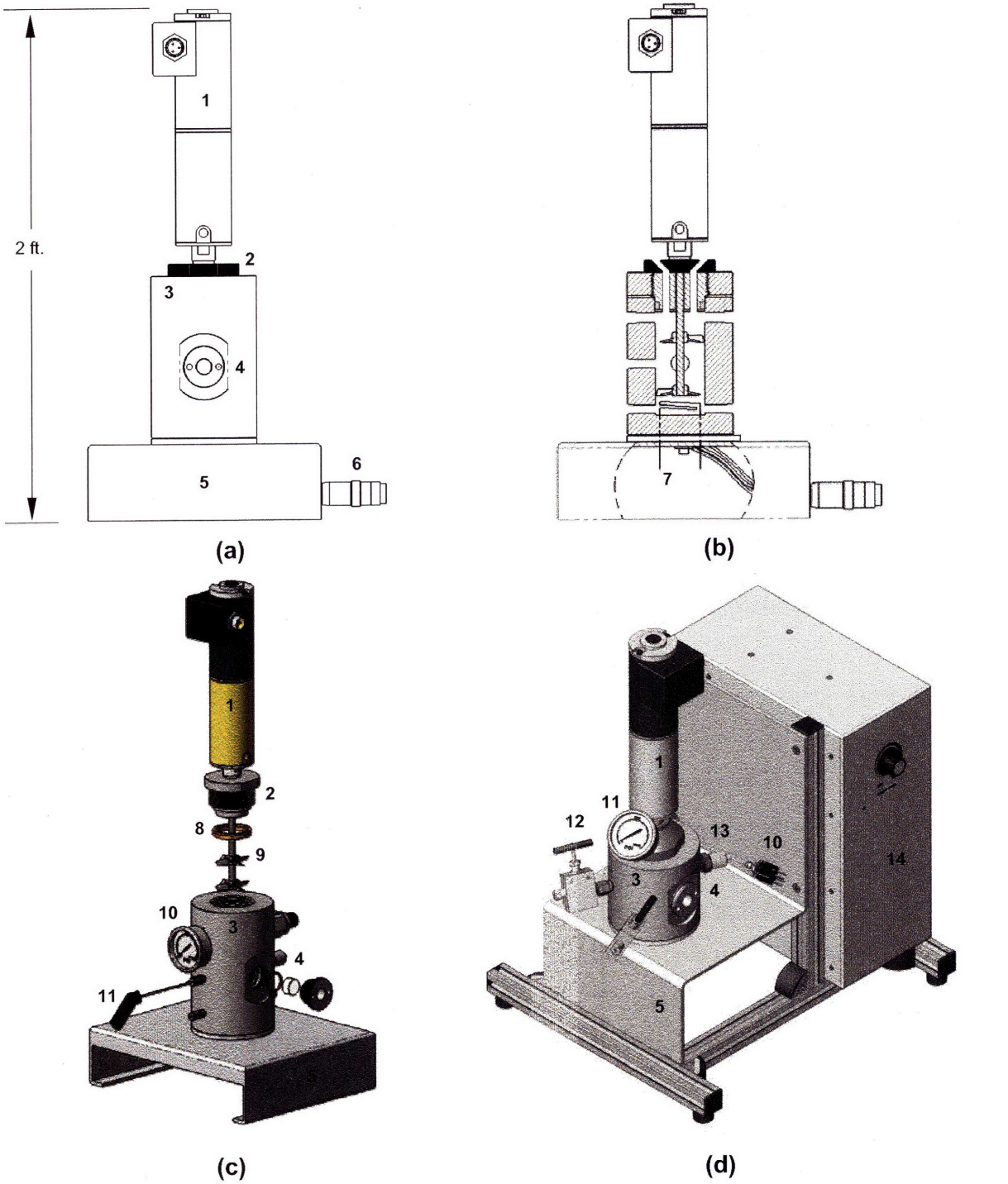

Figure 3-9. External **(a)**, internal **(b)**, and exploded **(c)** views of the reactor and external view of the reactor and mounting assembly **(d)** (adapted from Thar): (1) magnetic stirrer assembly; **(2)** primary seal cap; **(3)** reactor body; **(4)** window assembly consisting of a window cap; sapphire window; and o-ring **(5)** mounting stand; **(6)** connection to electrical enclosure; **(7)** cooling coil; **(8)** main spring-loaded seal; **(9)** impeller; **(10)** pressure transducer; **(11)** thermocouple; **(12)** valve; **(13)** rupture disc; **(14)** electrical enclosure. The reactor control system is not shown.

General Operating Procedures

1. **Vessel preparation and loading.** The window assemblies were installed in the reactor body in an identical fashion described by the general operating procedures for the view cells system, with the exception being that the vice and spanner pole were not used. Liquids were added to the vessel either by a graduated polypropylene Luer-Lok® syringe equipped with a 16-gauge x 1.5-in. needle, a 25-mL graduated glass pipet (VWR, *89003-530*), or a disposable polystyrene (VWR, *53283-710*) pipet equipped with a rubber bulb. Solids were added directly by a SS spatula or from wax weighing paper (VWR, *12578-121*) shaped into a cone. Charges could also be made during an experiment using a sampling/injection unit.

   The threads of the main cap were coated with the Teflon®-based dry aerosol lubricant. The main seal o-ring was attached to the cap and the cap/agitator assembly was fastened to the vessel by hand. The reactor inlet valve was then connected to the high-*P* manifold.

   The vessel pressure transducer, thermocouple, and agitator assembly leads were connected to controller **C-3**. One of the recirculation loop thermocouple leads was connected to the DAQ system and the other to controller **C-4**. Heating tapes attached in parallel to the section of the recirculation loop spanning from the vessel to the sampling/injection unit inlet were connected to variable autotransformer **VA-5** via a power strip. Likewise, tapes attached to the section of the recirculation loop spanning from the sampling/injection unit outlet to the vessel were connected in parallel by way of a power strip to variable autotransformer **VA-6**.

2. **Heating and stirring.** Temperature set-points were dialed into the reactor control unit (**C-3**) and agitation rates were set by adjusting the knob on the reactor's electrical enclosure. Agitation was typically set to 50%. Higher agitation rates led to unrepresentative sampling, as vortices were created that pushed the liquid phase up the vessel walls and exposed the ports responsible for CO_2 rich-phase sampling to liquid and *vice versa*.

   Unlike the view cells system, the reactor heating rate was unchangeable. It was also significantly lower, taking approximately 1.5 hours to heat to 100 °C (*vs.* 5 minutes

for the view cells). For temperature-sensitive experiments, materials were loaded to the vessel after the desired temperature was reached.

VA-5 and **VA-6** were each set to 90% for experiments requiring $100 < T < 150$ °C, 60% for $40 < T < 60$ °C, and 30% for $T < 40$ °C.

3. **Pressurization.** CO_2 from the high-*P* manifold entered the reactor system by opening **V-13** and placing **V-14** in the *b-c,* **V-15** in the *a-b,* **V-38** in the *b-c*, and **V-39** in the *a-b* positions. Ar was added by the identical valve configuration, but with **V-14** in the *a-b* position. The reactor inlet valve located on the cap was opened and then closed when the desired pressure was reached. Following pressurization, residual pressure that accumulated between the vessel inlet valve and manifold was vented by switching **V-38** to the *a-b* position while keeping **V-42** and **V-43** closed.

4. **Cooling.** Heating was terminated by reducing all set-point temperatures to 25 °C and tuning off all autotransformers. The reactor was allowed to cool to ambient *T* via natural convection. Since nearly all experiments performed in the reactor system were not *T*-sensitive, the cooling coil was rarely used.

5. **Venting.** CO_2 (or Ar) within the reactor was released at ambient *T* and was sent either directly to the vent or to the sparge chamber. With **V-38**, **V-41**, **V-43**, and the reactor inlet valve closed, CO_2 was sent directly to the vent by placing **V-39** in the *b-c*, **V-40** in the *b-c*, and **V-42** in the *a-b* positions. The reactor inlet valve was opened and CO_2 was released by slowly opening **V-41**. **V-41** was insulated with heating tape and interfaced with **VA-6**. **VA-6** was set to 30% to prevent valve damage due to CO_2 expansion during the venting process.

   When sending CO_2 to sparge chamber **SC-1**, a similar venting procedure was used, but with **V-42** in the *b-c* position and **V-43** opened.

6. **Vacuum.** The reactor system was connected to the view cells vacuum system via **V-34**. Vacuum was achieved by powering the pump, switching **V-39** to the *b-c* and **V-40** to the *a-b* positions, and opening **V-34**.

7. **Unloading and cleaning.** Following the vent step, the recirculation pump and agitator were shut off and the cap/agitator assembly was disconnected from the

process control unit, unfastened, and set aside. In some cases, the cap/agitator assembly was difficult to loosen by hand and required removal with a pipe wrench.

The contents of the vessel were removed primarily by a 25-mL glass pipet equipped with a rubber bulb and placed in a 300-mLbeaker. A ca. 1-mL disposable glass pipet equipped with a latex bulb was used to reach locations inaccessible to the 25-mL pipet (e.g., underneath the cooling coil). HPLC-grade acetonitrile or dichloromethane via a solvent wash bottle were sprayed thoroughly around the interior walls and ports until the vessel was approximately half full (ca. 50 mL). The solvent was then removed via pipet and placed in the wash collection beaker.

The vessel was refilled with 50 mL of solvent and the cap/agitator assembly was reconnected to the control unit and refastened to the vessel. The recirculation pump and agitation were turned on and the solvent was allowed to agitate for ca. 15 minutes. Agitation and recirculation were terminated and the solvent was transferred to the collection beaker. This procedure was then repeated. If both recirculation loops were used in an experiment, the procedure was repeated three times so that each loop was rinsed twice.

The cap/agitation assembly was removed from the process control unit and vessel. The o-ring was removed and placed in the wash collection beaker. The cap threads were positioned over the beaker and rinsed with solvent. Solvent trapped in the recirculation loops was removed by placing a tube that supplied high-velocity air (from a nozzle in the fume hood) into the supply ports that fed each loop.

All rinses were transferred to 100-mL collection bottles by way of a polypropylene funnel, wrapped with Parafilm®, and stored for further analysis in a refrigerator at 4 °C. The required total rinse volume varied for all experiments and was typically 200 – 400 mL.

For experiments in which CO_2 was vented through the sparge chamber, the cleaning procedure described in the view cells system was used.

3.2.5. Sight Gauge

The sight gauge was used to measure the volume expansion of CXLs. A PID for the sight gauge system is given in **Figure 3-10**. The liquid level sight gauge (**SG**) was an off-the-shelf model (Jerguson, *17-T-32*) that was modified under our instructions by the MIT Central Machine Shop (MIT CMS) to include additional ports. A similar model gauge was used by Timko (2004) to measure the partition coefficients of several benzoyl halides in CO_2/H_2O mixtures (see **Section 1.6**). Due to space restrictions in the G2 System, the assembled gauge and auxiliary equipment was operated in a fume hood adjacent to the high-*P* manifold.

The gauge consisted of a 316 SS rectangular liquid chamber (ca. 11 in. length x 2 in. width x 2 in. depth) that came standard with 1/2-in. FNPT ports at the top and bottom (2-in. x 2-in.) surfaces. The front and back (11-in. x 2-in.) faces each had rounded-edge rectangular slots (ca. 10.25-in. x 1.75-in.) that allowed visual access into the vessel. The side (11-in. x 2-in.) surfaces were nearly completely solid, with the exception of five custom-added 1/8 -in. FNPT ports. The front and back chamber faces were sandwiched by carbon-steel covers (Jerguson, *V-2-7-A4*) housing borosilicate glass windows (Jerguson, *V-16756-7*) and fastened together with nuts and bolts. The vessel's primary seals were made by placing Grafoil® gaskets (Jerguson, *V-13143-7*) between the windows and rounded-edge slots of the front and back faces. Fiber cushion gaskets (Jerguson, *V-18980-7*) were placed between the windows and covers to avoid damage during compression. Since the vessel underwent expansion and contraction during temperature cycling, lock washers (Jerguson, *V15528-J1*) were used with special nuts and bolts (Jerguson, *P7705-B71*) to ensure the integrity of the seal. Bolt arrangements and fastening instructions can be found in documentation provided by the manufacturer. The sealing surfaces needed to be trued and refashioned by the MIT CMS, as the vessel was damaged during preceding work. A manufacturer cut sheet that provides additional dimensions, port orientations, and the sealing configuration for the gauge is shown in **Figure 3-11**.

The manufacturer-specified MAWP of the gauge was ca. 193 bar (2800 pisa) at 423 K (150 °C). Higher-pressure cells (MAWP of ca. 310 bar [4,500 pisa]) were also available from the manufacturer, but were not purchased since we were already in possession of the vessel and did not require higher *P*-ratings.

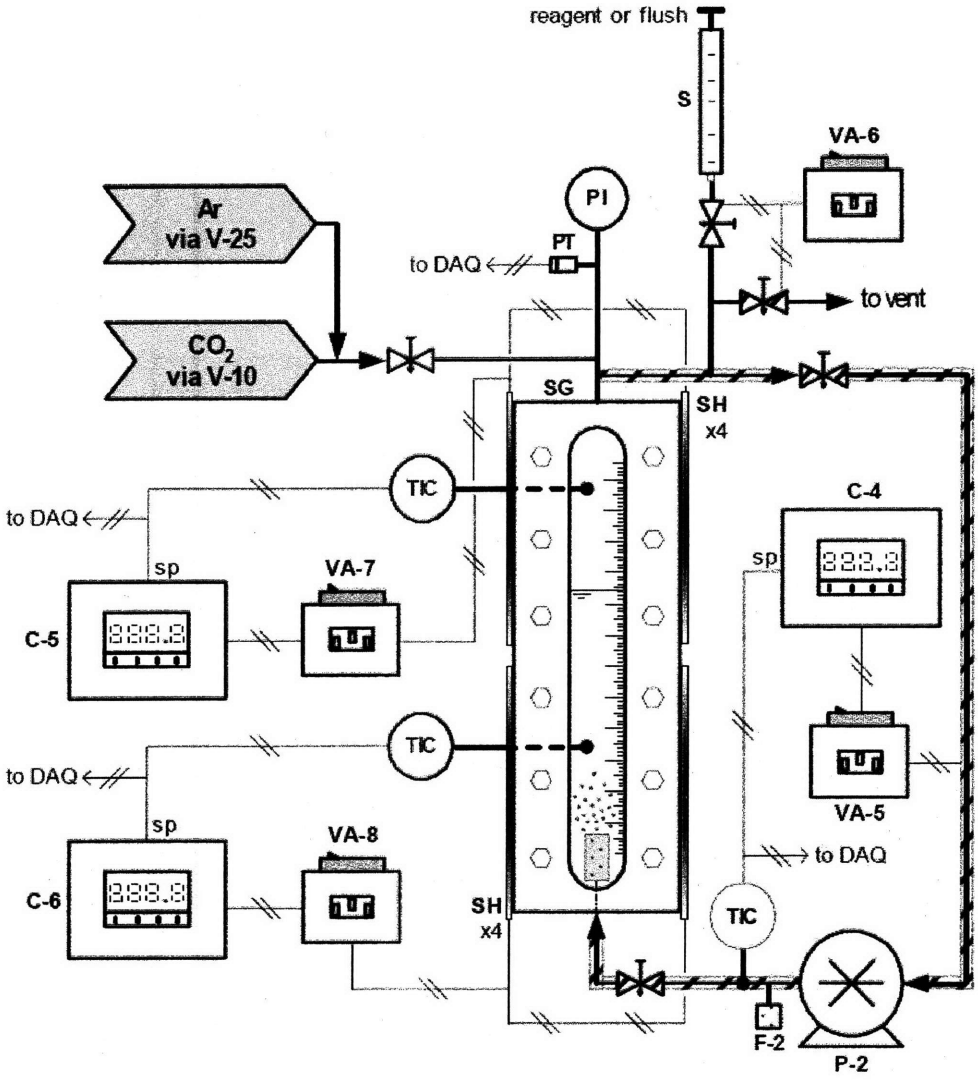

Figure 3-10. Piping and instrumentation diagram for the sight gauge system.

Gauge *P* was monitored by a pressure gauge (**PI**; [identical to **PI-1**]) and a DAQ-interfaced transducer (identical to **PT-1**). The transducer was calibrated with a high-accuracy pressure gauge (Omega, *549003-1079*, ca. 0–345 bar [0–5000 pisa] span, accuracy ± 0.1% of reading) to ensure accurate *P* readings. Given the relatively large size of the gauge, *T* was measured at the top and bottom sections of the vessel via J-type dual-element thermocouples

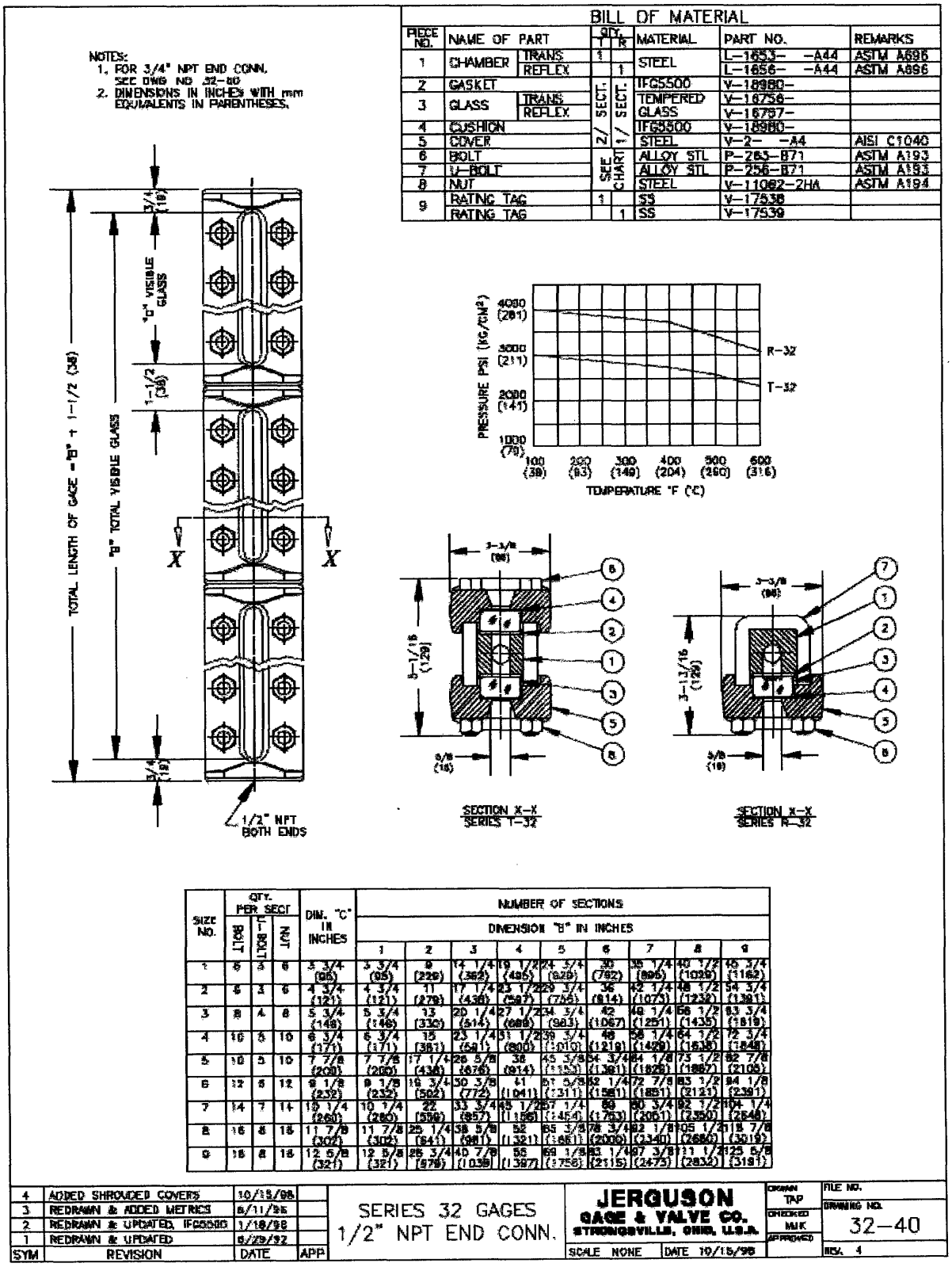

SIZE NO.	QTY. PER SECT BOLT	U-BOLT	NUT	DIM. "C" IN INCHES	NUMBER OF SECTIONS — DIMENSION "B" IN INCHES 1	2	3	4	5	6	7	8	9
1	6	3	6	3 3/4 (95)	3 3/4 (95)	9 (229)	14 1/4 (362)	19 1/2 (495)	24 3/4 (629)	30 (762)	35 1/4 (895)	40 1/2 (1029)	45 3/4 (1162)
2	6	3	6	4 3/4 (121)	4 3/4 (121)	11 (279)	17 1/4 (438)	23 1/2 (597)	29 3/4 (756)	36 (914)	42 1/4 (1073)	48 1/2 (1232)	54 3/4 (1391)
3	8	4	8	5 3/4 (146)	5 3/4 (146)	13 (330)	20 1/4 (514)	27 1/2 (698)	34 3/4 (883)	42 (1067)	49 1/4 (1251)	56 1/2 (1435)	63 3/4 (1619)
4	10	5	10	6 3/4 (171)	6 3/4 (171)	15 (381)	23 1/4 (591)	31 1/2 (800)	39 3/4 (1010)	48 (1219)	56 1/4 (1429)	64 1/2 (1638)	72 3/4 (1848)
5	10	5	10	7 7/8 (200)	7 7/8 (200)	17 1/4 (438)	26 5/8 (676)	36 (914)	45 3/8 (1153)	54 3/4 (1391)	64 1/8 (1629)	73 1/2 (1867)	82 7/8 (2105)
6	12	6	12	9 1/8 (232)	9 1/8 (232)	19 3/4 (502)	30 3/8 (772)	41 (1041)	51 5/8 (1311)	62 1/4 (1581)	72 7/8 (1851)	83 1/2 (2121)	94 1/8 (2391)
7	14	7	14	10 1/4 (260)	10 1/4 (260)	22 (559)	33 3/4 (857)	45 1/2 (1156)	57 1/4 (1454)	69 (1753)	80 3/4 (2051)	92 1/2 (2350)	104 1/4 (2648)
8	16	8	16	11 7/8 (302)	11 7/8 (302)	25 1/4 (641)	38 5/8 (981)	52 (1321)	65 3/8 (1661)	78 3/4 (2000)	92 1/8 (2340)	105 1/2 (2680)	118 7/8 (3019)
9	18	8	18	12 5/8 (321)	12 5/8 (321)	25 3/4 (979)	40 7/8 (1038)	56 (1387)	69 1/8 (1756)	83 1/4 (2115)	97 3/8 (2475)	111 1/2 (2832)	125 5/8 (3191)

SYM	REVISION	DATE	APP
4	ADDED SHROUDED COVERS	10/15/98	
3	REDRAWN & ADDED METRICS	8/11/95	
2	REDRAWN & UPDATED, IFG5500	1/18/95	
1	REDRAWN & UPDATED	6/29/92	

SERIES 32 GAGES
1/2" NPT END CONN.

JERGUSON GAGE & VALVE CO.
STRONGSVILLE, OHIO, U.S.A.

SCALE NONE DATE 10/15/98

DRAWN TAP | CHECKED MJK | APPROVED

FILE NO.
DRAWING NO. 32-40
REV. 4

Figure 3-11. View cell dimensions and specifications (courtesy of Jerguson).

(**TI**; Omega, *SIC316SS-125U-6-DUAL*, accuracy ± 0.1 °C). Each thermocouple was connected to both a local controller (**C-5** and **C-6**, respectively; [identical to C-1]) and the DAQ system. Temperature set-points were identical for the top and bottom portion of the vessel and attained (within ± 0.5 °C) by interfacing the controllers with variable autotransformers (**VA-7** and **VA-8**, respectively; [identical to **VA-1**]) and several strip heaters (Chromalox, *NSA-711*) mounted against the chamber's side surfaces.

Gauges of this type were typically heated by submerging the entire apparatus in a constant-*T* fluid bath. Given (1) the relatively large size of the vessel, (2) the lack of equipment required for heating, circulating, and maintaining an isothermal bath at elevated temperatures (e.g., $T > 80$ °C), (3) safety concerns associated with large volumes of hot fluids, and (4) the overall cumbersome nature of working with submerged equipment, we instead decided to equip the vessel with electrical band heating. In order to provide adequate heat transfer to the chamber, it was necessary to mount the heating strips against the chamber surfaces. This was not a trivial task, as the bolts joining the covers only permitted direct access to sections of the chamber's side surfaces that were too small to accommodate the heaters. To overcome this challenge, aluminum blocks (ca. 1.5 in. length x 1 in. width x 0.25 in. depth) were fabricated at the MIT Student Machine Shop (MIT SMS) and placed between each cover bolt and adhered to the chamber using a high-*T* conductive heat sink silicone compound (McMaster-Carr, *10405K79*). Holes were drilled in the center of some blocks to allow placement over sections of the chamber surface that contained ports and fittings. With the bolt and aluminum surfaces now flush, the heating strips were in intimate contact with the vessel. The strip heaters were mounted against the chamber by tightly twisting SS wire (McMaster-Carr, *9882K35*) around the bolts and heater surfaces.

Four strip heaters were wired together in parallel, mounted at the top section of the vessel, and interfaced with a thermocouple, **C-5**, and **VA-7**. Two of these heaters were placed on each of the top sides of the chamber. Similarly, four heaters were mounted at the bottom section of the vessel and interfaced with a thermocouple, **C-6** and **VA-8**. Each side of the chamber therefore had four strip heaters mounted to it — two that belonged to the top heating zone, and two to the bottom heating zone.

To accurately quantify the volume-expansion of CXLs, the gauge was equipped with an aluminum scale. The scale was a portion of a 1/4 in.-thick measuring tape that was fixed to the front window using a high-*T* adhesive kit (McMaster-Carr, *66725A23*). A single-piston metering

pump (**P-2**) equipped with a 7-μm inlet filter (**F-2**) was used to circulate the CO_2-rich phase within the liquid phase at a rate of 8 mL·min^{-1}. To further promote mixing, the terminus of the recirculation loop was fitted with a frit (Alltech Associates, *9402*) that dispersed CO_2 into the liquid phase as fine droplets. All tubing and fittings within the recirculation loop were wrapped tightly with insulated heating tape and maintained at the vessel T (within ± 0.5 °C) via a thermocouple/controller (**C-4**)/variable autotransformer (**VA-5**) combination identical to the view cells T-control system. Inlet and outlet valves were also wrapped in heating tape and heating was provided by **VA-6** set at 50%.

General Operating Procedures

1. **Vessel preparation and loading.** A Grafoil® gasket was placed on the chamber's sealing surface and a window was positioned on top of it. A fiber gasket was placed on top of the window and the cover was gently placed over this gasket. The bolts were then inserted into the cover. The gauge was flipped over and the opposite sealing face was exposed. The gasket/window/gasket/cover addition procedure was repeated. Lock washers and nuts were added to the bolts and tightened with an adjustable torque wrench to make the seal. Washer orientation, appropriate torque requirements, and ordering of bolt fastening can be found in the manufacturer documentation.

   Liquids were added to the vessel by connecting a graduated polypropylene Luer-Lok® syringe to a SS Luer-Lok® needle (McMaster-Carr, *6710A38*) that was connected to the a valve located at the top of the gauge. When adding viscous liquids, the valve was heated by setting **VA-6** to 30%. The reactor inlet valve was connected to the high-P manifold.

   The vessel pressure transducer and thermocouple leads were connected to the DAQ system. The gauge's top thermocouple was connected to controller **C-5**, the bottom thermocouple to **C-6**, and recirculation loop thermocouple to **C-4**. The top portion heating strip assembly was connected to variable autotransformer **VA-7** and the bottom assembly to **VA-8**. Heating tapes attached in parallel to the recirculation loop were connected to **VA-5** via a power strip. Likewise, tapes attached to the liquid

injection valve and vent valve were connected in parallel by way of a power strip to **VA-6**.

2. **Heating.** The desired temperature set-points were dialed into the controllers and the variable autotransformers were turned on. The autotransformers were set to 90% for experiments requiring 100 < T < 150 °C, 60% for 40 < T < 60 °C, and 30% for T < 40 °C.

3. **Pressurization.** CO_2 from the high-*P* manifold entered the sight gauge system by opening **V-10**. Ar was added by opening **V-25**. Since both gases were connected to the gauge via a cross (and not a three-way valve), header contamination was avoided by keeping **V-25** closed while **V-10** was opened and *vice versa*. The inlet valve located at the top of the gauge was opened and then closed when the desired pressure was reached.

4. **Cooling.** Heating was terminated by reducing all set-point temperatures to 25 °C and turning off all autotransformers. The gauge was allowed to cool to ambient *T* via natural convection.

5. **Venting.** CO_2 (or Ar) within the gauge was released at ambient *T* within the fume hood (and not the vent header located within the high-*P* manifold). The vessel was vented by slowly opening the vent valve. **VA-6** was set to 30% to prevent valve damage due to CO_2 expansion during the venting process.

6. **Unloading and cleaning.** Following the vent step, the recirculation pump was shut off. The gauge was drained by loosening a union found at the end of the recirculation loop and collecting the contents in a 300-mL beaker. The union was refastening and HPLC-grade acetonitrile or dichloromethane was added to the gauge via a syringe at the liquid injection valve. The pump was turned on and the solvent wash was allowed to recirculate for ca. 15 minutes. Recirculation was terminated and the solvent was transferred to the collection beaker by loosening the union. This procedure was repeated for a total of three times. Solvent trapped in the recirculation loop was removed by loosening a union located at the pump inlet and connecting a tube that supplied high-velocity air (from a nozzle located in the fume hood). All solvent rinses were transferred to waste.

3.2.6. Cloud-Point Apparatus

The cloud-point apparatus was used to determine multi-component mixture critical points and solubility limits of CO_2/liquid and CO_2/solid systems. A PID for the cloud-point apparatus is shown in **Figure 3-12**. A 25-mL view cell (**VC-1**) was configured such that the lower portion of the vessel was connected to a manual pressure generator (**PG**; HiP, *37-6-30*). The generator was essentially a cylindrical chamber whose volume varied depending on the placement of an internal piston that traversed its length. Turning the generator handle counterclockwise, for example, moved the piston away from the cell and increased the volume of the system by making more chamber volume accessible.

Temperature indication and control was identical to that of the view cells system discussed in **Section 3.2.2**. Pressure, however, was measured by a much more accurate digital gauge (**PI**; Omega, *549003-1079*, ca. 0–345 bar [0–5000 pisa] span, accuracy ± 0.1% of reading).

In a typical experiment, CO_2 and a compound of interest were added to the vessel and the pressure of the multiphasic system was increased above the $P_{c,mix}$ or the solubility limit to produce a single-phase condition. The pressure of the system was then reduced slowly by adjusting the manual pressure generator. As $P_{c,mix}$ or the solubility limit was approached, the single-phase mixtures became cloudy (hence, 'cloud-point') and phase segregation followed immediately thereafter.

It was necessary to elevate the generator (and piping leading to it) relative to the cell, as operation at lower elevations resulted in precipitation within the chamber and piping lines rather than the cell itself.

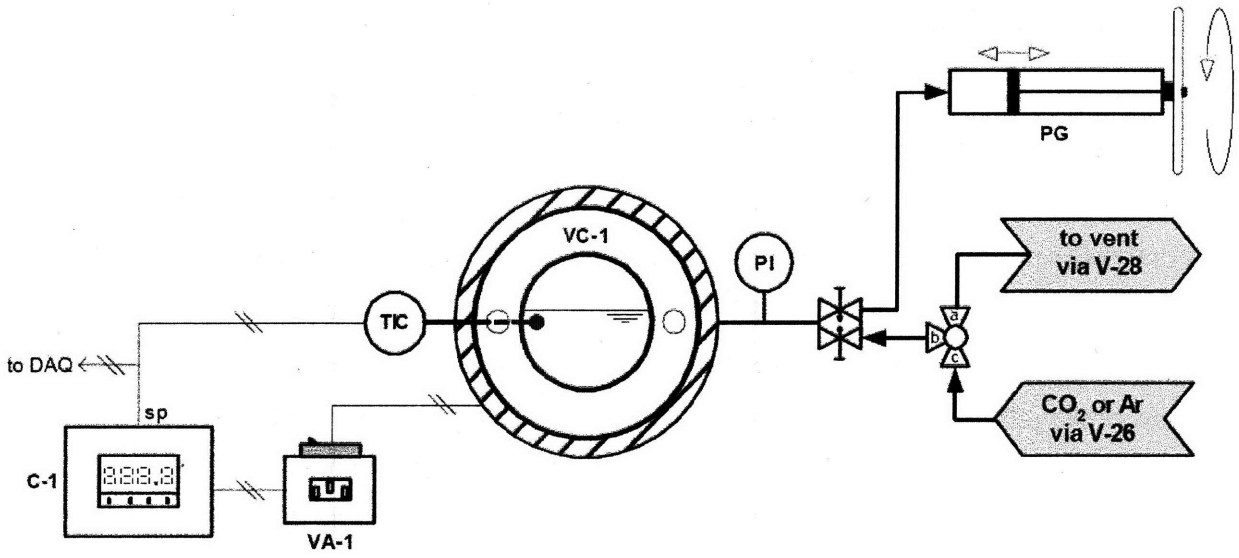

Figure 3-12. Piping and instrumentation diagram for the reactor system.

General Operating Procedures

The general operating procedures for the cloud-point apparatus was nearly identical to those of the view cells system. Deviations from these procedures are delineated below:

3. **Pressurization.** CO_2 (or Ar) from the high-*P* manifold entered the sight gauge system by placing the three-way valve in *b-c* position.

5. **Venting.** CO_2 (or Ar) within the cell was released by placing the three-way valve in the *a-b* position.

6. **Unloading and cleaning.** The pressure generator was cleaned by filling the chamber with solvent and dispensing the rinse into a waste beaker. The piston was first placed in a position farthest from the handle by turning the handle clockwise until it did not move (accessible chamber volume ≈ 0 mL). A tube was connected to the generator and placed in a beaker containing solvent. The chamber was filled by placing the piston in a position closest to the handle by turning the handle counterclockwise until it did not move (accessible chamber volume ≈ 11 mL). The solvent was dispensed into a waste beaker and the process was repeated a total of three times.

3.2.7. Ultrasonic View Cell

The ultrasonic view cell was used to generate CO_2-in-liquid and liquid-in-CO_2 microemulsions in CXL systems, thereby facilitating interfacial mass transport. A piping and instrumentation diagram for the ultrasonic view cell system is shown in **Figure 3-13**. A 25-mL view cell (**VC-4**) — modified by the manufacturer per our instructions to expand the top port from 1/8-in (**Figure 3-6**) to 3/8-in. FNPT — was configured to accommodate a 20 kHz flanged titanium ultrasonic horn (**UH**; Sonics & Materials, *A06963PRB*). The horn was similar to that used by Timko (2004), with the exception of a slightly smaller tip diameter to allow enough clearance between the cell port walls and the horn tip during operation. Contact of the cell walls with any portion of the horn between the flange (or 'nodal point') and tip during operation would decrease the horn's ability to generate emulsions (e.g., decreased energy efficiency) and also result in horn and cell damage (e.g., abrasion and pitting).

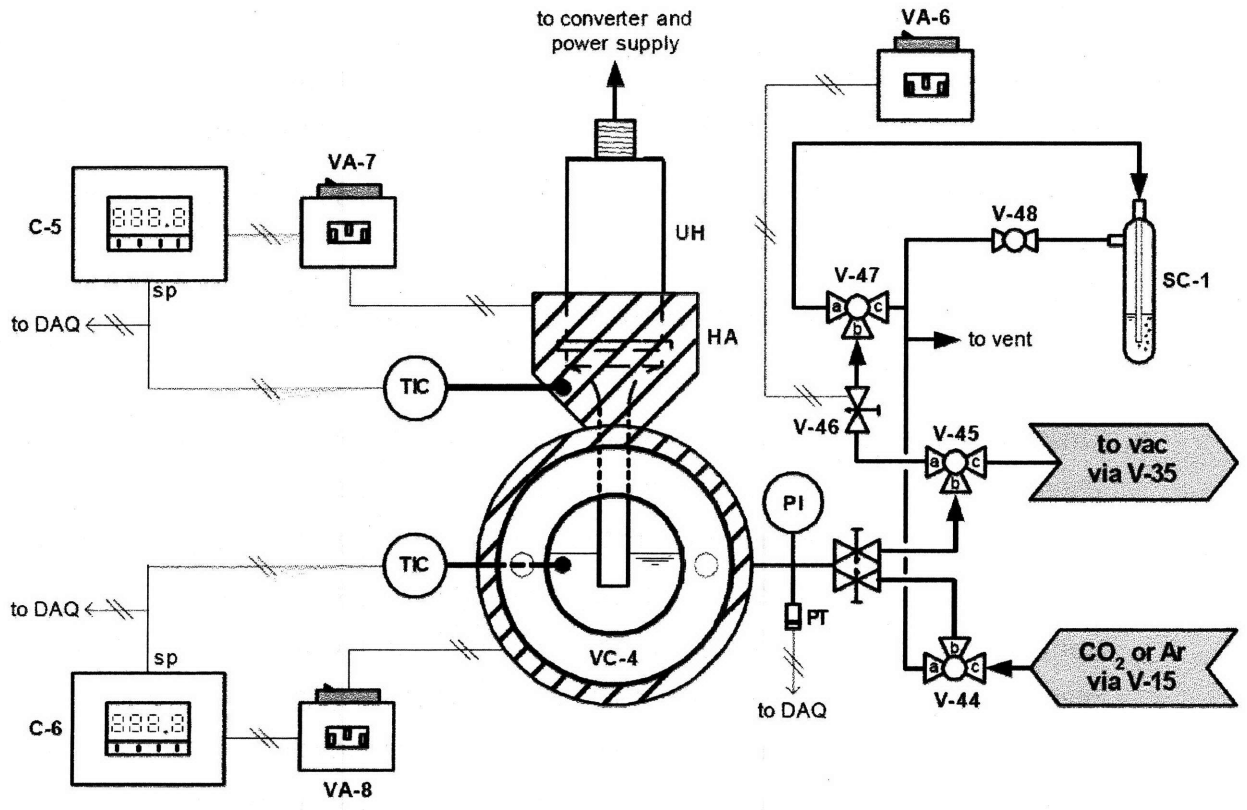

Figure 3-13. Piping and instrumentation diagram for the ultrasonic view cell system.

The horn was inserted into the vessel by way of a custom-designed 316 SS adapter (**HA**) shown in **Figure 3-14**. The adapter was constructed at the MIT CMS per our instructions and consisted of a cap and body. The cap was used to form the seal between the horn and the body. The body oriented the horn such that it could be inserted into the view cell via the 3/8-in. FNPT port. A 1/8-in. bored-through port was tapped in the top portion of the body to allow for adapter-specific *T* measurement and control and also provide a recirculation line for fluids that may accumulate in the dead-volume (conical) region of the body. A fluoropolymer-encapsulated viton o-ring (McMaster-Carr, *93445K218*) was placed around the horn and against the flange on the side closer to the tip. A copper gasket (1.50 in. OD . x 1.25 in. ID) — cut from 1/16-in. thick sheet stock with a die and punch set and trimmed with scissors — was placed on the other side of the flange. The seal was made by tightening the cap to the body via an adjustable torque wrench (set to 50 ft.-lbs.), which compressed the fluoropolymer-encapsulated o-ring against the body sealing surface. Several other o-ring/gasket combinations were experimented with (e.g., substituting a fluoropolymer-encapsulated o-ring for the copper gasket, using alternative o-ring materials of construction, etc.), but the fluoropolymer-encapsulated viton/copper combination proved to be the most robust.

Earlier observations made by Timko (2004) showed that turbidity and microemulsion particle size distributions (and hence reaction rates for mass-transfer limited reactions) varied with horn standoff distance (i.e., the distance between the horn and the liquid/CO_2 interface). To study this effect more quantitatively, two adapters were fabricated; one was designed for the insertion of the horn into the bottom of the vessel such that the tip faced upwards (as in the work of Timko [2004]), and the other for the insertion of the horn into the top of the vessel (**Figure 3-13** and **Figure 3-14**) such that the tip faced downwards. The adapters were identical in every aspect except for the length of the horn tip allowed to protrude from the body. In the 'tip upwards' design the horn protruded ca. 0.25 in. into the vessel and ca. 1.0 in. in the 'tip downwards' design. In addition to standoff distance, we decided to invert the horn ('tip downwards' design) in order to investigate the effect of this orientation on emulsion formation. The 'tip downwards' design offered additional processing benefits, as the dead-volume portion of the body was oriented such that liquids and solids resided mainly in the optically-accessible and ultrasonically-stimulated portion of the cell. Photographs of the adapters, horn, and the horn/adapter assembly are shown in **Figure 3-15**.

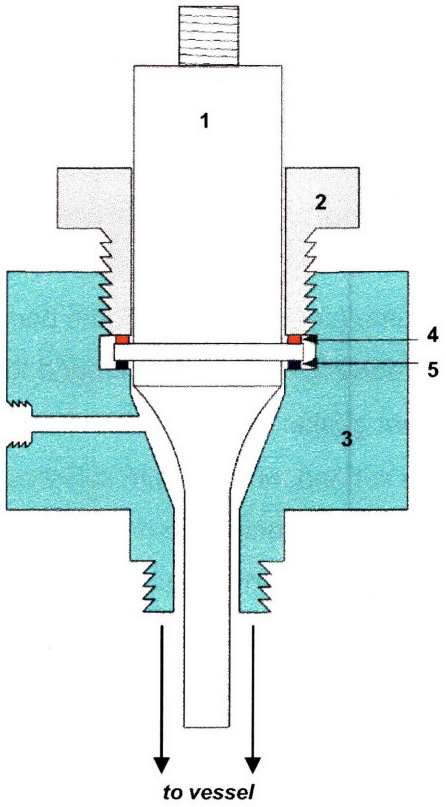

Figure 3-14. Illustration of the ultrasonic horn and adapter assembly: **(1)** horn; **(2)** cap; **(3)** body; **(4)** fluoropolymer-encapsulated viton o-ring; **(5)** copper gasket.

The adapter shown in **Figure 3-14** was actually a third-generation design based originally on an adapter designed by Lee Lai Yeng, a Singapore-MIT Alliance (SMA) Ph.D. candidate visiting our group in the Summer of 2004. The second-generation design was modified slightly from Ying's original design to accommodate a smaller-tipped horn and include the appropriate dimensions and fittings to fit the horn in our cell. The third-generation design expanded upon the second-generation design by: (1) reducing the overall bulkiness of the adapter, (2) decreasing the body dead-volume zone, (3) adding a *T*-control/recirculation port, and (4) increasing the clearance between the portion of the horn within the cap and the body threads, as o-rings and gaskets that expanded upon compression and thermal cycling seized in the threads, making it difficult to remove the horn.

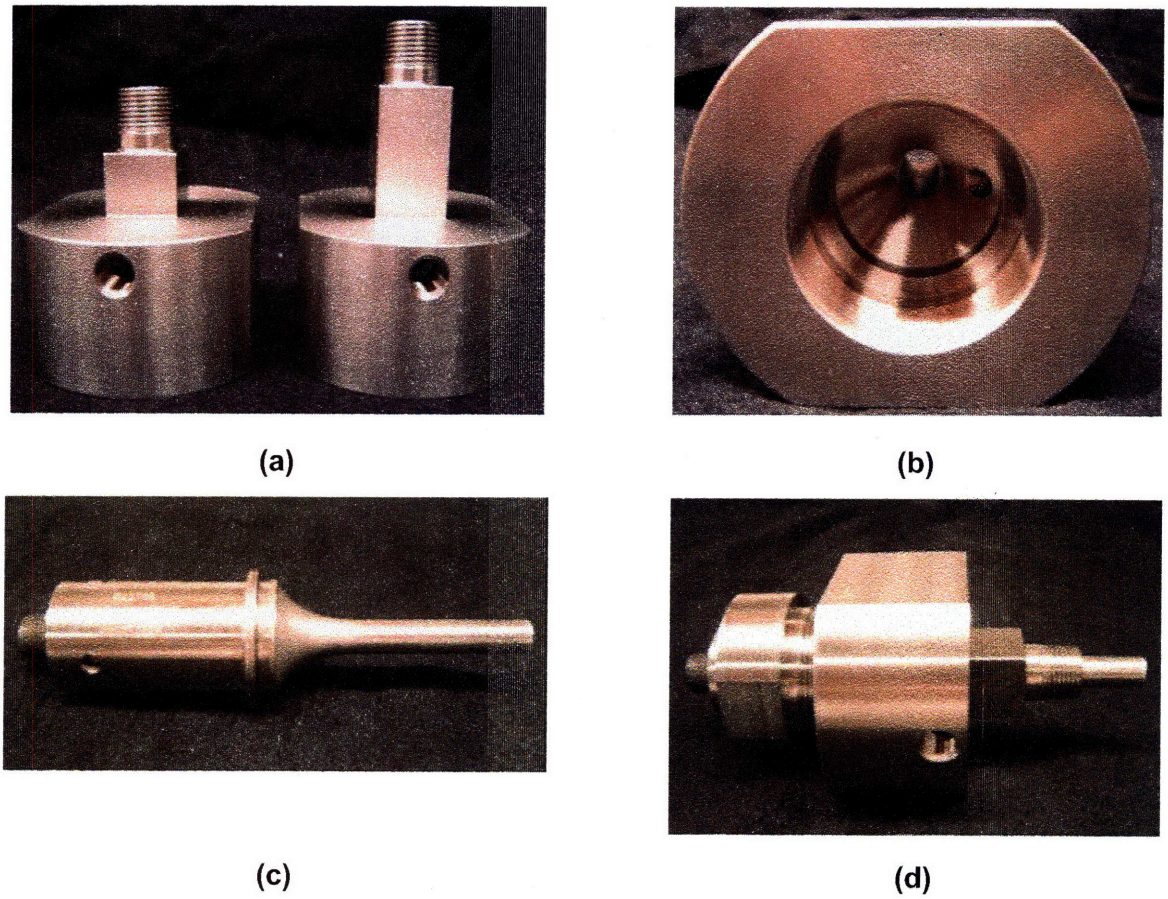

Figure 3-15. Photographs of the ultrasonic horn and adapter (photos/ Ciccolini). **(a)** adapter body for mounting the horn tip downwards (*left*) and upwards (*right*); **(b)** interior view and sealing surface of the body; **(c)** ultrasonic horn; **(d)** horn/adapter assembly ('tip downwards' design).

The instrumentation components and fittings configuration for the ultrasonic view cell is shown in **Figure 3-16**. Cell *P* was monitored by a pressure gauge (**PI**; Swagelok, *PGI-63C-PG5000-LAQX*, ca. 0–345 bar [0–5000 pisa] span, accuracy ± 1.5% of span [5 bar or 75 pisa]) and a DAQ-interfaced transducer (identical to **PT-3**). Cell *T* was measured by a J-type dual-element thermocouple (**TI**; Omega, *SIC316SS-125U-6-DUAL*, accuracy ± 0.1 °C) connected to both a local controller (**C-6**; [identical to **C-1**]) and the DAQ system. Adapter *T* was measured by an identical thermocouple and interfaced with controller **C-5** (identical to **C-1**) and the DAQ system. Temperature set-points for the cell were attained (within ± 0.5 °C) by interfacing the **C-6** with a variable autotransformer (**VA-8**; [identical to **VA-1**]) and insulated heating tape (Omega, *STH051-080*) wrapped tightly around the exterior cell wall. *T* set-points for the adapter

were identical to those of the cell and were attained by interfacing **C-7** (identical to **C-1**) with **VA-7** (identical to **VA-1**) and with heating tape wrapped tightly around the adapter body.

The ultrasonic horn was connected to an analog power supply unit (Branson, *S-450A*) by way of a converter containing a piezoelectric crystal. The power supply was used to control the duty cycle (i.e., ratio of 'on' to 'off' time; 100% duty cycle = continuous ultrasound) and power output (i.e., intensity of ultrasound). The converter transformed electrical power from the supply into high-frequency mechanical energy and imparted this energy to the horn tip. In simple terms, high-frequency vibrations of the horn tip created sound waves, and when placed near the interface of two dense fluids, droplets of each phase disperse into one another (see Timko [2004] for a more in-depth discussion of the mechanisms governing emulsion formation for general liquid/liquid and CO_2/liquid mixtures).

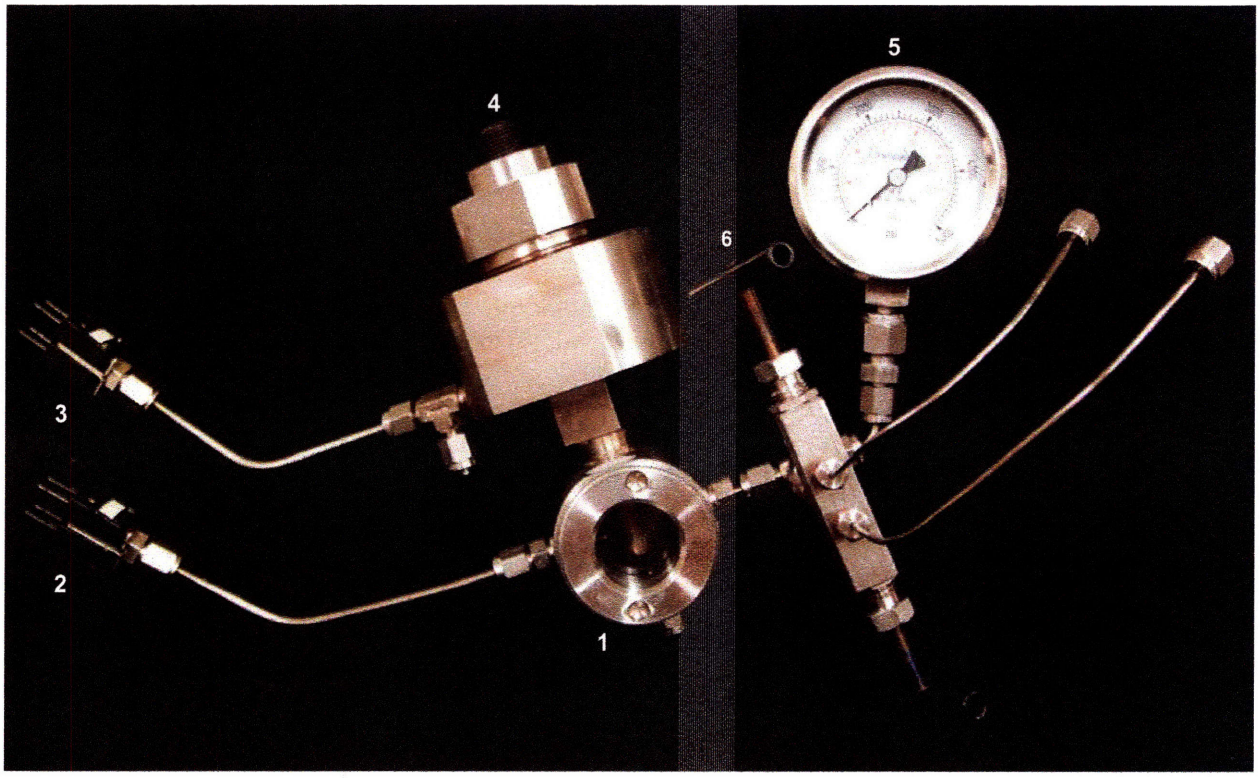

Figure 3-16. Photograph of the ultrasonic view cell (**VC-4**) (photo/ Ciccolini). **(1)** 25-mL view cell with the front window assembly installed; **(2)** cell thermocouple; **(3)** adapter thermocouple; **(4)** horn/adapter assembly ('tip downwards' design); **(5)** pressure gauge; **(6)** three-way two stem valve.

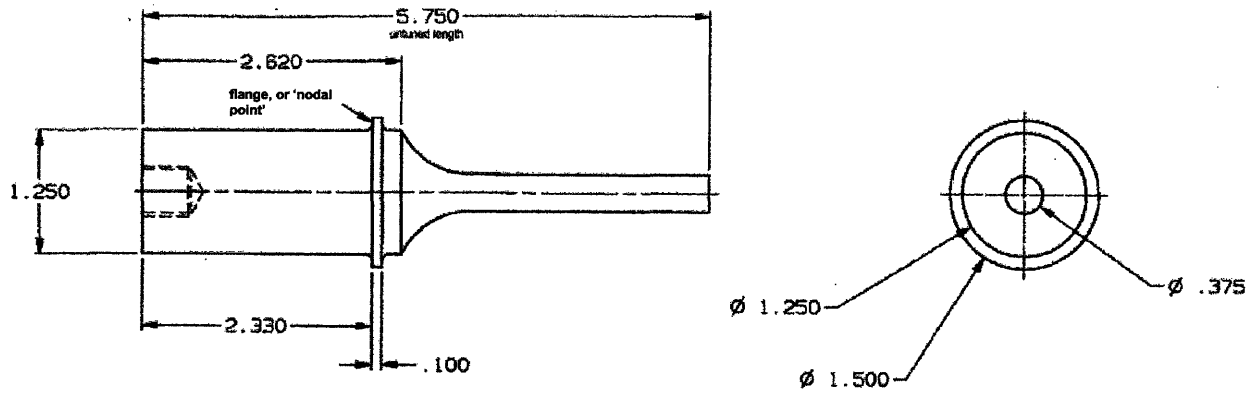

Figure 3-17. Dimensions (in inches) for the ultrasonic horn (adapted from Sonics & Materials).

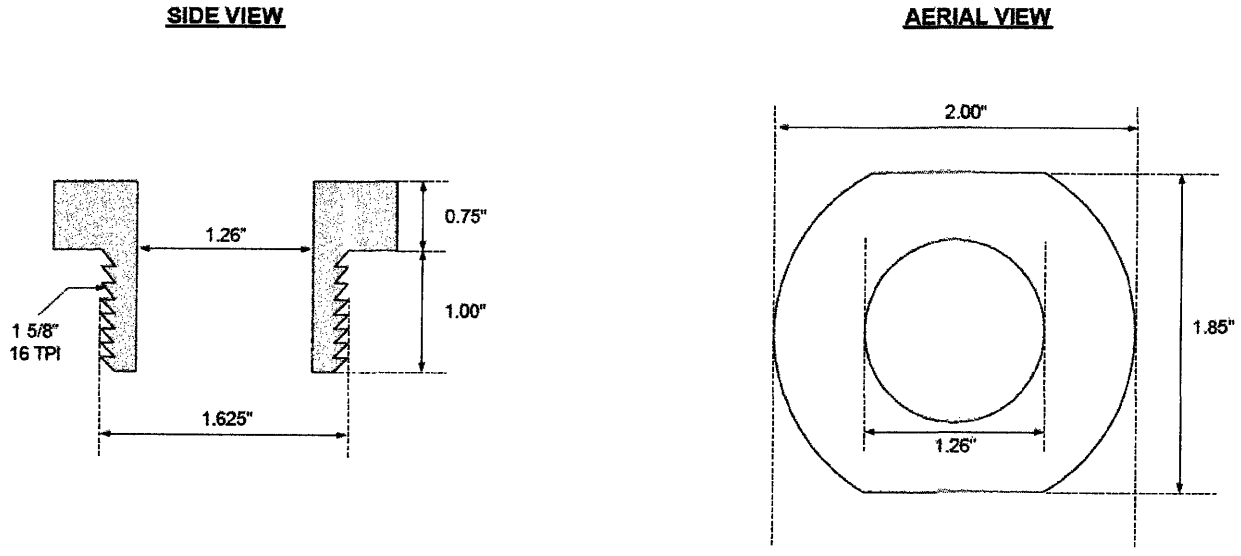

Figure 3-18. Dimensions (in inches) for the cap portion of the ultrasonic horn adapter.

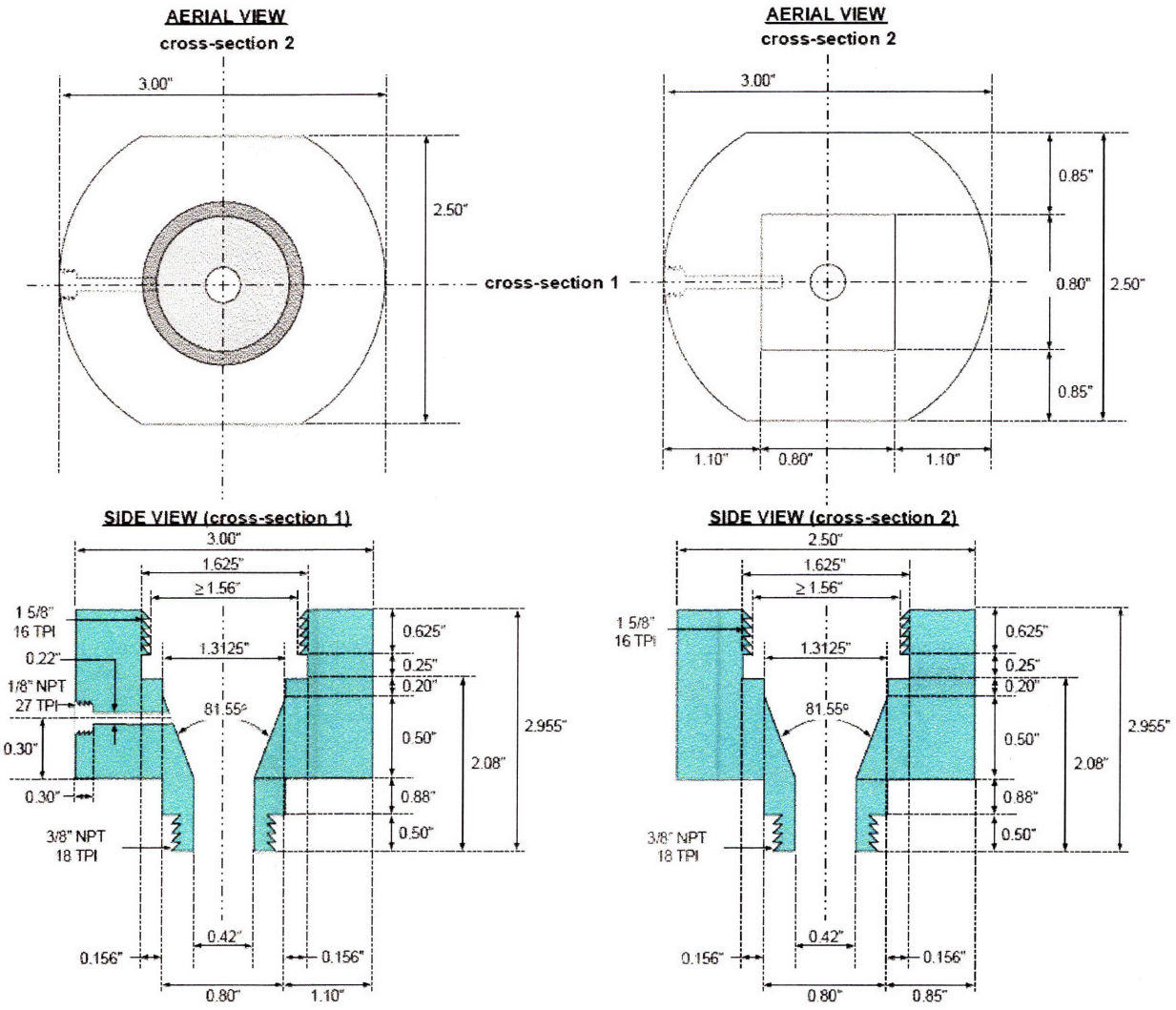

Figure 3-19. Dimensions (in inches) for the body portion of the ultrasonic horn adapter when the horn tip faces downwards.

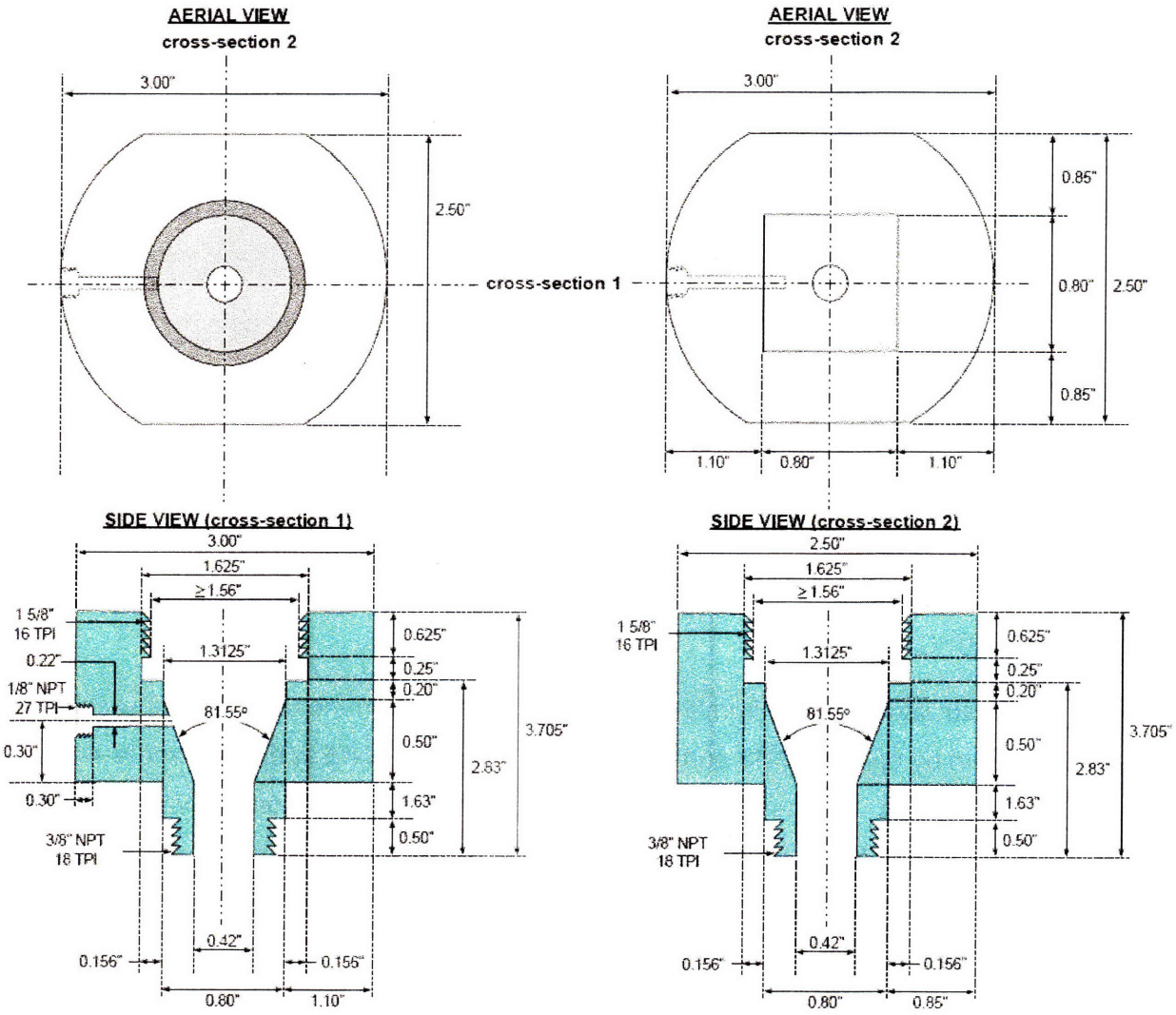

Figure 3-20. Dimensions (in inches) for the body portion of the ultrasonic horn adapter when the horn tip faces upwards.

General Operating Procedures

The general operating procedures for the ultrasonic view cell system were similar to those of the view cells system. Deviations from these procedures are delineated below:

1. **Vessel preparation and loading.** To prevent galling and stripping of the threads, the adapter cap was dressed with a high-*T* anti-seize compound (HiP, *SS-30*). The adapter's internal sealing surface was cleaned with a cotton swap. The o-ring and gasket was added to the horn and was placed into the body of the adapter. The cap was fastened to the body by hand. The adapter body was placed within a vice and the cap was tightened to 50 ft.-lbs. [ca. 68 N·m] using an adjustable torque wrench.

   The vessel was mounted in the ultrasound bay of the G2 System and connected to the high-*P* manifold. The converter was connected to the horn by hand and then to the power supply. The vessel was supported by clamping both the cap of the adapter and converter to a ring stand.

2. **Heating.** The desired temperature set-points were dialed into the controllers and the variable autotransformers were turned on. The autotransformers were set to 90% for experiments requiring $100 < T < 150$ °C, 60% for $40 < T < 60$ °C, and 30% for $T < 40$ °C.

3. **Pressurization.** CO_2 from the high-*P* manifold entered the ultrasonic view cell system by opening **V-13** and placing **V-14** in the *b-c,* **V-15** in the *b-c,* and **V-44** in the *b-c* positions. Ar was added by the identical valve configuration, but with **V-14** in the *a-b* position. Following pressurization, residual pressure that accumulated between the vessel inlet stem and manifold was vented by switching **V-44** to the *a-b* position while keeping **V-47** in the *b-c* position and **V-48** closed.

4. **Sonication.** After reaching *T* and *P*, the desired duty cycle and power output values were set on the power supply and sonication was initiated. During the first few pulses, the pressure decreased due to increased absorption of CO_2 into the previously unmixed liquid phase. Sonication was terminated until additional CO_2 was added to the system and the desired *P* was reached.

5. **Cooling.** Heating was terminated by reducing all set-point temperatures to 25 °C and turning off all autotransformers. The cell was allowed to cool to ambient *T* via natural convection.

6. **Venting.** CO_2 (or Ar) within the cell was released at ambient *T*, with sonication off, and was sent either directly to the vent or to the sparge chamber. With **V-46** and the outlet stem closed, CO_2 was sent directly to the vent by placing **V-45** in the *a-b* and **V-47** in the *b-c* positions. The outlet stem was opened and CO_2 was released by slowly opening **V-46**. **V-46** was insulated with heating tape and interfaced with **VA-6**. **VA-6** was set to 30% to prevent valve damage due to CO_2 expansion during the venting process.

   When sending CO_2 to sparge chamber **SC-1**, a similar venting procedure was used, but with **V-47** in the *b-c* position and **V-48** opened.

7. **Vacuum.** The ultrasonic view cell system was connected to the vacuum system via **V-35**. Vacuum was achieved by powering the pump, switching **V-45** to the *b-c* and position and opening **V-35**.

8. **Unloading and cleaning.** The cap was removed from the adapter and the horn was removed from the vessel. Several rinses were made to the cap and body threads, interior of the body, horn, o-ring, and gasket. All rinses were combined with the cell rinses and stored for future analysis.

3.3. Analytical/Sampling Equipment and Procedures

3.3.1. At-condition Sampling/Injection Units

At-condition sampling and liquid injections were made possible by connecting a six-way valve (**SV**; Valco, *C6UW*) equipped with a sample loop (**SL**; Valco, *SL100CUW* series) to the desired vessel. A piping diagram and photographs of a sampling/injection unit are shown in **Figure 3-21**. Needle valves (**V-a** and **V-b**; HiP, *15-21AM1NMA*) were placed on each side of the sample loop to ensure the containment of high-*P* samples when changing valve positions (*vide infra*). **V-a** was fitted with a SS Luer-Lok® needle (McMaster-Carr, *6710A65*) that enabled a liquid-tight connection with a Luer-Lok® syringe (**S**) needed while flushing the sample loop or adding reagents. **V-b** was fitted with a length of tubing that was directed either to the inverted-buret apparatus during $[CO_2]_l$ measurements (see **Section 3.3.2**), a volumetric flask, vial, or waste beaker. When the unit was used for sampling purposes, pump **P-2** was used to continuously recirculate vessel contents through the sample loop to ensure that the sample was representative of the vessel contents. In addition, all tubing connecting to and from the unit was wrapped tightly with heating tape and controlled to the *T* of the vessel. Using resources available at the MIT Student Machine Shop (MIT SMS), the components of the unit were mounted on a compact and portable aluminum panel.

The vessel contents were exposed to the sample loop by placing the **SV** knob in the 'northeast' position, which connected ports 1 & 2, 3 & 4, and 5 & 6 shown in **Figure 3-21**. Ports 1 & 6, 2 & 3, and 4 & 5 were connected by placing the knob in the 'northwest' position.

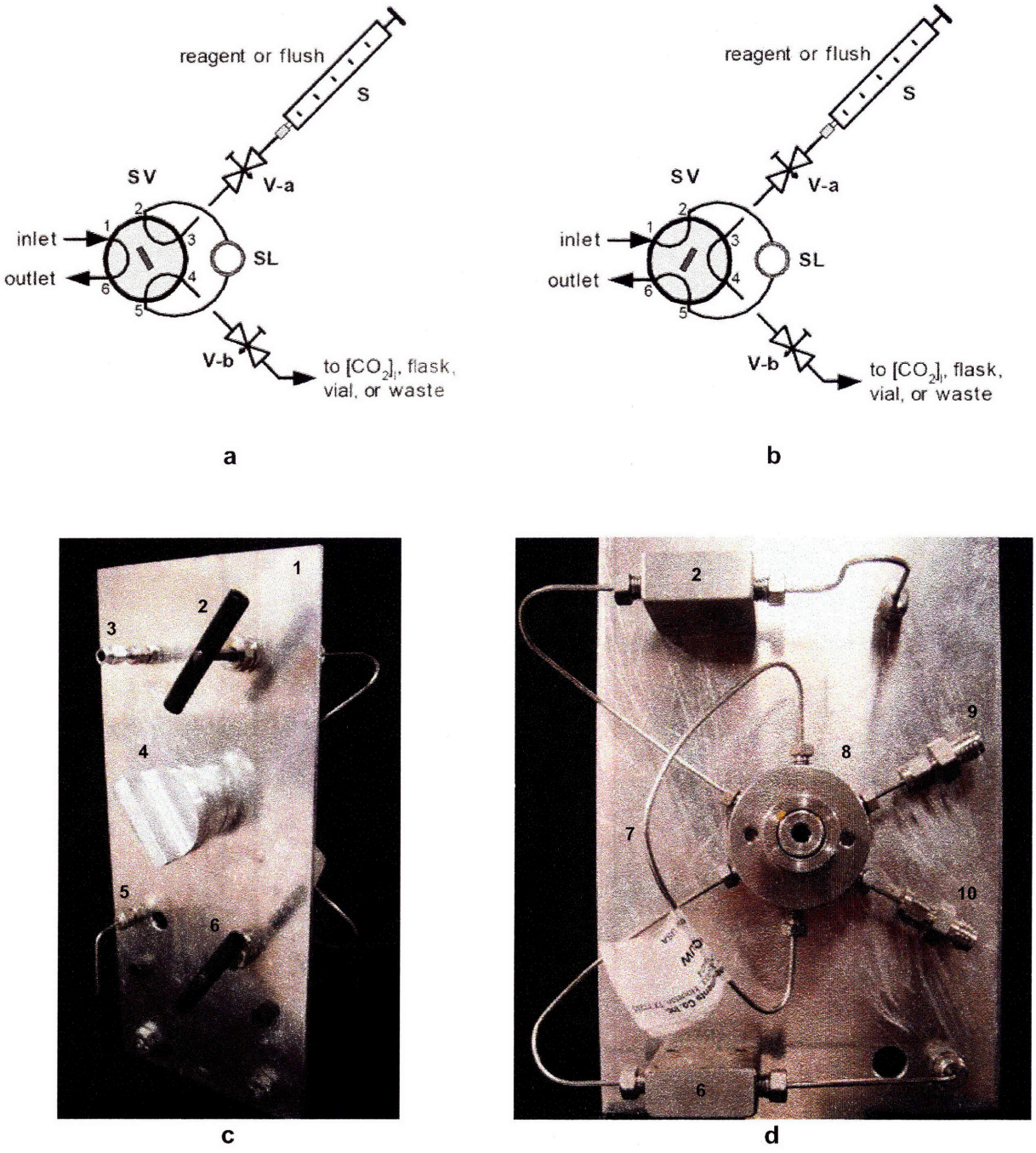

Figure 3-21. Piping diagram for the sampling/injection unit. Valve configurations for knob in the 'northwest' **(a)** and 'northeast' **(b)** positions. Photographs of the front **(c)** and back of the unit (**d**) (photos/ Ciccolini): **(1)** mounting panel; **(2)** valve **V-a**; (3) Luer-Lok® needle; **(4)** knob (in the 'northwest' position); **(5)** tubing length to flask, vial, or waste; **(6)** valve **V-b**; **(7)** sample loop; **(8)** six-way valve **SV**; **(9)** connection to pump outlet when used for sampling, connection to manifold when used for injections; **(10)** return connection to vessel.

General Operating Procedures

Mixture Sampling

The sampling unit inlet line was connected to the pump outlet and the outlet line to the vessel (e.g., **Figure 3-8**). **SV** was placed in the 'northeast' position. In this valve position, contents from the vessel entered the unit, passed through the sample loop, and returned to the vessel. Following recirculation through the loop for ca. 5 minutes (and when the sample loop *T* matched that of the vessel), **SV** was switched quickly to the 'northwest' position. In this position, the contents of the sample loop were isolated from the vessel and trapped between **V-a** and **V-b**. The vessel contents continued to recirculate through the unit, but not through the sample loop.

When preparing a sample for HPLC analysis, a short length of tubing was added to **V-b** and directed to a volumetric flask. **V-b** was opened slowly and the contents of the sample loop expanded into the flask. A syringe that contained HPLC-grade dichloromethane or acetonitrile was connected to the Luer-Lok® needle and **V-a** was opened. The sample loop was flushed with solvent and directed to the flask. The syringe was disconnected and the sample loop was dried with high-velocity air (supplied from a nozzle located in the fume hood). **V-a** and **V-b** were closed and **SV** was switched quickly to the 'northeast' to refill the sample loop.

Reagent Injection

The sampling unit inlet line was connected to the high-*P* manifold and the outlet line to the vessel (e.g., **Figure 3-5**). **SV** was placed in the 'northwest' position. In this valve position, CO_2 (or Ar) from the manifold vessel directly entered the vessel without entering the sample loop. Sample loop size was identical to the desired injection volume. Sample loops of volume larger than the injection volume were not used, as portions of the injection would have been lost to the dead-volume tubing that connected the Luer-Lok® needle to the loop. For a desired reagent injection of 0.5 mL, for example, the six-way valve was equipped with a 0.5-mL (Valco, *SL500CUW*) sample loop and a syringe containing ca. 1 mL of reagent was fixed to the Luer-Lok® needle. With **V-a** and **V-b** open, the entire 1-mL aliquot was dispensed. The volume of the injection in excess of the sample loop and dead-volume flowed out of the unit from **V-b** and was collected in a waste beaker. To prevent drainage from the loop due to gravity, **V-a** and **V-b** were closed during the flow of excess reagent from **V-b**. At this point, the loop was filled

completely with reagent. The high-*P* manifold was then pressurized to a *P* higher than that of the vessel and **SV** was switched quickly to the 'northeast' position. In this valve position, the vessel was exposed to the sample loop contents (and not the dead-volume). With vessel *P* < manifold *P*, liquid was quickly injected into the vessel. Excess CO_2 was flushed through the loop and into the vessel to ensure the complete addition of reagent.

Following the injection, **SV** was placed in the 'northwest' position. **V-b** was opened slowly and the remaining contents of the loop were directed to a waste beaker. The sample loop was flushed several times with solvent and dried with air.

3.3.2. Inverted-Buret Apparatus

The gas content of a pressurized liquid sample can be determined by directing the sample to an inverted gas buret filled with a liquid and observing the displaced volume. The inverted-buret apparatus was therefore used in conjunction with the reactor system and sampling/injection unit to measure the liquid-phase concentration of CO_2 in several CXL systems. A derivation of the relationship between $[CO_2]_l$ and volume displacement data is presented in **Section 6.5.1**.

The PID for the inverted-buret apparatus is shown in **Figure 3-22**. A 50-mL graduated gas buret (**B**; VWR, *14210-332*) was filled completely with DI water, inverted in a crystallizing dish (VWR, *89000-292*) also containing DI water, and clamped to a ring stand. A length of SS tubing was inserted approximately 2 in. into the buret and connected to **SV** via **V-b** (see **Section 3.3.1**). CO_2 was continuously bubbled through the bath water via two frits (Alltech Associates, *9402*) placed at opposite ends of the dish. A needle valve insulated with heating tape and interfaced with a variable autotransformer (**VA-6**; identical to **VA-1**) controlled the CO_2 sparge rate. Had the bath not been sparged, a portion of the CO_2 from the sample may have dissolved in the water (rather than displacing the water) and resulted in inaccurate displacements. The bath was agitated with a Teflon®-coated octagon-shaped magnetic stir bar (**SB**; VWR, *58948-116*) driven externally by a stir plate (**SP-3**; VWR, *58940-158*). Bath *T* was measured with a mineral spirit-filled general-purpose thermometer (**TI**; identical to **TI-4**) and the atmospheric *P* by way of a dial barometer (**PI**; VWR, *15551-024*). The unit was operated on a table adjacent to the G2 System.

In a typical experiment, the reactor system was used to recirculate a liquid-phase sample through **SV-1** (**Figure 3-8**). A sample was isolated from the system (see **Section 3.3.1**)

and directed to **B** by slowly opening **V-b**. Due to the reduced *P* at the exit of **V-b**, CO_2 rapidly evolved from the liquid sample, expanded into the gas buret, and displaced the water within it.

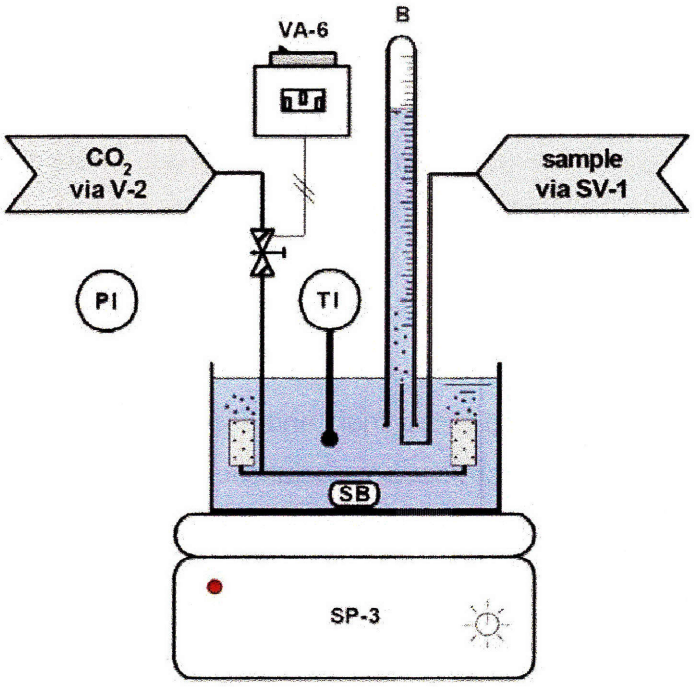

Figure 3-22. Piping and instrumentation diagram for the inverted-buret apparatus.

General Operating Procedures

The bath dish was filled 75% with DI water supplied from our laboratory station. CO_2 sparging was initiated by opening **V-2** and then slowly adjusting the inlet valve such that the flow of CO_2 into the water did not result in violent bubbling or overflow. **VA-6** was set to 30% to prevent valve damage due to CO_2 expansion. Agitation was initiated and the bath thermocouple was placed in the center of the bath via a clamp mounted to a ring stand. The atmospheric pressure gauge was placed in the immediate vicinity of apparatus.

After allowing the bath to saturate for ca. 15 minutes, a 25-mL graduated glass buret (VWR, *89003-530*) equipped with a rubber bulb was used to add CO_2-saturated water from the bath into the gas buret. When the gas buret was filled completely, a finger tip was placed over the inlet to create a water-tight seal. The gas buret was then inverted, placed beneath the bath liquid level, and clamped to the ring stand. The opening of the gas buret was located at approximately half of the distance between the bottom of the dish and the liquid level and far

enough away from either frit to avoid contamination with CO_2 from the manifold. When this procedure was done correctly, all air bubbles were absent from the gas buret prior to taking a sample. The tubing connected to **SV-1** via **V-b** was placed under the liquid level and into the gas buret.

A sample was directed to the gas buret by following the sampling procedure described in **Section 3.3.1** After recording the displaced water volume and all other necessary data (i.e., bath *T*, atmospheric *P*, and bath and buret liquid-level heights), the water remaining in the gas buret was poured back into the bath. The gas buret was refilled and the sampling process was repeated. The buret was rinsed with HPLC-grade acetone and dried with high-velocity after five samples were taken and the bath water was changed and re-saturated after twenty samples were taken. This was done to avoid gas buret and bath contamination (and hence measurement inaccuracies) with the organic portion of the incoming liquid sample.

3.3.3. Volume Determination Unit

The volume determination unit was used to determine vessel and piping system volumes. Accurate vessel volumes were needed to determine charge amounts for arriving at desired reagent concentrations. The PID for the volume determination unit is given in **Figure 3-23**. The unit consisted of a 50-mL 316 SS cylindrical pressure vessel (**PV**; Swagelok, *SS-4CS-TW-50*, MAWP of ca. 70 bar [1000 pisa] at 311 K [38 °C]) and pressure gauge (**PI**; Swagelok, *PGI-63C-PG3000-LAQX*, ca. 0 – 205 bar [0–3000 pisa] span, accuracy ± 1.5% of span [3 bar or 45 pisa]). The unit was operated in a fume hood adjacent to the G2 System.

In a typical volume determination experiment, Ar was loaded to the pressure vessel, adjusted to a known pressure, expanded into the vessel of interest, and allowed to equilibrate to ambient temperature. Using the volume of the determination unit and the system pressures before and after the expansion, vessel volume was calculated assuming ideal gas behavior (*vide infra*).

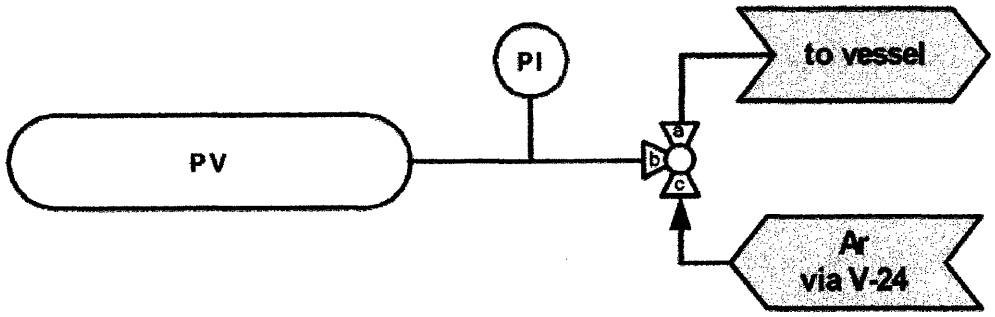

Figure 3-23. Piping and instrumentation diagram for the volume determination unit.

General Operating Procedures

The volume determination unit was connected to the vessel of interest via a short length of tubing of negligible volume. The unit was connected to the high-*P* manifold via **V-24** and Ar was added by placing the unit's three-way valve in the *b-c* position. When the pressure reached ca. 1500 pisa, the three-way valve was switched to the *a-b* position and Ar was expanded into the vessel. The final pressure was recorded, the unit was emptied by opening an outlet valve on the vessel, and the procedure was repeated for a total of five times.

Since Ar at ambient *T* and the pressures used here for volume determination behaves ideally, the ideal gas law for an isothermal expansion process was assumed:

$$P_i \underline{V}_i = P_f \underline{V}_f \qquad \textbf{(3-1)}$$

where P_i is the initial pressure (i.e., *P* of the volume determination unit after the Ar charge), $\underline{V}_i$ is the initial volume (i.e., volume of the unit, $\underline{V}_{du}$), P_f is the final pressure (i.e., *P* of the unit and vessel after the expansion), and $\underline{V}_f$ is the final volume (i.e., volume of the unit *and* the vessel, $\underline{V}_v$). All pressures were absolute. With $\underline{V}_i = \underline{V}_{du}$ and $\underline{V}_f = \underline{V}_{du} + \underline{V}_v$, equation **(3-1)** can be rearranged to solve for the volume of the vessel:

$$\underline{V}_v = \underline{V}_{du}\left[\frac{P_i}{P_f} - 1\right] \qquad \textbf{(3-2)}$$

The volume of the unit (V_{du}) was 56.6 ± 0.2 mL, which includes the volume associated with the pressure vessel, gauge, tubing, and three-way valve. $\underline{V}_{du}$ was determined by charging ca. 105

bar (1515 pisa) of Ar to the vessel and recording its mass on a balance (VWR, *11379-194*). The density of Ar at the experimental *T* and *P* conditions was also determined using the ideal gas law. With the density and moles of Ar known, $\underline{V}_{du}$ was easily determined. Comparison of densities predicted by the ideal gas law and a highly-accurate equation-of-state provided by the National Institute of Standards and Technology (NIST) revealed deviations (at our operating conditions) of less than 5%.

3.3.4. Off-gas Detection Unit

The off-gas detection unit was used to measure CO_2 evolution from solid CO_2/amine complexes. A PID for the unit is given in **Figure 3-25**. The unit consisted of a 125-mL glass collecting tube (**GT**; Supelco, 02-2161) that was equipped with stopcocked inlets and outlets and a rubber septum. The chamber was sampled by puncturing the septum with a 200-μL gas-tight syringe equipped with a SS needle (**GS**; Supelco, *20738,* MAWP of ca. 1 bar [15 pisa] at 298 K [25 °C]). Chamber *P* was monitored by a pressure gauge (**PI**; Omega, *DPG1000B-15G*, ca. 0–1 bar [0–15 pisa] span, accuracy ± 0.25% of span). The gauge was connected to the chamber via rubber vacuum pump hosing. Cell *T* was measured by a J-type single-element thermocouple (**TI**; Omega, *GJMQSS-062G-6*, accuracy ± 0.1 °C) that was connected to a local controller (**C-4**; [identical to **C-1**]). Temperature set-points were attained (within ± 0.5 °C) by interfacing the controller with a variable autotransformer (**VA-5**; [identical to **VA-1**]) and insulated heating tape (Omega, *STH051-080*) wrapped tightly around the exterior chamber wall. The thermocouple was placed between the exterior chamber wall and the heating tape. The chamber was agitated with a Teflon®-coated octagon-shaped magnetic stir bar (**SB**; VWR, *58948-116*) driven externally by a stir plate (**SP-3**; VWR, *58940-158*). The unit was operated in a fume hood adjacent to the G2 System. Gas samples obtained from the unit were injected into our laboratory's gas chromatography (GC) unit configured to detect light gases.

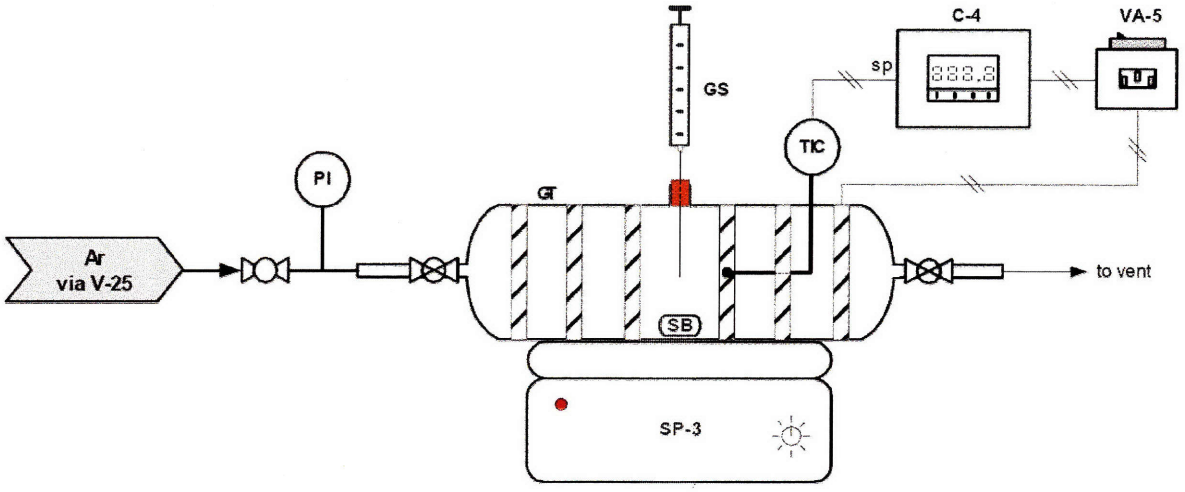

Figure 3-24. Piping and instrumentation diagram for the off-gas detection unit.

3.3.5. High-Pressure Liquid Chromatography System

In the Spring of 2006, our group acquired several Waters HPLC system components and the associated computer control system from Professor Kenneth A. Smith. The system was originally used by Professor Jackie Y. Ying's group, but had been out of service for approximately a year. After performing some minor in-house servicing of these components and adding some of our own, a fully-functional HPLC system was created. A diagram illustrating the connectivity of the system components is given in **Figure 3-25** and a photograph of the system is given in **Figure 3-26**. Details of the HPLC analytical methods used for the detection of compounds for specific reactions or phase behavior studies are provided in their chapters of discussion.

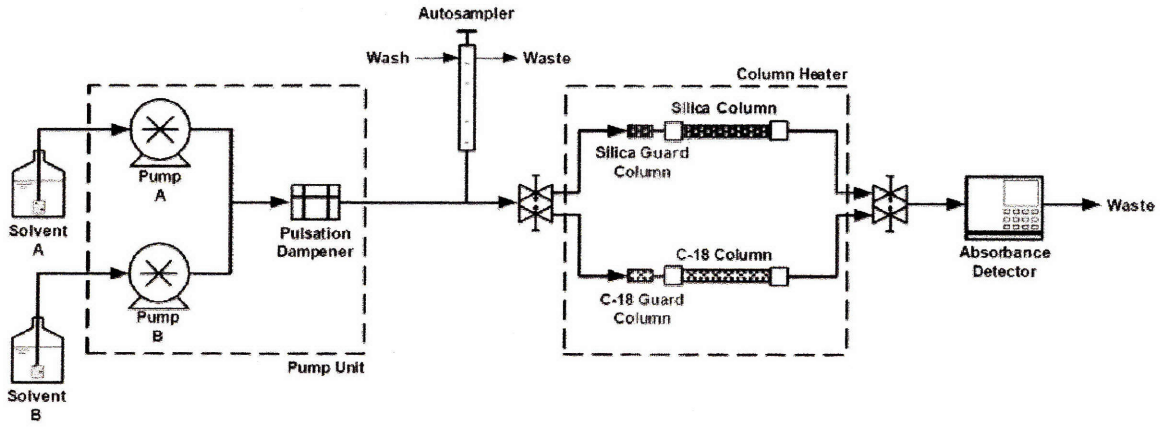

Figure 3-25. Piping diagram for the HPLC system.

The system was configured with two-stem, three-way valves to allow for the interchangeable use of either a Si-based chromatography column (Alltech, *70006*, 250 mm length x 4.6 mm OD) for normal-phase detection of non-polar compounds or a C-18-based column (Alltech, *70066*, 250 mm length x 4.6 mm OD) for reverse-phase detection of polar compounds. A guard cartridge — essentially a disposable miniature version of the column — was placed before each column to protect from clogging, saturation, and degradation that would have otherwise occurred in the column (Si: Alltech, *96125*; C-18: Alltech, *96121*). The columns were mounted vertically within a column heater.

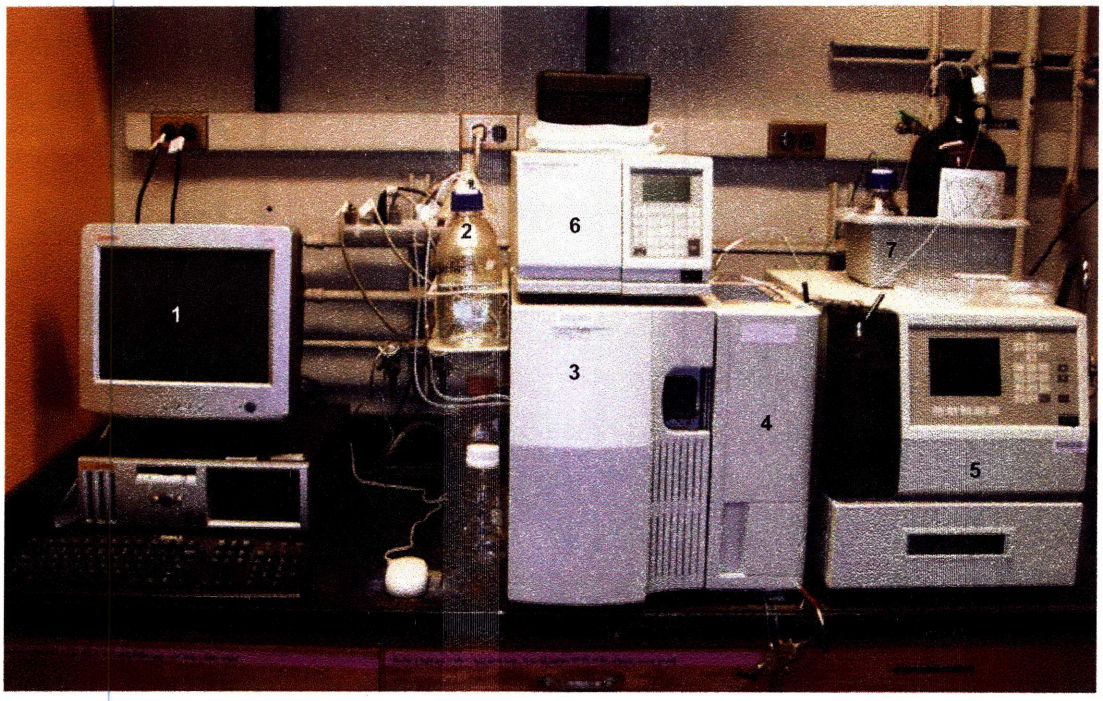

Figure 3-26. Photograph of the HLPC system (photo/ Ciccolini): **(1)** computer; **(2)** solvent bottles; **(3)** pump unit; **(4)** column heater; **(5)** autosampler; **(6)** absorbance detector; **(7)** waste accumulation. The columns (not shown) were mounted within the column heater enclosure.

A binary piston-pump system (Waters, *1525*) capable of operating in either isocratic or gradient mode delivered HPLC-grade solvent to the columns. Each pump contained two heads whose outlets were directed to a flow pulsation dampener. Solvents were stored in 1-L feed bottles (VWR, *89000-240*) and placed at an elevation higher than the pump heads. A small portion of the feed bottle cap was left open to the atmosphere in order avoid vacuum formation during solvent consumption. Vacuum formation when using volatile solvents (e.g.,

dichloromethane) led to vapor entrainment in the solvent feed lines and cavitation within the pump.

Exiting the pump, the mobile phase entered a variable-injection volume autosampler (Waters, *717 Plus*). The autosampler was equipped with interchangeable carousels capable of housing either 96 1-mL sample vials or 48 3-mL sample vials. Given the relatively large number of samples generated in the experiments in this work, only the 96 position carousel (with 1-mL sample vials [VWR, *66015-702*]) was used. The injector within the autosampler was routinely flushed with HPLC-grade dichloromethane. Mobile phase and injection compounds exiting the columns were directed to a dual-wavelength UV/Vis absorbance detector (Waters, *2487*). All system components — excluding the manual two-stem three-way valves — were connected to a computer (Compaq, *Evo*) and controlled by the *Breeze* software suite (Waters). *Breeze* provided a user-friendly GUI and several tools to analyze injection data.

General Operating Procedures

The computer and all HPLC components were turned on and the two-stem valves were configured to allow flow through a column. The solvent containers were filled and the pump enclosure was opened. Each pump was primed by opening the priming valve, inserting a 10-mL plastic syringe (Waters, *WAT010337*) into the priming valve port, and withdrawing several syringe aliquots of solvent. The priming valve was closed when gas bubbles were no longer visible in the solvent lines leading to the pump heads. Samples were placed in the carousel and loaded into the autosampler. The HPLC control software was loaded and a desired method and sample queue was established. In general, the system was allowed to equilibrate (i.e., solvent flow through the column) for 60 minutes and the autosampler injector was flushed for 15 minutes prior to the first injection and after the last injection. In between injections, the system was equilibrated and the injector was flushed for 6.5 minutes each. The absorbance detector and pumps were programmed to automatically shut down after the last step in the sample queue. Sample chromatograms obtained from the HPLC system are shown in **Sections 7.2** and **9.2**.

3.4. Safety Considerations

Laboratory safety was taken very seriously and was essential to the successful completion of this project. Project-related safety concerns and their corresponding precautionary procedures with respect to the nature of the chemicals used and the elevated pressures and temperatures of our experimental work are delineated in **Table 3-1**.

Table 3-1. Safety concerns and precautionary procedures followed.

SAFETY CONCERN	PRECAUTIONS TAKEN
Hazardous Chemicals	• Thoroughly reviewed available Material and Safety Data Sheets (MSDS) prior to the handling of all chemicals. • Used appropriate and chemically-compatible personal protective equipment (PPE), the minimum including goggles with side shields, gloves, and a lab coat. • Used chemicals in fume hood or equally-ventilated area. • Stored, labeled, and disposed of all chemicals in accordance to the guidelines established by MIT Environmental Health and Safety (EHS) department.
Elevated Pressures	• Thoroughly reviewed all equipment and fittings operating instructions and documentation and identified maximum allowable working conditions. • Installed all high-pressure equipment and associated fittings in a well-ventilated areas and within a shatter-proof, thick-walled enclosures. • Installed pressure relief valves or rupture discs on all high-pressure vessels.
Elevated Temperatures	• Thoroughly reviewed all equipment and fittings operating instructions and documentation and identified maximum allowable working conditions. • Cooled materials or used heavily-insulated gloves before handling.

3.5. Recommendations

The G2 System described in the previous sections was very effective at conducting reactions and phase behavior experiments discussed in this work. The following recommendations will increase the System's versatility for chemical processing in CO_2-based media:

- **Enhance process control.** Adding pneumatic valves and a process control panel such that the user can feed chemicals and manipulate valves and operating conditions from a satellite process control station will minimize exposure to high-*P* and high-*T* conditions.
- **Upgrades.** Replacing pump **P-2** with one that provides a larger flow rate (e.g., with one like **P-1**) would enhance mixing and decrease equilibration times. Adding magnetically-coupled mixing drives (such as the one for reactor) to the view cells would similarly enhance mixing in multi-phasic systems. Replacing the current fluoropolymer o-rings for the reactor and view cells systems, decreasing window size, and upgrading to hastelloy-C construction would enable the user to achieve operation at higher temperatures. One should consult the manufacturer for advice for achieving higher temperatures (e.g., $T > 150$ °C) prior to operation outside of the current maximum allowable working conditions. Magnet-within-tube-type mixers would allow for fluid recirculation at these conditions.
- **Go continuous.** Installation and operation of syringe pumps in alternating phases (i.e., one pump fills as the other dispenses) and back-pressure regulators will allow the user to perform semi-batch and continuous reactions and also post-reaction separations.
- **Add additional *in situ* sampling methods.** On-line sampling integration and automation with the HPLC system would eliminate the need for sample preparation and allow for continuous and phase-specific analyses of reaction mixtures.

3.6. Equipment and Instrumentation Symbol Key

Table 3-2. Equipment and instrumentation symbol key.

Symbol	Label	Description	Manufacturer
Valves			
	V-1,2,9–11,13,25,30, 31,41,46	Two-way needle valve	
	V-3,4,22–24,32–36, 43,48	Two-way ball valve	
	V-16–21		
	V-12,14,15,26,27,38, 39	Three-way ball valve	
	V-28,29,40,42,44,45, 47		
	(vessel-specific)	Stopcock	
	(vessel-specific)	Two-stem needle valve	
	V-8	Check valve	
	V-5,6,7	Pressure relief valve	
	RD	Rupture disc	
	SV	Sampling Valve, 6-way	
Instrumentation and Control			
	PI	Pressure indication (gauge)	
	TI	Temperature indication	
	TIC	Temperature indication and control	
	PT	Pressure transducer	
	VA	Variable autotransformer	
	C	Controller	

Table 3-2 (continued). Equipment and instrumentation key.

Symbol	Label	Description	Notes
Instrumentation and Control (cont.)			
	n/a	Thermocouple	
	n/a	Instrumentation signal via electrical wiring to controller and/or DAQ	
		Insulated with heating tape	
	SH	Strip heater	
n/a	sp	Set point	
Vessels			
not shown	R	Reactor, 100-mL	
	VC	View Cell, 25-mL	
	SG	Sight gauge	
	PV	Pressure vessel	
	GC	Gas chamber	
Miscellaneous Equipment, Fittings, and Symbols			
not shown	AA	Agitator assembly	
	B	Buret, 50-mL	
	CC	Cooling coil	
	CH	Chiller	
	CT	Cold trap	
	GS	Gas syringe	
	HA	Horn adapter	
	HX	Heat exchanger	
	I	Impeller	
	P	Pump	
	PG	Pressure generator	
	S	Syringe	
	SC	Sparge chamber	
	SL	Sample loop	
	SP	Stir plate	
	UH	Ultrasonic horn	
	VP	Vacuum pump	
	WB	Water bath	

Table 3-2 (continued). Equipment and instrumentation key.

Symbol	Label	Description	Manufacturer
Miscellaneous Equipment, Fittings, and Symbols (cont.)			
	F	Filter, 7μm	
	n/a	Frit	
	SB	Stir bar, teflon encapsulated	
	RG-1	Regulator	
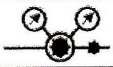	RG-2	Regulator	
	n/a	Sealed line	
	n/a	Indicates liquid level	
n/a	CFS	Cooling fluid supply	
	CFR	Cooling fluid return	

4. A Review of Carbon-Nitrogen Bond Formation in Carbon Dioxide-Based Media

4.1. Motivation

The editorial board of *Advances in Nitrogen Heterocycles* report that over half of all known organic compounds are heterocycles, with a large fraction of these containing nitrogen heteroatoms. Commercial interest in nitrogen heterocycles is fueled by their medicinal attributes. Penicillin, for example, is a well-known naturally-occurring nitrogen heterocycle used for its antimicrobial activity. This and other examples of pharmacologically-significant nitrogen heterocycles are shown in **Figure 4-1**.

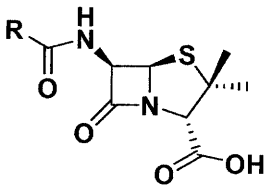

Penicillin®
antibiotic

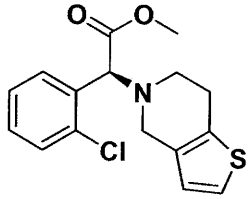

Bristol-Myers Squibb's Plavix®
antiplatelet

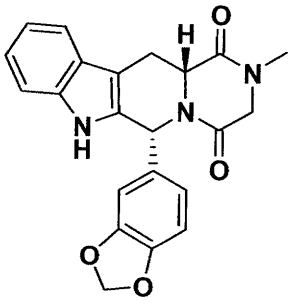

Eli Lilly's Cialis®
vasodilator

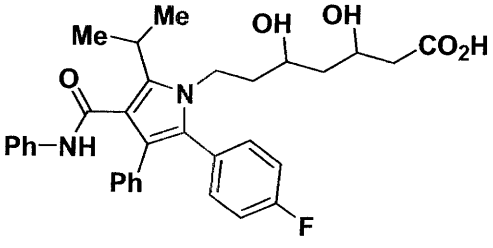

Merck's Lipitor®
statin

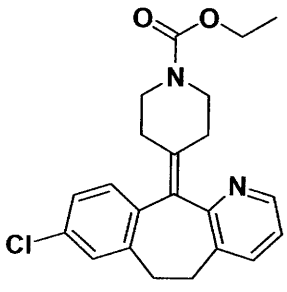

Schering-Plough's Claritin®
antihistamine

Figure 4-1. Examples of some nitrogen heterocycles with medicinal attributes.

Several carbon-nitrogen (C-*N*) bond-forming reactions involving amines are required during the synthesis of the compounds shown in **Figure 4-1**. Given the significance and widespread use of complex nitrogen heterocycles, it is fitting to explore methods for their synthesis using environmentally-benign reaction media. This chapter introduces the concept of C-*N* bond-formation in CO_2-based media and provides a review of synthetic transformations performed to date.

4.2. The Reaction of Carbon Dioxide with Amines

C-*N* bond-formation in CO_2-based media is complicated by the facility of nucleophilic amines to react with carbon dioxide. The reaction of CO_2 with amines is well-documented in the literature (Alauzun et. al., 2008; Aresta, et al., 2000 and 2002; Aroonwilas et al., 2007; Caplow, 1968; Chaturvedi et al., 2007; Dell'Amico et al., 2003; Diaf et al., 1993; Dijkstra et al., 2007; Dunetz et al., 1995; Ewing et al., 1980; Francis, 1954; Frasco et al., 1963; Fischer et al., 2003; George et al., 2002; Hampe et al., 2003; Heldebrant et al., 2005; Jessop et al., 2005; Khanna et al., 1999; Kirsch et al., 2000; Liu et al., 2006; Masuda et al., 2005; Ochiai et al., 2008; Park et al., 2003; Ramachandran et al., 1998; Rudkevich et al., 2005; Sakakura et al., 2007; Sharma, 1965; Stastny et al., 2007; Vaidya et al., 2007; Wen et al., 1995; Yoshikatsu et al., 2007; Xie et al., 2004; Xu et al., 2004). In the presence of carbon dioxide, primary and secondary amines (**1**) can react reversibly to form carbamic acids (**2**) and ammonium carbamate salts (**3**):

$$\underset{\mathbf{1}}{RNH_2} \overset{CO_2}{\rightleftharpoons} \underset{\mathbf{2}}{RNHCO_2H} \overset{RNH_2}{\rightleftharpoons} \underset{\mathbf{3}}{RNHCO_2^-\,{}^+H_3NR} \qquad \textbf{(4-1)}$$

In low-dielectric, aprotic media such as CO_2, carbamic acid formation proceeds through an amine-carbon dioxide coordination complex (**4**) (see **Section 10.4.1** and references therein):

$$RNH_2 + CO_2 \rightleftharpoons \underset{\mathbf{4}}{RNH_2 \cdots CO_2} \qquad \textbf{(4-2)}$$

In the absence of added base and water, a second amine molecule acts as a hydrogen transfer agent in the formation of carbamic acid:

$$RNH_2\cdots CO_2 + RNH_2 \rightleftharpoons RNHCO_2H + RNH_2 \quad \textbf{(4-3)}$$

Finally, an amine molecule reacts with carbamic acid in acid-base type chemistry to form the carbamic salt:

$$RNHCO_2H + RNH_2 \rightleftharpoons RNHCO_2^- {}^+H_3NR \quad \textbf{(4-4)}$$

Both primary and secondary amines are capable of participating in the reaction mechanisms described by equations **(4-2) – (4-4)**. Tertiary amines, however, require a base-catalyzed hydration mechanism (Vaidya et al., 2007) that is not discussed here. In reaction media such as water, carbamic acid is instead formed by the medium-assisted protonation of a zwitterion intermediate (i.e., a zwitterion forms instead of **4** in equation **[4-2]** and is protonated by water instead of another free amine molecule in equation **[4-3]**, see **Section 10.4.1**).

When CO_2 is added to neat amines or amine-rich solutions, carbamate salt formation is often accompanied by the precipitation of a white solid. The reaction and phase behavior properties associated carbamate salt formation within CO_2/amine systems has attracted considerable attention among researchers and industrial practitioners. Aqueous monoethanolamine (MEA) and other amine-containing solutions, for example, are used on an industrial scale to scrub CO_2 from effluent gas streams (Aroonwilas et al., 2007). Conversely, other researchers have proposed the use of CO_2 for the selective isolation of amines from reaction mixtures (Xie et al., 2004).

Masuda and coworkers (2005) investigated the reaction of carbon dioxide and ω-(1-napthyl)alkylamines in conventional solvents and found that carbamic acid and salt formation depended on the physical properties of the solvent employed. Various solutions of 3-naphthalen-1-yl-propylamine (**5**) were sparged with CO_2 at 298 K (25 °C) and the analysis of the resulting carbamic acid (**6**) and carbamic salt (**7**) was performed by *in situ* ^1H and ^{13}C NMR, IR, and absorption and fluorescence spectroscopy. Summarized in **Figure 4-2**, Masuda and coworkers found that solutions of amine **1** in DMSO, DMF, or pyridine (protophilic, highly dipolar, and aprotic solvents) produce carbamic acid **6** quantitatively. In dioxane (protophilic, dipolar, and aprotic), carbamic acid and a minor amount of carbamic salt was formed. In contrast, in MeCN (protophobic, dipolar, and aprotic), benzene, or $CHCl_3$ (apolar and aprotic), and 2-PrOH or MeOH (dipolar and amphiprotic), carbamic salt **7** is formed over carbamic acid **6**. In MeOH, ammonium carbonates and bicarbonates of amine **5** were also detected and

suspected to be a result of water contamination. Importantly, the Masuda study revealed that carbamic acids and ammonium carbamate salts were soluble in certain solvents. Therefore, the failure to observe a white, solid precipitate does not exclude the possibility of CO_2/amine reaction products.

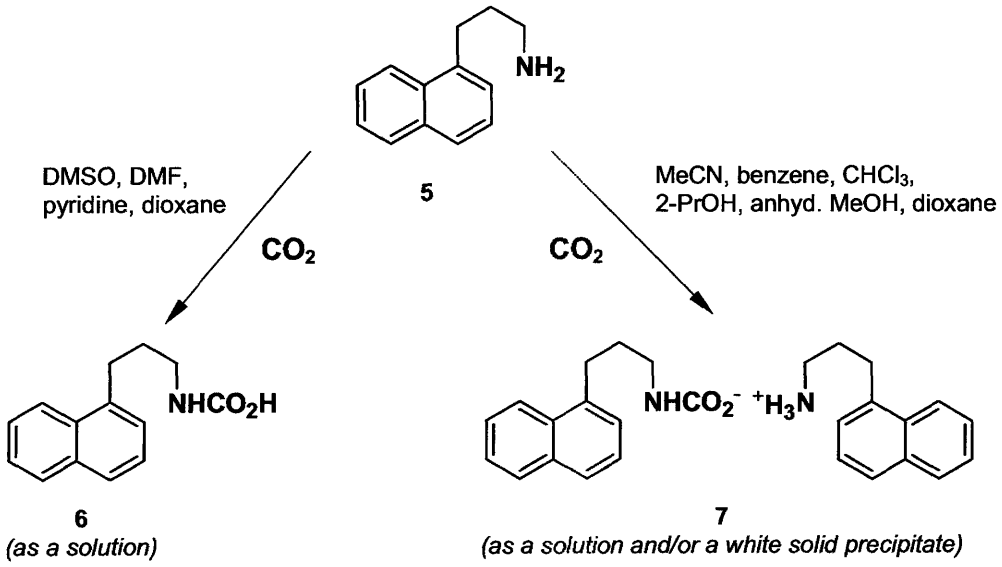

Figure 4-2. Reaction of 3-naphthalen-1-yl-propylamine with carbon dioxide in various solvents at 298 K (25 °C).

For primary amines, an increase in basicity generally increases the rate of carbamic acid formation (Sharma, 1965; Ewing et al., 1980; Caplow, 1968). The analysis for secondary amines is complicated by the introduction of steric effects. Fisher and coworkers (2003) monitored the reaction of benzylamine and *N*-benzylamine derivatives in neat CO_2 via on-line ^1H NMR spectroscopy at 323 K (50 °C) and 80 – 200 bar (1150 – 2900 psia) and found that carbamic acid formation was suppressed with increasing *N*-substituent size (see **Figure 4-3**). Carbamic acid was detected for *N*-methyl-benzylamine (**7**), but not for *N*-isopropyl-benzylamine (**8**) and *N*-tert-butyl-benzylamine (**9**). *N*-substitution in these cases actually led to an increase in amine nucleophilicity relative to the parent benzylamine, suggesting that steric effects were the controlling factor in carbamic acid formation. Carbon dioxide reacted with benzylamine (**6**) and phenethylamine (**10**) to form the CO_2-insoluble carbamic salts, making spectroscopy measurements for these amines unattainable. Importantly, the Fischer study revealed that carbamic acid derivatives (but not carbamate salt derivatives) were soluble in CO_2.

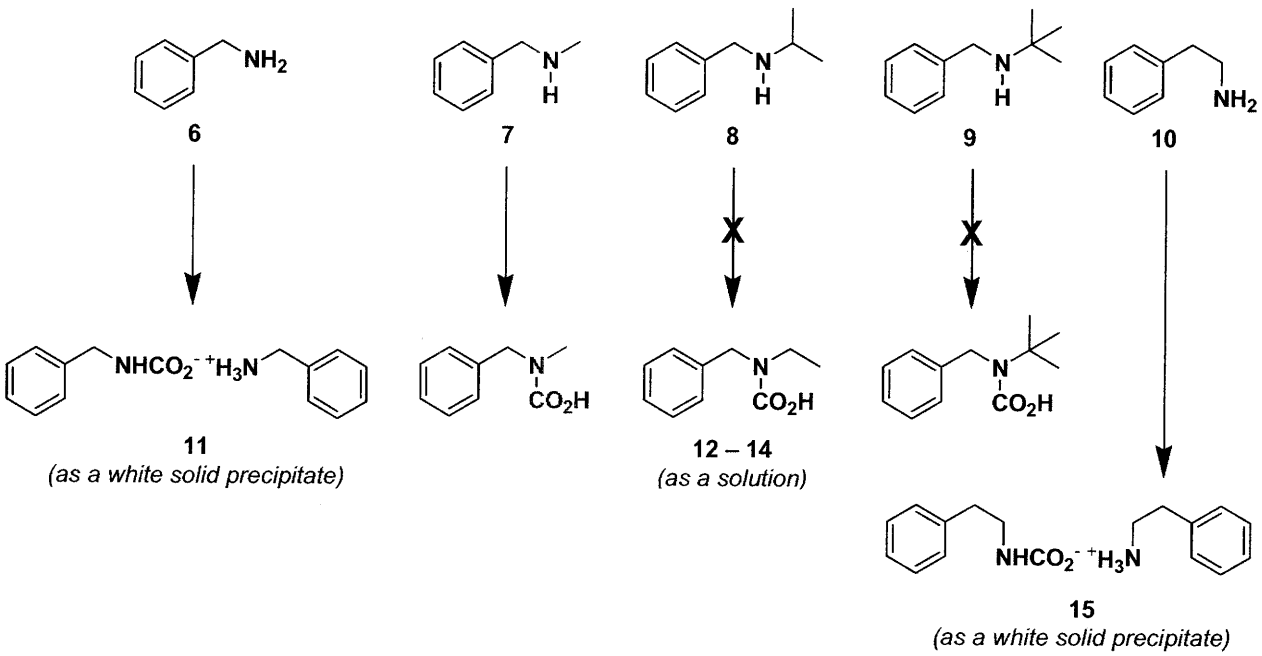

Figure 4-3. Reaction of amines with neat carbon dioxide at 323 K (50 °C) and 80 – 200 bar (1150 – 2900psia).

In a similar high-pressure NMR spectroscopy study, Dijkstra and coworkers (2007) examined the reaction of isopropylamine with neat CO_2 and observed a variation in carbamic acid formation as a function of process operating conditions. The authors did not comment on whether or not carbamate salts formed during their experiments. Shown in **Figure 4-4**, increasing pressure at constant temperature shifts the equilibrium towards 'free' amine and CO_2. This behavior is straightforward and is ascribed to Le Chatlier's principle. The decrease in the equilibrium ratio of carbamic acid to free amine at fixed CO_2 density with increasing *T* suggests that carbamic acid formation is an exothermic process and that the Gibbs free energy change of reaction increases with increasing temperature.

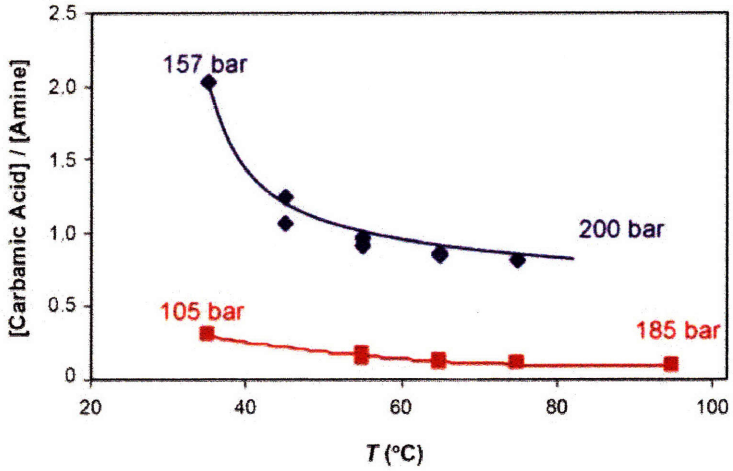

Figure 4-4. Equilibrium carbamic acid and amine concentration ratios for the reaction of carbon dioxide with isopropylamine plotted as a function of temperature and pressure (adapted from Dijkstra et al., 2007).

Dijkstra and coworkers (2007) also reported on the effect of solvent properties on carbamic acid formation for the carbon dioxide/isopropylamine reaction system. The authors found that carbamic acid was formed quantitatively in DMSO, whereas a mixture of carbamic acid and carbamate salt was observed for dioxane. Their results agree with observations reported earlier by Masuda and coworkers (2005) (see **Figure 4-2**).

4.3. Review of Synthetic Transformations

4.3.1 Carbon Dioxide as both a Raw Material and Solvent

Carbamic acid and ammonium carbamate salt formation from amines and CO_2 make CO_2-based media an attractive solvent for C-*N* bond-forming reactions that involve these intermediates. For these processes, CO_2 serves as both a solvent *and* raw material. Sakakura and coworkers (2007) recently published a comprehensive review of synthetic transformations involving carbon dioxide as a raw material, several of which include substrates that bear amine functionality. A discussion of these transformations is provided below:

Synthesis of Ureas and Urethanes

Since syntheses of ureas (**16**) and urethanes (**17**) from the amine/CO_2 reaction system are well-documented in the literature (Dell'Amico et al., 2003; Sakakura et. al., 2007; Chaturvedi et al., 2007 and references therein), we have limited our discussion to a broad overview. Shown schematically in **Figure 4-5**, ureas are produced from the reaction of dehydrated carbamic acids and ammonium carbamate salts with amines. Urethanes (or carbamates) are produced from reactions of carbamic acids and ammonium carbamate salts with alkylating agents.

Shi and coworkers (2000), for example, observed carbamate formation during the synthesis of amides from pyrrolidine and diphenylselenophosphinic chloride in the presence of potassium carbonate:

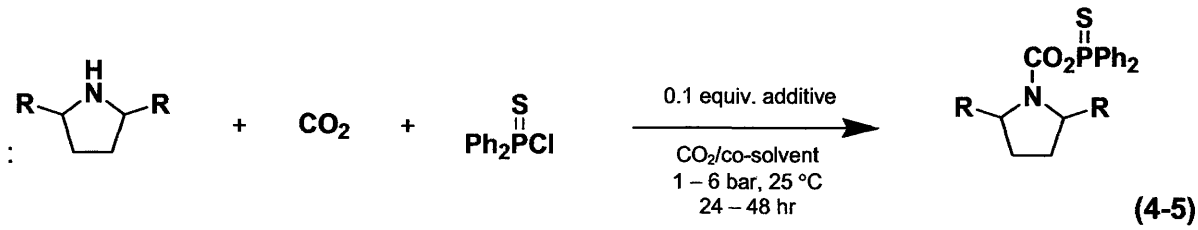

(4-5)

The authors proposed that the carbamate was the addition product of diphenylselenophosphinic chloride with the carbamic acid formed by the reaction of pyrrolidine with carbon dioxide. For reactions performed in the absence of CO_2, the authors attribute carbamic acid to the generation of carbon dioxide from the acid-catalyzed decomposition of potassium carbonate. Steric effects played an important role in the reaction, as carbon dioxide insertion decreased with increasing chloride substituent size.

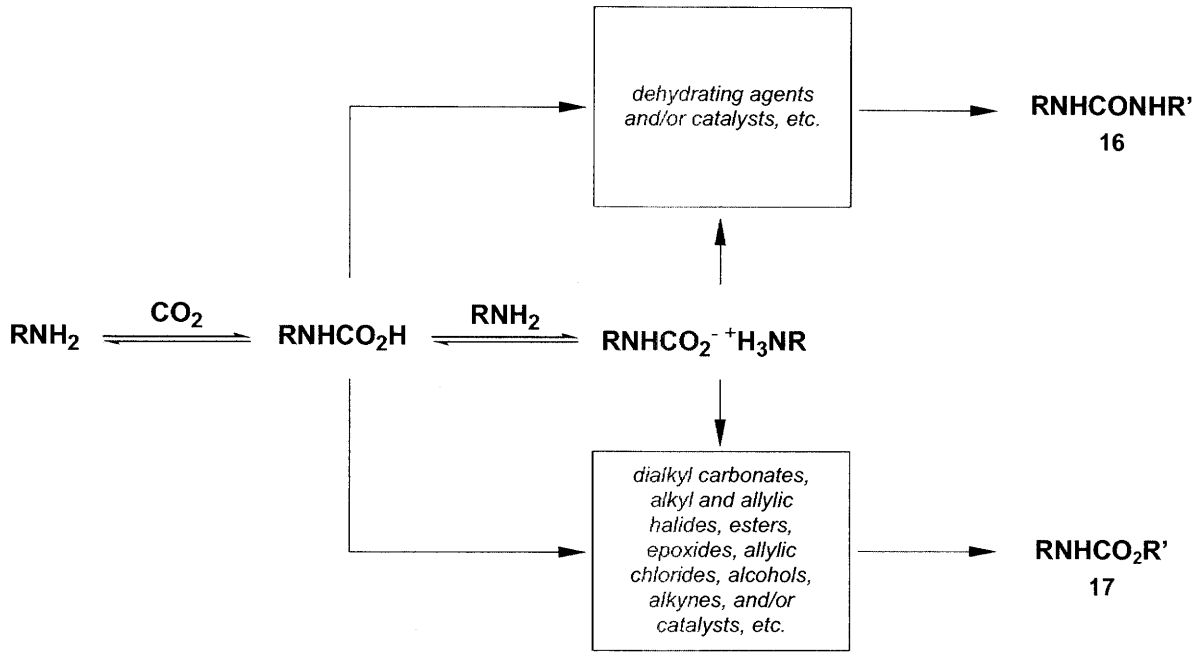

Figure 4-5. Urea and urethane derivate synthesis from the reaction of carbon dioxide and amines.

Synthesis of Quinazoline Derivatives

Mizuno and coworkers (2002 and 2004) reported the synthesis of quinazolines (**19**) from the reaction of aminobenzonitriles (**18**) with carbon dioxide in the presence of a catalytic amount of base:

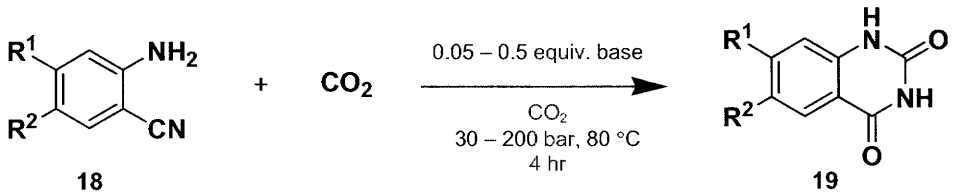

(4-6)

The authors proposed that the reaction proceeded via the intramolecular cyclization of the intermediate carbamate salt formed by the reaction of the amine with carbon dioxide. The reaction did not proceed to a quantifiable amount in the absence of base, which indicated its importance for carbamic acid formation and/or ring-closure. Increasing the pressure from 30 to 100 bar increased product yield by 15%. Although the authors did not comment on the phase

behavior of the reaction mixture, we presume that the increase in yield is due to the increase in reaction-phase CO_2 concentration.

Oxazolidinone Synthesis

Several reports exist for the synthesis of 2-oxazolidinones (**21** – **22**) from the reaction of aziridines (**20**) with carbon dioxide:

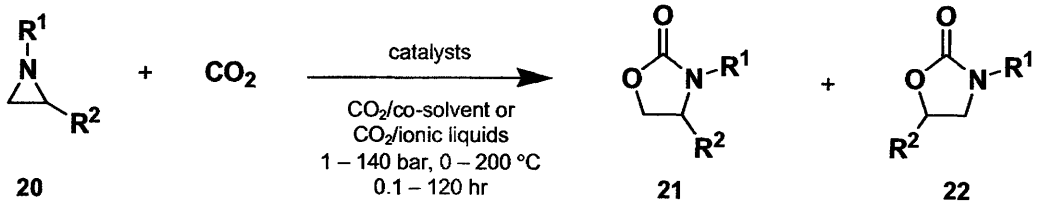

20 **21** **22** **(4-7)**

Sudo and coworkers (2003 and 2004) performed the reaction in a CO_2/co-solvent mixture at atmospheric pressure and observed exclusive selectivity for the 4-substituted product (**21**). The authors proposed a reaction mechanism involving the ring-opening of the **20** followed by the reaction of this intermediate with carbon dioxide to form carbamic acid. The carbamic acid subsequently underwent intramolecular cyclization to afford compound **21**.

Kawanami and coworkers (2005) investigated the reaction of 2-methyl-aziridine (R^1 = H, R^2 = Me) in both CO_2/co-solvent and CO_2/ionic liquid mixtures at elevated pressures and observed a biphasic reaction system that contained an upper, lower-density CO_2-rich supercritical-like phase and a lower, higher-density ionic liquid-rich liquid phase. They too observed selectivity for **21**. Product yield increased with pressures up to 80 bar and decreased thereafter. The authors ascribed the increase in yield below 80 bar to an increase in the liquid reaction-phase CO_2 concentration and postulated that the decrease in yields at higher pressures was due to the partitioning of the substrate to the CO_2-rich phase.

Miller and coworkers (2004), however, performed the reaction in CO_2/co-solvent mixtures and observed selectivity for the 5-substituted product (**22**) when using bulky amine substituents.

Bhanage and coworkers (2003) synthesized 2-oxazolidinones (**24**) by reacting aminoalcohols (**23**) with carbon dioxide in CO_2/co-solvent mixtures in the absence of additives:

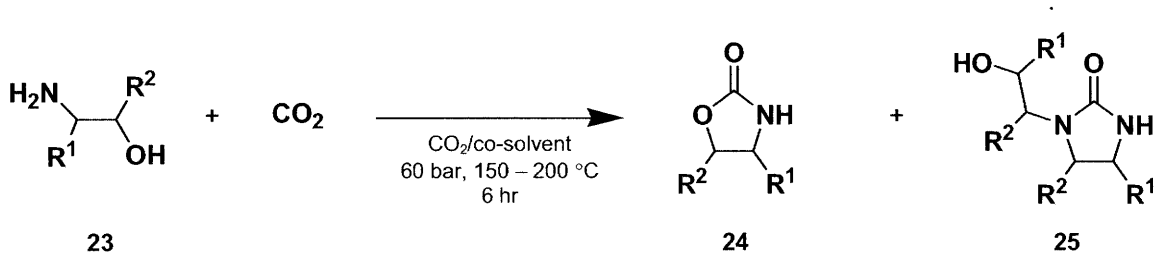

(4-8)

Selectivity for the desired 2-oxazolidinone (**24**) was comprised by the formation of undesired cyclic ureas (**25**) and decreased with increasing temperature.

Several reports also exist for the synthesis of 2-oxazolidinones (**27**) from the reaction of carbon dioxide with propargylamines (**26**) (Maggi et al., 2007; Costa et al., 1996; Feroci et al., 2005; Shi et al., 2002; Kayaki et al., 2006):

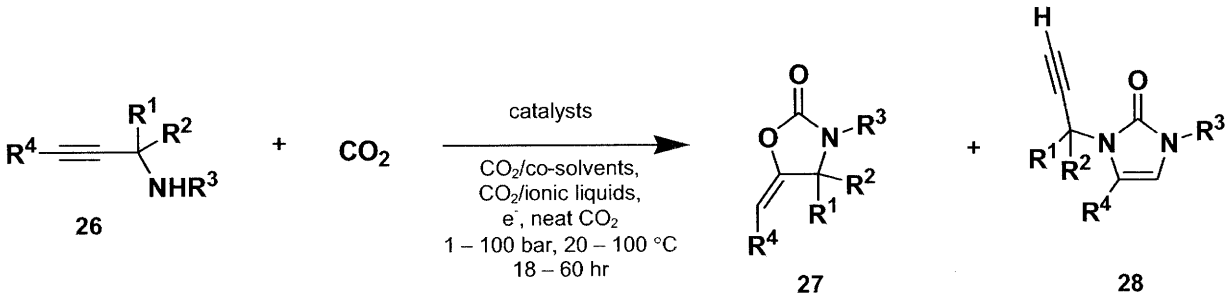

(4-9)

A majority of the reports for this reaction observe exclusive selectivity for the desired 2-oxazolidinones (**27**). Shi and coworkers (2002), however, observed a significant and variable amount of competitive cyclic urea (**28**) formation when employing propargylamine ($R^1 = R^2 = R^3 = R^4 = H$) and palladium-based catalysts in CO_2/co-solvent mixtures. Their study revealed that catalyst choice and amine functionality played important roles in reaction selectivity. They also observed an increase in selectivity for **27** with decreasing temperatures and increasing pressures.

Kayaki and workers (2006) recently performed this reaction in neat CO_2 and in the absence of any catalyst and found that 2-oxazolidinone yield varied appreciably with amine functionality and operating pressure. Product yield increased with pressures up to 60 bar and decreased thereafter. Visual observations revealed binary phase behavior that consisted of an upper, lower-density CO_2-rich supercritical-like phase and a lower, higher-density amine-rich liquid phase. Similar to the study by Sudo and coworkers (2003 and 2004), the authors attributed the initial increase in yield with pressure to the increase in carbamic acid and salt formation in the amine-rich liquid reaction phase. The authors also postulated that substrate partitioning to the CO_2-rich phase was responsible for reduced yields at higher pressures.

In separate studies, 2-oxazolidinones (**27**) were synthesized from the three-component coupling of amines with carbon dioxide and propargyl alcohols (**29**) (Costa et al., 1996; Gu et al., 2005):

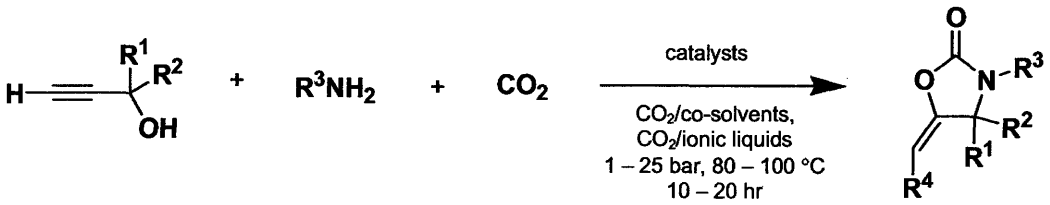

29 **27** **(4-10)**

Using a CO_2/ionic liquid mixture, Gu and coworkers (2005) extended the reaction to include a variety of amines and alcohols. Yield increased with increasing pressure again, presumably due to the increase in CO_2 concentration in the liquid reaction phase.

4.3.2 Carbon Dioxide as a Solvent

Formamide Synthesis

Jessop and coworkers (1994 and 1996) reported on the synthesis of formamides (**33**) in carbon dioxide via the reaction of amines with formic acid (**32**) generated from the *in situ* hydrogenation of carbon dioxide:

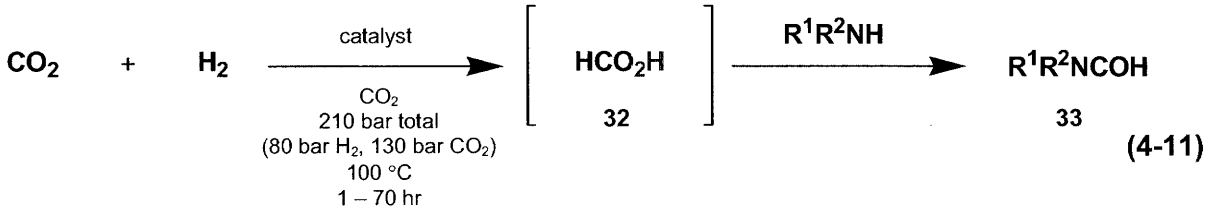

(4-11)

Unlike the previous examples, carbamic acid and ammonium salt formation compromised reaction efficiency. When using certain amines, the authors observed a deviation from mono-phasic behavior to systems that contained an upper, lower-density CO_2-rich supercritical-like phase believed to contain the catalyst, hydrogen, and formic acid, and a lower, higher-density liquid or solid amine-rich carbamic acid or salt phase. The authors attribute reduced reaction rates and yields for these amines to phase partitioning.

Pyrrolidine Synthesis

Wittmann and coworkers (2001) synthesized pyrrolidines (**35**) via the intramolecular hydroaminomethylation reaction involving ethylmethallylicamine (**34**), carbon monoxide and hydrogen:

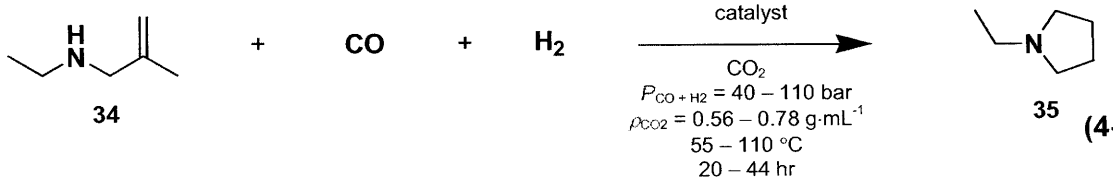

(4-12)

Their study revealed that whereas cyclic amides (or lactams) were the major products produced when performing this transformation in conventional solvents, saturated nitrogen heterocycles of type **35** were formed predominantly when using CO_2. The authors attribute this switch in selectivity to the reversible conversion of amine intermediates to carbamic acids that impeded reaction pathways leading to the lactam. On-line NMR measurements involving amine **34** and carbon dioxide confirmed the formation of the carbamic acid. In this case, CO_2 was thought to serve as both a solvent and *N*-protecting group. A discussion of phase behavior was not presented.

Tetrahydropyridine Synthesis

Shi and coworkers (2004) reported the imino-Diels-Alder reaction of imines (**36**) with Danishefsky's diene (**37**) to yield tetrahydropyridines (**38**):

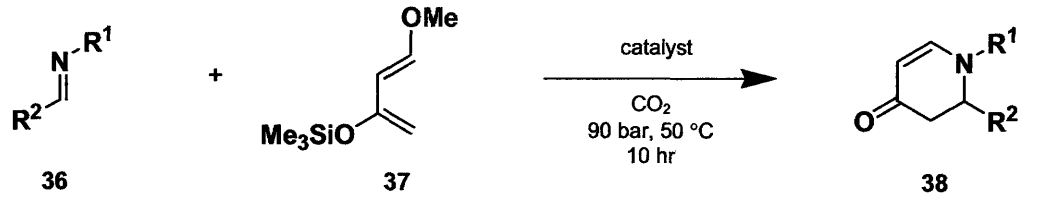

36 **37** **38** **(4-13)**

The authors did not mention the formation of carbamic acid nor did they provide a discussion of phase behavior.

Diaryl Amine Synthesis

Developed in collaboration with our laboratory under the Cambridge-MIT Institute partnership program (see **Section 1.7**), Smith and coworkers (2004 and 2005) from Professor Holmes' group developed protocols to synthesize diaryl amines (**41**) form *N*-silyl amines (**39**) and aryl halides (**40**):

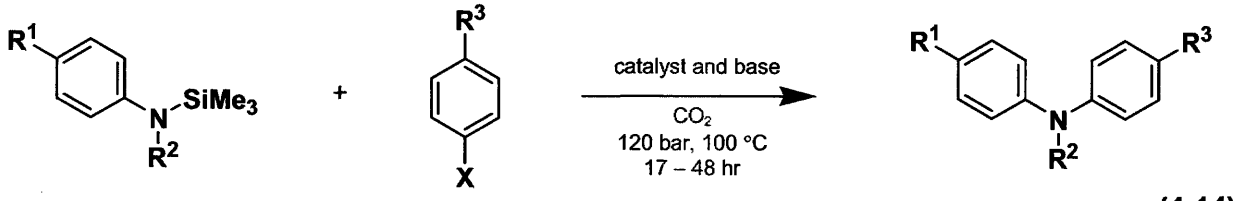

39 40 41 (4-14)

The cross-coupling reaction cited above was suppressed when employing more nucleophilic and less-sterically demanding *N*-silyl amines (**42**), possibly due to the formation of carbamic acid (**43**):

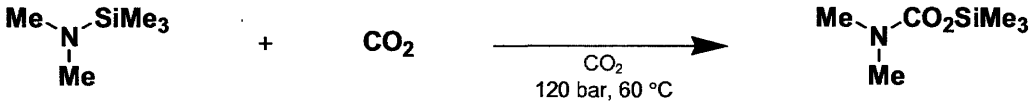

42 43 (4-15)

The authors also extended the scope of the reaction to include the intramolecular arylation of sulfonamides (**44**) to form tetrahydroquinolines (**45**):

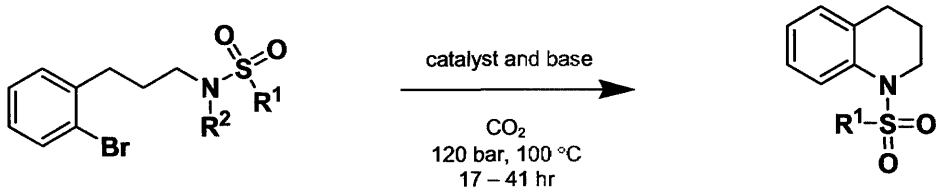

44 45 (4-16)

4.4. Conclusions and a Path Forward

The transformations reviewed in this chapter made it clear that in order to successfully engineer carbon-nitrogen bond-forming reactions in CO_2-based media, a firm understanding of phase behavior and the reaction of carbon dioxide with amines was required. We discovered that solvent choice, amine functionality, and process operating conditions all had significant impacts on carbamic acid and salt formation; carbamic acid and salt formation was suppressed when adding bulky *N*-substituents to primary amines and when operating at low pressures and high temperatures. Importantly, we found that while some reactions benefit from carbamic acid formation, the efficiency of several other processes diminish because of it.

Despite the modest level of research dealing with amine chemistry in CO_2-based media, when we began our studies, there were no general strategies that would allow for the development of a wide range of carbon-nitrogen bond-forming reactions. Motivated by the importance of nitrogen-containing compounds in the pharmaceutical and fine chemical industries and a growing commercial interest in utilizing environmentally-friendly syntheses, we specifically developed a program to explore the synthesis of nitrogen heterocycles in CO_2-based media. Our strategies involved chemically-modifying amines and/or operating at conditions that suppress carbamic acid interference. In addition, and unlike previous reports of C-*N* bond-formation, we complimented reconnaissance studies of feasible synthetic routes in CO_2-based media with quantitative analyses of reaction phase behavior and its impact on reaction efficiency. The remaining chapters discuss the experimental and theoretical variables explored for selected model reactions.

4.5. References

Alauzun, J., Besson, E., Mehdi, A., Reyé, C., and Corriu, R. J. P. *Reversible Covalent Chemistry of CO_2: An Opportunity for Nano-Structured Hybrid Organic-Inorganic Materials.* Chem. Meter., **2008**, *20*, 503-513.

Aresta, M. And Dibenedetto, A. *Development of Environmentally Friendly Synthesis: Use of Enzymes and Biomimetic Systems for the Direct Carboxylation of Organic Substrates.* Rev. Molec. Biotech., **2002**, 90, 113-128.

Aresta, M., Ballivet-Tkatchenko, D., Dell'Amico, D. B., Bonnet, M. C., Boschi, D., Calderazzo, F., Faure, R., Labella L., and Marchetti, F. *Isolation and Structural Determination of Two Derivatives of the Elusive Carbamic Acid.* Chem. Commun., **2000**, 1099-1100.

Aroonwilas, A. and Veawab, A. *Integration of CO_2 Capture Unit using Single- and Blended-Amines into Supercritical Coal-Fired Power Plants: Implications for Emission and Energy Management.* Int. J. Greenhouse Gas Contr., **2007**, *1*, 143-150.

Bhanage, B. M., Fujita, S.-I., Ikushima, Y., and Arai, M. Synthesis of Cyclic Ureas and Urethanes from Alkylene Diamines and Amino Alcohols with Pressurized Carbon Dioxide in the Absence of Catalysts. Green Chem., **2003**, *5*, 340-342.

Caplow, M. *Kinetics of Carbamate Formation and Breakdown.* J. Am. Chem. Soc., **1968**, *90*, 6795-6803.

Chaturvedi, D., Mishra, N., and Mishra, V. *Various Approaches for the Synthesis of Organic Carbamates.* Curr. Org. Synth., **2007**, *4*, 308-320.

Costa, M., Paolo, G., Chiusoli, P., and Rizzardi, M. *Base-Catalysed Direct Introduction of Carbon Dioxide into Acetylenic Amines.* Chem. Commun., **1996**, 1699-1700.

Dell'Amico, D. B., Calderazzo, F. Labella, L. Marchetti, F., and Pampaloni, G. *Converting Carbon Dioxide into Carbamato Derivatives.* Chem. Rev., **2003**, *103*, 3857-3897.

Diaf, A., Enick, R. M., and Beckman, E. J. *Molecular Redesign of Expanded Polystyrene to Allow Use of Carbon Dioxide as a Foaming Agent. I. Reversible Binding of CO_2.* J. Appl. Poly. Sci., **1993**, *50*, 835-844.

Dijkstra, Z. J., Doornbos, A. R., Weyten H., Ernsting, J. M., Elsevier, C. J., and Keurentjes, J. T. F. *Formation of Carbamic Acid in Organic Solvents and in Supercritical Carbon Dioxide.* J. Supercrit. Fluids, **2007**, *41*, 109-114.

Dunetz, J. R., Ciccolini, R. P., Fröling, M., Papp, S. M., Allen, A. J., Holmes, A. B., Tester, J. W., and Danheiser, R. L. *Pictet-Spengler Reactions in Multiphasic Supercritical Carbon Dioxide/CO_2-Expanded Liquid Media. In Situ Generation of Carbamates as a Strategy for Reactions of Amines in Supercritical Carbon Dioxide.* Chem. Commun., **2005**, 4465-4467.

Ewing, S. P., Lockshon, D., and Jencks, W. P. *Mechanism of Cleavage of Carbamate Anions.* J. Am. Chem. Soc., **1980**, *102*, 3072-3084.

Feroci, M., Orsini, M., Sotgiu, G., Rossi, L., and Inesi, A. *Electrochemically Promoted C-N Bond Formation from Acetylenic Amines and CO_2. Synthesis of 5-Methylene-1,3-oxazolidin-2-ones.* J. Org. Chem., **2005**, *70*, 7795-7798.

Fischer, H., Gyllenhaal, O., Vessman, J., and Albert, K. *Reaction Monitoring of Aliphatic Amines in Supercritical Carbon Dioxide by Proton Nuclear Magnetic Resonance Spectroscopy and Implications for Supercritical Fluid Chromatography.* Anal. Chem., **2003**, *75*, 622-626.

Francis, A. W. *Ternary Systems of Liquid Carbon Dioxide.* J. Phys. Chem., **1954**, *58*, 1099.

Frasco, D. L. *Infrared Spectra of Ammonium Carbamate and Deuteroammonium Carbamate.* J. Chem. Phys., **1964**, *41*, 2134-2140.

George, M. and Weiss, R. G. *Chemically Reversible Organogels via "Latent" Gelators. Aliphatic Amines with Carbon Dixode and Their Ammonium Carbamates.* Langmuir, **2002**, *18*, 7124-7135.

Gu, Y., Zhang, Q., Duan, Z., Zhang, J., Zhang, S., and Deng, Y. *Ionic Liquid as an Efficient Promoting Medium for Fixation of Carbon Dioxide: A Clean Method for the Synthesis of 5-Methylene-1,3-oxazolidin-2-ones from Propargylic Alcholos, Amines, and Carbon Dioxide Catalyzed by Cu(I) under Mild Conditions.* J. Org. Chem., **2005**, *70*, 7376-7380.

Hampe, E. M. and Rudkevich, D. M. Exploring Reversible Reactions between CO_2 and Amines. Tetrahedron, **2003**, *59*, 9619-9625.

Heldebrant, D. J., Jessop, P.G., Thomas, C. A., Eckert, C. A., and Liotta, C. L. *The Reaction of 1,8-Diazabicyclo[5.4.0]undec-7-ene (DBU) with Carbon Dioxide.* J. Org. Chem., **2005**, *70*, 5335-5338.

Jessop, P.G., Heldebrant, D. J., Li, X., Eckert, C. A., and Liotta, C. L. *Reversible Nonpolar-to-Polar Solvent.* Nature, **2005**, *426*, 1102.

Jessop, P. G., Hsiao, Y., Ikariya, T., and Noyori, R. *Homogeneous Catalysis in Supercritical Fluids: Hydrogenation of Supercritical Carbon Dioxide to Formic Acid, Alkyl Formates, and Formamides.* J. Am. Chem. Soc., **1996**, *118*, 344-355.

Jessop, P. G., Hsiao, Y., Ikariya, T., and Noyori, R. *Catalytic Production of Dimethylformamide from Supercritical Carbon Dioxide.* J. Am. Chem. Soc., **1994**, *116*, 8851-8852.

Kayaki, Y., Yamamoto, M., Suzuki, T., and Ikariya, T. Carboxylative Cyclizations of Propargylamines with Supercritical Carbon Dioxide. Green Chem., **2006**, *8*, 1019-1021.

Khanna, R. K. and Moore, M. H. *Carbamic Acid: Molecular Structure and IR Spectra.* Spectrochim. Acta Part A, **1999**, *55*, 961-967.

Kirsch, M., Korth, H.-G., Sustmann, R., and de Groot, H. *Carbon Dioxide but Not Bicarbonate Inhibits N-Nitosation of Secondary Amines. Evidence for Amine Carbamates as Protecting Groups.* Chem. Res. Toxicol., **2000**, *13*, 451-461.

Kawanami, H., Matsumoto, H., Ikushima, Y. Effective scCO2-Ionic Liquid Reaction System Based on Symmetric Aliphatic Ammonium Salts for the Rapid CO_2 Fixation with Aziridine to 2-Oxazolidinone. Chem. Lett., **2005**, *34*, 60-61.

Liu, Yingxin, Jessop, P. G., Cunningham, M., Eckert, C. A., and Liotta, C. L. *Switchable Surfactants.* Science, **2006**, *313*, 958-960.

Maggi, R., Bertolotti, C., Orlandini, E., Oro, C., Sartori, G., and Selva, M. *Synthesis of Oxazolidinones in Supercritical CO_2 under Heterogeneous Catalysis.* Tetrahedron Lett., **2007**, *48*, 2131-2134.

Masuda, K., Ito, Y., Horiguchi, M., and Fujita, H. *Studies on the Solvent Dependence of the Carbamic Acid Formation from ω-(1-naphthyl)alkylamines and Carbon Dioxide.* Tetrahedron, **2005**, *61*, 213-229.

Mizuno, T., Iwai, T., and Ishino, Y. *The Simple Solvent-Free Synthesis of 1H-quinazoline-2,4-diones using Supercritical Carbon Dioxide and Catalytic Amount of Base.* Tetrahedron Lett., **2004**, *45*, 7073-7075.

Mizuno, T. and Ishino, Y. *Highly Efficient Synthesis of 1H-quinazoline-2,4-diones using Carbon Dioxide in the Presence of Catalytic Amount of DBU.* Tetrahedron Lett., **2002**, *58*, 3155-3158.

Miller, A. W., Nguyen, S. T. *(Salen)chromium(III)/DMAP: An Efficient Catalyst System for the Selective Synthesis of 5-Substituted Oxazolidinones from Carbon Dioxide and Aziridines.* Org. Lett., **2004**, *6*, 2301-2304.

Ochiai, B., Yokota, K., Fujii, A., Nagai, D., and Endo, T. *Reversible Trap—Release of CO_2 by Polymers Bearing DBU and DBN Moieties.* Macromolecules, **2008**, *41*, 1229-1236.

Park, J.-Y., Yoon, S. J., and Lee, H. *Effect of Steric Hindrance on Carbon Dioxide Absorption into New Amine Solutions: Thermodynamic and Spectroscopic Verification through Solubility and NMR Analysis.* Environ. Sci. Technol., **2003**, *37*, 1670-1675.

Ramachandran, B. R., Halpern, A. M., Glendening, E. D. *Kinetics and Mechanism of the Reversible Dissociation of Ammonium Carbamate: Involvement of Carbamic Acid.* J. Phys. Chem. A, **1998**, *102*, 3934-3941.

Rudkevich, D. M. and Xu, H. *Carbon Dioxide and Supramolecular Chemistry.* Chem. Commun., **2005**, 2651-2659.

Sakakura, T., Choi, J.-C., and Yasuda, H. *Transformation of Carbon Dioxide.* Chem. Rev., **2007**, *107*, 2365-2387.

Sharma, M. M. *Kinetics of Reactions of Carbonyl Sulphide and Carbon Dioxide with Amines and Catalysis by Brönsted Bases of the Hydrolysis of COS.* Trans. Faraday. Soc., **1965**, *61*, 681-688.

Shi, M. and Shen, Y.-M. *Transition-Metal-Catalyzed Reactions of Propargylamine with Carbon Dioxide and Carbon Disulfide.* J. Org. Chem., **2002**, *67*, 16-21.

Shi, M. and Cui, S.-C., and Li, Q.-J. *Lithium Heptadecafluorooctanesulfonate Catalyzed Mannich-type and aza-Diels-Alder Reactions in Supercritical Carbon Dioxide.* Tetrahedron, **2004**, *60*, 6163-6167.

Shi, M., Jiang, J.-K., Shen, Y.-M., Feng, Y.S., and Lei, G.-X. *An Unexpected Carbon Dioxide Insertion in the Reaction of Trans-2,4-Disubstituted Azetidine, Trans-2,5-Disubstituted Pyrrolidine, or Trans-2,6-Disubstituted Piperidine with Diphenylthiophosphinic Chloride and Diphenylselenophosphinic Chloride.* J. Org. Chem., **2000**, *65*, 3443-3448.

Smith, C. J., Tsang, M. W. S., Holmes, A. B., Danheiser, R. L., and Tester, J. W. *Palladium Catalyzed Aryl Amination Reactions in Supercritical Carbon Dioxide. Org. Biomol. Chem.*, **2005**, *3*, 3767-3781.

Smith, C. J., Early, T. R., Tsang, M. W. S., Holmes, A. B., and Shute, R. E. *Palladium Catalyzed Cross-Coupling Reactions of Silylamines.* Chem. Commun., **2004**, *17*, 1976-1977.

Stastny, V. and Rudkevich, D. M. *Separations Using Carbon Dioxide.* J. Am. Chem. Soc., **2007**, *129*, 1018-1019.

Sudo, A., Morioka, Y., Sanda, F., Endo, T. *N-Tosylaziridine, a New Substrate for Chemical Fixation of Carbon Dioxide via Ring Expansion Reaction under Atmospheric Pressure.* Tetrahedron Lett., **2004**, *45*, 1363-1365.

Sudo, A., Morioka, Y., Koizumi, E., Sanda, F., Endo, T. *Highly Efficient Chemical Fixations of Carbon Dioxide and Carbon Disulfide by Cycloaddition to Aziridine under Atmospheric Pressure.* Tetrahedron Lett., **2003**, *44*, 7889-7891.

Vaidya, P. D. and Kenig, E. Y. *CO_2-Alkanolamine Reaction Kinetics: A Review of Recent Studies. Chem. Eng. Technol.*, **2007**, *30*, 1467-1474.

Wen, N. and Brooker, M. H. *Ammonium Carbonate, Ammonium Bicarbonate, and Ammonium Carbamate Equilibria: A Raman Study.* J. Phs. Chem., **1995**, *99*, 359-368.

Wittmann, K., Wisniewski, W., Mynott, R., Leitner, W., Kranemann, C. L., Rische, T., Eilbracht, P., Kluwer, S., Ernsting, J. M., and Elsevier, C. J. *Supercritical Carbon Dioxide as Solvent and Temporary Protecting Group for Rhodium-Catalyzed Hydroaminomethylation.* Chem. Eur. J., **2001**, *7*, 4584-4689.

Yoshikatsu, I. and Horiguchi, M. *Solvent-dependent Effect by Carbon Dioxide on the Photoreactions of (9-anthryl)alkylamines.* Tetrahedron, **2007**, *63*, 12286-12293.

Xie, X., Liotta, C. L., and Eckert, C. A. *CO_2-Protected Amine Formation from Nitrile and Imine Hydrogenation in Gas-Expanded Liquids.* Ind. Eng. Chem. Res., **2004**, *43*, 7907-7911.

Xu, H. and Rudkevich, D. M. *CO_2 in Supramolecular Chemistry: Preparation of Switchable Supramolecular Polymers.* Chem. Eur. J., **2004**, 10, 5432-5442.

5. AMINE CARBAMATION AND PICTET-SPENGLER REACTIONS IN CARBON DIOXIDE-EXPANDED LIQUID MEDIA

5.1. Motivation

The Pictet-Spengler (P-S) reaction is a representative synthetic reaction that produces pharmacologically-significant tetrahydroisoquinolines and indole alkaloids (Whaley et. al., 1951; Cox et al. 1995). In its simplest form, the P-S reaction consists of the acid-catalyzed condensation of β-arylethylamines (**1**) with carbonyl compounds (e.g., aldehydes [R^1CHO]) to yield tetrahydroisoquinolines (**3**) via an iminium ion intermediate (**2**):

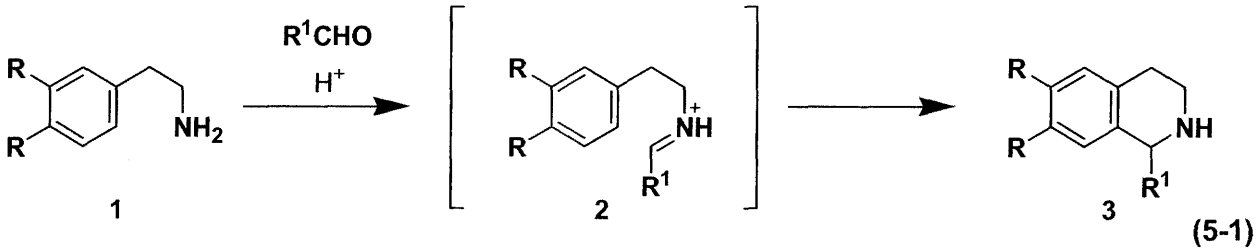

(5-1)

In conventional solvents at similar operating conditions, ring closure (**2** → **3**) is accelerated by the presence of electron-donating groups (R) in the aromatic ring of compound **1**. Ring closure is reported as most effective when employing formaldehyde (R^1 = H) and strong acids (e.g., HCl). A racemic mixture of tetrahydroisoquinoline enantiomers results when aldehydes other than formaldehyde are used. Preferential enantiomer synthesis can be achieved via specialty catalysts or by adding plane-of-attack-restricting functional groups to the α-carbon of the amine group.

Pictet-Spengler chemistry can also be extended to include the synthesis of tetrahydro-β-carbolines (**4**) from β-indolylethylamines (**6**) and their respective iminium ion intermediates (**5**):

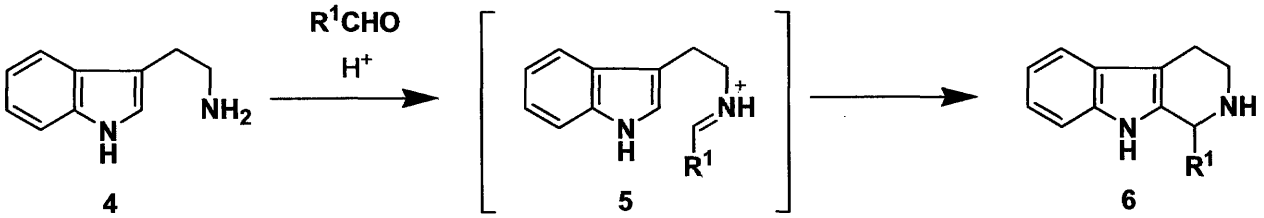

(5-2)

Both variants of the Pictet-Spengler reaction are frequently used for the synthesis of active pharmaceutical compounds. Eli Lilly and Co., for example, utilize the P-S reaction during the synthesis of their blockbuster erectile dysfunction drug Cialis® (see **Figure 4.1**) (Dunn, 2005; Revell et al. 2004). Other nitrogen heterocycle compounds derived from tetrahydroisoquinolines and tetrahydro-β-carbolines are shown in **Figure 5-1**.

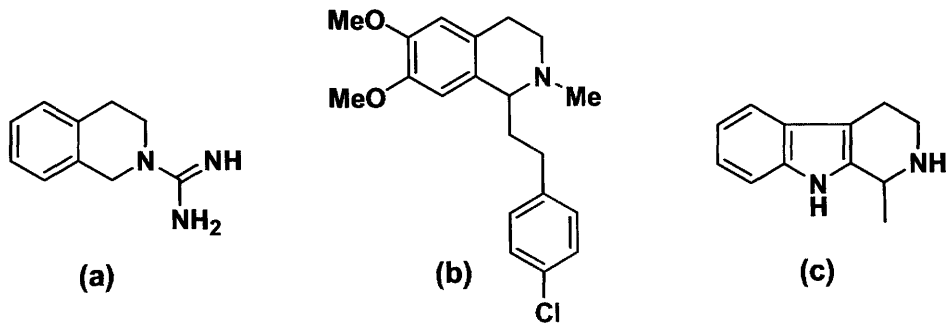

Figure 5-1. Examples of tetrahydroisoquinoline and tetrahydro-β-carboline derivatives with pharmacological attributes: Debrisoquine, antihypertensive **(a)**; Papaverine, vasodilator **(b)**; Tetrahydroharman, antimalarial **(c)**.

Although our decision to study the P-S reaction was driven largely by the medicinal attributes of the compounds it affords, the transformation was particularly attractive because it is relative simple when compared to other nitrogen heterocycle synthesis approaches. In addition, extensive studies of the P-S reaction in conventional solvents exist and offered insight for experimental design and comparison to reactions performed in CO_2-based media.

5.2. Synthetic Methodology

5.2.1. Nitrogen Protection via Amine Carbamation

Unfortunately, initial attempts led by Allen (2004) and Dunetz (2005) to perform the Pictet-Spengler reaction (see equation **[5-1]**) in $scCO_2$ were unsuccessful. Two separate reactions of 3,4-dimethoxyphenethyl amine (**7**) (ca. 11 mmol charge) with formaldehyde (HCHO) in the presence of a catalytic amount of *p*-toluene sulfonic acid (TsOH) failed to yield the desired tetrahydroisoquinoline (**8**) in quantifiable amounts:

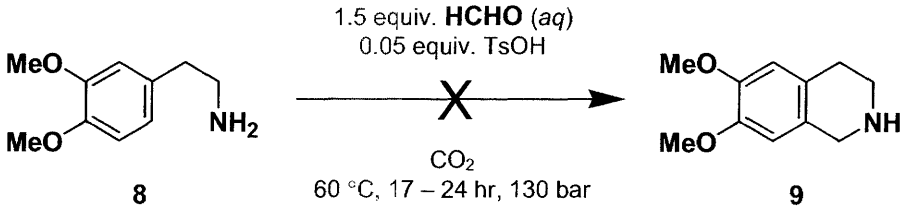

8 **9** **(5-3)**

Instead, the reaction mixture was comprised nearly entirely of oligomeric byproducts that were uncharacterizeable by conventional column chromatography and nuclear magnetic resonance (NMR) analysis. Amine **8** was consumed completely in both runs, indicating that competitive byproduct formation pathways were the primary reason for the trace yield of tetrahydroisoquinoline **9**. As a side note, the term 'equiv.' in equation **(5-3)** refers to the molar equivalent of a reagent employed in a reaction based on the initial amine charge. In the previously-described reactions, 1 equiv. = 11 mmol of amine **8**, and so the amount of formaldehyde and acid added were 15.6 mmol and 0.55 mmol, respectively.

The tendency for nucleophilic amines of type **8** to react with carbon dioxide to form carbamic acid and ammonium carbamate salts (see **Section 4.2)** may be the cause of the low yield. Control experiments with amine **8** and CO_2 at operating conditions corresponding to equation **(5-3)** revealed the formation of a CO_2-insoluble white solid (suspected to be the carbamic salt) that was later verified as reaction product between the two (for a more detailed discussion of the reaction of amine **8** with CO_2, see **Section 7.3.3**). Following this observation, we hypothesized that intermediate iminium ion formation was suppressed due to competitive acid-catalyzed condensation (polymer-forming) reactions involving the aldehyde and carbamic salt. Poor yield may have also been due to the partitioning of the amine from the bulk CO_2

phase. In contrast, tetrahydroisoquinoline **9** was produced with excellent yield when the reaction was performed in toluene at conditions identical to equation **(5-3)**.

Motivated by the observations of Fischer and coworkers (2003), we decided to investigate the effect of adding nitrogen (*N*) protecting groups on the reaction of amines with CO_2 medium. In general, the reaction of amines with CO_2 is suppressed by adding electron-withdrawing and/or bulky functional groups to primary amines (see **Section 4.2**). Electron-withdrawing groups decrease the nucleophilicity of the amine and bulky functional groups introduce steric effects, both of which reduce the reaction rate with CO_2. We therefore decided to chemically modify the original amine such that it would be 'inert' in the CO_2 solvent medium, but still able to participate in the P-S reaction.

N-substituted derivatives of amine **8** were synthesized by Dunetz (2005) and treated as 0.5 M solutions in hexane at ambient *T* and *P* with CO_2 in the form of dry ice. We assumed that a reaction of a given amine with CO_2 under these relatively mild conditions (via the observation of a carbamic salt precipitation) would also indicate salt formation at reaction conditions in CO_2. As seen from **Figure 5-2**, amine derivatives with sterically-demanding (compounds **11** and **12**) and electron-withdrawing groups (compound **13**) appeared inert to carbon dioxide.

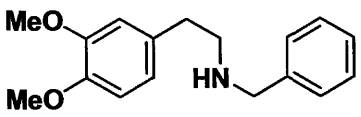

10
(white precipitate formed)

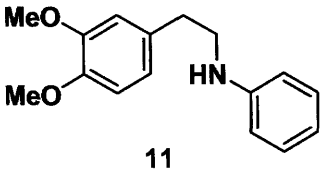

11
(no precipitate observed)
[P-S yield: <5%]

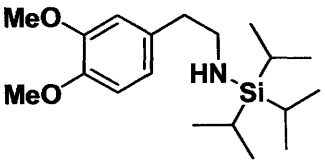

12
(no precipitate observed)
[P-S yield: 60%]

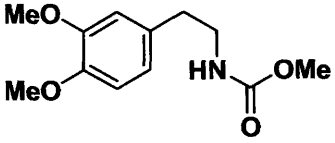

13
(no precipitate observed)
[P-S yield: 99%]

Figure 5-2. Carbamic salt formation and Pictet-Spengler reaction yields obtained for several substituted amine derivates. Reaction conditions: 1.5 equiv. HCHO (*aq*), 0.05 equiv. TsOH, benzene, 60 °C, 3h.

Compounds **11** – **13** were then used as starting materials for the P-S reaction in benzene at identical operating conditions. Reaction of compound **11** suffered from preferential addition of formaldehyde to aniline ring, resulting in a molar yield less than 5%. A substantial portion of compound **12** underwent cleavage of the triisopropylsilyl protecting group to yield a 60:40 molar % mixture of the corresponding tetrahydroisoquinoline **9** and amine **8**. Compound **13**, however, participated in the Pictet-Spengler reaction (more correctly, an *acyl*-Pictet-Spengler reaction) to form the corresponding tetrahydroisoquinoline quantitatively.

The conversion of amines to their less-nucleophilic carbamate derivatives appears to be an effective way to inhibit the undesired reaction with carbon dioxide. Though an additional synthetic step, amine carbamation prior to the P-S reaction served two benefits: (1) *N*-acyliminium ions demonstrate enhanced reactivity towards cyclization (Maryanoff et al., 2004), and (2) *N*-protection is a common strategy used in amine chemistry and would have likely been incorporated in earlier stages of a multi-step syntheses. Carbamates themselves are also important, having many applications in the agricultural, fine-chemical, and pharmaceutical industries. The carbamate functionality, for instance, appears in Schering-Plough's antihistamine Claritin® (see **Figure 4.1**).

In order to test the effectiveness of carbamate cyclization via the acyl-P-S reaction in CO_2, Allen (2004) and Dunetz (2005) performed several control experiments with carbamate **12** as starting material in place of amine **8**. Results of this initial screening study are presented in **Table 5-1**. The main conclusion drawn from these experiments was that carbamates underwent desired the desired acyl-Pictet-Spengler reactions with yields in CO_2-based media comparable to that of toluene and without interference with the CO_2 medium (compare entries 1 & 2). Though preliminary, the data also suggest that: (1) reaction rates in CO_2 were slower when compared to toluene (compare entries 1 – 3 and 11 & 12), (2) the addition of water to the CO_2 medium had a negative impact on yield (compare entries 3 & 4), (3) higher temperatures were required for reactions involving benzaldehyde (R^1 = Ph) and isopropyl aldehyde (R^1 = *i*-Pr) when compared to those involving formaldehyde (R^1 = H) (compare entries 1, 7, & 9), and (4) faster reaction rates and higher yields were obtained when performing the reaction under neat conditions (compare entries 1 & 5, 6 & 7, and 8 & 9). We will address the advantage of using carbon dioxide instead of performing neat reactions in **Section 5.5**.

Table 5-1. Yields obtained for the acyl-Pictet-Spengler reaction of a model carbamate with formaldehyde in carbon dioxide and toluene.

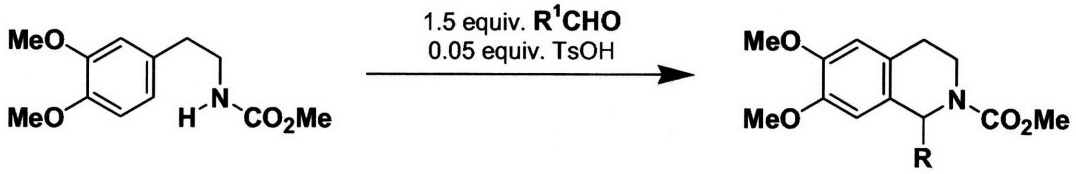

13 **14 – 16**

Entry [a]	Solvent	R^1	*t* hr	*T* °C	*P* bar	Product	Yield [b] %
1	toluene	H	3	60	ca. 1.01	**14**	98
2	CO_2	H	8	60	138	**14**	84
3	CO_2	H	17	60	138	**14**	88
4	CO_2/H_2O	H	17	60	138	**14**	81
5	neat	H	3	60	ca. 1.01	**14**	100
6	neat	Ph	2	85	ca. 1.01	**15**	81
7	toluene	Ph	2	85	ca. 1.01	**15**	21
8	neat	*i*-Pr	23	80	ca. 1.01	**16**	77
9	toluene	*i*-Pr	23	80	ca. 1.01	**16**	39
							Conversion %
10	CO_2/H_2O	H	3	60	138	**14**	64
11	toluene	Ph	15	80	ca. 1.01	**15**	100
12	CO_2	Ph	17	80	138	**15**	50

[a] for experimental details, see Allen (2004); [b] isolated yield by column chromatography.

After successfully demonstrating acyl-Pictet-Spengler cyclization reactions of carbamates in CO_2, our next task was to identify and develop a carbamate synthesis scheme in line with environmental considerations underscored by this work. Commercially, carbamates (e.g., polyurethane) are synthesized from the reaction of an alcohol with an isocyanate generated from the reaction of a primary amine with phosgene. This route is environmentally undesirable, as it involves the use of phosgene (toxic and corrosive) and liberates hydrochloric acid. As mentioned in **Section 4.3.1**, several alternative synthetic routes to carbamates exist, many of which involving amines and carbon dioxide as starting materials (Chaturvedi et al.,

2007; Dell'Amico et al., 2003). These are particularly advantageous methods because the conversion of amine substrates to carbamates occurs *in situ*, hence utilizing CO_2 as both a reagent and reaction medium.

In our opinion, the most attractive of these methods from practicality and environmental standpoints is the use of dimethyl carbonate (DMC, $CO(OMe)_2$) as a 'green' methylating agent (Selva et al., 2008; Pacheco et al., 1997) for the *in situ* conversion of amines to methyl carbamates (Aresta et al., 1991; Selva et al., 2002 and 2005). Unlike other alkylating agents, dimethyl carbonate is considered green because it is non-toxic, biodegradable, and is produced industrially from a relatively clean process, and generates only methanol and carbon dioxide as waste (Selva et al., 2008).

The widely-accepted mechanism for amine carbamation involving the CO_2/DMC reaction system involves the methylation of the ammonium carbamic salt formed by the reaction of CO_2 with amines (Tundo et al., 2002, 2005, and 2007; Selva et al., 2006):

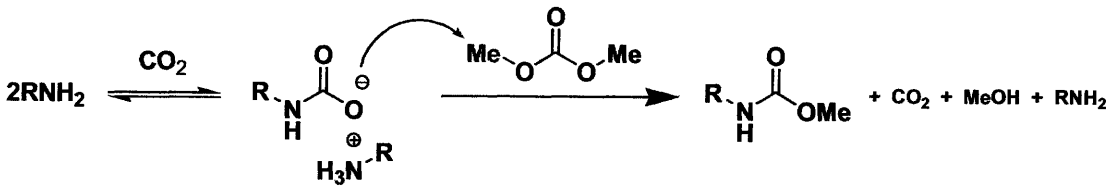

(5-4)

The $B_{Al}2$ alkylation mechanism shown in equation **(5-4)** has been reported to occur for reaction temperatures above 373 K (100 °C). Below this temperature, DMC acts as an acylating agent, with amine carbamation occurring through a $B_{Ac}2$ mechanism (Aresta et al., 1991):

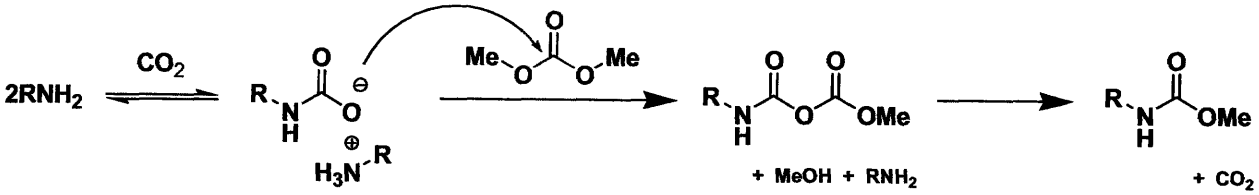

(5-5)

In equation **(5-5)**, the carbamic salt adds to the carbonyl carbon of DMC, resulting in a carbamic-carbonic anhydride intermediate that undergoes decarboxylation to yield the

carbamate. Below 373 K (100 °C), the carbamate can also be generated from the direct reaction of the amine with the carbonyl carbon of DMC:

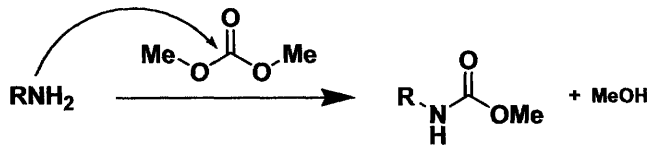

(5-6)

In addition to desired carbamation pathways, dimethyl carbonate at temperatures above 373 K (100 °C) can react with the amine via undesired methylation pathways:

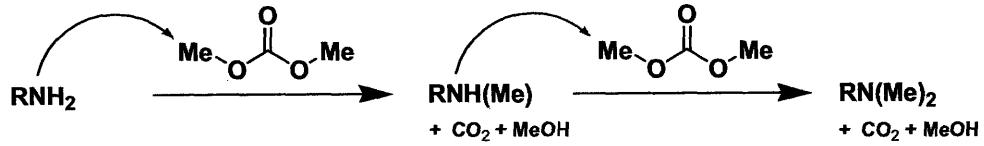

(5-7)

5.2.2. Synthetic Protocol and Variables Explored

In summary, we propose a two-step, single-reactor protocol for the synthesis of nitrogen heterocycles in carbon dioxide that involves:

(1) the synthesis of a carbamate from the reaction of an amine with carbon dioxide and a dialkyl carbonate ($CO(OR_2)_2$), and

(2) the synthesis of a nitrogen heterocycle from the acyl-Pictet-Spengler reaction of the *in situ* generated carbamate with an aldehyde in the presence of an acid:

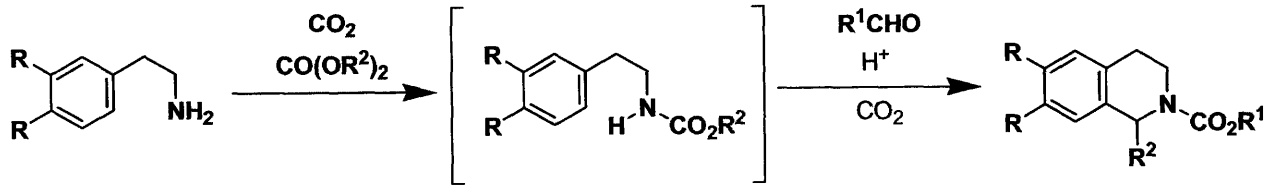

(5-8)

The protocol described by equation **(5-8)** was also extended to include the synthesis of tetrahydro-β-carbolines from carbamates generated *in situ* from β-indolylethylamines.

The overall yield of any multi-step synthetic process is invariably limited by its lowest-yielding step. Tertiary amine byproducts (i.e., $RN(Me)_2$) produced in the amine carbamation step, for example, do not participate in the P-S reaction (no *N*-H site available for the addition of the aldehyde). In addition, once-methylated amines (i.e., RNHMe) form in the presence of CO_2 form carbamic acids (see **Figure 4-3**) and would likely lead to oligomeric formation during the P-S step. A critical goal therefore became the optimization of reaction conditions such that alkylation of the carbamic salt was promoted over the amine. A series of optimization experiments were performed for this and the P-S step in order to elucidate the effects of reactant functionality and the temperature-pressure-concentration operating space on product conversion, yield, and selectivity.

5.3. Experimental Approach

Supercritical fluid extraction-grade (99.9999% purity, Airgas) carbon dioxide and 99.5+% purity reagents were used for all reactions discussed in this chapter. Unless noted otherwise, experiments were performed using the 25-mL view cells (**VC-1** and **VC-2**, often in parallel) and operating/reaction work-up procedures described in **Section 3.2.3**. Actual vessel volumes were calculated via the volume determination unit (see **Section 3.3.3**) and were 34.1 ± 0.3 mL for **VC-1** and 31.8 ± 0.3 mL for **VC-2**. **VC-1** was slightly larger in volume due to internal surface boring that was needed to remove pitting corrosion after extensive exposure to concentrated acids at elevated temperatures.

In a typical experiment, amine and dialkyl carbonate were simultaneous loaded to the reactor at ambient conditions. The vessel headspace was purged using gaseous argon (99.9999% purity, Airgas). Carbon dioxide was added until a pressure of ca. 35 bar (515 psia) was reached and the reaction mixture was heated to the desired temperature for the carbamation step. Additional CO_2 was added while the vessel heated and was topped off at the desired pressure once the temperature reached the set point. Care was taken not to initially charge the CO_2 in its liquid state at ambient conditions (e.g., adding CO_2 at $T < T_{c,CO_2}$ and $P > P_{vp,CO_2}(T)$). Doing so would have resulted in large and unsafe pressure increases upon heating to reaction conditions. The reactor was rapidly cooled after the desired reaction time by placing the vessel on a bed of ice. The vessel was vented and the CO_2 phase sparged into dichloromethane. All vessel and fitting surfaces in contact with the reaction mixture were

thoroughly washed with dichloromethane and submitted to Dunetz (2005) for isolation by column chromatography and further analytical analyses (e.g., NMR, GC-MS, etc.). We should note that dichloromethane is hardly a green solvent and would not be used when perforiming this and similar processes on an industrial scale.

When performing the acyl-P-S step, the vessel was cooled to the desired set-point via natural convection and reagents were injected using the at-condition sampling unit and procedures described in **Section 3.3.1**. Appropriately-sized sample loops were used to accommodate the necessary aldehyde and acid volumes. All reactions in conventional solvents were performed in the Danheiser synthetic organic chemistry group by Dunetz (2005). Experimental and product isolation details can be found in Dunetz's doctoral thesis (2005).

5.4. Screening of the Amine Carbamation Reaction

5.4.1. Carbamation of *β*-arylethylamines

Results of our screening study with 3,4-dimethoxyphenethyl amine (**8**) are presented in **Table 5-2**. Photographs of the reactor contents were taken during the progression of the reaction and are shown in **Figure 5-3**. 3,4-dimethoxyphenethyl amine and the dialkyl carbonates were miscible liquids at ambient conditions. Upon the addition of CO_2 to the amine/dialkyl carbonate mixture (see **Figure 5-3a**) at ambient conditions, a white solid precipitate formed and was dispersed in the entire volume of the liquid phase (see **Figure 5-3b**). As *T* approached 353 K (80 °C), the solid (suspected to be the carbamic salt) dissolved in the liquid phase (see **Figure 5-3c**). This observation suggested that (1) the salt melted to form a liquid phase that was miscible with the dialkyl carbonate, (2) the salt dissolved in the dialkyl carbonate due to increased solubility at higher *T*, and/or (3) the salt dissociated at higher *T* to afford a mixture of free amine and CO_2 (and potentially carbamic acid). With the exception of entry 11, all reactions at the conditions listed in **Table 5-2** were biphasic and consisted of an upper, lower-density CO_2-rich supercritical-like phase and a lower, higher-density organic-rich liquid phase (see **Figure 5-3d**). At 373 K (100 °C) (entry 11), three phases existed: (1) an upper, lower-density CO_2-rich supercritical-like phase, (2) a middle, intermediate-density dialkyl carbonate-rich liquid phase, and (3) a lower, higher-density amine-rich liquid phase (see **Figure 5-3e**). Carbamates **13** and **14** were solids at ambient conditions. For a more detailed discussion of dynamic reaction phase behavior, see **Section 7.3**.

Table 5-2. Yields obtained for carbamation optimization experiments involving the reaction of 3,4-dimethoxyphenethyl amine with carbon dioxide and dialkyl carbonates.

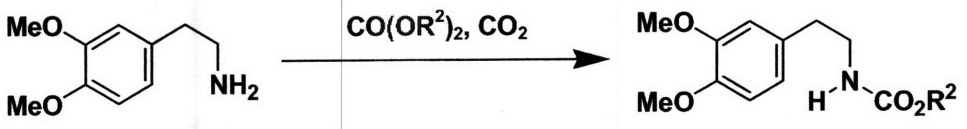

8

13 R^2 = Me
14 R^2 = Bn

Entry	R^2 (equiv.) [a]	*t* hr	*T* K (°C)	$P_i - P_f$ [b] bar	Yield [c] %
		Variable: Reaction Time (t)			
1	Me (1.5)	6	403 (130)	118 – 132	50 [d]
2	Me (1.5)	14	403 (130)	125 – 132	58 [d]
3	Me (1.5)	24	403 (130)	118 – 132	62 *
		Variable: Dialkyl Carbonate Equivalents (R^2 equiv.)			
4	Me (1.1)	24	403 (130)	118 – 132	48
3	Me (1.5)	24	403 (130)	118 – 132	62
5	Me (2.0)	24	403 (130)	118 – 132	66
6	Me (7.5)	24	403 (130)	118 – 132	77
		Variable: Pressure (P)			
7	Me (1.5)	24	403 (130)	ca. 2 [e]	47
8	Me (1.5)	24	403 (130)	98	55
3	Me (1.5)	24	403 (130)	118 – 132	62
9	Me (1.5)	24	403 (130)	132 – 142	59
10	Me (1.5)	24	403 (130)	180 – 187	55
		Variable: Temperature (T)			
11	Me (1.5)	24	373 (100)	118 – 125	54 (77) [f]
12	Me (1.5)	24	383 (110)	115 – 135	56 (62) [g]
3	Me (1.5)	24	403 (130)	118 – 132	62
13	Me (1.5)	24	423 (150)	118 – 134	61
		Variable: Base [h,i]			
4	Me (1.1)	24	403 (130)	118 – 132	48
14[h]	Me (1.1)	24	403 (130)	118 – 132	44
15[i]	Me (1.1)	24	403 (130)	118 – 132	37 [i]
		Variable: Dialkyl Carbonate (R^2)			
5	Me (2.0)	24	403 (130)	118 – 132	66
16	Bn (2.0)	24	403 (130)	118 – 132	69

* denotes 'optimal' conditions for carbamate synthesis; [a] 1 equiv. = 12.6 mmol of **8**; [b] P_i = initial *P* at *t* = 0 h, P_f = final *P* at *t*. [c] isolated yield of products by column chromatography at complete conversion of **8** unless noted otherwise, reproducibility ± 2%; [d] incomplete conversion of **8**; [e] reaction in a sealed tube under gaseous CO_2, *P* not monitored and estimated to be the vapor pressure of toluene; [f] estimated yield based on 75% conversion of **8**; [g] estimated yield based on 90% conversion of **8**; [h] experiment performed with 1.1 equiv. *N*,*N*-diisopropylethylamine (Hünig's base); [i] experiment performed with 1.1 equiv. cesium carbonate.

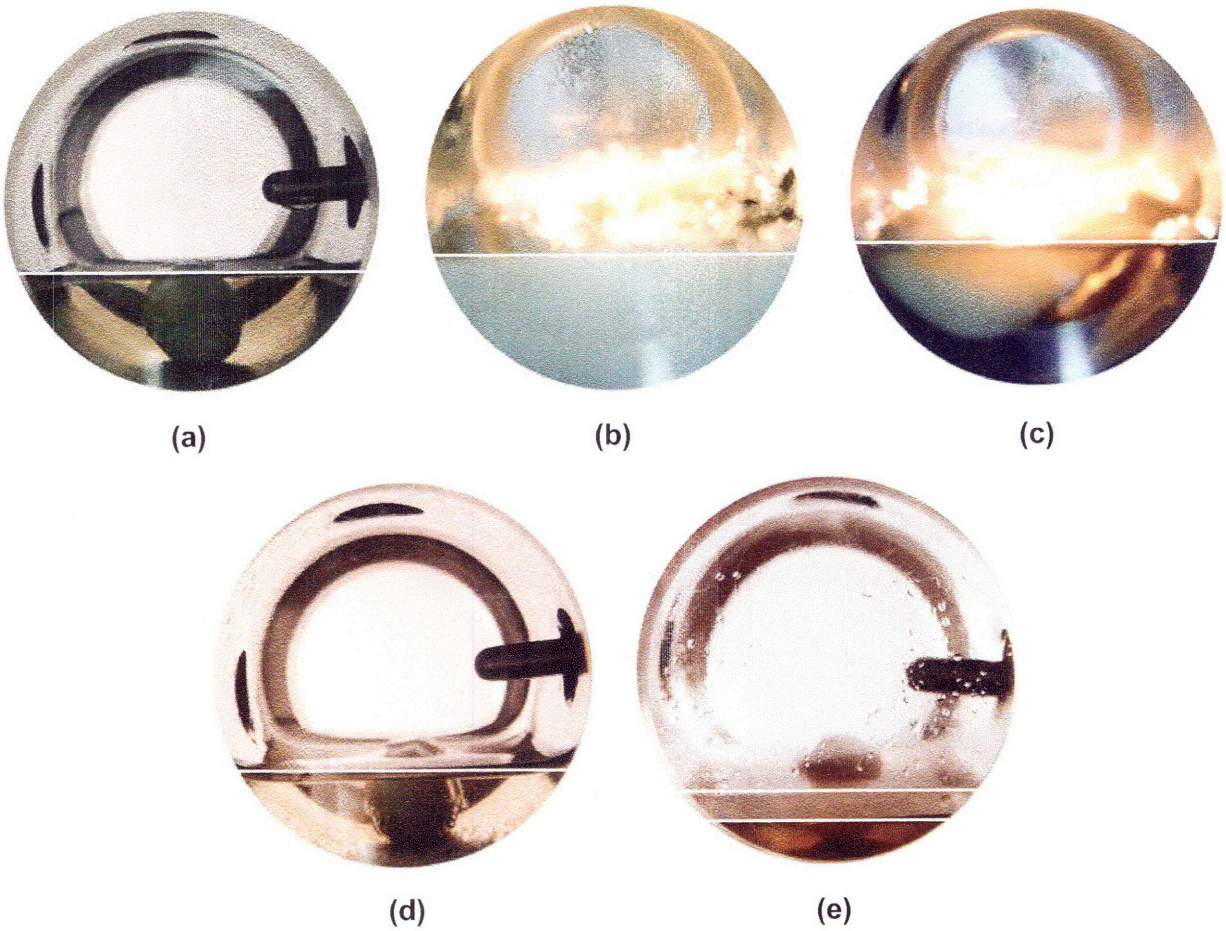

Figure 5-3. Phase behavior observed during the carbamation of β-arylethylamines: a liquid phase consisting of amine and dialkyl carbonate **(a)**; an upper, lower-density CO_2-rich supercritical-like phase and a lower, higher-density organic-rich liquid phase with an amine-rich solid precipitate dispersed throughout the entire phase **(b)**; an upper, lower-density CO_2-rich supercritical-like phase and a lower, higher-density organic-rich liquid phase with an amine-rich solid precipitate dissolving in the phase **(c)**; an upper, lower-density CO_2-rich supercritical-like phase and a lower, higher-density organic-rich liquid phase **(d)**; an upper, lower-density CO_2-rich supercritical-like phase, a middle, intermediate-density dialkyl carbonate-rich liquid phase, and a lower, higher-density amine-rich liquid phase **(e)**. The solid object visible in **(a)**, **(d)**, and **(e)** is a magnetic stir bar. Lines are drawn to indicate phase boundaries.

At 403 K (130 °C), complete conversion of amine **8** was realized between 14 and 24 hr (compare entries 1 – 3) and produced a reaction mixture containing the desired carbamate and a mixture of undesired alkylation products **15** – **16** and a styrene-like product **17**:

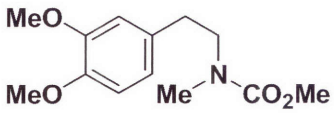

15

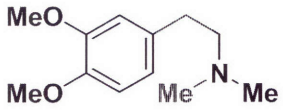

16

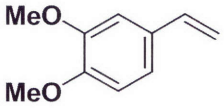

17

Several control experiments were performed in order to understand the mechanism by which the byproducts were formed. Compound **15** was not detected after exposing purified carbamate **13** to DMC (at reaction conditions of entry 3), indicating that it was formed by the carbamation of once-methylated amine (rather than methylation of the desired carbamate product). This control also revealed that carbamate products were thermally stable. Compound **16** was heated in the presence of DMC at 403 K (130 °C) and was converted nearly entirely to byproduct **17**. Products **16** and **17** were also observed when performing the reaction of amine **8** with DMC and in the absence of CO_2. These controls confirmed our hypothesis that product **17** was a consequence of competitive amine alkylation. The detection and mechanistic origins of **15** – **17** indicate that DMC acts predominantly as an alkylating (as opposed to an acylating agent) at these conditions. Byproduct formation mechanisms are summarized in **Figure 5-4.**

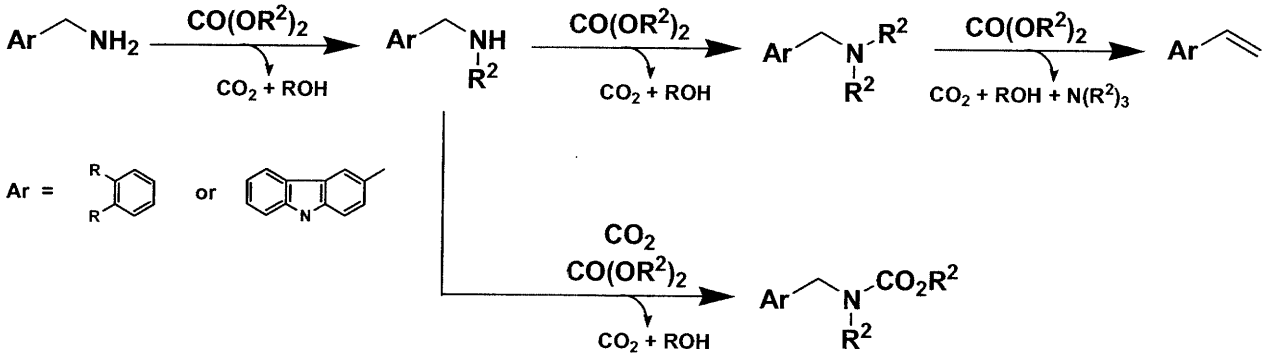

Figure 5-4. Byproduct formation pathways for the amine carbamation step.

Increasing the amount of DMC employed relative to the amine resulted in a substantial increase in carbamate **13** yield (compare entries 3 and 4 – 6) relative to byproducts **15** – **17**. Carbamate yield increased initially with increasing *P* and decreased at the higher end of the pressure range (compare entries 3 and 7 – 10). Carbamate yield increased with decreasing temperature. Reactions at $T < 403$ K (130 °C) required longer reaction times for complete amine conversion (compare entries 3 and 11 – 13). A thorough discussion of these findings in terms of reaction kinetics and phase behavior is presented in **Sections 7.4** and **7.5**. Briefly, carbamate selectivity is proportional to the concentration of carbon dioxide in the liquid reaction phase ($[CO_2]_l$). $[CO_2]_l$ increases with increasing pressure (see **Section 6.5**), thereby favoring

carbamic salt formation over amine alkylation. Selectivity drops at higher pressures because the dialkyl carbonate partitions to the CO_2-rich phase, leaving behind an amine-rich liquid phase that has a lower CO_2 concentration. Increasing the amount of DMC employed relative to the amine dilutes byproducts (e.g., MeOH) that have been shown to decrease carbamate selectivity and also enhances the ability for the reaction-phase to dissolve CO_2. At lower temperatures, liquid-phase CO_2 concentrations are larger, carbamic salts are more stable, and acylation is preferred over alkylation.

Initially thought to facilitate the desired carbamation reaction, the addition of *N,N*-diisopropylethylamine (Hünig's base) and cesium carbonate actually had a negative impact on carbamate yield (compare entries 4 and 14 – 15). Finally, benzyl carbamates were successfully synthesized in slightly better yields by employing dibenzyl carbonate (DBC) in place of DMC (compare entries 5 and 16). At 403 K (130 °C), the phase behavior for reaction involving DBC was identical to that involving DMC (see **Figure 5-3d**).

In all cases, the difference in molar yield from 100% was a mixture of approximately 50:25:25 molar % **16**:**17**:**15**. A carbamate yield of 60%, for example, indicates that based on a 100 mole amine charge, the resulting reaction mixture would contain 60:20:10:10 moles of carbamate:**16**:**17**:**15**. The mass recovery for each experiment was > 95% and carbamate yield was reproducible to 2%.

5.4.2. Carbamation of β-indolylethylamines

Following the successful carbamation of β-arylethylamines, the reaction was extended to include β-indolylethylamines. Results of our screening study with tryptamine (**18**) are presented in **Table 5-3**. Photographs of the reaction phase behavior for carbamation reactions involving tryptamine at specified conditions are shown in **Figure 5-5**. Tryptamine is a solid at ambient conditions and was essentially insoluble in DMC at all reaction conditions (see **Figure 5-5a**). Addition of CO_2 to the biphasic solid amine/liquid DMC mixture at ambient conditions caused the DMC-rich liquid phase to turn milky white, indicating that carbamic salts formed from the reaction occurred between CO_2 and the trace amount of tryptamine dissolved in this phase. As T approached 383 K (110 °C), the DMC-rich liquid phase cleared and the amine-rich solid phase melted and remained insoluble in either the CO_2- or DMC-rich phases (see **Figure 5-5b**). In the absence of CO_2, the melting point of tryptamine is ca. 387 K (114 °C).

Table 5-3. Product yields obtained for carbamation optimization experiments involving the reaction of tryptamine with carbon dioxide and dialkyl carbonates.

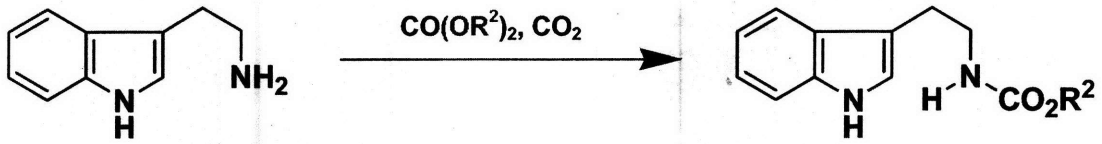

18

19 R^2 = Me
20 R^2 = Bn

Entry	R^1 (equiv.) [a]	MeOH equiv.	t hr	T K (°C)	$P_i - P_f$ [b] bar	Yield [c] %
1	Me (10)	0	24	403 (130)	118 – 134	45
2	Me (10)	2	24	403 (130)	118 – 135	40
3	Me (10)	0	24	378 (105)	125	20[d]
4	Me (10)	20	24	378 (105)	118 – 125	15
5	Bn (2)	0	24	403 (130)	125 – 132	50
6	Bn (5)	0	24	403 (130)	135 – 139	58*
7	Bn (2)	0	24	373 (100)	118 – 123	44
8	Bn (2)	0	66	373 (100)	125 – 130	56 (66) [e]
9	Bn (4)	0	66	373 (100)	129 – 132	60 (67) [f]

* denotes 'optimal' conditions for carbamate synthesis; [a] equivalents of amine varied due to vessel volume restrictions: 1 equiv. = 12.6 mmol of **18** for entry 1, 5, 7 & 8, 4.7 mmol for entries 2 – 4, 5.1 mmol for entry 6, and 6.4 for entry 9. [b] P_i = initial P at t = 0 h, P_f = final P at t. [c] isolated yield of products by column chromatography at complete conversion of **18** unless noted otherwise, reproducibility ± 2%; [d] incomplete conversion of **15**; [e] estimated yield based on 85% conversion of **18**; [f] estimated yield based on 90% conversion of **18**.

Compared with reactions involving 3,4-dimethoxyphenethyl amine (**8**), reactions with tryptamine afforded significantly less carbamate (compare entries 1 & 3 of **Table 5-3** with entries 6 & 11 of **Table 5-2**). A styrene-like byproduct analogous to **17** was not detected in appreciable amounts; major byproducts of tryptamine runs were instead the once- and twice-alkylated amines, which suggested that amine alkylation rates were slower when compared with amine **8**. Treatment of tryptamine carbamate **19** with DMC at reaction conditions of entry 1 did not result in the methylation or acylation of the indole nitrogen. Lowering the temperature below 383 K (110 °C) led to decreased conversion and yield (compare entries 1 & 3) and caused the tryptamine-rich phase to remain a separate, solid phase (see **Figure 5-5c**).

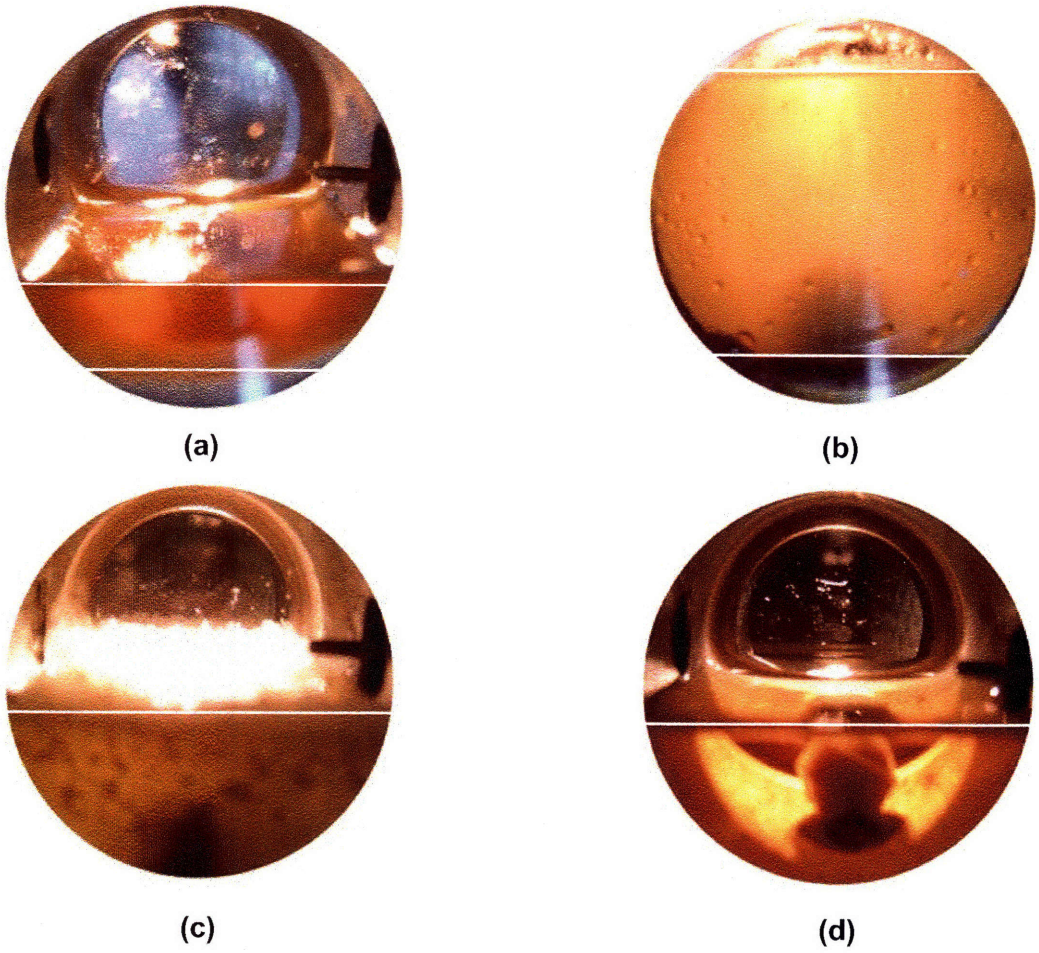

Figure 5-5. Phase behavior observed during the carbamation of β-indolylethylamines: a liquid phase consisting of dialkyl carbonate and solid amine **(a)**; an upper, lower-density CO_2-rich supercritical-like phase, a middle, intermediate-density dialkyl carbonate-rich liquid phase, and a lower, higher-density amine-rich liquid phase **(b)**; an upper, lower-density CO_2-rich supercritical-like phase, a middle, intermediate-density dialkyl carbonate-rich liquid phase with a dispersed amine-rich solid phase **(c)**; an upper, lower-density CO_2-rich supercritical-like phase and a lower, higher-density organic-rich liquid phase **(d)**. The solid object visible in each photograph is a magnetic stir bar. Lines are drawn to indicate phase boundaries.

Suspecting that triphasic phase behavior may have been an attributing factor to decreased yields, methanol was added to the system to increase the solubility of tryptamine in the DMC-rich liquid phase. Although methanol helped solubilize tryptamine at ambient conditions (see **Figure 5-5d**), addition of CO_2 at reaction conditions resulted in precipitation of an amine-rich liquid phase (see **Figure 5-5b**). The addition of methanol also resulted in lower yields (compare entries 1 & 2 with entries 3 & 4), possibly due to solvation effects mentioned in the previous section. Higher yields and a biphasic reaction system (see **Figure 5-5d**) were

obtained when dimethyl carbonate was replaced with dibenzyl carbonate (compare entries 1 & 2 with entries 3 & 4). DBC is more polar than DMC and it dissolves less CO_2 at similar pressures (see **Section 6.7**). Increased CO_2/DBC mixture polarity compared to the CO_2/DMC system allows for the dissolution of the tryptamine-rich phase. In addition to phase behavior effects, higher yields may also be attributed to the slower alkylation of the amine relative to the carbamic salt. Lower temperatures resulted in increased yields at the expense of longer reaction times (compare entries 5, 7, & 8). Lastly, an increase in the amount of DBC employed increased yield (compare entries 8 and 9).

5.5. Screening of the Pictet-Spengler Reaction

5.5.1. Cyclization of Carbamates Derived from β-arylethylamines

After optimizing the amine carbamation step, we turned our attention to a scoping study of the two-step nitrogen heterocycle synthesis protocol described by equation **(5-8)**. A variety of amines, aldehydes, and acids were employed and the results are delineated in **Table 5-4**. Initiation of the acyl-Pictet-Spengler reaction by injection of aldehyde and acid led to a triphasic system, consisting of consisting of: (1) an upper, lower-density CO_2-rich supercritical-like phase, (2) a middle, intermediate-density aqueous-rich liquid phase, and (3) a lower, higher-density organic-rich liquid phase (see **Figure 5-6**). Unlike the amine carbamation step, selection of temperature and pressure for the acyl-Pictet-Spengler step was somewhat arbitrary. A temperature of 353 K (80 °C) was selected to ensure the complete conversion of carbamate within 24 hr. Pressure was adjusted to ensure the complete injection of aldehyde and acid into the vessel. Yields reported in **Table 5-4** are therefore unoptimized with regard to process operating conditions. In many cases, however, the yield of the acyl-P-S was very close to that of the amine carbamation step, indicating a high reaction efficiency.

In the following analysis of the two-step protocol, the yield of the amine carbamation step for similar entries was assumed identical and was justified by the reproducibility of this step within ± 2%. Phenethylamine and 3,4-dimethoxyphenethylamine successfully underwent cyclization to their respective tetrahydroisoquinoline derivatives in nearly identical yields (compare entries 1 & 2). This is noteworthy given the complications associated with the P-S cyclization of phenethylamine in conventional solvents (Whaley et. al., 1951). At this point, we were not sure if the success of the electron-neutral ring-closure could be attributed to the nature

Table 5-4. Product yields obtained for the two-step tetrahydroisoquinoline synthesis protocol involving amine carbamation followed by the acyl-Pictet-Spengler reaction.

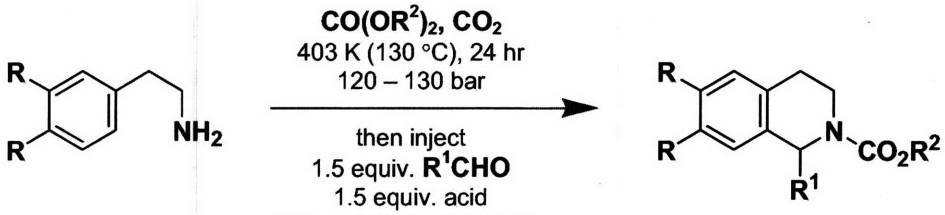

8 R = MeO
19 R = H

21 – 28

Entry	Amine	R^1 [a]	R^2 (equiv.) [b]	Acid [c]	Product	Yield (%) [d]
1	**19**	H	Me (2.0)	H_2SO_4	**21**	52
2	**8**	H	Me (2.0)	H_2SO_4	**22**	54
3	**8**	H	Me (2.0)	TFA	**22**	62
4	**8**	H	Me (7.5)	H_2SO_4	**22**	63
5	**8**	Ph	Me (2.0)	H_2SO_4	**23**	56
6	**8**	Ph	Me (7.5)	H_2SO_4	**23**	69
7	**8**	*i*-Pr	Me (2.0)	H_2SO_4	**24**	53
8	**8**	*i*-Pr	Me (7.5)	H_2SO_4	**24**	71
9 [e]	**8**	CO_2Me	Me (2.0)	H_2SO_4	**25**	49
10	**8**	H	Bn (2.0)	TFA	**26**	67
11	**8**	Et	Bn (2.0)	TFA	**27**	71
12	**8**	Ph	Bn (2.0)	H_2SO_4	**28**	57
			Failed			
13	**8**	2-furyl [f]	Me (2.0)	H_2SO_4	—	n/a
14	**8**	*p*-MeC_6H_4 [g]	Bn (2.0)	TFA	—	n/a
15	**8**	Ph	Bn (2.0)	TFA	—	ca. 0
16 [h]	**8**	Ph	Bn (2.0)	TFA	—	ca. 0
17	**8**	Ph	Bn (2.0)	TFA [i]	—	ca. 0

[a] formaldehyde (R^1 = H) added as a 37 wt% solution in H_2O, all other aldehydes neat; [b] 1 equiv. = 12.6 mmol of **8** or **19**; [c] unless noted otherwise, H_2SO_4 added as 9 M solution in H_2O, TFA as 50 vol% solution in H_2O. [d] isolated yield of products by column chromatography at complete conversion of **8** or **19**, reproducibility ± 2%; [e] methyl glyoxylate (R^1 = CO_2Me) generated *in situ* from the injection of its dimethyl acetal derivative; [f] 2-furaldehyde; [g] *p*-methoxybenzaldehyde; [h] experiment performed with 37 mmol MeOH; [i] TFA added neat.

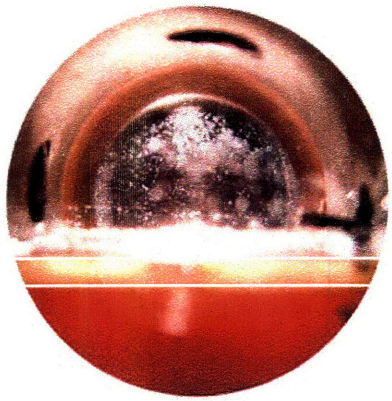

Figure 5-6. Phase behavior observed during the acyl-Pictet-Spengler reaction: a liquid phase consisting of amine and dialkyl carbonate: an upper, lower-density CO_2-rich supercritical-like phase, a middle, intermediate-density aqueous-rich liquid phase, and a lower, higher-density organic-rich liquid phase. Lines are drawn to indicate phase boundaries.

of the CO_2-based solvent medium, or due to the transformation of the amine to its carbamate derivative. Methyl and benzyl carbamates (compare entries 3 & 5 with 10 & 12) and aliphatic and aromatic aldehydes (compare entries 1, 5, 7, & 9) successfully participated in the acyl-Pictet-Spengler reaction. Yields increased when substituting trifluoroacetic acid (TFA) for the 'greener' sulfuric acid (H_2SO_4) (compare entries 1 & 3), which was ascribed to the sensitivity of some carbamate groups to H_2SO_4. Treatment of carbamate **14** with concentrated sulfuric acid, for example, led to complete cleavage of the carbamate group. Decomposition of the carbamate to yield free amine in this environment would subsequently lead to undesired polymerization reactions and the subsequent reduction in tetrahydroisoquinoline yield. Importantly, we found that benzyl carbamates are compatible with H_2SO_4 in the presence of carbon dioxide (entry 12); attempts to perform acyl-Pictet-Spengler cyclizations with benzyl carbamates under similar conditions in toluene led to cleavage of the carbamate group. Also, we observed that the overall yield for this two-stage process improves as the amount of DMC employed relative to the amine increases (compare entries 1 & 4, 5 & 6, and 7 & 8). This effect is due to the increase in carbamate yield during the amine carbamation step.

The use of 2-furaldehyde (entry 13) and *p*-methoxybenzaldehyde (entry 14) led to the formation a coal-like carbon solid that was insoluble in several organic solvents and not subjected to further analysis. Neat TFA or in solutions of water and methanol was ineffective at promoting the acyl-P-S reaction for entries 15 – 17.

5.5.2. Cyclization of Carbamates Derived from β-indolylethylamines

Extension of the two-step protocol to include β-indolylethylamines proved initially to be a significant challenge. First, the use of tryptamine in place of 3,4-dimethoxyphenethyl amine at similar operating conditions during the amine carbamation step resulted in significantly lower yields. This complication was eventually overcome by replacing DMC with DBC (see **Section 5.4.2**). Second, poor yields were obtained when performing the acyl-Pictet-Spengler step with DBC-derived benzyl carbamate (compare entry 1 of **Table 5-5** with entry 12 of **Table 5-4**). We suspected that the electron-withdrawing carbamate group decreased the nucleophilicity of the aliphatic nitrogen (i.e., the desired site of aldehyde addition for the acyl-P-S step) to an extent that would favor the undesired reactions of the aldehyde with the more nucleophilic indole nitrogen and ring. To test this hypothesis, the methyl carbamate derivative of tryptamine was prepared by Dunetz (2005) and treated with a combination of aldehydes (i.e., HCHO, *i*-PrCHO, and PhCHO) and acids (i.e., H_2SO_4 and TFA) in the absence of CO_2. Of the combinations explored, the only reaction that proceeded to modest yield (i.e., 40 molar %) was the reaction with PhCHO and H_2SO_4. Consistent with our hypothesis, all other reactions gave a mixture comprised predominantly of various side products that were a result of electrophilic addition of aldehydes to the indole ring.

Table 5-5. Unoptimized product yields obtained for the two-step tetrahyrdo-β-carboline synthesis protocol involving amine carbamation followed by the acyl-Pictet-Spengler reaction.

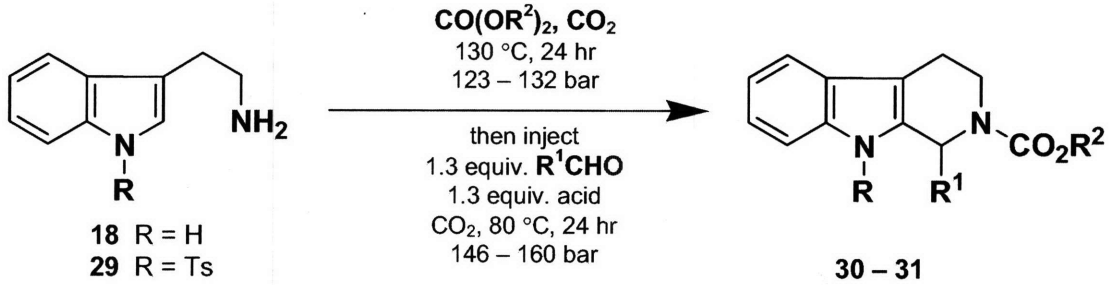

18 R = H
29 R = Ts

30 – 31

Entry	R	R^1	R^2 (equiv.) [a]	Acid [b]	Product	Yield [c] %
1	H	Ph	Bn (2)	H_2SO_4	**30**	20
2	Ts	H	Bn (5)	TFA	**31**	61

[a] equivalents of amine varied due to vessel volume restrictions: 1 equiv. = 12.6 mmol of **15** for entry 1 and 5.0 mmol of **27** for entry 2; [b] H_2SO_4 added as 9 M solution in H_2O, TFA as 50 vol% solution in H_2O. [c] isolated yield of products by column chromatography at complete conversion of **18** or **29**, reproducibility ± 2%.

In order to promote the desired cyclization, it was therefore necessary to (1) increase the nucleophilicity of the aliphatic nitrogen and (2) decrease the nucleophilicity of the indole ring. To satisfy the first condition, we chose to leave the benzyl carbamate group on the aliphatic nitrogen because it offered protection from CO_2 and was less electron-withdrawing than the methyl carbamate group. In addition to providing a more nucleophilic addition site for the aldehyde when compared to the methyl carbamate group, the addition of the benzyl carbamate via DBC also allowed for increased yields in the carbamation step. To address the second condition, the electron-withdrawing tosyl group (Ts) was added to indole nitrogen. Finally, TFA was used in place of H_2SO_4 in order to prevent cleavage of the more sensitive benzyl carbamate group. The chemical modification of tryptamine and the use of DBC in place of DMC successfully afforded the desired tetrahyrdo-β-carboline (compare entries 1 & 2) in a yield comparable to that of tetrahydroisoquinolines. Phase behavior for this reaction was identical to that shown in **Figure 5-6**.

5.6. Conclusions and Recommendations

In summary, we have successfully developed a versatile, CO_2-based synthetic protocol that produces nitrogen heterocycles. Our method involves the *in situ* carbamation of amines from the reaction with carbon dioxide and a dialkyl carbonate and the subsequent acyl-Pictet-Spengler cyclization of these carbamates by reaction with an aldehyde in the presence of acid. The conversion of amines to their carbamate derivatives offered suitable *N*-protection against the reaction of amines with CO_2. The amine carbamation step was highly sensitive to process operating conditions and was optimized after careful examination of byproduct formation pathways and the pressure-temperature-concentration space. For nearly all reactions studied, the acyl-Pictet-Spengler step proceeded nearly quantitatively and did not require optimization. Specific conclusions that can be drawn from this work include:

The Amine Carbamation Reaction (see **Chapter 7** for additional conclusions)

- Methyl and benzyl carbamate derivatives of β-arylethylamines and β-indolylethylamines were synthesized by employing dimethyl and dibenzyl carbonates, respectively. A temperature of 403 K (130 °C) was required to achieve complete amine conversion within 24 hr;

- The reaction was multi-phasic for the conditions explored and consisted of an upper, lower-density CO_2-rich supercritical-like phase and lower, higher-density organic-rich liquid phase(s);
- Carbamate selectivity was compromised by the competitive alkylation of the amine. Selectivity increased with: (1) an increase in pressure up to the pressure at which the dialkyl carbonate partitioned from the liquid phase and decreases thereafter, (2) an increase in the amount of dialkyl carbonate employed relative to the amine, and (3) a decrease in temperature, and
- At similar operating conditions, dibenzyl carbonate produced carbamates derived from β-indolylethylamines in larger yields.

The acyl-Pictet-Spengler Reaction

- Tetrahydroisoquinolines and tetrahyrdo-β-carbolines were synthesized from carbamates derived from β-arylethylamines and β-indolylethylamines, respectively, by employing a variety of aldehydes and acids;
- The reaction was multi-phasic for the conditions explored and consisted of an upper, lower-density CO_2-rich supercritical-like phase and lower, higher-density aqueous-rich and organic-rich liquid phases;
- Aliphatic and aromatic aldehydes, and organic (aqueous trifluoroacetic) and inorganic (aqueous sulfuric) acids successfully participated in the reaction, and
- Electron-withdrawing groups added to the indole nitrogen of β-indolylethylamines increased the efficiency of the desired cyclization pathway.

The scoping study of the acyl-Pictet-Spengler presented in the previous sections revealed several opportunities for future study. The following are recommendations that will facilitate the development and potential commercialization of this and similar processes (for recommendations regarding the amine carbamation step, see **Chapter 7**):

- **Process optimization and kinetic analysis:** explore the effect of process operating conditions (particularly carbon dioxide density) on the selectivity and rate of nitrogen heterocycle formation. It may be possible to operate some reactions at pressures and temperatures lower than those used in this study. Mentioned earlier in **Section 5.2.1**, it may be beneficial from a kinetic standpoint to run some reactions under neat conditions (i.e., depressurization after the amine carbamation step). The addition of carbon dioxide, however, has been shown to buffer sulfuric-acid containing systems that would otherwise not proceed under neat conditions (see **Section 5.4.1**). Carbon dioxide may also result in rate enhancements due to phase behavior effects. Under certain operating conditions, for example, it may be possible to partion excess dialkyl carbonate and byproducts from the amine carbamation step to the CO_2-rich phase, thereby concentrating (and possibly accelerating) the carbamate and aldehyde-rich phases. Alternatively, it may also be possible to selectively partition the desired nitrogen heterocycle product to the CO_2-rich phase and perform a relatively easy product isolation step.
- **Concerning reaction stereoselectivity:** add a functional group to the α-carbon of either a β-arylethylamine or β-indolylethylamine and explore the effect of process operating conditions on reaction stereoselectivity. Changes in stereoselectivity with CO_2 density would be a significant finding.

5.7. References

Aresta, M. and Quaranta, E. *Mechanistic Studies on the role of Carbon Dioxide in the Synthesis of Methylcarbamates from Amines and Dimethylcarbonate in the Presence of CO_2.* Tetrahedron, **1991**, 47, 9489-9502.

Allen, A. J. *Green Chemistry: Dense Carbon Dioxide and Water as Environmentally Benign Reaction Media.* S. M. Thesis, Chemical Engineering Department, Massachusetts Institute of Technology, Cambridge, MA, **2004**.

Cox, E. D. and Cook, J. M. *The Pictet-Spengler Condensation: A New Direction for an Old Reaction.* Chem. Rev., **1995**, *95*, 1797-1842.

Chaturvedi, D., Mishra, N., and Mishra, V. *Various Approaches for the Synthesis of Organic Carbamates.* Curr. Org. Synth., **2007**, *4*, 308-320.

Dell'Amico, D. B., Calderazzo, F. Labella, L. Marchetti, F., and Pampaloni, G. *Converting Carbon Dioxide into Carbamato Derivatives.* Chem. Rev., **2003**, *103*, 3857-3897.

Dunetz, J. R. *I. Synthesis of Indolines and Indoles via Intramolecular [4+2] Cycloaddition of Ynamides and Conjugated Enynes. II. Synthesis of Nitrogen Heterocycles in Supercritical Carbon Dioxide.* Ph. D. Thesis, Chemistry Department, Massachusetts Institute of Technology, Cambridge, MA, **2005**.

Dunn, P. J. *Synthesis of Commercial Phosphodiesterase(V) Inhibitors.* Org. Proc. Res. & Dev., **2005**, *9*, 88-97.

Fischer, H., Gyllenhaal, O., Vessman, J., and Albert, K. *Reaction Monitoring of Aliphatic Amines in Supercritical Carbon Dioxide by Proton Nuclear Magnetic Resonance Spectroscopy and Implications for Supercritical Fluid Chromatography.* Anal. Chem., **2003**, *75*, 622-626.

Maryanoff, B. E., Zhang, H.-C., Cohen, J. H., Turchi, I. J., and Maryanoff, C. A. *Cyclizations of N-Acyliminium Ions. Chem. Rev.* **2004**, *104,* 1431-1628.

Pacheco, M. A. and Marshall, C. L. *Review of Dimethyl Carbonate (DMC) Manufacture and Its Characteristics as a Fuel Additive.* Energy & Fuels, **1997**, *11,* 2-29.

Revell, J. D., Srinivasan, N., and Ganesan, A. *Two Concise Syntheses of Cialis via the N-Acyliminium Pictet–Spengler Reaction.* Synlett, **2004**, *8*, 1428–1430

Selva, M. and Perosa, A. *Green Chemistry Metrics: A Comparative Evaluation of Dimethyl Carbonate, Methyl Iodide, Dimethyl Sulfate and Methanol as Methylating Agents.* Green Chem., **2008**, *10*, 457–464.

Selva, M., Perosa, A., Tundo, P., and Brunelli, D. *Selective N,N-Dimethylation of Primary Aromatic Amines with Methyl Alkyl Carbonates in the Presence of Phosphonium Salts.* J. Org. Chem. **2006**, *71*, 5770-5773.

Selva, M., Tundo, P., Perosa, A., and Dall'Acqua, F. *Synthesis of Methyl Carbamates from Primary Aliphatic Amines and Dimethyl Carbonate in Supercritical CO_2: Effects of Pressure and Cosolvents and Chemoselectivity.* J. Org. Chem. **2005**, *70*, 2771-2777.

Selva, M., Tundo, P., and Perosa, A. *The Synthesis of Alkyl Carbamates from Primary Aliphatic Amines and Dialkyl Carbonates in Supercritical Carbon Dioxide.* Tetrahedron Lett. , **2002**, *43*, 1217–1219.

Tundo, P., Perosa, A., and Zecchini, F., Eds. *Methods and Reagents for Green Chemistry. An Introduction.* Wiley & Sons: New Jersey, **2007**.

Tundo, P., Bressanello, S., Loris, A., and Sathicq, G. *Direct Synthesis of N-Methylurethanes from Primary Amines with Dimethyl Carbonate.* Pure Appl. Chem., **2005**, *77*, 1719–1725.

Tundo, P. and Selva, M. *The Chemistry of Dimethyl Carbonate.* Acc. Chem. Res., **2002**, *35*, 706-716.

Whaley, W. M. and Govindachari, T. R. *Organic Reactions.* New York: John Wiley and Sons, **1951**.

6. PHASE EQUILIBRIA DATA AND ENGINEERING CORRELATIONS FOR THE CARBON DIOXIDE/DIMETHYL CARBONATE SYSTEM

6.1. Motivation

During our study of the amine carbamation reaction in **Chapter 5**, we observed a significant change in product selectivity with operating pressure. We suspected that phase behavior effects were at play and decided to perform an extensive experimental and theoretical phase equilibria study of the carbon dioxide/dimethyl carbonate (DMC) system in order to quantify the effect of process operating conditions on reaction system phase behavior. The purpose of this chapter is to develop models and engineering correlations from experimental data that can be used to predict the phase behavior properties of the carbamation reaction medium *a priori*. Specifically, we measured mixture critical pressures, and liquid-phase densities, species concentrations, and volume expansion — all as a function of temperature and pressure. Prior to this work, this property set for the CO_2/DMC system were not available. The importance of these properties on amine carbamation reaction efficiency will become clear in this and the following chapter.

We begin our discussion by introducing the concept of equation-of-state-based phase equilibria modeling and formulate a model for the CO_2/DMC system. In following sections, we use this model to correlate experimental phase equilibria data. Carbamation reactions were typically performed dilute with respect to amine and so system phase behavior is believed to behave closely to that of the binary CO_2/dialkyl carbonate mixture. In latter sections, we extend our analysis to include other dialkyl carbonates and also address the effects of amines and reaction byproducts (e.g., MeOH) on the phase behavior of the binary mixture.

6.2. Equation-of-State-Based Modeling Approach

A cubic equation-of-state (EOS)-based approach was used for the vapor-liquid equilibrium (VLE) modeling of the CO_2/DMC system. Unlike alternative modeling methods — such as excess Gibbs free energy-based methods or statistical mechanics-based and higher-order EOSs — cubic EOSs are often capable of accurately predicting equilibrium and critical phenomena for a wide range of systems and without the need for fitting a large number of empirical parameters. In addition, computational procedures for generating VLE predictions from cubic EOSs are well-documented and relatively simple. Cubic EOSs are made even more popular by their availability in a variety commercial process simulation software packages (e.g., Aspen®, ChemCAD®, Hysys®).

All theoretical VLE predictions presented herein were generated using Aspen Plus® 2004 steady state process simulation software. With practice, the Aspen Plus® 2004 (Aspen, 2004) graphic user interface offered a convenient and straightforward way of producing VLE predictions without the need for time-intensive manual EOS manipulation and coding. We selected the Redlich-Kwong-Aspen (RK-Aspen) EOS (Mathias, 1983) over other cubics available in Aspen Plus® because it offered several desirable modeling characteristics for CO_2-based systems, including:

- an empirical polar parameter in the molecular attraction term, which improves the prediction of pure-component vapor pressures of polar species (e.g., DMC);
- a molecular attraction term that is adjusted to account for components that are in their supercritical state (e.g., CO_2), which enhances agreement with *PVT* data;
- mixing rules that contained several binary interaction parameters, which makes it well-suited for combinations of small and large molecules (e.g., CO_2 and DMC), and
- mixing rules that contained temperature-dependent binary interaction parameters, which made the equation more robust.

The RK-Aspen EOS is shown in equation **(6-1)**:

$$P = \frac{RT}{V-b} - \frac{a}{V(V-b)} \qquad \textbf{(6-1)}$$

where P is pressure, R is the universal gas constant, T is temperature, V is molar volume, a is the molecular attraction term, and b is the molecular co-volume term. The RK-Aspen EOS was extended to mixtures by simple quadratic mole fraction-averaging of pure-component values:

$$a = \sum_i \sum_j x_i x_j \left(a_i a_j\right)^{0.5} \left(1 - k_{a_{ij}}\right) \tag{6-2}$$

$$b = \sum_i \sum_j x_i x_j \frac{b_i + b_j}{2} \left(1 - k_{b_{ij}}\right) \tag{6-3}$$

where i and j are component indices, and k is a binary interaction parameter applied to both the a and b terms and is assumed linear in temperature:

$$k_{a_{ij}} = k^0_{a_{ij}} - k^1_{a_{ij}} \frac{T}{1000} \tag{6-4}$$

$$k_{b_{ij}} = k^0_{b_{ij}} - k^1_{b_{ij}} \frac{T}{1000} \tag{6-5}$$

Unfortunately like other EOS/mixing rule combinations within Aspen Plus®, equations **(6-2)** – **(6-5)** could not be easily edited, nor could mixing rules from another EOS be used for the RK-Aspen EOS and *vice versa*.

The pure-component molecular attraction (a_i) and co-volume terms (b_i) were determined by applying stability criteria $\left(\left(\delta P / \delta V\right)_T = \left(\delta^2 P / \delta V^2\right)_T = 0\right)$ at the critical temperature (T_c) and critical pressure (P_c):

$$a_{c_i} = 0.42747 \frac{R^2 T_{ci}^2}{P_{c_i}} \tag{6-6}$$

$$b_i = 0.08664 \frac{R T_{c_i}}{P_{c_i}} \tag{6-7}$$

$$a_i = a_{c_i} \alpha_i \tag{6-8}$$

where:

$$\alpha_i = \left[1 + m_i \left(1 - T_{r_i}^{0.5}\right) - p_i \left(1 - T_{r_i}\right)\left(0.7 - T_{r_i}\right)\right]^2 \tag{6-9}$$

$$m_i = 0.48508 + 1.55191\omega_i - 0.15613\omega_i^2 \quad \textbf{(6-10)}$$

$$T_{r_i} = \frac{T}{T_{c_i}} \quad \textbf{(6-11)}$$

and α is a factor that adds T-dependence to the a term and is used to correlate pure-component vapor pressure, m is a constant correlated as a function of the acentric factor (ω), and p is an empirical adjustable polar parameter that enhances the accuracy of pure-component vapor pressure for polar species.

For components above their supercritical temperature ($T > T_c$), equation **(6-9)** is replaced by:

$$\alpha_i = \left[\exp\left(c_i\left(1 - T_{r_i}^{d_i}\right)\right)\right]^2 \quad \textbf{(6-12)}$$

$$c_i = 1 + \frac{m_i}{2} + 0.3p_i \quad \textbf{(6-13)}$$

$$d_i = 1 - \frac{1}{c_i} \quad \textbf{(6-14)}$$

For a multi-component system involving a coexisting vapor (v) and liquid (l) phase, equilibrium modeling begins by equating the fugacities (f) of each component:

$$\hat{f}_i^v = \hat{f}_i^l \quad \textbf{(6-15)}$$

where ^ denotes a mixture property. When using an equation-of-state, fugacities are expressed in terms of fugacity coefficients (ϕ):

$$\hat{f}_i^v = \hat{\phi}_i^v P y_i \quad \textbf{(6-16)}$$

$$\hat{f}_i^l = \hat{\phi}_i^l P x_i \quad \textbf{(6-17)}$$

where y_i and x_i are the mole fractions of component i in the vapor and liquid phases, respectively. Equating equations **(6-16)** and **(6-17)** results in the governing expression for liquid-vapor phase equilibrium:

$$\frac{x_i}{y_i} = \frac{\hat{\phi}_i^v}{\hat{\phi}_i^l} \tag{6-18}$$

Fugacity coefficients can be conveniently determined directly from a pressure-explicit EOS like the RK-Aspen EOS by employing the Helmholtz energy (A) departure function for the mixture:

$$RT\, ln\hat{\phi}_i = \left(A - A^{\circ}\right) + RT\left(\hat{Z} - 1\right) \tag{6-19}$$

and

$$A - A^{\circ} = -\int_{\infty}^{V}\left(P - \frac{RT}{V}\right)dV + RT\ln\hat{Z} \tag{6-20}$$

$$\hat{Z} = \frac{PV}{RT} \tag{6-21}$$

where the superscript $^{\circ}$ denotes the evaluation of a property under ideal-gas state conditions, $\hat{Z}$ is the compressibility factor for the mixture, and P takes the form of the EOS (see equation **[6-1]**). For a more detailed derivation of phase equilibrium, see Tester and Modell (1997).

Aspen Plus® utilizes proprietary algorithms that iteratively solve equation **(6-18)** and generate P-x_i-y_i and T-x_i-y_i data given user inputs. While the input-output framework of Aspen Plus® calculation algorithms made it easy to use, caution was taken when considering the reliability of simulation results. Two primary concerns were (1) the reliability of the Aspen Plus® VLE prediction algorithms, and (2) the ability of the RK-Aspen EOS to accurately predict the CO_2/DMC system phase behavior. Both concerns were addressed and are discussed in **Section 6.3**.

6.3. Vapor-Liquid Equilibria Modeling

6.3.1. Data Regression

As shown in the previous section, phase equilibria of a multi-component system can be predicted by simply using an equation-of-state (equipped with mixing rules) and the T_c, P_c, and ω of each component. Physical properties for CO_2 and DMC are listed in **Table 6-1**. For most mixtures, however, the accuracy of vapor-liquid equilibrium predictions are increased significantly when binary interaction parameters (regressed from experimental VLE data) are applied to the EOS via the mixing rules.

VLE data and modeling for the CO_2/DMC system were relatively scarce prior to this work, with the exception of two reports (Camy et al., 2003; Im et al. 2004). Combined, these sources provided data from 310 – 373 K (37 – 100°C). Im and coworkers (2004) used the Peng-Robinson EOS to regress their experimental P-x_i-y_i data and reported T-specific binary interaction parameter pairs. Their mixing rules were similar to those given in equations **(6-2)** – **(6-5)**, but with the exception that $k^1_{a_{ij}} = k^1_{b_{ij}} = 0$. As a result, a different pair of interaction parameters was required for each modeled T of interest. To overcome the burden of employing T-specific interactions parameters, we decided to regress experimental data reported by Im and coworkers with the RK-Aspen EOSin order to obtain a single set of binary interaction parameters that can be employed at all temperatures. Rather than regress a pair of binary interaction parameters from P-x_i-y_i data at each T, Aspen Plus® was used to regress the entire T-P-x_i-y_i data set and interaction parameters that varied as a function of T in the form of equations **(6-4)** and **(6-5)** were obtained. Data reported by Camy and co-workers (2003) was sparser and less consistent when compared to data from Im and coworkers and were therefore not included in the regression analysis.

Table 6-1. Pure-component properties for carbon dioxide and dimethyl carbonate (Poling et al., 2001).

Property	CO_2	DMC
T_c (K)	304.21	557
P_c (bar)	73.83	48
ω	0.225	0.336

6.3.2. Results and Discussion

Parameter regression results for the RK-Aspen EOS are listed in **Table 6-2**. Before regressing binary interaction terms, the polar parameter for DMC (p_{DMC}) was first regressed from pure-component vapor pressure (P_{vp}) data measured by Rodriguez and coworkers (2002). P_{vp} predictions for pure DMC by the RK-Aspen EOS using the regressed p_{DMC} value were improved only marginally.

Binary interaction terms, however, had a significant impact on the accuracy of VLE predictions. Without fitted-parameters, the RK-Aspen EOS resulted in a 7% average absolute deviation (AAD) in experimental pressures for a specified experimental x_i. Adding the regressed p_{DMC} and binary interaction parameters to the EOS significantly increased the accuracy of the fit, resulting in a 2.4% AAD. An AAD of 2.2% in x_i and 0.8% in y_i was observed at a specified experimental pressure, indicating that predictions were slightly more accurate for the vapor phase than the liquid phase. Using the regressed p_{DMC} and setting all binary interaction terms to zero resulted in a 6.8% AAD with respect to pressure. Setting p_{DMC} to zero and using the regressed interaction parameters did not affect the AAD with respect to pressure. Finally, regression of interaction parameters with p_{DMC} set to zero resulted in a different set of parameters and only slightly increased the AAD with respect to pressure.

Due to the differences in EOS choice and mixing rules, a direct comparison of binary interaction parameters could not be made between this work and those previously reported. Although the AADs found in this study were relatively small, we nevertheless decided to validate the accuracy of the Aspen Plus® regression algorithm. VLE data for the well-studied CO_2/toluene system were regressed using the Peng-Robinson EOS equipped with a single binary interaction parameter and compared with values reported in the literature. The Aspen Plus®-regressed interaction parameter was found to be within 10% of the value reported by Peng and Robinson (1976) (i.e., 0.10 vs. 0.09).

Table 6-2. Regressed RK-Aspen EOS parameters and vapor-liquid equilibrium prediction deviations from experimental data for the carbon dioxide/dimethyl carbonate system.

RK-Aspen EOS Parameter Set[a]						AAD[b] (%)		
p_{DMC}	$k^0_{a_{ij}}$	$k^1_{a_{ij}}$	$k^0_{b_{ij}}$	$k^1_{b_{ij}}$	T (K)	*P*	*x*	*y*
0.0388	-0.0402	-0.0263	0.0065	-0.1017	310.27	2.9	2.8	0.8
					320.36	2.3	2.2	1.0
					330.30	2.1	1.9	0.7
					340.27	2.4	2.0	0.9
					average	***2.4***	***2.2***	***0.8***
0	0	0	0	0	310.27	6.2		
					320.36	6.0		
					330.30	7.6		
					340.27	8.3		
					average	***7.0***		
0.0388	0	0	0	0	310.27	5.9		
					320.36	5.7		
					330.30	7.4		
					340.27	8.1		
					average	***6.8***		
0	-0.0402	-0.0263	0.0065	-0.1017	310.27	2.7		
					320.36	2.3		
					330.30	2.0		
					340.27	2.4		
					average	***2.4***		
0	-0.0532	0.0080	0.0000	-0.0848	310.27	3.0		
					320.36	2.4		
					330.30	2.1		
					340.27	2.4		
					average	***2.5***		

[a] $p_{CO_2} = 0$

[b] $\text{AAD} = \left(\frac{100}{n}\right)\sum_{1}^{n}\left|\frac{J_{\text{experimental}} - J_{\text{calculated}}}{J_{\text{experimental}}}\right|$, where n is the number of data points and J is the variable of interest

Graphical comparisons between the experimental VLE data and the RK-Aspen EOS predictions for the CO_2/DMC system are shown in **Figure 6-1**. As the AAD values suggest, the RK-Aspen EOS accurately fits the experimental data sets from which the interaction parameters were regressed. Extrapolation to higher temperatures also results in good agreement with experimental data.

In general, EOSs equipped with mixing rules that employ *T*-dependent interaction parameters most accurately predict VLE behavior when used in the experimental *T*-range from which parameters were regressed. The accuracy of the prediction is often compromised when extrapolating to significantly higher temperatures. In the absence of experimental data, though, extrapolation with interaction parameters regressed from lower-*T* data tends to be more accurate than not having interaction parameters at all.

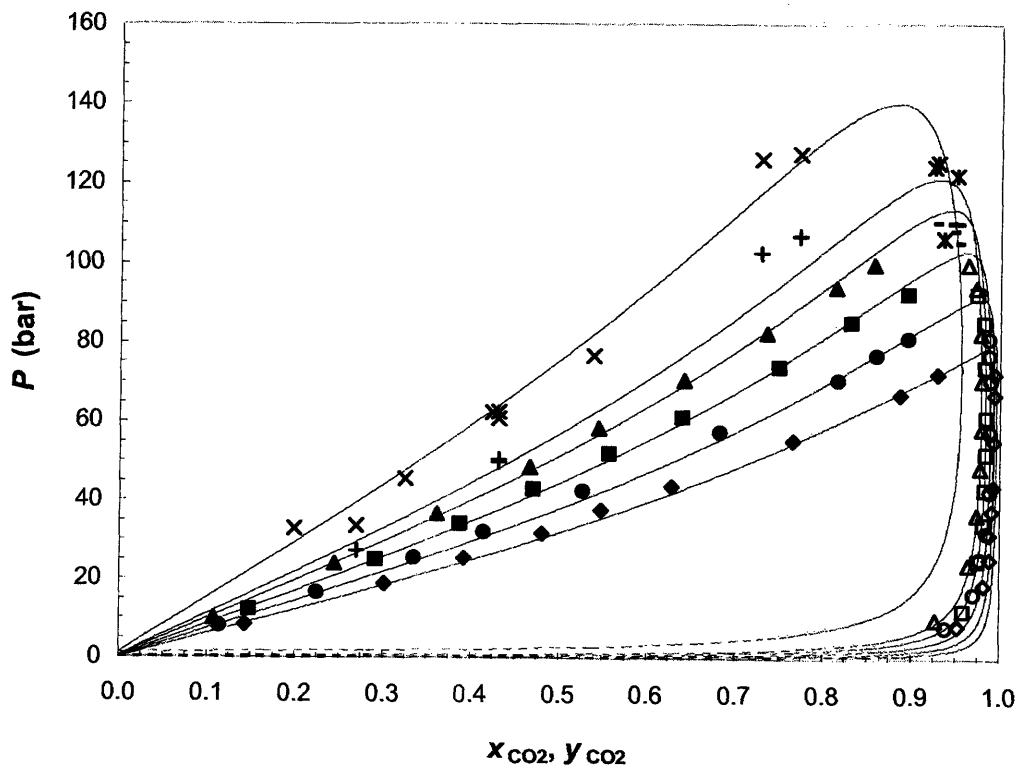

Figure 6-1. Vapor-liquid equilibria data and modeling for the carbon dioxide/dimethyl carbonate system: RK-Aspen EOS P-x_i (—) and P-y_i (- - -) by this work; experimental (P-x_i, P-y_i) data by Im et al. (2004) at 310.3 K (37.1 °C) (♦,◊); 320.4 K (47.2 °C) (●,○); 330.3 K (57.2 °C) (■,□); 340.3 K (67.1 °C) (▲,Δ); experimental (P-x_i, P-y_i) data by Carney et al. (2003) at 348.1 K (75.0 °C) (+,–); 373.6 K (100.4 °C) (×,*).

Aspen Plus® VLE calculation algorithms were further validated by manually manipulating and coding the RK-Aspen EOS (see equation **[6-1]**) and governing equilibrium expression (see equation **[6-18]**) into Matlab®. The code was developed by Kurt Frey in our group; Frey's research focuses on the design and validation of an EOS that aims at predicting accurate pure-component and mixture properties, including phase equilibria and densities (Frey et al., 2007). A comparison between experimental VLE data and the RK-Aspen predictions from Aspen Plus® and manual coding (see **Figure 6-2**) reveals that Aspen Plus® is indeed a reliable resource for VLE predictions.

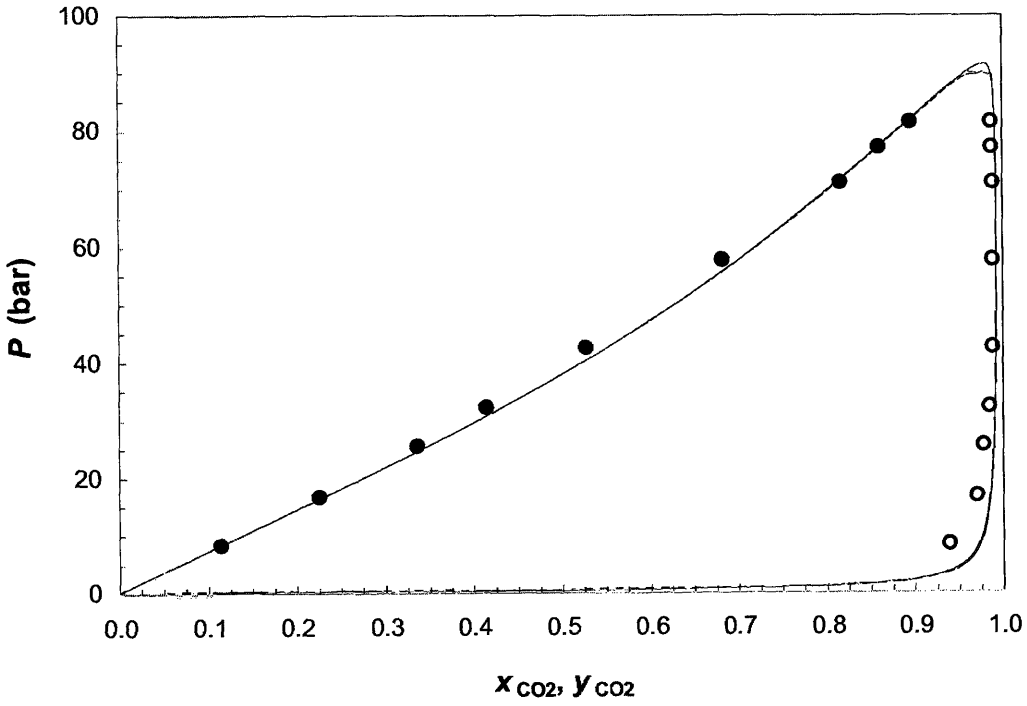

Figure 6-2. Comparison of vapor-liquid equilibria data for the carbon dioxide/dimethyl carbonate system with Aspen Plus® and manual EOS modeling methods: RK-Aspen EOS via Aspen Plus® by this work (—); RK-Aspen EOS via manual coding in Matlab® by this work (- - -); experimental data (P-x_i, P-y_i) by Im et al. (2004) at 320.4 K (47.2 °C) (•,○).

Equilibrium diagrams shown in **Figure 6-1** and **Figure 6-2** are extremely important for the design of CO_2-based processes; they are used identify the number of phases present and the phase-specific component distributions at a given set of process operating conditions. Consider, for example, if we were interested in identifying the phases present and the distribution of components within a CO_2/DMC mixture at 320 K (47 °C). As shown by **Figure 6-2**, the phase envelope at 320 K terminates at a mixture critical pressure ($P_{c,mix}$) of approximately 91 bar. Above 91 bar, the mixture is in its supercritical state, and only a single phase exists with a composition corresponding to that of the initial DMC and CO_2 charge. Below 91 bar, a lower-density vapor phase and a higher-density liquid phase co-exist in equilibrium. Phase-specific compositions can be found by drawing a horizontal line at the pressure of interest and noting the two points at which the line intersects the isotherm. The left-most point of intersection corresponds to P-x_i curve and liquid-phase phase compositions can subsequently be found by drawing a vertical line down to the x-axis. The right-most point of intersection corresponds to the P-y_i curve and vapor-phase phase compositions can similarly be found by drawing a vertical line down to the x-axis. At 60 bar and 320 K (47 °C), for example, the mole fractions of CO_2 in the liquid (x_{CO_2}) and vapor (y_{CO_2}) phases would be ca. 0.72 and 0.99, respectively. Since by definition $\sum_i x_i = \sum_i y_i = 1$, the mole fractions of DMC in each phase can be found by from $x_{DMC} = 1 - x_{CO_2}$ and $y_{DMC} = 1 - y_{CO_2}$.

At fixed temperature, phase-specific densities and component compositions approach each other as pressure is increased from ambient conditions and eventually become identical at a pressure infinitesimally close to $P_{c,mix}$. x_{CO_2} increases continuously with pressure up to $P_{c,mix}$. y_{CO_2} initially increases with increasing pressure, remains relatively constant for 1.01 bar << $P < P_{c,mix}$, and then decreases in the vicinity of the $P_{c,mix}$. This phenomenon becomes more pronounced at higher temperatures (see **Figure 6-1**). For fixed $T_2 > T_1$, larger pressures are required to arrive at an identical x_{CO_2} . For example, in order to arrive at an x_{CO_2} = 0.72 at 373 K (100 °C), an operating pressure of 116 bar would be needed (compared to 60 bar at 320 K, *vide supra*).

6.4. Mixture Critical Points and Modeling of the *P-T* Envelope

6.4.1. Experimental Approach and Equipment Validation

Supercritical extraction-grade (99.9999% purity, Airgas) carbon dioxide and HPLC-grade anhydrous dimethyl carbonate (99.9+%, Sigma-Aldrich) were used without further purification for all phase behavior studies discussed in this and latter sections. Experimental mixture critical pressures were determined using the cloud-point apparatus and operating procedures described in **Section 3.2.6**. Before measuring mixture critical pressures for the CO_2/DMC system, the apparatus and experimental techniques were first validated by benchmarking $P_{c,mix}$ literature data for the well-studied CO_2/toluene system against this work. **Figure 6-3** shows agreement between experimental data obtained for the CO_2/toluene system from our apparatus with that obtained by Ziegler and coworkers (1995).

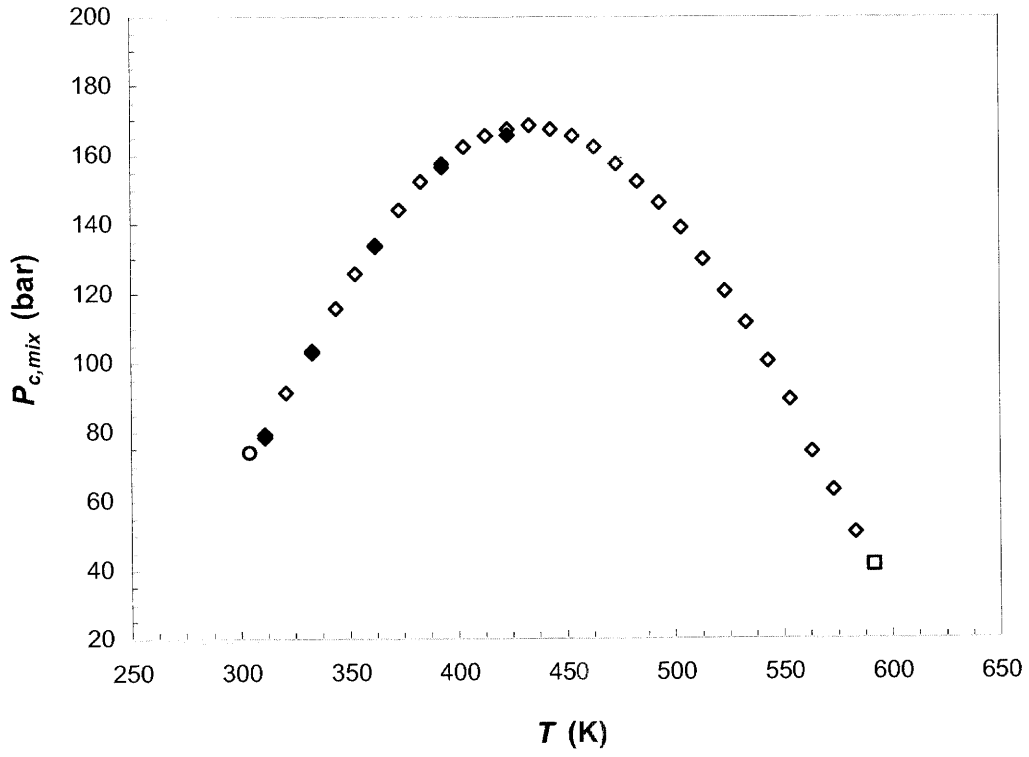

Figure 6-3. Mixture critical points for the carbon dioxide/toluene system: this work (♦); Ziegler et al. (1995) (◊); P_c of pure toluene (□); P_c of pure CO_2 (○).

6.4.2. Results and Discussion

To more fully understand the effect of process operating conditions on the phase behavior of the CO_2/DMC system, a *P-T* envelope was constructed using the RK-Aspen EOS and validated against our experimental data. The *P-T* envelope for the CO_2/DMC binary mixture was calculated by generating several isotherms in the $T_{c,CO_2} < T < T_{c,DMC}$ and noting the $P_{c,mix}$ value predicted at each *T*.

Representative isothermal equilibria trends are shown in **Figure 6-4** and reveal key aspects of the CO_2/DMC system. Like many CO_2-based binary systems, increasing the temperature from T_{c,CO_2} to $T_{c,DMC}$ results in a maximum value of $P_{c,mix}$ before it decreases to a value close to that of the critical pressure of pure DMC ($P_{c,DMC}$). The isotherms shift vertically upwards at $x_{CO_2} = 0$ as *T* increases, which corresponds to an increase in the vapor pressure of

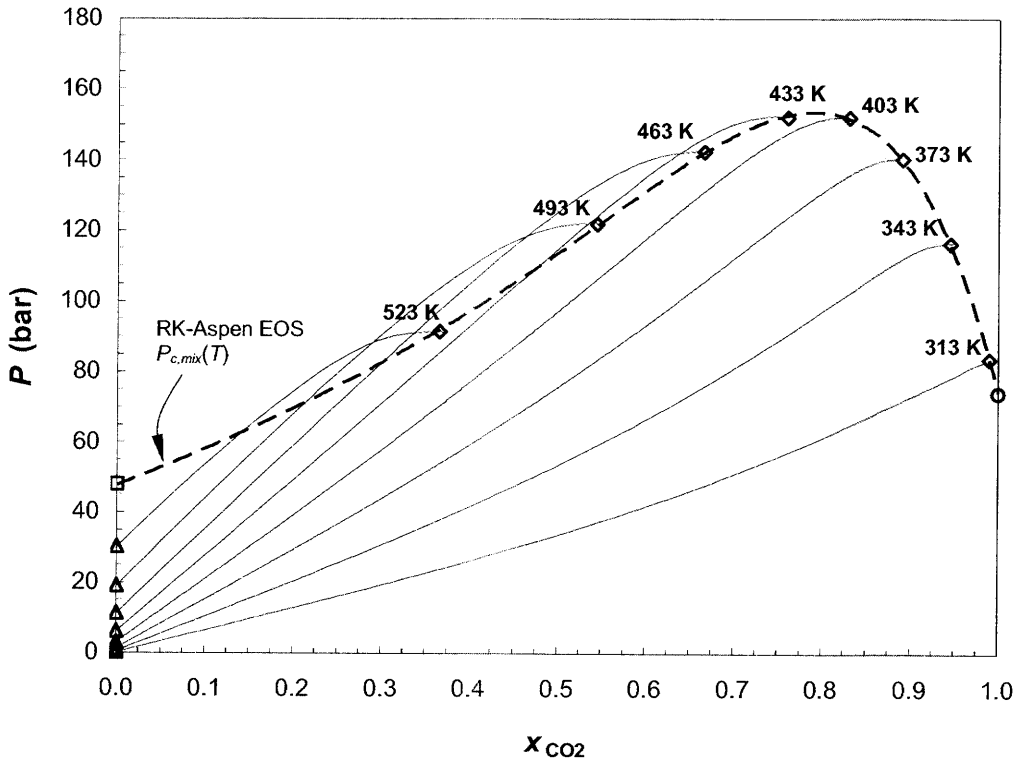

Figure 6-4. Vapor-liquid equilibria and mixture critical point predictions for the carbon dioxide/dimethyl carbonate system: RK-Aspen EOS $P\text{-}x_i$ (—); mixture critical points for plotted isotherms (◊) and for entire range by (- - -); P_c of pure DMC ($x_{CO2} = 0$) (□); P_c of pure CO_2 ($x_{CO2} = 1$) (○); Vapor pressure of pure DMC at each plotted temperature (Δ).

pure DMC. The phase envelope 'shrinks' with increasing temperature; that is, the maximum value of x_{CO_2} and y_{CO_2} reached for each isotherm decreases with increasing T (see **Figure 6-5**). Discussed in greater detail in **Section 6.5**, this trend correlates with the maximum-possible molar concentration of carbon dioxide permitted in the liquid phase at a given T.

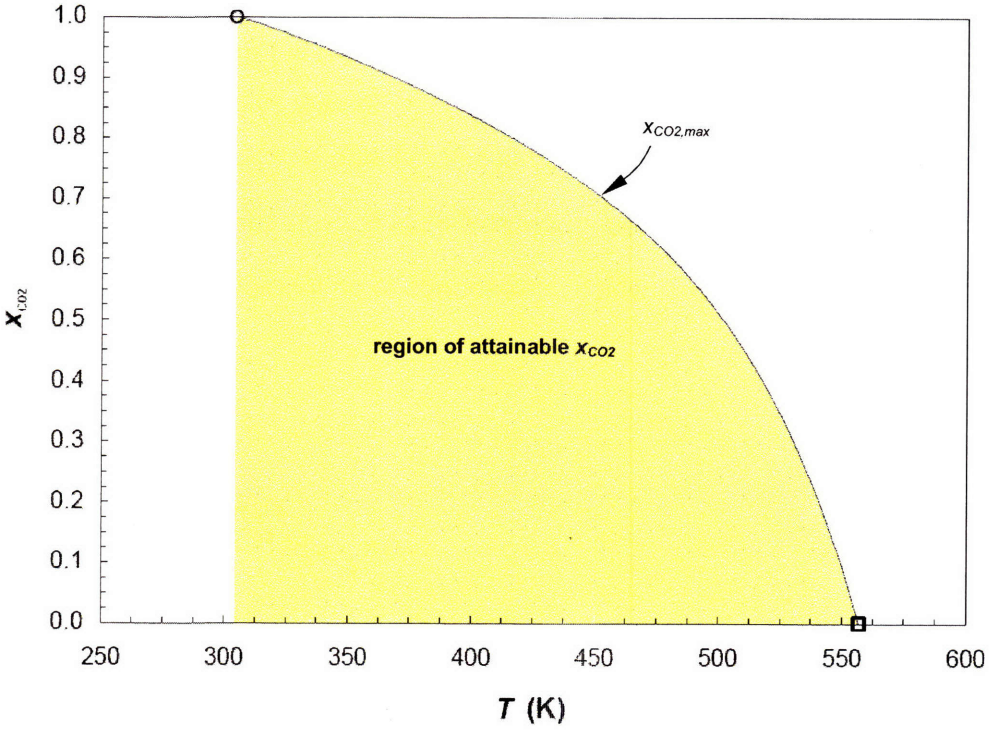

Figure 6-5. Maximum-possible liquid-phase mole fractions for the carbon dioxide/dimethyl carbonate system plotted as a function of temperature: RK-Aspen EOS (—) (also identical to equation **[6-22]**); T_c of pure CO_2 (x_{CO2} = 1) (○); T_c of pure DMC (x_{CO2} = 0) (□).

The experimental and RK-Aspen EOS-predicted P-T envelope for the CO_2/DMC binary system is shown in **Figure 6-6**. Experimental and calculated mixture critical point data reveal similar trends with temperature, with the RK-Aspen EOS over-predicting values by an AAD of 6.7% (see **Table 6-4** in **Section 6.11.1**). Also shown in the **Figure 6-6** are the vapor pressure curves for pure CO_2 and DMC, which connect to the mixture P-T envelope at their respective critical points. As expected, the RK-Aspen EOS does an excellent job at predicting the vapor pressures of both pure CO_2 and DMC, with an AAD of 0.60% when compared to experimental data.

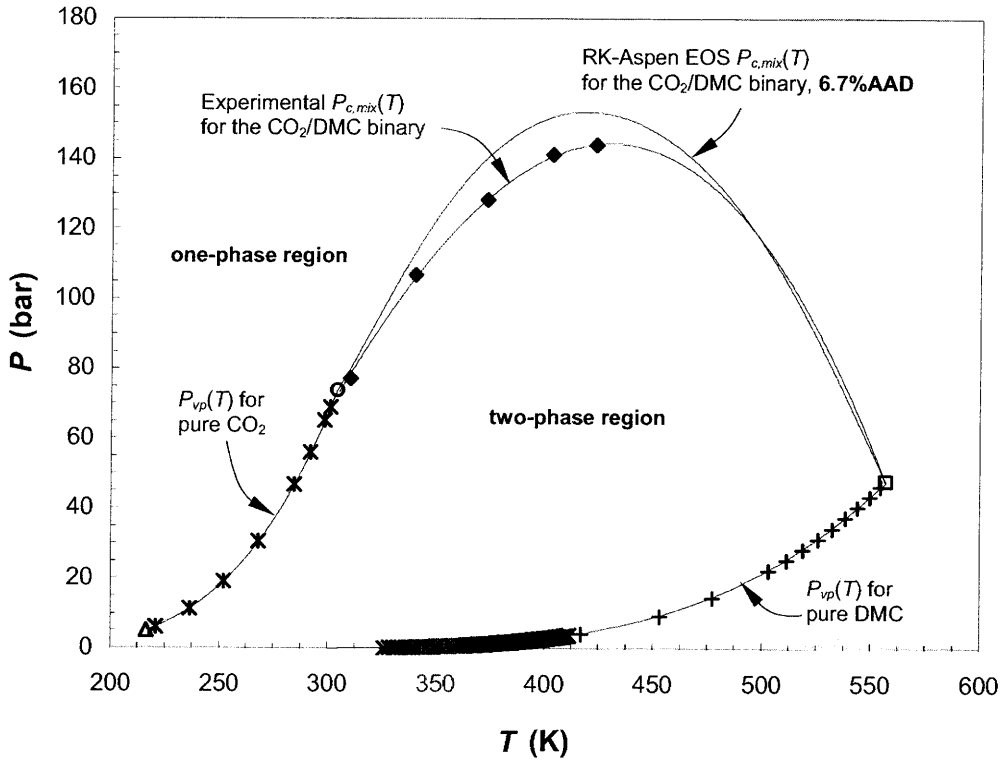

Figure 6-6. Experimental and calculated *P-T* envelope for the carbon dioxide/dimethyl carbonate system: $P_{vp}(T)$ for pure CO_2 trendline from NIST correlation (2005) (identical to equations **[6-22]** and **[6-23]**), RK-Aspen EOS by this work (∗), triple-point of pure CO_2 (Δ) from NIST; $P_{vp}(T)$ for pure DMC trendline by equation **(6-23)** (identical to equation **[6-22]**), experimental data by Rodriguez et al. (2002) (×), RK-Aspen EOS by this work(+); $P_{c,mix}(T)$ for the CO_2/DMC mixture from RK-Aspen EOS by this work (identical to equation **[6-22]**), experimental data by this work (♦); P_c of pure CO_2 (○); P_c of pure DMC (□).

Mixture and pure-component data and predictions for the *P-T* envelope were well-correlated by a cubic polynomial series given by equation **(6-22)**:

$$\text{property} = \alpha T^3 + \beta T^2 + \chi T + \delta \qquad \textbf{(6-22)}$$

Pure-component vapor pressure data were better correlated by the Antoine equation:

$$\ln P_{vp}(T) = A - \frac{B}{T - C} \qquad \textbf{(6-23)}$$

A list of regressed parameters and fit deviations for equations **(6-22)** and **(6-23)** are given in **Table 6-5** of **Section 6.11.1**.

6.5. Liquid-Phase Densities and Species Concentration Correlations

6.5.1. Experimental Approach and Equipment Validation

Experimental liquid-phase CO_2 concentrations ($[CO_2]_l$) were measured using a combination of the reactor (see **Section 3.2.4**), at-condition sampling unit (see **Section 3.3.1**), and inverted-buret apparatus (see **Section 3.3.2**) and their corresponding operating instructions. The gas (i.e., CO_2) content of a liquid sample can be calculated from the volume of fluid displaced when the gas effluent stream is directed into an inverted buret. The buret is typically filled with a higher-density incompressible fluid that is immiscible with the gas of interest. Step-by-step illustrations for the inverted buret method are shown in **Figure 6-7**. A liquid sample was taken a desired T and P and the composition of the liquid sample at these conditions was represented by the appropriate P-x_i isotherm shown in **Figure 6-4**. With the buret filled completely with water and inverted into a water bath, the liquid sample was directed to the buret (see **Figure 6-7a**). Since the buret was operated at ambient conditions, the reduction in P from experimental conditions resulted in the rapid release of CO_2 from the liquid sample ($x_{CO_2} \rightarrow 0$ as $P \rightarrow 1.01$ bar, see **Figure 6-7b**) and the subsequent displacement of the higher-density water-rich phase (see **Figure 6-7c**). The liquid portion of the sample either

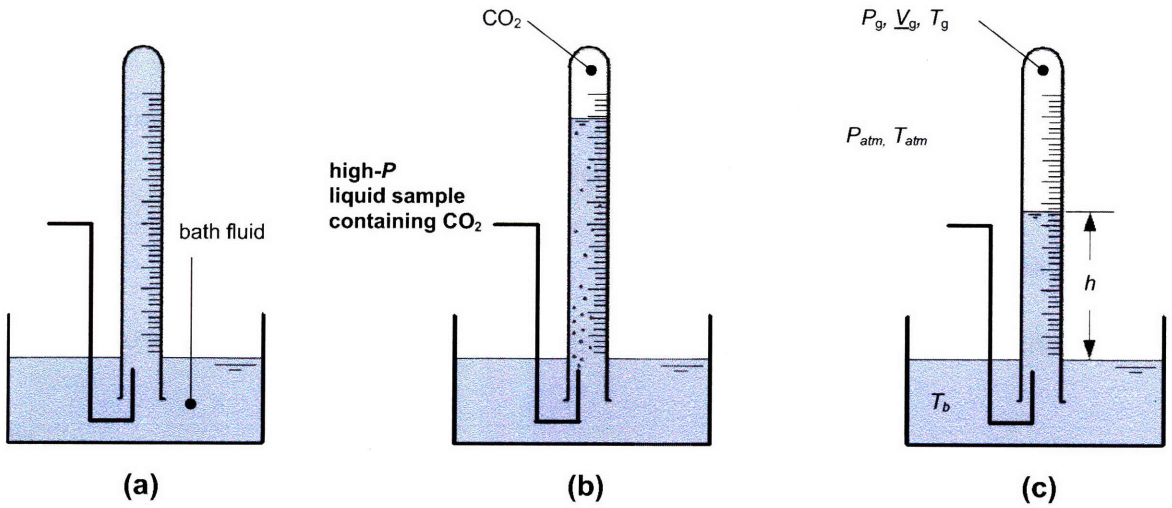

Figure 6-7. Step-by-step illustrations for the inverted-buret method used to measure liquid-phase carbon dioxide concentrations: buret initially filled completely with water prior to adding a liquid sample containing CO_2 **(a)**; CO_2 evolves from the sample and displaces the higher-density water-rich phase **(b)**; buret filled with a lower-density CO_2 phase (top) and higher-density water-rich phase (bottom) **(c)**.

dissolves in water or remains dispersed in the water as a separate phase. Although CO_2 does not have a large solubility in water at ambient T and P (Valtz et al., 2004), the water bath was constantly sparged with CO_2 in order to saturate the water and limit the driving force for CO_2 absorption. Lower-than-actual $[CO_2]_l$ values would have been observed had CO_2 from the sample absorbed into the liquid phase instead of displacing the water (*vide infra*).

By definition, liquid-phase CO_2 molar concentration was determined from the number of moles of CO_2 within the buret (n_{CO_2}) and the volume of the sample loop ($\underline{V}_s$):

$$[CO_2]_l = \frac{n_{CO_2}}{\underline{V}_s} \tag{6-24}$$

Assuming leak-free connections and neglecting absorption into the bath, n_{CO_2} was identical to the amount of moles in the original sample. The moles of CO_2 were calculated from the ideal gas law, as CO_2 behaves ideally at ambient T and P:

$$n_{CO_2} = \frac{P_{CO_2}\underline{V}_g}{RT_g} \tag{6-25}$$

where P_{CO_2} is the CO_2 partial pressure, $\underline{V}_g$ is the gas volume within the buret, and T_g is the gas temperature. P_{CO_2} was found by performing a pressure balance about the inverted-buret system:

$$P_{atm} = P_g + P_h(T_{bath}) = \left(P_{CO_2} + P_{vp,bath}(T_{bath})\right) + P_h(T_{bath}) \tag{6-26}$$

where P_{atm} is the atmospheric pressure, P_g is the gas pressure within the buret and is the sum of P_{CO_2} and the bath vapor pressure ($P_{vp,b}$) evaluated at the bath temperature (T_{bath}), and P_h is the bath fluid hydrostatic pressure within the buret at T_{bath} and is given by:

$$P_h(T_{bath}) = \rho_{bath}(T_{bath})gh \tag{6-27}$$

where ρ_{bath} is the density of the bath evaluated at T_{bath}, g is the gravitational constant, and h is the distance between the buret and bath liquid levels.

The bath CO_2 sparge rate was small enough and agitation rate high enough such that the entire system was isothermal (i.e., $T_{bath} = T_g = T_{atm}$). T_{bath} typically ranged from 293 – 303 K (20 – 30 °C). The bath was assumed to behave like pure water (i.e., $\rho_{bath} = \rho_{l,H_2O}$ and $P_{vp,bath} = P_{vp,H_2O}$). This was a valid assumption given the low solubility of CO_2 in water at ambient conditions. Also, since $\underline{V}_s$ was significantly smaller than the bath fluid volume (104 μL vs. 300 mL), bath contamination due to the liquid portion of the sample (≤ 104 μL) was assumed negligible. As a secondary precaution, bath fluid was changed after ten samples were taken.

Experimental ρ_{l,H_2O} and P_{vp,H_2O} data for the observed T_{bath} range were determined from NIST correlations and were fit well by equations **(6-22)** and **(6-23)**, respectively. Regressed parameters and correlation deviations are listed in **Table 6-6** of **Section 6.11.2**. The distance between the buret and bath liquid levels typically ranged from 12 – 25 in. $\underline{V}_g$ was read from the buret scale and typically ranged from 3 – 30 mL. Calculations of $P_{vp,b}$ and P_h revealed that both ranged from 0.02 – 0.06 bar, indicating that $P_{CO_2} \approx P_{atm}$ for the conditions studied. Calculation of n_{CO_2} with NIST correlations revealed that the ideal gas law assumption in equation **(6-25)** was justified, as a 0.5% AAD was obtained.

With experimental $[CO_2]_l$ data and liquid-phase mole fractions available from the RK-Aspen EOS, the density of the liquid-phase mixture was calculated from the following expression:

$$\rho_l = \frac{\bar{M}_l}{x_{CO_2}}[CO_2]_l \qquad \textbf{(6-28)}$$

where $\bar{M}_l$ is the average molecular mass of the liquid-phase mixture and is defined as:

$$\bar{M}_l = \sum_i x_i M_i \qquad \textbf{(6-29)}$$

Similarly, the relationship between liquid-phase DMC concentration ($[DMC]_l$) and density was given by:

$$\rho_l = \frac{\bar{M}_l}{x_{DMC}}[DMC]_l = \frac{\bar{M}_l}{\left(1 - x_{CO_2}\right)}[DMC]_l \qquad \textbf{(6-30)}$$

A relationship between $[DMC]_l$ and $[CO_2]_l$ was established by combining equations **(6-28)** and **(6-30)**:

$$[DMC]_l = \frac{x_{DMC}}{x_{CO_2}}[CO_2]_l = \frac{\left(1 - x_{CO_2}\right)}{x_{CO_2}}[CO_2]_l \qquad \textbf{(6-31)}$$

Before measuring liquid-phase CO_2 concentrations for the CO_2/DMC mixture, the inverted-buret apparatus and associated experimental techniques were first validated by benchmarking $[CO_2]_l$ literature data for the well-studied CO_2/toluene system against this work. As shown by **Figure 6-8**, data obtained for the CO_2/toluene system from our apparatus matched closely to that measured by Park and coworkers (Park et al., 1990).

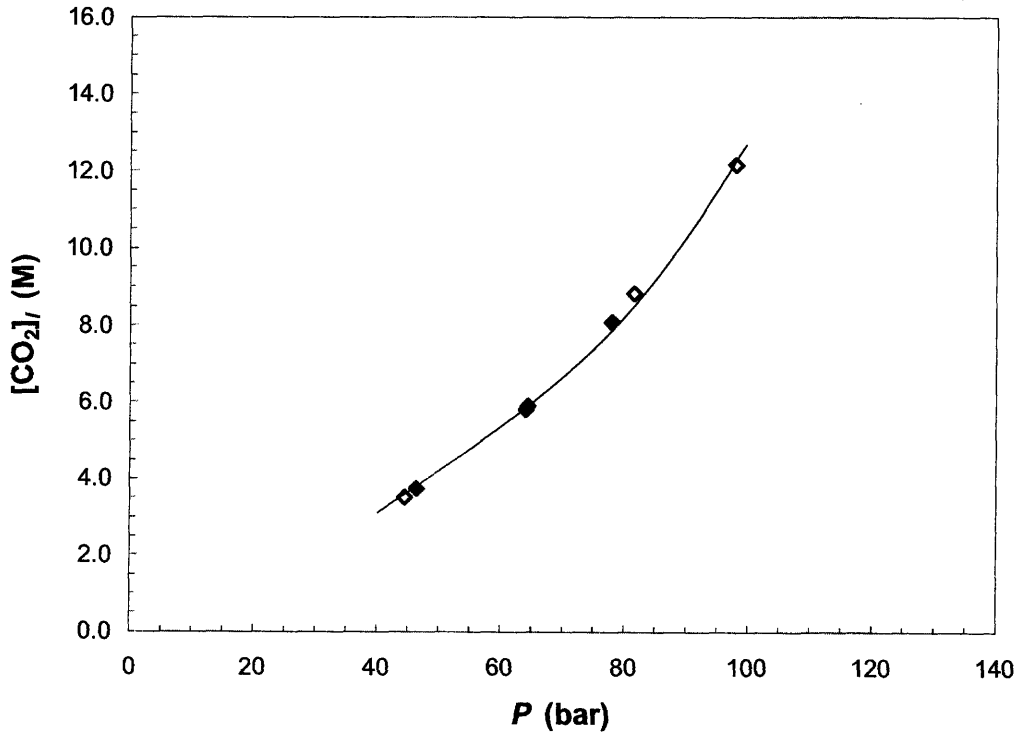

Figure 6-8. Experimental liquid-phase carbon dioxide concentration data for the carbon dioxide/toluene system at 333.2 K (60 °C): this work (♦); Park et al. (1990), calculated from equation **(6-28)** (◊). The trendline is drawn to serve as a guide for the eye and no physical basis is intended.

With the inverted-buret apparatus validated, the overall ability to accurately sample multiple phases (e.g., liquid phases as well as vapor phases) and multiple components (e.g., organic compounds as well as CO_2) was assessed. Using the CO_2/toluene system and same experimental set-up, multiple liquid and vapor-phase samples were taken and each were analyzed for CO_2 content via the inverted-buret method and toluene content via HPLC. Sample preparation and sampling procedures are described in **Section 3.3.1** and HPLC operating instructions in **Section 3.3.5**. Toluene resolved at ca. 8.5 minutes when using the C-18 column with a mobile phase ratio of 60:40 vol% acetonitrile:water at an isocratic flowrate of 1 mL·min^{-1}. The absorbance detector was set to 254 nm and the autosampler injection volume to 25 μL.

The toluene content of a known-volume sample was determined by injecting the solution into the HPLC system and determining the concentration via a linear calibration curve made from toluene standards:

$$[\text{toluene}] = c_1(\text{HPLC Peak Area}) + c_0 \qquad \textbf{(6-32)}$$

where c_1 and c_0 are the slope and intercept of the calibration curve, respectively. Toluene standards were prepared by diluting known masses into various-sized volumetric flasks. The number of moles toluene (n_{toluene}) in the HPLC sample were found from:

$$n_{\text{toluene}} = \underline{V}_w[\text{toluene}] \qquad \textbf{(6-33)}$$

where $\underline{V}_w$ is the total volume of solvent washed through the sample loop used to prepare the sample. All wash volumes were adjusted such that the injections fell within the range of the calibration curve. The liquid-phase concentration of toluene ([toluene]$_l$) was subsequently calculated from:

$$[\text{toluene}]_l = \frac{n_{\text{toluene}}}{\underline{V}_s} \qquad \textbf{(6-34)}$$

The volume of the sample loop ($\underline{V}_s$, 104 μL) was determined by injecting a solution of known toluene concentration through the sample loop ([toluene]$_s$) and then washing the loop with pure solvent. With the total wash volume ($\underline{V}_w$) and the concentration of the wash ([toluene]$_w$) known via equation **(6-32)**, $\underline{V}_s$ was calculated from:

$$\underline{V}_s = \frac{[\text{toluene}]_w}{[\text{toluene}]_s}\underline{V}_w \tag{6-35}$$

With the moles of CO_2 and toluene known in each phase via the inverted-buret method and HPLC, respectively, the mole fractions of CO_2 in each phase were calculated by:

$$x_{CO_2} = \left.\frac{n_{CO_2}}{n_{CO_2} + n_{\text{toluene}}}\right|_{\text{liquid-phase sample}} \tag{6-36}$$

$$y_{CO_2} = \left.\frac{n_{CO_2}}{n_{CO_2} + n_{\text{toluene}}}\right|_{\text{vapor-phase sample}} \tag{6-37}$$

As shown by **Figure 6-9**, VLE data obtained for the CO_2/toluene system generated from our apparatuses and sampling/analytical techniques matched very closely to that measured by Park and coworkers (1990).

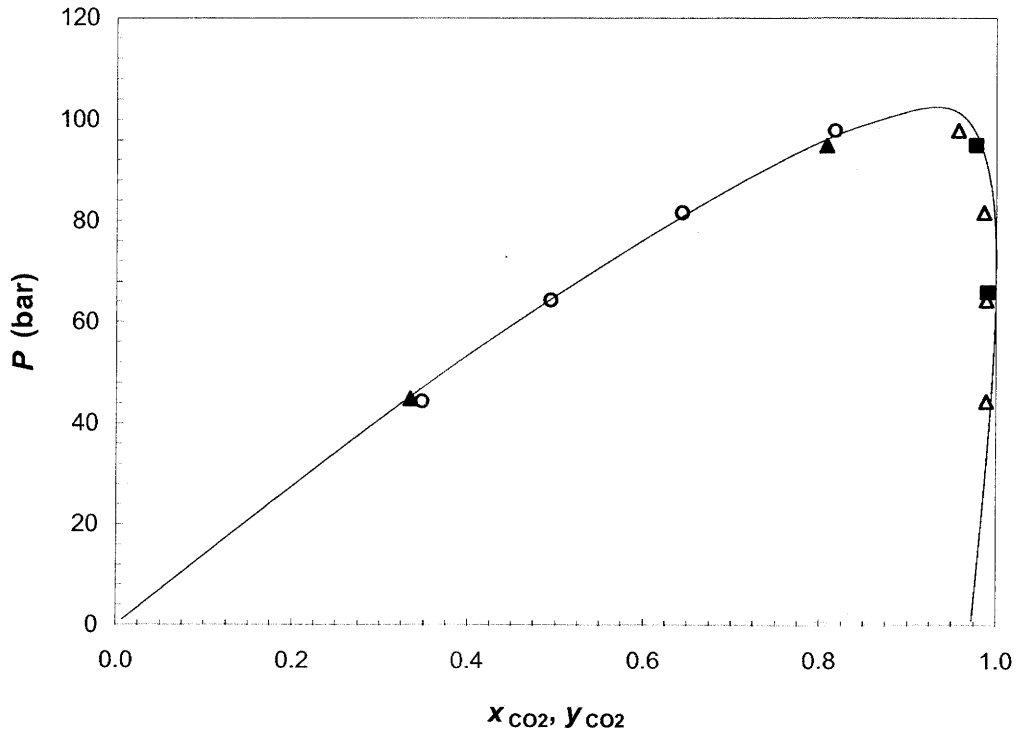

Figure 6-9. Experimental vapor-liquid equilibria data for the carbon dioxide/toluene system at 333.2 K (60 °C): (P-x_i, P-y_i) data by this work (♦, ▲); Park et al. (1990) (◊, Δ). The trendline is drawn to serve as a guide for the eye and no physical basis is intended.

6.5.2. Results and Discussion

Liquid-phase CO_2 concentration data for the carbon dioxide/dimethyl carbonate system plotted as a function of pressure for several isotherms is shown in **Figure 6-10**. A comparison between experimental and RK-Aspen EOS-calculated liquid-phase densities and component concentrations is given in **Table 6-7** of **Section 6.11.2**. Isotherms were selected to match the temperatures of VLE data sets currently available in the literature (Camey et al. 2003; Im et al., 2004).

At fixed temperature, $[CO_2]_l$ increases with increasing pressure. At higher temperatures, larger pressures were required to arrive at a similar $[CO_2]_l$. For example, in order to arrive at a $[CO_2]_l$ of 8 mol·L^{-1} at 310 K (37 °C), a pressure of ca. 40 bar would be required, whereas a pressure of ca. 94 bar would be required at 373 K (100 °C). Data were well-correlated by a linear model of the form:

$$\text{property} = \alpha P + \beta \qquad \textbf{(6-38)}$$

A list of regressed parameters and fit deviations for equations **(6-38)** are given in **Table 6-8** of **Section 6.11.2**.

Extrapolation of $[CO_2]_l$ by equation **(6-38)** up to the $P_{c,mix}$ for each isotherm revealed that the maximum possible $[CO_2]_l$ ($[CO_2]_{l,\,max}$) decreases with increasing temperature. Compared to experimental data, RK-Aspen EOS-calculated values deviated by an overall AAD of 8.7%. Calculated values diverged from the linear extrapolation at pressures within ca. 15% of the $P_{c,mix}$, resulting in a $[CO_2]_{l,\,max}$ that is ca. 12% lower than predicted by equation **(6-38)**. Although we have not confirmed this experimentally, deviations in $[CO_2]_l$ from linearity with respect to pressure for the CO_2/DMC system are expected to occur, as non-linear density and composition fluctuations are experienced in the vicinity of $P_{c,mix}$. Non-linear composition behavior, for example, was observed in experimental and RK-Aspen EOS-calculated P-x_i diagrams in the vicinity of $P_{c,mix}$, and becomes more pronounced at elevated T (see **Figure 6-1** and **Figure 6-4**). Deviation in $[CO_2]_l$ from linearity has been observed experimentally for other CO_2/co-solvent systems and is discussed in **Section 6.8**. Extrapolation of equation **(6-38)** to the $P \rightarrow 1.01$ bar region for each isotherm revealed the solubility of carbon dioxide in a saturated CO_2/DMC mixture at these conditions.

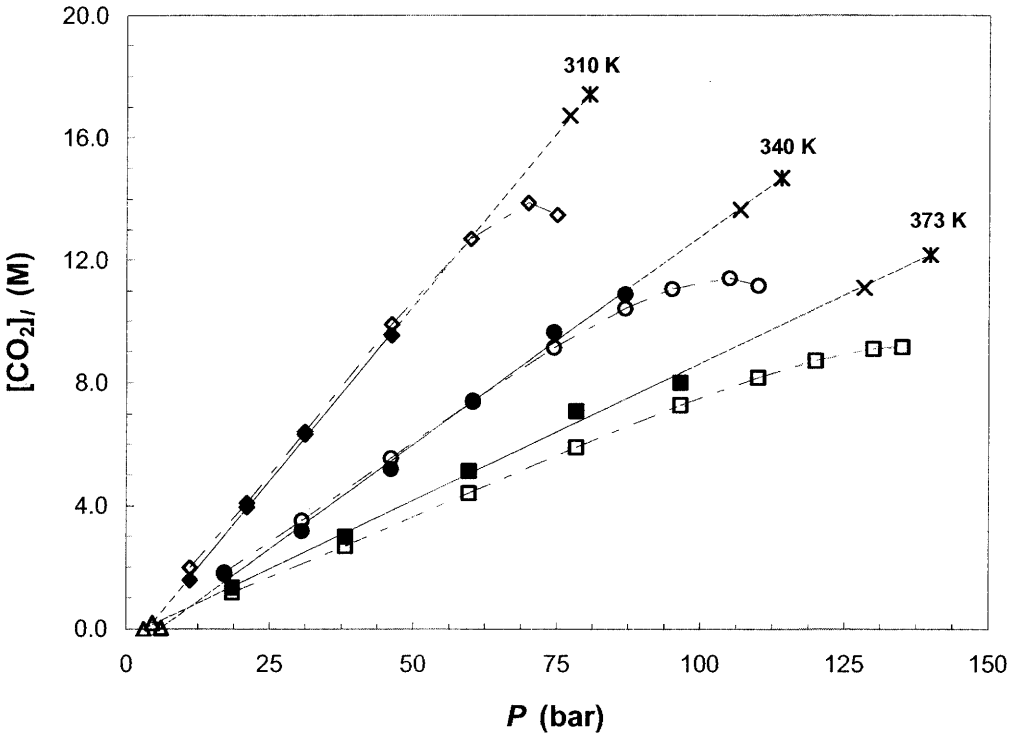

Figure 6-10. Liquid-phase carbon dioxide concentrations plotted as a function of pressure and temperature for the carbon dioxide/dimethyl carbonate system: (experimental, RK-Aspen EOS-calculated) at 310.15 K (37 °C) (♦, ◊); 339.65 K (66.5 °C) (•, ○); 373.15 K (100 °C) (■, □); RK-Aspen EOS (– - –); equation **(6-38)** (—); extrapolation by equation **(6-38)** to $[CO_2]_{l,max}$ (- - -); experimental mixture critical pressure (×); RK-Aspen EOS-calculated mixture critical pressure (∗); extrapolated value of $[CO_2]_l$ by equation **(6-38)** as $P \rightarrow 1.01$ bar for each isotherm (Δ).

When plotted as a function x_{CO2}, experimental $[CO_2]_l$ data sets for each isotherm collapsed onto a single trend (see **Figure 6-11**) that was correlated well by:

$$\text{property} = \alpha x_i + \beta \qquad \textbf{(6-39)}$$

Regressed parameters for equation **(6-39)** are also provided in **Table 6-8**.

This trend is a significant finding, as it provides a method of estimating the $[CO_2]_l$ at any *P-T* condition. To do so, we would first generate a *P-x*$_i$ diagram using the RK-Aspen EOS at a temperature of interest (see **Figure 6-4**). With x_{CO2} known as a function of pressure up to the $P_{c,mix}$ (see **Figure 6-6**), $[CO_2]_l$ can be readily determined from equation **(6-39)**.

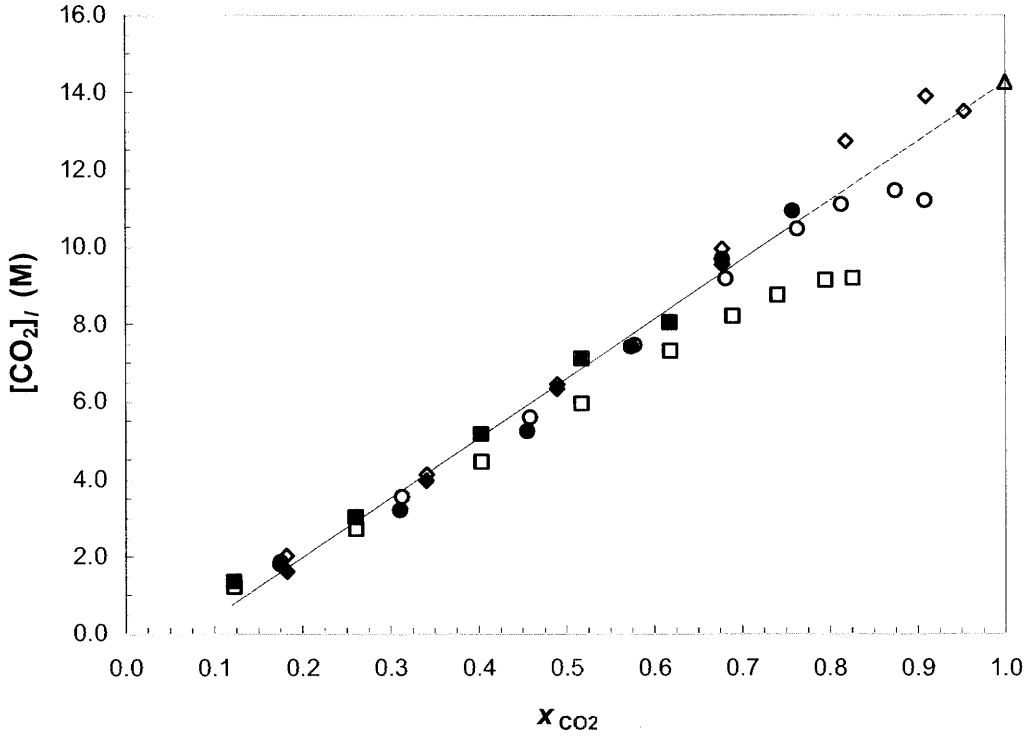

Figure 6-11. Liquid-phase carbon dioxide concentration plotted as a function of liquid-phase carbon dioxide mole fraction and temperature: (experimental, RK-Aspen EOS-calculated) at 310.15 K (37 °C) (♦, ◊); 339.65 K (66.5 °C) (•,○); 373.15 K (100 °C) (■, □); equation **(6-39)** (—); extrapolation by equation **(6-39)** (- - -); extrapolated value of $[CO_2]_l$ by equation **(6-39)** as $x_i \rightarrow 1$ (Δ).

Extrapolation to $x_{CO2} = 0$ revealed a non-zero intercept, which is indicative of experimental error in $[CO_2]_l$ data as well as error in x_{CO2} predictions by the RK-Aspen EOS. Extrapolation to $x_{CO2} = 1$ revealed an overall maximum attainable liquid-phase CO_2 concentration for the CO_2/DMC system of ca. 14 mol·L^{-1}. Since $x_{CO2} \rightarrow 1$ only for $T \approx T_{c,CO_2}$ (see **Figure 6-5**), $[CO_2]_{l,max}$ is largest for $T \approx T_{c,CO_2}$ and decreases continuously to zero as $T \rightarrow T_{c,DMC}$. Combining equations **(6-22)** and **(6-39)**, $[CO_2]_{l,max}$ was plotted as a function of temperature and is shown in **Figure 6-12**. The trend was regressed to the form of **(6-22)**, with parameters listed in **Table 6-9** of **Section 6.11.2**.

Liquid-phase densities were calculated from $[CO_2]_l$ data via equation **(6-28)** and are also given in **Table 6-7** of **Section 6.11.2**. Unlike $[CO_2]_l$, ρ_l did not trend with either P or x_{CO2}.

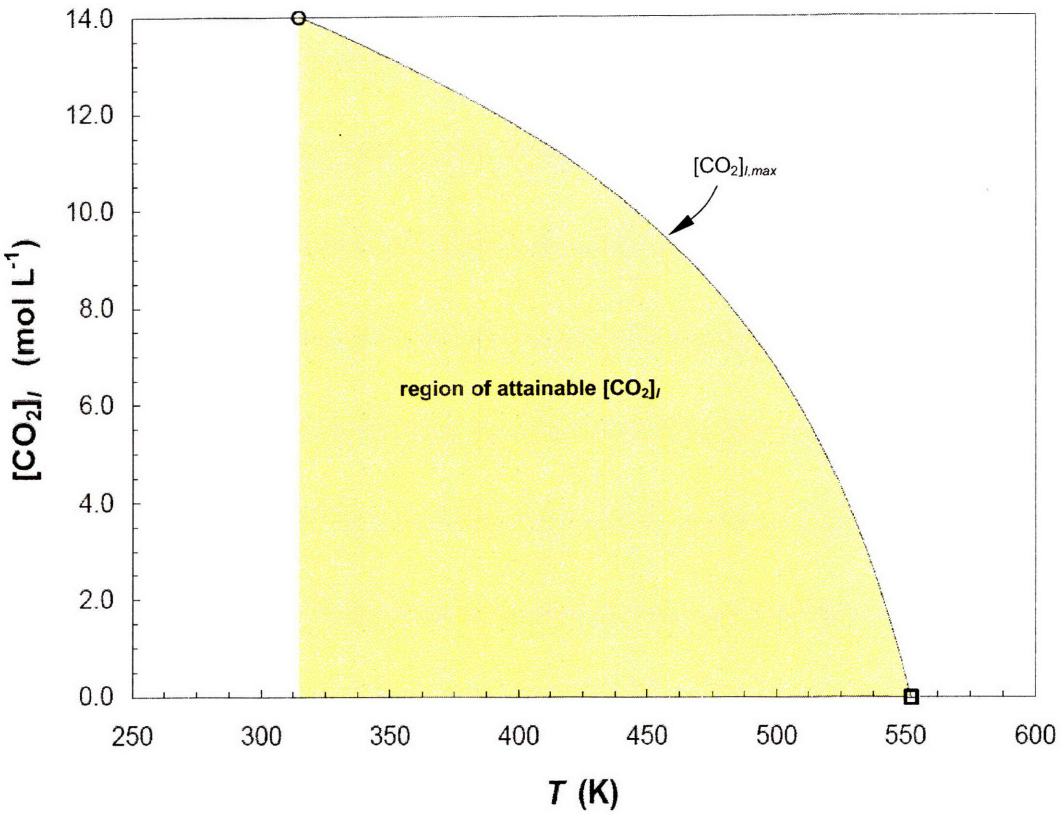

Figure 6-12. Maximum-possible liquid-phase carbon dioxide concentrations ($P \approx P_{c,mix}$) for the carbon dioxide/dimethyl carbonate system plotted as a function of temperature: T_c of pure CO_2 (○); T_c of pure DMC (□).

An interesting and often overlooked property of many CO_2-expanded solvent systems is that the concentration of CO_2 in the expanded-liquid phase tends to be larger than the concentration of pure CO_2 ($[CO_2]_{pure}$) when compared at the same T and P. Pure CO_2 concentration data were measured at 339.65 K (66.5 °C) for several pressures and compared with $[CO_2]_l$ data obtained for the CO_2/DMC system. As seen from **Figure 6-13** and **Figure 6-28** of **Section 6.11.2**, $[CO_2]_l$ was larger than $[CO_2]_{pure}$ for all experimental conditions. The ratio of $[CO_2]_l$ to $[CO_2]_{pure}$ was largest at low T and decreased with increasing temperature. Larger-than-neat CO_2 concentrations make CO_2-expanded liquids desirable mediums for reactions with CO_2-rate dependence (e.g., reactions in which CO_2 is a reactant or catalyst).

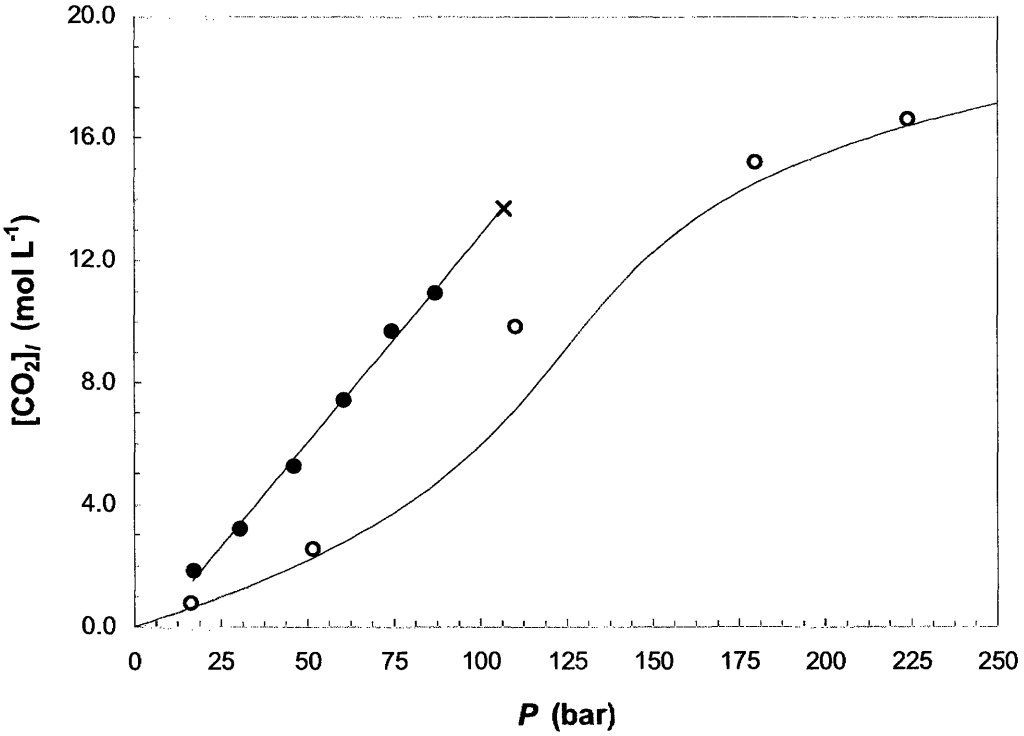

Figure 6-13. Liquid-phase carbon dioxide concentrations for the carbon dioxide/dimethyl carbonate system and pure carbon dioxide concentrations plotted as a function of pressure at 339.65 K (66.5 °C); experimental liquid-phase carbon dioxide concentration data (•); equation **(6-38)** (—); extrapolation by equation **(6-38)** to $[CO_2]_{l,max}$ (- - -); experimental mixture critical pressure (×); pure carbon dioxide concentration data (○); NIST correlation (– - –).

Liquid-phase DMC concentrations for the carbon dioxide/dimethyl carbonate system were also determined from equation **(6-28)** and are plotted as a function of pressure and temperature in **Figure 6-14**. At fixed temperature, $[DMC]_l$ decreased linearly with increasing P and was well-correlated by equation (**6-38**). Regressed parameters are provided in **Table 6-8** of **Section 6.11.2**.

Extrapolation of equation **(6-28)** up to the $P_{c,mix}$ for each isotherm revealed that the $[DMC]_l$ at $x_{CO2,max}$ increased with increasing T. Similar to the $[CO_2]_l$ data set, RK-Aspen EOS-calculated $[DMC]_l$ values deviated from linearity at P within ca. 15% of the $P_{c,mix}$. Extrapolation of experimental data to the $P \rightarrow 1.01$ bar region (pure DMC, $x_{CO2} = 0$) at each isotherm

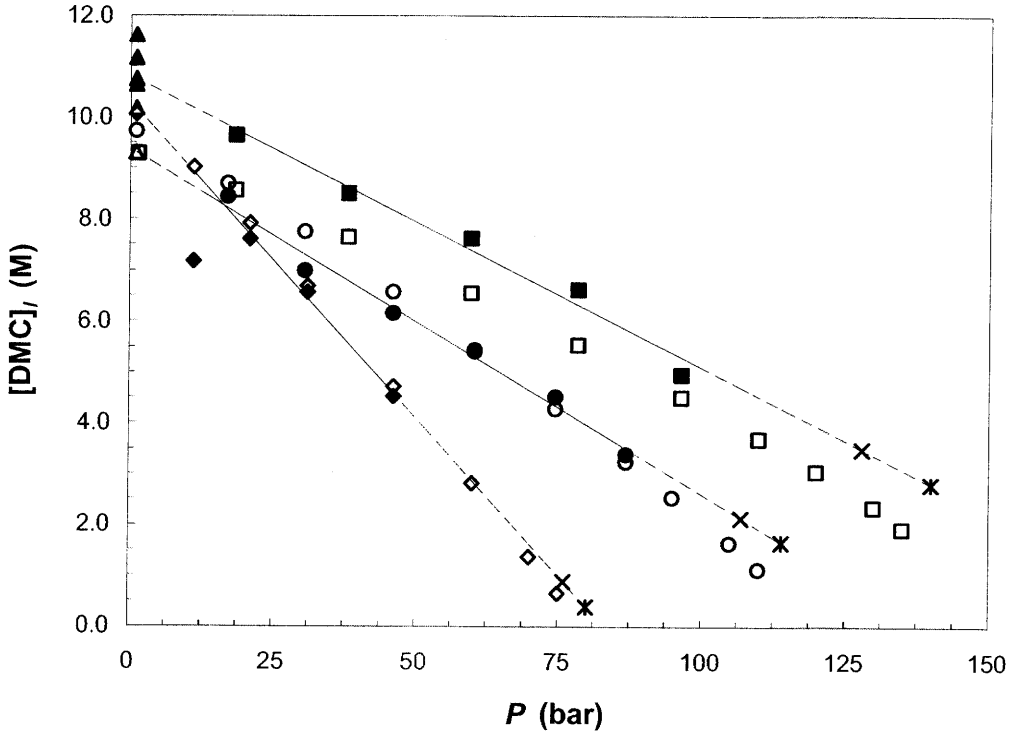

Figure 6-14. Liquid-phase dimethyl carbonate concentrations plotted as a function of pressure and temperature for the carbon dioxide/dimethyl carbonate system: (experimental, RK-Aspen EOS-calculated) at 310.15 K (37 °C) (♦, ◊); 339.65 K (66.5 °C) (•, ○); 373.15 K (100 °C) (■, □); RK-Aspen EOS (– - –); equation **(6-38)** (—); extrapolation by equation **(6-38)** to $[DMC]_{l,min}$ (- - -); experimental mixture critical pressure (×); RK-Aspen EOS-calculated mixture critical pressure (∗); extrapolated value of $[DMC]_l$ by equation **(6-38)** as $P \rightarrow 1.01$ bar for each isotherm (Δ); pure DMC density data by Steele et al. (1997) for each isotherm (▲).

revealed pure-component densities that deviated from data reported in the literature (Steele et al., 1997) by an AAD of 7%.

When plotted as a function x_{CO2}, experimental $[DMC]_l$ data sets for each isotherm also collapsed onto a single trend (see **Figure 6-29** of **Section 6.11.2**) that was correlated well by equation **(6-39)**. Extrapolation to $x_{CO2} = 1$ revealed that DMC concentration of ca. 2 mol·L^{-1}. $[DMC]_l$ at $x_{CO2,\,max}$ was also plotted as a function of temperature and is shown in **Figure 6-30** of **Section 6.11.2**. The trend was regressed to the form of **(6-22)**, with parameters listed in **Table 6-9** of **Section 6.11.2**.

6.6. Liquid-Phase Volume Expansion Correlations

6.6.1. Experimental Approach and Equipment Validation

Experimental volume expansion data were collected using the sight gauge apparatus and operating procedures described in **Section 3.2.5.** The apparatus calibrated by dispensing known amounts of water (typically 0.5-mL increments via a 50-mL stopcocked buret (VWR, *17527-106*) and recording the corresponding scale reading. Given the gauge's irregular internal geometry due to the various port and fittings along the chamber length, the resulting calibration curve consisted of a series of linear segments (as opposed to a single linear trend). As shown by **Figure 6-15**, data for each portion were regressed so that a volume could be determined as a function of scale reading.

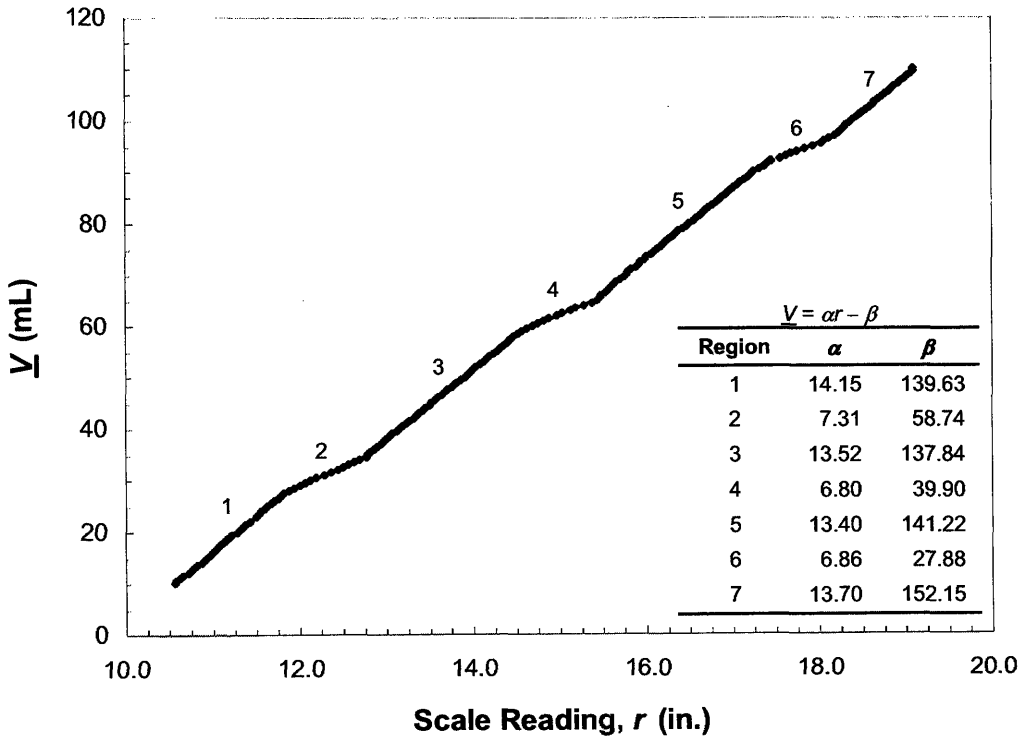

Figure 6-15. Calibration curve for the sight gauge apparatus: experimental data (♦); linear fits for each section (—).

With volume known as a function of scale reading, the volume expansion ($\Delta \underline{V} / \underline{V}^0$) of the liquid phase was defined as:

$$\frac{\Delta \underline{V}}{\underline{V}^0} = \left[\frac{\underline{V}(T,P) - \underline{V}^0(T, P_{vp,\mathrm{DMC}})}{\underline{V}^0(T, P_{vp,\mathrm{DMC}})} \right] \times 100 \qquad \textbf{(6-40)}$$

where $\underline{V}(T, P)$ is the liquid-phase mixture volume at a given T and P and $\underline{V}^0(T, P_{vp,\mathrm{DMC}})$ is the volume of pure DMC at the given T and corresponding vapor pressure prior to the addition of CO_2.

Before investigating the volume expansion of the CO_2/DMC system, the sight gauge apparatus and experimental techniques were validated by benchmarking volume expansion literature data for the well-studied CO_2/toluene system against this work. As seen from **Figure 6-16**, data obtained for the CO_2/toluene system from our apparatus matched very closely to that measured by Lazzaroni and coworkers (2005).

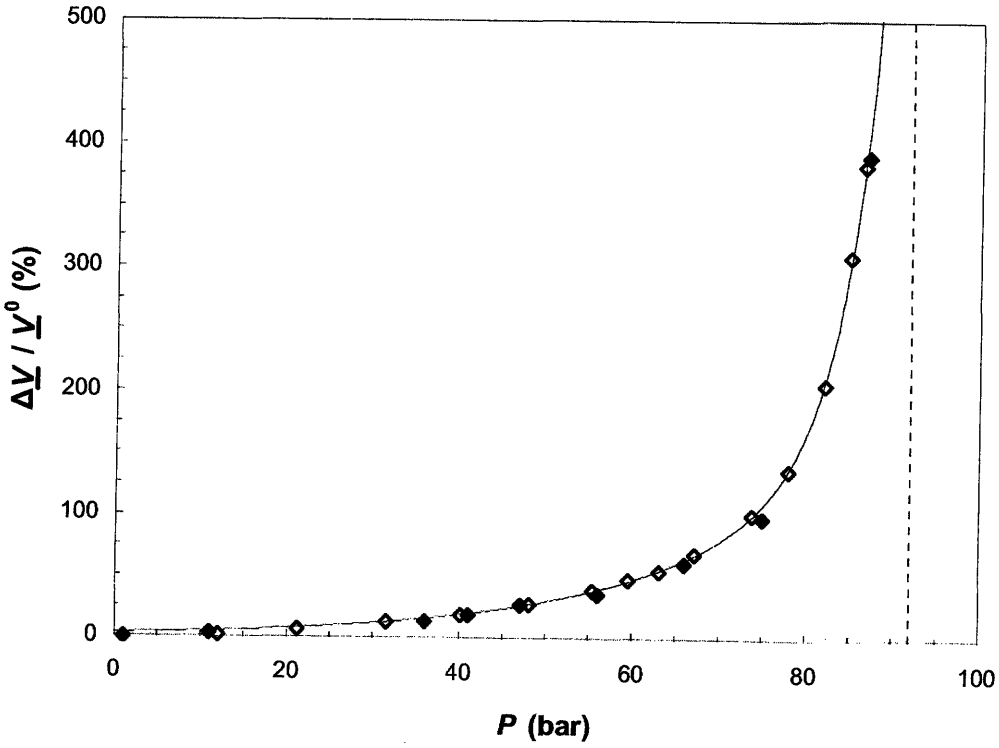

Figure 6-16. Liquid-phase volume expansion data for the carbon dioxide/toluene system at 323 K (50 °C): this work (♦); Lazzaroni et al. (2005) (◊); mixture critical pressure by Ziegler et al. (1995) (- - -). The solid line is drawn to serve as a guide for the eye and no physical basis is intended.

6.6.2. Results and Discussion

Liquid-phase volume expansion data for the carbon dioxide/dimethyl carbonate system plotted as a function of pressure and temperature is shown in **Figure 6-17**. A comparison between experimental and RK-Aspen EOS-calculated liquid-phase densities and component concentrations is given in **Table 6-10** of **Section 6.11.3**. Like the $[CO_2]_l$ data sets, isotherms were selected to match temperatures of VLE data sets currently available in the literature (Camey et al. 2003; Im et al., 2004).

As seen by **Figure 6-17**, volume expansion values of several hundred percent were obtained. At fixed temperature, liquid-phase volume expansion increased exponentially with increasing pressure and was correlated well by the following expression:

$$\frac{\Delta \underline{V}}{\underline{V}^0} = \alpha \exp(\beta P) + \chi \exp(\delta P) \qquad \textbf{(6-41)}$$

Regressed parameters for equation **(6-41)** are listed in **Table 6-11** of **Section 6.11.3**. At higher temperatures, larger pressures were required to obtain a similar $\Delta \underline{V} / \underline{V}^0$. For example, in order to arrive at a $\Delta \underline{V} / \underline{V}^0$ of 400% at 310 K (37 °C), a pressure of ca. 65 bar would be required, whereas a pressure of ca. 136 bar would be required at 373 K (100 °C).

Compared to experimental data, RK-Aspen EOS-calculated $\Delta \underline{V} / \underline{V}^0$ values differed by an AAD of 31.8%, with deviations becoming more pronounced at higher T. These large deviations were likely due to the inability of the RK-Aspen EOS to accurately predict the liquid-phase volumes. As shown by **Figure 6-31** of **Section 6.11.3**, the RK-Aspen EOS under-predicts the pure-component saturated liquid density of dimethyl carbonate (use to calculate $\underline{V}(T, P_{vp,\,DMC})$ in equation **[6-40]**) by 12 – 30%, with the largest deviations of this range occurring at higher T. Also, given the 8.7% AAD for liquid-phase CO_2/DMC mixture densities (see **Table 6-7** of **Section 6.11.2**), large deviations in EOS-calculated $\Delta \underline{V} / \underline{V}^0$ values from experimental data were not surprising.

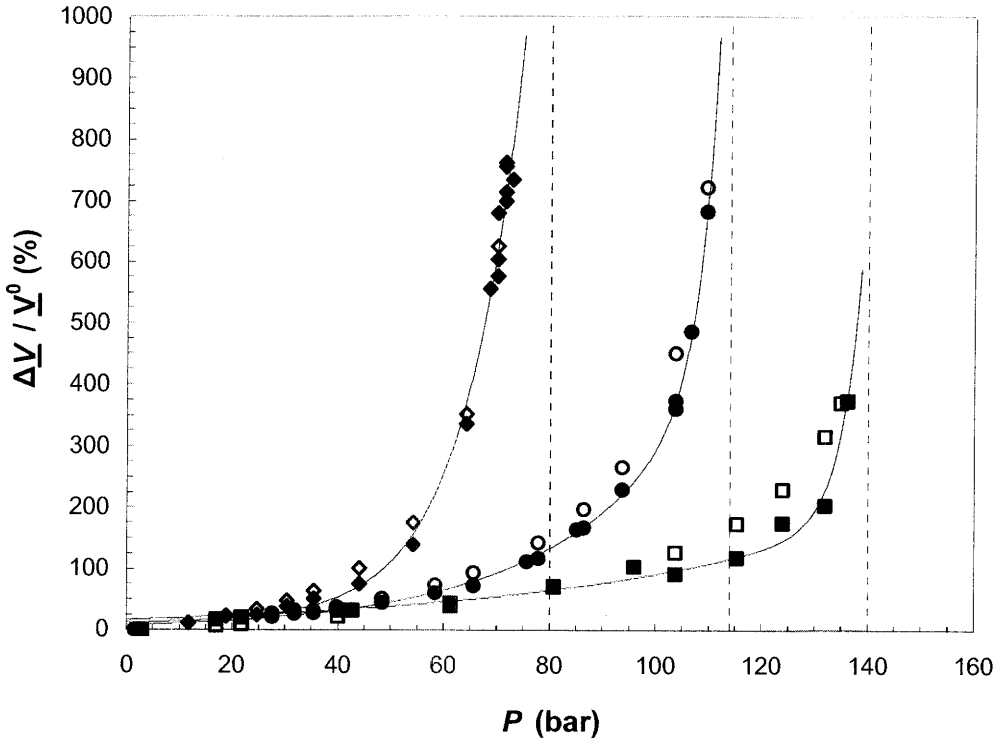

Figure 6-17. Liquid-phase volume expansion plotted as a function of pressure for the carbon dioxide/dimethyl carbonate system at several temperatures: (experimental, RK-Aspen EOS-calculated) at 310.25 K (37.1 °C) (♦, ◊); 340.15 K (67.1 °C) (•,○); 373.55 K (100.4 °C) (■, □); equation **(6-41)** (—); RK-Aspen EOS-calculated mixture critical pressures for each isotherm (- - -).

When plotted as a function x_{CO2}, experimental $\Delta\underline{V} / \underline{V}^0$ data sets collapsed onto a single trend (see **Figure 6-18**) that was correlated well by:

$$\frac{\Delta\underline{V}}{\underline{V}^0} = \alpha \exp(\beta x_i) + \chi \exp(\delta x_i) \qquad \textbf{(6-42)}$$

Regressed parameters for equation **(6-42)** are also provided in **Table 6-11** of **Section 6.11.3**. Using equation **(6-42)**, we can estimate $\Delta\underline{V} / \underline{V}^0$ at any *P-T* condition. For example, at a given *T*, we would first generate a *P*-x_i diagram using the RK-Aspen EOS (see **Figure 6-4**). With x_{CO2} known as a function of *P* up to the $P_{c,mix}$ (see **Figure 6-6**), we could easily determine $\Delta\underline{V} / \underline{V}^0$ by employing equation **(6-42)**. The maximum-possible liquid-phase volume expansion ($\Delta\underline{V} / \underline{V}^0_{max}$) decreased with increasing temperature (see **Figure 6-32** of **Section 6.11.3)**.

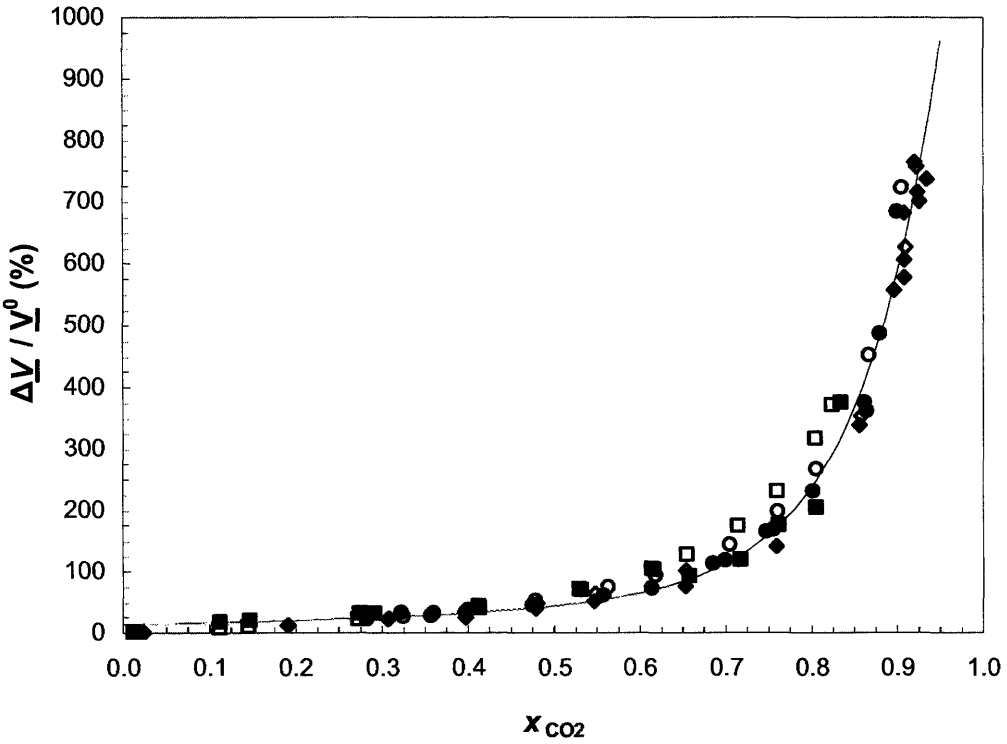

Figure 6-18. Liquid-phase volume expansion plotted as a function of liquid-phase carbon dioxide mole fraction for the carbon dioxide/dimethyl carbonate system at several temperatures: (experimental, RK-Aspen EOS-calculated) at 310.25 K (37.1 °C) (♦, ◊); 340.15 K (67.1 °C) (•,○); 373.55 K (100.4 °C) (■, □); equation **(6-42)** (—).

6.7. Investigation of Additional Carbon Dioxide/Dialkyl Carbonate Systems

In **Section 5.4**, we found that replacing dimethyl carbonate with dibenzyl carbonate (DBC) at similar operating conditions led to increased yields for the amine carbamation reaction. In order to determine if this yield enhancement was ascribed to differences in phase equilibria for the two binary systems (e.g., increased $[CO_2]_l$), we turned to a brief VLE study of the CO_2/DBC mixture.

In order to compare $[CO_2]_l$ values for the CO_2/DMC system against other dialkyl carbonate systems, we first decided to model the P-T-x_i behavior of these systems using the RK-Aspen EOS. As shown by the rearrangement of equation **(6-28)**, $[CO_2]_l$ is proportional to liquid-phase CO_2 mole fraction and density and the inverse of mixture average molecular weight:

$$[CO_2]_l = \frac{x_{CO_2}\rho_l}{\bar{M}_l} \qquad \textbf{(6-28)'}$$

At an identical x_{CO2}, and assuming that liquid-phase densities at the given x_{CO2} are comparable for the CO_2/dialkyl carbonate systems, we would expect smaller $[CO_2]_l$ values for the higher-molecular weight dialkyl carbonates (i.e., DBC [242.27 g·mol^{-1}] < DEC [118.13 g·mol^{-1}] < DMC [90.08 g·mol^{-1}]). To compensate for this disparity, higher operating pressures would be needed for CO_2/higher-molecular weight dialkyl carbonate systems to achieve similar $[CO_2]_l$ values for the CO_2/DMC system.

Due to the lack of data in the literature, ChemDraw® Ultra 7.0 was used to estimate the pure-component critical properties of DBC via the group contribution method developed by Joback and coworkers (Joback, 1984; Joback et al., 1987):

$$T_b = 198 + \sum_k N_k (tbk) \qquad \textbf{(6-43)}$$

$$T_c = T_b\left[0.584 + 0.965\sum_k N_k (tck) - \left\{\sum_k N_k (tck)\right\}^2\right]^{-1} \qquad \textbf{(6-44)}$$

$$P_c = \left[0.113 + 0.0032N_{atoms} - \sum_k N_k (pck)\right]^{-2} \qquad \textbf{(6-45)}$$

$$V_c = 17.5 + \sum_k N_k (vck) \tag{6-46}$$

where T_b is the normal boiling point, V_c is the critical molar volume, N_{atoms} is the number of atoms that comprise the molecule, *tbk*, *tck*, *pck*, and *vck* are group contribution terms specific to a functional group (e.g., $-CH_2-$, $\equiv CH$, $-NH-$, etc.), and N_k is the number of times these group occur within the molecule.

ChemDraw® does not provide an estimate of the acentric factor; although group contribution methods also exist for the estimation of ω, a quick estimate was obtained from the principal of corresponding-states:

$$\omega = \frac{0.291 - Z_c}{0.080} \tag{6-47}$$

where Z_c is the critical compressibility factor defined as:

$$Z_c = \frac{P_c V_c}{R T_c} \tag{6-48}$$

More accurate estimations of ω are also available from three-parameter forms of the corresponding-states expression given in equation **(6-47)**, but were not used due to their increased complexity. Pure component properties for DBC are listed in **Table 6-12** of **Section 6.11.4.** Due to the lack of pure-component DBC vapor pressure data and VLE data for the CO_2/DBC system in the literature, the polar term and binary interaction terms for the RK-Aspen EOS were set to zero.

VLE predictions for the CO_2/DBC system at 340.3 K (67.1 °C) along with experimental data and predictions for the CO_2/DMC and CO_2/diethyl carbonate (DEC) systems are presented in **Figure 6-19**. Similar to the CO_2/DMC procedures discussed in **Section 6.2**, the RK-Aspen EOS polar term for DEC was regressed from pure-component DEC vapor pressure data reported by Rodriguez and coworkers (2002) and binary interactions terms were regressed from CO_2/DEC system VLE data provided by Im and coworkers (2004). Regressed parameters can be found in **Table 6-13** of **Section 6.11.4**.

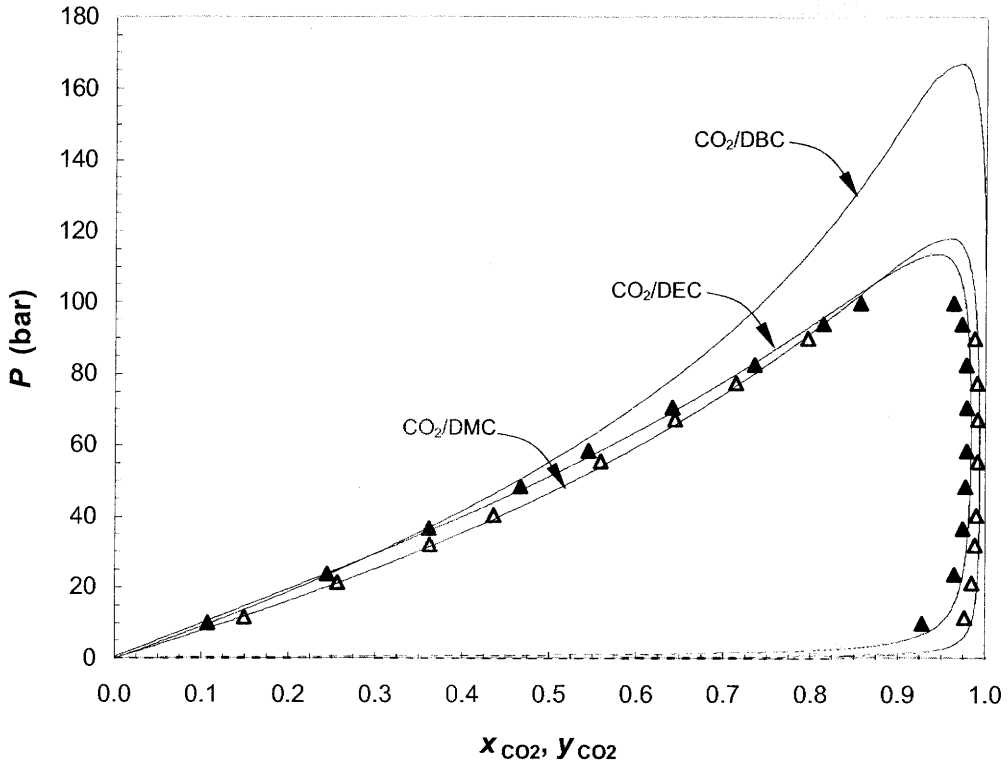

Figure 6-19. Vapor-liquid equilibria data and modeling for the carbon dioxide/dimethyl, /diethyl, and /dibenzyl carbonate systems at 340.3 K (67.1 °C): RK-Aspen EOS for P-x_i (—) and P-y_i (- - -); experimental (P-x_i, P-y_i) data by Im et al. (2004) for the CO_2/DMC system (▲) and CO_2/DEC system (Δ).

A comparison of experimental data and RK-Aspen EOS VLE predictions for the CO_2/DMC and CO_2/DEC systems over a wide range of conditions revealed that the CO_2/DEC system has larger x_{CO2} values at an identical P and T (see **Figure 6-33** of **Section 6.11.4**), and larger $P_{c,mix}$ and $x_{CO2,max}$ values at identical T (see **Figure 6-34** of **Section 6.11.4**). Deviations in x_{CO2} for the two systems became more pronounced at higher T due to the more-rapidly increasing slope of the P-x_i diagram for CO_2/DMC (especially in the vicinity of $P_{c,mix}$). Deviations at higher T were also attributed to the more pronounced upwards shifting of the phase envelope for the CO_2/DMC system at $x_{CO2} = 0$ because of DMC's higher vapor pressure (e.g., DMC has a P_{vp} 2.8 times larger than that of DEC over the range 350 – 400 K [ca. 77 – 127 °C]). It is not until pressure approaches $P_{c,mix}$ for the CO_2/DMC system where x_{CO2} for the CO_2/DMC system becomes larger.

When compared to the CO_2/DMC system, RK-Aspen EOS predictions for the CO_2/DBC system revealed larger x_{CO2} values at an identical P and T for the low-P end of each isotherm and significantly smaller x_{CO2} values as P approached $P_{c,mix}$ (see **Figure 6-33** of **Section 6.11.4**). Caution was taken, however, when interpreting predictions for the CO_2/DBC system, as the lack of experimental pure-component DBC critical constants and absence of regressed EOS terms are likely to decrease the accuracy of RK-Aspen EOS predictions. As a control, critical constants for pure DMC were estimated in an identical fashion as that of DBC and all regressed EOS terms for the CO_2/DMC system were set to zero. Resulting VLE predictions at 340.3 K (67.1 °C) deviated from the predictions made by the RK-Apsen EOS by an AAD of 7.4%. Combined with a 2.4% AAD of the RK-Aspen EOS prediction from experimental data, predictions for the CO_2/DBC system were likely to be off by at least 10%. Experimental $P_{c,mix}$ values (see **Table 6-3**), for example, were found to deviate from RK-Aspen EOS predictions by an AAD of 39.2%.

Assuming that both systems have comparable liquid-phase densities, larger x_{CO2} values for the CO_2/DMC system and DMC's smaller molecular mass suggest that it is likely for the CO_2/DMC systems to larger $[CO_2]_l$ values. To test this hypothesis, liquid-phase CO_2 concentrations for the CO_2/DBC system were measured at 339.65 K (66.5 °C) and are plotted as a function of pressure in **Figure 6-20**. As we expected, $[CO_2]_l$ data for the CO_2/DBC system were 2 – 4 times smaller when compared to the CO_2/DMC system at the same pressure, with deviations becoming more pronounced at higher P. As a result, higher pressures are needed to arrive at an identical CO_2/DMC system $[CO_2]_l$. Extrapolation of CO_2/DBC system data via equation **(6-38)** up to the experimentally-determined $P_{c,mix}$ revealed that $[CO_2]_{l,max}$ was

Table 6-3. Experimental and RK-Aspen EOS-calculated mixture critical pressures for the carbon dioxide/dibenzyl carbonate system.

T	$P_{c,mix,\ exp}$	$P_{c,mix,\ calc}$	AAD
K (°C)	bar		%
310.25 (37.1)	265	90	66.0
340.25 (67.1)	301	167	44.5
373.15 (100)	341	242	28.9
403.15 (130)	363	300	17.4
		average	***39.2***

ca. 9.3 M (compared to 13.7 M for the CO_2/DMC system). $[CO_2]_l$ data for the CO_2/DBC system were also well correlated by the linear model given in equation **(6-38)**. Regressed parameters for this system are given in **Table 6-14** of **Section 6.11.4**.

A comparison of experimental $[CO_2]_l$ data with RK-Aspen EOS calculations revealed an AAD 82.8% (see **Table 6-15** of **Section 6.11.4**). Despite these large errors, the RK-Aspen EOS accurately predicted the experimentally-observed trend of decreased $[CO_2]_l$ for larger-molecular weight dialkyl carbonate systems. RK-Aspen EOS-calculated $[CO_2]_l$ for the CO_2/DEC system are also shown in **Figure 6-20** and were approximately 9.6% smaller than experimental data for the CO_2/DMC system at identical *P* and *T* conditions. Considering that the RK-Aspen EOS-calculated values for the CO_2/DMC system at these conditions differ from experimental data by approximately 5.2%, we can conclude that $[CO_2]_l$ values for the CO_2/DEC system are relatively

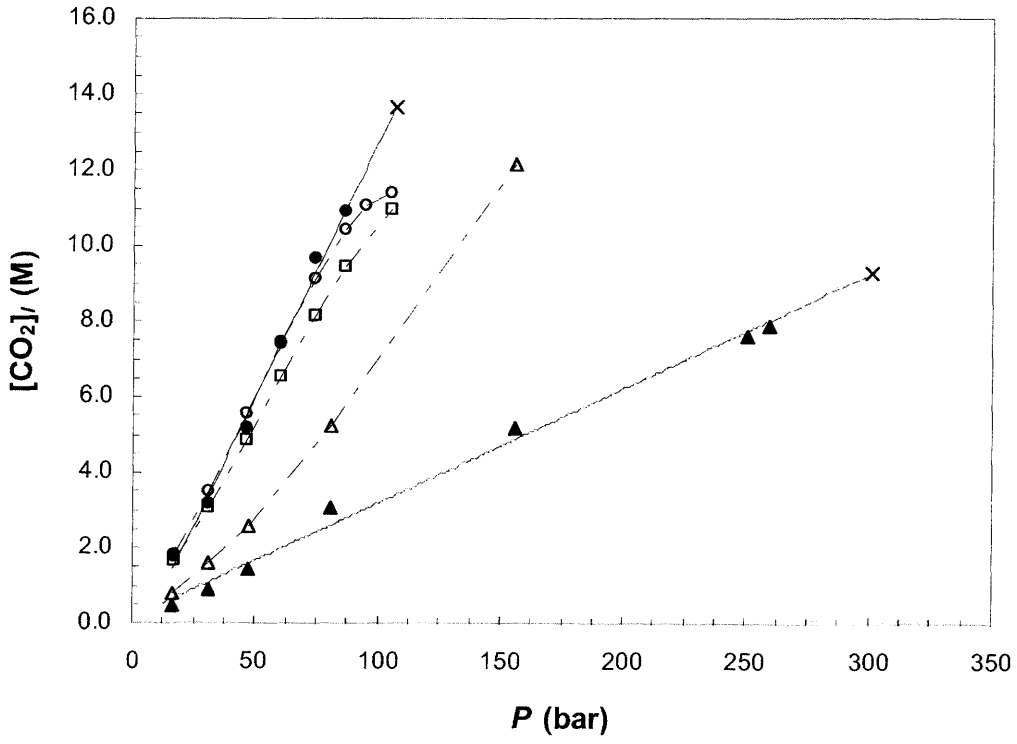

Figure 6-20. Liquid-phase carbon dioxide concentrations plotted as a function of pressure for the carbon dioxide/dimethyl, /diethyl, and /dibenzyl carbonate systems at 339.65 K (66.5 °C): experimental data for the CO_2/DMC system (•) and CO_2/DBC system (▲); RK-Aspen EOS predictions for the CO_2/DMC system (○), CO_2/DEC system (□), and CO_2/DBC system (Δ); extrapolation by equation **(6-38)** (- - -) to $[CO_2]_{l,max}$; experimental mixture critical pressure (×).

small. RK-Aspen EOS-calculated pure-component mixture densities for the dialkyl carbonates at 339.65 K (66.5 °C) were comparable (e.g., DBC [920 $kg \cdot m^{-3}$], DEC [806 $kg \cdot m^{-3}$], and DMC [877 $kg \cdot m^{-3}$]), indicating that deviations in predicted $[CO_2]_l$ values for the systems — and in general — were attributed primarily to differences in x_{CO2} and molecular size.

6.8. Effect of Additives on Binary CO_2/DMC Phase Equilibria

In this section, we discuss the effects of amine carbamation reaction system components (i.e., methanol and a model amine) on phase equilibria properties of the CO_2/DMC binary system. The procedure for predicting multi-component VLE is nearly identical to the methodology for binary systems discussed in **Section 6.2**, but with the exception that the initial feed concentrations of all components must be specified. As we have shown in previous sections of this chapter, the accuracy of EOS-based VLE predictions relies heavily on the availability of binary interaction parameters for all component pairs that comprise a multi-component mixture.

6.8.1. Methanol Composition Effects

Using the procedures outlined in **Section 6.3**, RK-Aspen EOS binary interaction parameters for the CO_2/MeOH and MeOH/DMC systems were regressed from experimental VLE data reported by Bezanehtak and coworkers (2002) and Yunhai (2005), respectfully. The RK-Aspen EOS polar term used for MeOH was obtained from Mathias (1983). A list of regressed parameters is provided in **Table 6-16** of **Section 6.11.4**. The RK-Aspen EOS matches closely with experimental VLE data, which was very promising when considering modeling complexities often associated with highly non-linear dependence of liquid-phase mole fractions in the vicinity of the mixture critical point for the CO_2/MeOH system and (see **Figure 6-21**) and non-ideal azeotropic behavior for the MeOH/DMC system (see **Figure 6-35** of **Section 6.11.4**).

Compared to the CO_2/DMC system for the conditions studied, the CO_2/MeOH exhibits mixture critical points that were only slightly larger, with deviations becoming more pronounced at higher temperatures. P-x_i isotherms for the CO_2/MeOH system deviated strongly from linearity for pressures in the vicinity of the $P_{c,mix}$. Most noteworthy were the significantly-smaller

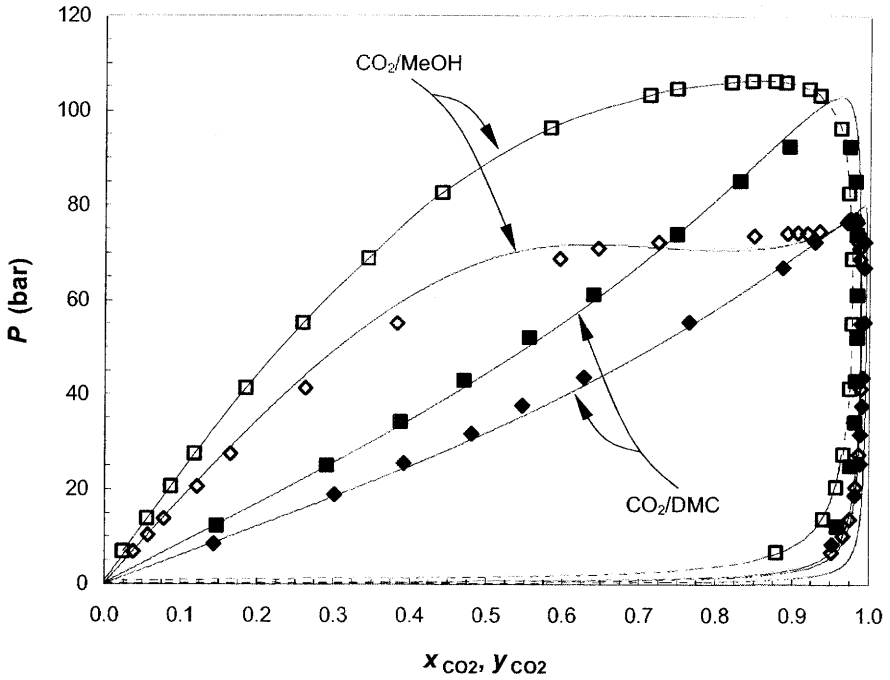

Figure 6-21. Vapor-liquid equilibria data and modeling for the carbon dioxide/methanol and carbon dioxide/dimethyl carbonate systems: RK-Aspen EOS for P-x_i (—) and P-y_i (- - -); experimental data for the CO_2/MeOH system by Hong et al. (1988) at 310 K (36.85 °C) (◊) and 330 K (56.85 °C) (□); experimental data for the CO_2/DMC system by Im et al. (2004) at 310.3 K (37.1 °C) (♦) and 330.3 K (57.2 °C) (■).

values of x_{CO2} achieved for the CO_2/MeOH system when operating at identical P and T conditions for the CO_2/DMC system. As discussed in detail in **Section 6.7**, this behavior is often accompanied by a decrease in $[CO_2]_l$ when compared to systems of similar liquid-phase mixture densities and smaller average molecular weights. A comparison of experimental data for the CO_2/DMC and CO_2/MeOH systems at nearly identical operating conditions (see **Figure 6-22**) reveals that higher pressures are needed in the CO_2/MeOH system to achieve $[CO_2]_l$ values equal to that of the CO_2/DMC system. $[CO_2]_l$ for the CO_2/MeOH system approach those of the CO_2/DMC system as pressure approaches the $P_{c,mix}$. Since liquid-phase mixture densities for both systems were nearly identical at these conditions and CO_2/MeOH mixture average molecular weights were actually smaller than that of the CO_2/DMC system, it appears that the difference in x_{CO2} at a given pressure is substantial enough to result in lower $[CO_2]_l$ values.

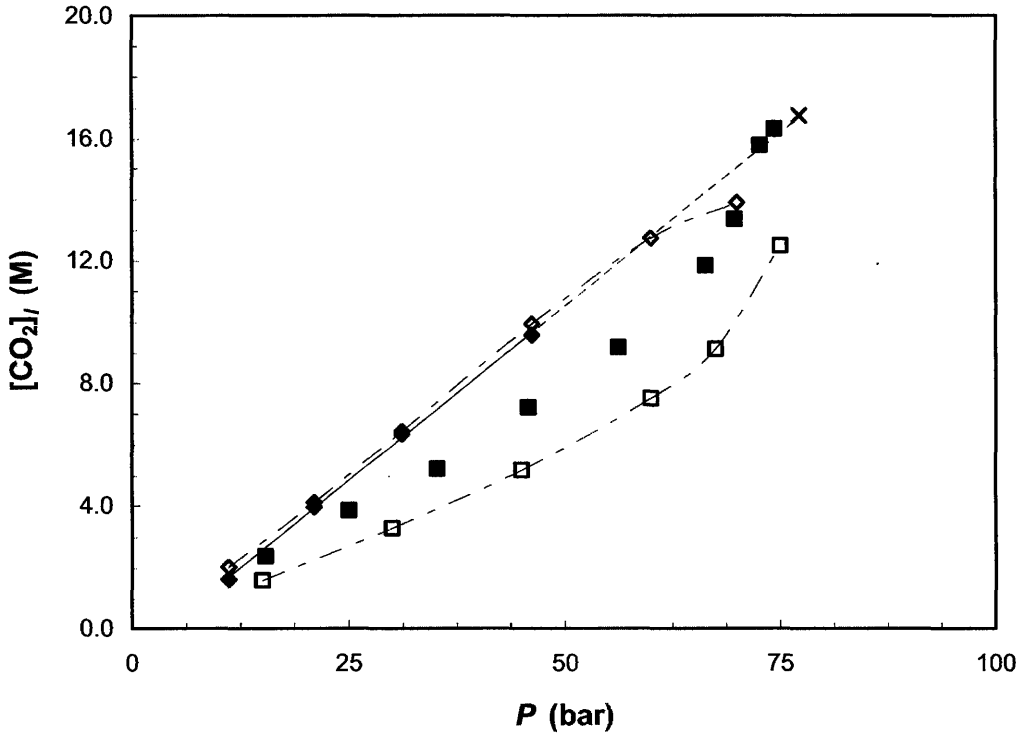

Figure 6-22. Liquid-phase carbon dioxide concentrations plotted as a function of pressure and temperature for the carbon dioxide/methanol and carbon dioxide/dimethyl carbonate systems: (experimental, RK-Aspen EOS-calculated) data for the CO_2/MeOH system calculated from Bezanehtak et al. (2002) at 308.15 K (35 °C) (■, □); for the CO_2/DMC system by this work at 310.15 K (37 °C) (♦, ◊); RK-Aspen EOS (– - –); equation **(6-38)** (—); extrapolation by equation **(6-38)** to $[CO_2]_{l,max}$ for the CO_2/DMC system (- - -); experimental mixture critical pressure for the CO_2/DMC system (×);

RK-Aspen EOS-calculated values of $[CO_2]_l$ for the CO_2/MeOH system deviated strongly from experimental values due to the failure of the EOS to predict accurate mixture molar volumes for this system. Noteworthy is how $[CO_2]_l$ for the CO_2/MeOH system deviates significantly from linearity with respect to pressure in the vicinity of the $P_{c,mix}$. Correlating $[CO_2]_l$ with a linear extrapolation method used for DMC, for example, would result in an inaccurate prediction of $[CO_2]_{l,\,max}$ (see **Figure 6-23**). Given that the P-x_i isotherms for the CO_2/DMC system are more linear than those of the CO_2/MeOH, it is likely that smaller deviations in $[CO_2]_{l,\,max}$ would be incurred when using a linear extrapolation for the CO_2/DMC system.

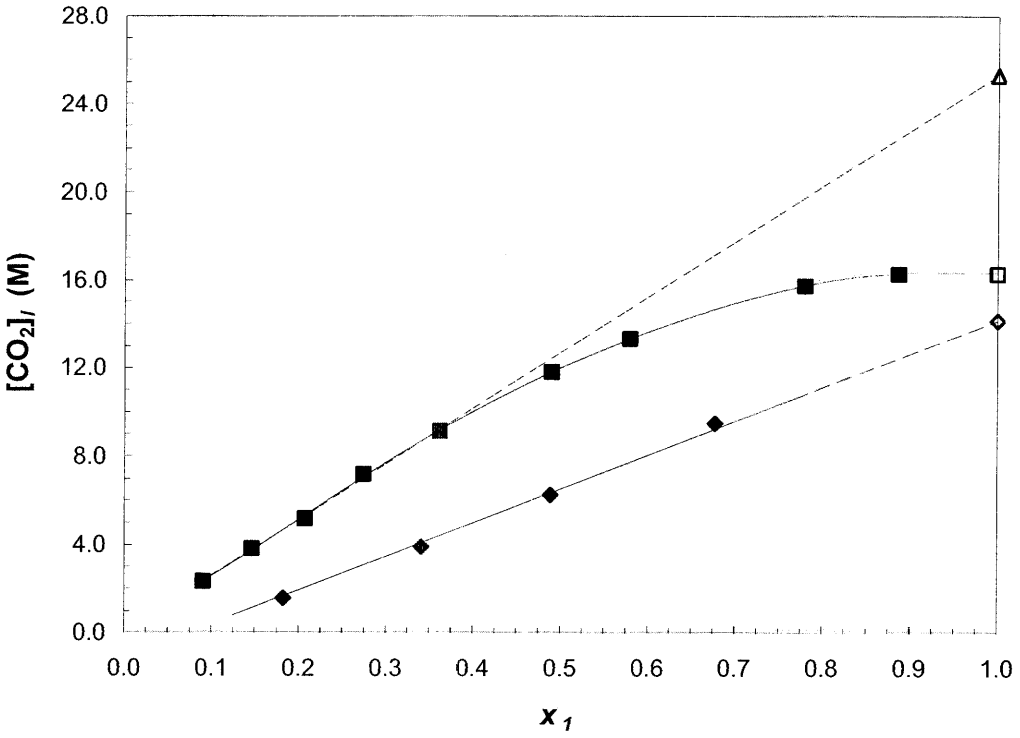

Figure 6-23. Liquid-phase carbon dioxide concentration plotted as a function of liquid-phase carbon dioxide mole fraction and temperature: experimental data for the CO_2/MeOH system calculated from Bezanehtak et al. (2002) at 308.15 K (35 °C) (■); experimental data for the CO_2/DMC system by this work at 310.15 K (37 °C) (♦); linear extrapolation (- - -) to $[CO_2]_l$ as $x_i \rightarrow 1$ for the CO_2/MeOH system (Δ) and CO_2/DMC system (◊); extrapolation (– - –) to $[CO_2]_l$ as $x_i \rightarrow 1$ for the CO_2/MeOH system (□).

Experimental volume expansion data for the CO_2/MeOH system were also compared to those obtained at similar conditions for the CO_2/DMC system. As shown by **Figure 6-24**, $\Delta\underline{V} / \underline{V}^0$ for the CO_2/MeOH were significantly smaller when compared at the same pressure. Similar to x_{CO2} and $[CO_2]_l$, $\Delta\underline{V} / \underline{V}^0$ for the CO_2/MeOH and CO_2/DMC systems were comparable only in the vicinity of the $P_{c,mix}$ for the CO_2/DMC mixture. RK-Aspen EOS-calculated $\Delta\underline{V} / \underline{V}^0$ values deviated strongly from experimental values also due to the failure of the EOS to predict accurate mixture molar volumes for this system.

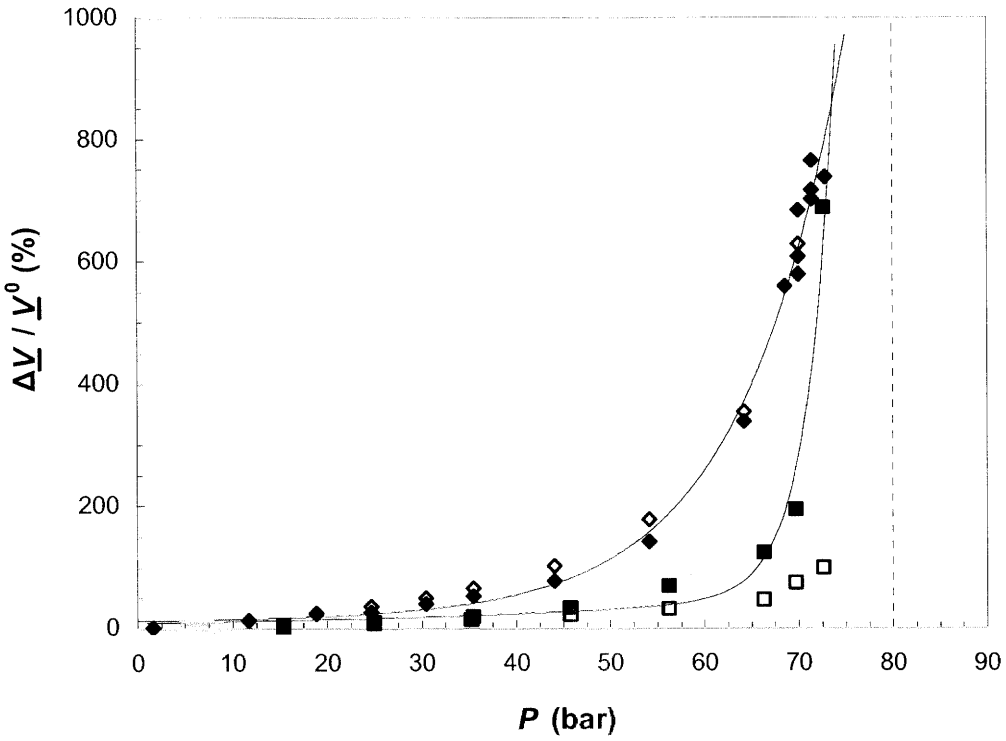

Figure 6-24. Liquid-phase volume expansion plotted as a function of pressure for the carbon dioxide/methanol and carbon dioxide/dimethyl carbonate systems: (experimental, RK-Aspen EOS-calculated) data for the CO_2/MeOH system by Bezanehtak et al. (2002) at 308.15 K (35 °C) (■, □); for the CO_2/DMC system by this work at 310.15 K (37 °C) (♦, ◊); equation **(6-41)** (—); RK-Aspen EOS-calculated mixture critical pressure for the CO_2/DMC system (- - -).

VLE predictions for the binary CO_2/MeOH system offer helpful insights towards the effect of MeOH when added to DMC in the presence of CO_2. Calculations and experimental data suggest that a liquid-phase richer in MeOH, for example, would experience lower $[CO_2]_l$ and $\Delta \underline{V} / \underline{V}^0$ values when compared to the CO_2/DMC binary at similar operating conditions. To test this hypothesis, $[CO_2]_l$ data were measured for a CO_2/50:50 vol% DMC:MeOH mixture (feed $x_{MeOH} = 0.68$) at several pressures. As expected, the results indicated a decrease in $[CO_2]_l$ with increased MeOH content (see **Figure 6-25**). RK-Aspen EOS VLE calculations performed for the ternary CO_2/MeOH/DMC system for a wide range of methanol feed concentrations reveal similar behavior. In a similar EOS-based modeling study of the CO_2/MeOH/DMC system, Piñero and coworkers (2007) also found that an increase in methanol feed composition at constant *T* and *P* led to a decrease in the liquid-phase carbon dioxide mole fraction.

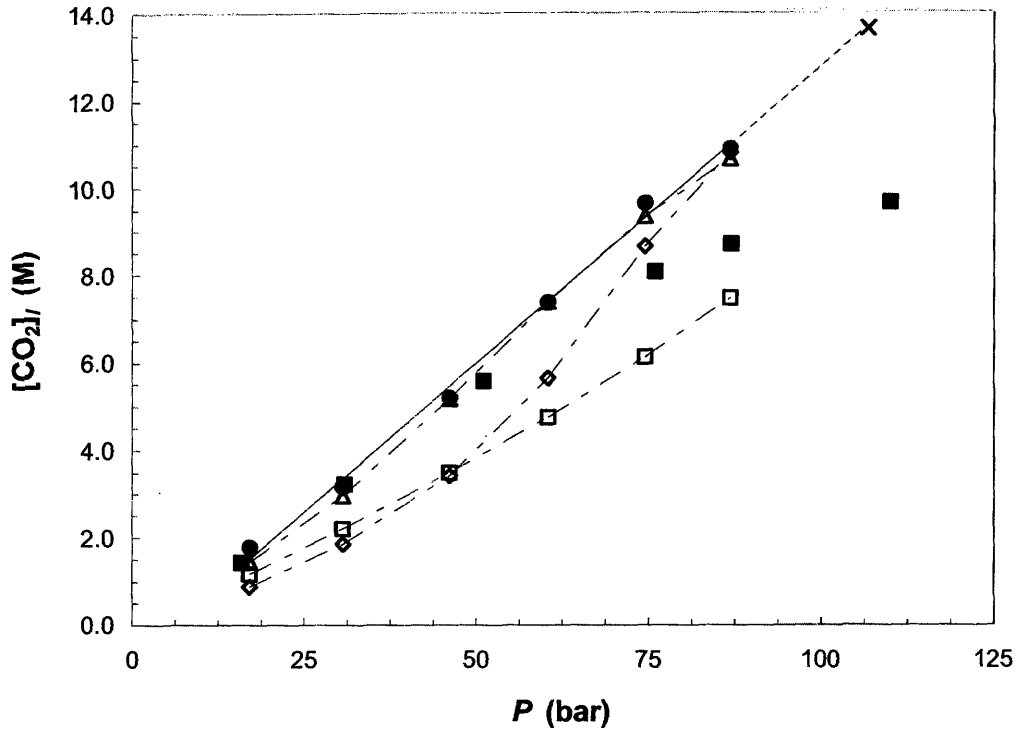

Figure 6-25. Liquid-phase carbon dioxide concentrations plotted as a function of pressure and temperature for the carbon dioxide/methanol, carbon dioxide/dimethyl carbonate, and carbon dioxide/methanol/dimethyl carbonate systems at 339.65 K (66.5 °C): experimental data for the CO_2/DMC system (feed $x_{MeOH} = 0$) (•) and CO_2/MeOH system (feed $x_{MeOH} = 0.68$); RK-Aspen EOS-calculated data for the CO_2/MeOH system for feed $x_{MeOH} = 0$ (□), $x_{MeOH} = 0.25$ (Δ), and $x_{MeOH} = 0.75$ (◊). RK-Aspen EOS (– - –); equation **(6-38)** (—); extrapolation by equation **(6-38)** to $[CO_2]_{l,max}$ (- - -) for the CO_2/DMC system; experimental mixture critical pressure (×) for the CO_2/DMC system;

6.8.2. Amine Composition Effects

The effects of amine concentration on the phase equilibria of the CO_2/DMC system are complicated by the tendency for nucleophilic amines to react with CO_2 to form carbamic acids and salts. VLE calculations for CO_2/amine systems are most representative of actual system behavior at elevated temperatures, as carbamic acid formation decreases at these conditions (see **Section 4.2**). Neat 3,4-dimethoxyphenethylamine (DMPA) — the amine selected for amine carbamation and Pictet-Spengler cyclizations in **Chapter 5** — for example, reacts instantaneously with carbon dioxide to form a solid alkyl ammonium carbamic salt (see **Section 7.3.3**) for 298 K (25 ° C) < T < 373 K (100 °C). Above 100 °C, the solid transforms into a liquid phase that is either the 'free' amine and/or mixture of free amine, carbamic acid, and/or the carbamic salt.

Using the calculation methods described in **Section 6.7**, the VLE of the CO_2/DMPA was modeled and is compared to the CO_2/MeOH and CO_2/DMC systems in **Figure 6-28**. Pure component properties for DMPA calculated by group contribution can be found in **Table 6-17** of **Section 6.11.4**. RK-Aspen EOS calculations indicate that the CO_2/amine has the largest $P_{c,mix}$ and x_{CO2} values that are intermediate the two binaries. Calculations also suggest that $[CO_2]_l$ values would be smallest for the CO_2/amine system which is not surprising given the large relatively molecular mass of the amine (181 g·mol^{-1}) in comparison to DMC (90 g·mol^{-1}) and MeOH (32 g·mol^{-1}) (see **Figure 6-27**). Similar to our analysis of the CO_2/MeOH system, it is likely that increased liquid-phase amine concentrations in the CO_2/DMC system would result in reduced $[CO_2]_l$ and $\Delta\underline{V} / \underline{V}^0$ values.

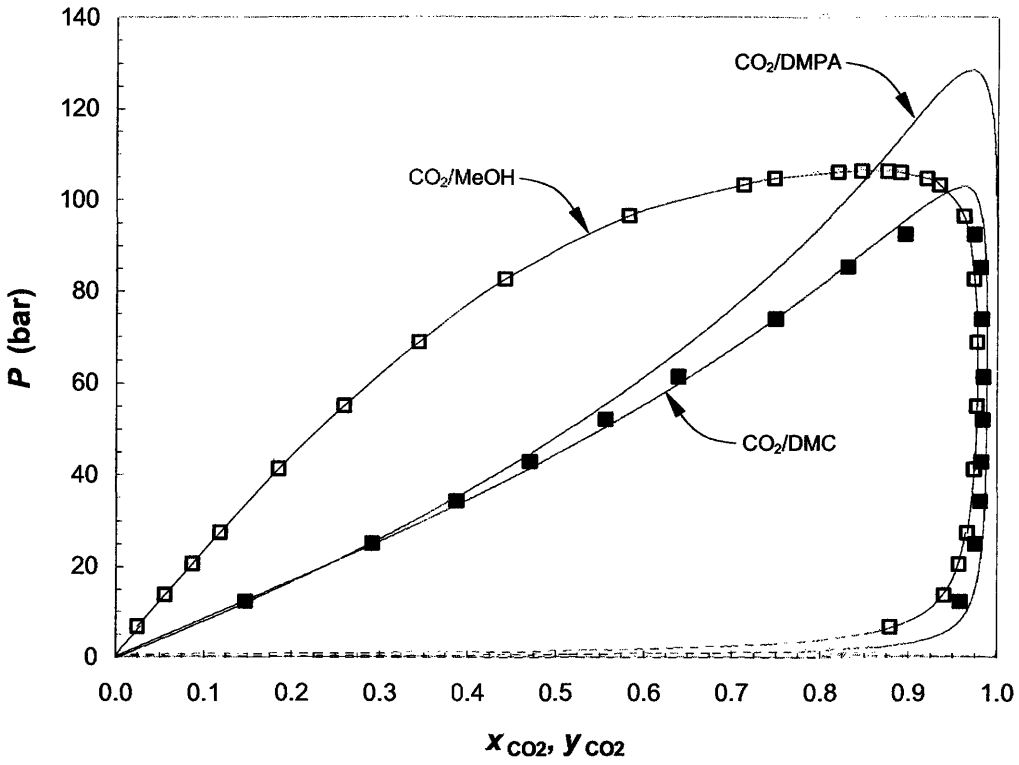

Figure 6-26. Vapor-liquid equilibria data and modeling for the carbon dioxide/methanol, carbon dioxide /dimethyl carbonate, and carbon dioxide/3,4-dimethoxyphenethylamine systems: RK-Aspen EOS for P-x_i (—) and P-y_i (- - -); experimental data for the CO_2/MeOH system by Hong et al. (1988) at 330 K (56.85 °C) (□); experimental data for the CO_2/DMC system by Im et al. (2004) at 330.3 K (57.2 °C) (■); RK-Aspen EOS (—); RK-Aspen EOS prediction for the CO_2/DMPA system at 330 K (56.85 °C).

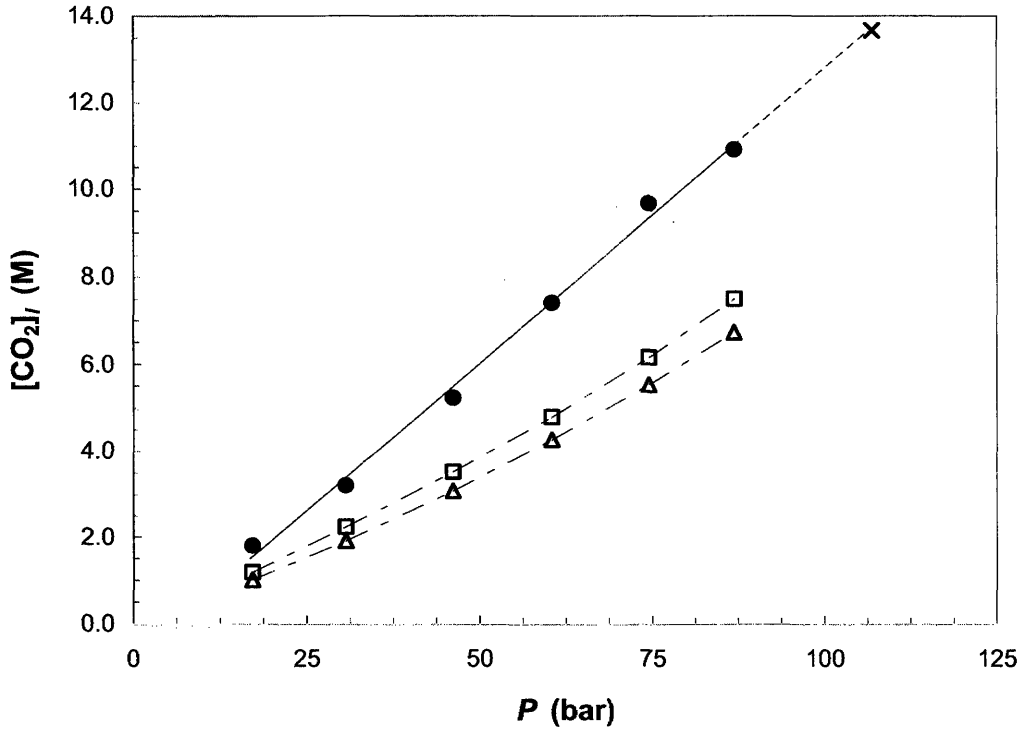

Figure 6-27. Liquid-phase carbon dioxide concentrations plotted as a function of pressure and temperature for the carbon dioxide/methanol, carbon dioxide/dimethyl carbonate, and carbon dioxide/ 3,4-dimethoxyphenethylamine systems at 339.65 K (66. 5 °C): experimental data for the CO_2/DMC system (•); RK-Aspen EOS-calculated data for the CO_2/MeOH system (□) and CO_2/DMPA system (Δ);RK-Aspen EOS (– - –); equation **(6-38)** (—); extrapolation by equation **(6-38)** to $[CO_2]_{l,max}$ for the CO_2/DMC system (- - -); experimental mixture critical pressure for the CO_2/DMC system(×);

6.9. Conclusions and Recommendations

In this chapter, we reported on our vapor-liquid equilibria study for the carbon dioxide/dimethyl carbonate (DMC) system. We specifically measured mixture critical pressures and liquid-phase densities, species concentrations, and volume expansion over a wide range of operating conditions. Importantly, we developed an equation-of-state model and empirical engineering correlations that can be used to predict VLE properties for this system in P-T-x_i regimes for which data are not currently available. The experimental and modeling procedures we developed can be adapted and applied to a variety of other CO_2/solvent mixtures. Specific conclusions that can be drawn from this work include:

- Binary interaction and vapor pressure parameters for the RK-Aspen EOS were regressed from existing experimental P-T-x_i data. With these parameters, the EOS was capable of reproducing experimental data VLE within an AAD of 2.4%;
- Mixture critical pressure ($P_{c,mix}$) data were measured for 310 K (37 °C) < T < 423 K (150 °C) and were correlated well by a third-order polynomial. The RK-Aspen EOS over-predicted experimental $P_{c,mix}$ data by an AAD of 6.7%;
- Liquid-phase carbon dioxide concentration ($[CO_2]_l$) data were measured for several pressures at 310 K (37 °C), 339.5 K (66.5 °C), and 373 K (100 °C). At fixed T, $[CO_2]_l$ increased with increasing pressure and was correlated well by a linear fit. The maximum-possible $[CO_2]_l$ (i.e., at $P \approx P_{c,mix}$) decreased with increasing temperature. Conversely, $[DMC]_l$ data decreased with increasing pressure and the $[DMC]_l$ at $P \approx P_{c,mix}$ increased with increasing temperature. When plotted as a function of x_{CO2}, liquid-phase species concentration collapsed onto a single, linear trend. $[CO_2]_l$ was 2 – 4 times larger than of pure CO_2 when compared at the same T and P. Liquid-phase densities were measured at these conditions and did not trend with either pressure or x_{CO2}. The RK-Aspen EOS deviated from experimental liquid-phase density and species concentration data by an AAD of 8.7%;
- Liquid-phase volume expansion ($\Delta\underline{V}/\underline{V}^0$) data were measured for several pressures at 310 K (37 °C), 340 K (67 °C), and 373 K (100 °C). At fixed T, $\Delta\underline{V}/\underline{V}^0$ increased with increasing pressure and was correlated well by the sum of two exponentials; The maximum-possible $\Delta\underline{V}/\underline{V}^0$ (i.e., at $P \approx P_{c,mix}$) decreased with increasing

temperature. When plotted as a function of x_{CO2}, $\Delta\underline{V}/\underline{V}^0$ data collapsed onto a single, exponential trend. The RK-Aspen EOS deviated from experimental liquid-phase volume expansion data by an AAD of 21.8%;

- Experimental measurements revealed that $[CO_2]_l$ for the CO_2/dibenzyl carbonate (DBC) system were 2 – 4 times smaller than of the CO_2/DMC system at identical T and P. $P_{c,mix}$ values for the CO_2/DBC system were significantly higher than that of the CO_2/DMC system. Without regressed parameters, the RK-Aspen EOS deviated from experimental $[CO_2]_l$ for the CO_2/DBC system by an AAD of 82.8% and $P_{c,mix}$ data by an AAD of 39.2%. RK-Aspen EOS calculations indicated that $[CO_2]_l$ varies for the mixtures in the order CO_2/DMC > CO_2/diethyl carbonate (DEC) > CO_2/DBC, and
- Experimental and RK-Aspen EOS calculations showed that introducing methanol to the CO_2/DMC binary system to form a ternary CO_2/DMC/MeOH system decreased $[CO_2]_l$. RK-Aspen EOS calculations suggested that introducing 3,4-dimethoxyphenethylamine (DMPA) to the CO_2/DMC system would similarly lead to reductions in liquid-phase carbon dioxide concentration.

The following recommendations would lead to significant improvements on the work discussed in this chapter:

1. Improve the Equation of State

- Modification of the RK-Aspen EOS to include volume translation will likely enhance the accuracy of liquid-phase density and volume expansion predictions.

2. Extend the VLE Data Sets

- Measure high-temperature (e.g., T > 100 °C) VLE data for the CO_2/DMC and improve the accuracy of the RK-Aspen EOS by regressing parameters from the expanded data set, and
- Measure the VLE of CO_2/DBC, CO_2/DMPA, and CO_2/DMC/MeOH systems over a wide range of operating conditions.

6.10. References

Aspen Plus version **2004**.1, Aspen Technology, Inc, Burlington, MA. USA.

Bezanehtak, K., Combes, G. B., Dehghani, F., and Foster, N. R. *Vapor-Liquid Equilibrium for Binary Systems of Carbon Dioxide + Methanol, Hydrogen + Methanol, and Hydrogen + Carbon Dioxide.* J. Chem. Eng. Data, **2002**, *47*, 161-168.

Camy, S., Pic, J.-S., Badens, E., and Condoret, J.-S. *Fluid Phase Equilibria of the Reacting Mixture in the Dimethyl Carbonate Synthesis from Supercritical CO_2.* J. Supercrit. Fluids, **2003**, *25*, 19-32.

Frey, K., Augustine, C., Ciccolini, R. P., Paap, S., Modell, M., and Tester, J. *Volume Translation in Equations of State as a means of Accurate Property Estimation.* Fluid Phase Equil., **2007**, *260*, 316-325.

Hong, J. H. and Kobayashi. Vapor-Liquid Equilibrium Studies for the Carbon Dioxide-Methanol System. Fluid Phase Equil., **1988**, *41*, 269-276.

Im, J., Kim, M., Lee, J., and Kim, H. *Vapor-Liquid Equilibria of Binary Carbon Dioxide + Alkyl Carbonate Mixture Systems.* J. Chem Eng. Data, **2004**, *49*, 243-245.

Joback, K. G. and Reid, R. C. *Estimation of Pure-Component Properties from Group-Contributions.* Chem. Eng. Commun., **1987**, *57*, 233-243.

Joback, K. G. *A Unified Approach to Physical Property Estimation using Multivariate Statistical Techniques.* S. M. Thesis, Chemical Engineering Department, Massachusetts Institute of Technology, Cambridge, MA, **1984**.

Lazzaroni, M. J., Bush, D., Brown, J. S., and Eckert, C. A. *High-Pressure Vapor-Liquid Equilibria of Some Carbon Dioxide + Organic Binary Systems.* J. Chem. Eng. Data, **2005**, *50*, 60-65.

Mathias, P. M. *A Versatile Phase Equilibrium Equation of State.* Ind. Eng. Chem. Process Des. Dev., **1983**, *22*, 385-391.

National Institute of Standards and Technology (NIST) Chemistry WebBook, Standard Reference Database Number 69, June 2005 Release, http://webbook.nist.gov/chemistry/.

Ng, H.-J. and Robinson, D. B. *Equilibrium Phase Properties of the Toluene-Carbon Dioxide System.* J. Chem. Eng. Data, **1978**, *23*, 325-327.

Ng, H.-J. and Robinson, D. B. *Equilibrium Phase Properties of the Toluene-Carbon Dioxide System.* J. Chem. Eng. Data, **1978**, *23*, 325-327.

Park, S.-D., Kim, C.-H., and Choi, C.-S. *Phase Equilibria and Mixture Densities Measurements of Carbon Dioxde-Toluene System under High Pressure.* Hwahak Konghak (J. Korean Inst. Chem. Eng .), **1990**, *28*, 438-443.

Piñero, R., Garcia, J., Sokolova, M., Cocero, M. J. *Modelling of the Phase Behavior for the Direct Synthesis of Dimethyl Carbonate from CO_2 and Methanol at Supercritical or Near Critical Conditions.* J. Chem. Therm., **2007**, *39*, 536-549.

Poling, B. E., Prausnitz, J. M., and O'Connell, J. P. *The Properties of Gases and Liquids, Fifth Edition* McGraw-Hill: New York, **2001**.

Rodriguez, A., Canosa, J., Dominguez, A., Tojo, J. *Isobaric Vapour-Liquid Equilibria of Dimethyl Carbonate with Alkanes and Cyclohexane at 101.3 kPa.* Fluid Phase Equil., **2002**, *198*, 95-109.

Rodriguez, A., Canosa, J., Dominguez, A., Tojo, J. *Isobaric Vapor-Liquid Equilibria of Diethyl Carbonate with Four Alkanes at 101.3 kPa.* J. Chem. Eng. Data, **2002**, *47*, 1098-1102.

Tester, J. W. and Modell, M. *Thermodynamics and Its Applications, Third Edition.* Prentice Hall: Upper Saddle River, **1997**.

Valtz, A., Chapoy, A., Coquelet, C., Paricaud, P., and Richon, D. *Vapor-Liquid Equilibria in the Carbon Dioxide-Water System, Measurement and Modelling From 278.2 to 318.2 K.* Fluid Phase Equil., **2004**, *226*, 333-344.

Yunhai, S., Honglai, L., Kun, W., Wende, X., Ying, H. *Measurements of Isothermal Vapor-Liquid Equilibrium of Binary Methanol/Dimethyl Carbonate System under Pressure.* Fluid Phase Equil., **2005**, *234*, 1-10.

Ziegler, J. W., Dorsey, J. G., Chester, T. L., and Innis, D. P. *Estimation of Liquid-Vapor Critical Loci for CO_2-Solvent Mixtures Using a Peak-Shape Method.* Anal. Chem., **1995**, *67*, 456-461.

Steele, W. V., Chirico, R. D., Knipmeyer, S. E., Nguyen, A. *Vapor Pressure, Heat Capacity, and Density along the Saturation Line, Measurements for Dimethyl Isophthalate, Dimethyl Carbonate, 1,3,5-Triethylbenzene, Pentafluorophenol, 4-tert-Butylcatechol, α-Methylstyrene, and N,N'-Bis(2-hydroxyethyl)ethylenediamine.* J. Chem. Eng. Data, **1997**, *42*, 1008-1020.

6.11. Experimental Data, Correlation Parameters, and Supplementary Figures

6.11.1. Mixture Critical Pressure Data and Correlation Parameters

Table 6-4. Experimental and RK-Aspen EOS-calculated mixture critical pressures for the carbon dioxide/dimethyl carbonate system.

T	$P_{c,mix,\ exp}$	$P_{c,mix,\ calc}$	AAD
K (°C)	bar		%
310.15 (37)	77	80	3.7
340.15 (67)	107	114	6.4
373.15 (100)	128	140	9.2
403.15 (130)	141	152	7.6
423.15 (150)	144	154	6.6
		average	***6.7***

Table 6-5. Regressed parameters for empirical *P-T* envelope correlations of the carbon dioxide/dimethyl carbonate system.

	Equation (6-22) Parameter Set property $= \alpha T^3 + \beta T^2 + \chi T + \delta$				
	$\alpha \cdot 10^7$	$\beta \cdot 10^4$	$\chi \cdot 10^1$	δ [b]	AAD [c]
Property [a]	K^{-3}	K^{-2}	K^{-1}	bar	%
$P_{c,mix,\ exp}$	–54.94	18.24	14.75	–390	0.80
$P_{c,mix,\ calc}$	12.22	–73.75	55.56	–970	0.85
$P_{vp,CO_2,exp}$	380	–219	43.81	–303	0.70
$P_{vp,DMC,exp}$	25.92	–24.01	7.51	–79.1	2.90
$x_{CO_2,max,calc}$	–0.8996	0.9953	–0.3818	5.951	1.57

	Equation (6-23) Parameter Set $\ln P_{vp}(T) = A - \frac{B}{T - C}$			
	A	B	C	AAD [c]
Property [a]	bar	K	K	%
$\ln P_{vp,CO_2,exp}$	10.71	1927	3.90	0.22
$\ln P_{vp,DMC,exp}$	10.27	3304	41.00	0.30

[a] all P in bar; [b] unitless for $x_{CO_2,max,calc}$; [c] refers to deviation between property and the empirical fit given by equations **(6-22)** or **(6-23)**.

6.11.2. Liquid-Phase Densities and Species Concentration Data and Correlation Parameters

Table 6-6. Regressed empirical correlation parameters for water vapor pressure and liquid-phase density from 293 – 303 K (20 – 30 °C).

	Parameter Set for Equations (6-22) $\text{property} = \alpha T^3 + \beta T^2 + \chi T + \delta$				
Property [a]	**α** K^{-3}	**β · 10⁴** K^{-2}	**χ · 10¹** K^{-1}	**δ** $kg \cdot m^{-3}$	**AAD** [b] %
$\rho_{H_2O,exp}$	0	-47.52	25.78	651	0.00
	Parameter Set for Equations (6-23) $\ln P_{vp}(T) = A - \frac{B}{T - C}$				
Property [a]	**A** bar	**B** K	**C** K		**AAD** [b] %
$\ln P_{vp,H_2O,exp}$	12.20	4110	35.57		0.09

[a] P in bar, ρ in $kg \cdot m^{-3}$; [b] refers to deviation between experimental property data and the empirical fit given by equations **(6-22)** or **(6-23)**.

Table 6-7. Comparison of experimental and RK-Aspen EOS-calculated liquid-phase densities and species concentrations for the carbon dioxide/dimethyl carbonate system.

P	$x_{CO2,\,calc}$	$[CO_2]_{l,\,exp}$	$[CO_2]_{l,\,calc}$	$[DMC]_{l,\,exp}$	$[DMC]_{l,\,calc}$	$\rho_{l,\,exp}$	$\rho_{l,\,calc}$	AAD
bar				M			$kg \cdot m^{-3}$	%
				T = 310.15 K (37 °C)				
11.1	0.1818	1.60	2.01	7.19	9.03	718	902	25.7
21.0	0.3411	3.95	4.11	7.63	7.93	861	895	4.0
31.1	0.4896	6.31	6.43	6.58	6.70	870	886	1.9
46.2	0.6775	9.52	9.92	4.53	4.72	827	862	4.2
							average	***8.9***
				T = 339.65 K (66.5 °C)				
17.1	0.1752	1.80	1.85	8.45	8.71	841	866	3.0
30.6	0.3126	3.18	3.53	7.00	7.76	771	855	10.9
46.1	0.4582	5.21	5.57	6.16	6.59	785	838	6.8
60.4	0.5776	7.40	7.44	5.41	5.44	813	817	0.6
74.5	0.6815	9.66	9.15	4.52	4.28	832	788	5.3
86.9	0.7631	10.91	10.43	3.39	3.24	785	751	4.3
							average	***5.1***
				T = 373.15 K (100 °C)				
18.5	0.1227	1.35	1.20	9.65	8.58	929	825	11.2
38.2	0.2608	3.00	2.70	8.51	7.66	899	809	10.1
59.7	0.4030	5.15	4.43	7.63	6.56	914	786	14.0
78.4	0.5168	7.09	5.92	6.63	5.54	910	750	16.5
96.5	0.6181	8.02	7.29	4.96	4.50	800	726	9.2
							average	***12.2***
							overall	***8.7***

Table 6-8. Regressed parameters for empirical liquid-phase component concentration correlations for the carbon dioxide/dimethyl carbonate system.

	Equation (6-38) Parameter Set property $= \alpha P + \beta$					
	$[CO_2]_l$			**$[DMC]_l$**		
T	***α***	***β***	**AAD**	***α***	***β***	**AAD**
K (°C)	**bar^{-1}**	**M**	**%**	**bar^{-1}**	**M**	**%**
310.15 (37 °C)	0.2267	-0.8329	2.2	-0.1238	10.3019	1.3
339.65 (66.5 °C)	0.1358	-0.7858	5.0	-0.0677	9.3819	3.2
373.15 (100 °C)	0.0891	-0.2658	3.6	-0.0572	10.8103	3.3
					overall	***2.6***
	Equation (6-39) Parameter Set property $= \alpha x_i + \beta$					
	$[CO_2]_l$			**$[DMC]_l$**		
	α	***β***	**AAD**	***α***	***β***	**AAD**
		M	**%**		**M**	**%**
	15.2756	-1.0910	8.1	-8.0673	10.0872	6.7

Table 6-9. Regressed parameters for empirical maximum-possible liquid-phase concentration correlations for the carbon dioxide/dimethyl carbonate system.

	Equation (6-22) Parameter Set property $= \alpha T^3 + \beta T^2 + \chi T + \delta$				
Property	**$\alpha \cdot 10^7$**	**$\beta \cdot 10^4$**	**$\chi \cdot 10^1$**	**δ**	**AAD**
$mol \cdot L^{-1}$	**K^{-3}**	**K^{-2}**	**K^{-1}**	**M**	**%**
$[CO_2]_{l,\,max}$	-13.740	15.20	-5.83	89.82	2.0
[DMC] at $x_{CO2,\,max}$	7.257	-8.03	3.08	-37.92	2.5

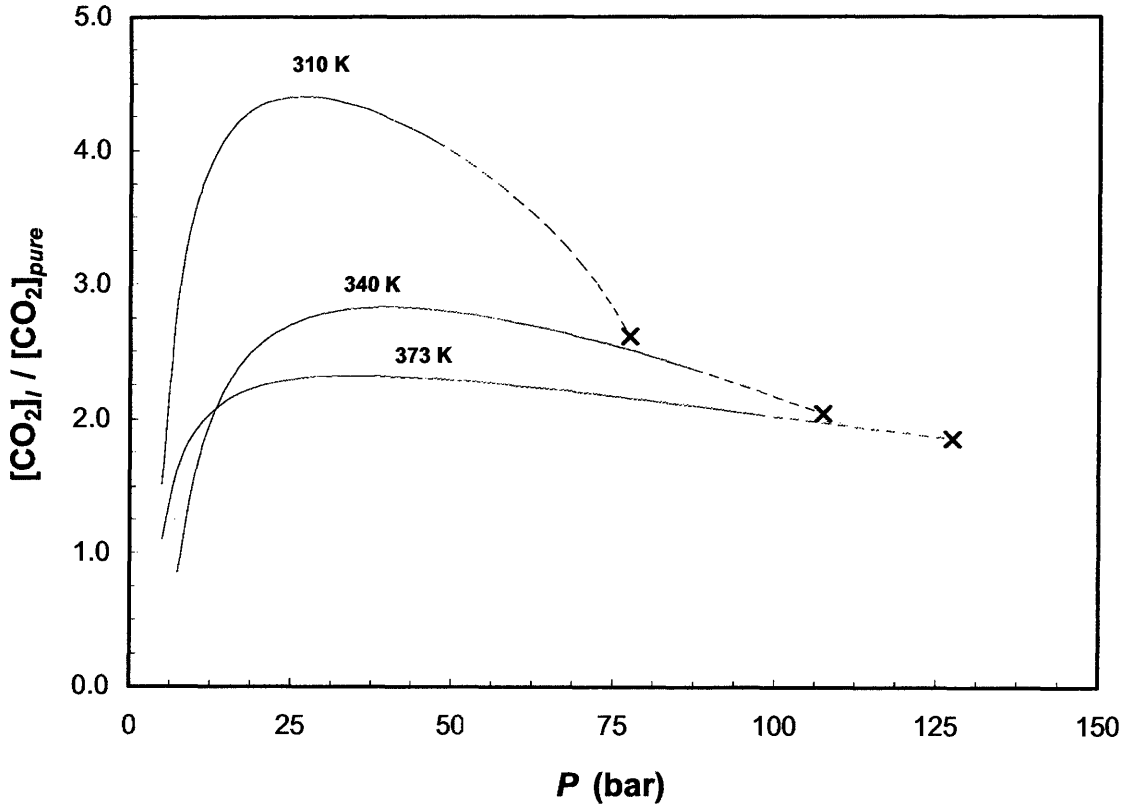

Figure 6-28. Ratio of liquid-phase carbon dioxide concentrations for the carbon dioxide/dimethyl carbonate system and pure carbon dioxide concentrations plotted as a function of pressure and temperature (—): $[CO_2]_l$ predicted by equation **(6-38)** and $[CO_2]_{pure}$ from NIST correlation; extrapolation of data by equation **(6-38)** (- - -); experimental mixture critical pressure (×).

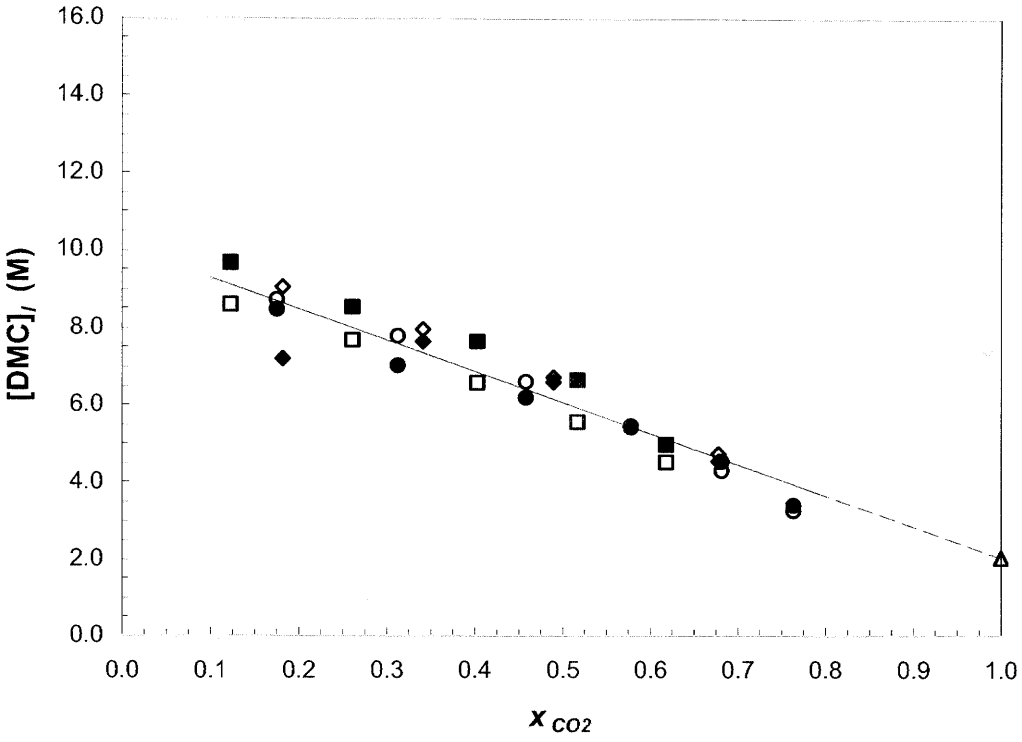

Figure 6-29. Liquid-phase dimethyl carbonate concentrations plotted as a function of liquid-phase carbon dioxide mole fraction at several temperatures: (experimental, RK-Aspen EOS-calculated) at 310.15 K (37 °C) (♦, ◊); 339.65 K (66.5 °C) (•,○); 373.15 K (100 °C) (■, □); experimental data fit by equation **(6-39)** (—); extrapolation of data by equation **(6-39)** (- - -); extrapolated value of $[DMC]_l$ by equation **(6-39)** as $x_i \rightarrow 1$ (Δ).

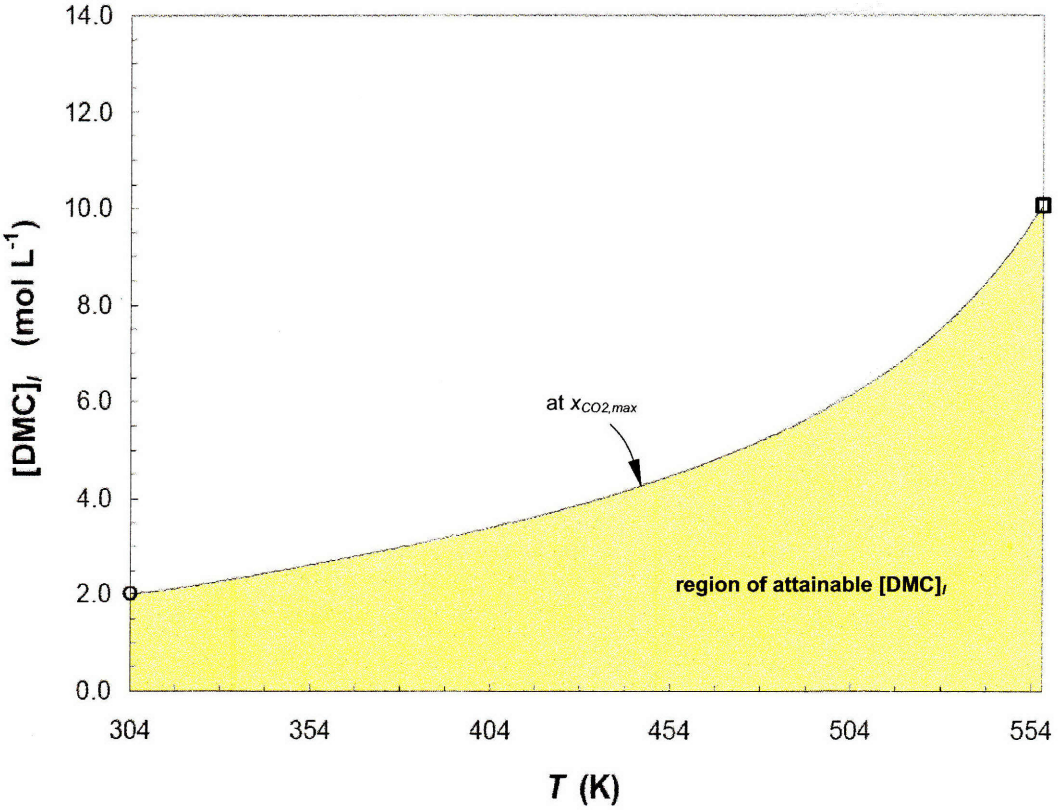

Figure 6-30. Liquid-phase dimethyl carbonate concentrations at maximum-possible liquid-phase carbon dioxide concentrations ($P \approx P_{c,mix}$) for the carbon dioxide/dimethyl carbonate system plotted as a function of temperature: T_c of pure CO_2 (○); T_c of pure DMC (□).

6.11.3. Liquid-Phase Volume Expansion Data and Correlation Parameters

Table 6-10. Comparison of experimental and RK-Aspen EOS-calculated liquid-phase volume expansion data for the carbon dioxide/dimethyl carbonate system.

P bar	$x_{CO2,\,calc}$	ΔV_{exp}	ΔV_{calc} %	AAD	P bar	$x_{CO2,\,calc}$	ΔV_{exp}	ΔV_{calc} %	AAD
				T = 310.25 K (37.1 °C)					
11.7	0.1913	12	12	0.2	68.5	0.8958	557	—	—
18.9	0.3080	23	23	2.1	70.0	0.9093	606	626	3.4
24.6	0.3966	25	34	38.3	70.0	0.9093	577	—	—
30.4	0.4799	39	48	24.2	70.0	0.9093	682	—	—
35.4	0.5478	51	64	24.6	71.4	0.9221	716	757	5.7
44.1	0.6535	76	101	33.2	71.4	0.9221	700	—	—
54.1	0.7614	140	177	25.8	71.4	0.9221	764	—	—
64.2	0.8576	337	353	4.7	72.9	0.9339	736	—	—
								average	***16.2***
				T = 340.15 K (67.1 °C)					
27.5	0.2819	26	22	17.0	77.9	0.7046	118	144	21.9
31.8	0.3247	33	27	17.6	85.1	0.7475	164	—	—
35.4	0.3596	27	31	15.0	86.5	0.7608	168	198	17.4
39.8	0.4004	33	37	13.2	93.7	0.8054	230	266	15.8
48.4	0.4782	45	52	15.1	103.8	0.8668	375	451	20.4
58.5	0.5623	61	74	21.4	103.8	0.8668	361	—	—
65.7	0.6178	73	94	29.7	106.7	0.8798	487	—	—
75.7	0.6854	113	—	—	109.6	0.9050	684	723	5.7
								average	***17.5***
				T = 373.55 K (100.4 °C)					
17.0	0.1115	18	8	57.1	103.8	0.6548	92	127	37.9
21.8	0.1452	20	10	49.2	115.3	0.7145	119	175	47.3
40.0	0.2720	32	23	28.8	124.0	0.7597	175	230	31.4
42.6	0.2906	32	—	—	131.9	0.8038	204	317	55.6
61.3	0.4118	40	43	8.3	136.2	0.8337	375	—	—
80.8	0.5288	70	71	1.7	140.5	0.9118	843	—	—
96.0	0.6135	103	104	1.0					
								average	***31.8***
								overall	***21.8***

Table 6-11. Regressed parameters for empirical liquid-phase volume expansion correlations for the carbon dioxide/dimethyl carbonate system.

	Equation (6-41) Parameter Set $\frac{\Delta V}{V^0} = \alpha \exp(\beta P) + \chi \exp(\delta P)$				
T	**$\alpha \cdot 10^1$**	**$\beta \cdot 10^2$**	**χ**	**$\delta \cdot 10^2$**	**AAD**
K	**%**	**P^{-1}**	**%**	**P^{-1}**	**%**
310.25 K (37.1 °C)	9.257	9.239	10.39	1.159	9.9
340.15 K (67.1 °C)	0.000	28.41	7.47	3.605	5.8
373.55 K (100.4 °C)	0.000	25.79	16.33	1.717	9.9
	Equation (6-42) Parameter Set $\frac{\Delta V}{V^0} = \alpha \exp(\beta x_i) + \chi \exp(\delta x_i)$				
	α	**β**	**$\chi \cdot 10^2$**	**δ**	**AAD**
	%		**%**		**%**
	13.53	2.07	2.504	11	12.1

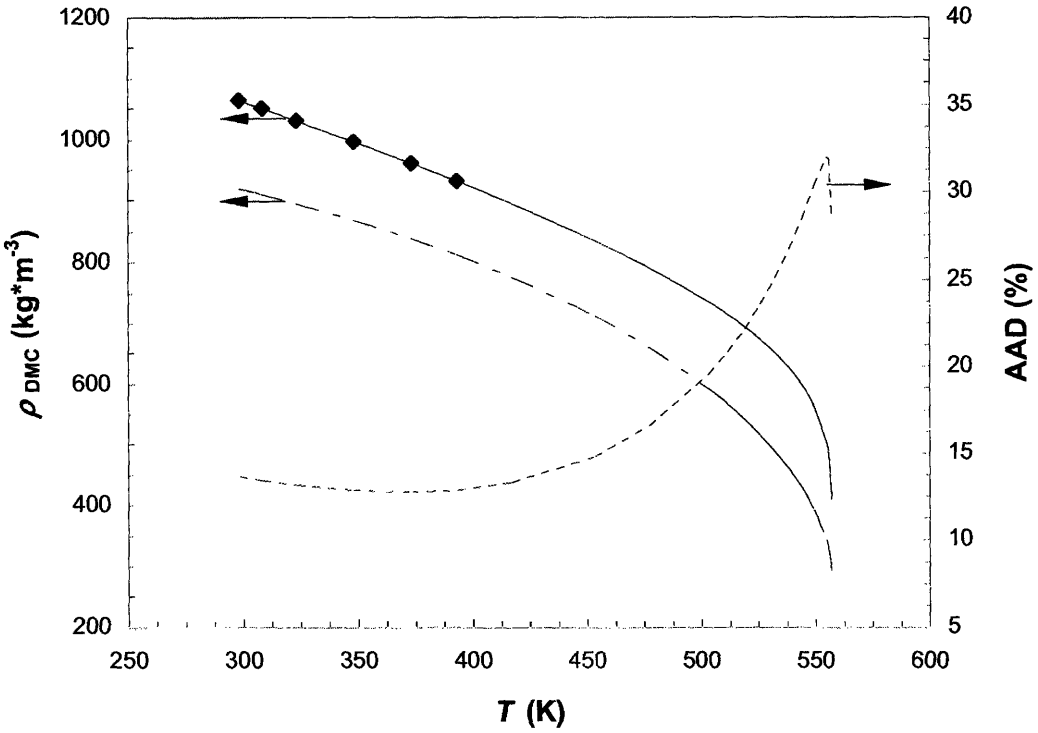

Figure 6-31. Comparison of experimental and calculated pure-component saturated liquid dimethyl carbonate density: experimental data (♦) and empirical correlation (—) by Steele et al. (1997); RK-Aspen EOS (– - –); deviation between experimental data and the empirical correlation with the RK-Aspen EOS (- - -).

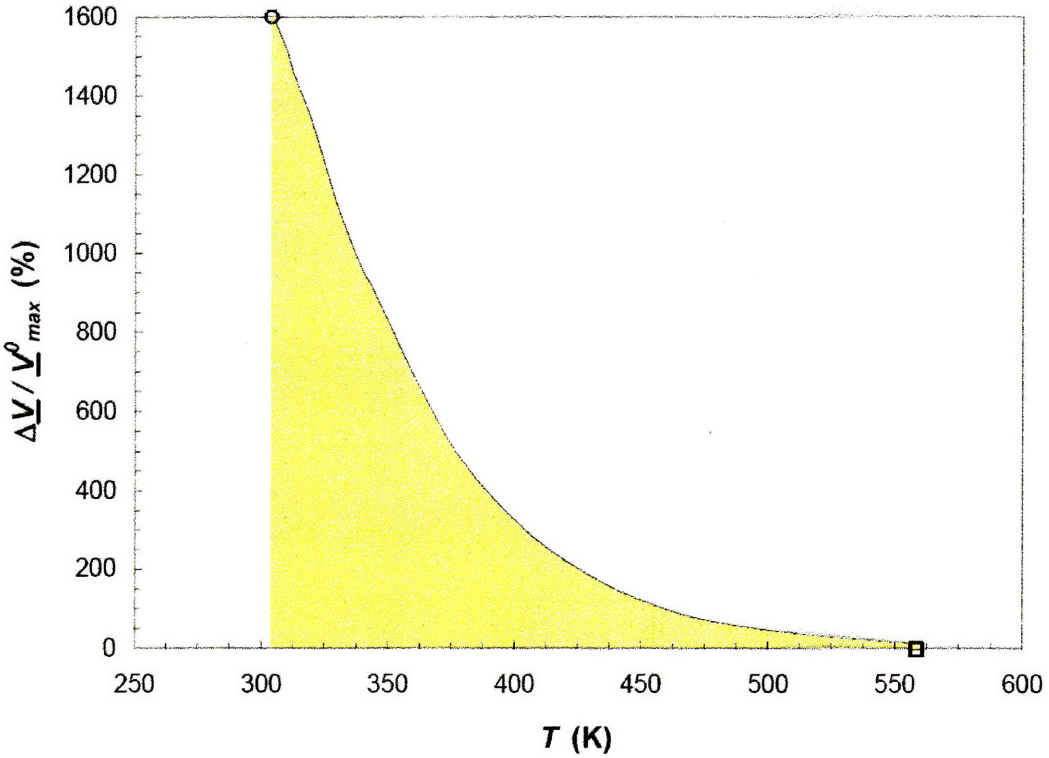

Figure 6-32. Maximum-possible liquid-phase volume expansion ($P \approx P_{c,mix}$) for the carbon dioxide/ dimethyl carbonate system plotted as a function of temperature: T_c of pure CO_2 (○); T_c of pure DMC (□).

6.11.4. Phase Equilibria Data and Correlation Parameters for other CO_2-based Mixtures

Table 6-12. Pure-component properties for diethyl and dibenzyl carbonates.

Property	DEC [a]	DBC [b]
T_c (K)	576.0	828.6
P_c (bar)	33.9	24.8
ω	0.485	0.472

[a] estimated by Im et al. (2004) using the Lydersen group contribution method; these are also the Apsen Plus® defaults; [b] estimated by the Joback group contribution method and calculated using ChemDraw®.

Table 6-13. Regressed parameters for the RK-Aspen EOS for the carbon dioxide/diethyl carbonate system.

p_{DEC}	$k^0_{a_{ij}}$	$k^1_{a_{ij}}$	$k^0_{b_{ij}}$	$k^1_{b_{ij}}$
0.4037	-0.0930	0.1914	-0.0510	0.1473

Table 6-14. Regressed parameters for empirical liquid-phase species concentration correlations for the carbon dioxide/dibenzyl carbonate system at 339.65 K (66.5 °C) by equation **(6-38)**.

T	α	β	AAD
K (°C)	bar^{-1}	M	%
339.65 (66.5 °C)	0.1358	-0.7858	9.5

Table 6-15. Comparison of experimental and RK-Aspen EOS-calculated liquid-phase component concentrations for the carbon dioxide/dibenzyl carbonate system.

P	$x_{CO2,\,calc}$	$[CO_2]_{l,\,exp}$	$[CO_2]_{l,\,calc}$	AAD	$\rho_{l,\,calc}$
bar		M		%	$kg \cdot m^{-3}$
16.6	0.1793	0.50	0.80	58.1	917
31.1	0.3148	0.93	1.60	71.9	913
47.1	0.4441	1.45	2.61	80.6	908
81.1	0.6583	3.09	5.24	69.7	889
156.0	0.9259	5.20	12.16	133.9	771
			average	***82.8***	

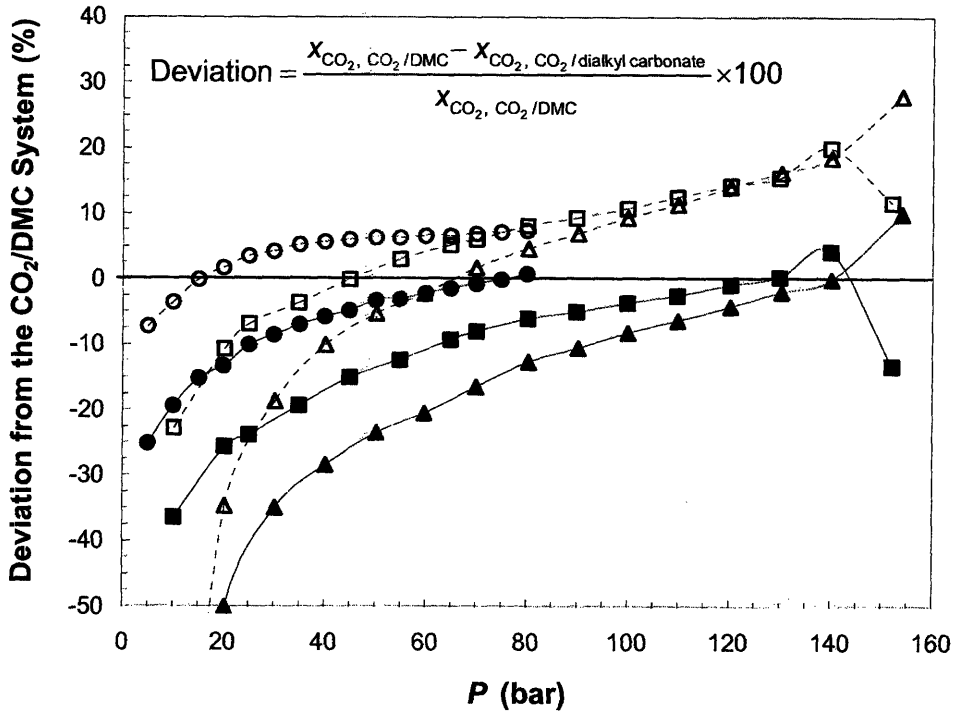

Figure 6-33. Deviations in liquid-phase mole fractions from the carbon dioxide /dimethyl carbonate system for the carbon dioxide/diethyl and /dibenzyl carbonate systems: RK-Aspen EOS predictions for (CO_2/DEC, CO_2/DBC) (—, - - -) at 310.15 K (37 °C) (•, ○); 373.15 K (100 °C) (■, □); 423.15 K (150 °C) (▲, Δ).

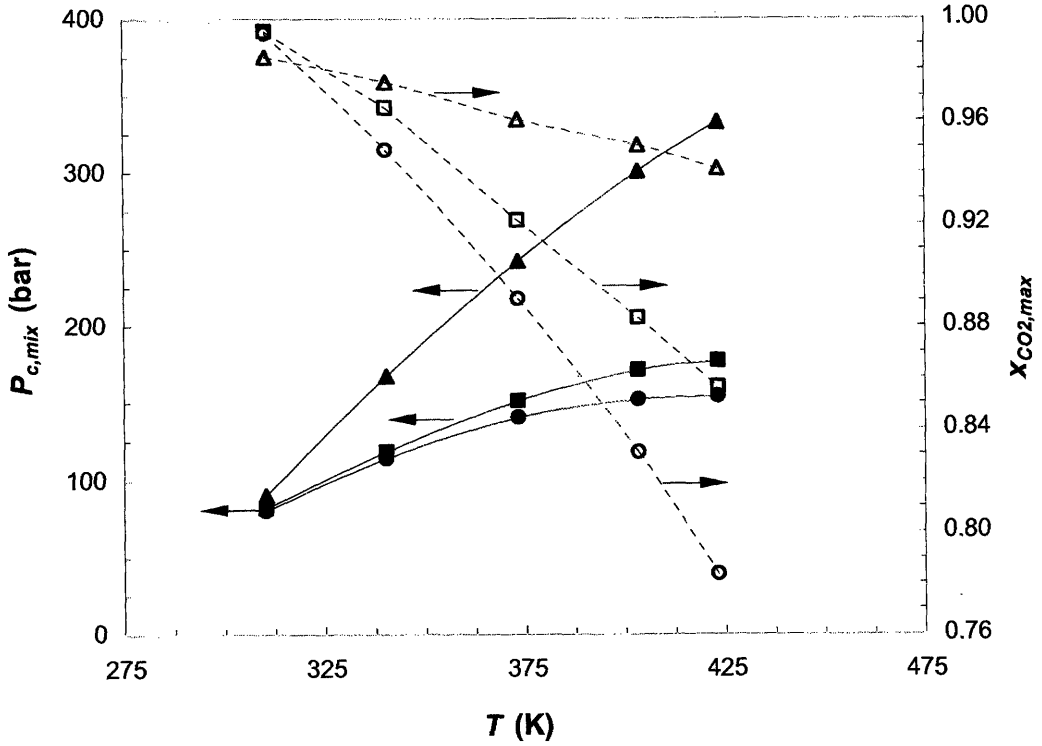

Figure 6-34. Comparison of mixture critical points and maximum-possible liquid-phase carbon dioxide mole fractions for the carbon dioxide/dimethyl, /diethyl, and /dibenzyl carbonate systems: RK-Aspen EOS predictions ($P_{c,mix}$, $x_{CO2,max}$) (—, - - -) for the CO_2/DMC system (•, ○); CO_2/DEC system (■, □); and CO_2/DBC system (▲, Δ).

Table 6-16. Regressed RK-Aspen EOS parameters for the carbon dioxide/methanol and methanol/dimethyl carbonate systems.

CO_2/MeOH System RK-Aspen EOS Parameter Set				
p_{MeOH}	$k^0_{a_{ij}}$	$k^1_{a_{ij}}$	$k^0_{b_{ij}}$	$k^1_{b_{ij}}$
0.2359	0.3528	-0.8373	0.2402	-0.6772
MeOH/DMC System RK-Aspen EOS Parameter Set				
p_{DMC}	$k^0_{a_{ij}}$	$k^1_{a_{ij}}$	$k^0_{b_{ij}}$	$k^1_{b_{ij}}$
0.0388	-1.3091	4.8521	-1.6829	5.9521

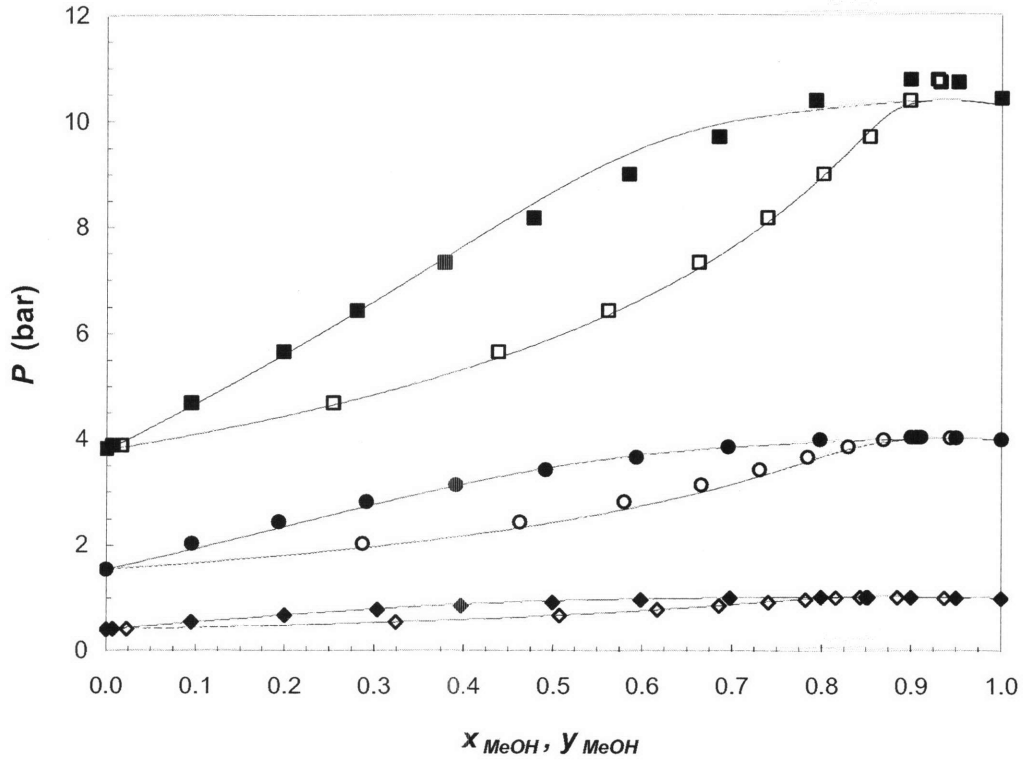

Figure 6-35. Vapor-liquid equilibria data and modeling for the methanol/dimethyl carbonate system: RK-Aspen EOS P-x_i (—) and P-y_i (- - -) by this work; experimental (P-x_i, P-y_i) data by Yunhai et a. (2005) at 337.4 K (64.2 °C) (♦,◊); 377.2 K (104.0 °C) (•,○); 391.2 K (118.0 °C) (■,□).

Table 6-17. Pure-component properties for 3,4-dimethoxyphenethylamine[a].

T_c	P_c	ω
K	bar	
751.2	29.09	0.421

[a] estimated by the Joback group contribution method using ChemDraw®

7. REVISITING AMINE CARBAMATION IN CARBON DIOXIDE-EXPANDED LIQUID MEDIA

7.1. Model Reaction and Variables Explored

Equipped with a quantitative understanding of phase equilibria for the carbon dioxide/dimethyl carbonate system over a wide range of temperature and pressure, we revisited the amine carbamation step in order to elucidate the effects of process operating conditions on reaction performance. Specifically, we probed the temperature-pressure-concentration (T-P-x_i) space for a model amine carbamation reaction, and in doing so, underscored the importance of coupling synthetic chemistry with reaction kinetics and phase equilibria.

3,4-dimethoxyphenethyl amine (DMPA) was selected as a model amine for carbamation via the carbon dioxide/dimethyl carbonate (DMC) reaction system:

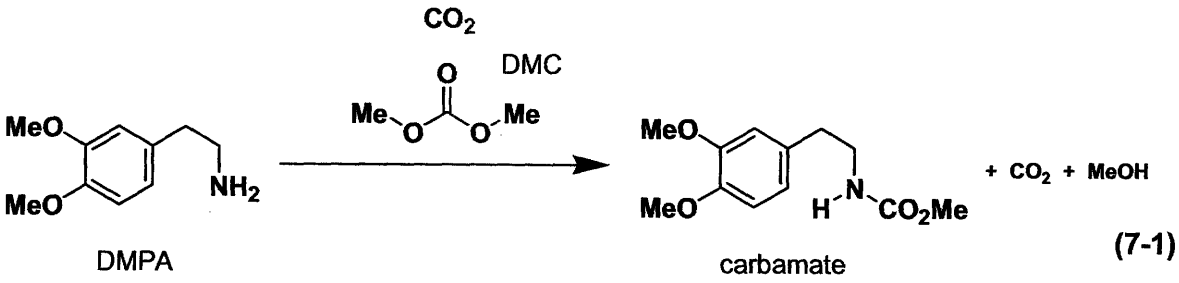

DMPA carbamate (7-1)

As previously discussed in **Section 5.4.1**, equation **(7-1)** was in competition with several amine alkylation pathways that generated byproducts of type **15 – 17**:

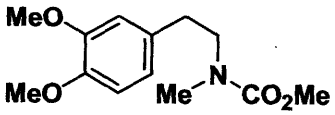

15

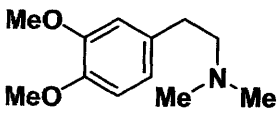

16

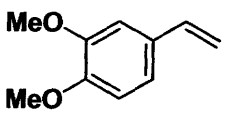

17

Due to sluggish conversion rates and more complex phase behavior at T< 100 °C, the majority of reactions discussed in this chapter were performed at 373 K (100 ° C) < T < 423 K (150 ° C). For temperatures within this range, a wide range of pressures and initial amine and dialkyl carbonate concentrations were explored. A discussion of each of these process operating conditions on reaction performance is presented in the following sections.

7.2. Experimental Approach and Analytical Methods

Supercritical extraction-grade (99.9999% purity, Airgas) carbon dioxide, HPLC-grade anhydrous dimethyl carbonate (99.9+%, Sigma-Aldrich), and high-purity 3,4-dimethoxyphenethyl amine (98+%, Sigma-Aldrich) were used without further purification for all experiments discussed in this chapter. Unless noted otherwise, all experiments were performed with the 25-mL view cell (**VC-2**) and operating/reaction work-up procedures described in **Section 3.2.3**. The actual vessel volume was 31.8 ± 0.3 mL (calculated using the volume determination unit [see **Section 3.3.3**]).

In a typical experiment, DMPA and DMC were loaded to the reactor simultaneously at ambient conditions. The vessel headspace was purged using gaseous argon (99.9999% purity, Airgas). Carbon dioxide was added until a pressure of ca. 35 bar (515 psia) was reached and the reaction mixture was heated to the desired temperature. Additional CO_2 was added while the vessel heated and was topped off at the desired pressure once the temperature reached the set point. Given the relatively high temperatures and time scales required for complete amine conversion (i.e., t = 14 – 24 hr at 130 °C, see **Section 5.4.1**), it was assumed that side reactions occurring in the absence of CO_2 (e.g., amine alkylation) during the loading stage took place to a negligible extent. It typically took ca. 10 min to reach reaction conditions. After the desired reaction time, the reactor was cooled to ambient T via natural convection. Depending on the operating pressure for a given run, CO_2 would exist in either its liquid or gaseous state after cooling (e.g., high-pressure runs yielded P > the vapor pressure of CO_2 at ambient T, thus making it a liquid). All reactions were performed on a time scale that accomplished complete conversion of the amine. This, in addition to the excellent thermal stability of reactions products, eliminated the need for post-reaction quenching. Examination of sparge solvent following the venting of CO_2 via high-pressure liquid chromatography (HPLC) (*vide infra*) revealed no detectable amount of reaction products. This observation indicated that a majority of reaction

products that may have been soluble in CO_2 at reaction conditions were not soluble in the gaseous or liquid form of CO_2 after cooling. Species that remained soluble in CO_2 after the cooling step were likely to precipitate within the vessel during the vent stage (gases being the exception). The sparge step was therefore abandoned and the CO_2-rich phase was instead vented into an open sample bottle for nearly all reported runs. All product-contacted vessel and fitting surfaces were thoroughly rinsed with acetonitrile, collected in a 200-mL volumetric flask, and diluted to the mark.

Samples of the carbamate and the major reaction byproduct **17** were isolated and purified from the crude model reaction mixture via column chromatography by Xiao Yin Mak of Danheiser's research group. Using these standards and the crude reaction mixture, an HPLC analytical method was developed that allowed for the quantification of products from the crude reaction mixture. Analysis method development was performed in collaboration with Professor Kathleen C. Swallow of the Merrimack College Chemistry Department. Detailed operating instructions for the HPLC system are given in **Section 3.3.5**. Due the polar nature of the reaction products, reverse-phase chromatography was employed, which utilized a non-polar C-18 chromatography column and polar mobile phase. Gradient mobile phase flow was used due to the quantity and structural similarity of compounds present in the reaction mixture. Excellent resolution was obtained when using an initial mobile phase ratio of 20:80 vol% acetonitrile:water that linearly increased to 80% acetonitrile over the span of 0.1 – 10 min following the injection. The mobile phase ratio was held constant at 80:20 vol% acetonitrile:water from 10 min until the termination of the run, which was typically 20 min. The mobile phase flowrate was held constant at 1 mL·min^{-1} for the entire run. The UV/Vis absorbance detector was set to 278 nm (the maximum absorbance of a carbamate solution in acetonitrile, determined experimentally) and the autosampler injection volume to 50 μL. A sample chromatogram with retention times (r_t) noted for the reaction products is shown in **Figure 7-1**. Retention times for the carbamate and byproduct **17** were identified by injecting standard solutions made from the isolated products provided by Mak. Given their resemblance to the carbamate, products **15** and **16** were assumed to elute at the peaks indicated in **Figure 7-1**. The methanol byproduct resolved at the same time as the acetonitrile injection solvent at an r_t equal to the residence time of the column. DMPA did not resolve when using this method, suggesting that it may have adhered to the guard column.

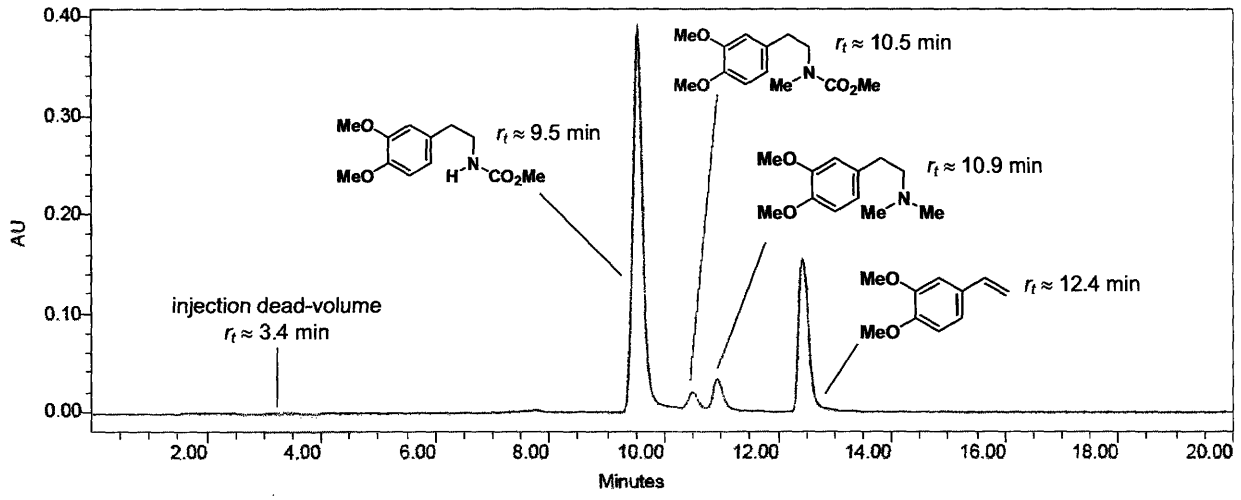

Figure 7-1. Sample high-pressure liquid chromatography chromatogram indicating the resolution of separated amine carbamation reaction products.

Carbamate yield for each run was determined by injecting a sample of known total volume into the HPLC system and determining the concentration via a linear calibration curve made from carbamate standards:

$$[\text{carbamate}] = c_1(\text{HPLC Peak Area}) + c_0 \qquad \textbf{(7-2)}$$

where c_1 and c_0 are the slope and intercept of the calibration curve, respectively. Carbamate standards were prepared by diluting known masses into various-sized volumetric flasks. The number of moles carbamate ($n_{carbamate}$) in the HPLC sample were found from:

$$n_{\text{carbamate}} = \underline{V}_w[\text{carbamate}] \qquad \textbf{(7-3)}$$

where $\underline{V}_w$ was the total volume of solvent used to wash the reactor and dilute the crude reaction mixture (200 mL). Wash and autosampler injection volumes were set so that (1) samples were within the calibration range, (2) the signal-to-noise ratio (i.e., base-line-to-peak height) was minimized, and (3) Beer's law was obeyed (i.e., AU < 1.0 for all injections). Yield was subsequently calculated from:

$$\text{Carbamate Yield} = \frac{n_{\text{carbamate}}}{n_{0,\text{ DMPA}}} \times 100 \qquad \textbf{(7-4)}$$

where $n_{0,DMPA}$ is initial DMPA charge.

7.3. Phase Behavior Considerations

To more fully understand the phase behavior of the reaction mixtures, solubility experiments for all pure-component binary pairs were performed over a wide range of T and P with and without CO_2 present.

7.3.1. The Amine/Dimethyl Carbonate System

3,4-dimethoxyphenethyl amine and dimethyl carbonate were liquids at ambient conditions (298 K, 1.01 bar) with densities of 1070 $kg \cdot m^{-3}$ and 1091 $kg \cdot m^{-3}$ (compared to 997 $kg \cdot m^{-3}$ for water at these conditions). In the absence of CO_2, both compounds were completely miscible for 298 K (25 °C) < T < 423 K (130 °C) (at pressures corresponding to the vapor pressure of the mixture at each temperature) and for amine concentrations ranging from 0.5 – 4 M. A photograph indicating representative DMPA/DMC system phase behavior for these conditions is shown in **Figure 7-2a.**

7.3.2. The Carbon Dioxide/Dimethyl Carbonate System

Phase equilibria properties for the carbon dioxide/dimethyl carbonate system over a wide range of T and P were discussed in **Chapter 6**. In summary, carbon dioxide dissolves in liquid dimethyl carbonate for all temperatures ranging between the freezing point and critical temperature of pure dimethyl carbonate (276 K [3 °C] < T < 557 K [284 °C]). At each temperature within this range, a biphasic system containing an upper, lower-density CO_2-rich phase and a lower, higher-density DMC-rich exists for pressures up to the mixture critical point ($P_{c,mix\,CO_2/DMC}$). Mixture critical pressures, phase-specific species compositions, and liquid-phase volume expansion varied with T and P according to the vapor-liquid equilibrium (VLE) correlations can be found in **Sections 6.3 – 6.6**. For $P > P_{c,mix\,CO_2/DMC}$, a single homogeneous phase exists with compositions corresponding to the total amount of DMC and CO_2 added to the system.

A single-phase mixture for the CO_2/DMC can also be obtained for $P < P_{c,mix\,CO_2/DMC}$ if the amount of DMC added to CO_2 is lower than the solubility limit at that given T and P. For example, if the solubility limit at 373 K (100 °C) and 10 bar was 5 kg DMC per 1 kg CO_2,

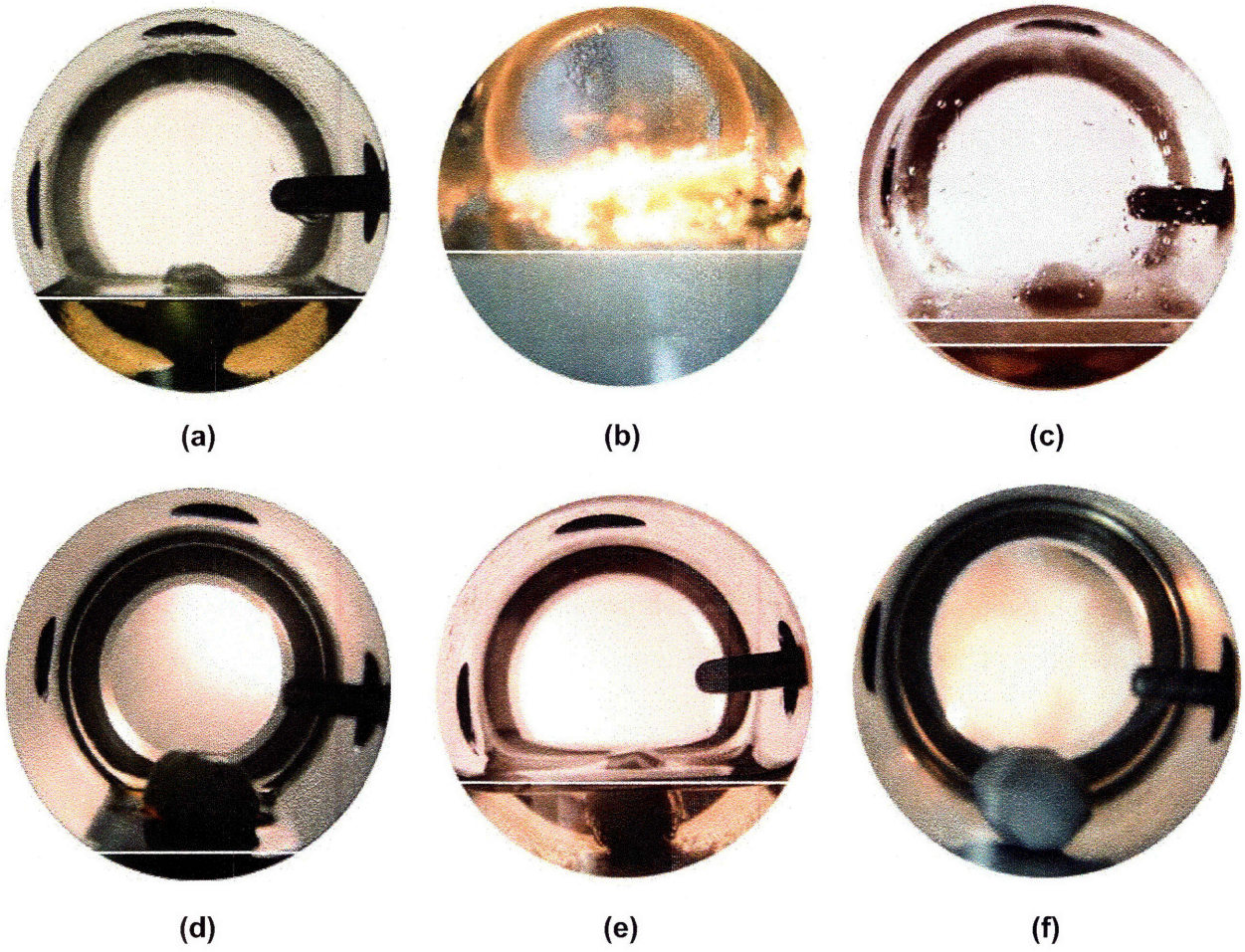

Figure 7-2. Phase behavior observed during the carbamation of 3,4-dimethoxyphenethyl amine with carbon dioxide and dimethyl carbonate: a liquid phase consisting of amine and dialkyl carbonate **(a)**; an upper, lower-density CO_2-rich supercritical-like phase and a lower, higher-density organic-rich liquid phase with an amine-rich solid precipitate dispersed throughout the entire phase **(b)**; an upper, lower-density CO_2-rich supercritical-like phase, a middle, intermediate-density dimethyl carbonate-rich liquid phase, and a lower, higher-density amine-rich liquid phase **(c)**; an upper, lower-density CO_2-rich supercritical-like phase and a lower, higher-density amine-rich liquid phase **(d)**; an upper, lower-density CO_2-rich supercritical-like phase and a lower, higher-density organic-rich liquid phase **(e)**; a supercritical-like CO_2-rich phase. The solid object visible in **(a)**, **(b)**, and **(c)** – **(f)** is a magnetic stir bar. Lines are drawn to indicate phase boundaries.

charging 4 kg to a reactor containing 1 kg of CO_2 would result in a single-phase mixture even though $P << P_{c,mix\ CO_2/DMC}$ at that T. In actuality, solubility limits of several organic compounds in CO_2 tend to be too low for practical application. That is, with a 25-mL reaction vessel volume and ca. 414 bar maximum allowable working pressure, the amount of DMC corresponding to its solubility limit over a wide range of T and P would still be significantly lower than the amount needed to perform reactions on a quantifiable scale. All reactions were therefore run at

conditions above the solubility limit, and because of this, biphasic behavior for all DMC charges was always observed when $P < P_{c,mix\ CO_2/DMC}$.

7.3.3. The Carbon Dioxide/Amine System

Initially a pale yellow viscous liquid, DMPA reacts instantaneously when exposed to CO_2 at ambient T (and mild P) to form a white solid. The solid persisted and appeared insoluble in carbon dioxide for 298 K (25 °C) < T < ca. 358 K (85 °C) and 1.01 bar < P < ca. 415 bar (6015 psia). In the presence of CO_2, the solid melted in the 353 – 363 K (80 – 90 °C) range to form a dark-brown liquid phase (see **Figure 7-2d**). Discoloration was likely due to the decomposition of impurities present in the initial charge. The liquid phase remained insoluble for 363 K (90 °C) < T < 423 K (150 °C) and 1.01 bar < P < ca. 414 bar. Two identical experiments varying in DMPA charge (12 and 0.2 mmol) gave essentially identical phase behavior results. Had the amine been completely soluble in CO_2, the resulting DMPA concentrations for these experiments would have been 371 and 37 mM, respectively.

Suspecting that the solid formed by from the addition of CO_2 to DMPA was a reaction product of the two components (e.g. carbamic acid and/or alkyl ammonium carbamic salt), a portion of the solid was isolated from the vessel and loaded into the off-gas detection unit (see **Section 3.3.4**). Much to our surprise, the solid remained stable in the absence of carbon dioxide at ambient conditions for several hours. This suggested a strong reaction between the basic amine and carbon dioxide and/or diffusion limitations preventing CO_2 offgassing from the solid matrix. If the sample was indeed a reaction product of carbon dioxide and the amine, increasing the temperature of the solid in an inert chamber would result in CO_2 offgassing, as the stability of carbamic salts and their carbamic acid precursors diminishes with increased T (see **Section 4.2**). In the absence of CO_2, the carbamic salt melted in the 373 – 383 K (100 – 110 °C) range to form a dark-brown liquid phase. As expected, sampling of the chamber headspace before and after melting revealed CO_2 evolution. Analysis of the chamber headspace was performed using our gas chromatography (GC) unit calibrated for the detection of light gases. Although confirmed to be a reaction product of CO_2 and the amine, it remains unclear if the solid was carbamic acid or the carbamic salt of the acid. In addition, it is not known whether the solid melts to form a liquid carbamic acid or carbamic salt phase, or decomposes to form 'free' DMPA and carbon dioxide.

7.3.4. The Carbon Dioxide/Carbamate System

The carbamate product is a white crystalline solid that melts at ca. 338 K (65 °C) in the absence of CO_2. In the presence of carbon dioxide at ca. 105 bar (1515 psia), the carbamate melted at ca. 313 K (40 °C). For 298 K (25 °C) < T < ca. 308 K (35 °C), the carbamate (in its solid form) remained insoluble in CO_2 for 1.01 < P < 415 bar (6015 psia). For T = 313 K (40 °C), 373 K (100 °C), and 403 K (130 °C), the carbamate (in its liquid form) completely dissolved in CO_2 at pressures of ca. 139 bar (2015 psia), 277 bar (4015 psia), and 346 bar (5015 psia), respectively. These values were determined using the cloud-point apparatus and operating instructions given in **Section 3.2.6**. 0.5 g of carbamate (ca. 2 mmol, the amount generated in a typical reaction) was used in this solubility experiment.

7.3.5. The Dimethyl Carbonate/Carbamate System

At reaction-scale concentrations, the carbamate readily dissolved in dimethyl carbonate for 298 K (25 °C) < T < 423 K (150 °C).

7.3.6. The Reaction System

With an understanding of component-component phase behavior, we turned to the analysis of the entire reaction mixture. For fixed DMPA and DMC charges, the following reaction phase behavior was observed:

- **298 K (25 °C) < T < ca. 358 K (85 °C):** *an upper, lower-density CO_2-rich supercritical-like phase, a middle, intermediate-density DMC-rich liquid phase, and a lower, higher-density amine-rich solid phase* (see **Figure 7-2b**).

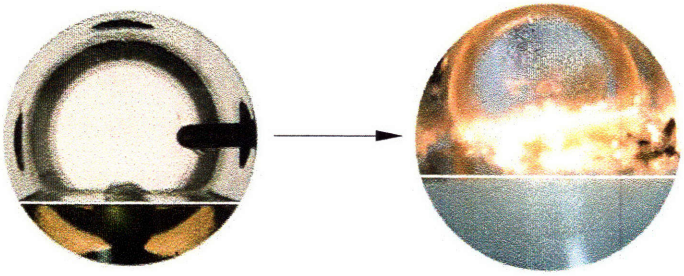

Figure 7-2a **Figure 7-2b**

- **373 K (100 °C):** *an upper, lower-density CO_2-rich supercritical-like phase, a middle intermediate-density DMC-rich liquid phase, and a lower higher-density amine-rich liquid phase* (see **Figure 7-2c**). As pressures approached $P_{c,mix\ CO_2/DMC}$, DMPA precipitated from an initial, single organic-rich liquid phase (see **Figure 7-2e**) to form a separate liquid phase. This suggested that DMPA — either in the form of free amine, carbamic acid, or carbamic salt — became insoluble as the polarity of the DMC-rich liquid phase decreased upon the absorption of CO_2. For pressures higher than $P_{c,mix\ CO_2/DMC}$, DMC partitioned to the CO_2-rich phase, resulting in *an upper, lower-density CO_2-rich supercritical-like phase and a lower, higher-density amine-rich liquid phase* (see **Figure 7-2d**). Based on the solubility experiments with carbamate and pure CO_2, it is likely that the carbamate partitions to the more polar organic-rich liquid phase for $P < 277$ bar (4015 psia).

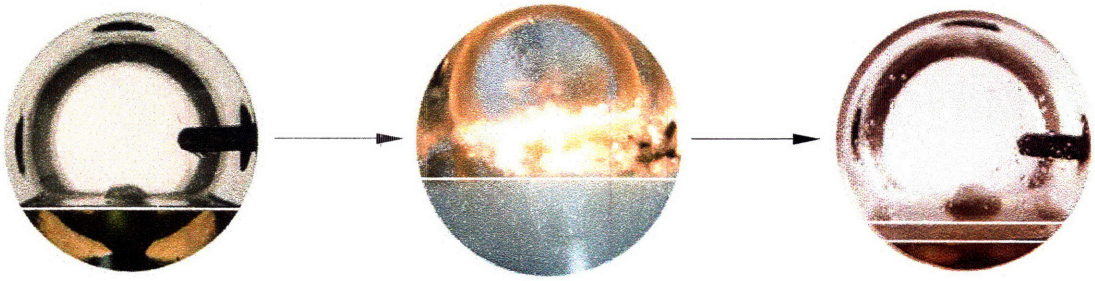

Figure 7-2a **Figure 7-2b** **Figure 7-2c**

for $P_{c,mix\ CO2/DMC} < P < P_{c,mix\ system}$

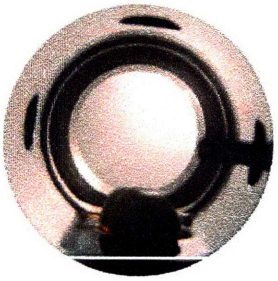

Figure 7-2d

- **383 K (110 °C) < *T* < 423 K (150 °C):** *an upper, lower-density CO_2-rich supercritical-like phase and a lower, higher-density organic-rich liquid phase* (see **Figure 7-2e**). Unlike the previous case, DMPA — either in the form of free amine, carbamic acid, or carbamic salt — remained soluble in the organic-rich liquid phase. At pressures higher than $P_{c,mix\ CO_2/DMC}$, DMC partitioned to the CO_2-rich phase, resulting in *an upper, lower-density CO_2-rich supercritical-like phase and a lower, higher-density amine-rich liquid phase* (see **Figure 7-2d**). At 403 K (130 °C) and P > 270 bar, the phase behavior of the system transitioned after ca. 1 hour to form a *single, homogenous supercritical-like phase* (see **Figure 7-2f**). Solubility control experiments with the CO_2/DMPA and CO_2/carbamate systems at similar concentrations, however, revealed that multiple existed at this operating condition. This finding suggests that the addition of polar materials to the CO_2-based system (e.g., DMC and byproducts such as methanol and compounds **15** – **17**) enhance its ability to solubilize the entire reaction mixture.

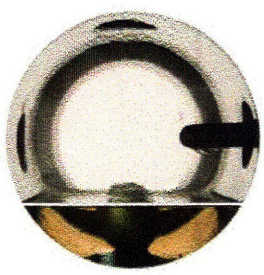

Figure 7-2a

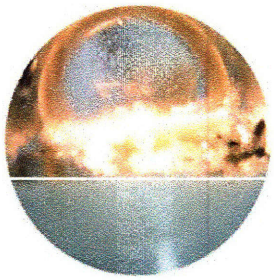

Figure 7-2b

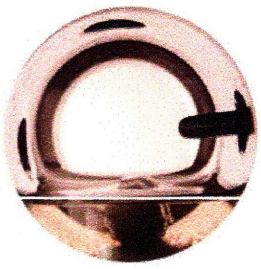

Figure 7-2e

for $P_{c,mix\ CO2/DMC} < P < P_{c,mix\ system}$

for $P > P_{c,mix\ system}$

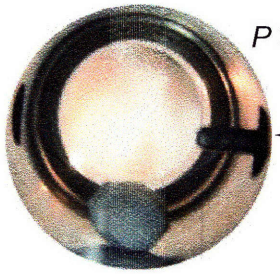

Figure 7-2f

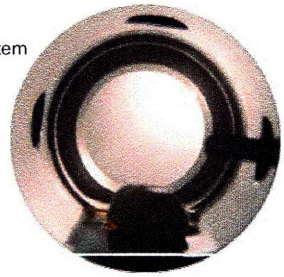

Figure 7-2d

The term 'rich' was used in the previous discussion to denote a phase that was concentrated with respect to a given component. For example, in a CO_2/DMC mixture, a 'DMC-rich' liquid phase indicates that the liquid-phase mole fraction (x_i) for DMC is larger than that of CO_2. This terminology was also used to describe phases that contained the majority of a particular component relative to its initial charge. For instance, although a CO_2/DMC mixture at $P \approx P_{c,mix\,CO_2/DMC}$ may have an x_{CO_2} larger than x_{DMC}, it is still referred to as 'DMC-rich' because most of the initial DMC charge resides in the liquid-phase (i.e., the vapor-phase mole fraction of DMC (y_{DMC}) is << 1, see **Section 6.2**).

7.4. Kinetic Model Formulation

7.4.1. Reaction Networks

Amine carbamation via the CO_2/DMC carbonate system occurs via the alkylation of the carbamic salt generated *in situ* from the reaction of CO_2 with an amine (see **Section 5.2**). As discussed in **Section 4.2** and from a quantum chemical perspective in **Section 10.4.1**, a widely-accepted method for forming carbamic salts in low-dielectric, aprotic mediums such as neat CO_2 begins with formation of coordination complex ($RNH_2 \cdots CO_2$) comprised of CO_2 and the amine:

$$RNH_2 + CO_2 \underset{k_{-1}}{\overset{k_1}{\rightleftharpoons}} RNH_2 \cdots CO_2 \qquad \textbf{(7-2)}$$

A second free amine molecule acts as a catalytic hydrogen transfer agent to facilitate carbamic acid ($RNHCO_2H$) formation:

$$RNH_2 \cdots CO_2 + RNH_2 \underset{k_{-2}}{\overset{k_2}{\rightleftharpoons}} RNHCO_2H + RNH_2 \qquad \textbf{(7-3)}$$

For polar media (and possibly CO_2-expanded DMC), the amine-CO_2 complex takes on the form of a zwitterion that can be protonated via another amine molecule or from the medium itself if it is protic. Finally, a free amine molecule reacts with carbamic acid in acid-base type chemistry to form a carbamic salt:

$$RNHCO_2H + RNH_2 \underset{k_{-3}}{\overset{k_3}{\rightleftharpoons}} RNHCO_2^- {}^+H_3NR \qquad \textbf{(7-4)}$$

The carbamic salt then undergoes methylation by DMC ($CH_3OCO_2CH_3$) to produce the desired carbamate ($RNHCO_2CH_3$):

$$RNHCO_2^- {}^+H_3NR + CH_3OCO_2CH_3 \xrightarrow{k_4} RNHCO_2CH_3 + CO_2 + CH_3OH + RNH_2 \quad \textbf{(7-5)}$$

Note that equation **(7-5)** is the overall reaction for the alkylation of the carbamic salt. In actuality, the reaction proceeds through a combination of several elementary reactions involving intermediates that are not shown here for brevity purposes. Rate constant k_4, then, is global rate constant that is a combination of elementary rate constants. The rate of carbamate formation via the alkylation of carbamic salts is therefore given by:

$$r_{RNHCO_2CH_3} = \frac{d[RNHCO_2CH_3]}{dt} = k_4[RNHCO_2^- {}^+H_3NR][CH_3OCO_2CH_3] \quad \textbf{(7-6)}$$

Since the amine reactions are thought to be at equilibrium, the concentrations of each component can be related by the thermodynamic equilibrium constant (K_i):

$$[RNHCO_2^- {}^+H_3NR] = \frac{k_3}{k_{-3}}[RNHCO_2H][RNH_2] = K_3[RNHCO_2H][RNH_2] \quad \textbf{(7-7)}$$

$$[RNHCO_2H] = \frac{k_2}{k_{-2}}[RNH_2 \cdots CO_2] = K_2[RNH_2 \cdots CO_2] \quad \textbf{(7-8)}$$

$$[RNH_2 \cdots CO_2] = \frac{k_1}{k_{-1}}[RNH_2][CO_2] = K_1[RNH_2][CO_2] \quad \textbf{(7-9)}$$

In actually, the equilibrium constant is the ratio of component activities (a_i) in solution. The equilibrium constant for equation **(7-2)**, for example, would be:

$$K_1 = \frac{a_{RNH_2 \cdots CO_2}}{a_{RNH_2} a_{CO_2}} = \frac{\gamma_{RNH_2 \cdots CO_2}}{\gamma_{RNH_2}\gamma_{CO_2}} \frac{[RNH_2 \cdots CO_2]}{[RNH_2][CO_2]} \quad \textbf{(7-10)}$$

For simplicity, we have lumped all activity coefficients (γ_i) into the equilibrium constant. Substituting the equations **(7-7)** – **(7-9)** into equation **(7-6)** yields:

$$r_{RNHCO_2CH_3} = \frac{d[RNHCO_2CH_3]}{dt} = k^*[RNH_2]^2[CO_2][CH_3OCO_2CH_3] \quad \textbf{(7-11)}$$

where $k^* = k_4K_3K_2K_1$.

Competitive alkylation reactions involving the free amine with DMC that yield byproducts **16** ($RN(CH_3)_2$) and **17** (R) are given by:

$$RNH_2 + CH_3OCO_2CH_3 \xrightarrow{k_5} RNHCH_3 + CO_2 + CH_3OH \quad \textbf{(7-12)}$$

$$RNHCH_3 + CH_3OCO_2CH_3 \xrightarrow{k_6} RN(CH_3)_2 + CO_2 + CH_3OH \quad \textbf{(7-13)}$$

$$RN(CH_3)_2 + CH_3OCO_2CH_3 \xrightarrow{k_7} N(CH_3)_3 + CO_2 + CH_3OH + R \quad \textbf{(7-14)}$$

Similar to equation **(7-4)**, only the overall alkylation reactions and global rate constants are presented. The rates of alkylated amine derivatives are given by:

$$r_{RNHCH_3} = \frac{d[RNHCH_3]}{dt} = k_5[RNH_2][CH_3OCO_2CH_3] \quad \textbf{(7-15)}$$

$$r_{RN(CH_3)_2} = \frac{d[RN(CH_3)_2]}{dt} = k_6[RNHCH_3][CH_3OCO_2CH_3] \quad \textbf{(7-16)}$$

$$r_{N(CH_3)_3} = \frac{d[N(CH_3)_3]}{dt} = k_7[RN(CH_3)_2][CH_3OCO_2CH_3] = r_R = \frac{d[R]}{dt} \quad \textbf{(7-17)}$$

Once-methylated amine ($RNHCH_3$) produced by equation **(7-11)** may also participate as a catalyst in the formation of the carbamic acid and carbamic salt intermediates during carbamate synthesis:

$$RNH_2\cdots CO_2 + RNHCH_3 \underset{k_{-2'}}{\overset{k_{2'}}{\rightleftharpoons}} RNHCO_2H + RNHCH_3 \quad \textbf{(7-3)'}$$

$$RNHCO_2H + RNHCH_3 \underset{k_{-3'}}{\overset{k_{3'}}{\rightleftharpoons}} RNHCO_2^- {}^+H_2CH_3NR \quad \textbf{(7-4)'}$$

$$RNHCO_2^- {}^+H_2CH_3NR + CH_3OCO_2CH_3 \xrightarrow{k_{4'}} RNHCO_2CH_3 + CO_2 + CH_3OH + RNHCH_3 \quad \textbf{(7-5)'}$$

$$r_{RNHCO_2CH_3} = \frac{d[RNHCO_2CH_3]}{dt} = k^{**}[RNH_2][RNHCH_3][CO_2][CH_3OCO_2CH_3] \quad \textbf{(7-6)'}$$

where $k^{**} = k_4 K_3 K_2 K_1$. The overall rate of carbamate formation is therefore given by the sum of equations **(7-6)** and **(7-6)'**.

$RNHCH_3$ may also react with CO_2 in a pathway similar to the free amine that ultimately leads to the production of the methylated carbamate byproduct **15** ($RNCH_3CO_2CH_3$):

$$RNHCH_3 + CO_2 \underset{k_{-8}}{\overset{k_8}{\rightleftharpoons}} RNHCH_3 \cdots CO_2 \quad \textbf{(7-18)}$$

$$RNHCH_3 \cdots CO_2 + RNH_2 \underset{k_{-9}}{\overset{k_9}{\rightleftharpoons}} RNCH_3CO_2H + RNH_2 \quad \textbf{(7-19)}$$

$$RNCH_3CO_2H + RNH_2 \underset{k_{-10}}{\overset{k_{10}}{\rightleftharpoons}} RNCH_3CO_2^{-}\ {}^{+}H_3NR \quad \textbf{(7-20)}$$

$$RNCH_3CO_2^{-}\ {}^{+}H_3NR + CH_3OCO_2CH_3 \xrightarrow{k_{11}} RNCH_3CO_2CH_3 + CO_2 + CH_3OH + RNH_2 \quad \textbf{(7-21)}$$

$$r_{RNCH_3CO_2CH_3} = \frac{d[RNCH_3CO_2CH_3]}{dt} = k^{***}[RNH_2][RNHCH_3][CO_2][CH_3OCO_2CH_3] \quad \textbf{(7-22)}$$

where $k^{***} = k_{11} K_{10} K_9 K_8$. In addition, $RNHCH_3$ may also participate as a catalyst in the formation of the carbamic acid and carbamic salt intermediates required for methylated carbamate (**15**) synthesis:

$$RNHCH_3 \cdots CO_2 + RNHCH_3 \underset{k_{-9'}}{\overset{k_{9'}}{\rightleftharpoons}} RNCH_3CO_2H + RNHCH_3 \quad \textbf{(7-19)'}$$

$$RNCH_3CO_2H + RNHCH_3 \underset{k_{-10'}}{\overset{k_{10'}}{\rightleftharpoons}} RNCH_3CO_2^{-}\ {}^{+}H_2CH_3NR \quad \textbf{(7-20)'}$$

$$RNCH_3CO_2^{-}\ {}^{+}H_2CH_3NR + CH_3OCO_2CH_3 \xrightarrow{k_{11'}} RNHCO_2CH_3 + CO_2 + CH_3OH + RNHCH_3 \quad \textbf{(7-21)'}$$

$$r_{RNCH_3CO_2CH_3} = \frac{d[RNCH_3CO_2CH_3]}{dt} = k^{****}[RNHCH_3]^2[CO_2][CH_3OCO_2CH_3] \quad \textbf{(7-22)'}$$

where $k^{****} = k_{11}K_{10}K_9K_8$. The overall rate of methylated carbamate (**15**) formation is therefore given by the sum of equations **(7-22)** and **(7-22)'**.

7.4.2. Carbamate Selectivity and Mechanism Validation

The selectivity for carbamate formation over alkylation byproducts is defined as:

$$S = \frac{r_{desired}}{\sum_i r_{undesired}} = \frac{r_{RNHCO_2CH_3}}{r_{RNHCH_3} + r_{RN(CH_3)_2} + r_{N(CH_3)_3} + r_{RNCH_3CO_2CH_3}} \qquad \textbf{(7-23)}$$

$$= \frac{\left(k^{*}[RNH_2] + k^{**}[RNHCH_3]\right)[RNH_2][CO_2]}{k_5[RNH_2] + k_6[RNHCH_3] + k_7[RN(CH_3)_2] + \left(k^{***}[RNH_2] + k^{****}[RNHCH_3]\right)[RNHCH_3][CO_2]}$$

With the majority of byproducts being the alkylated derivatives **16** and **17**, we can assume that upon formation, the once-methylated amine is rapidly converted to higher-order methylation products. Furthermore, if we assume that the concentration of free amine is larger than that of the once-methylated amine (i.e., $[RNH_2] >> [RNHMe]$), equation **(7-23)** simplifies to:

$$S = \frac{k^{*}[RNH_2]^2[CO_2]}{k_5[RNH_2] + k_6[RNHCH_3] + k_7[RN(CH_3)_2]} \qquad \textbf{(7-23)'}$$

Importantly, this expression ignores carbamate formed sans CO_2 by the acylation of the carbamic salt (see equation **[5-5]**) or free amine (see equation **[5-6]**) by DMC. In these mechanisms, the carbonyl carbon of the carbamate derives from the carbonyl group of DMC. In the carbamic salt alkylation mechanism (see equation **[7-5]**), the carbonyl carbon of the carbamate derives from CO_2. To distinguish among the mechanisms and validate our selectivity expression, a carbamation reaction was performed using isotopically-labeled carbon dioxide ($^{13}CO_2$) (99.5% purity, Sigma-Aldrich, *364592-Spec*). The resulting carbamate was isolated and purified via column chromatography by Mak, diluted in dichloromethane, and submitted for gas chromatography-mass spectroscopy (GC-MS) analysis. GC-MS analysis was performed by former Tester group member Dr. Michael Timko at the analytical chemistry facility of Aerodyne Research, Inc. Ratios of the $^{13}CO_2$ and $^{12}CO_2$ ion peaks from the GC-MS chromatogram revealed that ca. 35 molar% of the carbamate had incorporated $^{13}CO_2$. A control reaction using $^{12}CO_2$ at similar operating conditions revealed that ca. 10 molar% of the carbamate had

incorporated $^{13}CO_2$ (which is in line with the ca. 1% natural abundance of $^{13}CO_2$ in and given that the carbamate contains 12 carbons). It was intriguing that a higher incorporation of $^{13}CO_2$ was not observed. Incorporation less than 100% suggests that the acylating mechanism is partially at play and/or $^{12}CO_2$ liberated from DMC by all alkylation reactions (see equations **[7-5]** and **[7-12]** – **[7-14]**) participates in the carbamic salt alkylation mechanism to yield $^{12}CO_2$-carbamate. It is possible that the two carbon isotope forms of CO_2 compete for incorporation into the carbamate.

The incorporation of $^{13}CO_2$, detection of alkylated amine derivatives (**15** – **17**), lack of strong base, and high-T operating conditions all suggest that DMC acts predominantly as an alkylating agent. Consider, for example, typical reaction yield of 50 molar% carbamate, 5 molar% methylated carbamate (**15**), and 45 molar% alkylated amine derivatives (**16** and **17**). With a 35 molar% $^{13}CO_2$ uptake, this means that ca. 65 molar% ([0.35 × {50 + 5}] + 45) of the amine underwent alkylation the remaining 35 molar% acylation. 35 molar% is actually an overestimate, as it was not possible to quantify the amount of carbamate generated by the CO_2 liberated by DMC during alkylation (*vide supra*). These analyses therefore emphasize the importance of carbon dioxide concentration on carbamate selectivity.

7.5. Coupling Reaction Kinetics and Phase Behavior

As shown by the previous section, for efficient and selective amine carbamation, it was imperative to maximize contact between carbon dioxide and amine to form the requisite carbamic salt prior to alkylation by DMC. Based on the phase behavior discussion presented in **Section 7.3**, we are now able to make several assumptions regarding the phase at which the carbamation proceeded as function of T and P. Due to sluggish reaction rates for $T < 373$ K (100 °C) we have restricted our analysis to 373 K (100 °C) < T < 423 K (150 °C):

- **Reaction Condition 1: 373 K (100 °C) and $P < P_{c,mix\,CO_2/DMC}$.** Shown schematically in **Figure 7-3a**, reactions can proceed in three phases and at the two interfaces separating them. As discussed in **Section 6.5.2**, the concentration of pure CO_2 is approximately 2 – 4 lower than that of a DMC-rich liquid phase at the same conditions. Equation-of-state predictions suggested that the concentration of CO_2 in an amine-rich polar liquid phase are lower than that of a DMC-rich liquid phase (see

Section 6.8.2). Solubility control experiments revealed a low solubility of the amine (and/or carbamic acid and salt derivatives) in either the DMC- and CO_2-rich phases, and also a low solubility of DMC in the CO_2-rich phase at these conditions. All of these observations suggest that the carbamation reaction was likely to proceed at the interface between the DMC-rich and amine-rich phases. The reaction may also proceed to a lesser extent in either of the liquid-phases.

- **Reaction Condition 2: 383 K (110 °C) < T < 423 K (150 °C) and $P < P_{c,mix\ CO_2/DMC}$.** Shown schematically in **Figure 7-3b**, reactions can proceed in two phases and at the interface separating them. For reasons stated above, the carbamation reaction was likely to proceed in the organic-rich liquid phase. Also, since the concentration of CO_2 in the organic-rich liquid phase (comprised largely of DMC) is on the order of the reagents employed in many of the reactions (see **Section 6.5.2**), it was doubtful that the reaction was mass-transfer limited. The reaction at the interface between the CO_2-rich and DMC-rich phases was therefore assumed negligible. Carbamate selectivity was therefore maximized by maximizing the liquid-phase CO_2 concentration ($[CO_2]_l$).

- **Reaction Condition 3: 383 K (110 °C) < T < 423 K (150 °C) and $P_{c,mix\ CO_2/DMC} < P < P_{c,mix\ system}$.** Shown schematically in **Figure 7-3c**, reactions can proceed in two phases and at the interface separating them. With DMC partitioned to the CO_2 phase, the remaining amine-rich phase was now lower in CO_2 concentration. Due to the lack of amine solubility in the CO_2-rich phase, it was likely that the carbamation reaction took place at the interface.

- **Reaction Condition 4: 383 K (110 °C) < T < 423 K (150 °C) and $P > P_{c,mix\ system}$.** Shown schematically in **Figure 7-3d**, all reactions proceeded in a single, homogeneous phase.

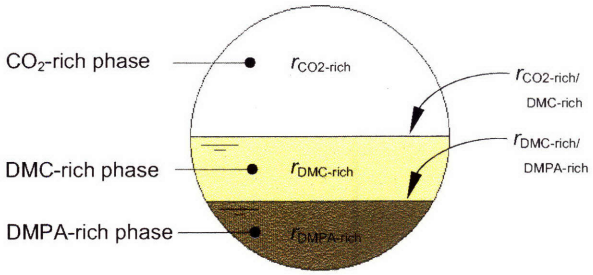

Reaction Condition 1:
373 K (100 °C)
$P < P_{c,mix\ CO_2\ /\ DMC}$

- $[CO_2]_{DMC\text{-rich}} > [CO_2]_{CO2\text{-rich}}$ and $[CO_2]_{DMPA\text{-rich}}$
- $[DMC]_{DMC\text{-rich}} > [DMC]_{CO2\text{-rich}}$ and $[DMC]_{DMPA\text{-rich}}$
- $[DMPA]_{DMPA\text{-rich}} > [DMPA]_{CO2\text{-rich}}$ and $[DMPA]_{DMC\text{-rich}}$

(a)

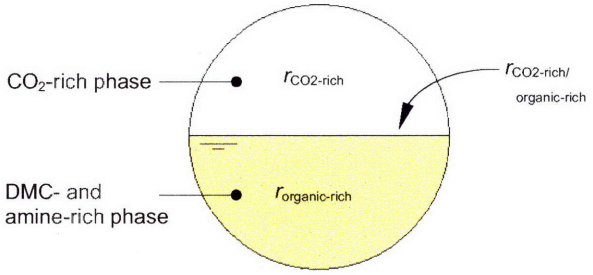

Reaction Condition 2:
383 K (110 °C) < *T* < 423 K (150 °C)
$P < P_{c,mix\ CO_2\ /\ DMC}$

- $[CO_2]_{organic\text{-rich}} > [CO_2]_{CO2\text{-rich}}$
- $[DMC]_{organic\text{-rich}} > [DMC]_{CO2\text{-rich}}$
- $[DMPA]_{organic\text{-rich}} > [DMPA]_{CO2\text{-rich}}$

(b)

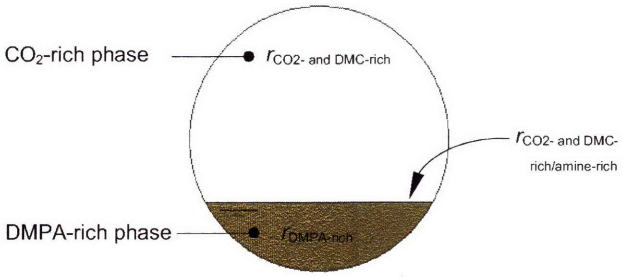

Reaction Condition 3:
383 K (110 °C) < *T* < 423 K (150 °C)
$P_{c,mix\ CO_2\ /\ DMC} < P < P_{c,mix\ system}$

- $[CO_2]_{CO2\text{-rich}} > [CO_2]_{DMPA\text{-rich}}$
- $[DMC]_{CO2\text{-rich}} > [DMC]_{DMPA\text{-rich}}$
- $[DMPA]_{DMPA\text{-rich}} > [DMPA]_{CO2\text{-rich}}$

(c)

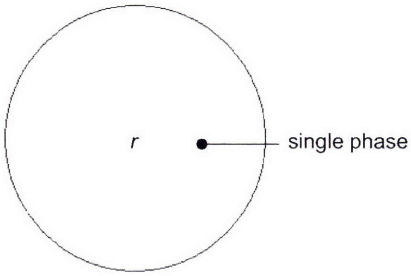

Reaction Condition 4:
383 K (110 °C) < *T* < 423 K (150 °C)
$P > P_{c,mix\ system}$

(d)

Figure 7-3. Schematic illustrations indicating the carbamation reaction phase as a function of temperature and pressure, where *r* denotes "reaction."

7.6. Reaction Performance

This section discusses the effects of several operating conditions on the performance of the model carbamation reaction. Carbamate yield (defined by equation **[7-4]**) at complete amine conversion was the metric used to evaluate reaction performance In all cases, the difference in molar yield from 100% was a mixture of byproducts **15** – **17**. Ratios of HPLC peak areas for the byproducts indicated an average product distribution of 6:2:1 **17:16:15**. A carbamate yield of 60 molar%, for example, indicates that based on a 100 mole amine charge, the crude reaction mixture contained approximately 60, 26, 9, 5 moles of carbamate, **17**, **16**, and **15**, respectively. Mass recovery was estimated to be > 95% for each run and carbamate yield was reproducible to ± 2%.

7.6.1. Pressure Effects

Similar to our initial screening work, a more detailed investigation of the model carbamation reaction revealed a strong relationship between carbamate selectivity and operating pressure. Reactions were performed with temperature held constant at 403 K (130 °C) and pressures ranging from 3 (40 psia) – 211 bar (3050 psia). Results of this study are presented in **Figure 7-4**. In the absence of CO_2, carbamate yield was approximately 54%. In the presence of CO_2, carbamate yield increased nearly linearly to as much as 75% with pressures up to ca. 131 bar (1900 psia). Qualitatively, the increase in yield with pressure was paralleled by an increase in the clarity of the crude reaction mixture (see **Figure 7-5**). Yield decreased to ca. 55% in the 131 bar < P < 270 bar (3915 psia) range before increasing to 80% at 404 bar (5860 psia).

Experimental observations indicated that for the 1.01 bar < P < ca. 131 bar (1900 psia) range, a biphasic reaction system was present and of the type shown in **Figure 7-2e** and **Figure 7-3b**. All reactions were performed dilute with respect to amine so that phase behavior would quantitatively resemble that of the CO_2/DMC system. To facilitate this discussion, VLE properties for the CO_2/DMC system calculated from correlations presented in **Chapter 6** are presented along with experimental yield data in **Table 7.1**. Increasing pressure at fixed temperature increases the liquid-phase concentration of CO_2 in the organic-rich reaction phase and therefore leads to increased carbamate selectivity (see equation **[7-23]'**).

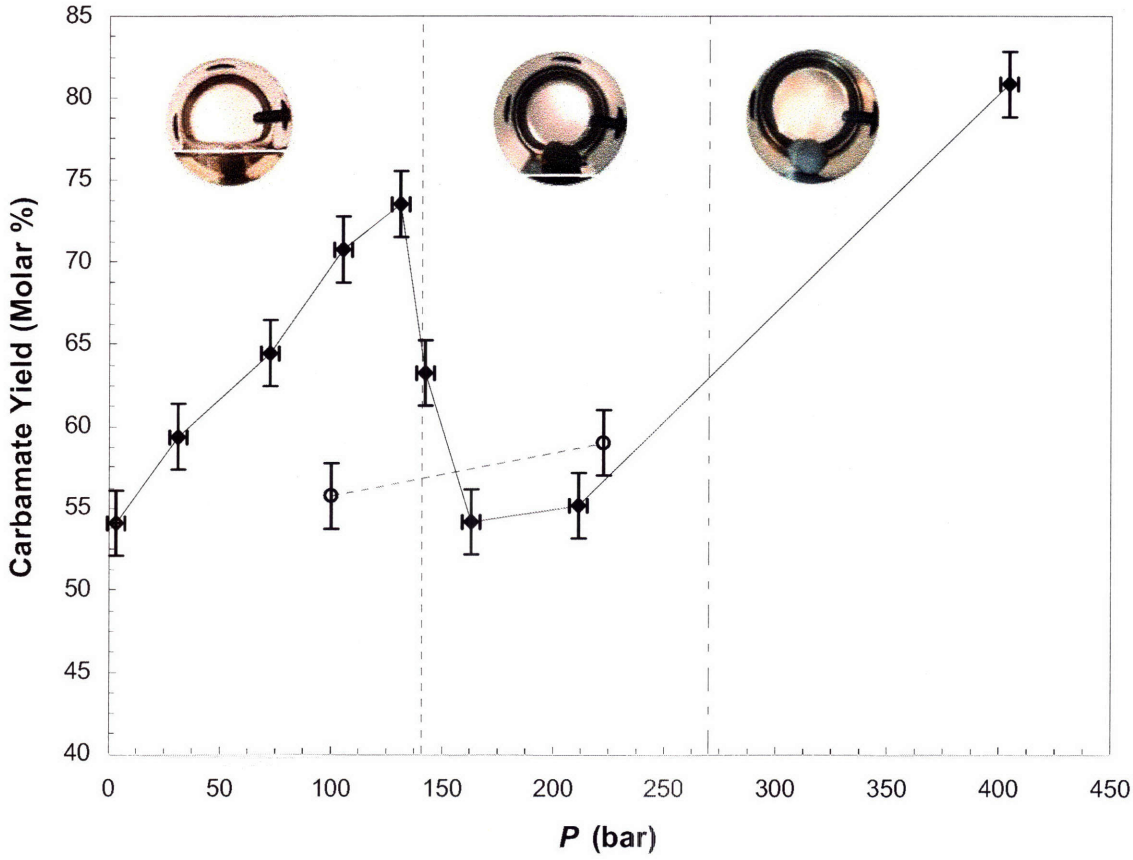

Figure 7-4. Carbamate yield at 403 K (130 °C) plotted as a function of pressure for the reaction of 3,4-dimethoxyphenethyl amine with carbon dioxide and dimethyl carbonate: reaction performed in the absence of CO_2 (□); using CO_2 (♦); using Argon (○). Experimental mixture critical point of the CO_2/DMC system (- - -) and entire reaction system (– - –) at 403 K. The solid line is used to guide the eye and no physical basis is intended. Reaction conditions: 6 mmol DMPA, 30 mmol (5 equiv.) DMC, 403 K (130 °C), 24 hr. All yields are reported at complete amine conversion and are reproducible within ± 2%. Pressures accurate to ± 3 bar; error bars shown for *P* instead correspond to the initial and final pressures of the reaction.

Increased operating pressure also leads to increased liquid-phase volume expansion, which has the effect of diluting components that diminish the solubility of CO_2 within this phase (i.e., both the liquid-phase mole fractions and concentrations of MeOH and DMPA are decreased and $[CO_2]_l$ increases, see **Section 6.8**). Increasing pressure also decreases liquid-phase viscosity and surface tension, which in turn increases convective transport rate of CO_2

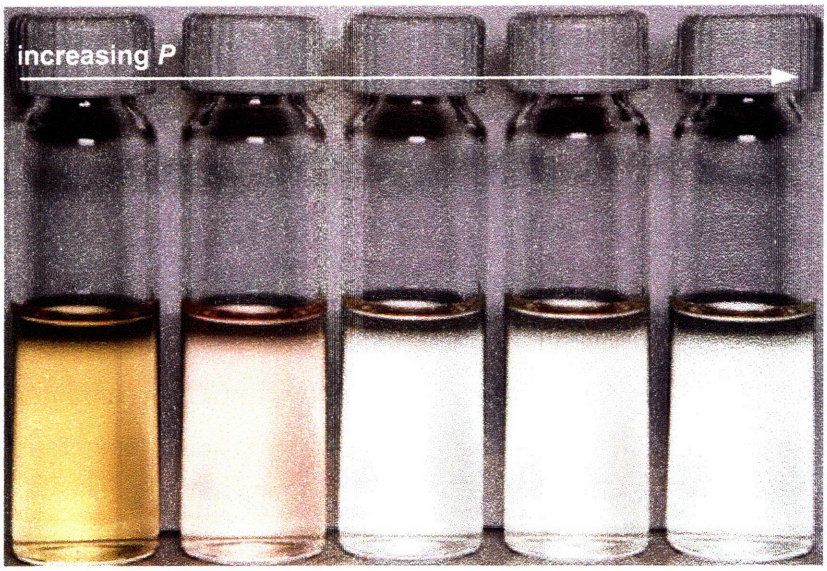

Figure 7-5. Photographs of the crude reaction mixture for the reaction of 3,4-dimethoxyphenethyl amine with carbon dioxide and dimethyl carbonate. Samples correspond to the first five data points of **Figure 7-4** and were diluted identically.

Table 7-1. Yield and phase equilibria data for the reaction of reaction of 3,4-dimethoxyphenethyl amine with carbon dioxide and dimethyl carbonate for various pressures at 403 K (130 °C).

P [a]	Yield [b]	$x_{CO_2, calc}$ [c]	$y_{CO_2, calc}$ [c]	$[CO_2]_l$ [d]	$[DMC]_l$ [d]	$\frac{\Delta V}{V^0}$ [e]	$[DMPA]_{l,l}$ [f]
bar	**%**			**M**		**%**	**M**
ca. 3 [g]	54			n/a			
31	59	0.1543	0.8647	1.27	8.84	19	1.44
72	64	0.3768	0.9110	4.66	7.05	31	1.30
105	71	0.5391	0.9090	7.14	5.74	51	1.13
131	73	0.6653	0.8917	9.07	4.72	91	0.89
142	63						
163	54			n/a			
211	55						
404 [h]	81						

$P_{c,mix\ CO_2/DMC}$ [i]	$x_{CO_2, max, calc}$	$[CO_2]_{l, max}$	$[DMC]_{l, min}$	$\frac{\Delta V}{V^0}_{max}$
bar		**M**		**%**
141	0.8317	11.61	3.38	311

[a] average reaction P; [b] yield by HPLC; [c] RK-Aspen EOS-calculated value; [d] from equation **(6-38)**; [e] from equation **(6-41)**; [f] initial liquid-phase concentration of DMPA calculated from $\underline{V}^0$ = 3.5 mL (volume of DMPA and DMC charged initially) and the volume expansion predictions at each pressure; [h] yield corrected by by ^{1}H NMR based on 50% amine conversion; [i] experimental value.

from the CO_2-rich to the organic-rich phase. This increase in transport rate would help maintain the liquid-phase equilibrium CO_2 concentration during the course of the reaction. Finally, it may also be possible that the change in reaction-phase polarity with the increase of CO_2-content preferentially favors carbamation over alkylation pathways via transition state free energy changes discussed in **Section 1.4.1**.

Surprisingly, modest carbamate yields were obtained even in the absence of CO_2. In addition to the amine acylation mechanism being partially at play, carbamate formation in this case may have also occurred from reaction of the amine with CO_2 evolved from the undesired alkylation pathways. Also noteworthy is how carbamate yield does not increase linearly with $[CO_2]_l$, as the selectivity expression predicts, further suggesting that solvation effects are at play.

For pressures larger than ca. 140 bar, dimethyl carbonate partitioned to the CO_2-rich phase (verified visually) and resulted in a biphasic reaction system of the type shown in **Figure 7-2d** and **Figure 7-3c**. The partition pressure at this condition coincides with the experimentally-determined mixture critical pressure of the CO_2/DMC system, indicating that experiments were indeed run dilute enough in amine to exhibit phase behavior properties of the CO_2/DMC system. Under these conditions, the liquid-phase concentration of $[CO_2]_l$ diminishes with the phase partitioning of DMC and the carbamation reaction is subsequently limited to the interface. Calculations indicated that the solubility of CO_2 in the polar, amine-rich liquid phase would be lower than that of a DMC-rich liquid phase (see **Section 6.8.2**). Crudely speaking, DMC acted like as a 'CO_2-sponge'; when DMC was removed from the amine-rich liquid phase, CO_2 was removed along with it. We therefore attribute the decrease in carbamate selectivity under these conditions to the decrease in CO_2 available to the amine (i.e., decreased concentration and phase segregation).

A reaction was also performed in the vicinity of the $P_{c,mix\ CO_2/DMC}$ such that the pressure increase typically observed in a reactions would increase the system pressure beyond the $P_{c,mix\ CO_2/DMC}$. As expected, an intermediate yield between a reaction at $P < P_{c,mix\ CO_2/DMC}$ and $P > P_{c,mix\ CO_2/DMC}$ was obtained. At $P > P_{c,mix\ system}$, all diffusion limitations disappeared and the carbamate reaction proceeded in a homogeneous reaction medium that resulted in high selectivity, but at the expense of longer reaction times (e.g., amine conversion in 24 hours = 50%). At 404 bar and 403 K, $[CO_2]$ = ca. 15 M, which is significantly higher than the $[CO_2]_{l,max}$ at these conditions.

Finally, to distinguish among pressure and phase behavior effects, Argon was substituted for carbon dioxide and carbamation reactions were performed at pressures both lower and higher than $P_{c,mix\,CO_2/DMC}$. No noticeable change in selectivity was observed, suggesting that phase behavior was the controlling factor.

7.6.2. Temperature Effects

Carbamation reaction temperature was varied between 373 K (100 °C) – 423 K (150 °C) with pressure held constant at 105 bar (1515 psia). Results of this study are presented in **Figure 7-6** and **Table 7-2**. Phase behavior for the 373 K (100 °C) run was triphasic (see **Figure 7-2c** and **Figure 7-3a**) and biphasic for the 373 K (100 °C) and 373 K (100 °C) runs (see **Figure 7-2e** and **Figure 7-3b**). Carbamate yield increased significantly with a decrease in reaction of temperature at the expense of increased reaction time. We attribute this increase in carbamate selectivity to several factors. First, at identical pressures, $[CO_2]_l$ increases with decreased temperature. Second, volume expansion is larger at lower temperatures, thereby diluting byproducts that decrease the liquid-phase CO_2 absorption to a larger extent. Third, carbamic salts are more stable at lower temperatures (see **Section 4.2**), which may result in the increase of the carbamation reaction rate relative to competitive byproduct formation rates. To distinguish among phase behavior and kinetic effects, we compared runs on of different temperatures on a comparable $[CO_2]_l$ basis and found that carbamate selectivity remained lower at higher temperatures. Compare, for example, the 403 K (130 °C) and 72 bar (1050 psia) run listed in **Table 7-1** with the 423 K (150 °C) and 105 bar (1515 psia) run listed in **Table 7-2**. Even with at lower $[CO_2]_l$ (4.66 vs. 6.22 M), the lower temperature run affords a higher carbamate yield. Even more noteworthy is how a better yield was obtained for the mass-transport limited triphasic mixture at 373 K (100 °C).

Higher yields at lower temperatures can also be ascribed to decreased methylation rates due to DMC acting more as an acylating agent at these conditions (Tundo et al., 2002, 2005, and 2007; Selva et al., 2006; Aresta et al., 1991):

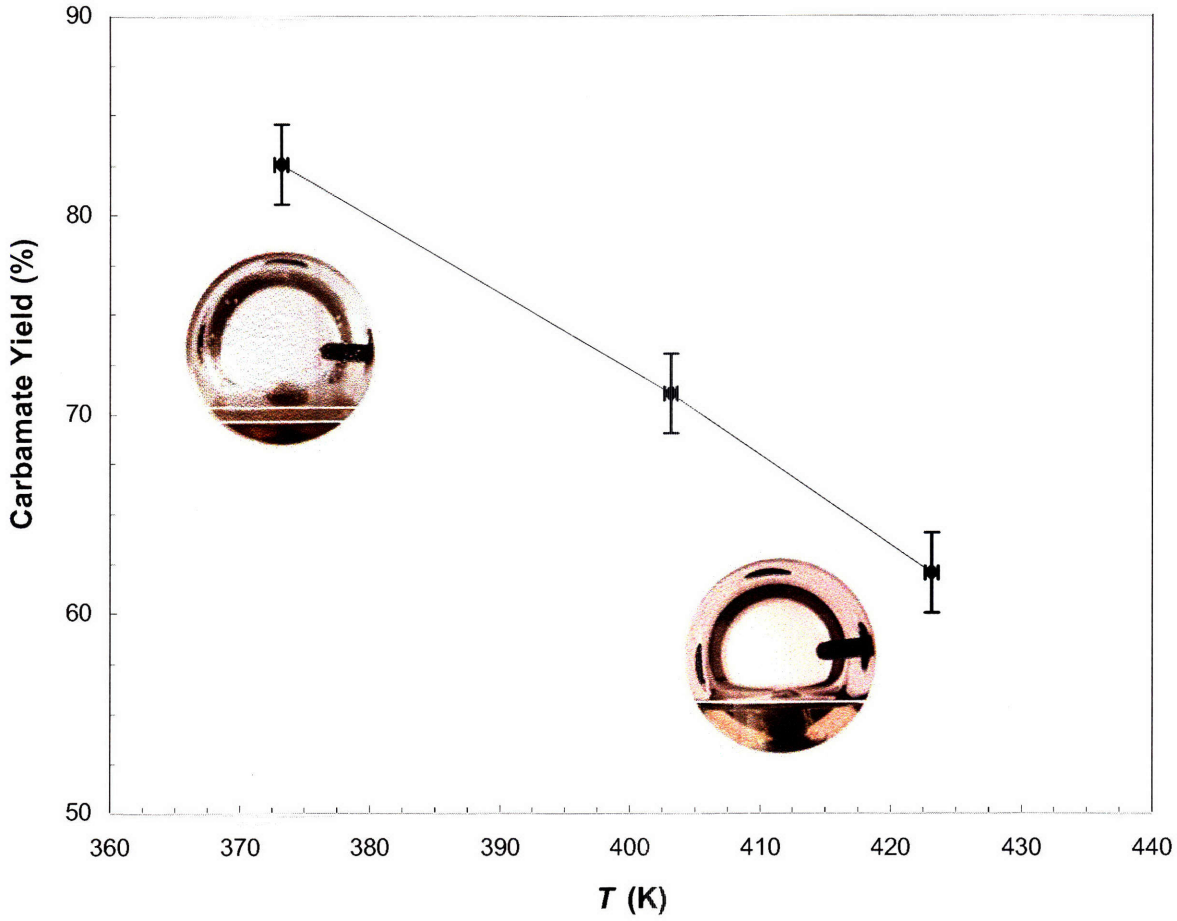

Figure 7-6. Carbamate yield plotted as a function of temperature for the reaction of 3,4-dimethoxyphenethyl amine with carbon dioxide and dimethyl carbonate. The solid line is used to guide the eye and no physical basis is intended. Reaction conditions: 6 mmol DMPA, 30 mmol (5 equiv.) DMC, 105 bar (1515 psia), 24 hr for 403 K (100 °C) and 423 K (150 °C) runs and 96 hr for 373 K (100 °C) run. All yields are reported at complete amine conversion and are reproducible within ± 2%. Temperature accurate to ± 0.5 °C.

Table 7-2. Yield and phase equilibria data for the reaction of reaction of 3,4-dimethoxyphenethyl amine with carbon dioxide and dimethyl carbonate for various temperatures at 105 bar (1515 psia).

T	Yield[a]	$x_{CO_2,calc}$[b]	$y_{CO_2,calc}$[b]	$[CO_2]_l$[c]	$[DMC]_l$[c]	$\frac{\Delta V}{V^0}$[d]	$[DMPA]_{l,l}$[e]
K (°C)	%			M		%	M
373 (100)	83	0.6633	0.9501	9.04	4.74	90	n/a[f]
403 (130)	71	0.5391	0.9090	7.14	5.74	51	1.13
423 (150)	62	0.4790	0.8686	6.22	6.22	41	1.21

T	$P_{c,mix\,CO_2/DMC}$[g]	$x_{CO_2,max,calc}$	$[CO_2]_{l,max}$	$[DMC]_{l,min}$	$\left(\frac{\Delta V}{V^0}\right)_{max}$
K (°C)	bar		M		%
373 (100)	128	0.8906	12.51	2.90	536
403 (130)	141	0.8317	11.61	3.38	311
423 (150)	144	0.7857	10.91	3.75	211

[a] yield by HPLC; [b] RK-Aspen EOS-calculated value; [c] from equation **(6-38)**; [d] from equation **(6-41)**; [e] initial liquid-phase concentration of DMPA calculated from $\underline{V}^0$ = 3.5 mL (volume of DMPA and DMC charged) and the volume expansion predictions at each pressure; [f] n/a due to phase separation; [g] experimental value.

7.6.3. Composition Effects

Several carbamation reactions were performed with different initial amine concentrations at 403 K (130 °C) and 105 bar (1515 psig). Results are presented in **Figure 7-7** and **Table 7-3**. Carbamate yield increased significantly with an increase in dimethyl carbonate equivalents (i.e., decreasing amine concentration). The effect saturated at 7.5 equiv., with little gains in yield achieved for large increases in the amount of DMC employed. Increasing the amount of DMC employed dilutes the amount of amine and MeOH present in solution, thereby increasing $[CO_2]_l$ for each run. Lower amine and MeOH content in higher-equivalent runs also allows the solution to expand to a larger extent, further diluting their detrimental effects on carbamate selectivity (see **Section 6.8**). To further explore the effect of MeOH content on carbamate selectivity, an amine carbamation reaction was performed at identical conditions to that of the 5 equiv. run presented, but with 2.5 equiv. of methanol doped in the system. As shown by **Table 7-3**, a significant decrease in carbamate yield resulted. In addition to lowering $[CO_2]_l$, MeOH may also selectively solvate the (charged) carbamic salt relative to the transition state complex, thereby decreasing the reaction rate of the carbamation reaction relative to competitive byproduct formation pathways (Selva et al., 2005).

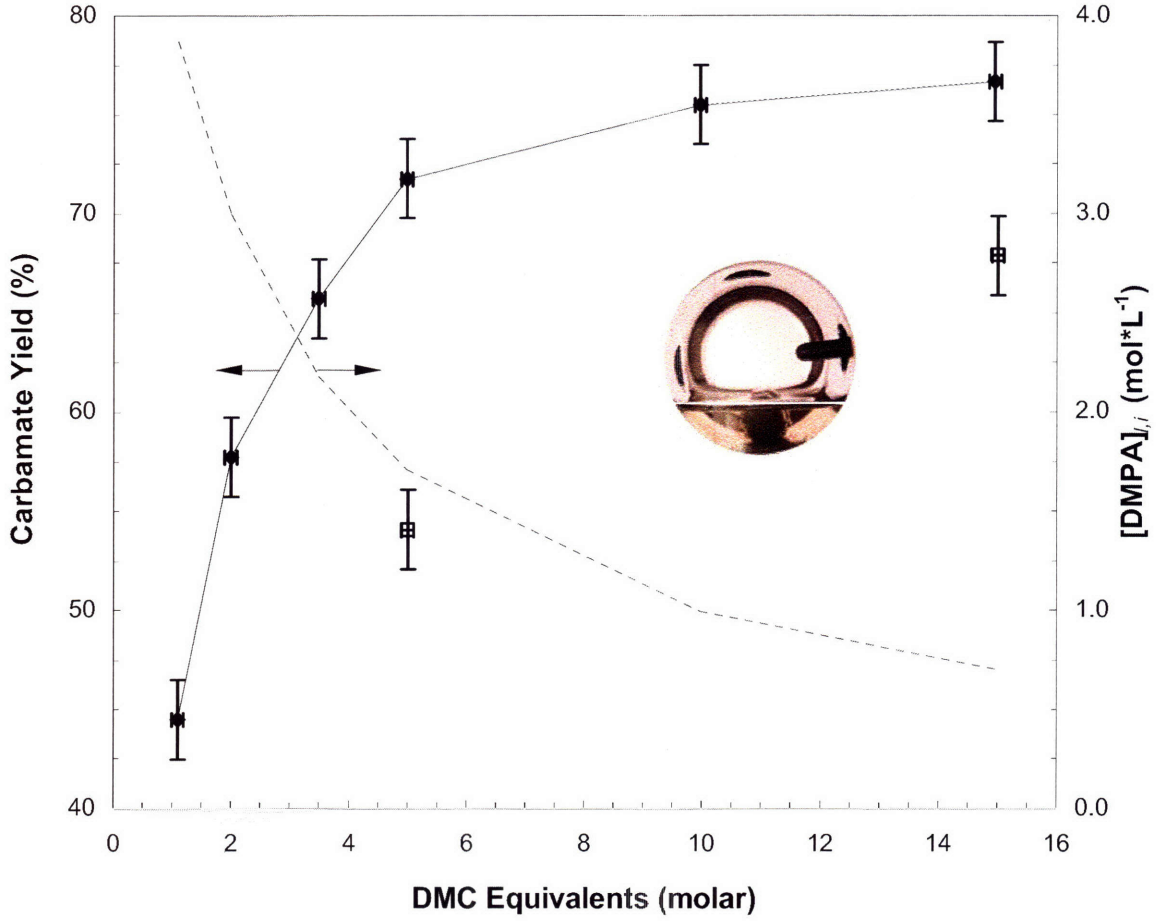

Figure 7-7. Carbamate yield plotted as a function of dimethyl carbonate equivalents for the reaction of 3,4-dimethoxyphenethyl amine with carbon dioxide and dimethyl carbonate: reaction performed in the absence of CO_2 (□); using CO_2 (♦). The solid line is used to guide the eye and no physical basis is intended. Reaction conditions: 6 mmol DMPA, 403 K (100 °C), 105 bar (1515 psia), 24 hr. All yields are reported at complete amine conversion and are reproducible within ± 2%. DMC equivalents are accurate to ± 1%.

It is also worth noting that the selectivity expression predicts a *decrease* in carbamate selectivity with decreasing amine concentration. Given that an *increase* in carbamate selectivity is observed, we therefore conclude that solvation and phase equilibrium effects are at play. In addition to an increase in $[CO_2]_l$, the impact of reduced amine concentration on selectivity may be offset by an increase in the rate constant of carbamic acid and salt formation (see equation **[7-23]'**) with increasing DMC equivalents.

Table 7-3. Yield data for the reaction of reaction of 3,4-dimethoxyphenethyl amine with carbon dioxide and dimethyl carbonate for various compositions 403 K (130 °C) and 105 bar (1515 psia).

DMC Equiv. molar	Yield [a] %	$\underline{V}^{0}$ [b] mL	$[DMPA]_{l,l}$ [c] M
1.1	44	1.52	3.87
2.0	58	1.97	2.99
3.5	66	2.71	2.17
5.0	72	3.46	1.71
5.0[d]	59	4.06	1.46
10.0	75	5.93	0.99
15.0	77	8.41	0.70

[a] yield by HPLC; [b] volume of DMPA and DMC charged; [c] initial liquid-phase concentration of DMPA calculated from $\underline{V}^{0}$; [d] with an additional 2.5 equiv. MeOH

7.7. Conclusions and Recommendations

In this chapter, we selected a model amine carbamation reaction involving 3,4-dimethoxyphenethylamine (DMPA), dimethyl carbonate (DMC), and carbon dioxide, and explored the effect of process operating conditions on reaction efficiency. We specifically identified phase behavior and measured carbamate yield and selectivity as functions of temperature, pressure, and starting material feed concentration. We also developed a governing kinetic selectivity expression that facilitated results interpretation and revealed conditions where carbamation would be preferred over undesired alkylation pathways. Specific highlights of this work include:

- The phase behavior of the reaction system varied significantly with process operating conditions:

  At 298 K (25 °C) < T < ca. 358 K (85 °C), the phase behavior was triphasic and consisted of an upper, lower-density CO_2-rich supercritical-like phase, a middle, intermediate-density DMC-rich liquid phase, and a lower, higher-density amine-rich solid phase.

  At 373 K (100 °C), the phase behavior was triphasic and consisted of an upper, lower-density CO_2-rich supercritical-like phase, a middle intermediate-density DMC-rich liquid phase, and a lower higher-density amine-rich liquid phase. Under these conditions, the carbamation reaction likely proceeded in the DMC-rich phase and/or the interface between the DMC-rich and amine-rich phases.

  At 383 K (110 °C) < T < 423 K (150 °C), the phase behavior was biphasic and consisted of an upper, lower-density CO_2-rich supercritical-like phase and a lower, higher-density organic-rich liquid phase. Under these conditions, the carbamation reaction likely proceeded in the organic-rich phase;

- Mechanistic studies with $^{13}CO_2$ at 403 K (130 °C) revealed a 35 molar% uptake of carbon dioxide into the carbamate product, indicating that (1) DMC acted primarily as an alkylating agent at these conditions, and (2) liquid-phase carbon dioxide concentration ($[CO_2]_l$) was a controlling factor of carbamate selectivity;

- At 403 K (130 °C), carbamate selectivity increased with increasing pressure up to the mixture critical point ($P_{c,mix}$). Increasing pressure for $P < P_{c,mix}$ increased $[CO_2]_l$, thereby increasing selectivity. Liquid-phase volume expansion ($\Delta \underline{V} / \underline{V}^0$) increased with increasing pressure and diluted the liquid-phase concentration of byproducts that were shown to reduce selectivity (e.g., methanol). Selectivity decreased at $P > P_{c,mix}$, as DMC partitioned from the organic-rich phase and resulted in a low-$[CO_2]_l$ amine-rich phase. Selectivity once again increased for $P > P_{c,mix\ system}$;
- At 105 bar (1515 psia), carbamate selectivity increased with decreasing temperature. Decreasing temperature increased $[CO_2]_l$ and $\Delta \underline{V} / \underline{V}^0$, thereby increasing selectivity for the reasons mentioned above. In addition, DMC is an acylating agent at reduced temperatures, which subsequently led to a decrease in the rate of competitive amine alkylation, and
- At 403 K (130 °C) and 105 bar (1515 psia), carbamate selectivity increased with an increase in the amount of dimethyl carbonate employed in the reaction. An increase in DMC content diluted the liquid-phase concentrations of the amine and other byproducts that reduced selectivity.

The following recommendations would lead to significant improvements on the work discussed in this chapter:

1. Revisit the Amine-CO_2 Reaction

- Unfortunately, we were unable to say for certain the exact composition of the amine-rich liquid phase observed during control experiments with carbon dioxide at elevated temperatures. *In situ* NMR and conductivity measurements would be helpful tools in identifying the form of amine present for changes in operating conditions (e.g., 'free' amine, carbamic acid, and/or carbamic salt form).

2. Build a Kinetic Model

- Measure phase-specific species concentrations as a function of reaction time and for changes in temperature, pressure, and starting material feed concentration and use

this information to create a kinetic model capable of predicting reaction rates as a function of process operating conditions.

- Perform $^{13}CO_2$ labeling studies for a range of temperatures and pressures in order to arrive at a more-complete understanding of the dual acylating/alkylating role of DMC.

3. Extend the Analysis to Include Dibenzyl Carbonate

- Perform similar rate, selectivity, and mechanistic studies using dibenzyl carbonate. Compared to DMC, it may be possible to obtain higher yields at milder operating conditions.

4. Apply Power Ultrasound

- Given the multi-phasic nature of the amine carbamation reaction, the use of power ultrasound may lead to enhanced reaction rates and possibly increased selectivity. In preliminary experiments, we were able to successfully generate CO_2/DMC microemulsions that remained turbid for ca. 15 minutes with a single pulse (see **Figure 7-8**).

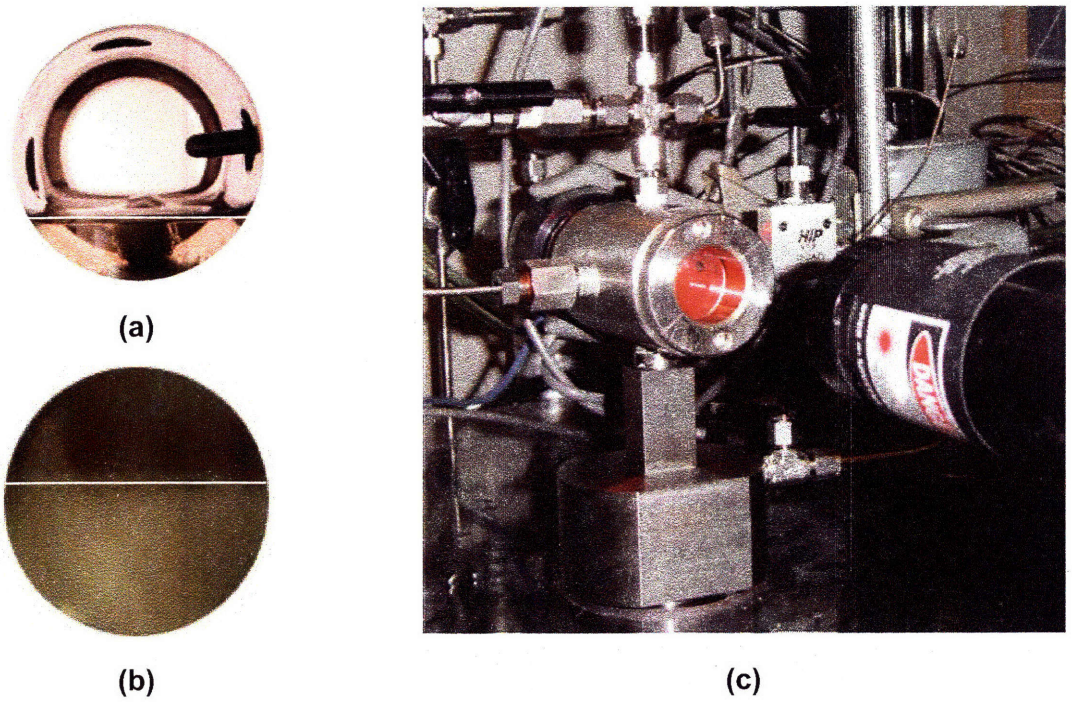

Figure 7-8. Application of power ultrasound to a biphasic carbon dioxide/dimethyl carbonate mixture: before ultrasound, an upper lower-density CO_2-rich supercritical-like phase and a lower, higher-density DMC-rich liquid phase (**a**); after ultrasound, an upper, lower-density CO_2-rich supercritical-like phase with dispersed DMC liquid droplets and a lower, higher-density DMC-rich liquid phase with dispersed CO_2 droplets (**b**); apparatus used for the determination of emulsion turbidity (**c**). Lines are drawn to indicate phase boundaries. Conditions: 130 °C, 100 bar, 20 kHz ultrasound frequency, 25% duty cycle (on a 1s cycle).

7.8. References

Aresta, M. and Quaranta, E. *Mechanistic Studies on the role of Carbon Dioxide in the Synthesis of Methylcarbamates from Amines and Dimethylcarbonate in the Presence of CO_2.* Tetrahedron, **1991**, 47, 9489-9502.

National Institute of Standards and Technology (NIST) Chemistry WebBook, Standard Reference Database Number 69, June 2005 Release, http://webbook.nist.gov/chemistry/.

Selva, M., Perosa, A., Tundo, P., and Brunelli, D. *Selective N,N-Dimethylation of Primary Aromatic Amines with Methyl Alkyl Carbonates in the Presence of Phosphonium Salts.* J. Org. Chem. **2006**, *71*, 5770-5773.

Selva, M., Tundo, P., Perosa, A., and Dall'Acqua, F. *Synthesis of Methyl Carbamates from Primary Aliphatic Amines and Dimethyl Carbonate in Supercritical CO_2: Effects of Pressure and Cosolvents and Chemoselectivity.* J. Org. Chem. **2005**, *70*, 2771-2777.

Tundo, P., Perosa, A., and Zecchini, F., Eds. *Methods and Reagents for Green Chemistry. An Introduction.* Wiley & Sons: New Jersey, **2007**.

Tundo, P., Bressanello, S., Loris, A., and Sathicq, G. *Direct Synthesis of N-Methylurethanes from Primary Amines with Dimethyl Carbonate.* Pure Appl. Chem., **2005**, *77*, 1719–1725.

Tundo, P. and Selva, M. *The Chemistry of Dimethyl Carbonate.* Acc. Chem. Res., **2002**, *35*, 706-716.

8. THE LAROCK INDOLE SYNTHESIS IN SUPERCRITICAL CARBON DIOXIDE

8.1. Motivation and Synthetic Methodology

The Larock indole synthesis is another representative synthetic method used to produce pharmacologically-significant nitrogen heterocycles (Larock et al., 1998). The Larock indole synthesis affords indoles (**3**) from the palladium-catalyzed coupling of an ortho-iodoaniline (**1**) and a disubstituted alkyne (**2**) and in the presence of base:

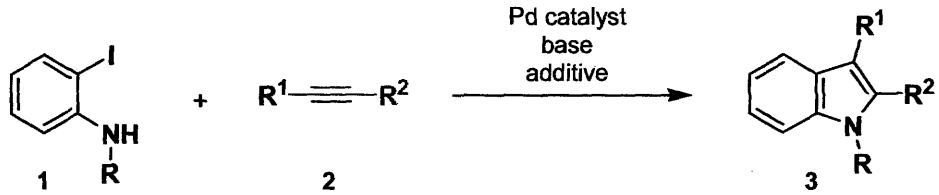

1 2 3 **(8-1)**

Like the Pictet-Spengler reaction discussion presented in **Chapter 5**, the Larock indole synthesis was studied extensively in conventional solvents, which offered insight for experimental design and comparison to reactions performed in CO_2-based media. Larock and coworkers (1998) found that indole yield in conventional solvents varied considerably with starting material functionality and the catalyst/additive choice. With the exception of a few cases, the authors reported exclusive selectivity towards the regioisomer in which the R^2 group is located adjacent to the indole nitrogen.

Using the Larock indole synthesis as a model transformation and building on the expertise of Professor Holmes' research group with palladium catalysis, our goal was to develop a robust reaction protocol to afford indoles in CO_2-based media. Unfortunately, our attempts at performing the Larock indole synthesis in supercritical carbon dioxide were not entirely successful. Due to Cambridge-MIT partnership program project deadlines and other priorities, we abandoned this chemistry prior to its optimization in order to pursue alternative transformations (see **Chapter 9**). In the following sections, we report on reaction and phase

behavior experiments that highlight critical areas to study in order to achieve this reaction in CO_2-based media.

8.2. Experimental Approach

All CO_2-based reactions and phase behavior studies presented in this chapter were performed using the experimental equipment and protocols described in **Section 5.3**. Reactions in conventional solvents were performed in the Danheiser group by Xiao Yin Mak.

8.3. Results and Discussion

Experimental results for the Larock indole synthesis study are summarized in **Table 8-1**. Before performing the reaction in $scCO_2$, we first explored the effects of catalyst, base, and additive loading on reaction efficiency in conventional solvents using 2-iodoaniline (**4**) and trimethylsilyl-hexyne (**7**) as a model substrates. Reaction of **4** and **7** at conditions reported by Larock and coworkers (1998) revealed a similar indole yield (compare entries 1 & 2), thereby validating our experimental procedures. Lithium chloride (LiCl) was used in place of tetrabutylammonium chloride (Bu_4NCl) for this experiment due to its availability at the time and because it had been reported by Larock and coworkers to give more reproducible results. Replacing dimethyl formamide (DMF) with toluene resulted in no measurable reaction (entry 3). The same was true when replacing the sodium acetate (NaOAc) base with triethylamine (Et_3N) and in the absence of LiCl (entry 4). Using a chlorine-based ligated palladium catalyst ($PdCl_2(PPh_3)_2$) in place of palladium(II) acetate ($Pd(OAc)_2$) eliminated the need for the addition of LiCl and ligand to the reaction system while still achieving modest indole yield (compare entries 4 & 5). Similar yields were obtained with substituting $Pd(OAc)_2$ with $PdCl_2(PPh_3)_2$ and adding ligand in the form of 1,1'-bis-(diphenylphosphino)-ferrocene (dppf) (compare entries 5 & 7). Running this reaction neat resulted in a significant decrease in indole yield due to incomplete starting material conversion, further emphasizing the importance of the role of solvent on improving reaction efficiency (compare entries 6 & 7). Although the authors reported that indole yield increased with the amount of alkyne employed in the reaction, we decided to run at reduced alkyne charges that still afforded modest indole yield.

Table 8-1. Yields obtained for Larock indole synthesis in supercritical carbon dioxide.

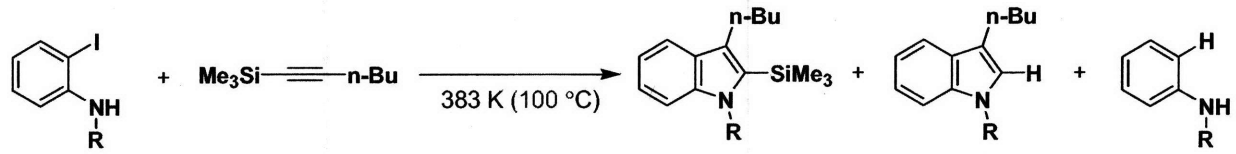

4 **R** = H
5 **R** = Me
6 **R** = $SiMe_3$

7

a

b

c

8a – c **R** = H
9a – c **R** = Me
10a – c **R** = $SiMe_3$

Entry	Solvent	*t* hr	R	7	Catalyst	Base (equiv.) [a]	Additive	Yield (%) [b] a:b:c
1 [c]	DMF	12	H	(5)	$Pd(OAc)_2$ (0.05)	NaOAc (5)	Bu_4NCl (1)	81:tr:tr
2 [c]	DMF	16.5	H	(5)	$Pd(OAc)_2$ (0.05)	NaOAc (5)	LiCl (1)	74:tr:tr
3	toluene	16.5	H	(5)	$Pd(OAc)_2$ (0.05)	NaOAc (5)	LiCl (1)	no rxn
4	toluene	14.5	H	(3)	$Pd(OAc)_2$ (0.1)	Et_3N (5)	—	no rxn
5	toluene	13.5	H	(3)	$PdCl_2(PPh_3)_2$ (0.1)	Et_3N (5)	—	64:tr:tr
6	neat	14.5	H	(10)	$Pd(OAc)_2$ (0.1)	Et_3N (5)	dppf (0.1)	25:tr:tr [d,e]
7	toluene	14.5	H	(3)	$Pd(OAc)_2$ (0.1)	Et_3N (5)	dppf (0.1)	65:tr:tr
8	CO_2 [f]	25.5	H	(3)	$Pd(OAc)_2$ (0.1)	Et_3N (5)	dppf (0.1)	22:15:15
9	toluene	15.5	Me	(3)	$PdCl_2(PPh_3)_2$ (0.05)	Et_3N (5)	—	67:14:tr
10	CO_2 [g]	13	Me	(3)	$PdCl_2(PPh_3)_2$ (0.05)	Et_3N (5)	—	20:10:33

[a] 1 equiv. = 2.5 mmol of amine **1**, all reactions performed at ca. 0.1 M amine; [b] isolated yield of products by column chromatography at complete conversion of amine **1** unless noted otherwise, "tr" refers to the trace detection of compounds **b** and **c**; [c] reaction performed at 373 K (100 °C); [d] incomplete conversion of amine **1**, balance was recovered starting material; [e] yield by ^{1}HNMR; [f] reaction performed at 161 bar (2315 psig); [g] reaction performed at 195 bar (2815 psig).

Replacing toluene with carbon dioxide for the reaction of 2-iodoaniline (**4**) and trimethylsilyl-hexyne (**7**) resulted in a significant decrease in indole **8a** yield (compare entries 7 & 8). Substantial amounts of desilylated indole product (**8b**) and deiodized amine (**8c**) were detected for this run. It is unclear whether or not the desilylated indole product (**8b**) was a result of desilylation of the alkyne prior to indole formation and/or decomposition of the desired indole product (**8a**). The use of 2-iodomethylaniline (**5**) in place of 2-iodoaniline also resulted in poor yields when compared to toluene (compare entries 9 & 10).

The tendency for nucleophilic amines of type **1** to react with carbon dioxide to form carbamic acid (see **Section 4.2)** may be the cause of the low yield. As shown by **Figure 8-1**,

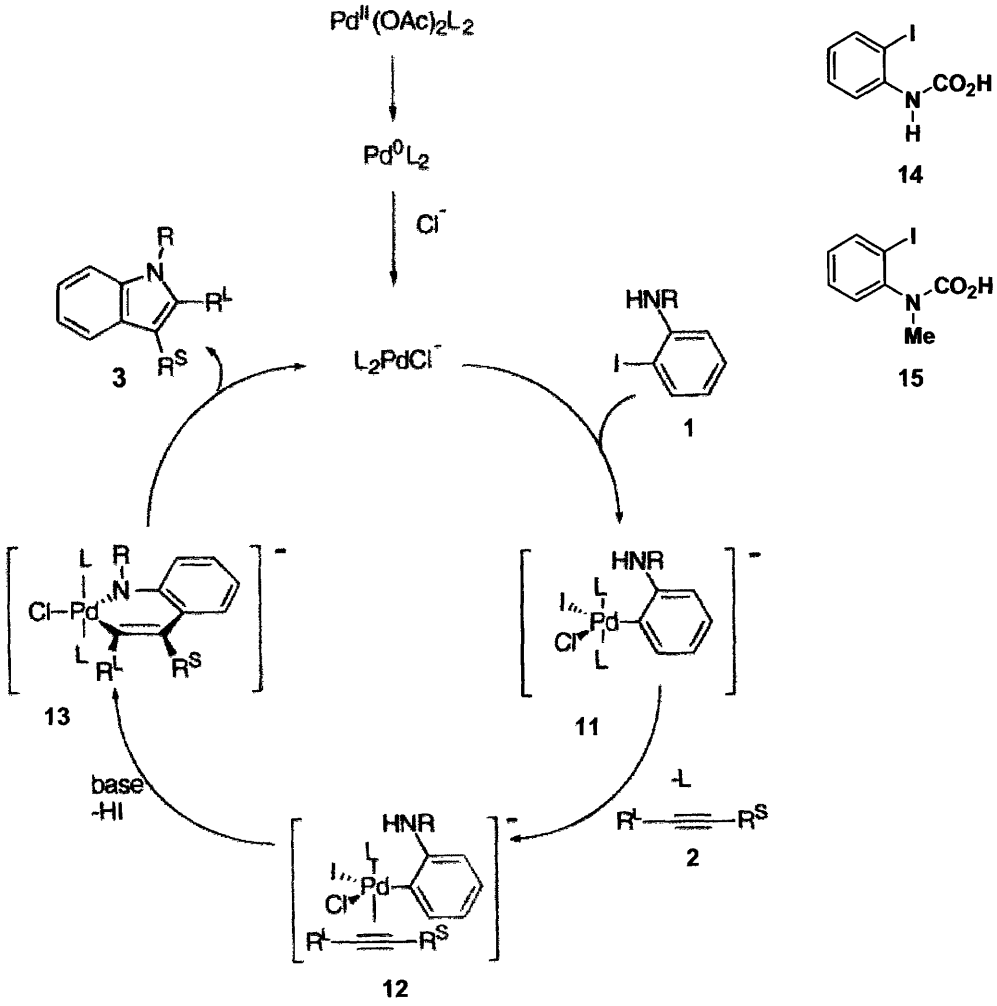

Figure 8-1. Proposed indole synthesis mechanism for the palladium-catalyzed reaction of ortho-iodoanilines and disubstituted alkynes (Larock et al., 1998).

Larock and coworkers (1998) propose that the synthesis of indoles occurs through several coordination complexes with ligated palladium (**11** – **13**). Formation of carbamic acid in the 2-iodoaniline case (**14**) could perhaps impede ring closure of intermediate **13** due to steric effects and/or decreased nitrogen nucleophilicity, thereby favoring deiodization mechanisms. In the case of 2-iodomethylaniline, formation of carbamic acid (**15**) could impede ring closure due to the lack of a requisite *N*-H bonding site in intermediate **12**. The formation of a dicarbamic acid in the 2-iodoaniline case would have a similar effect.

In addition to carbamic acid formation, the multi-phasic behavior of the reaction mixture in carbon dioxide may also account for the observed reduction in yield. In toluene, the Larock indole synthesis listed in **Table 8-1** (entries 7 and 9) are biphasic, consisting of an upper, lower-density liquid phase containing starting materials, and a lower, higher-density solid catalyst phase. In carbon dioxide, however, the reactions begin biphasic, consisting of an upper, supercritical-like CO_2-rich liquid phase containing starting materials (verified via control experiments) and a lower, higher-density solid catalyst phase, and soon transition to a triphasic system consisting of an upper, supercritical-like CO_2-rich liquid phase and a lower, higher-density organic-rich liquid phase with solid catalyst dispersed throughout the phase (see **Figure 8-2** and **Figure 8-3**). We suspect that the liquid phase formed during the CO_2-based reactions consists primarily of indole derivatives and possibly triethyl ammonium iodide (Et_3NI) generated from the reaction of the Et_3N with the iodine functionality of the amine (see **Figure 8-1**). The partitioning of starting materials across an additional phase in the CO_2-based experiments may impose mass-transport limitations that are detrimental to the desired indole formation reaction. Deiodinization of the amine, for example, may be accelerated by the partitioning of the amine and base from the CO_2-rich phase to the catalyst-containing liquid phase. It may also be possible for the alkyne and desired indole product to partition to phases where desilylation product formation pathways are preferred.

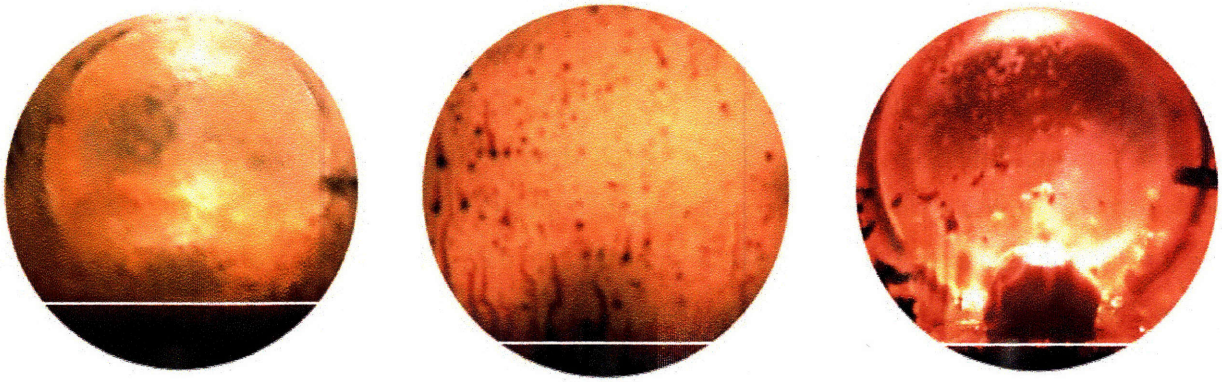

T = 298 K (25 °C)
P = 1.01 bar (15 psig)
t = 0 hr

(a)

T = 383 K (110 °C)
P = 161 bar (2315 psig)
$0.1 < t < 6$ hr

(b)

T = 383 K (110 °C)
P = 161 bar (2315 psig)
$6 < t < 25.5$ hr

(c)

Figure 8-2. Phase behavior observed during the Larock indole synthesis involving 2-iodoaniline and trimethylsilyl-hexyne: a liquid phase consisting of amine, alkyne, and base with solid catalyst and ligand dispersed throughout the phase **(a)**; an upper, lower-density CO_2-rich supercritical-like phase and a lower, higher-density solid catalyst and ligand phases **(b)**; an upper, lower-density CO_2-rich supercritical-like phase and a lower, higher-density organic-rich liquid phase with solid catalyst and ligand dispersed throughout **(c)**. The larger solid object visible in **(c)** is a magnetic stir bar. Reaction conditions: see entry 8 of **Table 8-1**. Lines are drawn to indicate phase boundaries.

T = 298 K (25 °C)
P = 1.01 bar (15 psig)
t = 0 hr

(a)

T = 383 K (110 °C)
P = 195 bar (2815 psig)
$0.1 < t < 6$ hr

(b)

T = 383 K (110 °C)
P = 195 bar (2815 psig)
$6 < t < 25.5$ hr

(c)

Figure 8-3. Phase behavior observed during the Larock indole synthesis involving 2-iodomethylaniline and trimethylsilyl-hexyne: a liquid phase consisting of amine, alkyne, and base with solid catalyst throughout the phase **(a)**; an upper, lower-density CO_2-rich supercritical-like phase and a lower, higher-density solid catalyst phase **(b)**; an upper, lower-density CO_2-rich supercritical-like phase and a lower, higher-density organic-rich liquid phase with solid catalyst dispersed throughout **(c)**. The larger solid object visible in all images is a magnetic stir bar. Reaction conditions: see entry 10 of **Table 8-1**. Lines are drawn to indicate phase boundaries.

As a side note, we observed another interesting phase behavior effect during this study that emphasizes the utility of carbon dioxide in separation processes. During solubility control experiments, we discovered a CO_2-based process that could be used to purify 2-iodoaniline (**4**). 2-iodoaniline was supplied as a brown crystalline solid comprised of large rod-shaped particles and agglomerates (see **Figure 8-4a**). At 298 K (25 °C) and $P > 140$ bar (2014 psig), the amine partitioned to the carbon dioxide phase, leaving behind an immiscible brown oil impurity that was responsible for the discoloration of the starting material. Reducing the pressure to the solubility limit ($P \approx 140$ bar [2014 psig]) resulted in the nucleation of white and significantly finer rod-shaped amine crystals (see **Figure 8-4b**). The melting point of the purified amine was much sharper (ca. 328 K [55 °C]) than the original starting material (ca. 321 – 325 K [48 – 52 °C]).

We should note that in this crude separation experiment, the purified amine precipitated on top of the impurity (which coated the bottom vessel surface) to form an amine/oil mixture. The sample shown in **Figure 8-4b** was therefore obtained by sampling the top portion of this mixture. Operating under continuous flow would overcome this complication; the CO_2/amine mixture can be transferred to a separate vessel where depressurization would afford the purified amine in the absence of the oil impurity.

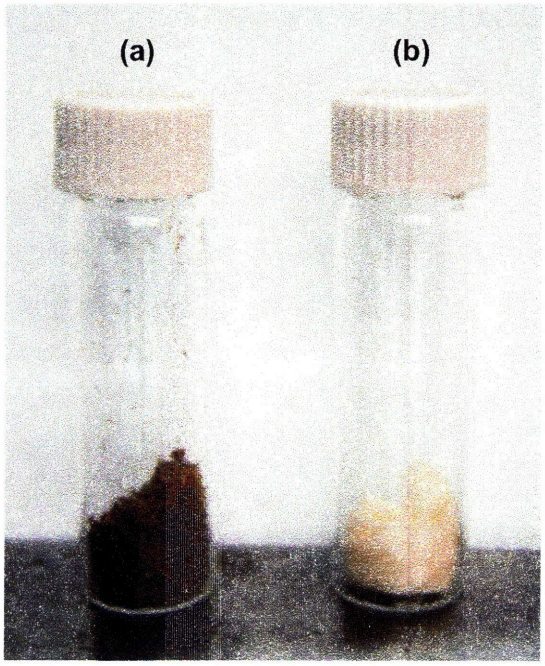

Figure 8-4. Photographs of 2-iodoaniline before **(a)** and after **(b)** purification using carbon dioxide.

8.4. Conclusions and Recommendations

In this chapter, we attempted to perform the Larock indole synthesis in carbon dioxide and found that yields and selectivities were significantly lower than when performed in conventional solvents. We postulated that the formation of carbamic acid and the multi-phasic nature of CO_2-based reactions may be responsible for the observed reduction in reaction efficiency. The following are recommendations for the development of the Larock indole synthesis in carbon dioxide-based media:

1. Characterize Byproduct Formation Pathways

- In separate control experiments, subject alkyne **7** and desired indole product **8a** to reaction conditions and analyze the resulting mixture for desilylation products (i.e., hexyne and byproduct **8b**, respectively). Desilylation can be avoided all together by using a more stable alkyne and/or one that does not contain silyl functionality. Exposure of 2-iodoaniline to reaction conditions in the absence of alkyne **7** may afford byproduct **8c**. Explore the effect of alkyne and base choice and concentrations on byproduct formation and reaction phase behavior.

2. Examine the Steric Inhibition of Carbamic Acid Formation

- The addition of bulkier *N*-protecting groups (e.g., t-Bu [see **Section 4.2**] or carbamate groups [see **Section 5.2**]) to 2-iodoaniline may suppress the formation of carbamic acid and possibly lead to increased indole yield and selectivity.

  Melanie Tsang, a member of Professor Holmes' research group on our CMI team, performed a reaction utilizing the previous recommendations and found a significant increase in desired indole yield:

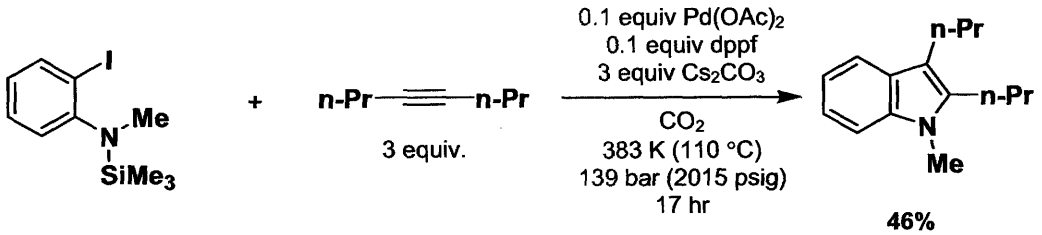

3. Explore the Effects of Phase Behavior

- Addition of co-solvents (e.g., ethyl acetate) or operating at higher densities (via a reduction of *T* and/or increase in *P*) may solubilize the liquid precipitate formed during CO_2-based reactions and possibly lead to increased reaction efficiency. Furthermore, the use of fluorinated ligands on the catalyst may enhance its solubility in CO_2 and increase the likelihood for a homogeneous reaction mixture.

8.5. References

Larock, R. C., Yum, E. K., and Refvik, M. D. *Synthesis of 2,3-Disubstituted Indoles via Palladium-Catalyzed Annulation of Internal Alkynes.* J. Org. Chem., **1998**, *63*, 7652-7662.

9. AMIDE AND LACTAM SYNTHESIS IN SUPERCRITICAL CARBON DIOXIDE

9.1. Motivation, Synthetic Methodology, and Variables Explored

Amides (R_2NCOR) are an important class of molecules that find wide-spread use in the pharmaceutical and fine chemical industries. In fact, 25% of known pharmaceuticals incorporate the carboxamide functional group (Ghose et al., 1999), including Eli Lilly's vasodilator Cialis® and Merck's statin Lipitor® (see **Figure 4.1**). Carey and workers (2006) recently reported that amide formation accounted for 8% of all reactions involved in the syntheses of drug candidates at Pfizer, GlaxoSmithKline, and AstraZeneca. In conventional solvents, amides are commonly formed from the reaction of amines with acylating agents (Montalbetti et al., 2005). These methods involve toxic and corrosive reagents and tend to generate large amounts of chemical waste due to their low atom-economy.

An attractive alternative to these standard methods for the synthesis of amides (**4**) involves the reaction of amines (**3**) with ketenes (**2**) generated *in situ* by the thermolysis of alkynyl ethers (**1**) (Ficini, 1954; Danheiser, 2006; Tidwell, 2006):

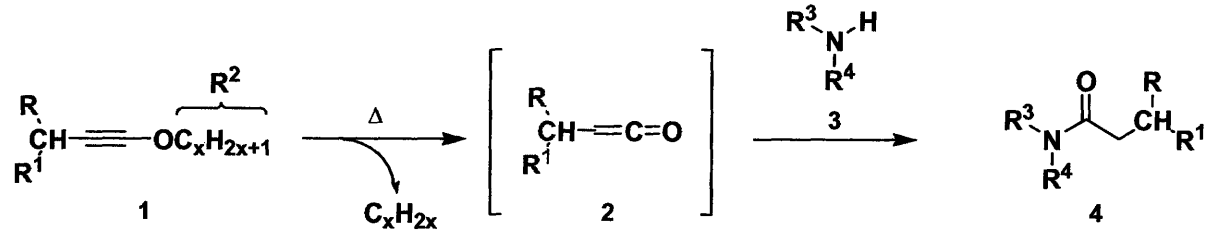

(9-1)

The proposed model reaction **(9-1)** has high atom-economy, with the only byproduct (in theory) being ethylene (R^2 = Et). In addition, the reaction requires activation by heating instead of the use of catalysts and other additives.

Lactams, or cyclic amides, (**6**) (e.g., Penicillin, see **Figure 4.1**) can be formed by the intramolecular variant of reaction **(9-1)** with aminoalkynyl ethers (**5**):

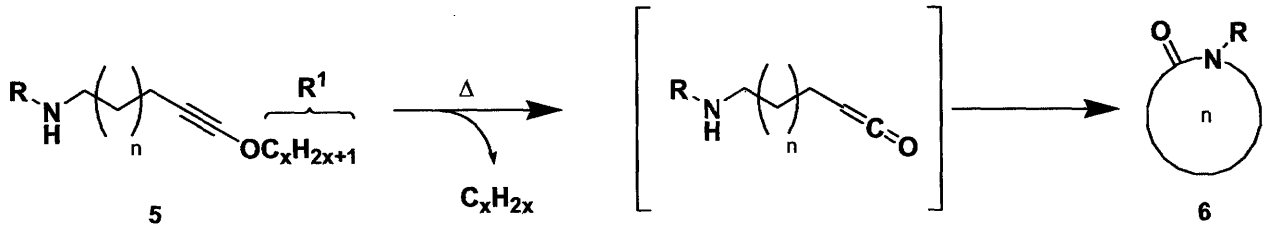

5 6

(9-2)

In this chapter, the performance and optimization of the proposed amide and lactam reactions in CO_2-based media are compared with the same reaction carried out in conventional solvents. Specifically, we explored reaction chemistry (including phase behavior, conversion, yield, and selectivity) by employing a variety of alkynyl ethers and amines over a wide range of process operating conditions (T, P, x_i, co-solvents).

9.2. Experimental Approach and Analytical Methods

Supercritical extraction-grade (99.9999% purity, Airgas) carbon dioxide and 99.5+% purity reagents were used for all reactions discussed in this chapter. Many of the amines were commercially available and were purified before use by Xiao Yin Mak and Julia Robinson of. Danheiser's synthetic organic chemistry group at MIT. All other reagents were synthesized by either Mak or Robinson. Amide formation experiments were performed using the 25-mL view cells (**VC-1** and **VC-2**, often in parallel) and operating/reaction work-up procedures described in **Section 3.2.3**. Lactam formation experiments were performed using the 50-mL view cell (**VC-3**). Actual vessel volumes were calculated via the volume determination unit (see **Section 3.3.3**) and were 34.1 ± 0.3 mL for **VC-1** and 31.8 ± 0.3 mL for **VC-2**, and 54.1 ± 0.4 mL for **VC-3**.

In a typical experiment, amine and alkynyl ether (or just the aminoalkynyl ether for lactam synthesis runs) were loaded to the reactor simultaneously at ambient conditions in a solution of dichloromethane and then concentrated by vacuum evaporation of the solvent. This method was used to deliver non-volatile specially-synthesized reagents; volatile amines were instead added neat after the loading and concentration of alkynyl ethers. Following all loading

and concentration steps, the vessel headspace was purged using gaseous argon (99.9999% purity, Airgas). Carbon dioxide was added until a pressure of ca. 35 bar (515 psia) was reached and the reaction mixture was heated to the desired temperature. Additional CO_2 was added while the vessel heated and was topped off at the desired pressure once the temperature reached the set point. It typically took ca. 10 min to reach reaction conditions, which was significantly shorter than the time required for complete conversion of starting materials. After the desired reaction time, the reactor was cooled to ambient *T* via placement on a bed of ice. Depending on the operating pressure for a given run, CO_2 would exist in either its liquid or gaseous state after cooling (e.g., high-pressure runs yielded $P >$ the vapor pressure of CO_2 at ambient *T*, thus making it a liquid). The reactor was vented by sparging the carbon dioxide into dichloromethane. All product-contacted vessel and fitting surfaces were thoroughly rinsed with dichloromethane and combined with the sparge solvent. All reactions in conventional solvents were performed by either Xiao Yin Mak or Julia Robinson in the Danheiser Laboratory. Unless noted otherwise, reported yields refer to isolated values obtained by column chromatography. Details regarding reagent preparation and product isolation are likely to be documented in the doctoral thesis of Mak (in preparation).

High-pressure liquid chromatography (HPLC) was used as a supplement to isolated yield data for the lactam synthesis study given difficulties encountered with byproduct co-elution during column chromatography. Samples of the lactam and dilactam (the only characterizable reaction products) were isolated and purified from the crude model reaction mixture via column chromatography by Mak. Using these purified compounds, an HPLC analytical method was developed that allowed for the direct quantification of products from the crude reaction mixture. Detailed operating instructions for the HPLC system are given in **Section 3.3.5**. Due the mildly polar nature of the reaction products, normal-phase column chromatography was employed, which utilized a silica column and a non-polar mobile phase. Excellent peak resolution was obtained when using an isocratic mobile phase flow of 2.5:97.5 vol% *i*-propanol:hexanes at 1 $mL \cdot min^{-1}$. The UV/Vis absorbance detector was set to 254 nm and the autosampler injection volume to 50 μL. A sample chromatogram with retention times (r_t) noted for the reaction lactam and dilactam products is shown in **Figure 9-1**. The dichloromethane injection solvent resolved

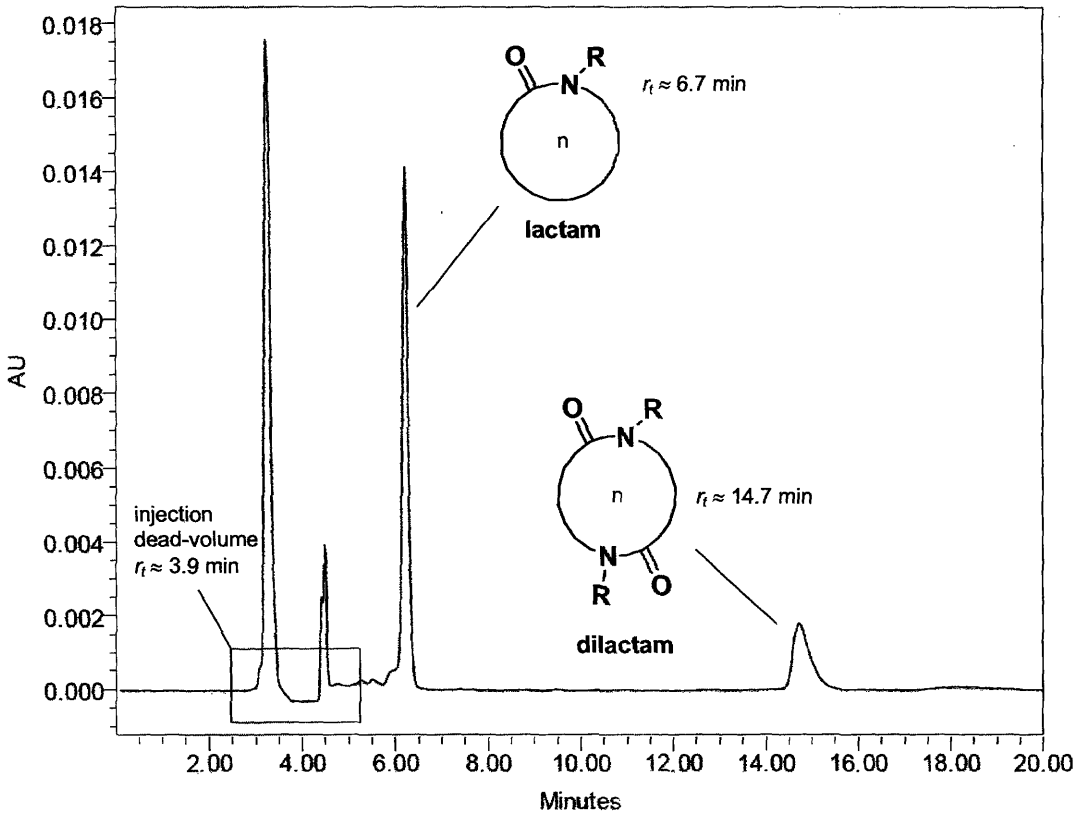

Figure 9-1. Sample high-pressure liquid chromatography chromatogram indicating the resolution of lactam synthesis reaction products.

at an r_t equal to the residence time of the column. Higher-molecular weight byproducts did not resolve when using this method, suggesting that they may have adhered to the guard column.

Product yields for each run were determined by injecting a sample of known total volume into the HPLC system and determining the concentration via a linear calibration curve made from the purified standards:

$$[\text{product}]_i = c_{i,1}(\text{HPLC Peak Area}) + c_{i,0} \qquad \textbf{(9-3)}$$

where $c_{i,1}$ and c_{i0} are the slopes and intercepts of the product-specific calibration curves, respectively. Lactam and dilactam standards were prepared by diluting known masses into various-sized volumetric flasks. The number of moles product (n_{product}) in the HPLC sample were found from:

$$n_{\text{product}_i} = \underline{V}_w [\text{product}]_i \qquad \textbf{(9-4)}$$

where $\underline{V}_w$ was the total volume of solvent used to wash the reactor (usually 100 mL). Wash and autosampler injection volumes were set so that (1) samples were within the calibration range, (2) the signal-to-noise ratio (i.e., base-line-to-peak height) was minimized, and (3) Beer's law was obeyed (i.e., AU < 1.0 for all injections). Yield was subsequently calculated from:

$$\text{Product Yield} = \frac{n_{\text{product}_i}}{n_{0,\text{amine}}} \times 100 \qquad \textbf{(9-5)}$$

where $n_{0,\text{amine}}$ is initial amine charge.

9.3. Amide Synthesis

9.3.1. Model Reaction

In order to explore the scope of the proposed amide synthesis protocol, we first needed to understand the effects of process operating conditions on reaction performance. 1-ethoxy-oct-1-yne (**6**) and *N*-butylbenzylamine (**7**) were selected as model reactants for several reasons:

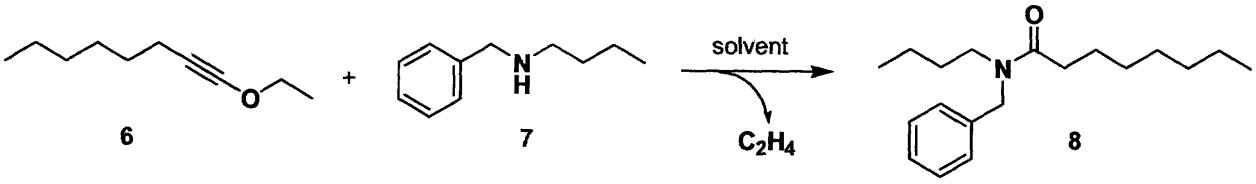

(9-6)

- ethoxy-substituted alkynyl ethers are thermally stable at ambient conditions, which limits their decomposition prior to reaction initiation during vessel loading, heating, and pressurization steps;
- based on our experience with the amine carbamation and Pictet-Spengler reactions (see **Chapters 5** and **7**) and from reports in the literature (see **Chapter 4**), bulky *N*-substituents suppressed the possibly-detrimental reaction of amines with CO_2, and
- long-chain alkyl groups on the ether and amine mimicked the functionality of the aminoalkynyl ethers used as starting materials for the synthesis of lactams.

At ambient conditions, alkynyl ether **6** and amine **7** were liquids and amide **8** a white solid.

9.3.2. Process Optimization and Phase Behavior Considerations

Discussed from a quantum chemical perspective in **Chapter 10**, the desired ketene amination reaction competes with ketene + ketene and ketene + alkynyl ether cycloaddition reactions. The facility of amines to react with carbon dioxide to form carbamic acids and salts also poses a potential barrier towards the successful development of this reaction in CO_2-based media. Carbamic acids formed from secondary amines, for example, could possibly block the desired addition of ketene to the amine (i.e., no free *N*-H site available for the transformation), and leads to (or enhances) byproduct formation. Phase behavior may also impact the course of the reaction. For instance, partitioning of the ketene to a concentrated phase lacking amine may promote the undesired cycloaddition reactions.

Interested in identifying operating conditions to avoid phase separation, we performed vapor-liquid equilibria (VLE) calculations for binary carbon dioxide and reaction system components using the RK-Aspen EOS and procedures described in **Chapter 6**. Due to their unavailability in the literature, pure-component properties were calculated via group contributions method (see **Section 6.7**). Shown in **Figure 9-2**, VLE calculations suggest that at constant temperature, the pressure required to arrive at a mono-phasic solution for each component (the mixture critical pressure, $P_{c,mix}$) varies in the order amide **8** > amine **7** > alkynyl ether **6** > ketene. These values were consistent with observations of decreased solubility in CO_2 with increased molecular size. Surprisingly, calculated $P_{c,mix}$ values were within ± 10 bar of the experimental values determined for the alkynyl ether, amine, and the amide from solubility control experiments.

Assuming ideal solution behavior for a reaction performed dilute with respect to all non-CO_2 species, we would expect the phase behavior of behavior of the system to follow that of its comprising binaries. If this assumption holds, the mixture critical pressure of the entire system ($P_{c,mix\ system}$) should be less than or equal to that of the highest binary mixture critical pressure. In order to completely solubilize the starting materials in CO_2, a $P > P_{c,mix\ CO2/amine}$ would be needed. Likewise, to completely solubilize all components, a $P > P_{c,mix\ CO2/amide}$ would be required. Although assuming ideal solution behavior is clearly a rough approximation, it provides a first-order estimate of appropriate operating conditions for mono-phasic behavior. More rigorous approaches involve the *T*-*P*-x_i VLE modeling of the 5-component mixture (see **Section 6.8**).

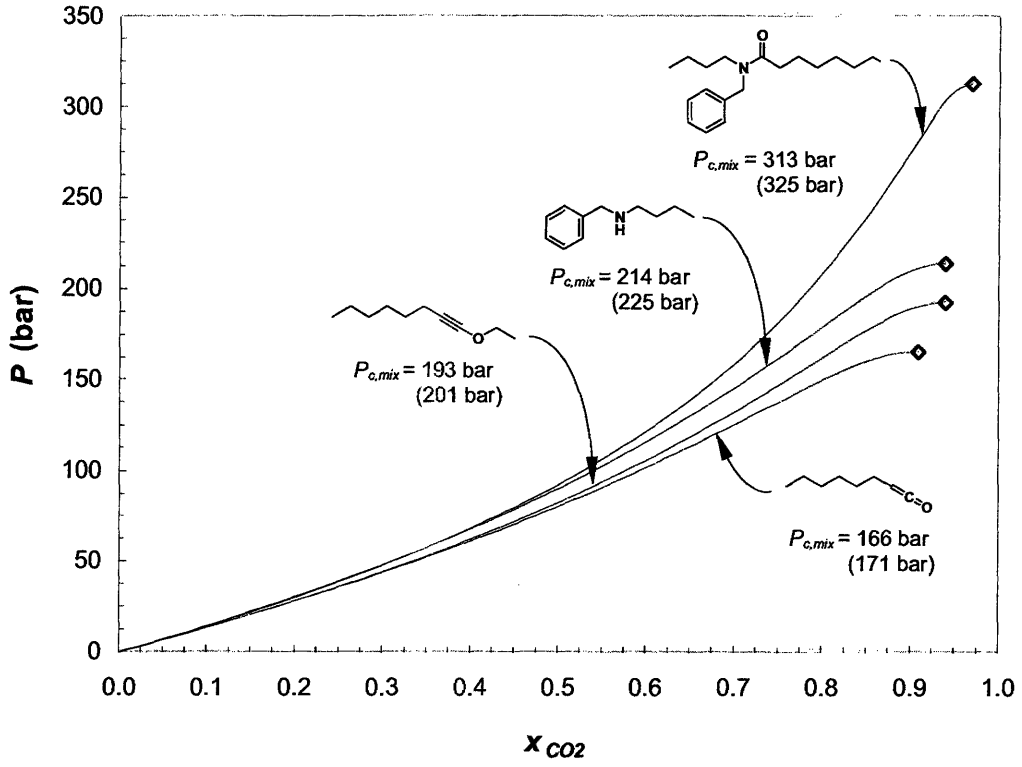

Figure 9-2. Vapor-liquid equilibrium predictions for the model amide formation reaction at 393 K (120 °C) and 403 K (130 °C): mixture critical pressures for each CO_2/species binary (◊). Numbers in parentheses are mixture critical pressure values at 403 K (130 °C).

Equipped with VLE predictions, we performed the reaction at several pressures and at temperatures shown to arrive at complete starting material conversion in conventional solvents within 24 hr. Results of our optimization experiments are presented in **Table 9-1**. Excellent yields of amide were obtained using this method and were comparable to those obtained in conventional solvents (compare entries 1 & 4). The reaction was slower in CO_2, requiring slightly larger temperatures to reach complete conversion within 24 hours (compare entries 2 & 3 with 1).

Photographs of the reaction mixture were taken during the course of the reaction and are presented in **Figure 9-3**. Descriptions of the phase behavior types are given in **Table 9-2**. In line with our initial hypothesis of ideal solution behavior, the pressures required to completely solubilize the starting materials were close to predicted values of $P_{c,mix\ CO2/amine}$ and also increased with increasing temperature (compare entries 2 & 3).

Table 9-1. Optimization of the model amide formation reaction.

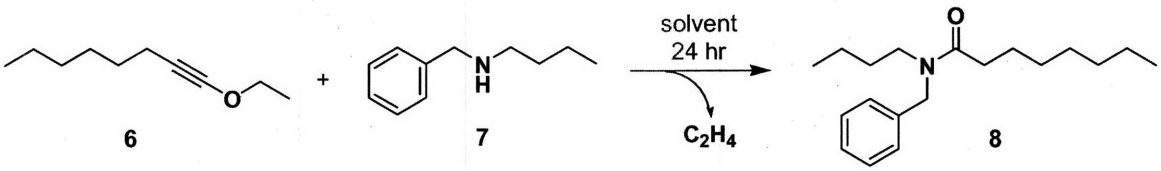

Entry	Solvent	*T* K (°C)	*P* bar (psia)	Phase Behavior type [a]	Conversion [b] %	Yield [c] %
1	Toluene	393 (120)	1.3 (19)	I	100	88
2	CO_2	393 (120)	211 (3165)	II	95	85
3	CO_2	393 (120)	384 (5765)	I	95	86
4	CO_2	403 (130)	228 (3415)	II	100	88

[a] for a detailed discussion of reaction phase behavior, see **Table 9-2**; [b] by 1H NMR; [c] isolated yield by column chromatography, based on 0.1 M charge of amine and 1-alkynyl ether.

Amide precipitation was observed upon formation for these runs, as $P < P_{c,mix\ CO2/amide}$. Increasing the pressure (entry 3) to $P > P_{c,mix\ CO2/amide}$ resulted in a mono-phasic reaction mixture for the entire duration of the reaction. Interestingly, product yield did not vary with operating pressure and phase behavior for over the range studied. The uniformity of product yields suggests that reactant partitioning from the CO_2-rich phase to the amide-rich phase (if any) did not reduce amide selectivity.

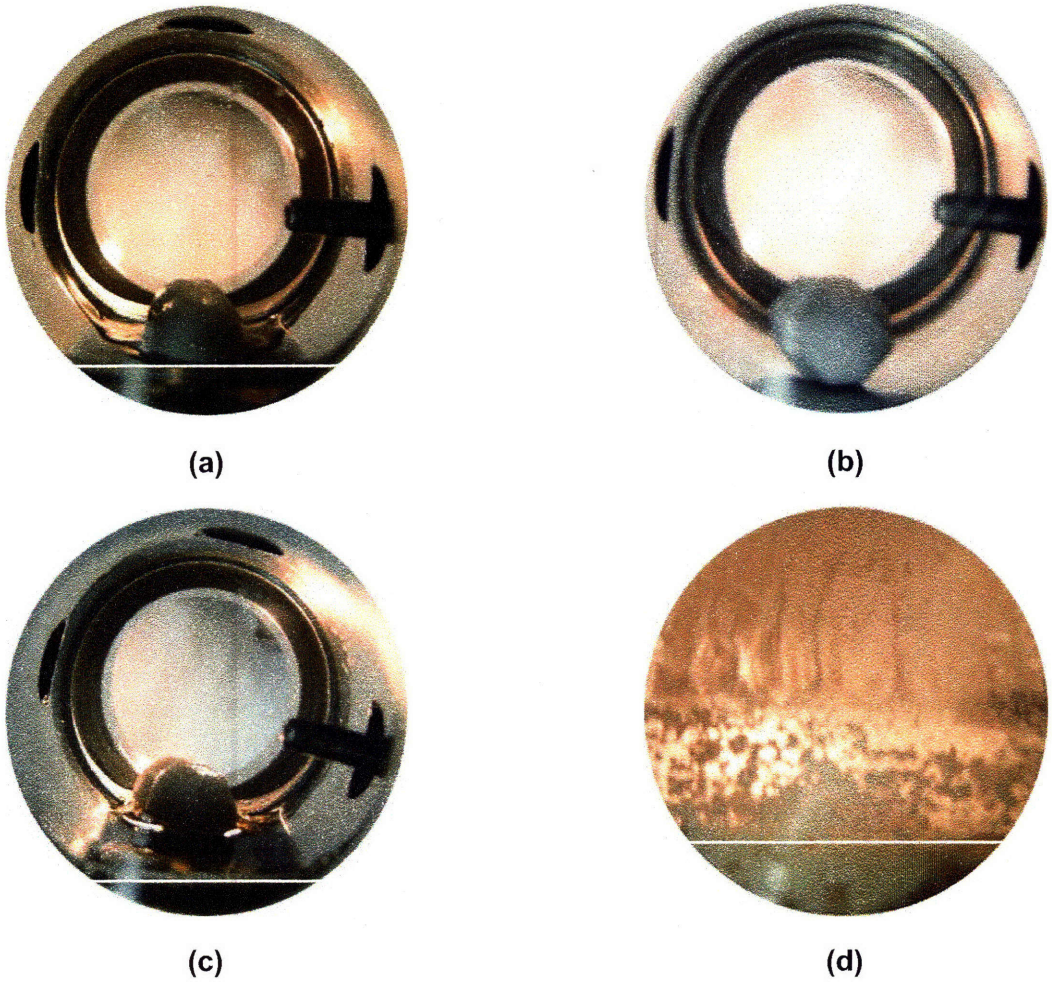

Figure 9-3. Phase behavior observed during amide synthesis in supercritical carbon dioxide: a liquid phase consisting of amine and alkynyl ether (a); a supercritical-like CO_2-rich phase **(b)**; an upper, lower-density CO_2-rich supercritical-like phase and a lower, higher-density organic-rich liquid phase **(c)**; an upper, lower-density CO_2-rich supercritical-like phase and a lower, higher-density organic -rich liquid phase with dispersed amine-rich solids throughout **(d)**. For a detailed discussion of reaction phase behavior, see **Table 9-2**. The solid object visible in **(a)** – **(c)** is a magnetic stir bar. Lines are drawn to indicate phase boundaries.

Table 9-2. Phase behavior descriptions for the synthesis of amides in supercritical carbon dioxide.

Visual observation of the reaction mixture and individual components in CO_2 over a wide range of operating conditions allowed us to categorize phase behavior into five types:

- **Type I**: Carbamic salts were not observed when heating and pressurizing from ambient conditions to reaction conditions. The reaction is monophasic for the entire duration of the reaction;
  Phase transitions: Figure 9-3a → Figure 9-3b

for $P < P_{c,mix}$ of reactants
$t = 0$ hr

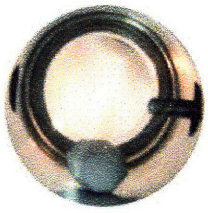

at reaction conditions
$t = 0.1 - 24$ hr

- **Type II**: Carbamic salts were not observed when heating and pressurizing from ambient conditions to reaction conditions. The reaction begins monophasic and becomes biphasic, consisting of an upper, lower-density CO_2-rich supercritical-like phase and a lower, higher-density organic-rich liquid phase. We suspect that the organic-rich liquid phase consists primarily of the amide product and the alkynyl ether, ketene, and amine are partitioned to the CO_2-rich phase;
  Phase transitions: Figure 9-3a → Figure 9-3b → Figure 9-3c

for $P < P_{c,mix}$ of reactants
$t = 0$ hr

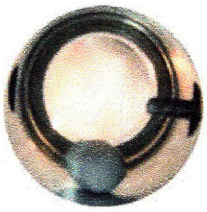

at reaction conditions
$t = 0.1 - 1$ hr

at reaction conditions
$t = 1 - 24$ hr

Table 9.2 (continued). Phase behavior descriptions for the synthesis of amides in supercritical carbon dioxide.

- **Type III**: Carbamic salts were not observed when heating and pressurizing from ambient conditions to reaction conditions. The reaction is biphasic, consisting of an upper, lower-density CO_2-rich supercritical-like phase and a lower, higher-density organic-rich liquid phase. We suspect that the organic-rich liquid phase consists primarily of the amine and amide, with the alkynyl ether and ketene partitioned to the CO_2-rich phase;
  Phase transitions: Figure 9-3a → Figure 9-3c

for $P < P_{c,mix}$ of reactants
t = 0 hr

at reaction conditions
t = 0.1 – 24 hr

- **Type IV**: Carbamic salts are observed upon the addition of CO_2 at ambient temperature. As T increases to approximately 353 – 373 K (80 – 100 °C), the salt melts, dissociates, and/or dissolves in the liquid alkynyl ether phase to form a single liquid phase that is soluble in CO_2 at the reaction conditions. The reaction begins mono-phasic and becomes biphasic, consisting of an upper, lower-density CO_2-rich supercritical-like phase and a lower, higher-density organic-rich liquid phase. After the disappearance of carbamic salt, species partitioning behavior is believed to be the same as type II;
  Phase transitions: Figure 9-3a → Figure 9-3d → Figure 9-3a → Figure 9-3b → Figure 9-3c

for $P < P_{c,mix}$ of reactants
t = 0 hr

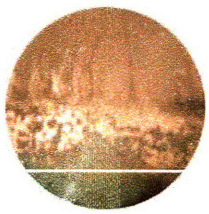

for $P < P_{c,mix}$ of reactants
and $T < T_{melt}$

for $P < P_{c,mix}$ of reactants
and $T > T_{melt}$

at reaction conditions
t = 0.1 – 1 hr

at reaction conditions
t = 1 – 24 hr

Table 9.2 (continued). Phase behavior descriptions for the synthesis of amides in supercritical carbon dioxide.

- **Type V:** Carbamic salts are observed upon the addition of CO_2 at ambient temperature. The salts do not melt, dissolve, and/or dissociate as temperature increases to reaction conditions. The reaction begins biphasic, consisting of an upper, lower-density CO_2-rich supercritical-like phase and a lower, higher-density organic-rich solid phase. The CO_2 phase is suspected to contain the alkynyl ether and ketene, whereas the solid phase is suspected to be the amine-rich carbamic salt. The reaction becomes triphasic, consisting of an upper, lower-density CO_2-rich supercritical-like phase, a middle, intermediate-density organic-rich liquid phase, and a lower, higher-density organic-rich solid phase. The solid phase remains the amine-rich carbamate salt. The middle liquid phase is suspected to consist primarily of the amide, with the alkynyl ether and ketene partitioned to the CO_2-rich phase. The solid phase eventually disappears as the reaction nears completion, yielding a biphasic system consisting of an upper, lower-density CO_2-rich supercritical-like phase and a lower, higher-density organic-rich liquid phase with portioning behavior of type II.
  Phase transitions: Figure 9-3a → Figure 9-3d → Figure 9-3c

for $P < P_{c,mix}$ of reactants
t = 0 hr

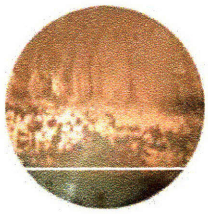

at reaction conditions
t = 0.1 – 10 hr

at reaction conditions
t = 10 – 24 hr

9.3.3. Scope of the Synthesis Protocol

Using the optimized process operating conditions revealed by earlier reconnaissance work (see **Section 9.3.1**), we extended the scope of the amide synthesis protocol by employing a variety of amines, alkynyl ethers, and ketenes. Since amide precipitation during the course of the reaction did not affect product yield, all experiments unless noted otherwise were performed at the minimum pressure required to solubilize the starting materials (i.e., $P_{c,mix\ CO2/reactants}$). Additionally, we chose to operate at these conditions because we suspected that reactant partitioning occurring for $P < P_{c,mix\ CO2/reactants}$ would negatively affect reaction performance.

Screening of Amines

Results of our screening study involving the reaction of amines with model alkynyl ether 1-ethoxy-oct-1-yne (**6**) are shown in **Table 9-3**. Amide yield increased depending on amine functionality in the order secondary > branched-primary > primary. Ignoring phase behavior effects for the moment, this observation is in line with the reactivity of amines with carbon dioxide. Carbamic acid formation diminishes with increasing *N*-substituent size; secondary and bulkier primary amines are likely to participate more effectively in the desired amination reaction due to reduced interference from the medium. This analysis, however, assumes that the reaction efficiency in the absence of CO_2 in conventional solvents is unaffected by the *N*-substituent choice. This is likely, as even the most sterically-demanding amines successfully undergo amide formation in yields nearly identical to those performed in CO_2 (compare entries 1a & 1b and 2a & 2b).

From a phase behavior perspective, decreased amide yields for certain amines may also be ascribed to dynamic reactant partitioning. Selectivity towards amide varies proportionally with amine concentration and inversely with ketene and alkynyl ether concentration (see **Section 10.4.3**). The preferential partitioning of the ketene or alkynyl ether from the bulk CO_2-rich phase containing the amine to the smaller-volume amide-rich liquid phase would lead to increased concentrations that would favor competitive cycloaddition reactions. Alternatively, if the amine partitioned to the amide-rich phase, leaving the ketene and alkynyl ether alone in the CO_2-rich phase to undergo side reactions.

To explore the effect of reactant partitioning on amide formation, we performed a reaction at an initial pressure that resulted in the partitioning of the alkynyl ether (and ketene) to the CO_2-rich phase (verified visually) (i.e., $P_{c,mix\ CO2/ketene} < P_{c,mix\ CO2/alkynyl\ ether} < P < P_{c,mix\ CO2/amine}$). The reaction was therefore biphasic, consisting of a CO_2-rich liquid phase containing the alkynyl ether and ketene, and a liquid-phase containing initially amine and becoming rich in amide as it formed (type III). Surprisingly, the yield for this experiment was essentially identical to that when performing the same reaction but without partitioning at the onset of the reaction (compare entries 4a & 4b). In both experiments, the concentrations of ketene and alkynyl ether were essentially equivalent, as the ketene and alkynyl ether resided in the larger-volume bulk CO_2-rich phase. This suggests that the amination reaction is desired over cycloaddition pathways at these conditions and even with imposed mass-transfer limitations. We expect different results had the experiment been performed such that the reaction was initiated with the

Table 9-3. Screening of amines for the amide synthesis protocol in supercritical carbon dioxide.

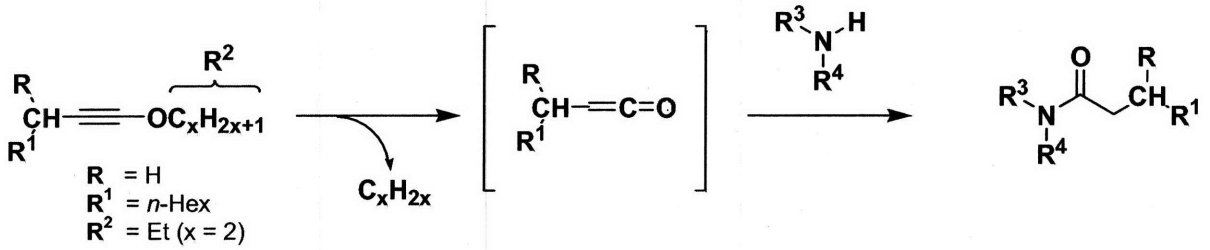

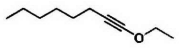

Entry	Amine	Solvent	*T* K (°C)	*P* bar (psia)	Phase Behavior type [a]	Product	Yield [b] %
1a	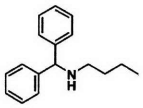	Toluene	393 (120)	1.3 (19)	I	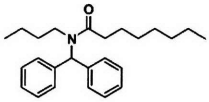	85
1b		CO_2	403 (130)	273 (4090)	II		88
2a	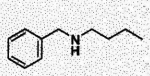	Toluene	393 (120)	1.3 (19)	I	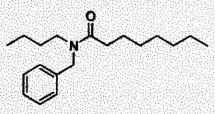	88
2b		CO_2	403 (130)	228 (3415)	II		88
3		CO_2	403 (130)	228 (3415)	II	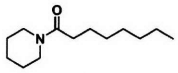	87
4a	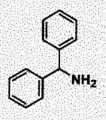	CO_2	403 (130)	298 (4465)	IV	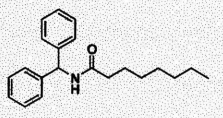	79
4b		CO_2	403 (130)	208 (3015)	III		78

[a] for a detailed discussion of reaction phase behavior, see **Table 9-2**; [b] isolated yield by column chromatography at complete conversion of 1-alkynyl ether, based on 0.1 M charge of amine and 1-alkynyl ether.

Table 9-3 (continued). Screening of amines for the amide synthesis protocol in supercritical carbon dioxide.

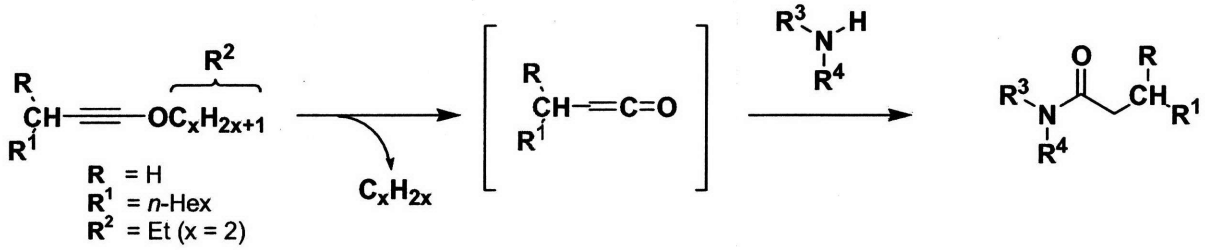

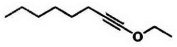

Entry	Amine	Solvent	T K (°C)	P bar (psia)	Phase Behavior type [a]	Product	Yield [b] %
5		CO_2	403 (130)	228 (3415)	IV	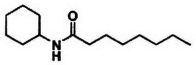	74
6		CO_2	403 (130)	229 (3440)	II	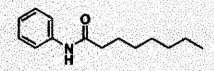	61
7		CO_2	403 (130)	274 (4115)	IV	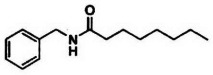	40

[a] for a detailed discussion of reaction phase behavior, see **Table 9-2**; [b] isolated yield by column chromatography at complete conversion of 1-alkynyl ether, based on 0.1 M charge of amine and 1-alkynyl ether.

ketene and alkynyl ether partitioned from the CO_2-rich phase containing the amine. In this case, the ketene and alkynyl ether would reside in a concentrated liquid phase that would favor cycloaddition reactions. This hypothesis could not be tested, as the alkynyl ether and ketenes had solubilities in CO_2 that were higher than the amines (i.e., $P_{c,mix\ CO2/ketene} < P_{c,mix\ CO2/alkynyl\ ether} < P_{c,mix\ CO2/amine}$)

The minimum pressure required to solubilize the reactants increased with the molecular size and relative reactivity with carbon dioxide (compare entries 1b & 2b and 6 & 7). Amines that showed signs of carbamic salt formation at ambient temperature still underwent the desired amination reaction in modest yields (entries 4a, 5, & 7). This suggests that there was an equilibrium shift to favor free amine over carbamic acid at higher temperatures and/or that the rate of carbamic acid formation was slower than ketene amination. Importantly, the lack of

carbamic salt formation at ambient temperature did not necessarily indicate that a reaction would perform better than one that did not exhibit this behavior (compare entries 5 & 6). The poor yield of the benzylamine case (entry 7) may be due to carbamic acid formation in the bulk CO_2-rich phase and/or enhanced carbamic acid formation in the more polar amide-rich liquid phase formed during the reaction.

Screening of Alkynyl Ethers and Ketenes

Results of our screening study involving the reaction of ketenes and alkynyl ethers using model amines are shown in **Table 9-4**. Substitution of the Et group with a *t*-Bu group in the alkynyl ether resulted in the generation of the identical ketene at a much faster rate; complete consumption of starting materials was achieved in 24 hr at 363 K (90 °C) (compared to 403 K [130 °C] for the R^2 = Et case). The *t*-Bu-substituted case afforded slightly less amide, potentially due to its higher thermal sensitivity (compare entries 1 and 2a). Surprisingly, yield was unaffected when performing the reaction using the *t*-Bu-substituted alkynyl ether at conditions when the amine was in its carbamic salt form at 363 K (90 °C) (compare entries 2b of **Table 9-4** with 4a of **Table 9-3**). This result suggests the amine participates in the reaction in its carbamic salt form or that the equilibrium to liberate free amine is fast enough to allow amide formation over ketene cycloaddition reactions.

A significant increase in amide selectivity relative to an elimination product for the reaction involving the –$OSi(Me)_2$*t*-Bu-substituted alkynyl ether was achieved by replacing toluene with CO_2 and decreasing reaction temperature (compare entries 3a & 3b with entries 4a & 4b). Carbamate- and geranyl- substituted alkynyl ethers also react to afford amides in good yields (entries 5a – 7). Diminished yields of entries 5b and 7 could be due to phase behavior effects (see previous section) or due to competitive side reactions. The inclusion of double bonds in the geranyl-substituted alkynyl ether (entry 7), for example, offer reactive sites where ketene cycloaddition reactions can occur (see **Section 10.4.3**).

Table 9-4. Screening of alkynyl ethers and ketenes for the amide synthesis protocol in supercritical carbon dioxide.

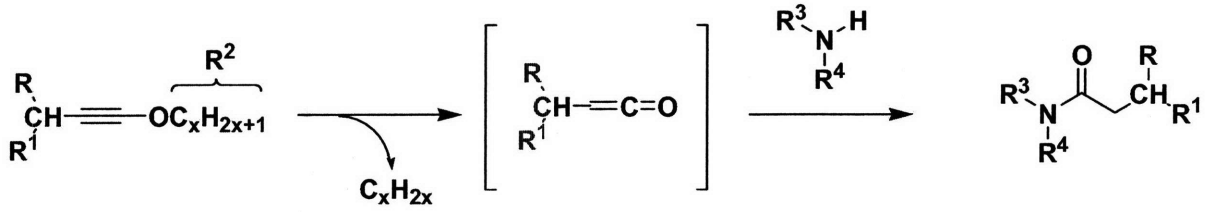

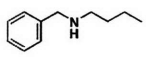

Entry	Alkynyl Ether	Solvent	*T* K (°C)	*P* bar (psia)	Phase Behavior type [a]	Product	Yield [b] %
1	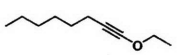	CO_2	403 (130)	228 (3415)	II	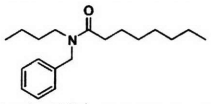	88
2a	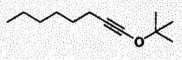	CO_2	363 (90)	298 (4465)	II	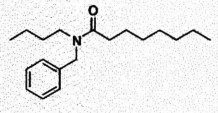	82
2b [c]	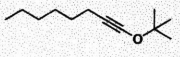	CO_2	363 (90)	229 (3315)	V	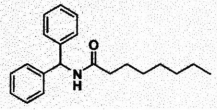	78
3a	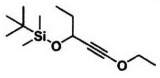	Toluene	393 (120)	1.7 (25)	II	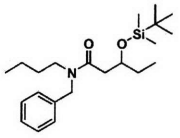	10 (80)
3b		CO_2	403 (130)	228 (3415)	II		56 (31)
4a	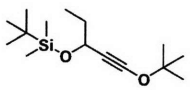	Toluene	363 (90)	0.5 (8)	II	+ 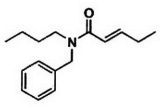	—
4b		CO_2	363 (90)	228 (3415)	II		80 (3)

[a] for a detailed discussion of reaction phase behavior, see **Table 9-2**; [b] isolated yield by column chromatography at complete conversion of 1-alkynyl ether, based on 0.1 M charge of amine and 1-alkynyl ether; [c] reaction performed with benzhydrylamine.

Table 9-4 (continued). Screening of alkynyl ethers and ketenes for the amide synthesis protocol in supercritical carbon dioxide.

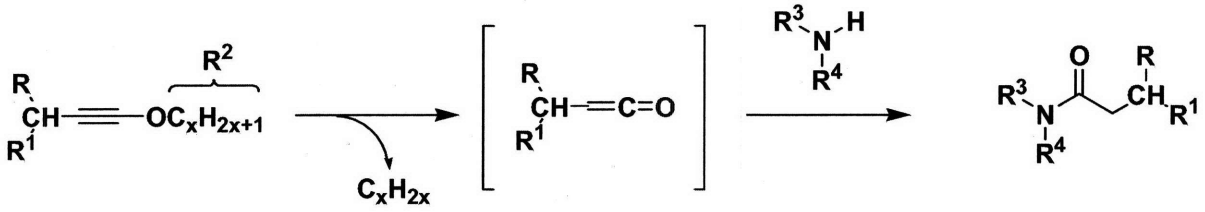

Entry	Alkynyl Ether	Solvent	*T* K (°C)	*P* bar (psia)	Phase Behavior type [a]	Product	Yield [b] %
5a	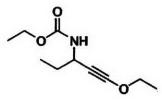	Toluene	403 (130)	1.7 (25)	II	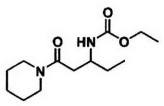	62
5b		CO_2	403 (130)	274 (4115)	II		66
6a	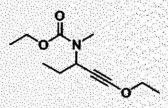	Toluene	403 (130)	1.7 (25)	II	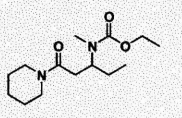	69
6b		CO_2	403 (130)	274 (4115)	II		85
7	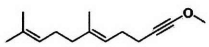	CO_2	403 (130)	274 (4115)	II	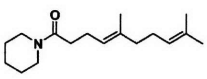	68

[a] for a detailed discussion of reaction phase behavior, see **Table 9-2**; [b] isolated yield by column chromatography at complete conversion of 1-alkynyl ether, based on 0.1 M charge of amine and 1-alkynyl ether.

9.4. Lactam Synthesis

9.4.1. Motivation and Model Reaction

Given our success with the amide formation via intermolecular pathways, we decided to investigate extending the method to intramolecular ring closure reactions. We selected the synthesis of large-ring lactams as a model system because these and other macrocycles are used as antibiotics, immunosuppressants, and anti-cancer agents (Atwood et al., 2004). Benzyl-(12-ethoxy-dodec-11-ynyl)-amine (**9**) was selected as a model aminoalkynyl ether and was essentially the unimolecular version of the model reaction involving 1-ethoxy-oct-1-yne (**6**) and *N*-butylbenzylamine (**7**) (MaGhee et al., 1994):

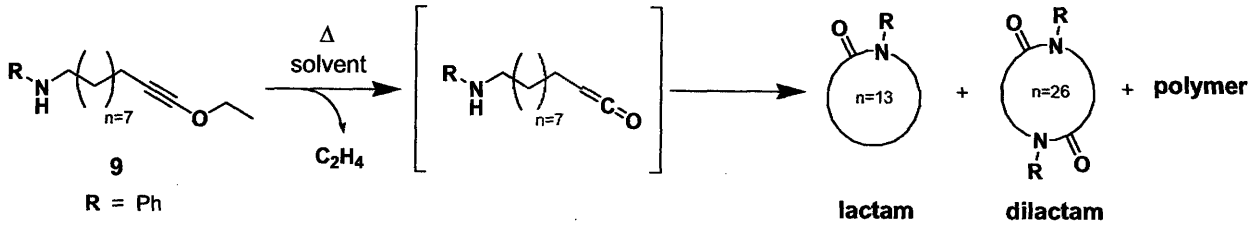

(9-7)

The principal difficulty in performing a unimolecular ring closure reaction lies in the competition between intramolecular cyclization and intermolecular polymerization. Shown schematically in **Figure 9-4**, once formed, the aminoketene can undergo desired intramolecular ring-closure to afford lactam or several other intermolecular pathways that produce higher-molecular weight macrocycles, such as dimers and polymers. Similar to the intermolecular version of this reaction, competitive pathways also include ketene + ketene and ketene + alkynyl ether cycloaddition reactions. A simple kinetic analysis reveals that lactam selectivity increases with increased starting material dilution and for conditions that increase k_{lac} relative to k_{poly}:

$$S_{lac} = \frac{k_{lac}}{k_{poly}} \frac{1}{[\text{ketene}]} \qquad \textbf{(9-8)}$$

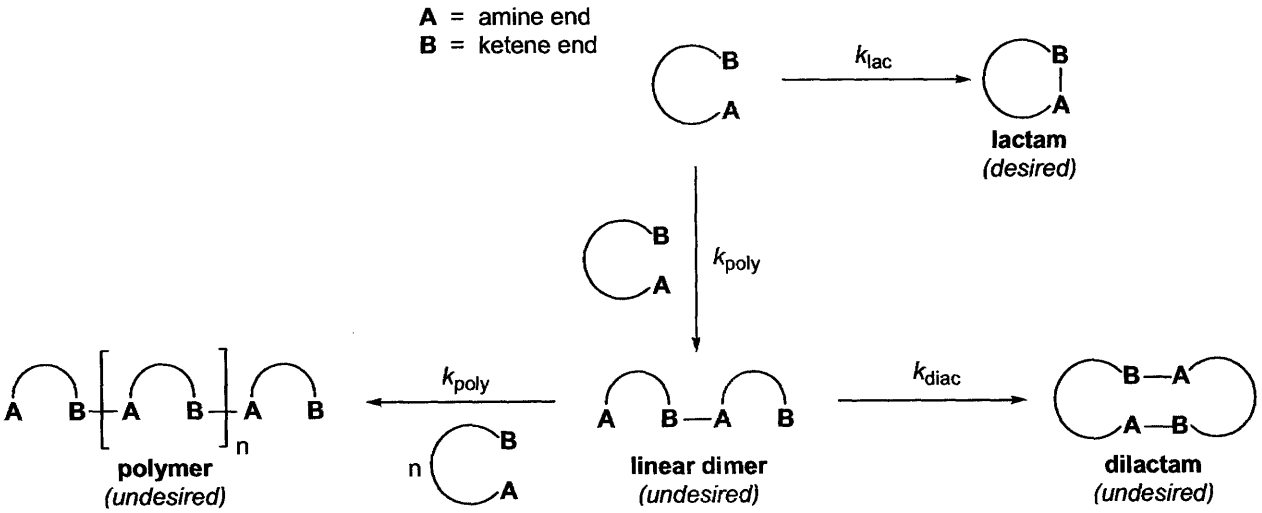

Figure 9-4. Lactam formation and competitive reaction pathways.

Our decision to perform this transformation in carbon dioxide was motivated in part by the work of Fürstner and coworkers (2001), who studied the effect of CO_2 density on the efficiency of olefin macrocyclization:

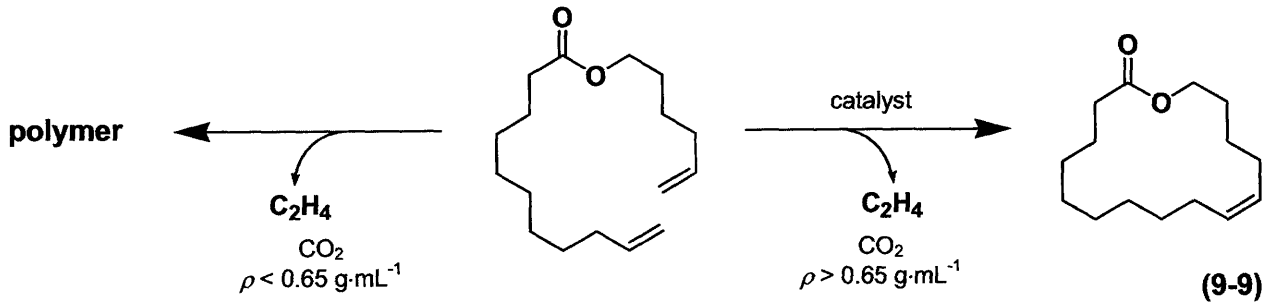

(9-9)

Shown in **Figure 9-5**, the authors report a significant increase in macrocycle selectivity with increasing density and attributed it to (1) solvophobic acceleration of the cyclization rate constant relative to polymerization rate constant, and (2) to an effective increase in dilution due to the increase number inert solvent molecules at higher densities. In conventional liquid solvents, dilution is obtained by decreasing the number of reactant molecules per unit volume (**Figure 9-5**, path **a**). According to equation (**9-8**), this leads to an increase in macrocycle selectivity. In CO_2, however, increasing the density of the medium at constant volume

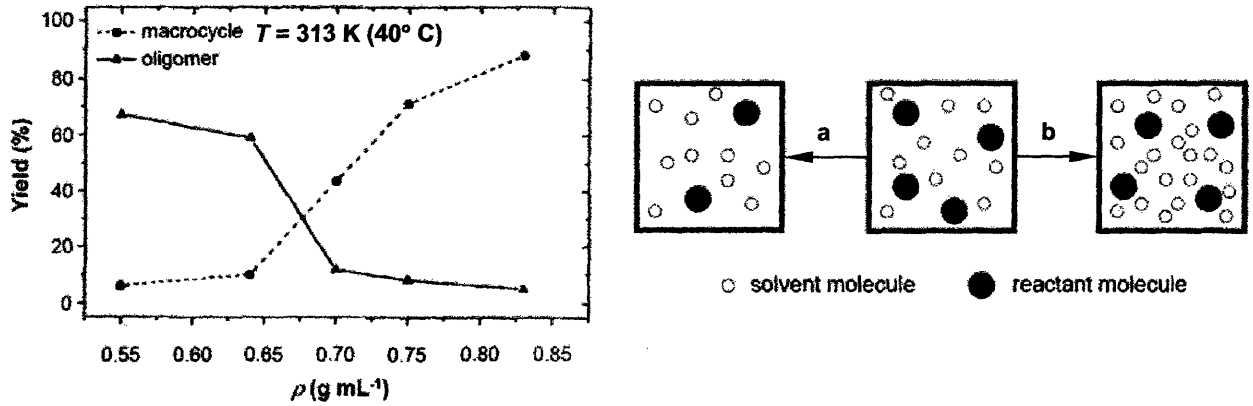

Figure 9-5. Macrocycle yield plotted as a function of carbon dioxide density and the schematic representation of dilution in conventional solvents (**a**) and carbon dioxide (**b**).

(via pressure) adds more solvent molecules without reducing the number of reactant molecules per unit volume. Although the reactant molar concentration is the same in this case, Fürstner and coworkers claim that the increased number of inert CO_2 solvent molecules suppresses competitive cyclization by reducing reactant-reactant interactions (**Figure 9-5**, path **b**). The density of toluene and carbon dioxide is plotted as a function of pressure and temperature in **Figure 9-6**. Although the mass density of toluene is comparable to CO_2 over a wide range of conditions, the molecular density is significantly smaller due to its smaller molecular mass. If the 'molecular dilution effect' claimed by Fürstner and coworkers was valid, one would expect an increase macrocycle selectivity in CO_2 when compared to larger-molecular weight conventional liquid solvents.

As we will show in the following section, we provide evidence to dismiss this 'molecular dilution effect' based on several well-defined experiments. Specifically, we determined the effect of solvent choice, temperature, pressures, densities, and substrate composition on lactam selectivity and yield. Our goal was to achieve selectivities and yields in CO_2 that were comparable to conventional liquid solvents, but at larger substrate concentrations, thereby increasing process throughput as well as solvent replacement.

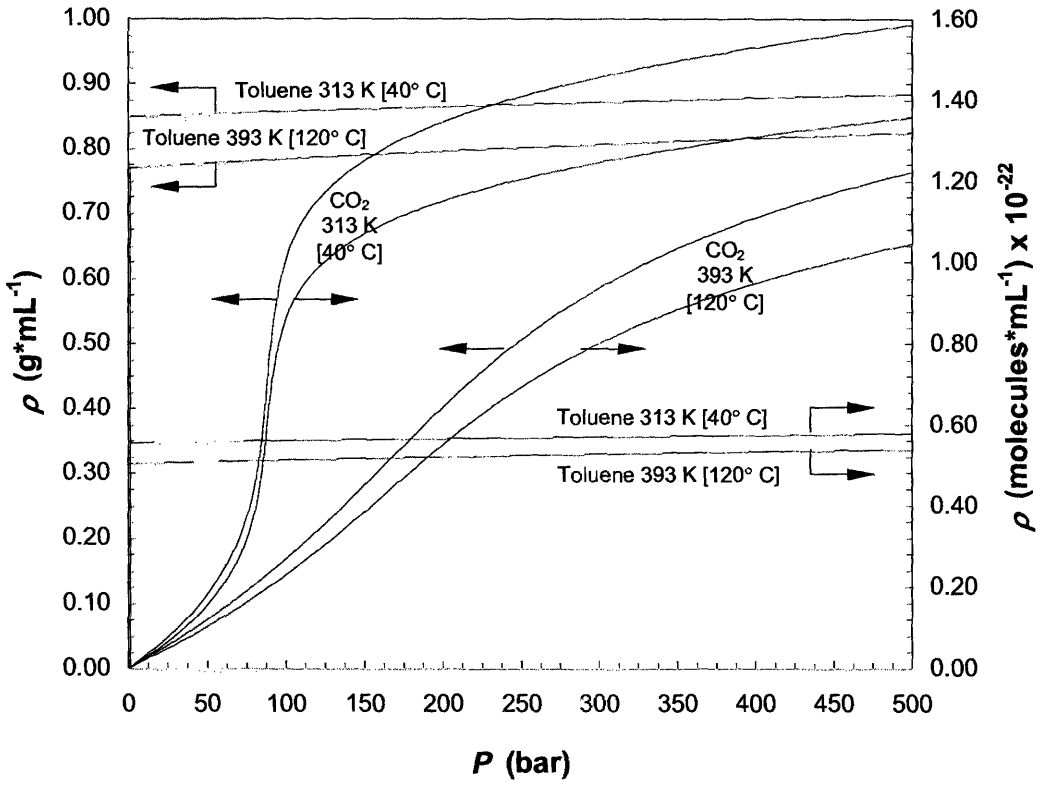

Figure 9-6. Mass and molecular density of carbon dioxide and toluene plotted as a function of pressure and temperature.

9.4.2. Results and Discussion

Results of our lactam synthesis study are delineated in **Table 9-5**. Lactam yields in xylenes were comparable to those reported by MaGee and coworkers (1994), which validated our experimental and analytical methods (entry 1). Since extremely large pressures would have been required to solubilize the starting material in CO_2 at these reaction conditions, several control experiments were performed at lower temperatures. 393 K (120 °C) was lowest possible temperature that allowed for complete conversion within 24 hr. Lactam yield was essentially insensitive to time exposed to reaction conditions beyond complete conversion (compare entries 2 & 3 and 5 & 7), solvent choice (compare entries 2 & 5 and 3 & 7), vessel material (compare entries 5 & 6), and temperature (compare entries 3 & 4). As expected, lactam yield decreased significantly with increasing substrate concentration (compare entries 4 & 9).

Table 9-5. Screening of the lactam synthesis protocol in supercritical carbon dioxide.

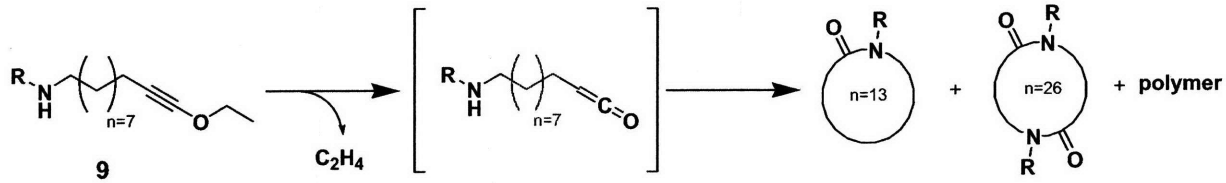

R = Ph

Entry	$[SM]_0$ M	Solvent	*t* hr	*T* K (°C)	*P* bar (psia)	Yield (%) [a] Lactam	Dilactam
1	0.001442	Xylenes	24	411 (138)	2.1 (30)	67 [b] (63)	0 [b] (0.5)
2	0.002	Toluene	3	411 (138)	2.1 (30)	54 (59)	(3)
3	0.002	Toluene	24	411 (138)	2.1 (30)	65 (60)	(2)
4	0.002	Toluene	24	393 (120)	1.3 (19)	(58)	(6)
5	0.002	Xylenes	3	411 (138)	2.1 (30)	63 (61)	(2)
6	0.002	Xylenes [c]	3	reflux	1.0 (15)	58 (60)	(6)
7	0.002	Xylenes	24	411 (138)	2.1 (30)	(61)	(1)
8	0.002	CO_2 [d]	24	393 (120)	322 (4665)	32 (33)	(7)
9	0.01	Toluene	24	393 (120)	1.3 (19)	(33)	(8)
10	0.01	CO_2 [d]	24	393 (120)	322 (4665)	22 (25)	7 (8)
11	0.002	CO_2/ Toluene [e]	24	393 (120)	322 (4665)	58 (45)	(9)

[a] isolated yield by column chromatography at complete conversion, numbers in parentheses indicate yield by HLPC; [b] yield reported by MaGee et al. (2004); [c] reaction performed using base-washed glass vessel; [d] reaction performed at 322 bar (4665 psia); [e] reaction performed at 322 bar and 10 %vol toluene.

Lactam selectivity was decreased significantly when performing the reaction in CO_2 at conditions identical to those of toluene (compare entries 4 & 8 and 9 & 10). Possible explanations for this observation are:

- **Physicochemical Effects.** The viscosity of CO_2 is approximately 5 times less than of toluene at our operating conditions. The substrate will likely have a higher diffusivity in CO_2. Higher diffusional encounter rates of aminoketene molecules may favor polymerization over cyclization;
- **Solvation Effects.** Compared to toluene, solvation effects in CO_2-rich mediums may increase polymerization rates and/or decrease amination rates.
- **Phase Behavior Effects.** Originally a liquid at ambient conditions (see **Figure 9-7a**), the substrate dissolves completely in CO_2 at the reaction conditions (see **Figure 9-7a**). After approximately 5 hours, a liquid precipitate forms and increases in volume for the duration of the experiment (see **Figure 9-7c**). Independent solubility control experiments with the lactam and dilactam at reactions conditions revealed that this phase was likely to be the dilactam and higher molecular weight compounds. If the substrate preferentially partitioned to the more polar and smaller-volume liquid phase, its concentration would increase significantly from that of the bulk CO_2-rich phase and subsequently result in decreased lactam selectivity (see equation **[9-8]**).

  To test this hypothesis, 10 vol% of toluene was added to the CO_2-rich reaction mixture in order to increase the solubility of these byproducts (entry 11). The volume of the observed liquid precipitate was significantly smaller and lactam yield increased by 12%.

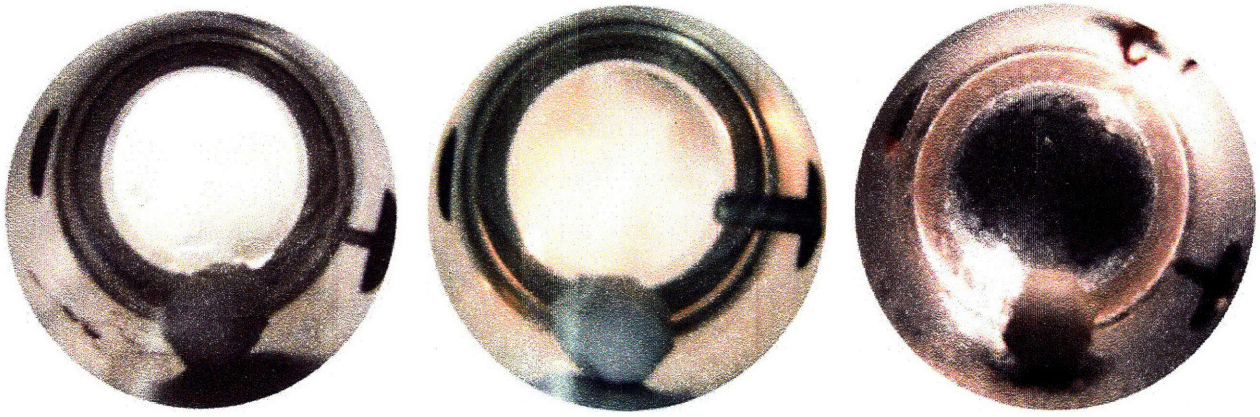

Figure 9-7. Sample high-pressure liquid chromatography chromatogram indicating the resolution of reaction products for the lactam synthesis reaction.

Given these findings, we find it unlikely for the 'molecular dilution effect' claimed by Fürstner and coworkers (2001) to be causing the observed results. From a kinetics standpoint, reaction rates depend on the moles of substrate per reaction volume and are less dependent on the concentration of 'inert' solvent molecules present. Like-like interactions are more likely to be reduced in the presence of viscous solvents rather than those with high molecular densities. Even if this dilution effect were true, the molecular density is related to mass density by the component molecular mass and is therefore a linear function of density. The sharp, nonlinear increase in macrocycle yield with CO_2 density shown in **Figure 9-5** suggests that other effects — such as phase behavior — are at play. Unfortunately, the authors do not comment on the solubility of the olefin in carbon dioxide as a function of operating conditions. We performed VLE calculations for the CO_2/olefin system at 313 K (40 °C) and found that the $P_{c,mix\ CO2/olefin} \approx$ 98 bar (ρ_{CO2} = 0.60), which coincides with the density at which Fürstner and coworkers (2001) observe the shift in macrocycle yield. We therefore suspect that at lower pressures, the olefin is insoluble in CO_2 and exists as a concentrated liquid phase that preferentially undergoes polymerization. For $P > P_{c,mix\ CO2/olefin}$, the system is homogenous (with the exception of the CO_2-insoluble catalyst), the substrate is more dilute, and cyclization is preferred.

9.5. Conclusions and Recommendations

In this chapter, we have successfully demonstrated the use of carbon dioxide as an environmentally-benign alternative to conventional solvents for the synthesis of a variety of amides. We proposed and optimized a high atom-economy and practical synthetic protocol that produces amides via the amination of ketenes generated *in situ* from the thermolysis of alkynyl ethers. More specifically,

- a variety of amines, alkynyl ethers, and ketenes participated actively in the reaction, producing amides in yields in CO_2 comparable to those of conventional solvents;
- experimental phase partitioning observations agreed well with EOS-based predictions and aided in the determination of operating conditions;
- amide yield increased in the order secondary > branched-primary > primary amines, suggesting that carbamic acid formation may have led to diminished reaction efficiency, and
- *t*-butoxy-substituted alkynyl ethers afforded ketenes faster than ethoxy-substituted ethers and allowed for a significant reduction in operating temperature.

Extension of the protocol to an intramolecular variant that afforded lactam revealed a significant decrease in selectivity when compared to conventional solvents. We suspected that phase behavior led to this discrepancy and were able to increase lactam selectivity by using CO_2/co-solvent mixtures.

Based on these findings, the following experiments are recommended to aide in the development of these and similar C-*N* bond-forming processes in CO_2-based media:

- investigate the kinetics associated with a model intermolecular amide formation reaction in CO_2 as a function of density and benchmark this data against conventional solvents;
- measure phase-specific species concentrations for model reactions involving secondary amines and primary amines in order to decouple the effect of carbamic acid formation and phase-partitioning on amide selectivity, and

- explore lactam selectivity as a function of CO_2 density and co-solvent choice/amount in CO_2/co-solvent mixtures.

9.6. References

Atwood, J. L. and Steed, J. W., Eds. Encyclopedia of Supramolecular Chemistry. Marcel Dekker: New York, **2004**.

Carey, J. S., Laffan, D., Thomson, C., and Williams, M. T. *Analysis of the Reactions Used for the Preparation of Drug Candidate Molecules.* Org. Biomol. Chem., **2006**, *4*, 2337-2347.

Danheiser, R. L., Ed. *Science of Synthesis. Volume 23: Three Carbon-Heteroatom Bonds: Ketenes and Derivatives.* Georg Thieme Verlag KG, **2006**.

Ficini, J. *Recherches sur les Ethers-Oxydes d'Ynols. Préparation et Réactions avec les Composés à H Mobile.* Bull. Soc. Chim. Fr., **1954**, 1367.

Fürstner, A., Ackermann, L., Beck, K., Hori, H., Koch, D., Langemann, K., Liebl, M., Siz, C., and Leitner, W. *Olefin Metathesis in Supercritical Carbon Dioxide.* J. Am. Chem. Soc., **2001**, *123*, 9000-9006.

Ghose, A. K., Viswanadhan, V. N., and Wendoloski, J. J. *A Knowledge-Based Approach in Designing Combinatorial or Medicinal Chemistry Libraries for Drug Discovery. 1. A Qualitative and Quantitative Characterization of Known Drug Databases.* J. Comb. Chem., **1999**, *1*, 55-68.

MaGee, D. I. and Ramaseshan, M. *Efficient Synthesis of Lactams by the Intramolecular Trapping of Ketenes.* Synlett, **1994**, 743-744.

Montalbetti, C. A. G. N. and Falque, V. *Amide Bond Formation and Peptide Coupling.* Tetrahedron, **2005**, *61*, 10827-10852.

Tidwell, T. T. Ketenes. Second Edition. Wiley & Sons: New York, **2006**.

10. *AB INITIO* INSIGHTS TOWARDS CARBAMIC ACID AND AMIDE FORMATION IN SUPERCRITICAL CARBON DIOXIDE

10.1. Motivation and Variables Explored

During the development of our previously-discussed experimental C-*N* bond-forming protocols, we also undertook a complimentary *ab initio* and semi-empirical quantum chemical modeling study of several model reactions. Coupled with vapor-liquid equilibrium predictions, kinetic modeling guides experimental design and offers the potential for a more-complete understanding of chemical processes proceeding in multi-phasic carbon dioxide-based media. In this chapter, we present the results of our theoretical investigation of the reaction of carbon dioxide with amines and also develop a kinetic model that describes the dynamics associated with amide synthesis in CO_2-based media. We specifically examine the effect of process operating conditions (e.g., *T*, solvent) and substrate functionality (e.g., *N*-substituents) on reaction rates and selectivity and compare these predictions with experimental observations.

10.2. Methodology

10.2.1. Transition State Theory

Transition state (TS) theory is a popular statistical mechanics-based theoretical approach used for approximating reaction rate constants. Since rigorous formulations of TS theory are well-documented in the literature (Steinfeld et al., 1999 and references therein), we limit our discussion here to the practical application of the theory. The rate constant (k) for a bimolecular reaction involving reactants A and B proceeding through a transition state complex in a one-dimensional reaction coordinate is given by:

$$k = L^{TS}\frac{k_B T}{h}\frac{\left(\frac{Q^{TS}}{V^{TS}}\right)}{\left(\frac{Q_A}{V_A}\right)\left(\frac{Q_B}{V_B}\right)}\exp\left(\frac{-\Delta E_0}{k_B T}\right) \quad \textbf{(10-1)}$$

where L^{TS} is the statistical factor, k_B is the Boltzmann constant, h is the Planck constant, Q is the total partition function, V is molar volume, ΔE_0 is the difference between the lowest energy states of the TS complex and the reactants (see **Figure 10-1**). The lowest energy state is referred to as the zero-point energy (E_{ZPE}) and corresponds to a molecule's vibrational energy at 0 K. ΔE_0 is defined as:

$$\Delta E_0 = E_{ZPE}\big|_{TS} - \sum_i E_{ZPE}\big|_{reactants} \quad \textbf{(10-2)}$$

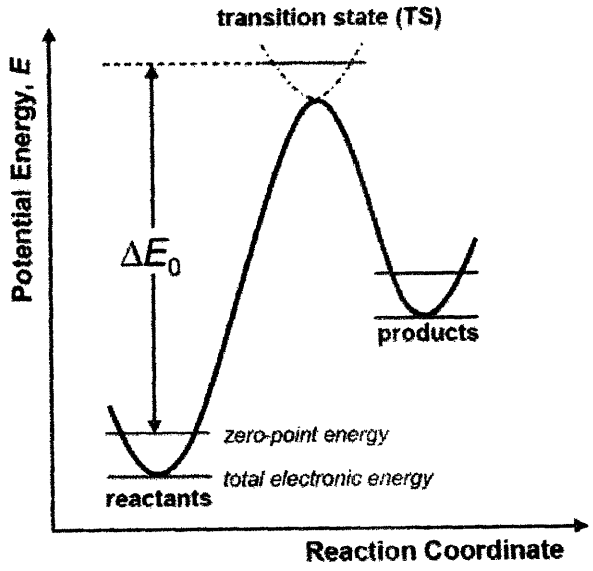

Figure 10-1. Reaction coordinate profile (adapted from Steinfeld et al. [1999]).

The total partition function depends on temperature and molecular structure and is comprised of rotational, translational, and vibrational energies:

$$Q(T) = q_{rot}\,q_{vib}\,q_{trans} \quad \textbf{(10-3)}$$

Contributions from nuclear transformations and electronic excited states have been omitted from equation (**10-3**), which is a valid assumption for non-fission/fusion type reactions and for transformations occurring at ground-state energies, respectively. An empirical tunneling term (q_{tun}) is often added to the partition function to account for deviations in TS theory from experimental observations (e.g., non-Arrhenius behavior) for reactions involving low energy barriers and/or the transfer of a hydrogen atom in the TS:

$$Q(T) = q_{rot} q_{vib} q_{trans} q_{tun} \tag{10-4}$$

Where in the simplest approximation:

$$q_{tun} = 1 + \frac{1}{24}\left(\frac{h\upsilon^{TS}}{k_B T}\right)^2 \left(1 + \frac{k_B T}{\Delta E_0}\right) \tag{10-5}$$

and υ^{TS} is the imaginary frequency calculated for the TS complex. Lastly, the statistical factor L^{TS} accounts for reactant symmetry and is defined as the total number of possible pathways leading to a transition state complex. Consider, for example, the extraction of a hydrogen atom from methane to produce a methyl radical. Since there are four hydrogens that upon abstraction would yield an identical TS complex, the statistical factor for this transformation is 4. When using the statistical factor, all symmetry numbers are omitted from the rotational partition function.

Equation (**10-1**) can also be related to thermodynamic quantities by:

$$k = L^{TS} \frac{k_B T}{h} \frac{\left(\frac{1}{V^{TS}}\right)}{\left(\frac{1}{V_A}\right)\left(\frac{1}{V_B}\right)} \exp\left(\frac{-\Delta G^{0,TS}}{RT}\right) \tag{10-6}$$

where $\Delta G^{0,TS}$ is the standard state Gibbs free energy difference between the TS complex and reactants and can be expressed in terms of standard state entropy (S) and enthalpy (H) changes:

$$\Delta G^{0,TS} = \Delta H^{0,TS} - T\Delta S^{0,TS} \tag{10-7}$$

Combining equations **(10-6)** and **(10-7)** gives:

$$k = L^{TS}\frac{k_B T}{h}\frac{\left(\frac{1}{V^{TS}}\right)}{\left(\frac{1}{V_A}\right)\left(\frac{1}{V_B}\right)}\exp\left(\frac{\Delta S^{0,TS}}{R}\right)\exp\left(\frac{-\Delta H^{0,TS}}{RT}\right) \qquad \textbf{(10-8)}$$

where R is the universal gas constant. The common standard state condition is 1.1 bar, 298 K (25 °C). For gas-phase calculations, the molar volumes V_j are determined from the ideal gas law ($V = RT/P$).

10.2.2. Computational Approach

Unlike stable reactant molecules, thermodynamic properties for the transient and unstable TS complex cannot be determined experimentally and must instead be estimated from semi-empirical and/or *ab initio* calculations. The Gaussian 03® (G03) software package (Gaussian, 2004) was used in this work for the estimation of partition functions and activation energy barriers required by TS theory. A combination of lower- and higher-level computational methods was used in the modeling of stable reactant and transition state structures. Computational time and data storage requirements scaled nonlinearly with the number of electrons, making higher-level calculation methods impractical for molecules with greater than 14 'heavy' (i.e., non-hydrogen) atoms. Unless stated otherwise, lower-level calculations were performed using the B3LYP/CBSB7 density functional theory (DFT) method and higher-level calculations refer to the CBS-QB3 complete basis set (CBS) method. Lower-level calculations gave reasonable estimates of entropy and partition functions and higher-level methods offered more accurate estimates of energy barriers of which rate constants depend exponentially. Due to time and computational limitations, large molecules were modeled as smaller versions that utilized the consitituent functional groups and reactive sites pertinent to the reaction in which they were involved. Since the reactive sites of large molecules were often isolated by several saturated carbons, the energetics of the simplified reactions were assumed to be similar to the real system. Due to the size of even some simplified reactions, only lower-level calculations could be completed.

All CBS-QB3 (higher-level) calculations were performed at 298 K (25 °C) and 1.01 bar. The quantum calculations return 0 Kelvin quantities, plus frequencies and moments of inertia

that allow for the computation of thermal corrections at any temperature. The following thermochemical properties were determined using the G03 output file:

$$\Delta E_0 = \text{CBS-QB3 (0 K)}\big|_{TS} - \sum_i \text{CBS-QB3 (0 K)}\big|_{\text{reactants}} \quad \textbf{(10-9)}$$

$$\Delta G^{0,TS} = \text{CBS-QB3 Free Energy}\big|_{TS} - \sum_i \text{CBS-QB3 Free Energy}\big|_{\text{reactants}} \quad \textbf{(10-10)}$$

$$\Delta H^{0,TS} = \text{CBS-QB3 Enthalpy}\big|_{TS} - \sum_i \text{CBS-QB3 Enthalpy}\big|_{\text{reactants}} \quad \textbf{(10-11)}$$

B3LYP/CBSB7 (lower-level) properties were also determined from the CBS-QB3 output file:

$$\Delta E_0 = \text{Sum of electronic and zero-point Energies}\big|_{TS} - \sum_i \text{Sum of electronic and zero-point Energies}\big|_{\text{reactants}} \quad \textbf{(10-12)}$$

$$\Delta G^{0,TS} = \text{Sum of electronic and thermal Free Energies}\big|_{TS} - \sum_i \text{S}\big|_{\text{reactants}} - \sum_i \text{Sum of electronic and thermal Free Energies}\big|_{\text{reactants}} \quad \textbf{(10-13)}$$

$$\Delta H^{0,TS} = \text{Sum of electronic and thermal Enthalpies}\big|_{TS} - \sum_i \text{Sum of electronic and thermal Enthalpies}\big|_{\text{reactants}} \quad \textbf{(10-14)}$$

$$\Delta S^{0,TS} = \text{S}\big|_{TS} - \sum_i \text{S}\big|_{\text{reactants}} \quad \textbf{(10-15)}$$

$$Q(T) = Q_{i,\text{ total V=0}} \quad \textbf{(10-16)}$$

Rate constants were determined by substituting equations **(10-9)** and **(10-16)** into equation **(10-1)**. Partition functions were evaluated at higher temperatures by accessing the checkpoint file generated by the 298 K calculation. Higher-level energies, such as the Free Energy, were estimated at higher T from:

$$G\big|_{T_2} = \left(G\big|_{298K} - \varepsilon_G\big|_{298K}\right) + \varepsilon_G\big|_{T_2} \quad \textbf{(10-17)}$$

where ε is the "thermal correction" of the property of interest. Rate constants were subsequently fit to the Arrhenius equation:

$$k = A\exp\left(\frac{-E_a}{RT}\right) \tag{10-18}$$

10.3. Model Reaction

The purpose of the following sections is to develop a kinetic model capable of describing the dynamics associated with our CO_2-based amide synthesis protocol discussed in **Chapter 9**:

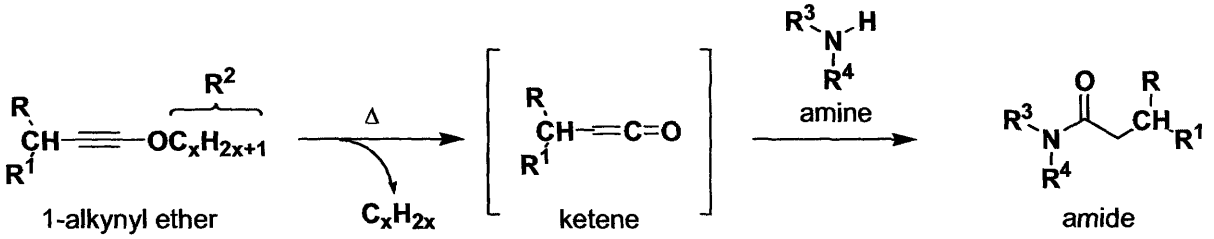

(9-1)

Most of the discussions in future sections pertain to the model reaction of 1-ethoxy-oct-1-yne with *N*-butylbenzylamine (see **Section 9.3.1**):

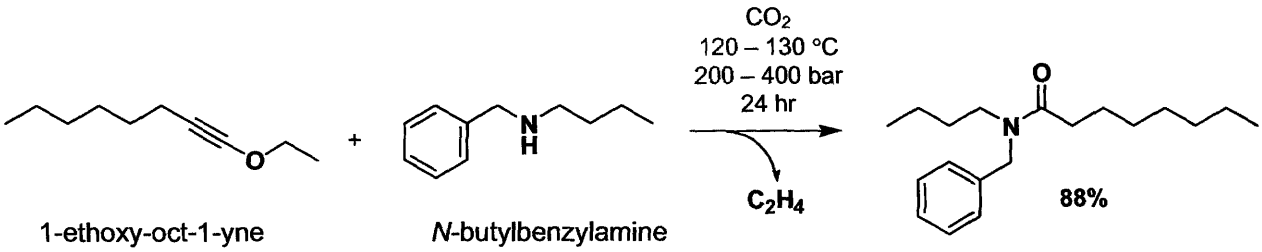

(9-6)

Unless noted otherwise, all rate and thermochemical property estimations are for reactions proceeding in an infinitely-dilute, mono-phasic gas-phase reaction medium with a dielectric constant of unity. Although the dielectric constant of carbon dioxide over our experimental range does not deviate significantly from unity, G03 is unable to account for reagent clustering effects (see **Section 1.4.1**). In addition, gas-phase G03 calculations are

unable to account for solvation effects that may arise due to the precipitation of polar liquid phases that were observed experimentally during some of the amide-forming reactions in CO_2 (see **Section 9.3.2**). Nonetheless, these calculations provide an initial estimate of the dynamics associated with amide synthesis and facilitate experimental design in the absence of kinetic data. Solvation effects were accounted for in some G03 calculations by using the integral equation formalism polarizable continuum model (IEFPCM) with the united atom topological (uahf) cavity model.

Benzyl groups and alkyl chains for large molecules were approximated by the addition of vinyl and ethyl groups, respectively. *N*-butylbenzylamine, for example, was modeled as ethylallylamine:

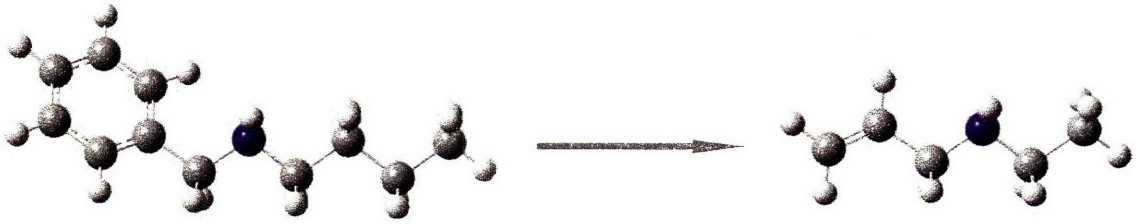

N-butylbenzylamine

ethylallylamine
('model' *N*-butylbenzylamine)

As we will show in **Section 10.4.2**, the influence of alkyl chain length in the vicinity of a transition state site typically diminishes beyond the second (ethyl) carbon. The vinyl group was selected to mimic the electrostatics imparted by the phenyl group. Although phenyl groups are sterically larger than the vinyl groups, both are flat and capable of similar rotation about sp^3 carbons. We suspect that the presence of an insulating sp^3 carbon between the phenyl group and nitrogen reduces the differences in steric contributions among the two amines. In order to estimate the level of error introduced by these approximations, higher-level calculations were performed on benzylamine and allylamine and their carbamic acid derivatives. Both molecules gave similar estimates of ΔG^0_{rxn} and ΔH^0_{rxn}. Due to the size of benzylamine, we were unable to calculate and compare the energy barriers associated with carbamic acid formation for the two amines.

10.4. Results and Discussion

The facility of amines to react with carbon dioxide to form carbamic acids poses a potential barrier towards the successful development of the proposed amide formation protocol in CO_2-based media. Carbamic acids formed from secondary amines, for example, could possibly block the desired addition of ketene to the amine (i.e., no free *N*-H site available for the transformation). The following section investigates carbamic acid formation from a quantum chemical perspective.

10.4.1. Carbamic Acid Formation

Equilibrium Calculations

Recalling our discussion from **Section 4.2**, Fischer and coworkers (2003) found that the addition of bulky functional groups to benzylamine suppressed carbamic acid formation in a neat, homogeneous CO_2 reaction medium (see **Figure 4-3**). From a quantum chemical perspective, the addition of sterically-demanding functional groups to a primary amine can suppress carbamic acid formation by (1) increasing the free energy change of the reaction ($\Delta\Delta G^0_{rxn} > 0$), and/or (2) increasing in the reaction energy barrier ($\Delta\Delta E_0 > 0$). In the overall reaction to form carbamic acid:

$$RNH_2 + CO_2 \underset{k_r}{\overset{k_f}{\rightleftharpoons}} RNHCO_2H \qquad \textbf{(10-19)}$$

these effects would be manifested by a decrease in the thermodynamic equilibrium constant (K) such that 'free' amine would be favored, and/or a decrease the forward reaction rate constant (k_f). To identify which of these two factors were at play, free energy equilibrium and transition state calculations were performed for a series of *N*-alkyl derivatives of our model benzylamine (allylamine).

To facilitate this analysis, we start by defining the thermodynamic equilibrium constant:

$$K = \exp\left(-\frac{\Delta G^0_{rxn}}{RT}\right) \qquad \textbf{(10-20)}$$

At equilibrium, the ratio of carbamic acid to free amine can be determined from the following expressions:

$$K_c = \frac{k_f}{k_r} = \frac{C^0_{RNHCO_2H}}{C^0_{RNH_2} C^0_{CO_2}} K = \frac{\left(\frac{1}{V_{RNHCO_2H}}\right)}{\left(\frac{1}{V_{RNH_2}}\right)\left(\frac{1}{V_{CO_2}}\right)} K = \frac{RT}{P} K \qquad \text{(for ideal gas phases)} \qquad \textbf{(10-21)}$$

$$K_c = \frac{k_f}{k_r} = \frac{[RNHCO_2H]_e}{[RNH_2]_e [CO_2]_e} \qquad \text{(for ideal gas phases)} \qquad \textbf{(10-22)}$$

where K_c is the concentration-based equilibrium constant, C_i^0 is the standard state species concentration which typically takes on the form of the molar volume for ideal gas-phase calculations ($V = RT/P$). Since the concentration of carbon dioxide is typically 10 – 100x larger than that of starting materials in CO_2-based processes, equation **(10-22)** can rearranged and simplified to:

$$\frac{[RNHCO_2H]_e}{[RNH_2]_e} = K_c [CO_2]_0 = \left[\frac{RT}{P} \exp\left(-\frac{\Delta G^0_{rxn}}{RT}\right)\right] [CO_2]_0 \qquad \textbf{(10-23)}$$

where $[CO_2]_0$ is the density of carbon dioxide at reaction conditions. At fixed density, equation **(10-23)** reveals that the equilibrium ratio of carbamic acid to free amine is directly proportional to K_c.

As shown from **Table 10-1**, the addition of small, electron-donating groups to ethylallylamine resulted in an equilibrium shift to favor carbamic acid (compare entries 1 – 3). This effect is likely ascribed to an increase in amine nucleophilicity, making it more likely to react with the electron-deficient carbon of CO_2. Methyl and ethyl groups do not appear sterically-demanding enough to inhibit carbamic acid formation. Although *i*-Pr and *t*-Bu groups also increase the nucleophilicity of ethylallylamine, it appears that sterics play a more important role; equilibrium shifts in these cases to favor free amine (compare entries 1, 4, & 5). Importantly, these trends are qualitatively consistent with experimental findings. Fischer and coworkers (2003), for example, found that in neat CO_2 at 323 K and 80 – 200 bar, carbamic acid formed for benzylamine and *N*-methylbenzylamine, but *not* for *N*-isopropyl- and *N*-tertbutylbenzylamine (see **Section 4.2**). In addition, Wittmann and coworkers (2001) observed carbamic acid formation in neat CO_2 at 313 K (40 °C) and 120 bar for ethyl-2-methylallylamine, which is very similar to our model ethylallylamine (entry 3) (see **Section 4.3.2**).

Table 10-1. CBS-QB3-calculated gas-phase thermochemical equilibrium properties for the reaction of amines with carbon dioxide at 298 K.

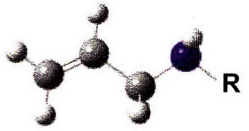

Entry	R	ΔG^0_{rxn}	$\Delta\Delta G^0_{rxn}$	ΔH^0_{rxn}	$K_c \cdot 10^5$
		kcal·mol^{-1}			M^{-1}
1	H	5.9	0	–4.1	116
2	Me	4.7	–1.2	–5.3	877
3	Et	5.5	–0.4	–5.1	227
4	*i*-Pr	6.2	0.3	–4.8	70
5	*t*-Bu	8.9	3.0	–2.8	0.7

In their experimental study involving isopropylamine and neat CO_2, Dijkstra and coworkers (2007) observed increased carbamic acid formation with (1) increased operating density at fixed temperature and (2) decreased temperature at fixed operating density (see **Section 4.2**). Intrigued by these findings, we turned our attention to an equilibrium study that probed the effects of process operating conditions on carbamic acid formation. The increase in carbamic acid formation with increased CO_2 density observed by the authors is straightforward and ascribed to Le Chatlier's principle. Le Chatlier's principle may similarly explain the observed decrease in carbamic acid formation at elevated temperatures; increased temperatures for an exothermic reaction (see **Table 10-1**), shifts the equilibrium shifts toward reactants (e.g., free amine). As shown by **Table 10-2**, calculations involving isopropylamine and its carbamic acid derivative at conditions explored by Dijkstra and coworkers also revealed an equilibrium shift to free amine with increased temperature. Our predictions show consistent trends with experimental data, although they are offset quantitatively by about an order of magnitude (see **Figure 10-2**). One reason for this discrepancy may be the inability of G03 gas-phase calculations to accurately capture solvation effects present in CO_2-based media. At 75 °C, for example, decreasing the calculated ΔG^0_{rxn} by 2 kcal·mol^{-1} would lead to nearly identical

Table 10-2. CBS-QB3-calculated free energy changes for the reaction of isopropylamine with carbon dioxide.

T		ΔG^0_{rxn}	$\Delta\Delta G^0_{rxn}$	$K_c \cdot 10^5$
K (°C)	Solvent	kcal·mol^{-1}		M^{-1}
298 (25 °C)	none	5.7	0	165
323 (50 °C)	none	6.7	1.0	82
323 (50 °C)	DMSO	4.0	—	5290
348 (75 °C)	none	7.5	1.8	57
373 (100 °C)	none	8.3	2.6	41

agreement. We have also neglected to correct the entropic portion of the ΔG^0_{rxn} to account for loss of rotations accompanied with two molecules becoming one. In addition, equation **(10-22)** assumes ideal solution behavior; a more rigorous alternative that is more applicable to this media is given by:

$$K_c = \frac{[RNHCO_2H]_e}{[RNH_2]_e\,[CO_2]_e}\,\frac{\hat{\phi}^v_{RNHCO_2H}}{\hat{\phi}^v_{RNH_2}\,\hat{\phi}^v_{CO_2}} \qquad \textbf{(10-24)}$$

where $\hat{\phi}_i^v$ is the species mixture fugacity coefficient. It may be possible that mixture fugacity coefficients in CO_2-based media deviate appreciably from unity and result in higher equilibrium ratios.

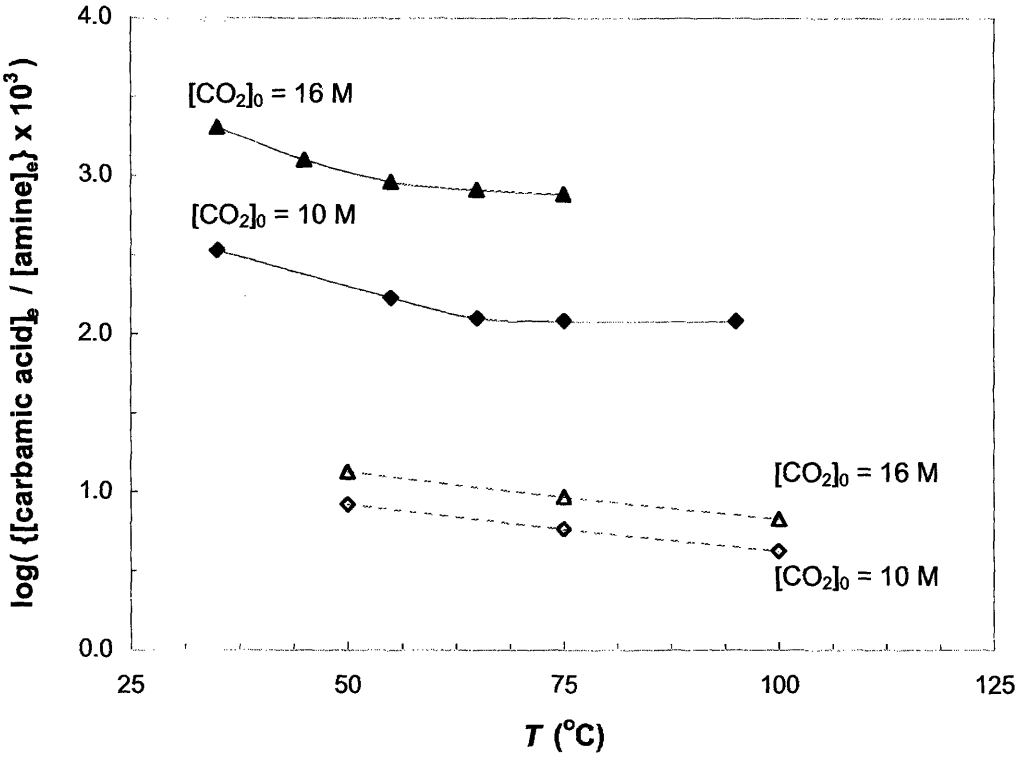

Figure 10-2. CBS-QB3-calculated equilibrium concentration ratios of carbamic acid and amine plotted as a function of temperature and carbon dioxide density for the reaction of carbon dioxide with isopropylamine: experimental data (—) by Dijkstra et al. (2007) for $[CO_2]_0$ = 16 M (▲) and 10 M (♦); calculations (- - -) by this work for $[CO_2]_0$ = 16 M (Δ) and 10 M (◊).

Dijkstra and coworkers (2007) also found that carbamic acid formation dependently greatly on solvent properties. Bubbling CO_2 into 0.1 M isopropylamine dimethyl sulfoxide (DMSO) solution at 298 K (25°C) and 1.01 bar, for example, led to the complete conversion of carbamic acid. The solubility in of CO_2 in DMSO at these conditions is significantly less than that of the neat CO_2 studies, which suggests that solvation effects were playing a dominant role. Interestingly, calculations using a DMSO electrostatic continuum solvation model (dielectric constant = 47) also revealed a dramatic increase in carbamic acid formation (see **Table 10-2**). These findings indicate that carbamic acid formation is preferred and potentially accelerated in polar liquid phases that are often present in multi-phasic CO_2-based systems.

Transition State Calculations

A careful review of the literature revealed the following mechanisms responsible for carbamic acid formation (Tsipis et al., 2005; Arstad et al., 2007):

(1) a single-step concerted reaction mechanism **(CA-1)**, and

(2) a two-step reaction mechanism **(CA-2)** involving amine-CO_2 coordination complex formation and amine-assisted protonation steps.

(3) a two-step reaction mechanism **(CA-2)''** involving zwitterion formation and amine-assisted protonation steps;

A summary of these mechanisms is presented in **Table 10-3**.

In the concerted reaction mechanism **(CA-1)**, C-*N* bond-formation and *N*-O hydrogen transfer occurs simultaneously in a 4-membered transition state (see **Figure 10-3a**). In their extensive gas-phase theoretical study of urea synthesis from ammonia and carbon dioxide, Tsipis and coworkers (2005) reported that the barrier associated with this mechanism was too high in energy to account for experimentally-observed urea formation rates. We extended the scope of their study to include a variety of primary and secondary amines and the results are presented in **Table 10-4**. Increasing the number of methyl groups added to ammonia led to a significant reduction in the energy barrier. We suspect that faster reaction rates are ascribed to the increased nucleophilicity of the amine upon addition of electron-donating groups. As previously mentioned, methyl groups are relatively small and one would not expect inhibitory effects due to steric interference. We also found a significant difference between lower- (B3LYP/CBSB7) and higher-level (CBS-QB3) barrier estimates. The error in the barrier for lower-level calculations ranges from +1 to –4 kcal·mol^{-1}, and seems to decrease rather consistently with each successive methyl group addition. Control calculations using even lower-level methods (e.g., B3LYP/6-31G(d')) revealed that that majority of the error between the lower- and higher-level calculations is due to the extrapolation to a complete basis set and not due to optimized geometry predictions. Lastly, all of these barriers make the reaction too slow to account for experimentally-observed carbamic acid formation (see previous section). For example, at 298 K (25 °C) and 403 K (130 °C, amide synthesis conditions), the rate constants

Table 10-3. Carbamic acid formation mechanisms.

$R^1R^2NH + O=C=O \rightleftharpoons [R^1R^2N\cdots H\cdots C(=O)=O]^{TS\ (CA\text{-}1)} \rightleftharpoons R^1R^2N{-}C(=O){-}OH$ (amine → carbamic acid)	**(CA-1)**
$R^1R^2NH + O=C=O \rightleftharpoons R^1R^2NH\cdots C(=O)=O \overset{R^1R^2NH}{\rightleftharpoons} [R^1R^2N(H\cdots NR^1R^2)C(=O)H]^{TS\ (CA\text{-}2)} \rightleftharpoons R^1R^2N{-}C(=O){-}OH + R^1R^2NH$	**(CA-2)**
$2R^1R^2NH \rightleftharpoons R^1R^2N(H)C(=O)N(H)R^1R^2 \overset{O=C=O}{\rightleftharpoons} [R^1R^2N(H\cdots NR^1R^2)C(=O)H]^{TS\ (CA\text{-}2)} \rightleftharpoons R^1R^2N{-}C(=O){-}OH + R^1R^2NH$	**(CA-2)'**
$R^1R^2NH + O=C=O \rightleftharpoons R^1R^2\overset{\oplus}{N}H{-}C(=O)O^{\ominus} \overset{R^1R^2NH}{\rightleftharpoons} [R^1R^2N(H\cdots NR^1R^2)C(=O)H]^{TS\ (CA\text{-}2)} \rightleftharpoons R^1R^2N{-}C(=O){-}OH + R^1R^2NH$	**(CA-2)''**

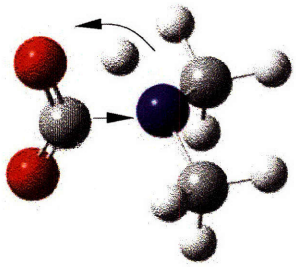

TS CA-1

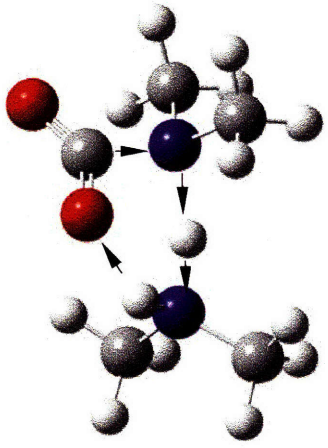

TS CA-2

Figure 10-3. Representative transition state structures leading to the formation of carbamic acid via the concerted **(CA-1)** mechanism and amine-assisted **(CA-2)** mechanism.

Table 10-4. CBS-QB3-calculated thermochemical and activation parameters for the reaction of amines with carbon dioxide via a concerted reaction mechanism **(CA-1)**.

			ΔE_0 (kcal·mol^{-1}) [a]			$\Delta G^{0,TS}$ (kcal·mol^{-1}) [b]		
Entry	**R^1**	**R^2**	**CBS-QB3**	**CBSB7**	**Δ [c]**	**CBS-QB3**	**CBSB7**	**Δ [c]**
1	H	H	45.1	43.7	1.4	53.6	52.3	1.3
2	H	Me	37.5	38.8	–1.3	47.0	48.3	–1.3
3	Me	Me	32.4	36.5	–4.1	42.3	46.5	–4.2

[a] refers to the difference in energies of the transition state and starting materials; [b] evaluated at 298 K (25 °C); [c] corresponds to the difference in values predicted by the two calculation methods.

for the concerted reaction involving CO_2 and dimethyl amine would be 2.9×10^{-17} and 2.9×10^{-11} $M^{-1}\cdot s^{-1}$, respectfully. With a typical initial concentrations of $[amine]_0$ = 0.1 M and $[CO_2]_0$ = 10.5 M (density at 130 °C and 250 bar), the largest rate of reaction would be a sluggish 2.6×10^{-6} $M\cdot day^{-1}$ at 130 °C (*vs.* instantaneously for the study by Dijkstra et al. [2007]).

Tsipis and coworkers (2007) proposed an alternative gas-phase carbamic acid formation mechanism that involved a second free amine molecule acting as a hydrogen transfer agent. In the **(CA-2)** mechanism, carbon dioxide and an amine form a coordination complex that undergoes amine-assisted hydrogen transfer to afford carbamic acid. The amine can also form a dimer in the **(CA-2)'** mechanism that combines with carbon dioxide in the **(CA-2)** transition state. Alternatively, in the **(CA-2)''** mechanism, nitrogen can add to carbon dioxide forming a a charge-separated intermediate known as a zwitterion. In protic media such as water, the medium itself can then serve as a hydrogen transfer agent and also protonate the zwitterion to form carbamic acid.

After extensive searching, we were unable to locate stable gas-phase zwitterion intermediates for a range of amines studied. This is not surprising given that a zero-dielectric gas-phase medium is unable to support charge separation of ionic species. All minimum energy searches involving an amine and carbon dioxide resulting in "loose" van der Waals coordination complexes that were 2 – 3 kcal·mol^{-1} less stable than the starting materials (see **Figure 10-4a)**. Switching to a water electrostatic continuum solvation model afforded a stable zwitterion species that was 6.4 kcal·mol^{-1} less stable than the starting materials (see **Figure 10-4b)**. Although the zwitterion is higher in energy, protonation in aqueous media would be significantly faster and result in higher carbamic acid formation rates. In their gas- and aqueous-phase

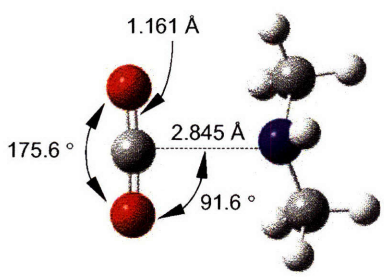

for complex: $\Delta G^{0,298\,K}_{rxn,\,gas\text{-}phase} = 2.6$ kcal·mol^{-1}

for carbamic acid: $\Delta G^{0,298\,K}_{rxn,\,gas\text{-}phase} = 4.5$ kcal·mol^{-1}

(a)

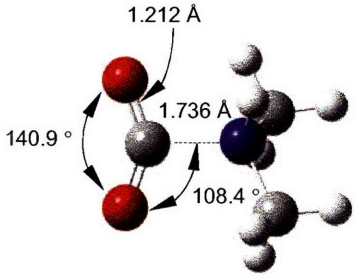

for zwitterion: $\Delta G^{0,298\,K}_{rxn,\,water} = 6.4$ kcal·mol^{-1}

for carbamic acid: $\Delta G^{0,298\,K}_{rxn,\,water} = 1.9$ kcal·mol^{-1}

(b)

Figure 10-4. Representative stable structures for the van der Waals coordination complex **(a)** and the zwitterion **(b)** formed from the reaction of carbon dioxide with amines.

theoretical study of zwitterion intermediates formed by the reaction of methylamine and formaldehyde, Hall and workers (1998) identified stable zwitterion species only when employing a water continuum model or by adding two water molecules in the vicinity of the gas-phase amine-aldehyde coordination complex. In light of these observations, and given that carbon dioxide is a low-dielectric medium, we have ruled out the possibility of zwitterion formation via the **(CA-2)''** mechanism for reactions proceeding in neat CO_2. Calculations also revealed that that the amine-CO_2 complex was ca. 3 kcal·mol^{-1} more stable than the amine-amine dimer of mechanism **(CA-2)'**. Furthermore, with the carbon dioxide is typically in large excess in these reactions, making **(CA-2)** the likely mechanism for carbamic acid formation.

Representative transition state structures for the **(CA-2)** mechanism were identified (see **Figure 10-3b**) and calculations for variety of amines are presented in **Table 10-5**. The barriers associated with the amine-assisted mechanism are ca. 22 kcal·mol^{-1} lower than those associated with the concerted reaction mechanism (compare entries 1 & 2 of **Table 10-5** with 1 & 3 of **Table 10-4**). Assuming for the moment a termolecular reaction, the rate constants for the amine-assisted reaction involving CO_2 and dimethyl amine would be 1.1×10^{-3} and 9×10^{-3} M^{-2}·s^{-1} at 298 K (25 °C) and 403 K (130 °C), respectfully. With typical initial concentrations of $[amine]_0 = 0.1$ M and $[CO_2]_0 = 10.5$ M, the reaction rate would be 81 M·day^{-1} at 130 °C, which is significant in comparison to the experimentally-observed time scale for amide

Table 10-5. CBS-QB3-calculated thermochemical and activation parameters for the reaction of amines with carbon dioxide via the amine-assisted **(CA-2)** mechanism.

			ΔE_0 (kcal·mol^{-1}) [a]		$\Delta G^{0,TS}$ (kcal·mol^{-1}) [b]	
Entry	**R^1**	**R^2**	**CBS-QB3 (CBSB7)**	**Δ [c]**	**CBS-QB3 (CBSB7)**	**Δ [c]**
1	H	H	21.6 (18.5)	3.1	40.0 (37.0)	3.0
2	Me	Me	3.7 (11.5)	–7.8	24.9 (32.7)	–7.8
3 [d]	Al	H	10.1 (14.0)	–3.9	30.5 (34.5)	–4.0
4	Al	Me	(12.5)	—	(34.0)	—
5 [e]	Al	Et	2.7 (15.1)	–12.4	25.7 (38.1)	–12.4
6	Al	*i*-Pr	(19.9)[f]	—	(42.8)	—
7 [g]	Al	*t*-Bu	—	—	—	—

[a] refers to the difference in energies of the transition state and starting materials; [b] evaluated at 298 K (25 °C); [c] corresponds to the difference in values predicted by the two calculation methods; [d] corresponds to our 'model' benzylamine, allylamine; [e] corresponds to our 'model' *N*-butylbenzylamine, ethylallylamine; [f] too large to calculate at CBS-QB3 level within a reasonable timeframe; [g] due to steric crowding, an energy minimum could not be determined.

formation (0.1 M·day^{-1}). However, $\Delta G_{rxn}^{0,403\,K}$ = 7.8 kcal·mol^{-1} and the resulting equilibrium ratio of carbamic acid to free amine is very small at 0.02.

Similar to our study of the concerted **(CA-1)** mechanism, adding an ethyl group to allylamine led to a decrease in the reaction barrier (compare entries 3 & 5). Although lower-level calculations for the **(CA-2)** transition state of *N*-isopropylallylamine revealed an increase in the barrier (compare entries 3 & 6), this observation remains suspect due to the systematic error associated with the level of computational theory. Several lower- and higher-level calculation attempts for the transition state structure involving *N*-tertbutylallylamine failed at the optimization step because of steric crowding. This finding may suggest that the forward reaction rate is very slow, if even possible at all.

In summary, the energy profile associated with carbamic acid formation in neat CO_2 is presented in **Figure 10-5**, with thermochemical and activation parameters given in **Table 10-8** of **Section 10.7**.

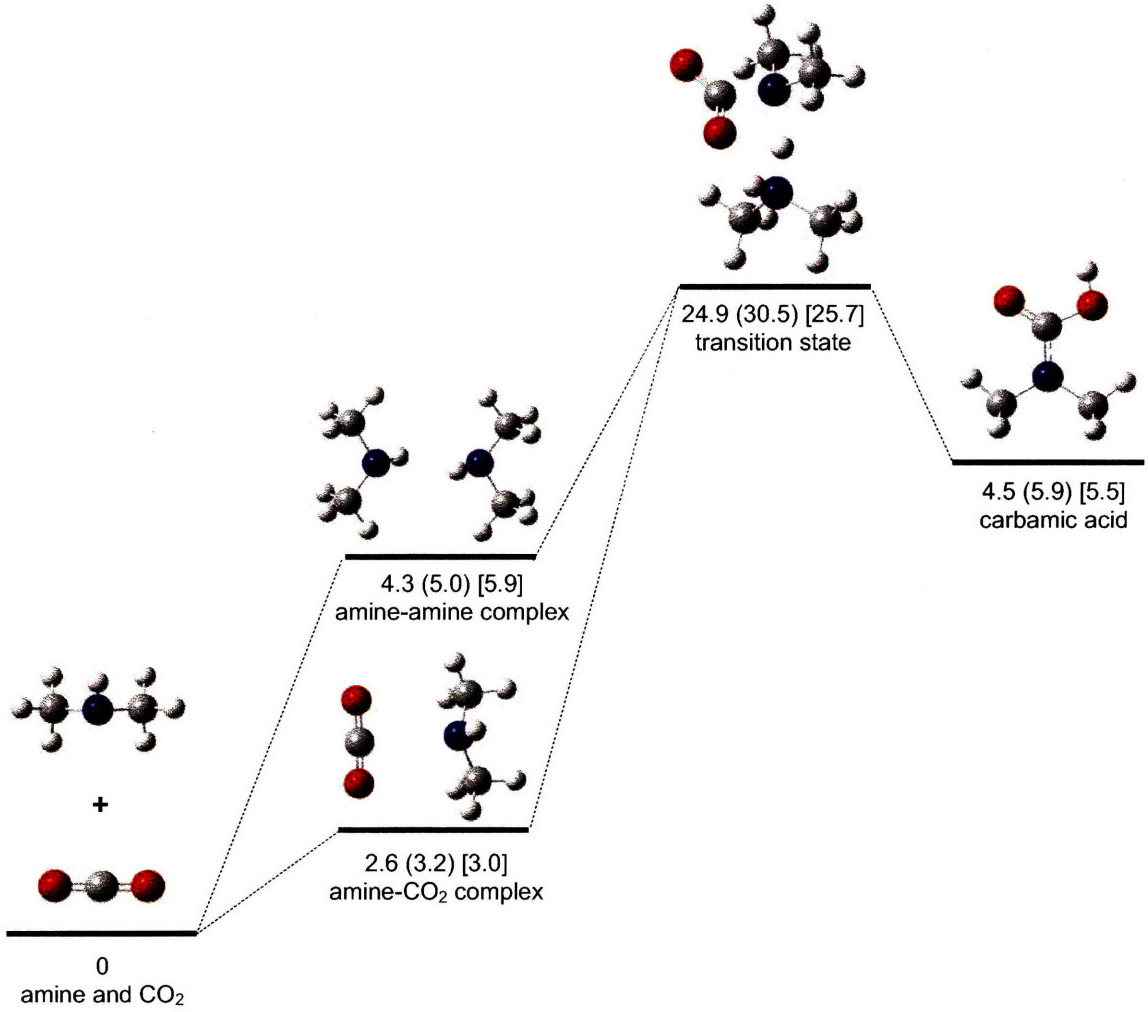

Figure 10-5. CBS-QB3-calculated (kcal·mol^{-1}) free energy diagram for the reaction of model amines with carbon dioxide at 298 K (25 °C): values listed for dimethyl amine; (allylamine, our model benzylamine); and [ethylallylamine, our model *N*-butylbenzylamine].

10.4.2. Ketene Formation

The formation of ketenes generated from the thermolysis of 1-alkynyl ethers has been reported to occur through a concerted 6-membered ring transition state involving hydrogen transfer (reviewed in Tidwell, 2006):

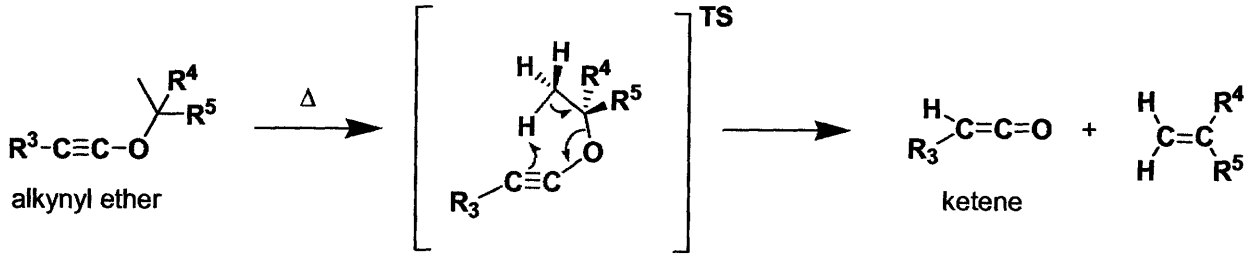

alkynyl ether ketene

(K-1)

Representative transition state structures for these transformations are shown in **Figure 10-6.** As shown by **Table 10-6**, fluctuations in thermochemical and activation parameters saturated after the addition of two sp^3 carbons to the R^3 group (compare entries 1 – 4). Surprising, we did not observe the quantifiable difference among reaction energy barriers as claimed by Moyano and coworkers (1998) in their experimental and semi-empirical AMI theoretical study (compare entries 2, 5, & 7). Calculation of rate constants in the form of the Arrhenius expression did however reveal larger reaction rate constants for *i*-Pr and t-Bu-substituted ethers relative to the Et-substitute ether, primarily due to increasing pre-exponential factors (*A*) (see **Table 10-8** in **Section 10.7**). All three cases were essentially irreversible, with a $\Delta G_{rxn}^{0,298\,K}$ of ca. –21 kcal·mol^{-1}.

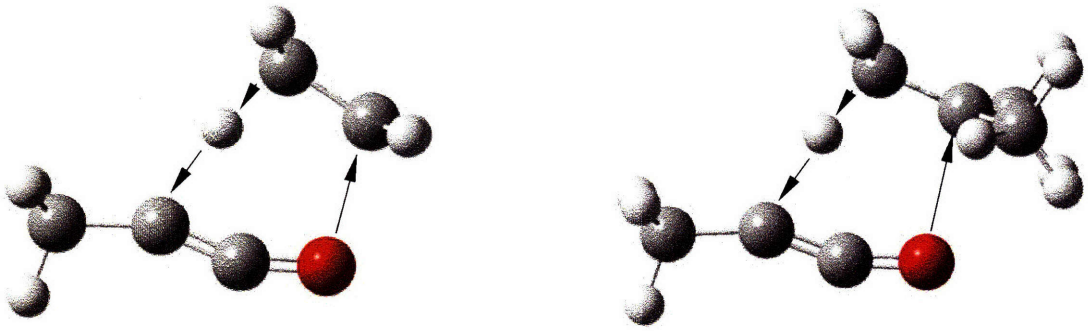

(a) (b)

Figure 10-6. Representative alkynyl ether thermolysis transition state structures leading to the formation of ketenes via the **(K-1)** mechanism: ethoxy-substituted alkynyl ether **(a)** and *t*-butoxy-substituted alkynyl ether **(b)**.

Table 10-6. CBS-QB3-calculated thermochemical and activation parameters for the thermolysis of alkynyl ethers.

Entry	R^3	R^4	R^5	ΔE_0 [a]	$\Delta H^{0,TS}$ [b,c]	$\Delta S^{0,TS}$ [b,c]
				(kcal·mol^{-1})		(cal·mol^{-1}·K^{-1})
ethoxy-substituted alkynyl ether (L^{TS} = 3)						
1	H	H	H	30.3	30.1 (46.3)	–2.4 (–4.4)
2	Me	H	H	31.6	31.8 (46.6)	1.1 (–7.7)
3	Et	H	H	31.0	30.6 (46.8)	–3.7 (–4.9)
4	*n*-Pr	H	H	31.0	30.6	–3.6
i-propoxy-substituted alkynyl ether (L^{TS} = 6)						
5	Me	H	Me	31.3	31.1 (43.8)	–4.0 (–6.7)
6	Et	H	Me	30.8	30.6	–2.6
t-butoxy-substituted alkynyl ether (L^{TS} = 9)						
7	Me	Me	Me	30.7	31.2 (40.5)	5.0 (–6.7)
8	Et	Me	Me	30.0	30.0	–0.7

[a] calculated at the CBS-QB3 level; [b] at 298 K (25 °C); [c] values in parentheses are reported by Moyano and coworkers (1987) using the semi-emperical AM1 method.

Importantly, our calculated activation energy barrier for the thermolysis of our model 1-ethoxy-but-1-yne (31 kcal·mol) is consistent to the experimental value reported by Moyano and coworkers (1987) for the similar 1-ethoxy-hept-1-yne (29 kcal·mol^{-1}). As shown by **Figure 10-8**, calculations suggest that temperatures of 398 K (125 °C) and 358 K (85 °C) are required for the complete conversion of ethoxy- and *t*-butoxy-substituted alkynyl ethers within our experimental 24-hr time frame, respectively. These findings agree quite satisfactorily with our experimental observations. Incomplete alkynyl ether was observed when employing ethoxy- and *t*-butoxy-substituted alkynyl ethers at 120 and 80 °C for 24 hr, respectively. Increasing temperature to 130 and 90 °C resulted in complete conversion.

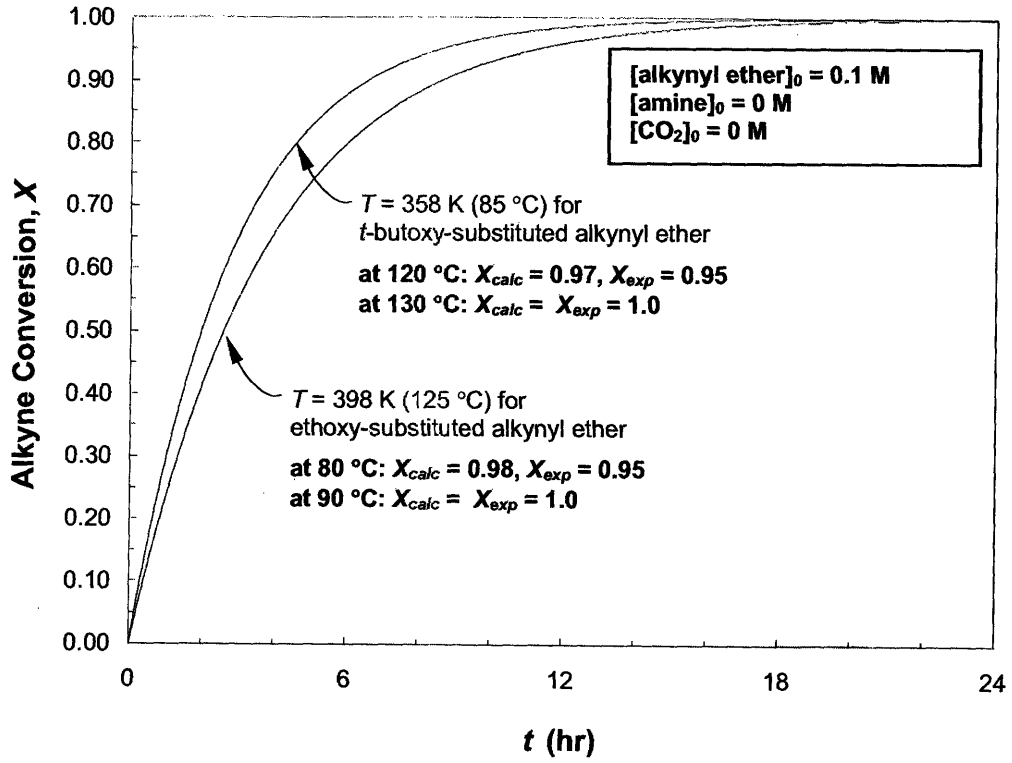

Figure 10-7. Predicted conversions of 1-ethoxy-hept-1-yne and 1-*t*-butoxy-prop-1-yne plotted as a function of time and temperature.

10.4.3. Ketene Cycloaddition Product Formation

In addition to competitive carbamic acid pathways, amide selectivity can be compromised the ketene cycloaddition pathways discussed below.

Ketene + Ketene Cycloaddition Reactions

Ketenes readily undergo [2 + 2] dimerizations that produce a variety of four-membered products. In the absence of catalysts, ketenes primarily form β-lactones and 1,3-cyclobutanediones via highly unsymmetrical concerted [$_{\pi}2_a$ + $_{\pi}2_a$] cycloaddition mechanisms (reviewed in Tidwell, 2006):

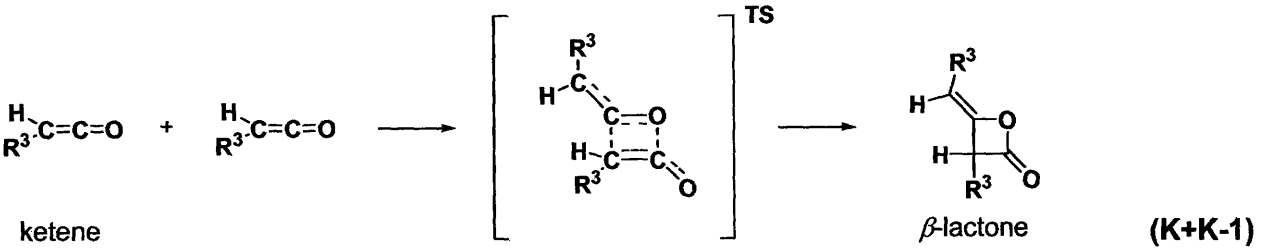

(K+K-1)

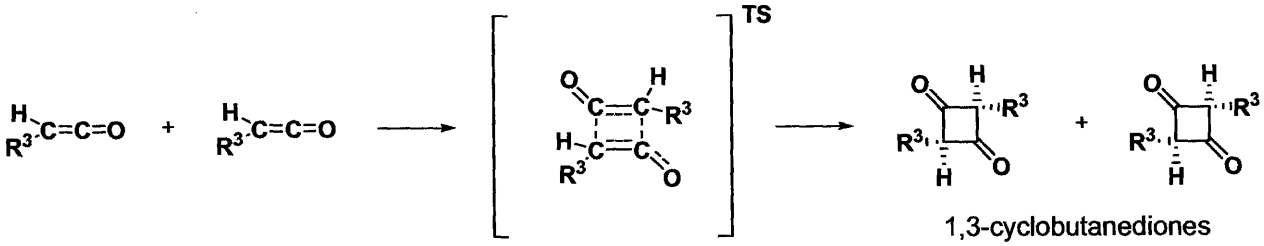

(K+K-2)

Representative transition state structures for these transformations are shown in **Figure 10-8**, with kinetic and thermochemical parameters given in **Table 10-8** in **Section 10.7**. Calculations indicated that the energy barrier associated with β-lactone formation was ca. 2.5 kcal·mol^{-1} higher than of the 1,3-cyclobutanedione formation reaction and was therefore considered negligible in comparison. Surprisingly, the lowest-energy transition state structure determined for the **(K+K-2)** mechanism was the one that afforded the *cis* stereoisomer. The barrier for the dimerization of propen-1-one (methylketene) by this mechanism was 14.9 kcal·mol^{-1} and was essentially irreversible with a $\Delta G_{rxn}^{0,298\,K}$ of –15.0 kcal·mol^{-1}.

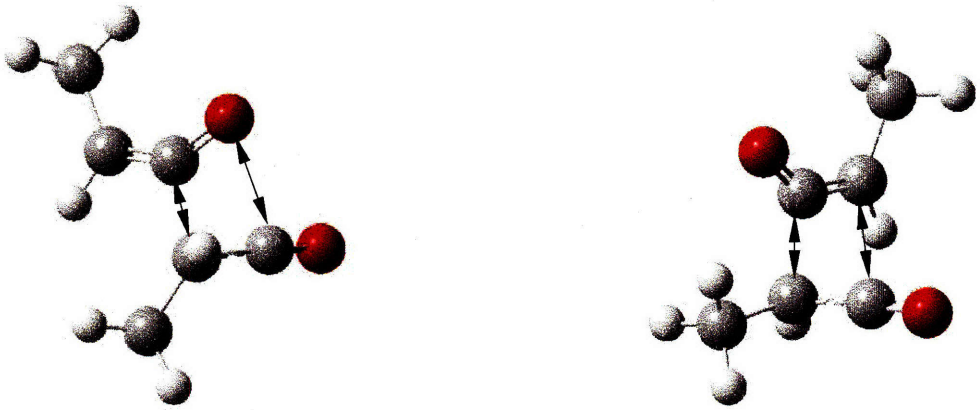

(a) (b)

Figure 10-8. Representative ketene + ketene cycloaddition transition state structures leading to the formation of β-lactones via the **(K+K-1)** mechanism **(a)** and 1,3-cyclobutanediones via the **(K+K-2)** mechanism **(b)**.

Ketene + Alkyne Cycloaddition Reactions

Ketenes can similarly undergo [2 + 2] cycloaddition reactions with the alkynyl ethers from which they were derived to form cyclobutenones (reviewed in Tidwell, 2006):

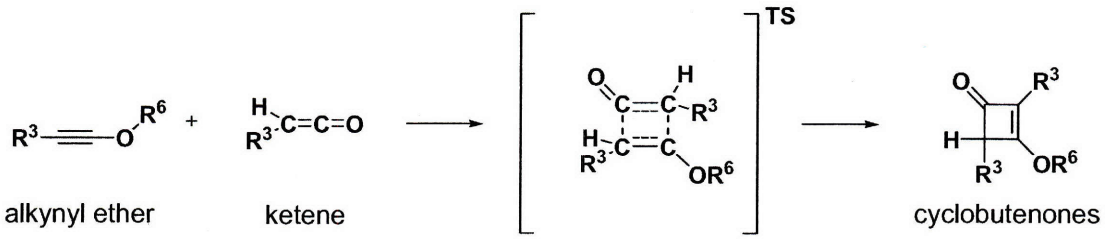

(K+Alk-1)

A representative transition state structure for this transformation is shown in **Figure 10-9**, with reaction rates and thermochemical properties given in **Table 10-8** in **Section 10.7**. The barrier for the cycloaddition of 1-ethoxy-prop-1-yne and propen-1-one by this mechanism was 15.4 kcal·mol^{-1} and was essentially irreversible with a $\Delta G_{rxn}^{0,298\,K}$ of –40.0 kcal·mol^{-1}.

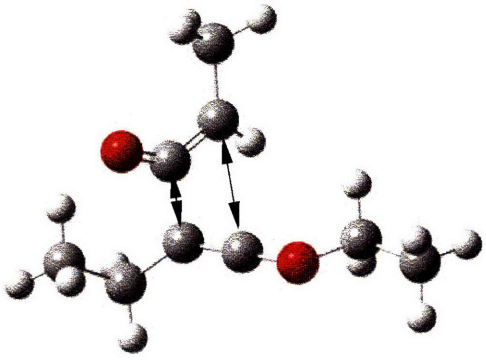

Figure 10-9. Representative ketene + alkynyl ether cycloaddition transition state structure leading to the formation of cyclobutenones via the **(K+Alk-1)** mechanism.

Ketene + Alkene Cycloaddition Reactions

Ketenes and alkenes can also participate in a mechanism very similar to **(K+Alk-1)** to yield cyclobutanones (reviewed in Tidwell, 2006). Calculations with but-1-en-1-one and ethylene (formed during the ketene formation step, see **Section 10.4.2**) revealed a barrier of 24.0 kcal·mol^{-1}, making the reaction insignificant when compared to ketene + alkynyl ether and ketene + ketene cycloaddition pathways.

Impact on Amide Formation

As shown by **Figure 10-10**, calculations indicate that the ketene will undergo competitive cycloaddition reactions on a time scale that would be detrimental to amide formation. This observation supports our theory that the partitioning of ketene to a more concentrated phase that is devoid of amine or that interference due to carbamic acid formation would indeed lead to byproduct formation. Unfortunately, our analytical capabilities were unable to detect cycloaddition products for cases where amide selectivity diminished.

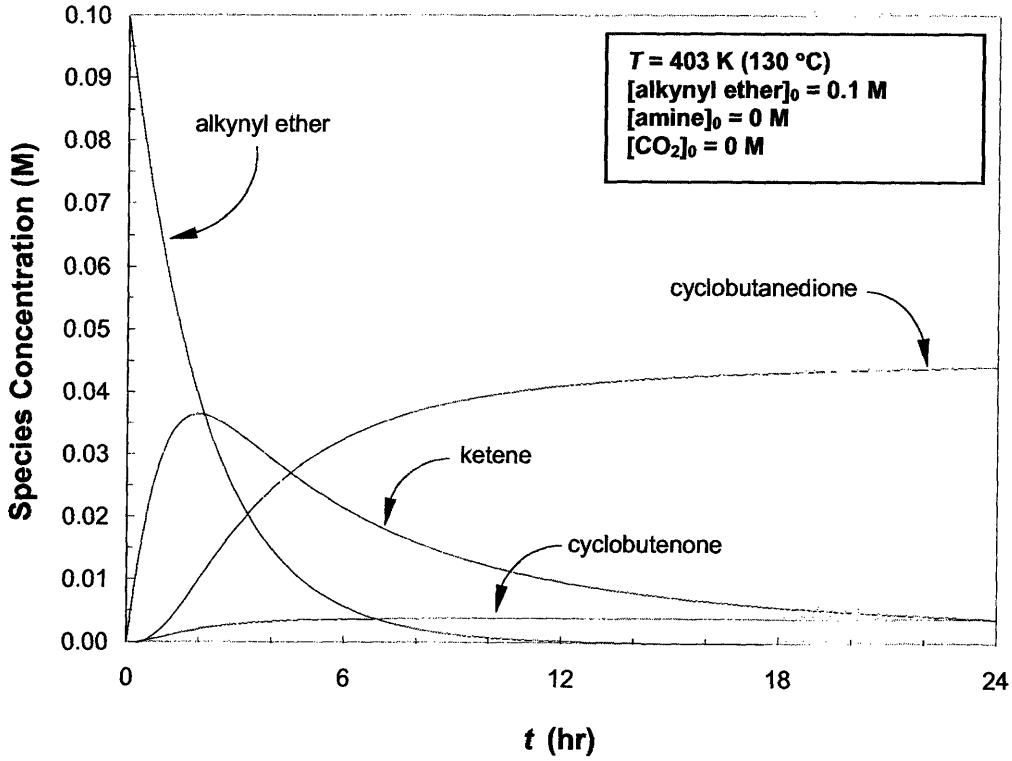

Figure 10-10. Predicted species concentrations profiles for the thermolysis of 1-ethoxy-hept-1-yne at 403 K (130 °C).

10.4.4. Amide Formation

Amide formation via the amination of ketenes has been reported to occur through the following reaction mechanisms (reviewed in Tidwell, 2006; Allen et al., 1999; Sung et al., 1998; Raspoet et al., 1998):

(1) a single-step concerted reaction mechanism **(A-1)**;

(2) a two-step reaction mechanism **(A-2)** involving amine-ketene complex formation (or amine-amine complex formation **[A-2]'**) and amine-assisted hydrogen-transfer steps, and

(3) a three-step reaction mechanism **(A-3)** involving amine-ketene complex formation (or amine-amine complex formation **[A-3]'**), an amine-assisted hydrogen-transfer step affording an enol intermediate, and an amine-assisted hydrogen-transfer step affording an amide.

A summary of these mechanisms is presented in **Table 10-7**.

In separate theoretical studies involving ketene ($H_2C=C=O$) and ammonia (NH_3), Raspoet and coworkers (1998) and Sung and coworkers (1998) found that the energy barriers associated with the concerted **(A-1)** mechanism involving NH_3 addition across the C=C bond were too large to account for experimentally-observed amide formation rates. For example, Raspoet and workers reported a QCISD(T)-calculated barrier of 41.6 kcal·mol^{-1}, which is very close to the MP4-calculated value of 42.0 kcal·mol^{-1} reported by Sung and coworkers (1998). Both studies failed to locate stable zwitterion intermediates for this transformation in both gas- and solvent continuum-phase calculations. Sung and coworkers (1998) found that the barrier was reduced significantly to 16.9 kcal·mol^{-1} when using an ammonia molecule as a hydrogen transfer agent in the **(A-2)** mechanism. This barrier was still too slow to account for reasonable amide formation rates.

In the more-likely **(A-3)** mechanism, an enol is formed by the amine-catalyzed addition of NH_3 across the C=O ketene bond. The enol subsequently undergoes amine-assisted hydrogen transfer to afford the desired amide. Sung and coworkers (1998) reported MP4-calculated barriers of 1.1 kcal·mol^{-1} for the enol-formation step (*vs.* 32.5 kcal·mol^{-1} for the uncatalyzed

Table 10-7. Amide formation mechanisms.

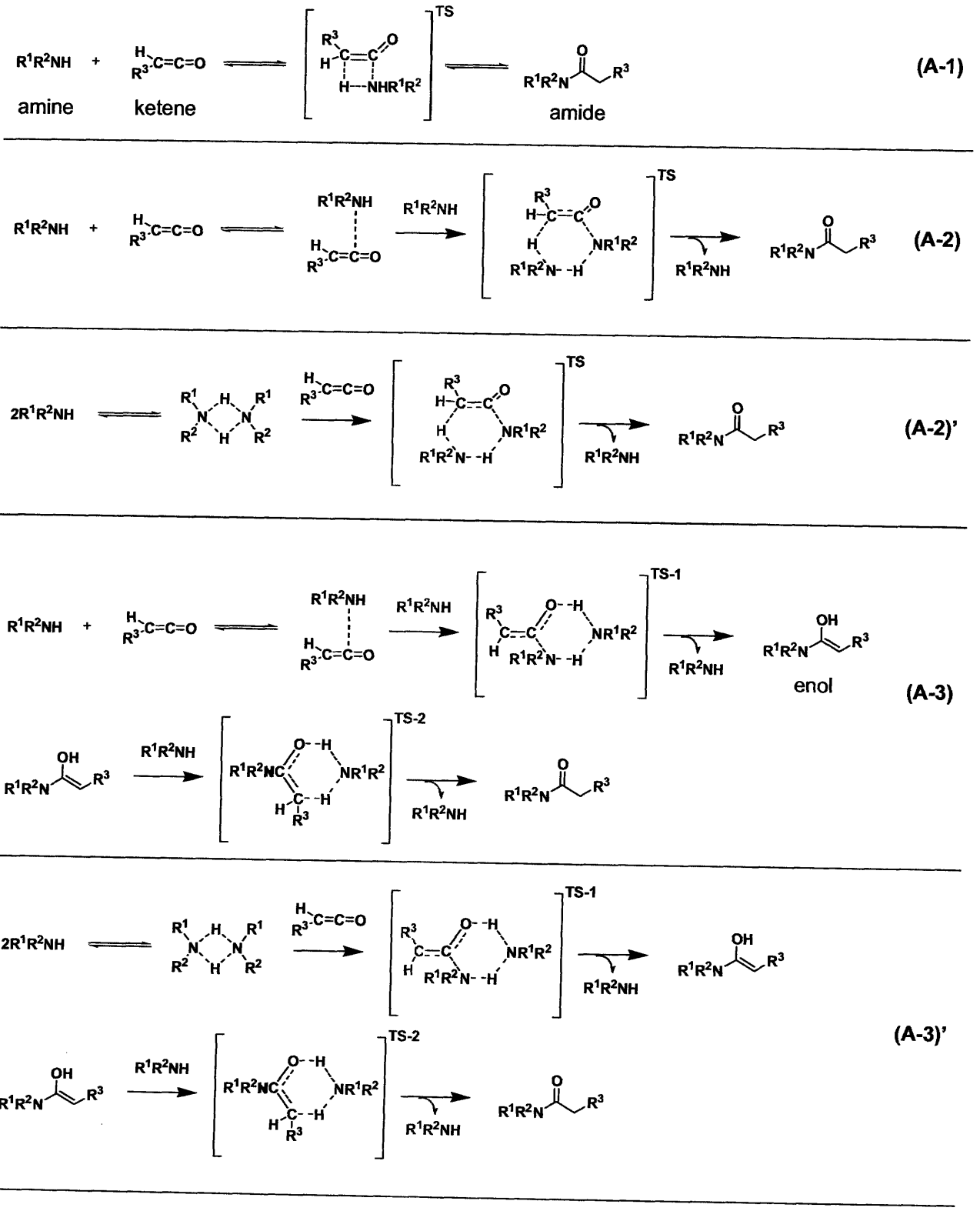

version of this step) and 9.2 kcal·mol^{-1} for the amide-formation step (*vs.* 39.8 kcal·mol^{-1} for uncatalyzed version of this step). This mechanism is supported further by the experimental spectroscopic detection of enol intermediates (Raspoet et al., 1998) and by the non-linear dependence of observed reaction rate constants with amine concentration (Allen et al., 1999) during the experimental amination of ketenes.

Based on these previous theoretical and experimental findings, we have therefore limited our modeling effort to the **(A-3)** mechanism and have assumed that the **(A-1)** and **(A-2)** mechanisms yield reaction rates too slow for reactants other than ketene and ammonia as well. Representative transition state structures for the **(A-3)** mechanism are shown in **Figure 10-11** and kinetic and thermochemical parameters are given in **Table 10-8** in **Section 10.7**. The energetics associated with enol and amide formation involving propen-1-one and dimethyl amine are shown in **Figure 10-12** and **Figure 10-13**, respectfully. The amine-amine complex was found to be ca. 2.5 kcal·mol^{-1} more stable than the ketene-amine complex, suggesting that **(A-3)** was preferred over the **(A-3)'** pathway.

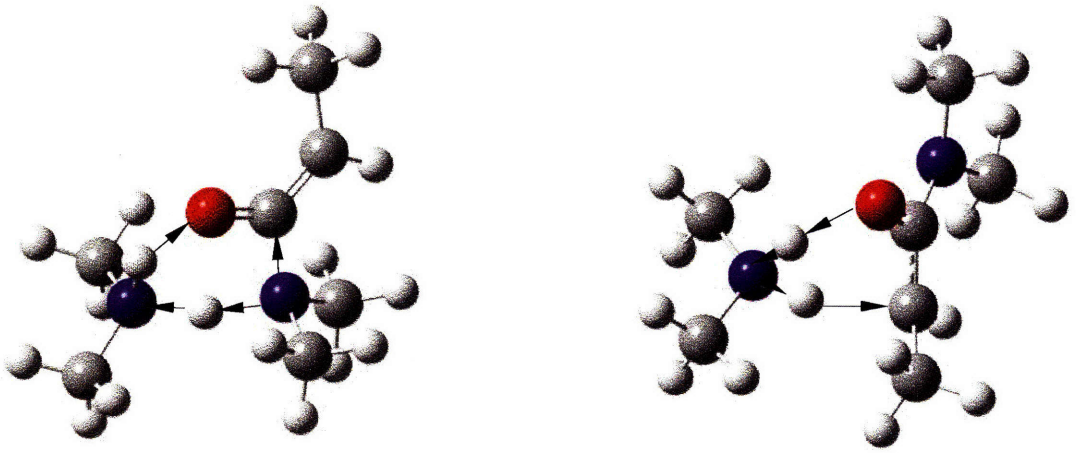

(a) **(b)**

Figure 10-11. Representative ketene amination transition state structures leading to the formation of enols **(a)** and amides **(b)** via the **(A-3)** mechanism.

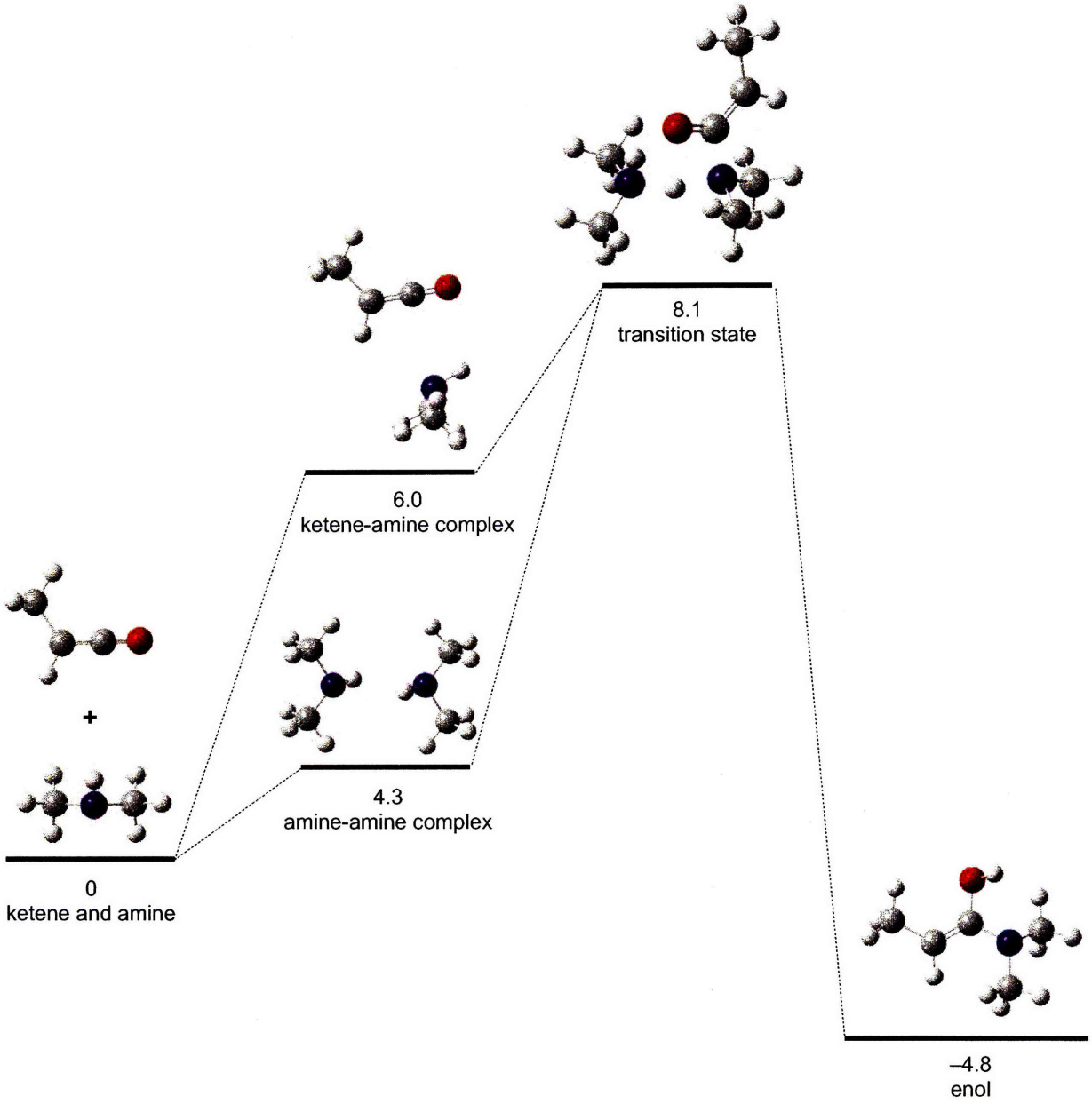

Figure 10-12. CBS-QB3-calculated (kcal·mol^{-1}) free energy diagram for the reaction of a dimethyl amine and methyl ketene to form an enol at 298 K (25 °C).

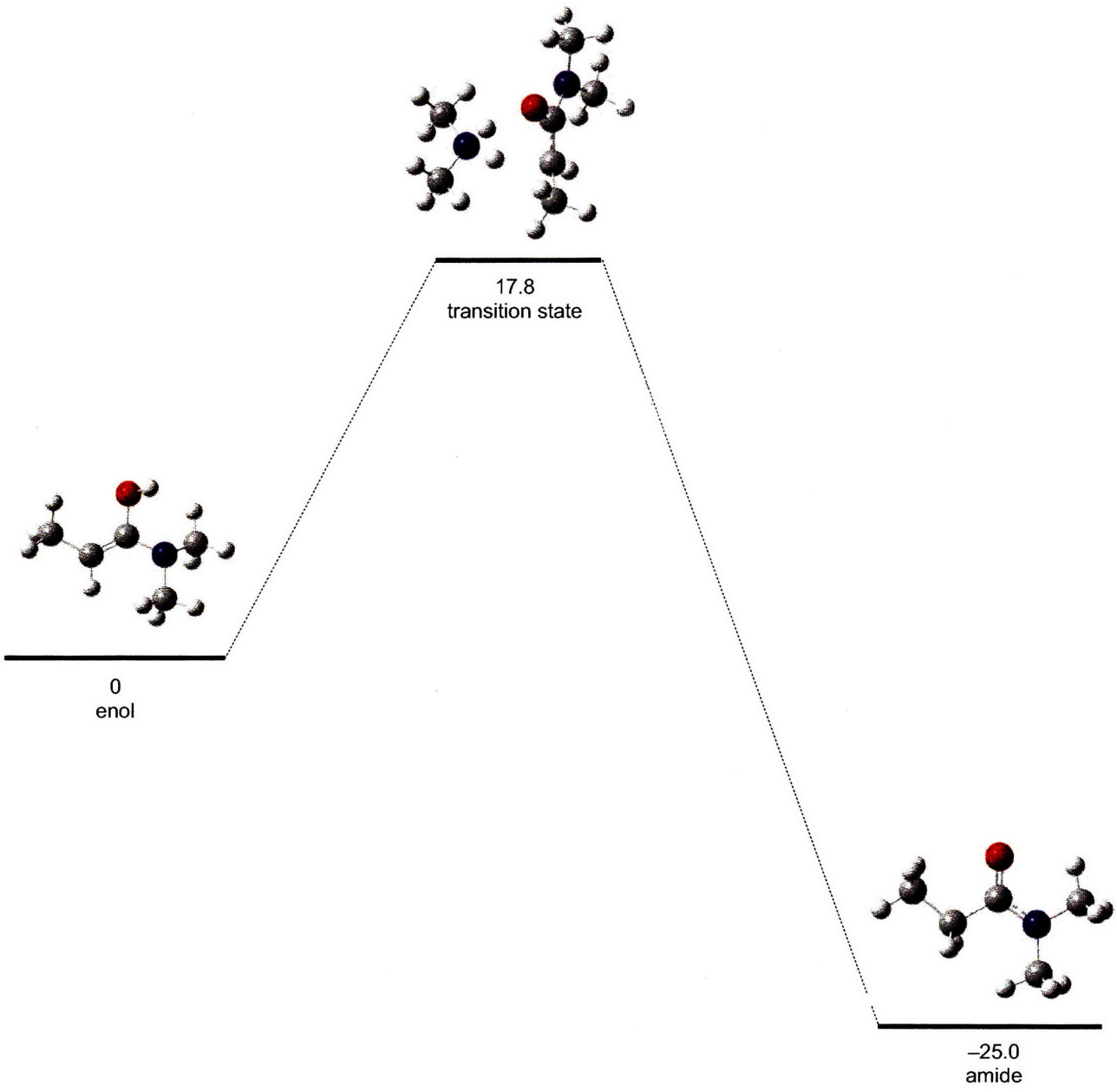

Figure 10-13. CBS-QB3-calculated (kcal·mol^{-1}) free energy diagram for the amine-assisted conversion of an enol to an amide 298 K (25 °C).

Putting the entire reaction system together, we found essentially what we have observed experimentally; the reaction proceeds to afford amide at 403 K (130 °C) nearly quantitatively and within a time-frame of 24 hr (see **Figure 10-14**). The thermolysis of alkynyl ether is the rate limiting step. Enol and amide formation steps appear significantly faster than competitive cycloaddition pathways. The complexation of the amine with carbon dioxide at early time does not seem to inhibit amide formation, suggesting that the equilibrium is shifted far enough to 'free' amine and/or that byproduct-formation rates are small in comparison to enol and amide formation. Lastly, carbamic acid formation appears to be negligible and does not interfere with the reaction at these conditions.

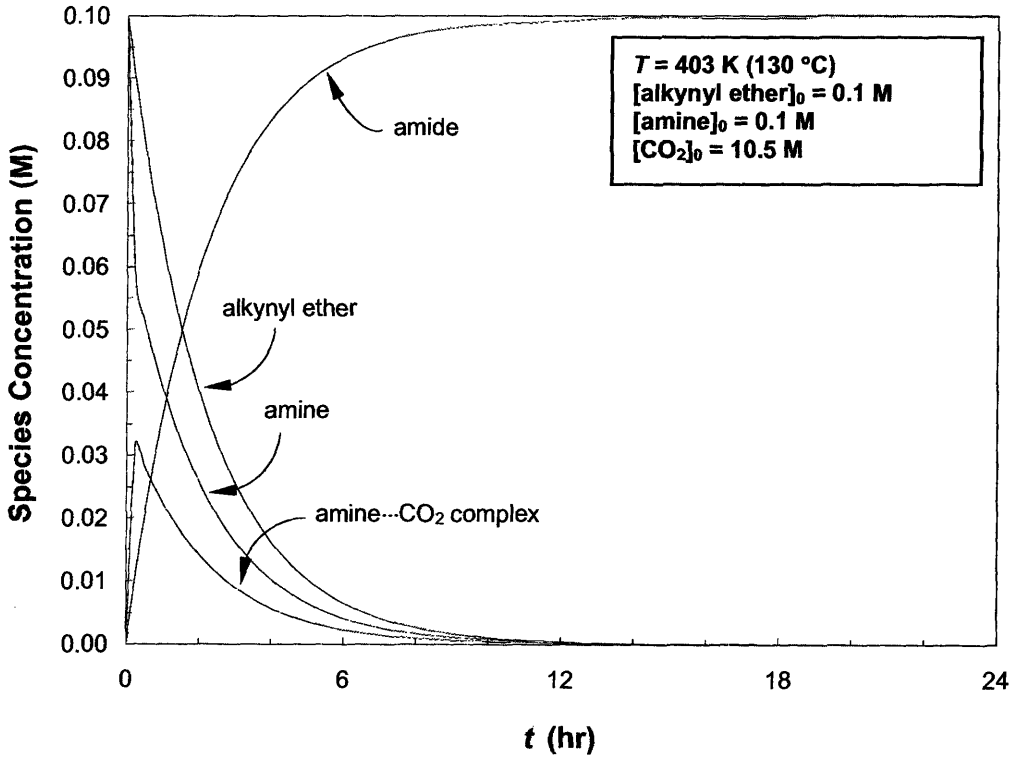

Figure 10-14. Predicted species concentration profiles for the reaction of ethylallylamine with the ketene formed *in situ* from the thermolysis of 1-ethoxy-hept-1-yne in carbon dioxide at 403 K (130 °C). The concentration of carbon dioxide corresponds to density of pure CO_2 at typical reaction conditions of 403 K and 250 bar.

10.5. Conclusions and Recommendations

In summary, we have systematically probed the mechanisms associated with carbamic acid and amide formation and subsequently developed an *ab initio* quantum chemical kinetic model capable of predicting the qualitative dynamics of our model reaction system. Specific highlights of this chapter include:

- The geometries and thermochemical properties of all stable species and transition state intermediates involved in carbamic acid and amide formation were determined using the CBS-QB3 and B3LYP/CBSB7 levels of computational theory. The B3LYP/CBSB7 method gave poor estimates of energy barrier estimates, with deviations becoming more pronounced with system size;

- Calculations suggested that carbamic acid formation in apolar, aprotic media such as neat CO_2 is likely to occur through an amine-assisted hydrogen transfer mechanism. Stable zwitterion intermediates could not be identified in gas-phase calculations but were identified when using a higher-dielectric continuum water solvation model.

  Energy barriers for the concerted carbamic acid formation mechanism were too large to account for experimentally-observed carbamic acid formation rates. The addition of small functional groups (e.g., methyl and ethyl) to primary amines led to a significant reduction in the energy barrier for both the concerted and amine-assisted reaction mechanisms. Conversely, sterically-demanding groups (e.g., *i*-propyl and *t*-butyl) led to higher barriers and free energy changes of reaction, which is in line with experimental observations of decreased carbamic acid formation with the addition of bulky functional groups. Calculations also indicated that the equilibrium concentration ratio of carbamic acid to free amine decreased with increasing temperature in a trend that was nearly identical to experimental observations (but off by a factor of 10). The use of a dimethyl sulfoxide continuum solvation model revealed a significant shift towards carbamic acid formation, which is also in line with experimental findings in the literature;

- The formation of ketenes from the unimolecular thermal decomposition of 1-alkynyl ethers was found to be the rate-limiting step for amide formation. Decomposition rates increased in the order *t*-butoxy- > *i*-propoxy- > ethoxy-substituted alkynyl

ethers, which is in line with both experimental and theoretical reports in the literature and also our own experimental observations. Temperature predictions for complete consumption of alkynyl ethers within a 24-hr time frame agreed well with our experimentally-observed amide formation rates;

- Calculations suggested that in the absence of amine, alkynyl ethers and ketenes readily undergo undesired cycloaddition reactions, and
- Amide formation in apolar, aprotic media such as neat CO_2 was modeled as a two-step process involving the amine-assisted formation of an enol followed by amine-assisted tautomerization to an amide. Concerted and uncatalyzed reaction barriers between amines and ketenes were found to be too large to account for experimentally-observed formation rates. Enol and amide formation rates were much faster than carbamic acid formation rates for the amines and operating conditions selected. As a result, calculations did not indicate interference from the carbon dioxide medium and was in agreement with our experimental observations for the model reaction system.

The following recommendations would lead to significant improvements on the work discussed in this chapter:

1. Refine the Kinetic Model

- Given time and computational constraints, only representative fragments of 'real' molecules were modeled at a high-level of theory. It may be possible to extend the size of the systems and enhance the accuracy of rate predictions. For example, in the enol and amide-formation steps, improvements can be made by modeling the reaction as ethylketene and ethylallylamine (instead of methylketene and dimethyl amine). Further improvement can be made by replacing the partition functions determined from fragments of the real molecule with values obtained from lower-level calculations for the entire molecule. By treating molecules as harmonic oscillators, we have also neglected the effect of hindered rotations for reactions in which there is a net loss of entropy (e.g., during carbamic acid and cycloaddition formation).

2. Include Solvent Effects

- Estimate and compare the rates of amide formation in conventional solvents (e.g. toluene) with gas-phase calculations by performing calculations in the presence of a solvent continuum model. Protic solvents may participate in amination and carbamic acid formation mechanisms by serving as hydrogen-transfer agents. For the gas-phase model, CO_2 microsolvation effects can be estimated by placing several carbon dioxide molecules in the vicinity of the transitions state and functional groups.

  Molecular dynamic simulations would offer a representative and potentially more accurate estimate of solvation effects in both conventional and carbon dioxide-based media. Running simulations at different carbon dioxide densities, for example, may reveal solvation effects that are common to many supercritical fluids.

3. Examine Lactam Formation

- Significant decreases in lactam (cyclic amide) yield and selectivity were obtained when performing the intramolecular variant of the model amide synthesis reaction. Even poorer selectivities were observed when switching the solvent from toluene to CO_2 (see **Section 9.4**). To decouple phase behavior and kinetic effects that may account for this discrepancy, compare reactions rates for aminoketene dimerization and cyclization using both toluene and CO_2 solvation models (*vide supra*).

4. Revisit Carbamic Acid Formation

- In **Chapter 9**, we found that amide selectivity decreased significantly when using benzylamine in place of *N*-butylbenzylamine. Aside from possible phase behavior effects, we postulated that this decrease could be due to interference from carbamic acid (see **Section 9.3.3**). Contrary to our experimental observations, our model predicts that the rate of carbamic acid formation for benzylamine would be *lower* than that of *N*-butylbenzylamine. Higher-level calculations on the full versions of these amines and inclusion of solvation effects may reveal that benzylamine is indeed more reactive towards CO_2.

10.6. References

Allen, A. D. and Tidwell, T. T. Amination of Ketenes: Kinetic and Mechanistic Studies. J. Org. Chem, **1999**, *64*, 266-271.

Arstad, B., Blom, R., and Swang, O. *CO_2 Absorption in Aquesous Solutions of Alanolamines: Mechanistic Insight from Quantum Chemical Calculations.* J. Phys. Chem. A, **2007**, *111*, 1222-1228.

Dijkstra, Z. J., Doornbos, A. R., Weyten H., Ernsting, J. M., Elsevier, C. J., and Keurentjes, J. T. F. *Formation of Carbamic Acid in Organic Solvents and in Supercritical Carbon Dioxide.* J. Supercrit. Fluids, **2007**, *41*, 109-114.

Fischer, H., Gyllenhaal, O., Vessman, J., and Albert, K. *Reaction Monitoring of Aliphatic Amines in Supercritical Carbon Dioxide by Proton Nuclear Magnetic Resonance Spectroscopy and Implications for Supercritical Fluid Chromatography.* Anal. Chem., **2003**, *75*, 622-626.

Gaussian 03, Revision W, Frisch, M. J.; Trucks, G. W.; Schlegel, H. B.; Scuseria, G. E.; Robb, M. A.; Cheeseman, J. R.; Montgomery, Jr., J. A.; Vreven, T.; Kudin, K. N.; Burant, J. C.; Millam, J. M.; Iyengar, S. S.; Tomasi, J.; Barone, V.; Mennucci, B.; Cossi, M.; Scalmani, G.; Rega, N.; Petersson, G. A.; Nakatsuji, H.; Hada, M.; Ehara, M.; Toyota, K.; Fukuda, R.; Hasegawa, J.; Ishida, M.; Nakajima, T.; Honda, Y.; Kitao, O.; Nakai, H.; Klene, M.; Li, X.; Knox, J. E.; Hratchian, H. P.; Cross, J. B.; Bakken, V.; Adamo, C.; Jaramillo, J.; Gomperts, R.; Stratmann, R. E.; Yazyev, O.; Austin, A. J.; Cammi, R.; Pomelli, C.; Ochterski, J. W.; Ayala, P. Y.; Morokuma, K.; Voth, G. A.; Salvador, P.; Dannenberg, J. J.; Zakrzewski, V. G.; Dapprich, S.; Daniels, A. D.; Strain, M. C.; Farkas, O.; Malick, D. K.; Rabuck, A. D.; Raghavachari, K.; Foresman, J. B.; Ortiz, J. V.; Cui, Q.; Baboul, A. G.; Clifford, S.; Cioslowski, J.; Stefanov, B. B.; Liu, G.; Liashenko, A.; Piskorz, P.; Komaromi, I.; Martin, R. L.; Fox, D. J.; Keith, T.; Al-Laham, M. A.; Peng, C. Y.; Nanayakkara, A.; Challacombe, M.; Gill, P. M. W.; Johnson, B.; Chen, W.; Wong, M. W.; Gonzalez, C.; and Pople, J. A.; Gaussian, Inc., Wallingford CT, 2004.

Hall, N. E. and Smith, B. J. *Solvation Effects on Zwitterion Formation.* J. Phys. Chem. A, **1998**, *102*, 3985-3990.

Moyano, A., Pericàs, M. A., Serratosa, F., and Valentí, E. *A Semiemperical (AM1, MNDO, and MINDO/3) Study on the Thermolysis of 1-Alkynyl Ethers. Reaction Analysis by Correlation of Localized Molecular Orbitals.* J. Org. Chem., **1987**, *52*, 5532-5538.

Raspoet, G. and Nguyen, M. T. *Amination of Ketenes: Evidence for a Mechanism Involving Enols of Amides as Intermediates.* J. Org. Chem., **1998**, *63*, 9669-9677.

Steinfeld, J. I., Francisco, J. S., and Hase, W. L. Chemical Kinetics and Dynamics. Prentice Hall: Upper Saddle River, **1999**.

Sung, K. and Tidwell, T. T. *Amination of Ketene: A Theoretical Study.* J. Am. Chem. Soc., **1998**, *120*, 3043-3048.

Tidwell, T. T. Ketenes. Second Edition. Wiley & Sons: New York, **2006**.

Tsipis, C. A. and Karipidis, P. A. *Mechanistic Insights into the Bazaroc Synthesis of Urea from NH_3 and CO_2 using Electronic Structure Calculation Methods.* J. Phys. Chem. A, **2005**, *109*, 8560-8567.

Vaidya, P. D. and Kenig, E. Y. *CO_2-Alkanolamine Reaction Kinetics: A Review of Recent Studies. Chem. Eng. Technol.*, **2007**, *30*, 1467-1474.

10.7. Model Formulation and Kinetic Parameters

Reaction Networks

The reaction network associated with amide formation in $scCO_2$ is summarized below:

$$\text{alkyne} \xrightarrow{k_1} \text{ketene} \qquad \textbf{(R-1)}$$

$$\text{ketene} + \text{ketene} \xrightarrow{k_2} \text{cyclobutanedione} \qquad \textbf{(R-2)}$$

$$\text{ketene} + \text{alkyne} \xrightarrow{k_3} \text{cyclobutenone} \qquad \textbf{(R-3)}$$

$$\text{amine} + \text{amine} \underset{k_{-4}}{\overset{k_4}{\rightleftharpoons}} \text{amine}\cdots\text{amine} \qquad \textbf{(R-4)}$$

$$\text{amine}\cdots\text{amine} + \text{ketene} \underset{k_{-5}}{\overset{k_5}{\rightleftharpoons}} \text{enol} + \text{amine} \qquad \textbf{(R-5)}$$

$$\text{enol} + \text{amine} \xrightarrow{k_6} \text{amide} + \text{amine} \qquad \textbf{(R-6)}$$

$$\text{amine} + CO_2 \underset{k_{-7}}{\overset{k_7}{\rightleftharpoons}} \text{amine}\cdots CO_2 \qquad \textbf{(R-7)}$$

$$\text{amine}\cdots CO_2 + \text{amine} \underset{k_{-8}}{\overset{k_8}{\rightleftharpoons}} \text{carbamic acid} + \text{amine} \qquad \textbf{(R-8)}$$

Mass balances for each species are delineated below and were solved using the ode15s routine in Matlab®:

$$r_{\text{alkyne}} = \frac{d[\text{alkyne}]}{dt} = -k_1[\text{alkyne}] - k_4[\text{alkyne}][\text{ketene}]$$

$$r_{\text{ketene}} = \frac{d[\text{ketene}]}{dt} = k_1[\text{alkyne}] - 2(k_2 + k_3)[\text{ketene}]^2 - k_4[\text{ketene}][\text{alkyne}]$$

$$-k_6[\text{ketene}][\text{amine}\cdots\text{amine}] + k_{-6}[\text{enol}][\text{amine}]$$

$$r_{\text{cyclobutanedione}} = \frac{d[\text{cyclobutanedione}]}{dt} = k_2[\text{ketene}]^2$$

$$r_{\text{cyclobutenone}} = \frac{d[\text{cyclobutenone}]}{dt} = k_3[\text{ketene}][\text{alkyne}]$$

$$r_{\text{amine}} = \frac{d[\text{amine}]}{dt} = -2k_4[\text{amine}]^2 + 2k_{-4}[\text{amine}\cdots\text{amine}] + k_5[\text{amine}\cdots\text{amine}][\text{ketene}]$$
$$-k_{-5}[\text{enol}][\text{amine}] - k_7[\text{amine}][CO_2] + k_{-7}[\text{amine}\cdots CO_2]$$

$$r_{\text{amine}\cdots\text{amine}} = \frac{d[\text{amine}\cdots\text{amine}]}{dt} = k_4[\text{amine}]^2 - k_{-4}[\text{amine}\cdots\text{amine}]$$
$$-k_5[\text{amine}\cdots\text{amine}][\text{ketene}] + k_{-5}[\text{enol}][\text{amine}]$$

$$r_{\text{enol}} = \frac{d[\text{enol}]}{dt} = k_5[\text{ketene}][\text{amine}\cdots\text{amine}] - k_{-5}[\text{enol}][\text{amine}] - k_6[\text{enol}][\text{amine}]$$

$$r_{\text{amide}} = \frac{d[\text{amide}]}{dt} = k_6[\text{enol}][\text{amine}]$$

$$r_{\text{amine}\cdots CO_2} = \frac{d[\text{amine}\cdots CO_2]}{dt} = k_7[\text{amine}][CO_2] - k_{-7}[\text{amine}\cdots CO_2]$$
$$-k_8[\text{amine}][\text{amine}\cdots CO_2] + k_{-8}[\text{carbamic acid}][\text{amine}]$$

$$r_{\text{carbamic acid}} = \frac{d[\text{carbamic acid}]}{dt} = k_8[\text{amine}][\text{amine}\cdots CO_2] - k_{-8}[\text{carbamic acid}][\text{amine}]$$

Table 10-8. CBS-QB3-calculated thermochemical properties, Arrhenius parameters, and rate constants for the amide synthesis reaction in carbon dioxide.

Reaction	ΔE_0	$\Delta G^{0,TS}$ [a]	ΔG^0_{rxn} [a]	ΔH^0_{rxn} [a]	E_a	A	k (298 K)	k (403 K)
	kcal·mol^{-1}						$M^{-1}\cdot s^{-1}$ [b]	
1 [c]	31.0	31.7	–22.8	–12.5	31.0	7.86E+12	1.54E–10	1.26E–04
1 [d]	30.8	31.3	–21.6	–10.5	31.0	2.60E+13	5.32E–10	4.29E–04
1 [e]	30.7	29.6	–21.0	–9.3	31.7	2.20E+15	1.33E–08	1.47E–02
2 [f]	14.9	27.2	–15.0	–28.5	15.6	4.78E+05	1.92E–06	1.76E–03
3 [g]	15.4	28.6	–40.0	–55.1	16.0	9.35E+04	1.77E–07	1.97E–04
4 [h]	—	—	4.3	–2.8	—	—	—	—
5 [i]	–7.9	8.2	–9.1	–15.1	–8.8	1.02E+02	2.92E+08	6.03E+06
			reverse rate		6.4	3.34E+06	6.42E+01	1.07E+03
6 [j]	6.7	18.0	–24.99	–23.72	7.7	4.96E+06	1.10E+01	3.23E+02
7 [k]	—	—	3.0	–3.4	—	—	—	—
8 [k]	6.6	22.7	5.5	–5.1	10.8	2.58E+10	3.61E+02	2.70E+04
			reverse rate		12.5	3.84E+13	3.73E+04	6.06E+06

[a] at 298 K (25 °C); [b] units of s^{-1} for Reaction 1; [c] modeled as 1-ethoxy-hept-1-yne (see entry 4 of **Table 10-6**); [d] modeled as 1-*i*-propoxy-prop-1-yne (see entry 6 of **Table 10-6**); [e] modeled as 1-*t*-butoxy-prop-1-yne (see entry 7 of **Table 10-6**); [f] modeled as methylketene; [g] modeled as methylketene and 1-ethoxy-prop-1-yne; [h] modeled as dimethylamine; [i] modeled as dimethyl amine and methylketene; [j] modeled as dimethyl amine and the enol of reaction 5; [k] modeled as ethylallylamine.